

Magnetism: Molecules to Materials IV. Edited by Joel S. Miller and Marc Drillon
Copyright © 2002 Wiley-VCH Verlag GmbH & Co. KGaA
ISBNs: 3-527-30429-0 (Hardback); 3-527-60069-8 (Electronic)

Magnetism: Molecules to Materials IV

Edited by J. S. Miller and M. Drillon

 **WILEY-VCH**

Magnetism: Molecules to Materials IV. Edited by Joel S. Miller and Marc Drillon
Copyright © 2002 Wiley-VCH Verlag GmbH & Co. KGaA
ISBNs: 3-527-30429-0 (Hardback); 3-527-60069-8 (Electronic)

Further Titles of Interest

J. S. Miller and M. Drillon (Eds.)
Magnetism: Molecules to Materials
Models and Experiments
2001. XVI, 437 pages
Hardcover. ISBN: 3-527-29772-3

J. S. Miller and M. Drillon (Eds.)
Magnetism: Molecules to Materials II
Molecule-Based Materials
2001. XIV, 489 pages
Hardcover. ISBN: 3-527-30301-4

J. H. Fendler (Ed.)
Nanoparticles and Nanostructured Films
1998. XX, 468 pages
Hardcover. ISBN: 3-527-29443-0

P. Braunstein, L. A. Oro, and P. R. Raithby (Eds.)
Metal Clusters in Chemistry
1999. XLVIII, 1798 pages
ISBN: 3-527-29549-6

Magnetism: Molecules to Materials IV. Edited by Joel S. Miller and Marc Drillon
Copyright © 2002 Wiley-VCH Verlag GmbH & Co. KGaA
ISBNs: 3-527-30429-0 (Hardback); 3-527-60069-8 (Electronic)

Magnetism: Molecules to Materials IV

Nanosized Magnetic Materials

Edited by
Joel S. Miller and Marc Drillon

 **WILEY-VCH**

Magnetism: Molecules to Materials IV. Edited by Joel S. Miller and Marc Drillon
Copyright © 2002 Wiley-VCH Verlag GmbH & Co. KGaA
ISBNs: 3-527-30429-0 (Hardback); 3-527-60069-8 (Electronic)

Prof. Dr. Joel S. Miller
University of Utah
315 S. 1400 E. RM Dock
Salt Lake City
UT 84112-0850
USA

Prof. Dr. Marc Drillon
CNRS
Inst. de Physique et Chimie
des Matériaux de Strasbourg
23 Rue du Loess
67037 Strasbourg Cedex
France

This book was carefully produced. Nevertheless, editors, authors and publisher do not warrant the information contained therein to be free of errors. Readers are advised to keep in mind that statements, data, illustrations, procedural details or other items may inadvertently be inaccurate.

Library of Congress Card No.: applied for

A catalogue record for this book is available from the British Library.

Die Deutsche Bibliothek - CIP Cataloguing-in-Publication-Data

A catalogue record for this publication is available from Die Deutsche Bibliothek

ISBN 3-527-30429-0

© WILEY-VCH Verlag GmbH, Weinheim (Federal Republic of Germany). 2002

Printed on acid-free paper.

All rights reserved (including those of translation in other languages). No part of this book may be reproduced in any form - by photoprinting, microfilm, or any other means - nor transmitted or translated into machine language without written permission from the publishers. Registered names, trademarks, etc. used in this book, even when not specifically marked as such, are not to be considered unprotected by law.

Composition: EDV-Beratung Frank Herweg, Leutershausen. Printing: betz-druck GmbH,
Darmstadt. Bookbinding: Wilh. Osswald + Co. KG, Neustadt
Printed in the Federal Republic of Germany.

Preface

The development, characterization, and technological exploitation of new materials, particularly as components in 'smart' systems, are key challenges for chemistry and physics in the next millennium. New substances and composites including nanostructured materials are envisioned for innumerable areas including magnets for the communication and information sector of our economy. Magnets are already an important component of the economy with worldwide sales of approximately \$30 billion, twice that of the sales of semiconductors. Hence, research groups worldwide are targeting the preparation and study of new magnets especially in combination with other technologically important properties, e. g., electrical and optical properties.

In the past few years our understanding of magnetic materials, thought to be mature, has enjoyed a renaissance as it is being expanded by contributions from many diverse areas of science and engineering. These include (i) the discovery of bulk ferro- and ferrimagnets based on organic/molecular components with critical temperature exceeding room temperature, (ii) the discovery that clusters in high, but not necessarily the highest, spin states due to a large magnetic anisotropy or zero field splitting have a significant relaxation barrier that traps magnetic flux enabling a single molecule/ion (cluster) to act as a magnet at low temperature; (iii) the discovery of materials exhibiting large, negative magnetization; (iv) spin-crossover materials that can show large hysteretic effects above room temperature; (v) photomagnetic and (vi) electrochemical modulation of the magnetic behavior; (vii) the Haldane conjecture and its experimental realization; (viii) quantum tunneling of magnetization in high spin organic molecules; (viii) giant and (ix) colossal magnetoresistance effects observed for 3-D network solids; (x) the realization of nanosize materials, such as self organized metal-based clusters, dots and wires; (xi) the development of metallic multilayers and the spin electronics for the applications. This important contribution to magnetism and more importantly to science in general will lead us into the next millennium.

Documentation of the status of research, ever since William Gilbert's *de Magnete* in 1600, provides the foundation for future discoveries to thrive. As one millennium ends and another beacons the time is appropriate to pool our growing knowledge and assess many aspects of magnetism. This series entitled *Magnetism: Molecules to Materials* provides a forum for comprehensive yet critical reviews on many aspects of magnetism that are on the forefront of science today.

Joel S. Miller
Salt Lake City, USA

Marc Drillon
Strasbourg, France

Contents

Preface	V
List of Contributors	XV
1 Bimetallic Magnets: Present and Perspectives	1
1.1 Introduction	1
1.2 Bimetallic Magnetic Materials Derived from Oxamato-based Complexes	2
1.2.1 Dimensionality and Magnetic Properties	2
1.2.2 Modulation of the Magnetic Properties	17
1.2.3 Dimensionality Modulation by a Dehydration-Polymerization Process	20
1.2.4 Alternative Techniques for the Studies of Exchange-coupled Systems	26
1.3 Bimetallic Magnets Based on Second- and Third-row Transition Metal Ions	28
1.3.1 Examples of Ru(III)-based Compounds	28
1.3.2 Mo, Nb, and W-cyanometalate-based Magnets	31
1.3.3 Light-induced Magnetism	36
1.4 Concluding Remarks	37
References	38
2 Copper(II) Nitroxide Molecular Spin-transition Complexes	41
2.1 Introduction	41
2.2 Nitroxide Free Radicals as Building Blocks for Metal-containing Magnetic Species	42
2.2.1 Electronic Structure	43
2.2.2 Coordination Properties	43
2.3 Molecular Spin Transition Species	46
2.3.1 Discrete Species	46
2.3.2 One-dimensional Species	50
2.4 Conclusion	61
References	62
3 Theoretical Study of the Electronic Structure of and Magnetic Interactions in Purely Organic Nitronyl Nitroxide Crystals	65
3.1 Introduction	65
3.2 Electronic Structure of Nitronyl Nitroxide Radicals	68

VIII Contents

3.2.1	Fundamentals	68
3.2.2	<i>Ab-initio</i> Computation of the Electronic Structure of Nitronyl Nitroxide Radicals	73
3.2.3	Spin Distribution in Nitronyl Nitroxide Radicals	78
3.3	Magnetic Interactions in Purely Organic Molecular Crystals	88
3.3.1	Basics of the Magnetism in Purely Organic Molecular Crystals	88
3.3.2	The McConnell-I Mechanism: A Rigorous Theoretical Analysis	90
3.3.3	Theoretical Analysis of Through-space Intermolecular Interactions	94
3.3.4	Experimental Magneto-structural Correlations	102
3.3.5	Theoretical Magneto-structural Correlations	105
	References	113
4	Exact and Approximate Theoretical Techniques for Quantum Magnetism in Low Dimensions	119
4.1	Introduction	119
4.2	Exact Calculations	121
4.3	Applications to Spin Clusters	125
4.4	Field Theoretic Studies of Spin Chains	129
4.4.1	Nonlinear σ -model	130
4.4.2	Bosonization	133
4.5	Density Matrix Renormalization Group Method	137
4.5.1	Implementation of the DMRG Method	139
4.5.2	Finite Size DMRG Algorithm	140
4.5.3	Calculation of Properties in the DMRG Basis	142
4.5.4	Remarks on the Applications of DMRG	142
4.6	Frustrated and Dimerized Spin Chains	144
4.7	Alternating (S_1, S_2) Ferrimagnetic Spin Chains	148
4.7.1	Ground State and Excitation Spectrum	149
4.7.2	Low-temperature Thermodynamic Properties	155
4.8	Magnetization Properties of a Spin Ladder	160
	References	168
5	Magnetic Properties of Self-assembled $[2 \times 2]$ and $[3 \times 3]$ Grids	173
5.1	Introduction	173
5.2	Polytopic Ligands and Grid Complexes	174
5.2.1	$[2 \times 2]$ Ligands	175
5.2.2	Representative $[2 \times 2]$ Complexes	176
5.2.3	$[3 \times 3]$ Ligands and their Complexes	187
5.3	Magnetic Properties of Grid Complexes	189
5.3.1	$[2 \times 2]$ Complexes	189
5.3.2	$[3 \times 3]$ Complexes	191
5.3.3	Magnetic Properties of $[2 \times 2]$ and $[3 \times 3]$ Grids	192

5.3.4	Potential Applications of Magnetic Grids to Nanoscale Technology	201
	References	202
6	Biogenic Magnets	205
6.1	Introduction	205
6.1.1	Magnetotactic Bacteria	205
6.1.2	Magnetosomes	206
6.1.3	Magnetite Magnetosomes	207
6.1.4	Greigite Magnetosomes	208
6.2	Magnetic Properties of Magnetosomes	209
6.2.1	Magnetic Microstates and Crystal Size	209
6.2.2	Single-domain (SD) and Multi-domain (MD) States	211
6.2.3	Superparamagnetic (SPM) State	211
6.2.4	Theoretical Domain Calculations: Butler–Banerjee Model	213
6.2.5	Local Energy Minima and Metastable SD States: Micromagnetic Models	214
6.2.6	Magnetic Anisotropy of Magnetosomes	215
6.2.7	Magnetosome Chains	217
6.2.8	Magnetic Properties of Magnetosomes at Ambient Temperatures	217
6.2.9	Low-temperature (<300 K) Magnetic Properties	218
6.2.10	Magnetosomes and Micromagnetism	220
6.2.11	Magnetosome Magnetization from Electron Holography	220
6.3	Mechanism of Bacterial Magnetotaxis	223
6.3.1	Passive Orientation by the Geomagnetic Field	223
6.3.2	Magneto-aerotaxis	225
6.4	Conclusion	227
	References	228
7	Magnetic Ordering due to Dipolar Interaction in Low Dimensional Materials	233
7.1	Introduction	233
7.2	Magnetic Ordering in Pure Dipole Systems	234
7.2.1	The Dipole–Dipole Interaction – A Well Known Hamiltonian?	234
7.2.2	Ordering Temperature – The Mean-field Approach	235
7.2.3	Dipolar Ordering in 3D Systems	238
7.2.4	Dipolar Ordering in 2D Systems	243
7.3	Strongly Correlated Extended Objects	246
7.3.1	Stacking of Magnetic Planes	246
7.3.2	3D of 1D – Bunching of Wires or Chains	248
7.3.3	2D of 1D – Planar Arrays of Magnetic Wires	250
7.3.4	2D of 0D – Planar Arrays of Magnetic Dots	252
7.3.5	1D of 0D – Lines of Magnetic Dots	254
7.4	Weakly Correlated Extended Systems	255

7.4.1	Low Dimensional Molecular-based Magnets	255
7.4.2	3D Ordering Due to Dipolar Interaction – A Model	261
7.5	Conclusion	265
	References	266
8	Spin Transition Phenomena	271
8.1	Introduction	271
8.2	Physical Characterization	272
8.2.1	Occurrence of Thermal Spin Transition	272
8.2.2	Magnetic Susceptibility Measurements	274
8.2.3	Optical Spectroscopy	275
8.2.4	Vibrational Spectroscopy	276
8.2.5	⁵⁷ Fe Mössbauer Spectroscopy	277
8.2.6	Calorimetry	279
8.2.7	Diffraction Methods	280
8.2.8	X-ray Absorption Spectroscopy	281
8.2.9	Positron-annihilation Spectroscopy	282
8.2.10	Nuclear Resonant Scattering of Synchrotron Radiation	283
8.2.11	Magnetic Resonance Studies (NMR, EPR)	284
8.3	Highlights of Past Research	285
8.3.1	Chemical Influence on Spin-crossover Behavior	285
8.3.2	Structural Insights	289
8.3.3	Influence of Crystal Quality	291
8.3.4	Theoretical Approaches to Spin Transition Phenomena	292
8.3.5	Influence of a Magnetic Field	299
8.3.6	Two-step Spin Transition	299
8.3.7	LIESST Experiments	306
8.3.8	Formation of Correlations During HS → LS relaxation	309
8.3.9	Nuclear Decay-induced Spin Crossover	313
8.4	New Trends in Spin Crossover Research	320
8.4.1	New Types of Spin Crossover Material	320
8.4.2	New Effects and Phenomena	326
	References	334
9	Interpretation and Calculation of Spin-Hamiltonian Parameters in Transition Metal Complexes	345
9.1	Introduction	345
9.2	The Spin-Hamiltonian	347
9.2.1	The SH	347
9.2.2	Eigenstates of the SH	348
9.2.3	Matrix Elements of the SH	349
9.2.4	Comments	352
9.3	The Physical Origin of Spin-Hamiltonian Parameters	352
9.3.1	Many-electron Wavefunctions and the Zeroth-order Hamiltonian	352
9.3.2	Perturbing Operators for Magnetic Interactions	355
9.3.3	Theory of Effective Hamiltonians	361

9.3.4	Equations for Spin-Hamiltonian Parameters	363
9.3.5	Formulation in Terms of Molecular Orbitals	371
9.4	Ligand Field and Covalency Effects on SH Parameters	380
9.4.1	Molecular Orbitals for Inorganic Complexes	380
9.4.2	Ligand Field Energies	381
9.4.3	Matrix Elements over Molecular Orbitals	385
9.4.4	“Central Field” versus “Symmetry Restricted” Covalency	392
9.4.5	Ligand-field Theory of Zero-field Splittings	395
9.4.6	Ligand-field Theory of the g-Tensor	396
9.4.7	Ligand-field Theory of Hyperfine Couplings	397
9.4.8	Table of Hyperfine Parameters	399
9.4.9	Examples of Ligand-field Expressions for Spin Hamiltonian Parameters	401
9.5	Case Studies of SH Parameters	414
9.5.1	CuCl_4^{2-} and the Blue Active Site: g and A^M Values	415
9.5.2	FeCl_4^- and the $\text{Fe}(\text{SR})_4^-$ Active Site: Zero-field Splitting (ZFS)	420
9.6	Computational Approaches to SH Parameters	423
9.6.1	Hartree–Fock Theory	424
9.6.2	Configuration Interaction	426
9.6.3	Density Functional Theory	427
9.6.4	Coupled-perturbed SCF Theory	428
9.6.5	Relativistic Methods	432
9.6.6	Calculation of Zero-field Splittings	433
9.6.7	Calculation of g-Values	435
9.6.8	Calculation of Hyperfine Couplings	444
9.7	Concluding Remarks	455
9.8	Appendix: Calculation of Spin–Orbit Coupling Matrix Elements	456
	References	458
10	Chemical Reactions in Applied Magnetic Fields	467
10.1	Introduction	467
10.2	Gas-phase Reactions	467
10.2.1	Gaseous Combustion	467
10.2.2	Carbon Nanotube and Fullerene Synthesis	468
10.2.3	Liquid-phase Reactions	470
10.2.4	Asymmetric Synthesis	470
10.2.5	Electrodeposition	471
10.3	Solid-phase Reactions	472
10.3.1	Self-propagating High-temperature Synthesis (SHS)	472
10.3.2	SHS Reactions in High Fields (1 to 20 T)	475
10.3.3	Time-resolved X-ray Diffraction Studies	476
10.3.4	Possible Field-dependent Reaction Mechanisms	479
10.4	Conclusions	479
	References	480
	Index	483

Magnetism: Molecules to Materials IV. Edited by Joel S. Miller and Marc Drillon
Copyright © 2002 Wiley-VCH Verlag GmbH & Co. KGaA
ISBNs: 3-527-30429-0 (Hardback); 3-527-60069-8 (Electronic)

List of Contributors

Prof. Richard B. Frankel
Physics Department
California Polytechnic State University
San Luis Obispo, CA 93407
USA

Prof. Bruce M. Moskowitz
Department of Geology and Geophysics
University of Minnesota
310 Pillsbury Drive SE
Minneapolis, MN 55455
USA

Yann Garcia, Hartmut Spiering,
Prof. Philipp Gütllich
Institute of Inorganic Chemistry
and Analytical Chemistry
Johannes Gutenberg University
Staudingerweg 9
55099 Mainz
Germany

Prof. Juan J. Novoa, Pilar Lafuente,
Prof. Mercè Deumal
Departament de Química Física,
Facultat de Química, and
CER de Química Teòrica,
Universitat de Barcelona,
Av. Diagonal 647
08028-Barcelona
Spain

Prof. Fernando Mota
Department of Chemistry
King's College London, Strand
London WC2R 2LS
UK

Prof. Pierre Panissod,
Prof. Marc Drillon
Institut de Physique et Chimie des
Matériaux de Strasbourg,
UMR CNRS 75040
23 rue du Loess
67037 Strasbourg
France

Dr. Quentin A. Pankhurst
Department of Physics and Astronomy
University College London
Gower Street
London WC1E 6BT
UK

Prof. Ivan P. Parkin
Department of Chemistry
University College London
20 Gordon Street
London WC1H 0AJ
UK

Dr. Paul Rey
CEA-Département de Recherche
Fondamentale sur la Matière Condensée
Service de Chimie Inorganique
et Biologique
Laboratoire de Chimie de Coordination
UMR CNRS 5046
17 rue des Martyrs
38054 Grenoble cedex 09
France

XIV List of Contributors

Prof. Victor I. Ovcharenko
Laboratory of polypsin compounds
International Tomography Center
Institutskaya 3A
630090 Novosibirsk
Russia

Dr. Frank Neese
Max-Planck-Institut für Strahlenchemie
Stiftstr. 34-36
45470 Mülheim/Ruhr
Germany

Prof. Edward I. Solomon
Stanford University
Department of Chemistry
Stanford, CA, 94305
USA

Prof. Olivier Kahn (deceased)
Prof. Corine Mathonière,
Dr. Jean-Pascal Sutter
Groupe des Sciences Moléculaires
Institut de Chimie de la Matière
Condensée de Bordeaux
CNRS
F-33608 Pessac
France

Dr. Jatinder V. Yakhmi
Technical Physics & Prototype
Engineering Division
Physics Group
Bhabha Atomic Research Center
Mumbai (Bombay) – 400 085
India

Prof. S. Ramasesha
Solid State & Structural Chemistry Unit
Indian Institute of Science
Bangalore 560 012
India

Prof. Laurence K. Thompson,
Zhiqiang Xu
Department of Chemistry
Memorial University of Newfoundland
St. John's, Newfoundland, A1B 3X7
Canada

Dr. Oliver Waldmann
Physikalisches Institut III
Universität Erlangen-Nürnberg
Erwin-Rommel-Str. 1
91058 Erlangen
Germany

1 Bimetallic Magnets: Present and Perspectives

Corine Mathonière, Jean-Pascal Sutter, and Jatinder V. Yakhmi

1.1 Introduction

An important branch of the molecular magnetism deals with molecular systems with bulk physical properties such as long-range magnetic ordering. The first molecular compounds with spontaneous magnetization below a critical temperature were reported during the eighties [1, 2]. These pioneering reports encouraged many research groups in organic, inorganic, or organometallic chemistry to initiate activity on this subject, and many new molecule-based magnets have been designed and characterized. A tentative classification can arise from the chemical nature of the magnetic units involved in these materials – organic- or metal-based systems and mixed organic–inorganic compounds. Of materials based only on magnetic metal complexes, several families such as the oxamato, oxamido, oxalato-bridged compounds and cyanide-bridged systems play an important role in the field of molecular magnetism. This contribution focuses mainly on molecule-based magnets involving oxamato and oxamido complexes. The most extensively used spin carriers are 3d transition metal ions. The magnetic interactions between these ions are now well understood and enable the rational synthesis of materials. This aspect will be highlighted in the first part of this contribution. The heavier homologs from the second and third series have been envisaged only recently for the construction of heterobimetallic materials. In the second part of this chapter we will briefly discuss the very encouraging first results obtained with such ions.

In 1995 Olivier Kahn wrote a paper reviewing the magnetism of heterobimetallic compounds [3]. An important part of this review was devoted to finite polynuclear compounds, which can be considered as models for the study of exchange interactions. Magnetic ordering is a three dimensional property, however, and the design of a molecule-based magnet requires control of the molecular architecture in the three directions of space. The results obtained in bimetallic supra-molecular materials by our group and others show different features:

- the dimensionality can be controlled by the stoichiometry of the reagents during the synthesis or by the number of solvation molecules;

¹ This chapter is dedicated to the memory of Professor Olivier Kahn who passed away suddenly on December 8, 1999. Many of the illustrative examples used in this contribution are results obtained by his group.

- in a chemical system, the magnetic properties can be modulated by the nature of metallic ions;
- these systems can be studied by alternative techniques which are complementary of the magnetic studies.

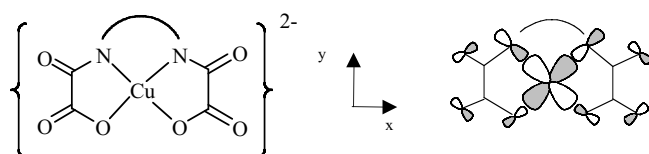
In the following text we will describe briefly the structures and magnetic properties of the compounds by emphasizing their main features. In particular, the magnetic properties will be summarized in terms of the exchange parameter J , the ordering temperature, T_C for a ferro(or ferri)magnetic material or T_N for an antiferromagnetic material, and the coercive field H_{coerc} , i. e. the magnetic field applied to cancel the permanent magnetization present in the material, which characterizes the hardness of a magnet.

1.2 Bimetallic Magnetic Materials Derived from Oxamato-based Complexes

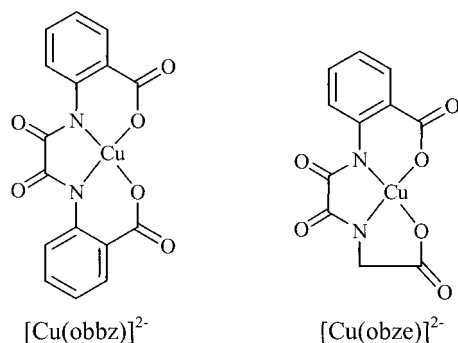
1.2.1 Dimensionality and Magnetic Properties

1.2.1.1 Cu^{II} Precursors

The general chemical strategy for the construction of bimetallic systems is based on the use of the bis-bidentate metal-complex as a complex-ligand. The bis-oxamato Cu^{II} precursors (shown in Scheme 1) and disymmetrical Cu^{II} complexes with two types of bridging units (oxamato and carboxylato) (shown in Scheme 2) have mainly been used for the preparation of extended bimetallic compounds.



Scheme 1



Scheme 2

$[\text{Cu}(\text{pba})]^{2-}$ (Table 1) was first described by Nonoyoma in 1976 [4] and at the end of the eighties it was used by Kahn and coworkers to design high-spin molecules, namely $(\text{LM})_2\text{Cu}(\text{pba})$ with $\text{M} = \text{Mn}^{\text{II}}, \text{Ni}^{\text{II}}$, L being a terminal ligand or bimetallic chains $\text{MCu}(\text{pba})$ [5, 6]. $[\text{Cu}(\text{opba})]^{2-}$ was later synthesized by Stumpf; this precursor enables the preparation of compounds with different dimensionality – high-spin molecules [7], chain and ladders compounds, honeycomb layers, and interlocked compounds (Table 1) [8].

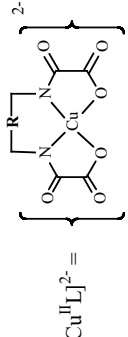
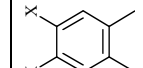
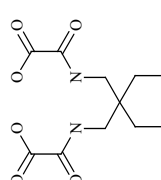
These Cu precursors were chemically modified through their ligand skeleton. The pba and opba ligands have been modified in two directions (Table 1):

- in the bridging moiety, by substituting the O (R_1 and R_2) atoms by N atoms, to increase the overlap of magnetic orbitals, because of the more pronounced diffuse character of the 2p(N) orbitals (next section);
- around the bridging moiety, by changing the nature of the R unit to modify the crystal packing of the molecules.

1.2.1.2 Mechanisms of Exchange Coupling

In the bimetallic systems obtained from reaction of Cu^{II} compounds with other transition metal ions, M, the magnetic ordering is ferrimagnetic. This means that exchange interactions between Cu and M ($S_{\text{Cu}} \neq S_{\text{M}}$ with S referring to the spin state of the metal) in the systems are a result of overlap between magnetic orbitals. If M has no orbital contribution (magnetically isotropic ion), the mechanism of the dominant $\text{Cu}^{\text{II}}\text{-M}$ interactions through an oxamato (or oxamido)-bridge is well understood. In fact, both the planar structure of the Cu^{II} complex and the four peripheral oxygen atoms give to the compound its efficient mediating character in terms of magnetic connector. The Cu^{II} ion has one unpaired electron occupying a d_{xy} orbital which is delocalized toward the nearest nitrogen and oxygen atoms and also toward the external oxygen atoms (Scheme 1). This magnetic orbital may overlap strongly with magnetic orbitals of other ions linked to the Cu^{II} brick by the four external oxygen atoms. Structural investigations of several compounds in this family have shown that the distances between the two metals, $\text{Cu}^{\text{II}}\text{-M}$, is approximately 5.3 Å. Going further in the quantification of the exchange interactions, the magnetic data can be interpreted in the paramagnetic regime with a phenomenological Hamiltonian in a spin-spin coupling scheme such as $H = -J\mathbf{S}_{\text{Cu}} \cdot \mathbf{S}_{\text{M}}$, where J is the isotropic interaction parameter. For example, in $\text{Cu}^{\text{II}}\text{-Mn}^{\text{II}}$ pairs, J has been found to be approximately -30 cm^{-1} . On the basis of experimental studies (magnetism and neutron diffraction) and theoretical investigations (DFT calculations), the dominant mechanism is spin delocalization from the Cu^{II} ion towards the planar skeleton of the N(O)-C-O bridging part of the ligand. A similar situation occurs for the $\text{Cu}^{\text{II}}\text{-Ni}^{\text{II}}$ pair, with additional Ni^{II} local anisotropy treated with the phenomenological zero-field splitting. The resulting J is higher, and has been estimated at $J = -100 \text{ cm}^{-1}$. For other couples, for instance $\text{Cu}^{\text{II}}\text{-Co}^{\text{II}}$, $\text{Cu}^{\text{II}}\text{-Fe}^{\text{II}}$, and $\text{Cu}^{\text{II}}\text{-Ln}^{\text{III}}$, the orbital contribution renders the interpretation of magnetic data using the simple scheme described above extremely difficult. For these species only qualitative interpretation of magnetic data has been achieved in order to determine the nature of exchange interactions between Cu^{II} and the other ion.

Table 1. Bis-oxamato Cu^{II} building blocks and resulting bimetallic compounds (M stands for magnet and m for metamagnet).

$[\text{Cu}^{\text{II}}\text{L}]^{2-} = \left\{ \begin{array}{c} \text{R} \\ \text{N} \quad \text{N} \\ \text{O} \quad \text{O} \\ \text{O} \quad \text{O} \\ \text{Cu} \end{array} \right\}^{2-}$		Bimetallic compound					
Ligand skeleton (R)	R_1 and R_2	Ligand abbreviation	Cluster	Chain	Ladder	Plane	Interlocked planes
	Y = OH	O	pbaOH	✓ (M)			
	Y = H	O	pba	✓ (m)			
	X = H	O	opba	✓	✓ (m)	✓ (M)	✓ (M)
	O and NMe		Meopba			✓ (M)	
	NMe		Me ₂ opba			✓ (M)	
	N-(CH ₂) _n -C ₆ H ₅		PhMe ₂ opbox			✓ (M)	
	n = 1, 3, 4		PhPr ₂ opbox			✓ (M)	
		PhBu ₂ opbox			✓ (M)		
X = Cl	O	opbaCl ₂	✓				
		O	bis-pba	✓			

1.2.1.3 Discrete Molecules

One of the first high-spin molecules was prepared in 1988. By using $[\text{Cu}(\text{pba})]^{2-}$ as the core and $[\text{Mn}(\text{Me}_6\text{-[14]ane-N}_4)]^{2+}$ as a peripheral complex it is possible to obtain a trinuclear linear CuMn_2 species [5]. No single crystal was obtained, and a structure in agreement with the magnetic properties was proposed. The compound has ferrimagnetic behavior with an irregular spin state structure resulting from the antiferromagnetic interaction between the peripheral Mn ions ($S_{\text{Mn}} = 5/2$) and the middle Cu ion ($S_{\text{Cu}} = 1/2$). The low-temperature magnetic behavior is characteristic of a high-spin ground state equal to $S = 9/2$. Efforts were later made to obtain structural information for such species [9]. Let us mention the result of Liao's group. They succeeded in isolating crystals of binuclear and trinuclear compounds with the Ni^{II} ion ($S_{\text{Ni}} = 1$) [7]. The compounds are obtained by reaction of CuL^{2-} ($\text{L} = \text{pba}, \text{pbaOH}$ and opba) with NiL^{2+} , L being tetraamine ligands, the final compounds having formula $(\text{L Ni})\text{CuL}$ or $(\text{L Ni})_2\text{CuL}^{2+}$ (the trinuclear species is shown in Fig. 1). The compounds have been magnetically characterized, and have the expected ferrimagnetic behavior with an $S = 3/2$ ground state with a zero-field splitting.

An other interesting example has been described by Ouahab and Kahn with the opbaCl_2 ligand (Table 1) and its Cu^{II} complex [10]. The reaction of the Cu^{II} precursor with ethylenediamine, en, and Mn^{II} in the solvent DMSO led to an unprecedented trinuclear species $\text{Mn}^{\text{III}}\text{Cu}^{\text{II}}\text{Mn}^{\text{III}}$. The structure of this species has been resolved (Fig. 2), and reveals that:

- the Mn^{III} has replaced the Cu^{II} in the cavity N_2O_2 of the opbaCl_2 ligand;
- the formation of the $[\text{Cu}(\text{en})_2]^{2+}$ complex, because of the strong affinity of the en for the Cu^{II} ; and, finally,
- the self-assembling process between the anionic $[\text{Mn}(\text{opbaCl}_2)]^-$ and the cationic $[\text{Cu}(\text{en})_2]^{2+}$ complexes.

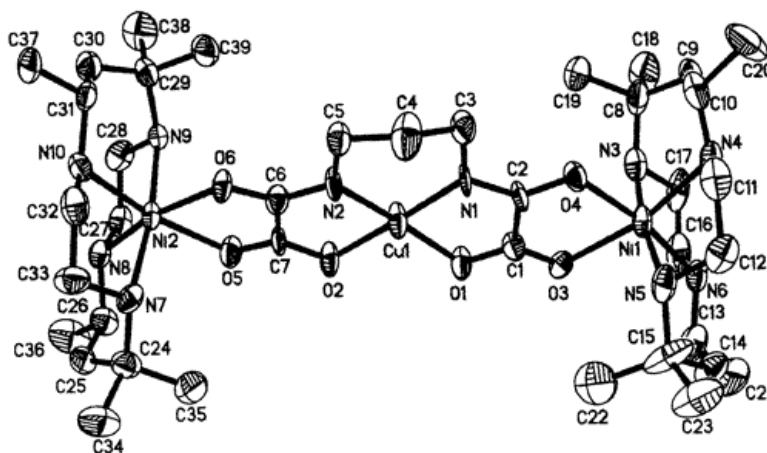


Fig. 1. Structure of the trinuclear cation $[\text{Ni}(\text{cth})_2\text{Cu}(\text{pba})]^{2+}$ [7] (reproduced with permission; Copyright 2001, the American Chemistry Society).

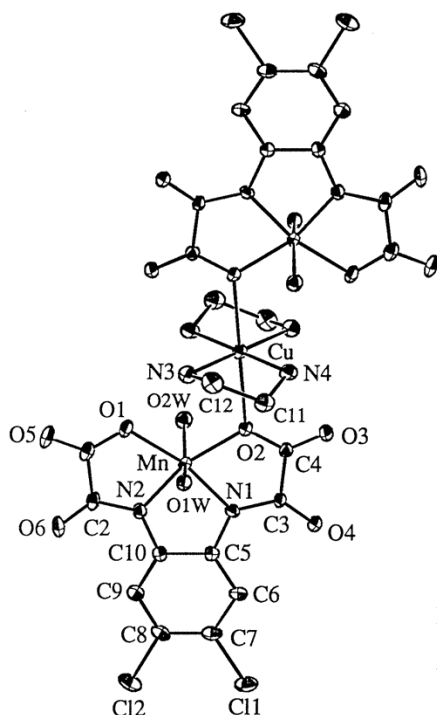
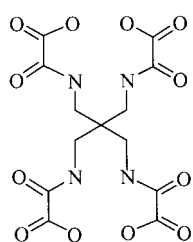


Fig. 2. Structure of the trinuclear species $\text{Cu}(\text{en})_2\text{Mn}(\text{Cl}_2\text{opba})(\text{H}_2\text{O})_2$ [10] (reproduced with permission; Copyright 2001, the American Chemistry Society).

The linkage between the two complexes is realized through apical Cu–O bonds of length 2.454 Å. The delocalization of the spin density of the Cu^{II} towards the oxygen atoms in the apical position has been postulated to be negligibly small, and the magnetic data have been interpreted in terms of zero-field splitting of the Mn^{III} ion.

More recently, Journaux et al. obtained an interesting dinuclear $\text{Na}_4[\text{Cu}_2(\text{bis-pba})]$ species by use of the bis-tetradentate ligand denoted bis-pba (Table 1 and Scheme 3) [11]. They succeeded in isolating dinuclear $\text{Na}_4[\text{Cu}_2(\text{bis-pba})]$ species, with weak intramolecular ferromagnetic interactions between the two Cu^{II} ($J \approx 1 \text{ cm}^{-1}$). The reaction of this dinuclear compound with four equivalent external complexes such as $[\text{Ni}(\text{cyclam})]^{2+}$ (cyclam = 1,4,8,11-tetraazacyclotetradecane) in acetonitrile or with $[\text{Cu}(\text{tmen})]^{2+}$ (tmen = *N, N, N, N*-tetramethylethylenediamine) in water affords hexanuclear anionic compounds of formula $\{\text{Ni}(\text{cyclam})\}_4\text{Cu}_2(\text{bis-pba})$ and $\{\text{Cu}(\text{tmen})(\text{H}_2\text{O})\}_2\{\text{Cu}_2(\text{bis-pba})\}$, respectively [12]. The structure of the Cu_6 species is shown in Fig. 3. It is made of two symmetry-related oxamato-bridged trinuclear units connected through the central carbon. In these hexanuclear species, the interactions through the oxamato bridge were found to be equal to $J = -342 \text{ cm}^{-1}$ for Cu_6 and -82 cm^{-1} for Cu_2Ni_4 . The weak ferromagnetic coupling between the two Cu^{II} ions within the dinuclear synthon was masked by intermolecular interactions and/or local anisotropy.

[Bis-pba]⁸⁻

Scheme 3

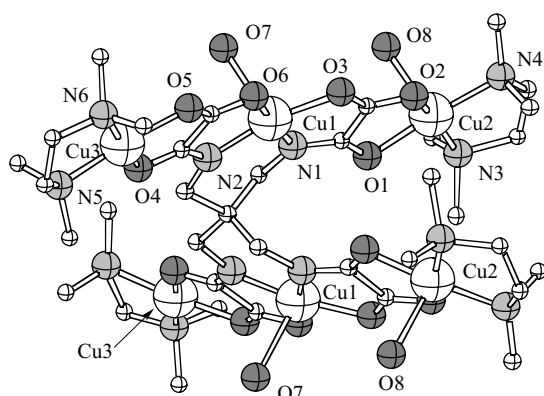


Fig. 3. Structure of the cationic hexanuclear unit $[\{\text{Cu}(\text{tmen})(\text{H}_2\text{O})\}_2\{\text{Cu}(\text{tmen})\}_2\{\text{Cu}_2(\text{bis-pba})\}]^{4+}$ [12] (reproduced with permission from Journal of Inorganic Chemistry).

1.2.1.4 One-dimensional Systems: Chain Compounds

When the dianionic Cu precursor is reacted with a 3d metal cation, M^{n+} , under stoichiometric conditions 1:1, neutral compounds of formula MCu_xS are obtained, S standing for solvent molecules. Different bimetallic chains have been structurally and magnetically described. The bimetallic chains with $\text{M} = \text{Mn}^{\text{II}}$ are described in detail in the review written in 1995 by Kahn. A typical example of a linear bimetallic chain is presented in Fig. 4. The magnetic properties of the chain compounds are well understood in the paramagnetic region (5–300 K), and are analyzed with theoretical models for ferrimagnetic one-dimensional systems, because of antiferromagnetic coupling between two different spins ($S_{\text{Mn}} = 5/2$ and $S_{\text{Cu}} = 1/2$) [13]. Below 5 K magnetic ordering occurs because of interchain interactions, which are governed by the crystal packing of the chains in the lattice. Actually, only one compound has ferromagnetic (F) ordering, with $T_{\text{C}} = 4.6$ K, namely $\text{MnCu}(\text{pbaOH})(\text{H}_2\text{O})_3$, which was the first molecule-based magnet belonging to the family described here [2]. Other compounds have antiferromagnetic (AF) ordering with T_{N} between 1.8 K and 5 K. The occurrence of F or AF magnetic ordering in these chain compounds is related to the interchain metal-metal separations of the type Mn–Cu for ferromag-

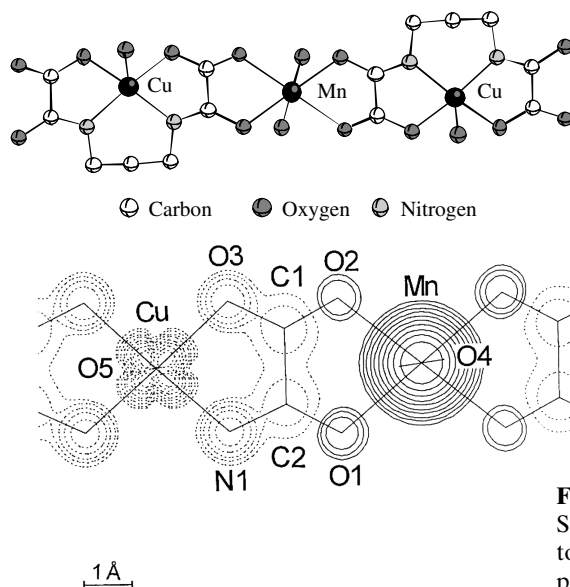


Fig. 4. MnCu(pba)(H₂O)₃ · 2H₂O (top) Structure of the chain compound (bottom) Spin density map deduced from polarized neutron diffraction data.

nets and Mn–Mn and Cu–Cu for antiferromagnets [14]. Some of these antiferromagnets behave as metamagnets, where a small applied magnetic field (between 1 or 2 kOe) can overcome the weak antiferromagnetic interchain interactions to induce a long-range ferromagnetic-like ordering. Note that for a few compounds there is no evidence of cooperative magnetic phenomena down to 1.8 K. They behave as quasi-perfect one-dimensional ferrimagnets; one example is MnCu(opba)(DMSO)₃ which has a zigzag chain structure [15].

Two interesting features of these bimetallic chain compounds can be mentioned in this section. First, the size of crystals (up to 15 mm³) of [MnCu(pba)(H₂O)₃ · 2H₂O] (Fig. 4) enabled the performance of further physical studies such as polarized neutron diffraction (p. n. d.) and optical spectroscopy (Section 1.2.4) [16, 17]. Secondly, the magnetic properties of compounds of formula [MnCu(pbaOH)] · xH₂O are strongly dependent on the water composition. Just above we mentioned the compound MnCu(pbaOH)(H₂O)₃, which behaves as a magnet at 4.6 K. It is possible to isolate another phase of this compound, MnCu(pbaOH)(H₂O)₃ · 2H₂O, which has three-dimensional antiferromagnetic ordering in zero fields with $T_N = 2.4$ K. The bimetallic chains in both compounds are identical but in the latter the hydrogen-bond network developed by the non-coordinated water molecules imposes crystal packing with short interchain Mn–Mn and Cu–Cu separations, inducing antiferromagnetic interactions between the chains. The compound also has metamagnetic behavior, because a field of 0.9 kOe is sufficient to overcome these interchain interactions giving rise to a ferromagnetic state [14]. When MnCu(pbaOH)(H₂O)₃ is heated to 130°C one water molecule bound in the apical position of the copper coordination sphere is removed, and the new compound, MnCu(pbaOH)(H₂O)₂, has long range ferromagnetic ordering at $T_C = 30$ K [18]. The release of H₂O reduces

the interchain distances, and this enhances the interchain exchange interactions by a factor of 40. In Section 1.2.3 we will encounter other examples of magnetic ordering controlled by the water content of the material; these lead to the concept of magnetic sponges.

1.2.1.5 Two-dimensional Systems: Layered Honeycomb Compounds

We have seen that magnetic ordering of chain compounds can occur, and is strongly related to solvent molecules which impose the organization of the crystal packing. The interchain magnetic interactions remain weak, however, and magnetic ordering occurs at low temperature. To increase these temperatures, chemists have to build compounds with higher dimensionality. This section is devoted to bidimensional compounds, which are prepared with the same building blocks as the one-dimensional compounds but with different stoichiometries. Almost all of these 2D compounds behave as ferrimagnets. Experimentally the long-range magnetic ordering is revealed by the temperature dependencies of the field-cooled magnetization (FCM, which is measured by cooling the sample within a very small field, usually $H < 20$ Oe) and by the in-phase (χ_M') and out-of-phase (χ_M'') molar susceptibilities in the ac mode. The non-zero value of χ_M'' indicates the presence of permanent magnetic moment within the sample. The critical temperatures, denoted T_C , are determined by the extremum of the derivative curve $d(\text{FCM})/dT$ or by the maximum of the χ_M' curve, if it exists. In both instances they correspond to the temperatures where remnant magnetization vanishes, the latter is measured by turning the field off at low temperature and then warming up the sample in strictly zero field. The field dependence of the magnetization measured at low temperature enables the determination of the coercive field.

The reaction of $(\text{NBu}_4)_2[\text{Cu}(\text{opba})]$ with Mn^{II} in DMSO in 3:2 stoichiometry yielded a compound of formula $(\text{NBu}_4)_2[\text{Mn}_2\{\text{Cu}(\text{opba})\}_3,4\text{DMSO}] \cdot 2\text{H}_2\text{O}$, which is a ferrimagnet below $T_C = 15$ K [15]. When Mn^{II} is replaced by Co^{II} , T_C increases to 29 K [19]. Unfortunately, no crystals were obtained for these compounds; a layered honeycomb structure was proposed for the anionic part (Fig. 5), for compatibility with the chemical formulas of the compounds and, of course, with the magnetic ordering occurring for temperatures higher than for the chain compounds. A theoretical approach was developed for a two-dimensional hexagonal model to derive an analytical expression for the molar magnetic susceptibility, χ_M , in the paramagnetic regime (40–300 K) using high-temperature expansions of the partition function [20]. Comparison of theory and experiment led to determination of the exchange parameter as $J = -33.1 \text{ cm}^{-1}$, which is close to values obtained for related finite or chain compounds.

The occurrence of magnetic ordering in these two dimensional compounds might result from intralayer magnetic anisotropy and/or interlayer interactions. The cations are probably located between the anionic layers, and it is possible that the magnetic properties of these materials can be tuned by changing the size of the cations and/or slight modification of the ligand. Table 2 summarizes the different results. The magnetic behavior of the Mn derivatives strongly depends on the size

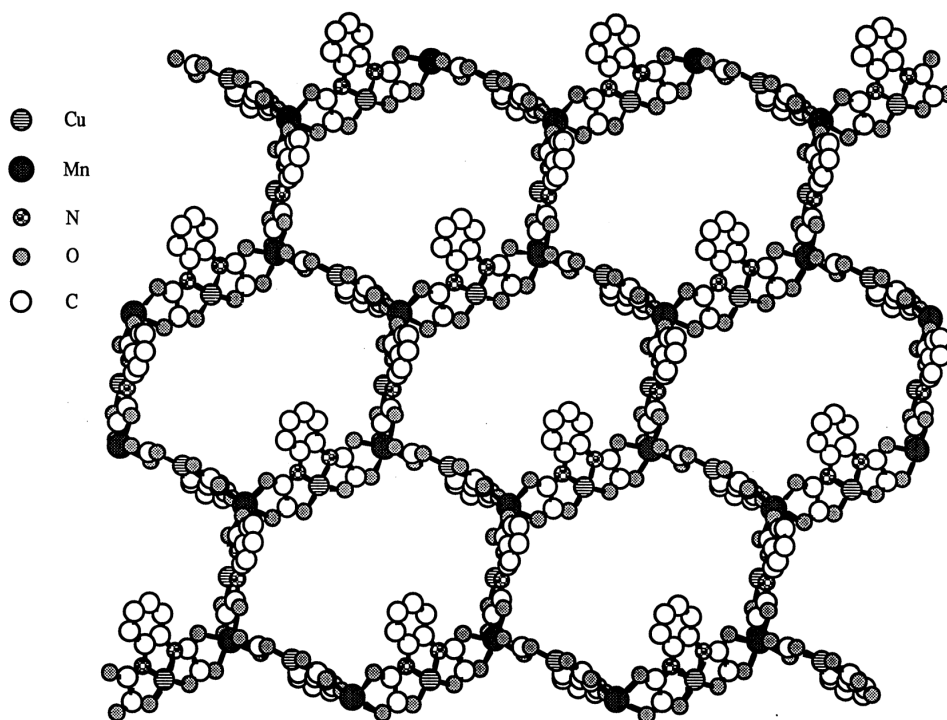


Fig. 5. Structure of a honeycomb layer.

of the cations. For large cations such as $[\text{Ru}(\text{bipy})_3]^{2+}$ magnetic ordering occurs at lower temperature [21], and for small cations such as alkali metals, the compounds have weak ferromagnetism [19], because of competition between antiferromagnetic interlayer interactions and ferrimagnetic intralayer interactions. In contrast, all the Co compounds are ferrimagnets with $T_C \approx 30$ K, irrespective of the cation. Such similar magnetic properties strongly suggests that the compounds adopt the same structure.

For some of these compounds XANES and EXAFS studies showed that each Mn^{II} is surrounded by three CuL complexes [22]. Journaux et al. compared experimental magnetic data with two theoretical models. One is based on a two-sublattice molecular field model in the mean field approximation, and is assumed valid for three-dimensional structures. The second already introduced above is adapted for hexagonal honeycomb layers. For all the examples studied the second approach led to good fitting of the magnetic data, and gave J values in good agreement with those deduced previously for other compounds of lower dimensionality. These structural and magnetic results lead to the conclusion that all these compounds are two-dimensional, with a honeycomb layered structure.

Finally, introduction of a cation with an intrinsic property, for instance chirality for cations such as nicot andambutol or the paramagnetic $[\text{FeCp}_2]^+$, has been envisaged [23, 24]. Chirality was introduced with the objective of inducing the for-

Table 2. Magnetic properties for the family of oxamato(oxamido)-bridged honeycomb layered ferrimagnets of formula $\text{Cat}^{\text{I}}[\text{M}_2^{\text{II}}(\text{CuL})_3]$ and $\text{Cat}^{\text{II}}[\text{M}_2^{\text{II}}(\text{CuL})_3]$.

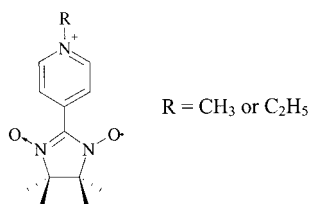
M^{II}	L	Cat	J (cm^{-1})	T_{C} (K)	H_{coerc} (Oe)	Ref.		
Mn	opba	NBu_4^+	-32	15	<10	[15]		
		NEt_4^+		17	<10	[19]		
		NMe_4^+		$T_{\text{N}} = 15$ K		[19]		
		K^+		$T_{\text{N}} = 15$ K		[19]		
		Na^+		$T_{\text{N}} = 15$ K		[19]		
		FeCp_2^{*+}		14	<20	[24]		
		CoCp_2^{*+}		13	<20	[24]		
		<i>nicot</i> $^{2+}$		$T_{\text{N}} = 15$ K		[23]		
		<i>ambutol</i> $^+$		$T_{\text{N}} = 15$ K		[23]		
		$\text{Ru}(\text{bipy})_3^{2+}$		12		[21]		
		PPh_4^+		-31.8	11.5	10	[22]	
		Meopba		PPh_4^+	-32.6	13	10	[22]
		Me ₂ opba		PPh_4^+	-30.5	8	10	[22]
		PhMe ₂ opbox		PPh_4^+		12.5	5	[26]
PhPr ₂ opbox	PPh_4^+		11.5	5	[26]			
PhBu ₂ opbox	PPh_4^+		13.5	5	[26]			
Co	opba	NBu_4^+		30.5	1400 (5 K)	[15]		
		NMe_4^+		33		[19]		
		Cs^+		34		[19]		
		K^+		33.5	2000 (5 K)	[19]		
		Na^+		31.5		[19]		
		FeCp_2^{*+}		27	3500	[24]		
		CoCp_2^{*+}		27.5	5300	[24]		

Notes: $\text{Cp}^* = \text{C}_5\text{Me}_5$, *nicot* is the chiral *N,N*-dimethylnicotinium species and *ambutol* is the chiral dimethylhydroxymethyl-2-ethylhydroxymethyl-1-propylammonium species.

mation of three dimensional coordination polymers in the same manner as for the 3D lattices obtained for the oxalato-bridged family discussed in another chapter of this series [25]. The magnetic cation was expected to increase the magnetic interaction between the layers, but the results were slightly disappointing, because no significant modifications of the magnetic properties were observed. These observations are, however, informative because they suggest future directions which might afford three-dimensional molecule-based magnets. In fact, a chiral cation can induce the formation of magnetic helicates only if it correctly fills the cavities formed by the three dimensional lattice. This obviously did not happen with the examples given above. Another way of filling the cavities of the anionic network is to use bulky ligands. The results obtained with the bulkier PhR₂opbox ligands (Table 1) designed on the basis of this strategy are not conclusive [26]. Note that the compound obtained with $[\text{FeCp}_2^*]^+$ enabled a Mössbauer study which revealed that the Fe^{III} ion begins to feel an internal field only at temperatures well below T_{C} . This clearly indicates that the cation between the layers is not directly involved in the long range magnetic ordering.

1.2.1.6 Interpenetrated Two-dimensional Networks: Interlocked Compounds

To increase the dimensionality further Kahn and coworkers imagined the use of a cation which would be capable of bridging two transition metal ions and which would be paramagnetic, thus increasing the magnetic density of the compounds. Cations belonging to the nitronyl nitroxide family, in which the unpaired electron is equally shared between the two N-O groups, have been envisaged (Scheme 4).



Scheme 4

The methyl and ethylpyridinium radical cations were used with success [27-29]. The structures of compounds with the formula (Etrad)₂[M₂{Cu(opba)}₃] have been investigated by single crystal X-ray studies for M = Mn, Co, and by powder X-ray studies for M = Mg, Ni [30, 31]. All the compounds are fully interlocked with a general architecture made of two equivalent two-dimensional networks, denoted A and B, each consisting of parallel honeycomb layers. Each layer is made up of edge-sharing hexagons with an M^{II} ion at each corner and a Cu^{II} ion at the middle of each edge (Fig. 5). The layers stack above each other in a graphite-like fashion, with a mean interlayer separation of 14.8 Å. The A and B networks are almost perpendicular to each other, and interpenetrate in such a way that at the center of each hexagon belonging to a network is located a Cu^{II} ion belonging to the other network (Fig. 6). The networks are further connected through the radical cations; this affords infinite chains of the kind Cu_A-Etrad-Cu_B-Etrad, where Cu_A and Cu_B belong to the A and B network, respectively.

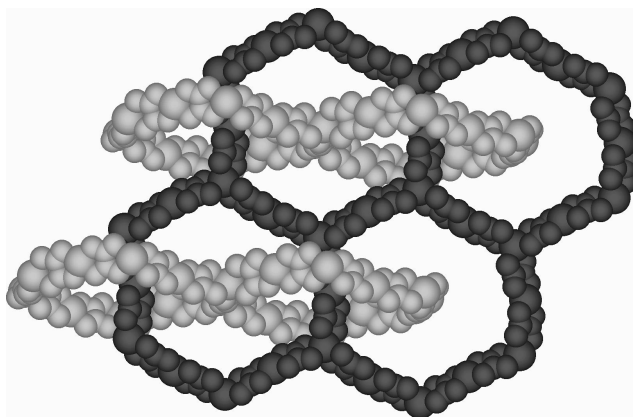


Fig. 6. Interpenetration of the two networks A and B.

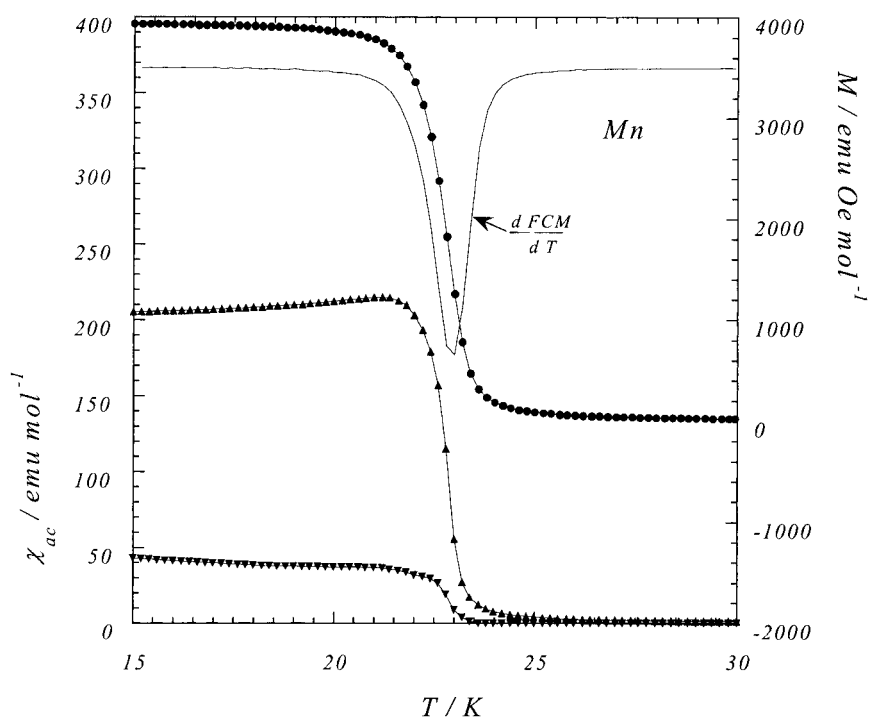


Fig. 7. FCM curve (●) and its derivative $d(\text{FCM})/dT$ (top) and in-phase χ'_M (▲) and out-of-phase χ''_M (▼) plots of ac susceptibilities (bottom) against T for $(\text{Etrad})_2[\text{Mn}_2\{\text{Cu}(\text{opba})\}_3]$.

Besides the aesthetic aspect of the structures, the compounds also had interesting magnetic properties. They behave as ferrimagnets with Curie temperatures in the range of 22–37 K (Figs. 7 and 8 and Table 3). The χ'_M and χ''_M curves can have two different general shapes, (i) a shape similar that of the FCM with $\chi'_M \gg \chi''_M$ as shown in Fig. 7, or (ii) a peak-like shape as shown in Fig. 8 with maximum values for very close temperatures. These differences are related to the coercivity of the material, case (i) applies for a very weak coercivity ($H_{\text{coerc}} < 10$ Oe) and case (ii) when a

Table 3. Magnetic properties for the family of oxamato(oxamido)-bridged interlocked ferrimagnets of formula $(\text{r-Rad})_2[\text{M}_2^{\text{II}}(\text{CuL})_3]$, where r = methyl- or ethylpyridinium.

M^{II}	L	Cat	T_C (K)	H_{coerc} (Oe)	Ref.
Mn	opba	Merad	23	<10	[15]
		Etrad	22.8	<10	[29]
Co	opba	Merad	34	3000 (5 K)	[15]
		Etrad	37	8500–24 000	[29]
Ni	opba	Etrad	28	500	[30, 31]
Mg	opba	Etrad	Paramagnet	Paramagnet	[31]

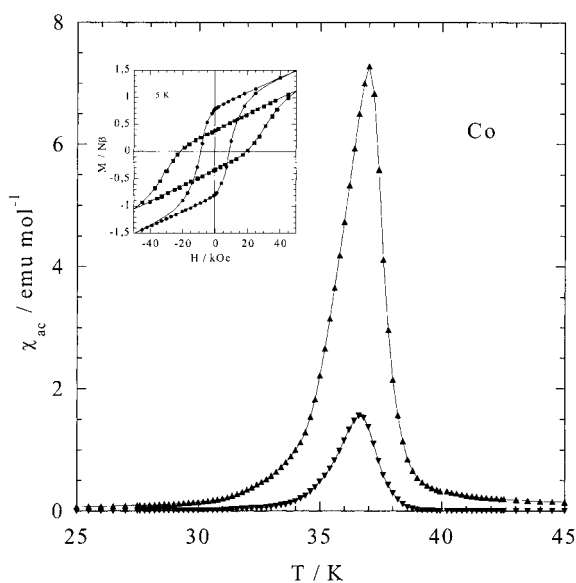


Fig. 8. In-phase χ'_M (\blacktriangle) and out-of-phase χ''_M (\blacktriangledown) ac susceptibilities (bottom) for $(\text{Etrad})_2[\text{Co}_2\{\text{Cu}(\text{opba})\}_3]$. The insert shows the field dependence of the magnetization for two samples with the largest (\bullet) crystals and smallest (\blacksquare) crystals.

significant coercivity ($H_{\text{coerc}} > 1000 \text{ Oe}$) exists. As a result of the formation of the 3D networks the Curie temperatures are effectively increased by up to 8 K for the Mn and Co compounds, compared with the layered compounds (Table 2). But the increase of T_C seems weak with regard to the three-dimensional connectivity of the compound. In fact, the interaction between the interlocked layers is weak, and has been estimated in $(\text{Etrad})_2[\text{Mg}_2\{\text{Cu}(\text{opba})\}_3]$. Because the Mg ion is diamagnetic, magnetic interactions occur only along the $\text{Cu}_A\text{--Etrad--Cu}_B\text{--Etrad}$ chains. They are ferromagnetic, as expected between Cu^{II} and a nitroxide group occupying the apical position. Neglecting intermolecular interactions, the magnetic data were analyzed by a chain model for $S = 1/2$ spins, leading to an exchange parameter of $J = 8 \text{ cm}^{-1}$, which is four times weaker in absolute values than the intralayer interaction [31].

1.2.1.7 Ladder and Honeycomb Lattices in 3d–4f Systems

The chemistry of the bis-bidentate Cu-oxamato complexes is not limited to the reaction with 3d transition metals. Impressive extended structures have been obtained when $[\text{Cu}(\text{opba})]^{2-}$ was reacted with lanthanide ions, Ln^{III} . The first compounds of this kind were reported in 1992 for the $\text{Ln}^{\text{III}}\text{--Cu}(\text{pba})$ system [32]. Two different structures have been described for compounds of general formula $\text{Ln}_2\{\text{Cu}(\text{pba})\}_3$. One consists of discrete ladders of Ln going from Tb to Yb, and Y, an architecture similar to that of $\text{Ln}_2\{\text{Cu}(\text{opba})\}_3$ shown in Fig. 9. The second results from condensed ladder-like motifs with a rearrangement of the rungs and is formed with Ln

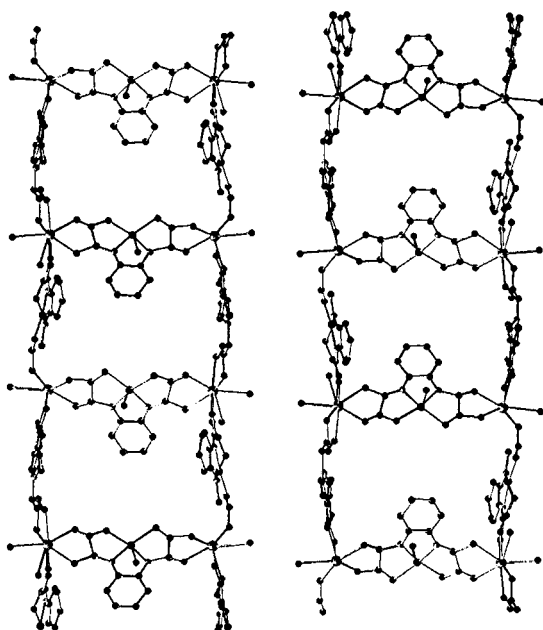


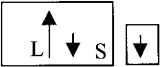
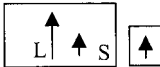
Fig. 9. Structure of the ladder-type compound $\text{Ln}_2\{\text{Cu}(\text{opba})\}_3$.

belonging to the beginning of the Ln series. Interestingly, compounds of formula $\text{Ln}_2\{\text{Cu}(\text{opba})\}_3$ crystallize with the same structure all along the lanthanide series. This structure consists of infinite ladders, parallel to each others, as shown in Fig. 9. The side-pieces of a ladder are made of $\text{Ln}_2\{\text{Cu}(\text{opba})\}_3$ units, and the rungs are made of $\text{Cu}(\text{opba})$ units that bridge two Ln atoms belonging to either side-pieces of the ladder. When seen along the direction of a rung the two edges of a ladder are in an eclipsed conformation. Each Ln^{III} ion is surrounded by three $\text{Cu}(\text{opba})$ units, its coordination sphere being completed by three water molecules.

As mentioned in the Section 1.2.1.2, the magnetic properties of compounds containing paramagnetic Ln ions are usually difficult to interpret. They are governed both by the thermal population of the Stark components of Ln^{III} and by the $\text{Ln}^{\text{III}}\text{-Cu}^{\text{II}}$ interaction. To extract information on the nature of the $\text{Ln}^{\text{III}}\text{-Cu}^{\text{II}}$ interaction the magnetic behavior of $\text{Ln}_2\{\text{Cu}(\text{opba})\}_3$ can be compared with that of $\text{Ln}_2\text{Zn}(\text{opba})_3$ for each Ln^{III} ion. Wide-angle X-ray scattering (WAXS) experiments strongly suggest that the Zn^{II} -containing compounds have also a ladder-type structure [33]. For a $\text{Ln}_2\text{Zn}(\text{opba})_3$ compound in which the only magnetic ion is Ln^{III} , the magnetic properties are entirely governed by the thermal population of the Stark components of Ln^{III} . The purpose here is not to enter into the details of the procedure but to restrict ourselves to reporting some results [34].

The simplest example is that where the lanthanide element is gadolinium. The ground state of Gd^{III} is a pure $S_{\text{Gd}} = 7/2$ spin state, orbitally non-degenerate. The $\text{Gd}^{\text{III}}\text{-Cu}^{\text{II}}$ interaction is weakly ferromagnetic. All the spins of the material

Table 4. Nature of the magnetic interaction between Ln^{III} and M^{II} ions, as determined by the experimental method described in the text.

Ln^{III} Compound	Ce	Pr	Nd	Sm	Eu	Gd	Tb	Dy	Ho	Er	Tm	Yb
Ni_3Ln_2	af	af	af	af	af	F	F	F	f			
Cu_3Ln_2	af	af	af	af	af	F	F	F			f	
CuLn pairs	AF		AF	AF		F	F	F	F	F	AF	
Kahn's prediction												
	Overall AF interaction					Overall F interaction						

AF – antiferromagnetic interaction, F – ferromagnetic interaction, af – proposed antiferromagnetic interaction, f – proposed ferromagnetic interaction.

tend to align along the same direction, and actually $\text{Gd}_2\{\text{Cu}(\text{opba})\}_3$ has long-range ferromagnetic ordering at 1.78 K [35]. The $\text{Tb}^{\text{III}}\text{--Cu}^{\text{II}}$ and $\text{Dy}^{\text{III}}\text{--Cu}^{\text{II}}$ interactions were also found to be ferromagnetic, and the appearance of long-range magnetic ordering was also established for $\text{Tb}_2\{\text{Cu}(\text{opba})\}_3$ and $\text{Dy}_2\{\text{Cu}(\text{opba})\}_3$ at 0.81 K and 0.74 K, respectively, by specific heat measurements [36]. For all the other Ln^{III} ions, the interaction is not ferromagnetic; it is either not detectable by the magnetic technique or very weakly antiferromagnetic. An ambiguity remains for Tm^{III} .

A similar series of compounds has been obtained with the $\text{Ni}(\text{opba})$ precursor. In the resulting $\text{Ln}_2\text{Ni}(\text{opba})_3$ compounds, the four-coordinated environment of the Ni ion was completed by a solvent molecule (DMSO in this case), as confirmed by EXAFS studies [37]. In the new geometry (pyramidal or octahedral), the Ni center is paramagnetic. When the procedure described above is used to extract magnetic information about the $\text{Ln}^{\text{III}}\text{--Ni}^{\text{II}}$ pair, ferromagnetic interactions are found in $\text{Ni}^{\text{II}}\text{--Gd}^{\text{III}}$, $\text{Ni}^{\text{II}}\text{--Tb}^{\text{III}}$, $\text{Ni}^{\text{II}}\text{--Dy}^{\text{III}}$ pairs and perhaps in $\text{Ni}^{\text{II}}\text{--Ho}^{\text{III}}$, and antiferromagnetic interactions are obtained for $\text{Ni}^{\text{II}}\text{--Ln}^{\text{III}}$ with Ln going from Ce to Eu. These conclusions, similar to those obtained for Ln–Cu pairs (except for Tm), are in line with the predictions of Kahn (Table 4) [38]. Results obtained for other Ln–Cu pairs seem in agreement with our results [39]. It has been pointed out that geometrical considerations do not seem to be crucial to the nature of exchange interaction between Ln and a 3d ion, irrespective to what happens in 3d–3d pairs.

Finally, one can notice that the stoichiometry $\text{Ln}_2\{\text{Cu}(\text{opba})\}_3$ might also correspond to two-dimensional compounds with a honeycomb-like structure, reminiscent of that shown in Fig. 5, and such a structure has actually been found [40]. During the synthetic process, however, partial hydrolysis of the oxamato groups into oxalato groups occurs. The formula of this compound is $\text{Nd}_2\text{Cu}(\text{opba})_{0.5}(\text{ox})_3 \cdot 9\text{DMF}$ with ox = oxalato and DMF = dimethylformamide. The Nd^{III} ions occupy the corners of the edge-sharing hexagons and the Cu^{II} ions occupy the middles of the edges. These edges are statistically made of $\text{Cu}(\text{opba})$ and $\text{Cu}(\text{ox})_2$ groups, with a probability of 0.5 for each. The Nd^{III} are surrounded by nine oxygen atoms, six arising from the bidentate oxamato or oxalato groups and three from DMF molecules. The

magnetic properties for this and related compounds with the Nd_2Cu_3 stoichiometry are rather unexpected. All the compounds have a quasi-non-magnetic ground state characterized by a $\chi_{\text{M}}T$ value tending to zero as the temperature approaches absolute zero. This situation results from an almost perfect compensation between the two Nd^{III} and the three Cu^{II} local magnetic moments. Such compensation can occur if the ratio $\rho = g_{\text{Nd}}/g_{\text{Cu}}$ is equal to a critical value which has been calculated as 1.73; g_{Nd} and g_{Cu} are the Zeeman factors of the local Kramers doublets of Nd^{III} and Cu^{II} , respectively. If the Nd^{III} and Cu^{II} magnetic moments coupled antiferromagnetically, but without accidental compensation, the behavior would be ferrimagnetic, and $\chi_{\text{M}}T$ would not tend to zero at low temperature.

1.2.2 Modulation of the Magnetic Properties

So far we have focused only on the temperature at which the magnetic ordering occurs, and the possibilities of increasing this temperature by controlling the dimensionality of the covalent skeleton of the compounds. This section is devoted to an other aspect of magnetic materials and their memory-effect characteristics. The memory effect is associated with a property of the material with hysteretic behavior with regard to a given perturbation. We already mentioned that the Co-containing magnets described in Sections 1.2.1.5 and 1.2.1.6 have T_{C} values almost twice as high as their Mn analogs. They also have large magnetic hysteresis loops with rather large coercive field values ($H_{\text{coerc}} > 1000$ Oe at 5 K), whereas the Mn compounds have rather weak coercive fields ($H_{\text{coerc}} < 10$ Oe). The former can be regarded as hard magnets, the latter as soft magnets. The coercive field for the interlocked Co compound also depends on the average size of the crystals, and values as large as 24 kOe can be reached for smaller crystallites (insert in Fig. 8).

It is well established that the coercivity of a magnet depends to some extent on morphologic factors such as grain size and shape, and the defects within the crystallites which would favor pinning of the ferromagnetic domain walls. The key property of a molecule-based magnet with a large value of coercivity seems, however, to be a chemical – the presence of magnetic centers with unquenched orbital momentum in the structure. In our example Mn^{II} is magnetically isotropic ion and cannot, therefore, prevent the domains from rotating freely when a field is applied. Replacing Mn^{II} , with an orbital singlet state (${}^6\text{A}_1$), by Co^{II} , with an orbital triplet ground state (${}^4\text{T}_1$), results in a dramatic increase in coercivity. Occasionally values are much higher than those of the commercial atom-based materials Fe_2O_3 or CrO_2 . Rather strong coercive fields are expected for molecular magnets in which Co^{II} ion is in distorted octahedral environment, because being magnetically anisotropic Co^{II} can assume preferred orientations. The intrinsic anisotropy of Co^{II} certainly also plays a role in intralayer anisotropy, which can be responsible for the increased T_{C} values compared with those of the Mn analogs.

An other interesting example is the behavior of the Ni^{II} interlocked derivative [30, 31]. First, the magnetization curves are rather unusual. The FCM curve recorded within a very small field (1 Oe) has a break at $T_{\text{C}} = 28$ K, characteristic of the long-range magnetic ordering, then passes through a maximum at 21 K, and finally de-

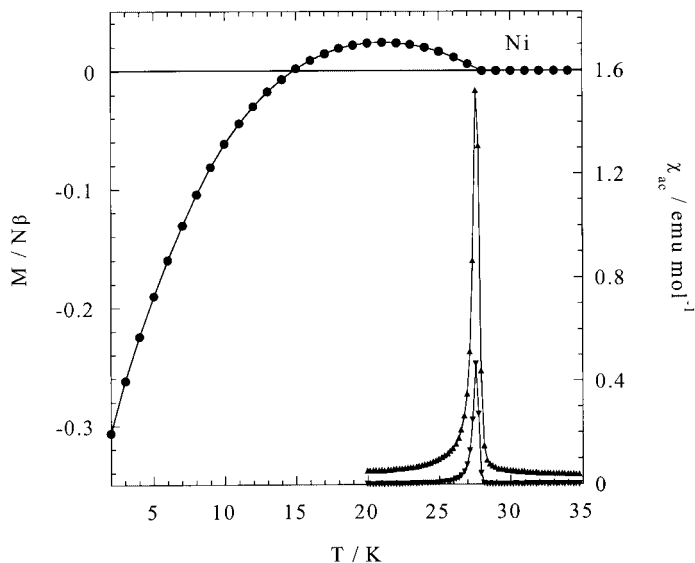


Fig. 10. FCM curve (●) (1 Oe) for $\text{Etrad}_2[\text{Ni}_2\text{Cu}_3]$. The figure also shows the in-phase, χ'_{ac} (▲), and out-of-phase, χ''_M (▼), versus T plots.

creases monotonically at lower temperatures (Fig. 10). The temperature at which the magnetization vanishes (15 K) is the so-called compensation temperature, denoted T_{comp} , and already observed for other ferrimagnets [25]. Below T_{comp} the magnetization is aligned in a direction opposite to that of the applied magnetic field. Also, whereas the coercive fields for manganese and cobalt derivatives increase when the temperature is reduced, the coercive field for $(\text{Etrad})_2[\text{Ni}_2\{\text{Cu}(\text{opba})\}_3]$ is highest (1.2 kOe) at T_{comp} , and decreases above and below T_{comp} .

The peculiar behavior of the Ni derivative has been studied in detail, and analyzed with the help of molecular field theory (MFT) and magnetic anisotropy [30, 41]. To study the stability of the negative magnetization several FCM curves have been recorded with increasing magnetic field. The FCM curve obtained with a field of 1000 Oe (Fig. 11) passes through zero for two different temperatures, namely T_{comp} and T_{CM} . Furthermore, depending on the measurement process (cooling or warming modes) double field-induced thermal hysteresis is observed for the magnetization curves FCM and FWM. The two curves are not superimposed, as they are normally for ferro(ferrimagnets), and the material strongly memorizes the strength of the magnetic field when cooling. For the same applied magnetic field (1 Oe) the FWM curve obtained after the sample was cooled in a field of 50 kOe is almost the mirror image of the FCM curve. To analyze these experimental data it is possible to use MFT, which at least reproduces qualitatively the experiments. Using the Néel theory for ferrimagnets [42], the compound may be described with three sublattices (Ni, Cu, Etrad) characterized by their local magnetization, M_{Ni} , M_{Cu} , and M_{Etrad} (Fig. 12). The antiferromagnetic interactions between M_{Ni} and M_{Cu} favor their antiparallel orientation whereas the ferromagnetic Cu^{II} -Radical interactions favor the M_{Cu} and

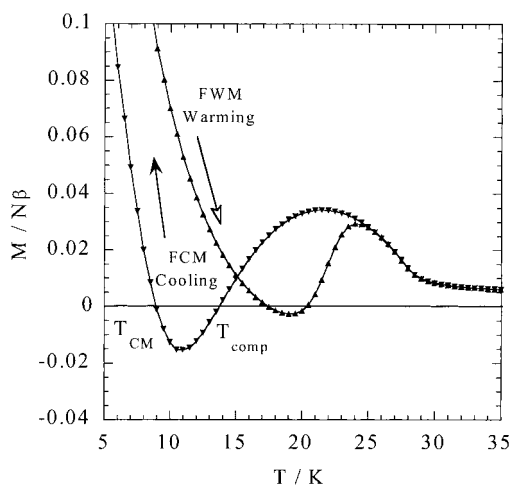


Fig. 11. Magnetization versus T curves for $(\text{Etrad})_2[\text{Ni}_2\{\text{Cu}(\text{opba})\}_3]$ obtained in cooling (FCM) or warming modes (FWM), recorded at 1000 Oe.

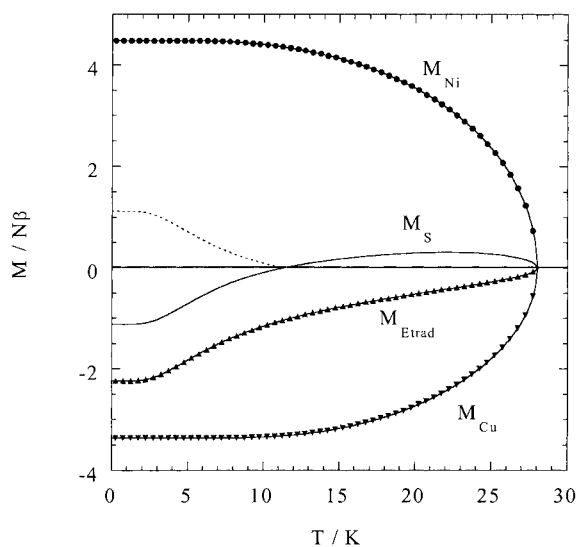


Fig. 12. Thermal dependence of the magnetization sub-lattices simulated with molecular field theory (\bullet) for M_{Ni} ; (\blacktriangledown) for M_{Cu} ; (\blacktriangle) for M_{Etrad} ; ($-$) for M_{S} .

M_{Etrad} orientation in the same direction. To simplify the discussion below, we note $M_{1/2} = M_{\text{Cu}} + M_{\text{Etrad}}$.

Below T_{C} , the total magnetization M_{S} is the algebraic sum of the two contributions M_{Ni} and $M_{1/2}$. M_{S} , first, is positive as T is lowered, M_{Ni} being larger in value than $M_{1/2}$. But M_{Ni} and $M_{1/2}$ have different thermal dependencies and the two contributions cancel out at the compensation temperature T_{comp} , M_{S} is then equal to zero. Below T_{comp} , $M_{1/2}$ becomes larger than M_{Ni} and M_{S} turns negative. This negative magnetization corresponds to a metastable state, which exists because the orientation of each sublattice is blocked by anisotropy (H_{coerc} is maximum at T_{comp} with a value of 1.2 kOe). As H_{coerc} decreases when the temperature is reduced fur-

ther, it might happen during the cooling mode measurement that H becomes higher than H_{coerc} . In this circumstance the negative magnetization state is no longer stable, and we observe the magnetic pole reversal at T_{CM} with $M_S > 0$ (Fig. 11). The same explanation applies for the warming mode process and explains the appearance of the double field-induced thermal hysteresis. The efficiency of hard magnets and ferrimagnets for information storage is well established. Molecular chemistry thus provides access to materials exhibiting memory effects related to the blocking of the magnetization and its temperature-dependent orientation. Interestingly, the use of a simple theory like MFT makes possible the design of compounds with desired properties by controlling T_C , H_{coerc} and T_{comp} .

These results show that by quite a small alteration of the synthetic steps, for instance by changing the metal ion M , the magnetic properties of molecule-based magnets can be modified. The Mn, Co, and Ni derivatives have the same general architectures, but the resulting magnets have very different features and these properties are simply related to the nature of the ion. The Mn derivative is a soft magnet (Mn being an isotropic ion), the Co derivative is a hard magnet (because of the strong intrinsic anisotropy of the Co ion), and the Ni derivative is an intermediate case in terms of coercive fields. For the Ni ion the anisotropy is weaker than for Co and finds its origin in the zero-field splitting effects. Its weaker anisotropy is responsible for the interesting compensated ferrimagnetic behavior. If the anisotropy is stronger no compensation temperature is observed, as shown for the Co derivative.

1.2.3 Dimensionality Modulation by a Dehydration-Polymerization Process

We have seen in Section 1.2.1.4 that the magnetic properties of some molecular compounds can be dramatically and reversibly modified by means of a mild dehydration-rehydration process. This class of compound has been named *molecular magnetic sponges* [43–46]. This is because they have “sponge”-like characteristics, viz. a reversible cross-over on dehydration to a polymerized long-range magnetically ordered state with spontaneous magnetization, and transform back into the isolated units underlying the initial non-magnetic phase on re-absorption of water, i. e. rehydration of both non-coordinated and coordinated water molecules. For some of these sponges a color change also occurs reversibly and simultaneously with the change in magnetic properties at the transition temperature corresponding to the dehydration-rehydration process.

The very first example of a molecule-based magnet obtained by reversible dehydration of a paramagnetic (or antiferromagnetic) species was $\text{MnCu}(\text{obbz}) \cdot n\text{H}_2\text{O}$ with $n = 5$ or 1 , and where “obbz” stands for oxamido(bis benzoato) (Scheme 2) [47]. The pentahydrate has a chain structure and has a long-range antiferromagnetic transition at $T_N = 2.3$ K, because of very weak interchain interaction. When four out of five water molecules are removed, however, this interaction strengthens and the monohydrate becomes a genuine magnet with $T_C = 14$ K. The dehydration process is reversible.

Because of the results obtained for the Co molecule-based magnets (Sections 1.2.1.5 and 1.2.1.6), study of such behavior in CoCu compounds seemed obvious. The linear chain compound $\text{CoCu}(\text{pbaOH})(\text{H}_2\text{O})_3 \cdot 2\text{H}_2\text{O}$, in which the ferrimagnetic chains interact antiferromagnetically ($T_N \approx 2 \text{ K}$) within the lattice, was transformed into $[\text{CoCu}(\text{pbaOH})(\text{H}_2\text{O})_3]$ on removal of two non-coordinated water molecules by thermal treatment. The three hydrate has ferromagnetic ordering at $T_C = 9.5 \text{ K}$. Removal of a third water molecule, occupying the apical position in the copper coordination sphere, yields a compound $[\text{CoCu}(\text{pbaOH})(\text{H}_2\text{O})_2]$ with high values of $T_C = 38 \text{ K}$ and $H_{\text{coerc}} = 5.66 \text{ kOe}$ at 2 K [43]. The dehydration process is not only reversible but also accompanied by color change, the blue pentahydrate turning deep purple when dehydrated into the ferromagnetic $\text{CoCu}(\text{pbaOH})(\text{H}_2\text{O})_2$, and vice versa upon rehydration.

The dehydrated compound $\text{CoCu}(\text{pba})\text{H}_2\text{O}$ was obtained by heating the parent blue compound, $\text{CoCu}(\text{pba})(\text{H}_2\text{O})_3 \cdot 2\text{H}_2\text{O}$ (isostructural with the Mn compound represented in Fig. 4) at 120°C under vacuum. If heating is stopped at 120°C , the compound $[\text{CoCu}(\text{pba})\text{H}_2\text{O}]$ begins to reabsorb water and the color changes back from purple to blue. The compound decomposes if heated above 175°C . The plot of $\chi_M T$ against T for $\text{CoCu}(\text{pba})(\text{H}_2\text{O})_3 \cdot 2\text{H}_2\text{O}$, with a minimum at 65 K , is indicative of magnetic behavior typical of a bimetallic one-dimensional $\text{Co}^{\text{II}}\text{-Cu}^{\text{II}}$ ferrimagnet chain, ordering antiferromagnetically at 7 K . The shortest interchain separations between metal atoms are Cu-Cu and Co-Co . The dehydrated analog $[\text{CoCu}(\text{pba})\text{H}_2\text{O}]$ is, however ferromagnetic, with spontaneous magnetization below 33 K , as confirmed by the $\chi_M T$ vs. T and ac-susceptibility data, and a large coercive field of 3 kOe at 2 K , arising from the magnetic anisotropy of the Co^{II} ion in octahedral surroundings. We believe that the bimetallic ferrimagnetic chains move closer to each other on loss of water molecules in such a manner that the shortest metal ion distances are now between the Co^{II} ions of one chain and the Cu^{II} ions of the adjacent chain. The dehydration–rehydration process, accompanied by the color change from blue to purple is totally reversible. If left to stand in air for ca. two days the dehydrated ferromagnetic compound regains the magnetic characteristics of the original hydrated compound. One can, of course, also achieve rehydration by adding water to the dehydrated compound in a controlled fashion.

In the following text, to describe the characteristics of the magnetic sponges we have chosen $\text{CoCu}(\text{obbz})(\text{H}_2\text{O})_4 \cdot 2\text{H}_2\text{O}$ as a representative example; this is described in sufficient detail below to bring the phenomenon of the softness of the molecular lattice into focus. The compound $\text{CoCu}(\text{obbz})(\text{H}_2\text{O})_4 \cdot 2\text{H}_2\text{O}$ is a binuclear and has four water molecules in the cobalt coordination sphere and two additional uncoordinated water molecules. The Co^{II} is in octahedral environment, and the Cu^{II} ion is in a square-planar environment. The $\chi_M T$ for $\text{CoCu}(\text{obbz})(\text{H}_2\text{O})_4 \cdot 2\text{H}_2\text{O}$ tends to zero as T is lowered, as expected for antiferromagnetically coupled $\text{Co}^{\text{II}}\text{Cu}^{\text{II}}$ pairs in a non-magnetic ground state (Fig. 13). The combined effect of distortion and spin-orbit coupling on Co^{II} in an octahedral environment gives rise to low-lying Kramers doublets among which only the ground Kramers doublet is thermally populated at low temperatures. The Co^{II} ion can then have an effective spin of only $S = 1/2$, and a very anisotropic g_{Co} tensor. An antiferromagnetic interaction between Co^{II} and Cu^{II} ($S_{\text{Cu}} = 1/2$) in such a situation

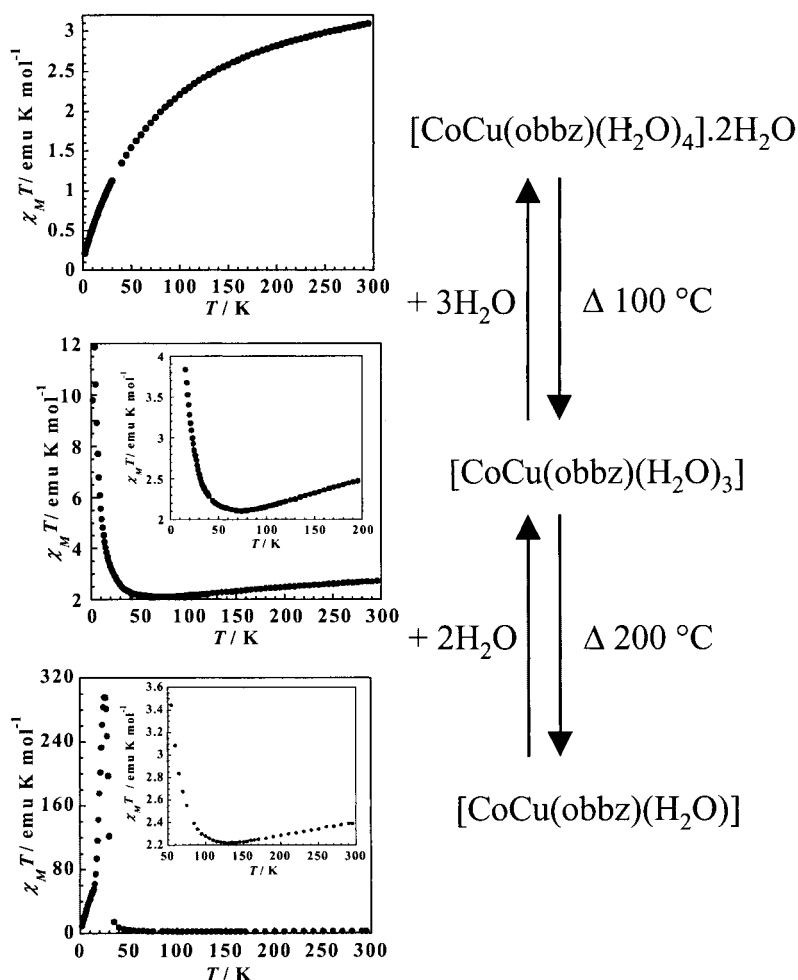


Fig. 13. $\chi_M T$ vs. T plots for $\text{CoCu}(\text{obbz})(\text{H}_2\text{O})_4 \cdot 2\text{H}_2\text{O}$ and its dehydrated versions to $\text{CoCu}(\text{obbz})(\text{H}_2\text{O})_3$ and to $\text{CoCu}(\text{obbz})(\text{H}_2\text{O})$ [46].

gives rise to a non-magnetic singlet state and a pseudo triplet state, split in zero field. Thermogravimetric analysis revealed that $\text{CoCu}(\text{obbz})(\text{H}_2\text{O})_4 \cdot 2\text{H}_2\text{O}$ could be dehydrated to give two well-defined new compounds. At approximately 100°C , the two non-coordinated water molecules leave along with one water molecule from the Co^{II} coordination sphere. The removal of these three water molecules is accompanied by a sort of polymerization process yielding a one-dimensional chainmagnetic compound $\text{CoCu}(\text{obbz})(\text{H}_2\text{O})_3$ for which the $\chi_M T$ vs. T plot has a minimum at 74 K, but no long range magnetic order is observed down to 2 K. Heating this compound further up to approximately 200°C resulted in the release of two more water molecules and development of the polymerization process to give a bulk fer-

paramagnetic compound $\text{CoCu}(\text{obbz})\text{H}_2\text{O}$ with long-range magnetic ordering below $T_C = 25\text{ K}$ (Fig. 13). The $\chi_{\text{M}}T$ vs. T plot for $\text{CoCu}(\text{obbz})\text{H}_2\text{O}$ is indicative of long-range magnetic ordering below T_C ; this is confirmed by FCM, ZFCM, and REM plots and by ac magnetic susceptibility data. Remarkably, this dehydration process was completely reversible inasmuch as if a sample of $\text{CoCu}(\text{obbz})\text{H}_2\text{O}$ is kept at room temperature in the close vicinity of a source of water it can slowly re-adsorb water and be transformed back into the original phase $\text{CoCu}(\text{obbz})(\text{H}_2\text{O})_4 \cdot 2\text{H}_2\text{O}$, the chemical composition, X-ray structure, and magnetic and optical behavior of which is exactly reproduced. The dehydration-rehydration process can be repeated as many times as desired without any degradation of the material, if the temperature does not exceed 275°C , the decomposition temperature.

Not only is $\text{CoCu}(\text{obbz})\text{H}_2\text{O}$ a magnet, but it is a hard magnet, because the field dependence of the magnetization at 5 K has a wide hysteresis loop with a coercive field of 3 kOe, indicating that Co^{II} must be in an octahedral environment, in contravention of the fact that this monohydrate has only one water molecule in the cobalt coordination sphere; this might suggest tetrahedral coordination of the Co^{II} ion. The octahedral environment around the Co^{II} ion can be restored only if the two water molecules which were removed from the coordination sphere of Co while dehydrating the trihydrate $\text{CoCu}(\text{obbz})(\text{H}_2\text{O})_3$ to the monohydrate $\text{CoCu}(\text{obbz})\text{H}_2\text{O}$ are replaced by two carboxylato oxygen atoms belonging to two neighboring chains, which would also raise the dimensionality of the compound $\text{CoCu}(\text{obbz})\text{H}_2\text{O}$ in compatibility with the long-range magnetic order displayed by $\text{CoCu}(\text{obbz})\text{H}_2\text{O}$. Interestingly, infrared and Raman spectroscopy data are in line with this proposition. The IR spectrum of $\text{CoCu}(\text{obbz})(\text{H}_2\text{O})_4 \cdot 2\text{H}_2\text{O}$ in the $1550\text{--}1620\text{ cm}^{-1}$ range has several intense and broad bands which can be assigned to the antisymmetric ν_{COO} vibrations of the monodentate carboxylato groups. The relative intensities of these features decrease for the trihydrate $[\text{CoCu}(\text{obbz})(\text{H}_2\text{O})_3]$ and new IR bands start appearing in the ranges $1600\text{--}1620\text{ cm}^{-1}$, and $1660\text{--}1690\text{ cm}^{-1}$, signifying antisymmetric ν_{COO} vibrations of the bridging carboxylato groups, and very asymmetrical carboxylato groups, respectively [44]. The relative intensities of these two groups of bands increase further as we pass from the trihydrate $[\text{CoCu}(\text{obbz})(\text{H}_2\text{O})_3]$ to the monohydrate $[\text{CoCu}(\text{obbz})\text{H}_2\text{O}]$.

This points to the formation of two Co–O bonds during dehydration, involving both bridging and strongly asymmetrical carboxylato groups at the expense of two Co– H_2O bonds. The Raman spectrum of $\text{CoCu}(\text{obbz})(\text{H}_2\text{O})_4 \cdot 2\text{H}_2\text{O}$ is dominated by the peak at 1415 cm^{-1} , arising from the symmetric ν_{COO} vibrations of the monodentate carboxylato groups. Upon dehydration this band shifts to higher energy and appears at 1428 cm^{-1} for $\text{CoCu}(\text{obbz})\text{H}_2\text{O}$, assignable to the symmetric ν_{COO} vibrations of the bridging carboxylato groups. Upon rehydration of the sample, in situ, the ν_{COO} mode shifted from 1428 back to 1415 cm^{-1} , even its half-width reverting from 10 to ca. 22 cm^{-1} , underlining the complete reversibility of the dehydration-rehydration process. It was, therefore, postulated that the compound $\text{CoCu}(\text{obbz})(\text{H}_2\text{O})_3$ has a chain structure and behaves as a one-dimensional ferromagnet without long-range ordering.

For the monohydrate $\text{CoCu}(\text{obbz})\text{H}_2\text{O}$ the chains associate to afford a network of higher dimensionality. The monodentate carboxylato groups of a chain create, upon

dehydration, Co–O bonds involving Co^{II} ions belonging to the neighboring chains. If it was so, the Co^{II} ion in $\text{CoCu}(\text{obbz})\text{H}_2\text{O}$ would be surrounded by six oxygen atoms, one arising from a water molecule, two from the oxamido group, one from a carboxylato groups, as shown schematically in Fig. 14. The shortest intermolecular metal-metal separation in $\text{CoCu}(\text{obbz})(\text{H}_2\text{O})_4 \cdot 2\text{H}_2\text{O}$ is 5.109 \AA between Co and Cu, which happens to be shorter than the intramolecular distance of 5.295 \AA . It seems, therefore, that in this case the molecular lattice was pre-formed to facilitate the equilibrium of Scheme 5 which gets displaced towards the right if conditions favor dehydration (i. e. vacuum or heating) whereas in the presence of excess water it gets displaced towards the left. The reversibility of the dehydration-polymerization process hinges on the simultaneous reversibility of:

- creation (breaking) of Co-carboxylato bonds, involving a step in the solid state, and
- breaking (creation) of Co-water bonds, a step occurring in a solid-liquid heterogeneous phase.

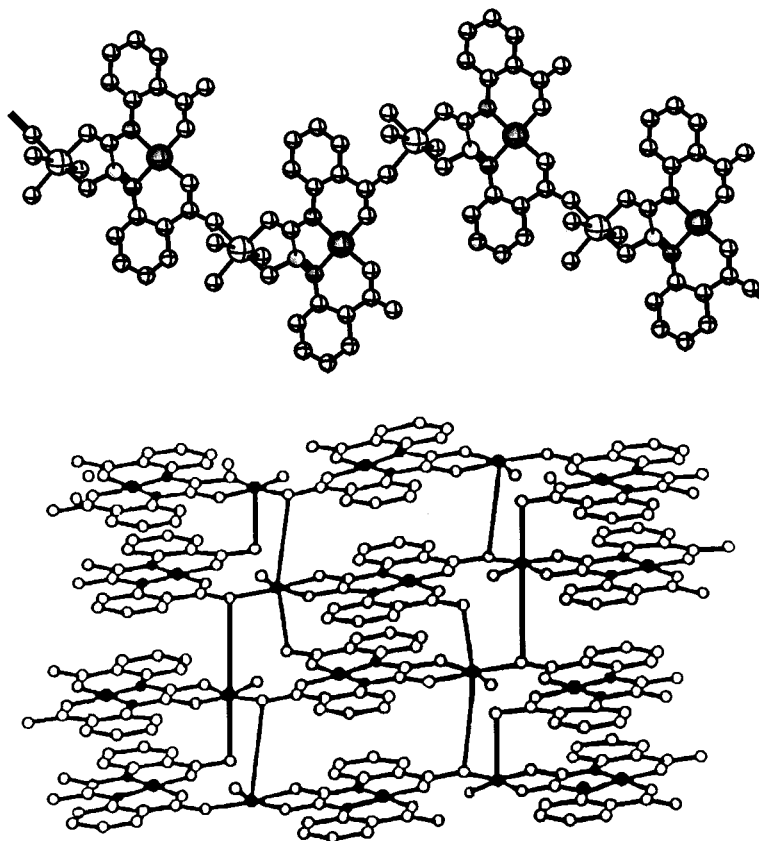
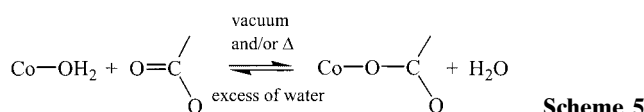


Fig. 14. Proposed chain structure for $\text{CoCu}(\text{obbz})(\text{H}_2\text{O})_3$ and the two-dimensional structure for $\text{CoCu}(\text{obbz})(\text{H}_2\text{O})$, obtained by association of chains [46].



The non-magnetic compound $\text{CoCu}(\text{obze})(\text{H}_2\text{O})_4 \cdot 2\text{H}_2\text{O}$ could also be grown as single crystals and converted to the ferrimagnetic state upon dehydration at 190°C , with T_C values of 20 K, and H_{coerc} of 1 kOe at 2 K. The color of the compound changed from violet to dull green on dehydration and back to violet on rehydration [45]. The structure of $\text{CoCu}(\text{obze})(\text{H}_2\text{O})_4 \cdot 2\text{H}_2\text{O}$ is isomorphous with that of $\text{MnCu}(\text{obze})(\text{H}_2\text{O})_4 \cdot 2\text{H}_2\text{O}$ [48], with the Co environment identical with that observed for $\text{CoCu}(\text{obbz})(\text{H}_2\text{O})_4 \cdot 2\text{H}_2\text{O}$. Interestingly, for both $\text{CoCu}(\text{obbz})(\text{H}_2\text{O})_4 \cdot 2\text{H}_2\text{O}$ and $[\text{CoCu}(\text{obze})(\text{H}_2\text{O})_4] \cdot 2\text{H}_2\text{O}$ the powder X-ray patterns were strongly modified on dehydration, although the compounds remained crystalline. Upon rehydration, the patterns returned to those of the starting compounds.

Reversibility of the dehydration-rehydration process is well-known for many hydrates. The novel and remarkable feature characterizing the *sponges* described here (summarized in Table 5), is the reversible release of coordinated water molecules, accompanied by a polymerization process. The Co–O bonds in $\text{CoCu}(\text{obbz})(\text{H}_2\text{O})_4 \cdot 2\text{H}_2\text{O}$, for instance, can be broken and created without destroying the fundamental molecular architecture, although it is modified reversibly. The dehydration process also increases the structural and magnetic dimensionality of this sponge from zero (for isolated molecules) to two or three, depending on the amount of dehydration; on rehydration the structure reverts to the original low dimensionality (Fig. 15). *Molecular magnetic sponges* are illustrative of the softness of the molecular lattice. Molecular chemistry thus provides a route to materials that can pass reversibly from a non-magnetic state to a magnetically ordered state, and the process of reversibility can be repeated without any fatigue of the molecule. This is certainly not possible by any of the simple solid-state chemical processing routes. Restoration of magnetic and physical properties upon rehydration points hopefully to important dividends to be reaped from a synergy between two seemingly di-

Table 5. Features of the $\text{Co}^{\text{II}}\text{Cu}^{\text{II}}$ molecular magnetic sponges after dehydration.

Compound	After dehydration	T_C (K)	H_{coerc} (Oe)	Color	Ref.
$\text{CoCu}(\text{pbaOH})(\text{H}_2\text{O})_3 \cdot 2\text{H}_2\text{O}$	$[\text{CoCu}(\text{pbaOH})(\text{H}_2\text{O})_2]$	38	5660 (2 K)	Blue to deep purple	[43]
$\text{CoCu}(\text{pba})(\text{H}_2\text{O})_3 \cdot 2\text{H}_2\text{O}$	$[\text{CoCu}(\text{pba})\text{H}_2\text{O}]$	33	300 (2 K)	Blue to purple	[45]
$\text{CoCu}(\text{obbz})(\text{H}_2\text{O})_4 \cdot 2\text{H}_2\text{O}$	$[\text{CoCu}(\text{obbz})\text{H}_2\text{O}]$	25	3000 (5 K)		[46]
$\text{CoCu}(\text{obze})(\text{H}_2\text{O})_4 \cdot 2\text{H}_2\text{O}$	$[\text{CoCu}(\text{obze})\text{H}_2\text{O}]$	20	1000 (2 K)	Violet to dull green	[45]

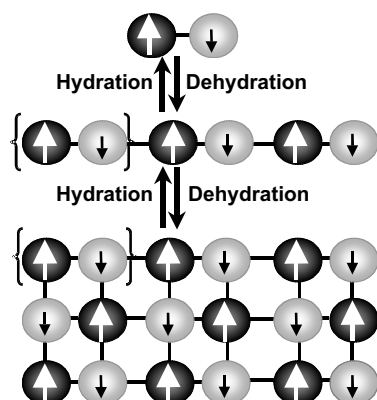


Fig. 15. The dehydration-polymerization process for ferrimagnetic precursor units [46]. The two steps, in particular, apply to $\text{CoCu}(\text{obbz})(\text{H}_2\text{O})_4 \cdot 2\text{H}_2\text{O}$ described in the text.

verse disciplines of molecular chemistry and materials science. The color change at a magnetic transition is a useful property for designing a molecular switching device, and the high value of H_{coerc} might make these molecular magnets useful in the construction of memory devices for storage of data if the T_{C} value can be increased to approximately room temperature, and the color change occurs within a few nanoseconds.

1.2.4 Alternative Techniques for the Studies of Exchange-coupled Systems

As mentioned in Section 1.2.1.4, the chain compounds can be crystallized and control of the temperature during the crystallization process enabled us to obtain crystals the size of which was sufficient for physical studies. We investigated single-crystal polarized neutron diffraction (p.n.d.) and optical spectroscopy for chain compounds to obtain precise and complementary information to that gathered by magnetic studies.

The p.n.d. technique enables the determination of spin-density maps, which give precise information on mechanisms governing the exchange interactions. For $\text{MnCu}(\text{pba})(\text{H}_2\text{O})_3 \cdot 2\text{H}_2\text{O}$ the spin density map (Fig. 4) reveals alternation of large positive spin densities (full lines) in the Mn^{II} region and weak negative spin densities (dotted lines) in the Cu^{II} region. Both positive and negative spin densities are delocalized from the metal ion towards its nearest neighbors. This delocalization is much more pronounced on the copper side than on the manganese side. This situation reflects the stronger covalency of the Cu–N (or O) bonds compared with the Mn–O bonds. A better way of comprehending the spin delocalization is to express the spin distribution with atomic spin populations. In the chain the Cu^{II} carries 76% of the negative spin density whereas the Mn^{II} carries 97.6%, which is consistent with the more covalent character of the bonds around the copper. Finally, the sum of the negative atomic spin populations is equal to $-1.05 \mu_{\text{B}}$, and that of the positive spin populations is equal to $+5.05 \mu_{\text{B}}$. This description is very close to a naive picture, when ignoring the spin delocalization, the metallic popu-

lation would be $P_{\text{Mn}} = g_{\text{Mn}}S_{\text{Mn}}$ and $P_{\text{Cu}} = -g_{\text{Cu}}S_{\text{Cu}}$, g_{Mn} and g_{Cu} being the local Zeeman factors. In fact, for antiferromagnetically $(\text{MnCu})_n$ systems, the spin populations on the metal centers in the ground state depend on the number of repeat units n [49]. It has been shown theoretically (DFT and DMRG approaches) that for an isolated MnCu pair ($n = 1$) the ground state corresponds to mixing of the $(+5/2, -1/2)$ state with the $(+3/2, +1/2)$ state. When n increases contamination of the $(+3/2, +1/2)$ state decreases, and then the ground state is only characterized by the $(+5/2, -1/2)$ component. These theoretical calculations are satisfactorily confirmed by the experimental results.

The single-crystal polarized optical spectra of $\text{MnCu}(\text{pba})(\text{H}_2\text{O})_3 \cdot 2\text{H}_2\text{O}$ at room temperature is shown Fig. 16 [17]. Strong polarization of the absorption is observed in the chain direction, because of the strong polarization of the Cu^{II} band at around 16000 cm^{-1} in this direction. They also reveal narrow and intense formally spin-forbidden Mn^{II} transitions ${}^6\text{A}_{1\text{g}} \rightarrow {}^4\text{A}_{1\text{g}}, {}^4\text{E}_{\text{g}}$ (O_h) around 24000 cm^{-1} activated by an exchange mechanism and strongly temperature-dependent [50]. Both polarization and thermal features of these bands have been interpreted in the pair mechanism, first introduced by Tanabe. In particular, these optical studies offer an alternative means of determining the exchange parameter with the detailed temperature-dependence studies of the spin-forbidden transitions. In the MnCu chain compound,

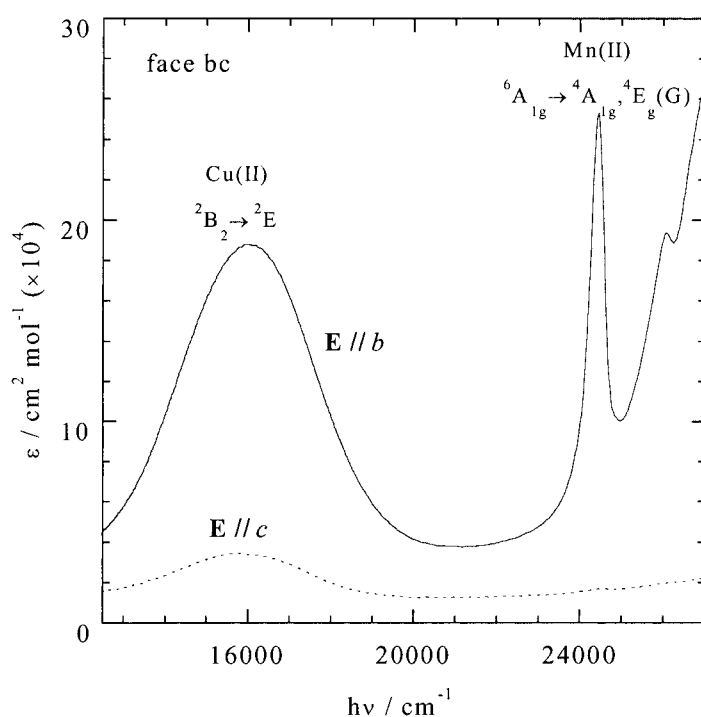


Fig. 16. Polarized optical absorption spectra at room temperature perpendicular to the bc face of a single crystal of $\text{MnCu}(\text{pba})(\text{H}_2\text{O})_3 \cdot 2\text{H}_2\text{O}$ [17].

J has been found to be $J_{\text{opt}} = -25 \text{ cm}^{-1}$, which is exactly the value deduced from magnetic studies. The optical technique also enables information to be obtained about the excited state reached. In fact, careful thermal study of the spin-forbidden Mn^{II} transitions reveals cold and hot components the energy difference of which has been directly related to J and J^* , where J^* is the exchange parameter between Cu^{II} and Mn^{II} in its first excited state. Our study revealed a J^* value equal to $+40 \text{ cm}^{-1}$. The change of sign between J (antiferromagnetic interaction between Cu^{II} and Mn^{II}) and J^* (ferromagnetic interaction between Cu^{II} and $\text{Mn}^{*\text{II}}$) is surprising, and not yet fully understood. This behavior has been already described for other MnCu compounds [51].

1.3 Bimetallic Magnets Based on Second- and Third-row Transition Metal Ions

The ions from the second and third transition metal series have been considered only very recently as spin carriers for the preparation of bimetallic magnets. These ions are characterized by more diffuse valence orbitals compared with their 3d congeners, a trend following the sequence $5d > 4d \gg 3d$. To magnetochemists a more diffuse singly occupied orbital suggests that an enhanced exchange interaction might be expected between magnetic centers. Spin-orbit coupling is also often observed for these ions, and is characteristic of compounds with magnetic anisotropy. A limitation might, however, be that the ground state of species containing 4d or 5d metal ions is usually derived from a strong field configuration, i. e. they are low-spin.

We will see below that the first information gathered from compounds containing transition metal ions from the second or third series suggests exciting possibilities for the preparation of bimetallic magnets with increased critical temperatures, with coercivity, or even with photomagnetic properties. They also address the question of the validity for 4d or 5d metal ions of rules applying for the analysis of the magnetic properties of bimetallic compounds containing only 3d metals ions.

1.3.1 Examples of Ru(III)-based Compounds

The first example of molecule-based magnets involving metal ions from the second or third transition metal series was an oxalate-bridged polymeric compound synthesized from the building block $[\text{Ru}^{\text{III}}(\text{oxalato})_3]^{3-}$ [52]. In this environment, the Ru ion has a low-spin d^5 electron configuration with a magnetic moment of $2.03 \mu_{\text{B}}$ at room temperature [53]. The reaction of $[\text{Ru}(\text{ox})_3]^{3-}$ with Mn^{II} , Fe^{II} , or Cu^{II} in the presence of tetrabutylammonium resulted in the formation of the two dimensional compound, $(\text{NBu}_4)[\text{M}^{\text{II}}\text{Ru}^{\text{III}}(\text{ox})_3]$, which has a honeycomb structure.

The molar magnetic susceptibility data for $(\text{NBu}_4)[\text{Fe}^{\text{II}}\text{Ru}^{\text{III}}(\text{ox})_3]$ are represented in Fig. 17 in the form of the $\chi_{\text{M}}T$ versus T plot. The minimum in the curve,

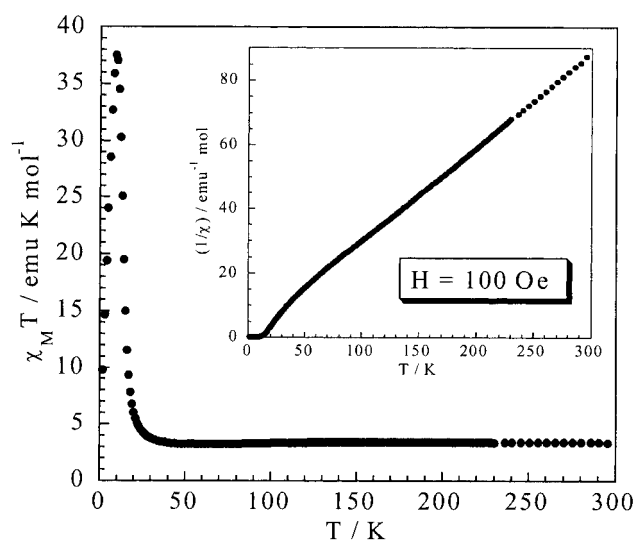


Fig. 17. $\chi_M T$ versus T curve for $(\text{NBu}_4)[\text{Fe}^{\text{II}}\text{Ru}^{\text{III}}(\text{ox})_3]$. In the inset, temperature dependence of $1/\chi_M$ [52] (reproduced with permission; Copyright 2001, the American Chemistry Society).

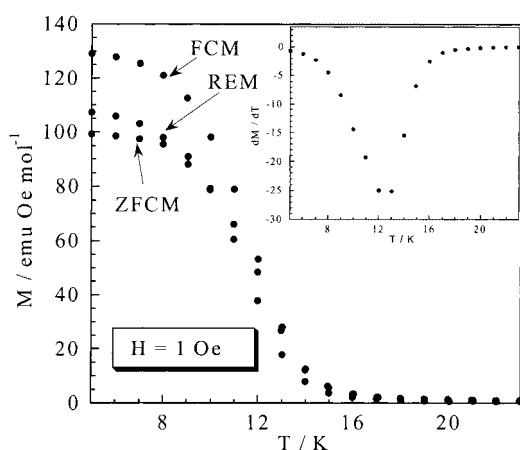


Fig. 18. Field-cooled magnetization (FCM), zero field cooled magnetization (ZFCM), and remnant magnetization (REM) plots for $(\text{NBu}_4)\text{Fe}^{\text{II}}\text{Ru}^{\text{III}}(\text{ox})_3$.

even if weakly pronounced, indicates ferrimagnetic behavior with a $\text{Ru}^{\text{III}}\text{-Fe}^{\text{II}}$ anti-ferromagnetic interaction. The low-temperature data suggest that the compound has long-range magnetic ordering. This is confirmed by the field cooled-magnetization (FCM) and remnant magnetization (REM) curves shown in Fig. 18. The FCM curve shows a steep rise of the magnetization below 13 K and the REM curve indicates that the remnant magnetization vanishes when the sample is heated to 13 K, behavior typical of a magnet. Confirmation of the three-dimensional ordering at $T_C = 13$ K was provided by the temperature dependencies of the ac magnetic responses. Both

the in-phase, χ'_M , and out-of-phase, χ''_M , ac magnetic susceptibilities pass through a maximum.

We have already mentioned that the coercivity of a magnet is governed by both chemical and structural factors. The chemical factor is the magnetic anisotropy of the spin carriers and the structural factors are the crystal lattice symmetry and the size and shape of the grains. In this species both Fe^{II} and Ru^{III} in distorted octahedral surroundings are orbital triplet ions with first-order orbital momentum. These ions therefore have magnetic anisotropy. The field dependence of the magnetization measured at 2 K for (NBu₄)[Fe^{II}Ru^{III}(ox)₃] reveals indeed the occurrence of a magnetic hysteresis loop, with a coercive field of 1.55 kOe.

In contrast with the previous compound, long-range magnetic ordering is not observed for (NBu₄)[Mn^{II}Ru^{III}(ox)₃] and (NBu₄)[Cu^{II}Ru^{III}(ox)₃] in the temperature domain investigated. The magnetic behavior of these two compounds indicates that the Cu^{II}-Ru^{III} interaction is antiferromagnetic whereas the Mn^{II}-Ru^{III} interaction is ferromagnetic. The magnetic behavior of the Mn^{II}-Ru^{III} and Fe^{II}-Ru^{III} compounds could be analyzed quantitatively with a theoretical model for a honeycomb lattice [54]. The spin Hamiltonian considered in the model is given in Eq. (1) where the index M refers to the classical spin ion, Mn^{II} or Fe^{II}. Both single-ion anisotropy for the M^{II} ion and anisotropic interaction have been neglected. The analytical expression used to fit the experimental data is given in Eq. (2). This expression is valid for honeycomb lattices with alternation of quantum S_{Ru} and classical S_M spins at the corners of the hexagons and for $T \gg |J|S/2$. For (NBu₄)[Fe^{II}Ru^{III}(ox)₃] least-squares fitting to the magnetic susceptibility data down to 20 K led to $J = -9.7 \text{ cm}^{-1}$, $g_{Ru} = 2.10$, and $g_{Fe} = 2.13$. For (NBu₄)[Mn^{II}Ru^{III}(ox)₃] fitting down to 5 K gave $J = 1.04 \text{ cm}^{-1}$, $g_{Ru} = 2.1$, and $g_{Mn} = 1.97$.

$$\mathbf{H} = -J \sum_{i,j} \mathbf{S}_{Ru,i} \cdot \mathbf{S}_{M,j} + \left(g_{Ru} \sum_i \mathbf{S}_{Ru,i} + g_M \sum_j \mathbf{S}_{M,j} \right) \cdot H\beta \quad (1)$$

$$\chi_M T = \frac{3}{8} \left[S^2 g_M^2 y_1 - S g_M g_{Ru} \frac{y_2}{2} + g_{Ru}^2 \frac{y_3}{4} \right] \quad (2)$$

where $y_1 = 0.3353 + 0.0186 K + 0.5049 K^2 + 0.4534 K^3$, $y_2 = -0.0009 + 2.0583 K - 0.3351 K^2 + 1.8454 K^3$, $y_3 = 1.0095 + 0.0214 K + 1.1352 K^2 + 0.5341 K^3$, $K = -JS/2kT$, and $S = [S_M(S_M + 1)]^{1/2}$

The magnetic properties of these compounds have revealed that with M = Mn the Ru^{III}-M^{II} interaction is ferromagnetic whereas it is antiferromagnetic with M = Cu and Fe. (NBu₄)[Cu^{II}Ru^{III}(ox)₃] is interesting because the nature of the interaction does not respect the symmetry rules valid for the 3d metal ions. It is now well understood that the nature of the interaction between two 3d magnetic centers is governed to a large extent by the relative symmetries of the magnetic orbitals [13]. A non-zero overlap integral between two magnetic orbitals favors an antiferromagnetic contribution whereas a zero overlap favors a ferromagnetic contribution. When the interaction occurs between ions carrying more than one unpaired electron the nature of the interaction is usually given by the weighted sum of each contribu-

tion. These rules are in accordance with the ferromagnetic interactions found for $\text{Cu}^{\text{II}}\text{-Cr}^{\text{III}}$ or $\text{Ni}^{\text{II}}\text{-Cr}^{\text{III}}$ oxalate compounds. The Ru^{III} ion in octahedral surrounding has a low-spin state arising from the t_{2g}^5 configuration. Each of the t_{2g} orbitals centered on Ru is orthogonal with the dx^2dy^2 type magnetic orbital of Cu^{II} . On the basis of the orbital symmetries a ferromagnetic $\text{Cu}^{\text{II}}\text{-Ru}^{\text{III}}$ interaction might have been expected but it is found to be antiferromagnetic in $(\text{NBu}_4)[\text{Cu}^{\text{II}}\text{Ru}^{\text{III}}(\text{ox})_3]$. Obviously, the symmetry rules which applied for analysis of the magnetic properties of polymetallic compounds formed with 3d metal ions seem not to be transposable to Ru^{III} . A reason might be that the spin-orbit coupling mixes the symmetry orbitals so that the eigenfunctions can no longer be labeled with the irreducible representations of the symmetry point groups. Study of more examples of exchanged coupled systems involving Ru^{III} will be necessary to rationalize this situation.

A second compound in which Ru^{III} is in exchange interaction with Mn^{II} has been described. It consists in a 3D network of $\text{Ru}(\text{acac})_2(\text{CN})_2$ units linked to Mn^{II} ions and has long-range magnetic ordering at approximately 4 K [55]. Interestingly, the magnetic behavior reveals that the $\text{Ru}^{\text{III}}\text{-Mn}^{\text{II}}$ interaction through the cyano ligand is ferromagnetic as through the oxalato-link in $(\text{NBu}_4)[\text{Mn}^{\text{II}}\text{Ru}^{\text{III}}(\text{ox})_3]$.

1.3.2 Mo, Nb, and W-cyanometalate-based Magnets

As for their 3d metal ion counterpart, cyanometalate derivatives of 4d and 5d ions have also been envisaged for the preparation of bimetallic magnets. For instance, $[\text{Nb}^{\text{IV}}(\text{CN})_8]^{4-}$, $[\text{Mo}^{\text{III}}(\text{CN})_7]^{4-}$, and $[\text{W}^{\text{V}}(\text{CN})_8]^{3-}$ afford extended three-dimensional networks in the presence of Mn^{II} ions. The structure of $[\text{Mn}_2(\text{H}_2\text{O})_5\text{Mo}(\text{CN})_7] \cdot 4\text{H}_2\text{O}$ is depicted in Fig. 19. In this compound the Mo^{III} center is linked through its CN ligands to seven Mn^{II} ions, and each Mn^{II} center is thus connected to either three or four Mo units, setting up a 3D network. The compounds formed with the three cyanometalates behave as magnets characterized by T_C values of approximately 50 K (50, 51, and 54 K, respectively, for the Nb [56], Mo [57, 58], and W [59] derivatives).

The magnetic properties of the two phases of compound $\text{Mn}_2(\text{H}_2\text{O})_5\text{Mo}(\text{CN})_7 \cdot x\text{H}_2\text{O}$ (phase α , $x = 4$ and phase β , $x = 4.75$) have been deeply investigated and revealed rather complex behavior. These studies have been described in detail and we will recall here only the general features of these materials. The temperature dependence of the magnetic susceptibility of $\text{Mn}_2(\text{H}_2\text{O})_5\text{Mo}(\text{CN})_7 \cdot 4\text{H}_2\text{O}$ (phase α) is represented in Fig. 20 as a plot of $\chi_M T$ against T . It is worth noting that in the temperature range above T_C , i. e. 300 to 50 K, $\chi_M T$ increases continuously as T is reduced. The plot of $1/\chi_M$ is also rather linear in the corresponding temperature domain and its extension leads to an intersection with the temperature axis at $T > 0$. Such features are usually characteristic of ferromagnetic interaction between the magnetic centers, and initial results were interpreted in this way. Polarized neutron diffraction study of a related $\text{Mn}^{\text{II}}/\text{Mo}(\text{CN})_7$ -based compound clearly established, however, that the $\text{Mn}^{\text{II}}\text{-Mo}^{\text{III}}$ interaction through the CN ligand is antiferromagnetic [60]. The spin density map shown in Fig. 21 reveals alternation of positive spin densities in the Mn ion region and negative spin density in the Mo region.

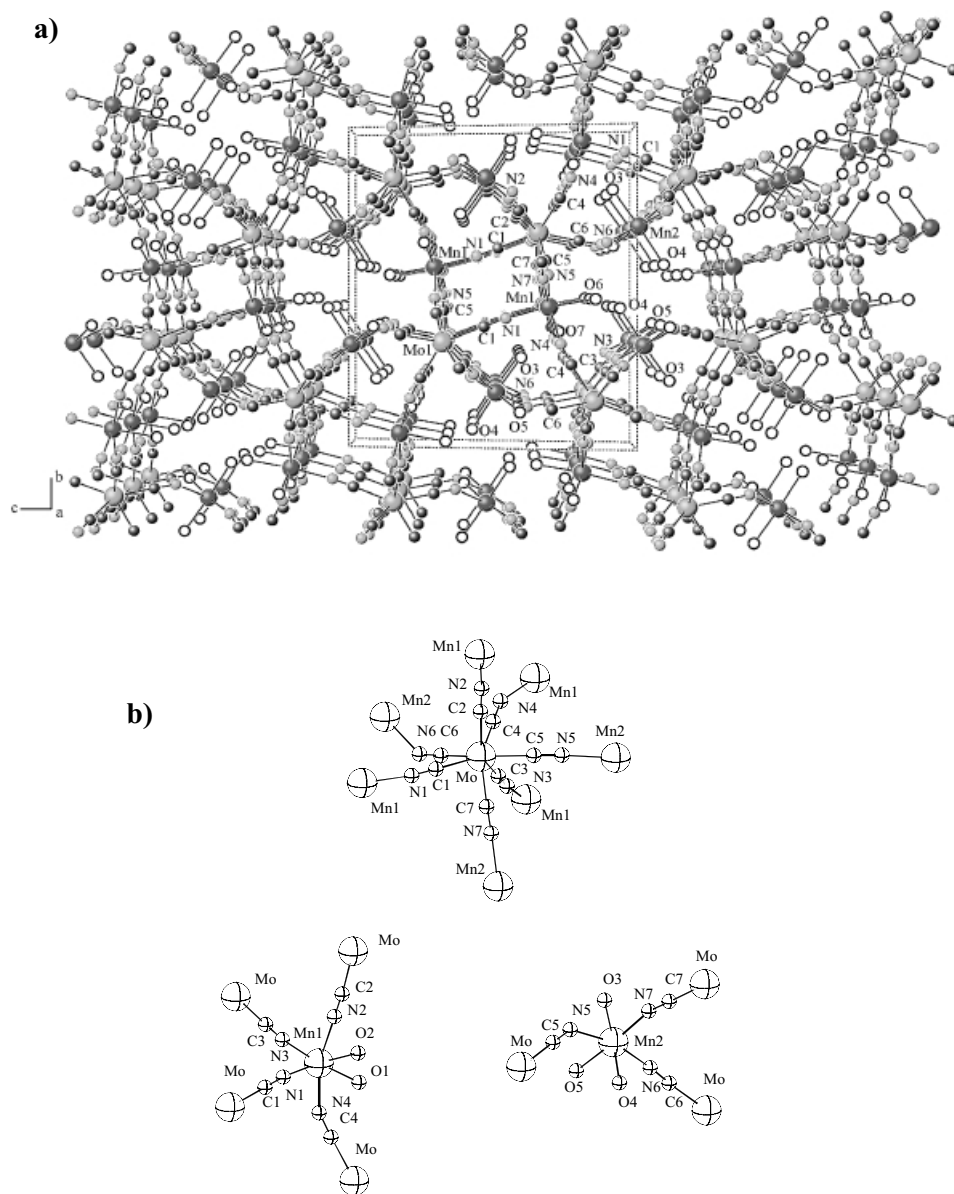


Fig. 19. $\text{Mn}_2(\text{H}_2\text{O})_5\text{Mo}(\text{CN})_7 \cdot 4\text{H}_2\text{O}$: (a) view of the 3D network; (b) coordination spheres of the Mo^{III} and Mn^{II} centers.

An important feature of $\text{Mn}_2(\text{H}_2\text{O})_5\text{Mo}(\text{CN})_7 \cdot x\text{H}_2\text{O}$ ferrimagnets is their strong magnetic anisotropy. Results from measurement of the dependence of M on T and M on H (Fig. 22), performed on oriented crystals, are explicit. The origin of this anisotropy is ascribed to the $4d^3$ low spin Mo^{III} ion ($S = 1/2$) in the $\text{Mo}(\text{CN})_7$

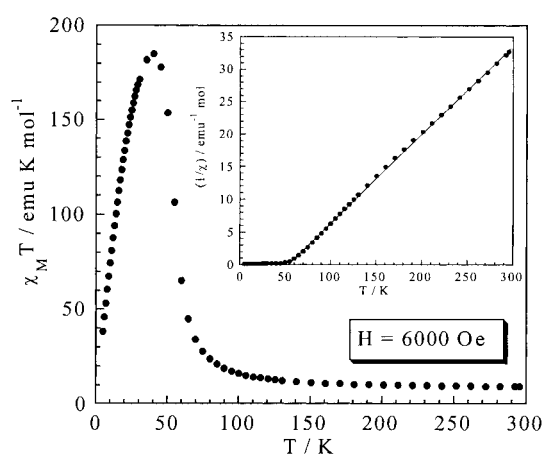


Fig. 20. Temperature-dependence of $\chi_M T$ for a polycrystalline sample of $\text{Mn}_2(\text{H}_2\text{O})_5\text{Mo}(\text{CN})_7 \cdot 4\text{H}_2\text{O}$ [57] (reproduced with permission; Copyright 2001, the American Chemistry Society).

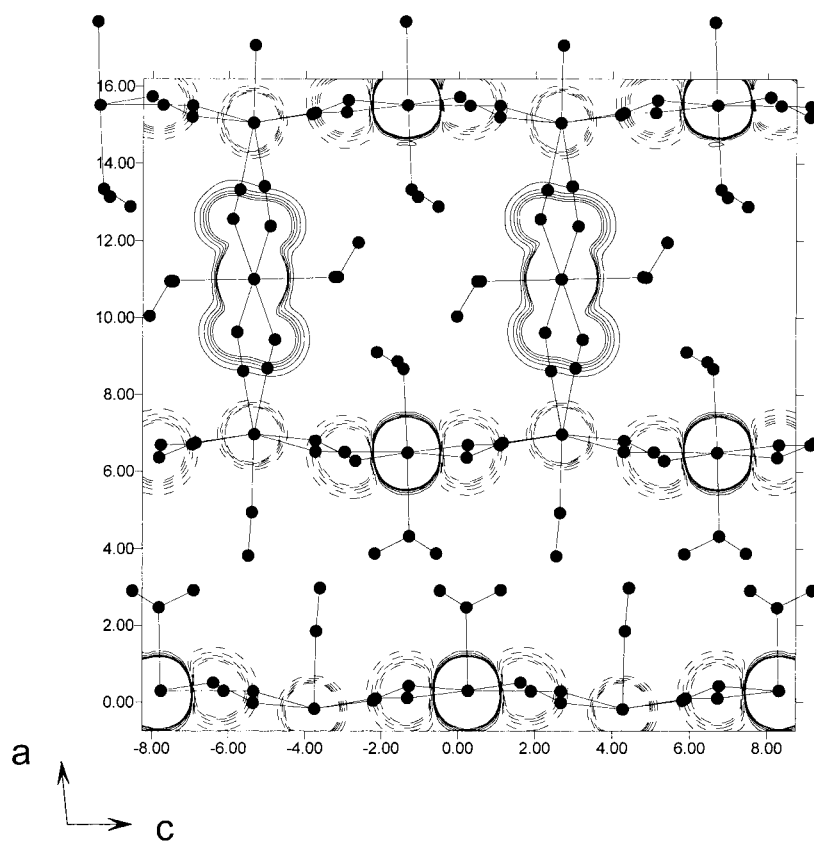


Fig. 21. Spin density map of the bi-dimensional compound, $\text{K}_2\text{Mn}_3(\text{H}_2\text{O})_6\text{Mo}(\text{CN})_7 \cdot 6\text{H}_2\text{O}$ at 4 K (applied field, 3 T) projected along the crystallographic b axis. Solid lines denote positive contours, dashed lines denote negative contours [60] (reproduced with the permission of the editor).

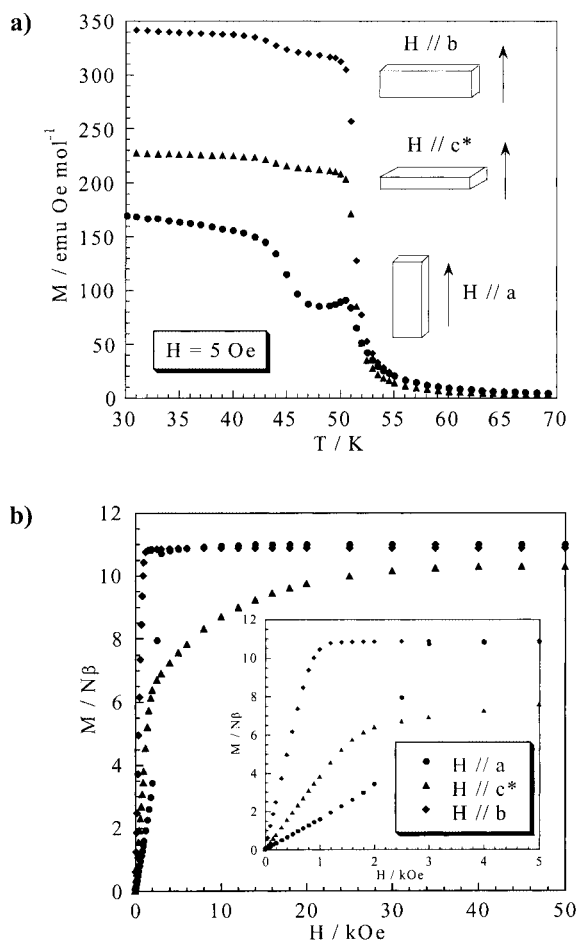


Fig. 22. (a) Temperature dependence of the magnetization for $\text{Mn}_2(\text{H}_2\text{O})_5\text{Mo}(\text{CN})_7 \cdot 4\text{H}_2\text{O}$ along the a , b , and c^* directions (external field $H = 5 \text{ Oe}$). (b). Field dependence of the magnetization at $T = 5 \text{ K}$ [57] (reproduced with permission; Copyright 2001, the American Chemistry Society).

environment for which the strongly anisotropic g tensor have been found [61, 62]. Other factors, e. g. the anisotropic components of the $\text{Mo}^{\text{III}}\text{-Mn}^{\text{II}}$ interaction resulting from the local spin-orbit coupling for the Mo^{III} , and the low symmetry of the crystal lattice might make significant contributions to the magnetic anisotropy of these compounds [63]. Despite the anisotropy, however, no coercivity is observed.

The magnetic properties of the $\text{Mn}_2(\text{H}_2\text{O})_5\text{Mo}(\text{CN})_7 \cdot x\text{H}_2\text{O}$ compounds are modified by partial dehydration leading to an increase in T_C up to 65 K and to the appearance of a magnetic hysteresis with a coercive field of 850 Oe at 5 K. An even more pronounced effect is observed for the bidimensional compound $\text{K}_2[\text{Mn}_3(\text{H}_2\text{O})_6\text{Mo}(\text{CN})_7] \cdot 6\text{H}_2\text{O}$ involving the same spin carriers; for this T_C is in-

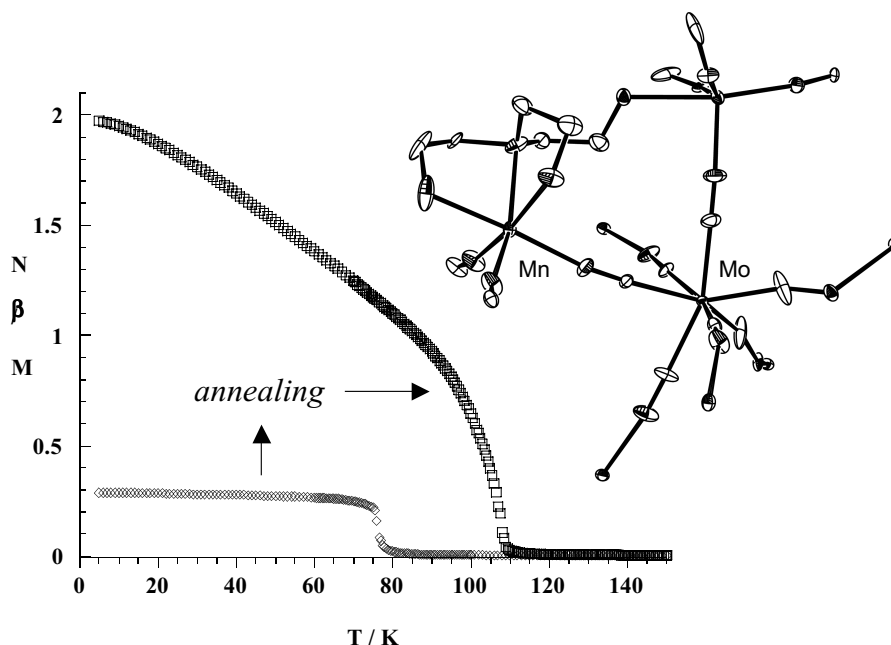


Fig. 23. Detail of the Mn–Mo connectivity in the 3D framework of $\text{Mn}_2(\text{tea})\text{Mo}(\text{CN})_7 \cdot \text{H}_2\text{O}$ and temperature-dependence of the magnetization ($H = 50$ Oe) before and after annealing.

creased from 39 to 72 K after H_2O is released from the network. For this compound dehydration also induces an increase in coercivity. Related effects are observed when pressure is applied to the compound [64]. These observations suggest that slight modification of the lattice and/or the coordination spheres of the metal ions might have an important effect on the magnetic properties of the compounds. Substitution of H_2O by an ancillary ligand in the coordination sphere of the M^{II} ion could be an easy way to control the conformation of such networks and, consequently, their magnetic properties. A first result in this direction has been obtained for the compound $\text{Mn}_2(\text{tea})\text{Mo}(\text{CN})_7 \cdot \text{H}_2\text{O}$, where *tea* stands for triethanolamine. For this compound the ordering temperature is 75 K and can be further increased to 106 K by smooth annealing (Fig. 23) [65]. The spin carriers and their connectivity in the compound with a T_{C} of 75 K are the same than those for the compound with $T_{\text{C}} = 51$ K; the different magnetic behavior is clearly the result of small conformational differences in the structure.

It is interesting to compare the magnetic properties of a compound like $\text{Mn}_2(\text{tea})\text{Mo}(\text{CN})_7 \cdot \text{H}_2\text{O}$ with a related compound, $\text{Mn}_3[\text{Fe}(\text{CN})_6]_2 \cdot 15\text{H}_2\text{O}$. For both compounds the metal ion of the cyanometalate unit bears a local spin of $S = 1/2$ but whereas the T_{C} for the compound formed with the 3d ion derivative is found at 9 K, the compound with the 4d ion, Mo^{III} , has T_{C} for 75 K and even higher after annealing. The same is also true for the compounds obtained with the cyanometalates of Nb^{IV} and W^{V} , which also have a local spin of $S = 1/2$.

1.3.3 Light-induced Magnetism

A recent issue in molecule-based magnets is light-driven magnetism, commonly called photomagnetism. For instance, long range magnetic order can be induced by light irradiation of Prussian-blue derivatives involving Fe–Co pairs. The photo-physical properties of metal ions from the second and third transition metal series is well documented, and their potential as photo-active building blocks in magnetic materials has been demonstrated with Mo^{IV} -based compounds. For instance, the three dimensional compound obtained by reaction of the diamagnetic $[\text{Mo}^{\text{IV}}(\text{CN})_8]^{4-}$ building block and Cu^{II} ions has paramagnetic behavior down to 2 K. When this compound is irradiated long-range magnetic interactions are observed (Fig. 24) [66–68]. The appearance of the magnetic interaction is a consequence of the photo-oxidation of Mo. Upon irradiation in the energy range of the intervalence charge-transfer band of the compound the diamagnetic Mo^{IV} transfers an electron to a neighboring Cu^{II} ion and becomes Mo^{V} which is paramagnetic with a local spin of $S = 1/2$. This magnetic center is then exchange-coupled with the remaining Cu^{II} paramagnetic centers and long-range correlation appears as the Mo^{IV} ions are oxidized to Mo^{V} . Related results are found for the chain compound $\text{Mn}^{\text{II}}(\text{L})_2(\text{H}_2\text{O})\text{Mo}^{\text{IV}}(\text{CN})_8 \cdot 5\text{H}_2\text{O}$, where L stand for a macrocyclic ligand [69].

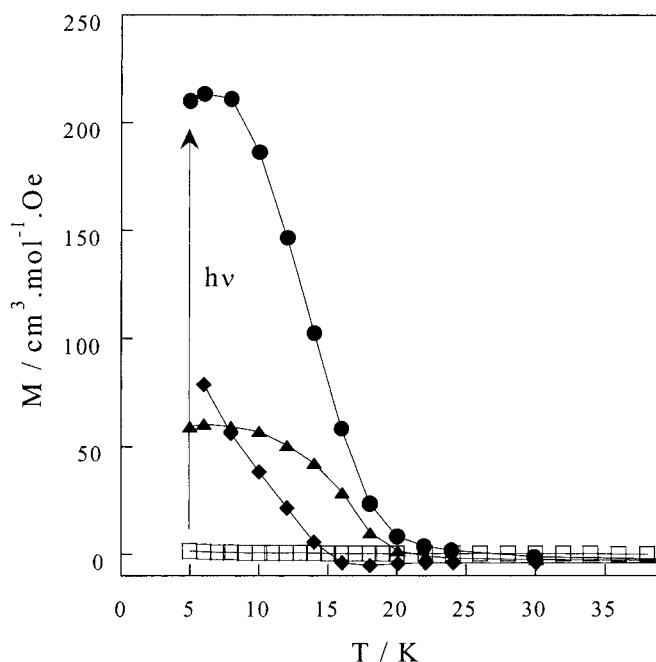


Fig. 24. Dependence of magnetization on T for the compound $\text{Cu}_2\text{Mo}(\text{CN})_8 \cdot 5\text{H}_2\text{O}$ before (\square) and after (FCM \bullet , REM \blacklozenge and ZFCM \blacktriangle) irradiation at 530 nm.

This section would not be complete without mention of the very promising results obtained with 4d and 5d metal ions in the construction of high-spin molecules (discussion of high-spin molecules is available elsewhere [9]). Starting from $[\text{M}(\text{CN})_8]^{3-}$ ($\text{M} = \text{Mo}^{\text{V}}$ or W^{V}) and Mn^{II} ions, well defined $\{\text{Mn}_9\text{M}_6\}$ molecular clusters with a ground state of $S = 39/2$ and $51/2$, respectively, for the W and Mo derivative, could be synthesized [70, 71]. Related compounds are obtained with the diamagnetic Mo^{IV} and W^{IV} building blocks; this suggests the possibility of photo-induced magnetism for these aggregates in the same way as for the 3D compounds [72].

The first molecule-based compound involving 4d metal ions and with long-range magnetic interactions was described in 1998. Since then a few more heterobimetallic magnets formed with building blocks comprising ions from the second or third transition series have been reported. A general feature of these materials is the temperature at which magnetic order is found $-T_C$ is significantly higher than for most of the related 3d ion-based magnets. The spin-orbit coupling occurring for these ions might, moreover, lead to materials with magnetic anisotropy, another important feature of magnets, as was found for Mo^{III} -based compounds. Although the limited number of compounds and the diversity of spin carriers studied do not currently enable conclusions to be drawn about general trends, it seems obvious that these ions warrant more systematic investigation.

1.4 Concluding Remarks

The prominent role of structural dimensionality and nature of the active magnetic centers on the main characteristics of magnets, which are the temperature below which spontaneous magnetization is observed and the magnetic anisotropy which confers a memory effect to the material, are now well established and understood. The supramolecular chemistry of open-shell architectures provides versatile access to compounds of desired topology and composition, and it is therefore possible to design materials with properties predetermined at synthesis. Molecule-based magnets with giant coercivity or complex magnetic behavior, e. g. multiple magnetization-inversion can be prepared rationally.

Until now most studies have been on 3d paramagnetic ions; only very recently have the heavier congeners, the 4d and 5d transition metal ions, been investigated. The first results gathered with such ions show that not only do they have all the features regarded as desirable in the contemporary study of molecular magnetism, for example magnetic anisotropy or photo-physical properties, but the materials obtained have spontaneous magnetization at temperature significantly higher than those found for related 3d analogs. This opens interesting perspectives for the preparation of high- T_C magnets and the number of molecule-based magnets involving these ions will certainly increase rapidly in the coming years.

References

- [1] J. S. Miller, J. C. Calabrese, H. Rommelman, S. R. Chittipedi, J. H. Zang, W. M. Reiff, A. J. Epstein, *J. Am. Chem. Soc.* **109** (1987) 769.
- [2] O. Kahn, Y. Pei, M. Verdaguer, J. P. Renard, J. Sletten, *J. Am. Chem. Soc.* **110** (1988) 782.
- [3] O. Kahn, *Adv. Inorg. Chem.* **43** (1995) 179.
- [4] K. Monoyama, H. Ojima, M. Monoyama, *Inorg. Chim. Acta* **20** (1976) 127.
- [5] Y. Pei, Y. Journaux, O. Kahn, *Inorg. Chem.* **27** (1988) 399.
- [6] Y. Pei, M. Verdaguer, O. Kahn, J. Sletten, J.-P. Renard, *Inorg. Chem.* **26** (1987) 138.
- [7] E.-Q. Gao, J.-K. Tang, D.-Z. Liao, Z.-H. Jiang, S.-P. Yan, G.-L. Wang, *Inorg. Chem.* **40** (2001) 3134.
- [8] O. Kahn, *Acc. Chem. Res.* **33** (2000) 647.
- [9] T. Mallah, A. Marvilliers, in J. S. Miller, M. Drillon (Eds.): *Magnetism: From Molecules to Materials, Vol. 2*, Wiley-VCH, Weinheim 2001, p. 189.
- [10] M. Fettouhi, L. Ouahab, A. Boukhari, O. Cador, C. Mathonière, O. Kahn, *Inorg. Chem.* **35** (1996) 4932.
- [11] A. Aukauloo, X. Ottenwaelder, R. Ruiz, Y. Journaux, Y. Pei, E. Rivière, B. Cervera, M. Carmen Munoz, *Eur. J. Inorg. Chem.* (1999) 209.
- [12] A. Aukauloo, X. Ottenwaelder, R. Ruiz, Y. Journaux, Y. Pei, E. Rivière, M. Carmen Munoz, *Eur. J. Inorg. Chem.* (2000) 951.
- [13] O. Kahn, *Molecular Magnetism*, VCH, Weinheim 1993.
- [14] V. Baron, B. Gillon, J. Sletten, C. Mathonière, E. Codjovi, O. Kahn, *Inorg. Chim. Acta* **235** (1995) 69.
- [15] H. O. Stumpf, Y. Pei, O. Kahn, J. Sletten, J.-P. Renard, *J. Am. Chem. Soc.* **115** (1993) 6738.
- [16] V. Baron, B. Gillon, A. Cousson, C. Mathonière, O. Kahn, A. Grand, L. Ohhrström, B. Delley, M. Bonnet, J.-X. Boucherle, *J. Am. Chem. Soc.* **119** (1997) 3500.
- [17] O. Cador, C. Mathonière, O. Kahn, *Inorg. Chem.* **39** (2000) 3799.
- [18] K. Nakatani, P. Bergerat, E. Codjovi, C. Mathonière, Y. Pei, O. Kahn, *Inorg. Chem.* **30** (1991) 3978.
- [19] O. Cador, D. Price, J. Larionova, C. Mathonière, O. Kahn, J. V. Yakhmi, *J. Chem. Mat.* **7** (1997) 1263.
- [20] J. Léandri, Y. Leroyer, S. V. Meshkov, Y. Meurdesoif, O. Kahn, B. Mombelli, D. Price, *J. Phys. Condens. Matter* **8** (1996) L271.
- [21] S. Turner, C. Michaut, O. Kahn, L. Ouahab, A. Lecas, E. Amouyal, *New J. Chem.* **19** (1995) 773.
- [22] C. Surville-Barland, R. Ruiz, A. Aukauloo, Y. Journaux, I. Castro, B. Cervera, M. Julve, F. Lloret, F. Sapina, *Inorg. Chimica Acta* **278** (1998) 159.
- [23] J.-C. Colin, Y. Journaux, *C. R. Acad. Sci. Chim.* **4** (2001) 207.
- [24] Y. Pei, S. Turner, L. Fournes, J. S. Miller, O. Kahn, *J. Mater. Chem.* **6** (1996) 1521.
- [25] M. Pilkington, S. Decurtins, in J. S. Miller, M. Drillon (Eds.): *Magnetism: From Molecules to Materials, Vol. 2*, Wiley-VCH, Weinheim 2001.
- [26] R. Ruiz, C. Surville-Barland, Y. Journaux, J.-C. Colin, I. Castro, B. Cervera, M. Julve, F. Lloret, F. Sapina, *Chem. Mater.* **9** (1997) 201.
- [27] H. O. Stumpf, L. Ouahab, Y. Pei, D. Grandjean, O. Kahn, *Science* **261** (1993) 447.
- [28] H. O. Stumpf, Y. Pei, O. Kahn, J. Sletten, J. P. Renard, *J. Am. Chem. Soc.* **116** (1994).
- [29] M. G. F. Vaz, L. M. M. Pinheiro, H. O. Stumpf, A. F. C. Alcântara, S. Golhen, L. Ouahab, O. Cador, C. Mathonière, O. Kahn, *Chem. Eur. J.* **5** (1999) 1486.

- [30] M. G. F. Vaz, H. O. Stumpf, N. L. Speziali, C. Mathonière, O. Cador, *Polyhedron* 20 (2001) 1761.
- [31] O. Cador, M. G. F. Vaz, H. O. Stumpf, C. Mathonière, O. Kahn, *Synth. Metals* 122 (2001) 559.
- [32] O. Guillou, O. Kahn, R. L. Oushoorn, K. Boubekeur, P. Batail, *Inorg. Chim. Acta* 198-200 (1992) 119.
- [33] M. L. Kahn, M. Verelst, P. Lecante, C. Mathonière, O. Kahn, *Eur. J. Inorg. Chem.* (1999) 527.
- [34] M. L. Kahn, C. Mathonière, O. Kahn, *Inorg. Chem.* 38 (1999) 3692.
- [35] M. Evangelisti, F. Bartolome, J. Bartolome, M. L. Kahn, O. Kahn, *J. Magn. Mag. Mat.* 196-197 (1999) 584.
- [36] M. Evangelisti, J. Bartolome, F. Mettes, L. J. de Jongh, M. L. Kahn, C. Mathonière, O. Kahn, *Polyhedron* 20 (2001) 1447.
- [37] M. L. Kahn, P. Lecante, M. Verelst, C. Mathonière, O. Kahn, *Chem. Mater.* 12 (2000) 3073.
- [38] O. Kahn, O. Guillou, in C. J. O'Connor (Ed.): *Research frontiers in magnetochemistry*, World Scientific, Singapore 1993.
- [39] J. P. Costes, F. Dahan, A. Dupuis, J. P. Laurent, *Chem. Eur. J.* 4 (1998) 1616.
- [40] C. Daiguebonne, O. Guillou, M. L. Kahn, O. Kahn, R. L. Oushoorn, K. Boubekeur, *Inorg. Chem.* 40 (2001) 176.
- [41] O. Cador, M. G. F. Vaz, H. O. Stumpf, C. Mathonière, *J. Magn. Magn. Mat.* 234 (2001) 6.
- [42] L. Néel, *Ann. Phys.* 3 (1948) 137.
- [43] S. Turner, O. Kahn, L. Rabardel, *J. Am. Chem. Soc.* 118 (1996) 6428.
- [44] J. Larionova, S. A. Chavan, J. V. Yakhmi, A. Gulbrandsen, J. Sletten, C. Sourisseau, O. Kahn, *Inorg. Chem.* 36 (1997) 6374.
- [45] S. A. Chavan, J. Larionova, O. Kahn, J. V. Yakhmi, *Phil. Mag. B* 6 (1998) 1657.
- [46] O. Kahn, J. Larionova, J. V. Yakhmi, *Chem. Eur. J.* 5 (1999) 3443.
- [47] K. Nakatani, J. Y. Carriat, Y. Journaux, O. Kahn, F. Lloret, J. P. Renard, Y. Pei, J. Sletten, M. Verdaguer, *J. Am. Chem. Soc.* 111 (1989) 5739.
- [48] Y. Pei, O. Kahn, K. Nakatani, E. Codjovi, C. Mathonière, J. Sletten, *J. Am. Chem. Soc.* 113 (1991) 6558.
- [49] O. Kahn, C. Mathonière, B. Srinivasan, B. Gillon, V. Baron, A. Grand, L. Ohrström, S. Ramashesha, *New J. Chem.* 21 (1997) 1037.
- [50] P. J. Mac Carthy, H. U. Güdel, *Coord. Chem.* 88 (1988) 89.
- [51] J. Ferré, M. Régis, *Solid State Com.* 26 (1978) 255.
- [52] J. Larionova, B. Mombelli, J. Sanchiz, O. Kahn, *Inorg. Chem.* 37 (1998) 679.
- [53] R. W. Olliff, A. L. Odell, *J. Chem. Soc.* (1964) 2467.
- [54] B. Mombelli, O. Kahn, Y. Leroyer, S. Meshkov, Y. Meurdesoif, *J. Phys.: Condens. Matter.* 10 (1998) 5187.
- [55] W. F. Yeung, W. L. Man, W. T. Wong, T. C. Lau, S. Gao, *Angew. Chem. Int. Ed. Engl.* 40 (2001) 3031.
- [56] M. Pilkington, S. Decurtins, *Chimia* 54 (2000) 593.
- [57] J. Larionova, R. Clérac, J. Sanchiz, O. Kahn, S. Golhen, L. Ouahab, *J. Am. Chem. Soc.* 120 (1998) 13088.
- [58] J. Larionova, O. Kahn, S. Golhen, L. Ouahab, R. Clérac, *Inorg. Chem.* 38 (1999) 3621.
- [59] Z. J. Zhong, H. Seino, Y. Mizobe, M. Hidai, M. Verdaguer, S.-I. Ohkoshi, K. Hashimoto, *Inorg. Chem.* 39 (2000) 5095.
- [60] J. A. Stride, B. Gillon, A. Goukassov, J. Larionova, R. Clérac, O. Kahn, *C. R. Acad. Sci. Paris, Chem.* 4 (2001) 105.

- [61] M. B. Hursthouse, K. M. A. Maijk, A. M. Soares, J. F. Gibson, W. P. Griffith, *Inorg. Chim. Acta* **45** (1980) L81.
- [62] G. R. Rossman, F. D. Tsay, H. B. Gray, *Inorg. Chem.* **12** (1973) 824.
- [63] O. Kahn, *Phil. Trans. R. Soc. Lond. A* **357** (1999) 3005.
- [64] J. Larionova, O. Kahn, J. Bartolome, R. Burriel, M. Castro, V. Ksenofontov, P. Gütlich, *Chem. Mater.* **11** (1999) 3400.
- [65] S. Tanase, F. Tuna, P. Guionneau, T. Maris, G. Rombaut, C. Mathonière, M. Andruh, O. Kahn, J.-P. Sutter, *Manuscript in preparation*.
- [66] G. Rombaut, M. Verelst, S. Golhen, L. Ouahab, C. Mathonière, O. Kahn, *Inorg. Chem.* **40** (2001) 1151.
- [67] S.-I. Ohkoshi, N. Machida, Z. J. Zhong, K. Hashimoto, *Synth. Met.* **122** (2001) 523.
- [68] S.-I. Ohkoshi, N. Machida, Y. Abe, Z. J. Zhong, K. Hashimoto, *Chem. Lett.* (2001) 312.
- [69] G. Rombaut, S. Golhen, L. Ouahab, C. Mathonière, O. Kahn, *J. Chem. Soc., Dalton Trans.* (2000) 3609.
- [70] J. Larionova, M. Gross, M. Pilkington, H. Andres, H. Stoeckli-Evans, H. U. Güdel, S. Decurtins, *Angew. Chem. Int. Ed. Engl.* **39** (2000) 1605.
- [71] Z. J. Zhong, H. Seino, Y. Mizobe, M. Hidai, A. Fujishima, S.-I. Ohkoshi, K. Hashimoto, *J. Am. Chem. Soc.* **122** (2000) 2952.
- [72] B. Sieklucka, J. Szklarzewicz, T. J. Kemp, W. Errington, *Inorg. Chem.* **39** (2000) 5156.

2 Copper(II) Nitroxide Molecular Spin-transition Complexes

Paul Rey and Victor I. Ovcharenko

2.1 Introduction

The design of molecular materials is attracting much interest from scientists, probably because it corresponds not only to a natural trend of chemical science and to an economic need of society but also to a clear and aesthetic aspect of the professional activity of chemists. Indeed, the molecular chemist is in the same situation as that of an architect who has building blocks at his disposal and seeks to build a functional structure. The building blocks at disposal of the chemist are atoms and molecular fragments from which an infinite number of structures may be designed; depending on functionality, however, the building blocks and assembling rules are different.

For example, molecular materials designed to have magnetic properties must include open shell fragments, transition metal ions or/and organic free radicals; these spin carriers must also be associated in such a way that the nature of the magnetic interactions is controlled to produce the desired bulk material property. The chemistry involved in the synthesis of molecular magnetic materials must therefore take into account the organization of all space; it is a challenging problem requiring chemical skill and intuition [1].

Pioneering investigations in this field produced extended structures in which bridging diamagnetic organic fragments mediated magnetic interactions between transition metal ions. Because most ligands mediate antiferromagnetic (spin-paired) interactions, efforts have been directed toward the synthesis of organic fragments able to link alternating, different, metal centers with the aim of obtaining ferrimagnetic structures [2–4]. Indeed, if the metal ions have different spins and are arranged regularly along a 1D (or any higher dimension) structure the resulting magnetic moment will never cancel out, irrespective of the nature (ferro- or antiferromagnetic) of the interaction. This strategy, however, suffers from an important synthetic drawback – the design of organic fragments able to organize multidimensional structures in which different metal ions are selectively and regularly arranged into two inter-penetrating sub-lattices.

This difficulty is easily overcome if one of the spins is carried by the bridging organic fragment itself. Indeed, alternation of spin carriers is then a consequence of coordination, and ferrimagnetism naturally follows from the presence of different organic ($S = 1/2$) and metallic ($S > 1/2$) magnetic centers. This strategy was

introduced in the eighties with the use of stable nitroxide free radicals as building blocks in the design of molecular magnetic materials [5, 6].

Fifteen years later it can be seen from examination of the literature that, among molecules or molecular assemblies relevant to molecular magnetism, those containing stable nitroxide free radicals are playing a particularly important role [1]. This situation is the consequence of their ability to assemble as purely organic crystals or to function as ligands towards metal ions. Thus, one understands the popularity of nitroxides in magnetic engineering, because the design of magnetic materials takes advantage of the flexibility of organic synthesis and of the diversity of magnetic situations found in coordination compounds.

2.2 Nitroxide Free Radicals as Building Blocks for Metal-containing Magnetic Species

Although nitroxides have been known for more than one hundred years [7], their chemistry was deeply investigated only in the sixties and seventies. Several hundred individual compounds characterized by the presence of at least one NO group have been prepared; these are classified as members of several classes of compound, depending on structural features related to stability [8–10].

As a general rule, the presence of protons in a position α to the oxyl group is the cause of bimolecular disproportionation of nitroxides; therefore, stable nitroxides are characterized by permethylated or aromatic substituents, or conjugated structures as shown in Fig. 1.

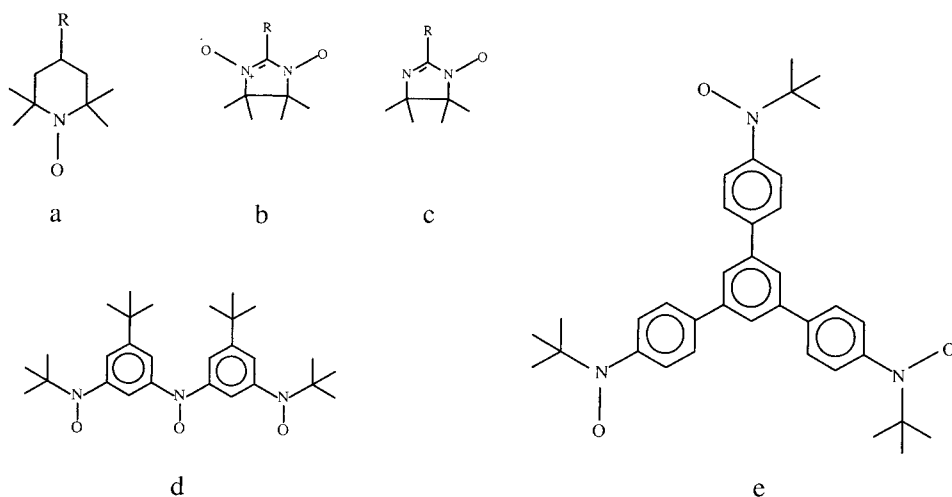


Fig. 1. Examples of nitroxide ligands: (a) piperidinyl (commercially available); (b) nitronyl; (c) imino; (d) and (e) aromatic polynitroxides.

Remembering that magnetism is a bulk property (or at least a finite collection of spin carriers), bridging ligands, such as nitronyl (b) and imino (c) nitroxides, and poly nitroxides, where nitroxyl groups are *m*-substituents of a phenyl ring (d and e), are particularly attractive. They all have several oxyl groups and unsaturated structures, enabling correlation of the unpaired spin density over the different coordination sites.

2.2.1 Electronic Structure

The magnetic orbital (semi-occupied molecular orbital) in nitroxides is well established as having π^* symmetry, in agreement with elementary molecular orbital theory [11]. Polarized neutron diffraction studies performed on nitronyl and imino nitroxides confirm these expectations. The important point to keep in mind is that both potential coordination sites (O,O in nitronyl and N,O in imino nitroxides) carry large and positive spin densities [12].

As sketched for nitronyl nitroxides in Fig. 2, both sites of coordination are equivalent; in particular they play the same role concerning overlap with d orbitals of transition metal ions.

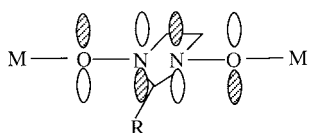


Fig. 2. Sketch of the magnetic orbital in nitronyl nitroxides. The sp^2 carbon atom carries a negative spin density. The methyl groups have been omitted.

2.2.2 Coordination Properties

The oxygen atom of the nitroxyl group has weak Lewis base properties and binds only to electron-acceptor metal centers. This is why the metal centers are surrounded by fluorinated electron-withdrawing ligands, e. g. hexafluoroacetylacetonato groups, in most studies devoted to the coordination chemistry of nitroxides. Most of our knowledge of the coordination behavior of the oxyl group comes from the pioneering work of Doedens who characterized structurally the first metal complexes of simple piperidinylnitroxides (Fig. 1a) [13, 14].

According to Lewis the oxyl group can be represented as a neutral form and another form in which the oxygen atom carries a formal negative charge (Fig. 3).



Fig. 3. Lewis representations of the oxyl group.

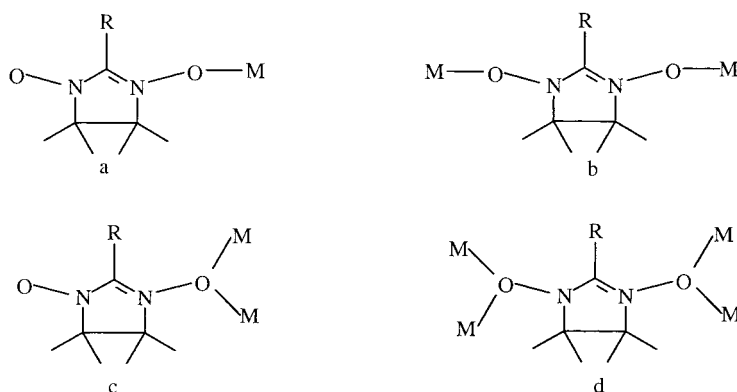


Fig. 4. Expected modes of binding of nitronyl nitroxides to metal ions: (a) non-bridging; (b) μ -1,3 bridging; (c) μ -1,1 bridging; (d) μ -1,1 and μ -3,3 bridging.

It is clear that the unpaired electron is delocalized on both atoms but that complexation can favor one of these limiting formulas. In Fig. 3b, taking into account the coordination properties of nitrones or alkoxides, one expects that the oxygen atom might function as a μ -1,1 bridging group as sketched in Fig. 4 for nitronyl nitroxides.

Although derivatives of metal-hexafluoroacetylacetonates usually correspond to coordination mode a or b and are discrete or 1D complexes, a few nickel(II) and cobalt(II) complexes with a μ -1,1 oxyl bridge have been characterized, and a manganese(II) complex probably has a structure corresponding to mode d. In contrast with nitronyl nitroxides, in all other nitroxides, e.g. piperidinyl nitroxides or the triradicals described in Figs. 1d and 1e, the oxyl group is never μ -1,1 bridging. This behavior must be related to steric crowding – in nitronyl and imino nitroxides one position α to the oxyl groups is not fully substituted, as observed in piperidinyl nitroxides for example, and steric crowding depends on the substituent in position 2.

Steric crowding is one of the main features governing the coordination properties of nitroxides. Obviously, for metal ions where a strong Jahn-Teller effect is operative one expects that steric crowding will play a major role, because bulky ligands are expected to be better accommodated in axial positions. The coordination geometry thus results not only from the steric demand of the ligand but also from the nature of the metal ions. Importantly, the coordination geometry will result in specific orientations of magnetic orbitals and will determine the nature and the magnitude of the magnetic interactions. Let us examine crude guidelines for designing complexes [6].

2.2.2.1 Oxygen Coordination

It is convenient to consider metal ions as different as possible. For example, manganese(II) which is highly isotropic and has five unpaired electrons is much different from copper(II) which has a single unpaired electron and is subject to strong Jahn–

Teller effect. For metal ions where numerous d orbitals are singly occupied, anyone interested in magnetic properties need not care much about the coordination geometry, because one at least of the metal magnetic orbitals will have the right symmetry for overlapping with the ligand magnetic orbital. In contrast, for copper(II), overlap with the unique half-filled d orbital depends on the axial or equatorial binding of the nitroxide ligand.

It has been observed that the structure of the nitroxide ligand can play a fundamental role in two ways. Bulky substituents favor axial coordination of the nitroxyl group in octahedral complexes because steric crowding is released; when the free radical ligand carries another donor group, e. g. to bridge two metal ions, the binding is also generally axial for reasons of steric crowding, at least when the metal center carries hexafluoroacetylacetonato groups. In this situation, the next metal ion can be regarded as a “bulky substituent”. This is the rule for nitronyl and imino nitroxides (two coordination sites), for which the expected (*and generally observed at room temperature*) binding geometry in polynuclear derivatives is axial. In contrast, in complexes of nitroxides which do not carry extra coordination sites and are not sterically demanding the observed binding geometry is equatorial. In the absence of reliable theoretical calculations it seems that the actual binding geometry is the result of a delicate balance between electronic and steric factors.

Therefore, because of a delocalized structure, the presence of two coordination sites and a steric demand which can be monitored through the bulkiness of the substituent in position 2, the coordination behavior of nitronyl nitroxides can be tuned to obtain specific complexes and, consequently, specific magnetic properties.

Considering first-row transition metal ions, coordination through the oxygen atom (all nitroxides except imino nitroxides) generally occurs such that the ligand magnetic orbital strongly overlaps with the metal orbital directed along the M–O bond. This situation results in strong antiferromagnetic metal–ligand interaction. Axial binding to an octahedral or square planar copper(II) complex, however, makes the ligand (π^*) and metal ($d_{x^2-y^2}$) magnetic orbitals orthogonal to each other. Accordingly, the interaction is ferromagnetic. Many of these complexes have been characterized in which the interaction can be as large as $+100 \text{ cm}^{-1}$ ($H = -J\mathbf{S}_1\mathbf{S}_2$) but, because the metal coordination sphere is often distorted, pseudo-orthogonality leads to weaker values of $10\text{--}30 \text{ cm}^{-1}$. Ferromagnetic behavior is also observed in a few Ni(II) complexes where accidental orthogonality also occurs.

2.2.2.2 Nitrogen Coordination

Coordination of nitrogen in imino nitroxides complexes occurs through the nitrogen lone pair which is in the plane of the imidazolidine ring and orthogonal to the π^* magnetic orbital. In this situation overlap and antiferromagnetic behavior are disfavored so that, roughly, the rule is opposite to that governing oxyl(oxygen) coordination – most interactions are ferromagnetic. This is particularly true for Cu(II) and Ni(II) (high-spin) complexes, all of which are characterized by ferromagnetic interactions. Interestingly, these interactions are large, $300\text{--}400 \text{ cm}^{-1}$ in copper(II) complexes and $>100 \text{ cm}^{-1}$ in nickel complexes.

Quantitatively, interactions are strong as expected for exchange coupled species where the spin carriers are directly bound. Actually, metal-nitroxide species belong to the only known system where exchange interactions spread over a energy range of 1000 cm^{-1} (-500 to $+500$) are observed.

In addition to variety in coordination mode, nature, and magnitude of exchange interactions, one must consider the consequence of including donor atoms in substituents in position 2 of a nitroxide ligand; this leads to more possibilities for the design of molecular magnetic species. In particular, this short account is devoted to copper(II) complexes of nitronyl and imino nitroxides, in which the substituent includes a nitrogen binding site in a non-chelating position for the oxyl group, which have peculiar magnetic properties.

2.3 Molecular Spin Transition Species

The preceding section stressed the diverse structural and magnetic situations encountered in nitroxide coordination chemistry and in particular in copper(II) complexes. As already mentioned, axial and equatorial binding which corresponds to opposite interactions depend on several factors. Spin pairing is probably a driving force for equatorial binding which is counterbalanced by steric effects favoring axial coordination. It is, therefore, not unexpected that, in complexes with a peculiar structure, the energy gap between axial and equatorial coordination should be very weak. As a consequence, these complexes would undergo conversion between these two forms and between two types of magnetic behavior under an appropriate perturbation.

Such behavior is, indeed, observed in copper(II) complexes with 3-pyridylnitronyl, 3-pyridylimino, and pyrazolyl nitroxides (Fig. 5).

These ligands are tridentate. Although nitrogen coordination should occur to any metal center, binding of the oxyl group requires use of acceptor metal fragments such as hexafluoroacetylacetonates ($\text{M}(\text{hfac})_2$). Structurally, these complexes belong to two classes.

2.3.1 Discrete Species

For LNPy and LIpy, depending upon the proportion of reactants, different complexes are obtained for each ligand. Among these are tetranuclear species, the structure of which is represented in Fig. 6 [15, 16]. They correspond to full participation of all coordination sites and have a cyclic structure including two intra-cyclic octahedral and two extra-cyclic penta-coordinated copper ions.

The only significant difference between the complexes of the nitronyl and the imino nitroxide resides in the environment of the extra-cyclic metal centers which are square pyramidal in the former and trigonal bipyramidal (nitrogen coordination) in the latter. Coordination features in both complexes are unexceptional, because

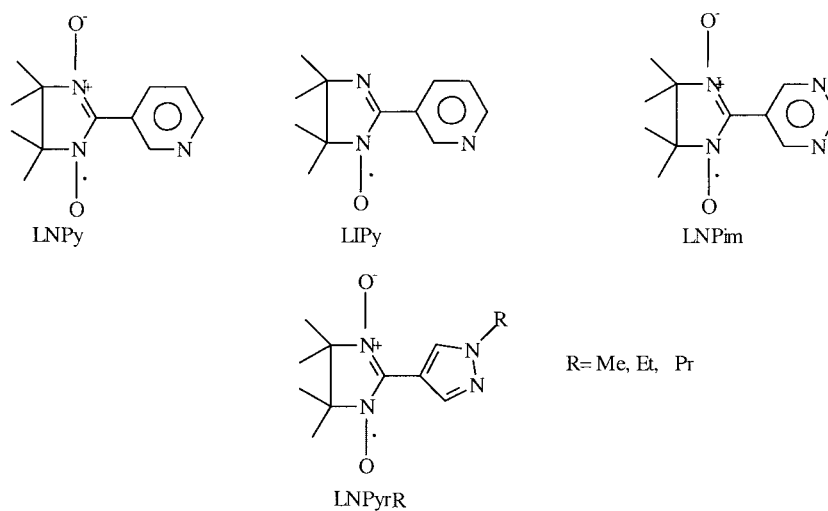


Fig. 5. Non-chelating nitroxides for which spin-transition-like behavior has been characterized.

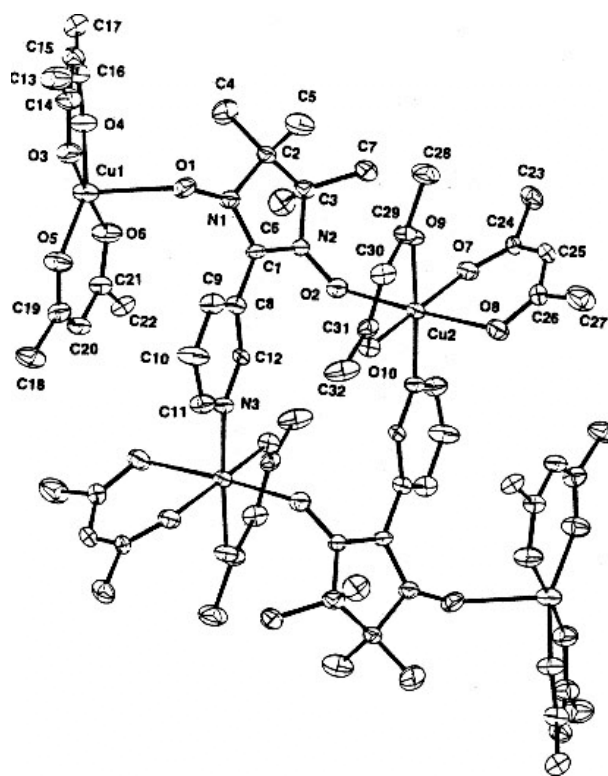


Fig. 6. Room temperature structure of the tetranuclear species $[\text{Cu}(\text{hfac})_2]_4(\text{LNPy})_2$. In the analogous complex derived from the imino nitroxide, $[\text{Cu}(\text{hfac})_2]_4(\text{LIPy})_2$, the extra-cyclic metal centers are trigonal bipyramidal.

similar arrangements are found for nitroxides carrying substituents of similar bulkiness, e. g. a phenyl group. In particular, the oxyl ligation to the intra-cyclic metal ion is axial at room temperature in both complexes, as is usually observed for bis(oxyl) bridging ligands. The presence of an additional binding site in the pyridyl fragment is, however, responsible for the formation of the cyclic structure observed.

The magnetic properties of both complexes are displayed in Fig. 7 as the temperature dependence of $\chi_M T$.

One observes two types of Curie behavior, one at high temperature (>120 K) corresponding to six independent $S = 1/2$ spins and another corresponding to two independent $S = 1/2$ spins below 90 K. Keeping in mind that, at room temperature, the coordination of all oxyl groups is axial and that such geometry results in a weak ferromagnetic interaction, the independence of the spins at high temperature is straightforward to understand. The apparent disappearance of four spins below 120 K is explained by a crystal structure at 50 K which shows that the axial

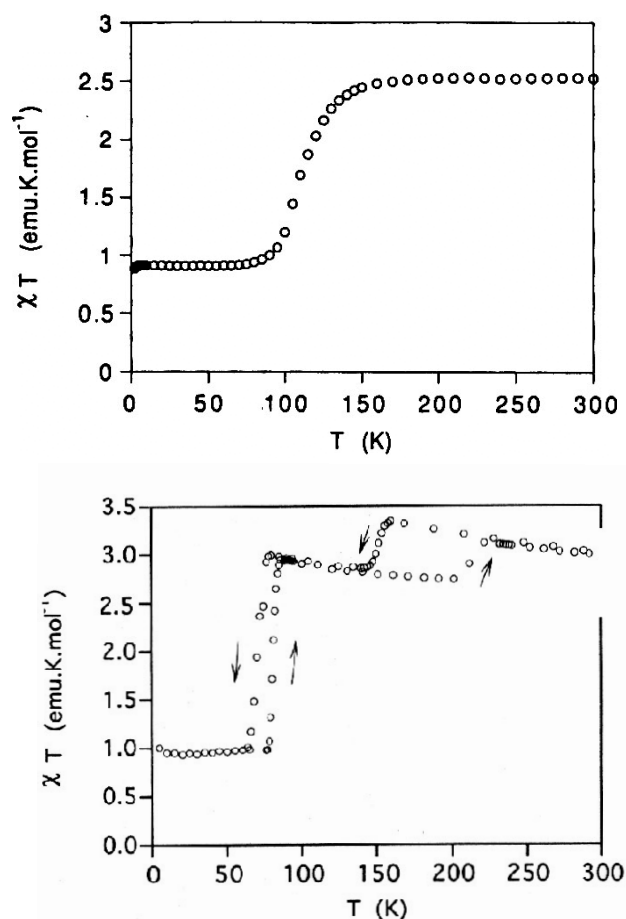


Fig. 7. Temperature dependence of $\chi_M T$ for $[\text{Cu}(\text{hfac})_2]_4(\text{NIT-3Py})_2$ (a) and $[\text{Cu}(\text{hfac})_2]_4(\text{IM-3Py})_2$ (b).

oxyl coordination to the intra-cyclic copper ion has switched to equatorial at low temperature. In this new geometry the interaction of the nitroxide ligand with the metal center is strongly antiferromagnetic, so the magnetic behavior corresponds to the two remaining uncoupled extra-cyclic copper(II) ions.

The analogous complex of the imino nitroxide has more complicated features. Because crystal breaking precludes the determination of the structure at low temperature, understanding of these features is more speculative. One observes at ca 70 K, however, a decrease of $\chi_{\text{M}}T$ which also corresponds to the pairing of four spins. The high-temperature behavior is far more complicated than that of the nitronyl nitroxide analog – because nitrogen bonding of the imino nitroxide to the extra-cyclic metal is ferromagnetic and large, the room temperature value of $\chi_{\text{M}}T$ is larger than that expected for independent spins and increases as the temperature decreases. There is then a transition to a $\chi_{\text{M}}T$ value corresponding to independent spins and then a new smooth increase down to 70 K. This second transition has been tentatively interpreted as a rearrangement of the extra-cyclic copper(II) coordination sphere from trigonal bipyramidal to square pyramidal. This switch occurs with a change of the nitrogen coordination from equatorial (short binding distance and large ferromagnetic coupling) to axial (large binding distance and weaker ferromagnetic coupling).

Another difference between the magnetic behavior of the two complexes has been observed. Whereas in the former the low-temperature transition occurs without hysteresis, in the latter both transitions have rather large hysteresis loops. This is in agreement with extensive rearrangement of the extra-cyclic metal center which, as shown by the room-temperature crystal structure, should affect neighboring molecules and occur cooperatively.

These compounds were the first examples of a new type of spin-transition behavior. It has been called molecular spin-transition because, in contrast with conventional Fe(II) or cobalt(II) spin-transition species, in these copper(II)-nitroxide complexes the change in spin multiplicity involves several open-shell fragments. Phenomenologically, however, structural and magnetic aspects of the changes are very similar in both.

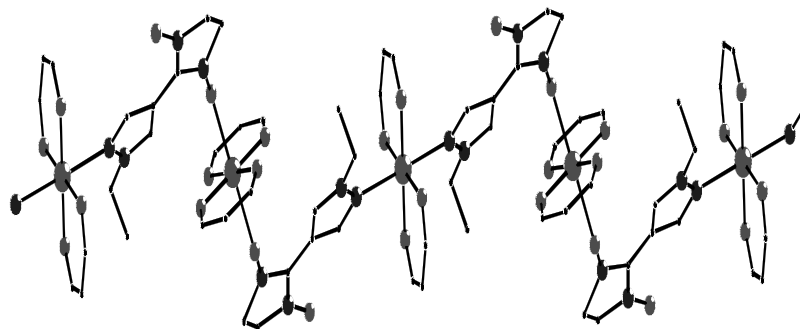
Although understanding of the structural features involved in the onset of the transition is poor, it is apparent that crystal packing is of utmost importance. Indeed, $[\text{Cu}(\text{hfac})_2]_4(\text{LIPy})_2$ crystallizes as two polymorphs and the molecular spin transition is observed in one only.

Both compounds have a cyclic structure but it was unknown whether 1D or 2D compounds could undergo such a conversion between two different magnetic and structural states. Attempts have been made using the 5-pyrimidyl-substituted nitronyl nitroxide (Fig. 5, LNPim), a tetradentate ligand, which gives a 1D structure in which similar cyclic fragments are linked by copper(II) ions through the second *m*-nitrogen of the pyrimidyl ring. In this compound, however, equatorial oxygen binding to the intra-cyclic metal is observed at room temperature; on heating no transition is observed before decomposition. Nevertheless, copper(II) derivatives of LnpyrR are 1D species with even richer magnetic behavior.

2.3.2 One-dimensional Species

These are derivatives of nitronyl nitroxides whose spin-labeled heterocycle contains a pyrazole fragment as substituents which may be easily modified [17]. These poly-functional nitroxides react with transition metal ions, forming complexes differing in structure and composition. In our study on $\text{Cu}(\text{hfac})_2$ complexes with LNPyrR we revealed a family of chain heterospin complexes with spin-crossover-like behavior at relatively high temperatures (130–230 K) [18–20]. Crystal cracking occurred for only one of the complexes (with LNPyrMe); it occurred in the region of the transition temperature. For all other heterospin complexes, structure determinations were successfully performed before and after the spin transition. This enabled tracing of the structural dynamics in the systems. Whereas repeated cooling/heating cycles led to considerable changes in unit-cell volumes, the cell contraction/expansion was generally reversible and X-ray analyses did not reveal any changes in crystal quality. For this reason we called these crystals “breathing crystals”. Spin-crossover-like behavior was found to be intrinsic to polymer chain compounds with a “head-to-head” or “head-to-tail” motif. Unexpectedly, only half the total number of spins participated in the spin-crossover-like effect. As mentioned above, for classical spin crossover compounds, the magnetic moment decreases (gradually, abruptly, stepwise, or with hysteresis) with temperature and usually the spins of all paramagnetic centers participate in this process [21]. In our work participation of only half the total number of spins in the spin transition needed a reasonable explanation.

Reactions of $\text{Cu}(\text{hfac})_2$ with LNPyrR in non-polar solvents (hexane or heptane) in a 1:1 ratio lead to chain polymer complexes $\text{Cu}(\text{hfac})_2(\text{LNPyrR})$ with a “head-to-head” ($\text{Cu}(\text{hfac})_2\text{LNPyrEt}$ and $\text{Cu}(\text{hfac})_2\text{LNPyrPr}$) or “head-to-tail” ($\text{Cu}(\text{hfac})_2\text{LNPyrMe}$ and $[(\text{Cu}(\text{hfac})_2)_2\text{LNPyrMe,LNPyrEt}]$) motif. Of particular interest are the magneto-structural correlations in these complexes. It is reasonable to start the discussion with $\text{Cu}(\text{hfac})_2\text{LNPyrEt}$. The structure of the “head-to-head” chain in $\text{Cu}(\text{hfac})_2\text{LNPyrEt}$ is shown in Fig. 8. The symmetry of the structure does not change when the temperature is reduced (Table 1). The most remarkable



- Cu
- O
- N

Fig. 8. The structure of the “head-to-head” chain in $\text{Cu}(\text{hfac})_2\text{LNPyrEt}$ at 293 K; the methyl and trifluoromethyl groups and the hydrogen atoms omitted for clarity.

Table 1. Crystal data for the chain complexes.

Compound	Cu(hfac) ₂ L ^{Me}	Cu ₂ (hfac) ₄ L ^{Me} L ^{Et}	Cu ₂ (hfac) ₄ L ^{Me} L ^{Et}	Cu(hfac) ₂ L ^{Et}
Molecular formula	C ₂₁ H ₁₉ CuF ₁₂ N ₄ O ₆	C ₄₃ H ₄₀ Cu ₂ F ₂₄ N ₈ O ₁₂	C ₂₁ H ₁₉ CuF ₁₂ N ₄ O ₆	C ₂₂ H ₂₁ CuF ₁₂ N ₄ O ₆
<i>FW</i>	714.94	1443.91	714.94	742.99
<i>T</i> (K)	293	293	115	115
Space group,	P2 ₁ /n	P-1	P-1	C2/c
<i>Z</i>	4	2	2	8
<i>a</i> (Å)	12.287(2)	12.420(2)	12.169(12)	30.516(5)
<i>b</i> (Å)	16.181(4)	15.802(3)	15.837(16)	9.540(2)
<i>c</i> (Å)	15.631(2)	15.865(2)	15.210(16)	25.194(4)
α (°)		84.87(1)	82.03(9)	
β (°)		86.76(1)	85.85(9)	
γ (°)		74.04(2)	76.13(8)	
Volume (Å ³)	2948(1)	2980.0(8)	2816(5)	6084(2)
<i>V/Z</i> (Å ³)	737	1490	1408	761
<i>D</i> _{calc} (g cm ⁻³)	1.611	1.609	1.702	1.592

Compound	Cu(hfac) ₂ L ^{Et}	Cu(hfac) ₂ L ^{Et}	Cu(hfac) ₂ L ^{Pr}	Cu(hfac) ₂ L ^{Pr}
Molecular formula	C ₂₂ H ₂₁ CuF ₁₂ N ₄ O ₆	C ₂₂ H ₂₁ CuF ₁₂ N ₄ O ₆	C ₂₃ H ₂₃ CuF ₁₂ N ₄ O ₆	C ₂₃ H ₂₃ CuF ₁₂ N ₄ O ₆
<i>FW</i>	728.97	728.97	742.99	742.99
<i>T</i> (K)	188	115	293	115
Space group,	C2/c	C2/c	C2/c	C2/c
<i>Z</i>	8	8	8	8
<i>a</i> (Å)	29.489(9)	29.324(10)	30.907(6)	29.968(3)
<i>b</i> (Å)	9.495(5)	9.438(5)	9.582(2)	9.654(1)
<i>c</i> (Å)	24.382(7)	24.236(8)	26.204(6)	25.720(3)
α (Å)				
β (Å)				
γ (Å)				
Volume (Å ³)	5835(4)	5748(4)	6342(2)	5894(1)
<i>V/Z</i> (Å ³)	730	719	793	737
<i>D</i> _{calc} (g cm ⁻³)	1.660	1.685	1.556	1.675

structural feature at 293 K is very short Cu–O and Cu–N axial distances – 2.237 and 2.375 Å, respectively, in the crystallographically independent centrosymmetric fragments CuO₆ and CuO₄N₂ (Table 2). As the temperature decreases the Cu–O_L axial distances in the CuO₆ fragments gradually increase to 2.260 at 188 K and to 2.281 Å at 115 K (Table 2). The Cu–O_{hfac} distances in the CuO₆ fragments also change. As the axial distances along the O_L–Cu–O_L axis are lengthened, the Cu–O_{hfac} bonds along one of the O_{hfac}–Cu–O_{hfac} directions are shortened by a comparable value (~0.043 Å). The shortening of the Cu–O_{hfac} distances from 2.028 to 1.985 Å leads to equalization of all Cu–O_{hfac} bond lengths in the CuO₆ fragments. At 188 K, the long axis of the Cu bipyramid in the CuO₄N₂ fragment is shifted to another position; the coordinated N atoms of the pyrazole heterocycles pass to the equatorial position ($d_{\text{Cu-N}} = 2.375\text{--}2.079$ Å), replacing two O_{hfac} atoms to the axial positions ($d_{\text{Cu-O}} = 1.996\text{--}2.269$ Å) (Table 2). As the temperature decreases further, the Cu–N_L distances in the CuO₄N₂ fragments shorten whereas the Cu–O_L distances in the CuO₆ fragments lengthen. It is, in general, reasonable to consider that the structural motion occurring in solid Cu(hfac)₂LNPyEt at reduced temperature is localized within the CuO₆ and CuO₄N₂ fragments, because the values of the angles and distances in the coordinated hfac-anions and LNPyEt remain the same, within experimental error. For the coordinated LNPyEt these values are, moreover, almost the same as those for the free ligand.

Figure 9 shows the temperature-dependence of the effective magnetic moment of Cu(hfac)₂LNPyEt. At room temperature the value of μ_{eff} is close to the theoretical value of $2.45 \mu_{\text{B}}$ for a system of non-interacting spins of Cu²⁺ and nitroxide based on the {Cu(hfac)₂LNPyEt} fragment. When the sample is cooled from room temperature to 225 K, μ_{eff} gradually decreases to $2.4 \mu_{\text{B}}$, thus manifesting non-trivial behavior. In all previously reported examples with the nitroxyl group coordinated axially to the Cu²⁺ ion, μ_{eff} increased at low temperatures as a result of a ferromagnetic exchange interaction. For the >N•O–Cu²⁺–O•–N< exchange cluster with rather long Cu–O distances (>2.4 Å) and an axially coordinated nitroxyl group the ferromagnetic exchange interaction has received a reliable theoretical explanation [15, 22]. It was noted, however, that shortening of the Cu–O_{O•–N} axial distances can lead to a situation where the antiferromagnetic exchange interaction prevails [22]. The unprecedented short Cu–O_L axial distance (2.237 Å) in the CuO₆ octahedron is the reason for the predominant antiferromagnetic interaction in the >N•O–Cu²⁺–O•–N< exchange clusters in solid Cu(hfac)₂LNPyEt over the temperature range 225–300 K. It is worthy of note that the exchange interaction is very sensitive to variation of the Cu–O_L distance. Low-temperature structural studies on Cu(hfac)₂LNPyEt showed that at 188 K the Cu–O_L distance lengthened by no more than ~0.02 Å (Table 2) but that the antiferromagnetic interaction in the >N•O–Cu²⁺–O•–N< exchange cluster vanished completely. The transition occurred abruptly at 220 K (Fig. 9). As the temperature decreased, the Cu–O_{O•–N} distance continued to increase, although the exchange interaction in the >N•O–Cu²⁺–O•–N< cluster remained ferromagnetic, because of which μ_{eff} increased until the temperature of ~25 K was reached. Below this temperature, μ_{eff} started to decrease rapidly as a result of the antiferromagnetic intermolecular interaction. The exchange parameters were estimated for Cu(hfac)₂LNPyEt in the

Table 2. Selected bond lengths (Å) and angles (°) for the chain complexes.

Cmpd.	Cu(hfac) ₂ L ^{Me}		Cu ₂ (hfac) ₄ L ^{Me} L ^{Et}		Cu(hfac) ₂ L ^{Et}		Cu(hfac) ₂ L ^{Et}	
	293	CuO ₅ N	115	CuO ₅ N	293	CuO ₆	188	CuO ₆
T (K)	293	CuO ₅ N	115	CuO ₅ N	293	CuO ₆	188	CuO ₆
Unit	CuO ₅ N	CuO ₅ N	CuO ₅ N	CuO ₅ N	CuO ₆	CuO ₆	CuO ₆	CuO ₆
Cu-OL	2.484(5)	2.510(5)	2.433(5)	2.465(5)	2.237(4)	2.260(3)	2.260(3)	2.260(3)
Cu-NL	2.329(5)	2.346(5)	2.314(5)	2.314(5)	1.965(4)	1.979(4)	1.960(4)	1.973(3)
Cu-O _{hfac}	1.936(4)	1.944(5)	1.954(4)	1.954(4)	2.028(5)	1.996(4)	2.007(4)	2.269(3)
	1.950(4)	1.953(5)	1.941(5)	1.941(5)				
	1.956(4)	1.924(4)	1.961(4)	1.961(4)				
	1.962(4)	1.946(4)	1.962(4)	1.962(4)				
N-O	1.288(6)	1.295(6)	1.274(6)	1.274(6)	1.312(6)		1.299(5)	
	1.287(8)	1.264(7)	1.272(6)	1.285(5)	1.266(7)		1.269(5)	
CuON	139.4(4)	148.1(4)	130.4(4)	148.4(3)	126.5(4)		125.2(3)	
Pz-CN ₂	13.3(7)	7.3(8)	7.7(10)	3.7(9)	10.3(9)	9.8(6)	9.2(5)	

Cmpd.	Cu(hfac) ₂ L ^{Er}		Cu(hfac) ₂ L ^{Pr}		Cu(hfac) ₂ L ^{Pr}		Cu(hfac) ₂ L ^{Pr}	
	293	CuO ₄ N ₂	203	CuO ₆	115	CuO ₆	115	CuO ₄ N ₂
T (K)	115	CuO ₄ N ₂	203	CuO ₆	115	CuO ₆	115	CuO ₄ N ₂
Unit	CuO ₆	CuO ₄ N ₂	CuO ₆	CuO ₄ N ₂	CuO ₆	CuO ₆	CuO ₆	CuO ₄ N ₂
Cu-OL	2.281(3)	2.055(4)	2.143(4)	2.144(4)	2.018(3)	2.415(3)	2.018(3)	2.018(3)
Cu-NL	1.958(4)	1.961(4)	2.474(5)	2.405(5)	1.959(3)	1.958(3)	1.959(3)	1.958(3)
Cu-O _{hfac}	1.985(4)	2.313(3)	1.952(4)	1.965(4)	2.263(2)	1.975(3)	2.263(2)	1.975(3)
			1.954(4)	1.952(4)				
			1.975(5)	1.965(4)				
			2.119(5)	1.980(4)				
			2.130(5)	1.968(4)				
N-O	1.300(5)	1.306(6)	1.302(6)	1.308(6)	1.309(4)		1.309(4)	
	1.271(6)	1.262(7)	1.273(7)	1.277(6)	1.276(5)		1.276(5)	
CuON	124.0(3)	128.0(4)	126.5(4)	123.7(4)	123.7(2)		123.7(2)	
Pz-CN ₂	9.1(5)	8.6(6)	7.4(7)	11.8(7)	9.7(4)		9.7(4)	

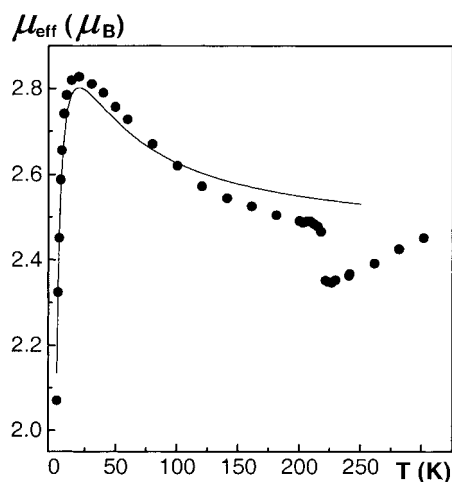


Fig. 9. Experimental dependence $\mu_{\text{eff}}(T)$ for $\text{Cu}(\text{hfac})_2\text{NITPyrEt}$. The solid line is the theoretical curve described in the text.

Table 3. Spin-crossover transition temperatures and optimum parameters for the theoretical curves of $\mu_{\text{eff}}(T)$ for the chain compounds.

	T (K)	g_{Cu}	J (cm^{-1})	nJ (cm^{-1})
$\text{Cu}(\text{hfac})_2\text{L}^{\text{Me}}$	146	2.13 ± 0.03	8.8 ± 0.2	-0.11 ± 0.02
$\text{Cu}(\text{hfac})_2\text{L}^{\text{Et}}$	220	2.00 ± 0.01	26 ± 6	-0.45 ± 0.05
$\text{Cu}(\text{hfac})_2\text{L}^{\text{Pr}}$	226	2.09 ± 0.02	-100 ± 2	-0.39 ± 0.03
$\text{Cu}_2(\text{hfac})_4\text{L}^{\text{Me}}\text{L}^{\text{Et}}$	131	2.12 ± 0.03	8.7 ± 0.6	-0.26 ± 0.01

temperature range 2–175 K by use of the cluster approximation and an isotropic spin Hamiltonian by the procedure suggested elsewhere [23]. Neglecting the relatively weak copper-nitroxyl exchange interaction across the paramagnetic ligand heterocycles, one can choose an exchange cluster $\{\text{Cu}^{2+} \dots >\text{N}^{\bullet}\text{O}-\text{Cu}^{2+}-\text{O}^{\bullet}-\text{N}<\}$, where the Cu^{2+} ions belong to the CuO_4N_2 and CuO_6 groups. The resulting optimum values of the g factor, exchange interaction (J) in the $>\text{N}^{\bullet}\text{O}-\text{Cu}^{2+}-\text{O}^{\bullet}-\text{N}<$ fragment, and intermolecular interaction (nJ) are listed in Table 3. The calculated curve is displayed as solid line in Fig. 9. In the approximation used nJ is actually a value averaged over the intermolecular interactions and the copper-nitroxyl interactions across the paramagnetic ligand heterocycles.

The motif of the $\text{Cu}(\text{hfac})_2\text{LNPyPr}$ polymer chain is identical (“head-to-head”) to that of $\text{Cu}(\text{hfac})_2\text{LNPyEt}$ (Fig. 8). The low-temperature bond length variation in the alternate CuO_6 and CuO_4N_2 coordination sites differs essentially from that of $\text{Cu}(\text{hfac})_2\text{LNPyEt}$, however. As the temperature decreases all bonds of the copper atoms with the donor atoms of the bridging LNPyPr ligand ($d_{\text{Cu}-\text{O}}$ and $d_{\text{Cu}-\text{N}}$) are shortened (Table 2). The shortening is more pronounced for $\text{Cu}-\text{O}_{\text{L}}$ than for $\text{Cu}-\text{N}_{\text{L}}$. It is reasonable to assume that the shortening of the $\text{Cu}-\text{N}_{\text{L}}$ bonds in $\text{Cu}(\text{hfac})_2\text{LNPyPr}$ is hindered by the propyl substituent, which is more bulky than ethyl in $\text{Cu}(\text{hfac})_2\text{LNPyEt}$. When a single crystal of $\text{Cu}(\text{hfac})_2\text{LNPyPr}$ was cooled to 203 K, the distances between the copper atom and the coordinated

nitroxyl oxygens in the CuO_6 groups decreased by $0.173 \pm 0.008 \text{ \AA}$, and by another $0.126 \pm 0.007 \text{ \AA}$ at 115 K, whereas the distances between the copper atom and the coordinated nitrogens of the pyrazole heterocycles in the CuO_4N_2 fragments decreased by only $0.069 \pm 0.010 \text{ \AA}$ at 203 K and by another $0.052 \pm 0.008 \text{ \AA}$ at 115 K. Whereas the $\text{Cu}-\text{O}_L$ distances in the CuO_6 fragments are significantly shortened, the $\text{Cu}-\text{O}_{\text{hfac}}$ distances in the CuO_6 groups along one of the $\text{O}_{\text{hfac}}-\text{Cu}-\text{O}_{\text{hfac}}$ “axes” are lengthened by 0.144 and $0.155 \pm 0.010 \text{ \AA}$ at 203 K and by another 0.144 and $0.133 \pm 0.008 \text{ \AA}$ at 115 K. The process that actually takes place in Jahn–Teller-distorted CuO_6 octahedral groups is replacement of the $\text{O}_L-\text{Cu}-\text{O}_L$ “octahedron axis”, which is elongated at room temperature and shortened by $0.598 \pm 0.008 \text{ \AA}$ on cooling, by the $\text{O}_{\text{hfac}}-\text{Cu}-\text{O}_{\text{hfac}}$ “axis”, which is elongated at low temperature and lengthened by $0.576 \pm 0.008 \text{ \AA}$ on cooling. This is vital to further discussion of the magnetic properties of $\text{Cu}(\text{hfac})_2\text{LNPyPr}$. The observed low-temperature rearrangement of the CuO_6 coordination fragments reflects the gradual shift of the nitroxyl oxygens from the axial to equatorial positions; this leads to strong antiferromagnetic exchange interactions in the $>\text{N}^{\bullet}\text{O}-\text{Cu}^{2+}-\text{O}^{\bullet}-\text{N}<$ exchange clusters. The $\mu_{\text{eff}}(T)$ curve, which smoothly decayed with temperature, falls abruptly below 230 K to a plateau at $\mu_{\text{eff}} \approx 1.8 \mu_{\text{B}}$ (Fig. 10), indicating that the antiferromagnetic interactions increase sharply in the clusters. This fall in μ_{eff} to $1.8 \mu_{\text{B}}$ shows that half of the total number of spins “vanish” in $\text{Cu}(\text{hfac})_2\text{LNPyPr}$ when the sample is cooled to 50 K. This is fully consistent with the decrease in the spin of the $>\text{N}^{\bullet}\text{O}-\text{Cu}^{2+}-\text{O}^{\bullet}-\text{N}<$ exchange cluster to $S = 1/2$ as a result of increased antiferromagnetic interaction. The exchange integral in the $>\text{N}^{\bullet}\text{O}-\text{Cu}^{2+}-\text{O}^{\bullet}-\text{N}<$ cluster was estimated at -100 cm^{-1} for the low-temperature range (Table 3; calculated curve shown as solid line in Fig. 10). Because of the high value of antiferromagnetic exchange, at $T < 50 \text{ K}$ the magnetic moment of $\text{Cu}(\text{hfac})_2\text{LNPyPr}$ is the sum of the residual spins of the exchange cluster and the Cu^{2+} ions of the CuO_4N_2 fragments. As for $\text{Cu}(\text{hfac})_2\text{LNPyEt}$, μ_{eff} decreases in the range 300–250 K (Fig. 3). Consequently, the distorted octahedral CuO_6 fragments, and the analogous units

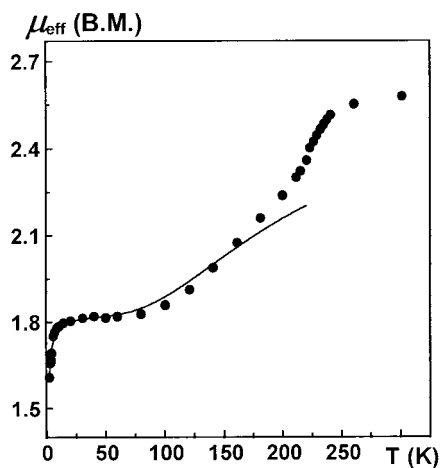


Fig. 10. Dependence $\mu_{\text{eff}}(T)$ for $\text{Cu}(\text{hfac})_2\text{NITPyPr}$. The solid line is the theoretical curve described in the text.

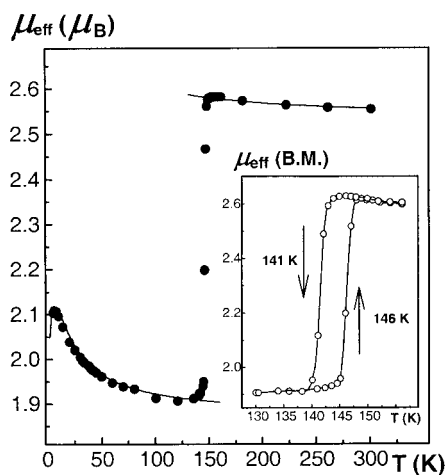


Fig. 11. Experimental dependence $\mu_{\text{eff}}(T)$ for $\text{Cu}(\text{hfac})_2\text{NITPyrMe}$. The solid line is the theoretical curve received as described in the text. Insert – hysteresis loop appearing as a result of repeated heating-cooling cycles.

in $\text{Cu}(\text{hfac})_2\text{LNPyEt}$, are responsible for the predominant antiferromagnetic exchange in the $>\text{N}\cdot\text{O}-\text{Cu}^{2+}-\text{O}\cdot\text{N}<$ clusters for the axially coordinated nitroxyl oxygens. As in $\text{Cu}(\text{hfac})_2\text{LNPyEt}$, the $\text{Cu}-\text{O}_L$ distances are short (2.317 Å) at room temperature. These distances are, moreover, shortened to 2.144 Å when the temperature is reduced to 203 K. A structural study on $\text{Cu}(\text{hfac})_2\text{LNPyPr}$ at 203 K clearly demonstrated a tendency of the coordinated nitroxyl oxygens in the CuO_6 units to pass from the axial to equatorial positions (Table 2). This structural motion in the CuO_6 units is the reason for the halving of μ_{eff} starting from 50 K.

It is worth noting that at 203 K the symmetry of the structure changes (Table 1). Structural solution for $\text{Cu}(\text{hfac})_2\text{LNPyPr}$ at this temperature enabled us to record the formation of flattened CuO_6 octahedra in the course of the transition, which is a very rare occurrence for Cu^{2+} complexes ($\text{Cu}-\text{O}_L$ 2.143 and 2.144 Å, $\text{Cu}-\text{O}_{\text{hfac}}$ 2.119, 2.130, 1.958, and 1.966 Å; Table 2). At 115 K, the initial symmetry of the structure was restored (Table 1).

Whereas for $\text{Cu}(\text{hfac})_2\text{LNPyPr}$ μ_{eff} decreases smoothly with temperature, for $\text{Cu}(\text{hfac})_2\text{LNPyMe}$ the $\mu_{\text{eff}}(T)$ curve reveals the presence of sharp transitions at 141 (cooling) and 146 (heating) K (Fig. 11). The only feature common to the magnetic behavior of the two compounds is that μ_{eff} is halved, indicating that half of the total number of spins have “vanished”. At room temperature μ_{eff} corresponds to two weakly coupled spins ($S = 1/2$); below 140 K it is close to the value typical for one spin ($S = 1/2$) per $\text{Cu}(\text{hfac})_2\text{LNPyMe}$ fragment. As the temperature decreases, μ_{eff} gradually increases over the whole temperature range 2–300 K, which is indirect evidence of the axial coordination of the nitroxyl O atoms to the Cu^{2+} ion at rather large $\text{Cu}-\text{O}_L$ distances. The experimental $\mu_{\text{eff}}(T)$ dependence was used to estimate the exchange integral. The experimental points in the transition region were excluded, and the values of μ_{eff} below the transition temperature were preliminarily re-normalized to the high-temperature range. As a result, the experiment with the optimum parameters presented in Table 3 was well approximated by $\text{Cu}^{2+}-\text{O}\cdot\text{N}<$ as an isolated exchange cluster model. The theoretical curve is presented in

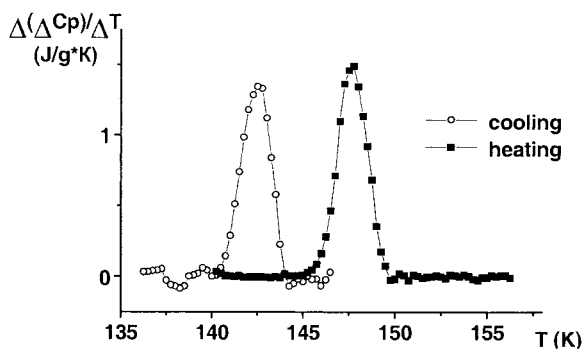
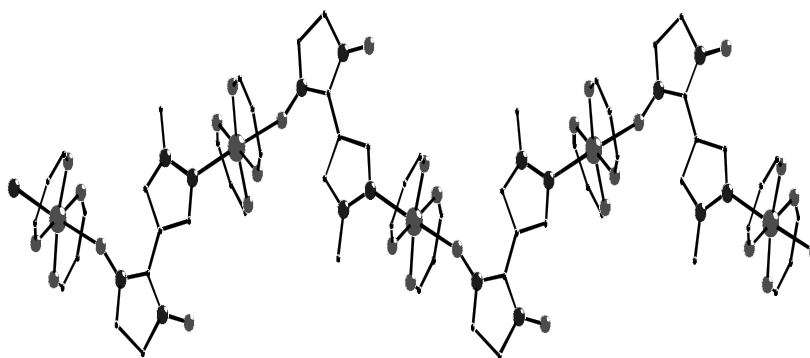


Fig. 12. Differential curves of specific heat against temperature for $\text{Cu}(\text{hfac})_2\text{NITPyrMe}$.

Fig. 11 as a solid line. The measurement cycle fulfilled at temperatures from those of liquid helium to room temperature and back was repeated many times for the same $\text{Cu}(\text{hfac})_2\text{LNPyMe}$ sample, and for samples obtained in different syntheses. The $\mu_{\text{eff}}(T)$ dependence was always reproduced with a narrow hysteresis loop of 5 K (Fig. 11, insert). The presence of a hysteresis is also confirmed by the differential curves of specific heat variation for the $\text{Cu}(\text{hfac})_2\text{LNPyMe}$ sample (Fig. 12).

Structural study of $\text{Cu}(\text{hfac})_2\text{LNPyMe}$ at 293 K has revealed a chain polymer structure of the compound (Fig. 13). The chain motif, however, differs essentially from the chain motifs of $\text{Cu}(\text{hfac})_2\text{LNPyEt}$ and $\text{Cu}(\text{hfac})_2\text{LNPyPr}$. In $\text{Cu}(\text{hfac})_2\text{LNPyMe}$ the chains are arranged on the basis of the “head-to-tail” principle. The copper atom is surrounded by two hfac ligands with short Cu–O distances in the equatorial plane and by the NO oxygen and pyrazole heterocycle nitrogen, belonging to different bridging LNPyMe, in the axial positions. The Cu–O_L distance to the axial nitroxyl oxygen is rather long (2.484 Å, Table 2); this explains the predominance of the ferromagnetic exchange interaction in the $\text{Cu}^{2+}\text{-O}\bullet\text{-N}<$ ex-



- Cu
- O
- N

Fig. 13. The structure of the “head-to-tail” chain in $\text{Cu}(\text{hfac})_2\text{NITPyrMe}$ at 293 K; methyl groups on the 2-imidazoline heterocycle, trifluoromethyl groups, and hydrogen atoms have been omitted for clarity.

change clusters. The shortest distances between the non-coordinated NO oxygens are long, 4.104 Å, and the shortest interchain F...F contacts are at least 2.922 Å. Consequently, the exchange interactions between the paramagnetic centers are concentrated in the $\text{Cu}^{2+}\text{-O}^\bullet\text{-N}$ exchange clusters. This was taken into account when choosing an isolated exchange cluster model for fitting the experimental $\mu_{\text{eff}}(T)$ dependence.

Because all CuO_5N coordination groups are identical at room temperature, the “disappearance” of only half of the total number of spins might not be explained without structural solution of the low-temperature phase (at $T < 140$ K). When a single crystal of $\text{Cu}(\text{hfac})_2\text{LNPyMe}$ was cooled, however, its quality deteriorated sharply and so was no longer suitable for X-ray diffraction analysis. Therefore full structure determination below the transition temperature was not performed. We simply found that on cooling the unit cell symmetry decreased to triclinic and the unit cell volume was reduced by $\sim 300 \text{ \AA}^3$. The nature of the magnetic spin transition in $\text{Cu}(\text{hfac})_2\text{LNPyMe}$ was understood by investigating the mixed-ligand complex $\text{Cu}_2(\text{hfac})_4(\text{LNPyMe}, \text{LNPyEt})$, readily isolated as an individual compound from a hexane solution with equimolar amounts of $\text{Cu}(\text{hfac})_2\text{LNPyMe}$ and $\text{Cu}(\text{hfac})_2\text{LNPyEt}$ and characterized by the same shape of the $\mu_{\text{eff}}(T)$ dependence (Fig. 14).

The structure of $\text{Cu}_2(\text{hfac})_4\text{LNPyMeLNPyEt}$ is similar to that of $\text{Cu}(\text{hfac})_2\text{LNPyMe}$. It is also built from infinite “head-to-tail” chains. Starting from room temperature, however, it contains two crystallographically independent copper atoms corresponding to CuO_5N alternate coordination units of two types. One has noticeably shorter Cu-O_L and Cu-N_L axial distances (Table 2). The copper atoms of these units form a considerably smaller angle ($\text{CuON } 130.4^\circ$) with the coordinated nitroxyl fragment. At low temperature the O_L and N_L donor atoms of these units pass to the equatorial position, whereas the axial positions are occupied by two oxygen atoms of the hfac ligands. When the $\text{Cu}_2(\text{hfac})_4(\text{LNPyMeLNPyEt})$ crystal is cooled to 115 K, the Cu-O_L distances decrease by 0.41 and the Cu-N_L

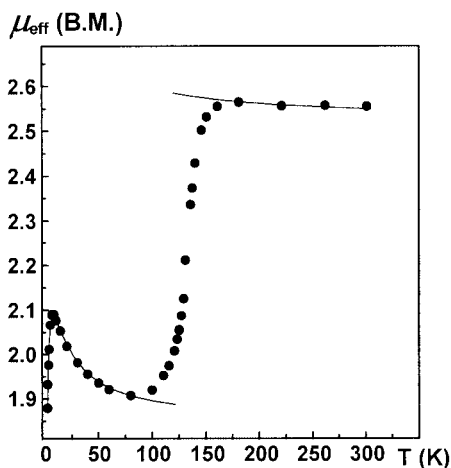


Fig. 14. Dependence $\mu_{\text{eff}}(T)$ for $\text{Cu}_2(\text{hfac})_4\text{NITPyMeNITPyEt}$ (calculated for the $\text{Cu}(\text{hfac})_2\text{NITPy}$ fragment).

distances by 0.27 Å. These are certainly substantial changes, the largest among all structural rearrangements occurring in the crystal on cooling. In CuO₅N units of the other type the Cu–O_L distances are shortened to a lesser extent (by 0.077 Å) and the Cu–N_L distances remain almost the same, within experimental error, as shown by a single-crystal study of Cu₂(hfac)₄(LNPyrMeLNPyrEt) at 115 K. The O_L and N_L atoms stay in the axial positions and all equatorial positions are occupied by the O_{hfac} atoms, for which Cu–O_{hfac} < 2 Å. Another motion recorded in the crystal on cooling is a change in the angle between the plane of the pyrazole ring and the plane of the CN₂ atoms of the O•–N–C=N–O fragment of the imidazoline heterocycle. At room temperature the angle is the same (7.5°), within experimental error, for all bridging L. At 115 K the angle decreases for half of the total number of the bridging L, containing the O atoms that are shifted from the axial to equatorial position in the coordination polyhedron; for the other half, which contain the O atoms remaining in the axial positions, the angle increases (Table 2). For the latter ligands, moreover, the N–O bond lengths are equalized to 1.286 Å whereas for the former both N–O distances in the O•–N–C=N–O fragment increase. Thus at 115 K the alternate bridging L, and the alternate coordination polyhedra CuO₅N, become non-equivalent. The only point which was not clarified during the crystal solution for Cu₂(hfac)₄(LNPyrMe,LNPyrEt) was – which of the ligands, LNPyrMe or LNPyrEt, undergoes these changes? For structural solution the methyl group in the ethyl fragment was taken with a weight of 0.5 for both crystallographically independent L.

The above structural changes occurring in Cu₂(hfac)₄(LNPyrMe,LNPyrEt) crystals in the range from 293 to 115 K make it possible to readily explain the form of the experimental $\mu_{\text{eff}}(T)$ dependence for this compound (Fig. 14). Because the polymer chains have a “head-to-tail” motif, the exchange interactions between the paramagnetic centers in the Cu²⁺–O•–N< exchange clusters prevail as they do in Cu(hfac)₂LNPyrMe. Because the oxygen atoms of the nitroxyl groups in the CuO₅N coordination sites are axial at room temperature, the exchange interactions in the Cu²⁺–O•–N< clusters are ferromagnetic (Table 3 gives the estimated exchange parameters for Cu₂(hfac)₄(LNPyrMeLNPyrEt) and Fig. 14 shows the theoretical curve (solid line)), leading to a smooth increase in μ_{eff} in the high-temperature phase in the range from 300 to 170 K. The same is observed for the low-temperature phase in the range from 80 to 10 K. As for Cu(hfac)₂LNPyrMe, in the transition range (170–180 K), the number of spins decreases by half. This is caused by the shift of the coordinated O_L atoms of the nitroxyl groups in half of the total number of CuO₅N units from the axial to equatorial position and, as a consequence, by the change of the exchange interaction in the Cu²⁺–O•–N< clusters from weak ferromagnetic to strong antiferromagnetic, leading to spin compensation in these units. Because both Cu(hfac)₂LNPyrMe and Cu₂(hfac)₄(LNPyrMeLNPyrEt) have the same (“head-to-tail”) motif of polymer chains and the same shape of the $\mu_{\text{eff}}(T)$ dependence, for the low-temperature phase of Cu(hfac)₂LNPyrMe one can admit an analogous structural rearrangement, leading to two structurally diverse coordination sites CuO₅N with essentially different exchange interactions in the Cu²⁺–O•–N< clusters.

Thus, a family of heterospin complexes of Cu(hfac)₂ with pyrazole-substituted nitronyl nitroxides has been found for which spin-crossover phenomena are ob-

served in the solid state. Direct X-ray diffraction studies of the single crystals of the complexes at different temperatures have revealed the structural rearrangements leading to these phenomena; these are crucial to understanding the magnetic properties. Experimental evidence has been obtained to support the assumption that the coordinated nitroxyl oxygens pass from axial to equatorial positions. The transition is accompanied by a change of the exchange interaction in the $\text{Cu}^{2+}\text{-O}^{\bullet}\text{-N}<$ clusters from weak ferromagnetic for the axial coordination of the nitroxyl group ($d_{\text{Cu-O}} > 2.4 \text{ \AA}$) to strong antiferromagnetic for the equatorial coordination of the nitroxyl oxygen ($d_{\text{Cu-O}} \approx 2 \text{ \AA}$), leading to spin compensation between the Cu^{2+} ion and the nitroxyl fragment. This rearrangement is dominated by the Jahn-Teller nature of the Cu^{2+} ion, because of which the coordination site is constructed as an elongated octahedron. The motif of the polymer chain (“head-to-tail” or “head-to-head”) is unimportant for initiation of the thermally induced spin-crossover transitions in the systems. In both the shortening of the Cu–O distance in the $\text{Cu}^{2+}\text{-O}^{\bullet}\text{-N}<$ exchange cluster as a result of the shift of the coordinated oxygen atom from the axial to equatorial position leads to halving of μ_{eff} (or to halving of the magnetic susceptibility) as recorded for $\text{Cu}(\text{hfac})_2\text{LNPyPr}$, $\text{Cu}(\text{hfac})_2\text{LNPyMe}$, and $\text{Cu}_2(\text{hfac})_4(\text{LNPyMeLNPyEt})$.

Rarely, it seems, the Cu–O axial distances in the $\text{Cu}^{2+}\text{-O}^{\bullet}\text{-N}<$ exchange cluster in the octahedron around the central atom are rather short (2.2–2.35 Å) at room temperature. This leads to predominant antiferromagnetic exchange interactions, despite the axial coordination in the $\text{Cu}^{2+}\text{-O}^{\bullet}\text{-N}<$ clusters. At high temperatures, therefore, μ_{eff} decreases for compounds ($\text{Cu}(\text{hfac})_2\text{LNPyEt}$ and $\text{Cu}(\text{hfac})_2\text{LNPyPr}$) with this structural feature. Still more exotic is the situation when the structural rearrangement at the magnetic transition temperature leads to a lengthening of Cu–O distances in the $>\text{N}^{\bullet}\text{-O-Cu}^{2+}\text{-O}^{\bullet}\text{-N}<$ exchange cluster, resulting in a shift of exchange from antiferromagnetic to ferromagnetic. Yet these coordination site dynamics are possible; we observed them for $\text{Cu}(\text{hfac})_2\text{LNPyEt}$. It is reasonable to believe that a structural rearrangement of this type occurred in the heterospin chains studied by Gatteschi et al. [24].

At low temperature for all the compounds under study we observed a considerable decrease (by 5–6%) in the unit cell volume (Table 1). The absolute value of the decrease was large (up to 300 Å³) in accordance with the decrease in the size of the unit cell. The greatest change was observed in the directions of infinite chains along which shortening of the Cu...Cu distances was most substantial. The least amount of compression or even lengthening at low temperatures (e. g. for $\text{Cu}(\text{hfac})_2\text{LNPyPr}$) was observed in the direction along which the Cu–O_{hfac} bonds lengthened. The crystals under study have different mechanical stability at low temperature above the spin-crossover transition point. The single crystals of $\text{Cu}(\text{hfac})_2\text{LNPyMe}$ generally cracked. The quality of the single crystals of $\text{Cu}_2(\text{hfac})_4(\text{LNPyMeLNPyEt})$ deteriorated considerably in the course of cooling and during the low-temperature X-ray experiment; the peak profiles of single-crystal reflections broadened and were not restored in their previous form at elevated temperature. The single crystals of $\text{Cu}(\text{hfac})_2\text{LNPyEt}$ and $\text{Cu}(\text{hfac})_2\text{LNPyPr}$ with a polymer chain “head-to-head” motif were described as “breathing” (during the cooling/heating cycles); after their cooling followed by an X-ray structural analysis and heating to room tempera-

ture the peak widths of their reflections were completely restored. The fact that $\text{Cu}(\text{hfac})_2\text{LNPyEt}$ and $\text{Cu}(\text{hfac})_2\text{LNPyPr}$ single crystals as macro-objects can undergo drastic reversible compression or expansion is another peculiarity of the heterospin compounds under discussion.

2.4 Conclusion

This short account illustrates the exceptional potential of nitronyl and imino nitroxides in the design of molecule-based magnetic materials. The fundamental bridging property of these ligands enables the building of extended structures in which one can “play” with the magnetic orbitals. But, importantly, the role of the substituent can be optimized to obtain specific structural arrangements and specific magnetic properties. Thus, it is shown how nitrogen containing non-chelating substituents might afford discrete cyclic or 1D structures depending on the nature of the heterocycle fragment. One should notice that these structural differences are the consequence of slight differences in the orientation of nitrogen coordination. In 1D compounds structural variety is augmented by the possibilities of head-to-head or head-to-tail coordination.

Such structural variety is reflected in magnetic properties. For copper(II) complexes, in which the Jahn-Teller effect operates, oxyl coordination can result in ferromagnetic or antiferromagnetic behavior. Owing to the plasticity of the coordination sphere, moreover, a complex might convert between these two types of behavior as a result of a perturbation; this is a new family of “spin-crossover species”.

Heterospin systems based on Cu(II) complexes with nitroxides are extremely interesting for performing detailed studies of a variety of effects associated with spin-crossover phenomena. Whereas few heterospin complexes with these effects have been found, magnetic transition regions were detected within a wide temperature range. For compounds described here this range is 30–250 K. The potential upper limit for the temperature of the spin-crossover-like phenomena generally accessible for such complexes is confined to the decomposition temperature, which is roughly estimated at 350–400 K. As for classical spin-crossover complexes, investigation of the relationship between the structural motion and the magnetic property variation might provide unique information for further quantum chemical analyses of the electronic structure of the exchange clusters. A valuable characteristic of heterospin complexes capable of spin-crossover transitions is their easy preparation as high-quality single crystals with mechanical stability over a wide temperature range. The single crystals are rich in easily functionalizable paramagnetic ligands. This opens up prospects of detailed rationalization of all atomic motion in the space of single crystals (i. e. structural dynamics in the range of phase transition) for determination of factors governing the form of the $\mu_{\text{eff}}(T)$ dependence, and for selective modification of magnetic transition characteristics by preliminary design of the paramagnetic ligand of desired structure. Additional possibilities for design of such complexes are afforded by solid solutions such as $\text{Cu}_2(\text{hfac})_4(\text{LNPyMe}, \text{LNPyEt})$.

Also, it seems quite feasible to determine the structural properties responsible for the mechanical instability which sometimes arises in crystals cooled below the spin-crossover transition temperature.

In our opinion, the exceptional ease of modification of the substituent makes these spin transition compounds more attractive than the classical compounds based on Fe or Co metal ions. In particular, use of chiral nitroxide ligands provides a unique opportunity to include optical properties.

References

- [1] For recent reviews, see: V. I. Ovcharenko, R. Z. Sagdeev, *Russ. Chem. Rev.* **1999**, 68, 345; *Magnetism: A Supramolecular Function* (Ed. O. Kahn), Kluwer Academic, Dordrecht, **1996**; *Mol. Cryst. Liq. Cryst.* (Eds.: K. Itoh, J. S. Miller, T. Takui), **1997**, 305/306, 1–586/1–520; *Mol. Cryst. Liq. Cryst.* (Ed.: O. Kahn), **1999**, 334/335, 1–712/1–706.
- [2] M. Verdaguer, A. Gleizes, J.-P. Renard, J. Seiden, *Phys. Rev. B* **1984**, 29, 5144.
- [3] O. Kahn, Y. Pei, M. Verdaguer, J.-P. Renard, J. Slatten, *J. Am. Chem. Soc.* **1988**, 110, 782.
- [4] J. S. Miller, J. C. Calabrese, H. Rommelmann, S. R. Chittipeddi, J. H. Zhang, W. M. Reiff, A.J. Epstein, *J. Am. Chem. Soc.* **1987**, 109, 769.
- [5] A. Caneschi, D. Gatteschi, R. Sessoli, P. Rey, *Acc. Chem. Res.* **1989**, 22, 392.
- [6] A. Caneschi, D. Gatteschi, P. Rey, *Progr. Inorg. Chem.* **1991**, 39, 331.
- [7] E. Freymy, *Ann. Chim. Phys.* **1845**, 15, 459.
- [8] A. R. Forrester, J. M. Hay, R. H. Thomson, *Organic Chemistry of Stable Free Radicals*, Academic Press, London, 180, **1968**.
- [9] E. G. Rozantsev, *Free Nitroxyl Radicals*, Plenum Press, New York, **1970**.
- [10] L. B. Volodarsky, V. A. Reznikov, V. I. Ovcharenko, *Synthetic Chemistry of Stable Nitroxides*, CRC Press, Boca Raton, USA, **1994**.
- [11] R. Brière, H. Lemaire, A. Rassat, *Bull. Soc. Chim. France* **1965**, 3273.
- [12] A. Zheludev, V. Barone, M. Bonnet, B. Delley, A. Grand, E. Ressouche, R. Subra, P. Rey, *J. Am. Chem. Soc.* **1994**, 116, 2019.
- [13] M. H. Dickman, R. J. Doedens, *Inorg. Chem.* **1981**, 20, 2681.
- [14] L. C. Porter, M. H. Dickman, R. J. Doedens, *Inorg. Chem.* **1988**, 27, 1548.
- [15] F. Lanfranc de Panthou, E. Belorizky, R. Calemzuk, D. Luneau, C. Marcenat, E. Ressouche, Ph. Turek, P. Rey, *J. Am. Chem. Soc.* **1995**, 117, 11247.
- [16] F. Lanfranc de Panthou, R. Calemzuk, D. Luneau, C. Marcenat, R. Musin, P. L. Öström, A. Grand, Ph. Turek, P. Rey, *Inorg. Chem.* **1996**, 35, 3484.
- [17] S. F. Vasilevsky, E. V. Tretyakov, O. M. Usov, Y. N. Molin, S. V. Fokin, Y. G. Shvedenkov, V. N. Ikorskii, G. V. Romanenko, R. Z. Sagdeev, V. I. Ovcharenko, *Mendeleev Commun.* **1998**, 216-218.
- [18] V. I. Ovcharenko, Magnetic Anomalies Inherent in Nonrigid Heterospin Molecule-Based Magnets. In: *VIIIth Int. Conf. Molecule-based Magnets*, San Antonio, Texas, September 16-21, 2000.
- [19] I. V. Ovcharenko, S. V. Fokin, G. V. Romanenko, Y. G. Shvedenkov, V. N. Ikorskii, E. V. Tretyakov, S. F. Vasilevsky, Thermally Induced Spin Transitions in Heterospin Systems. *XXth All-Russian Conf. Coordination Chemistry*, Rostov, Russian Federation, June 25–29, 2001.

- [20] I. V. Ovcharenko, Thermally Induced “Non-Classical Spin Transitions in Chain Polymer Heterospin Exchange Clusters”. In: *Polynuclear systems and CO₂ activation. The IIIrd All-Russian Conf. on Clusters Chemistry*. Tcheboxary, Russian Federation, August 20–25, 2001.
- [21] P. Gütllich, A. Hauser, H. Spiering, *Angew. Chem. Int. Ed. Engl.* **1994**, *33*, 2024–2054.
- [22] R. N. Musin, P. V. Schastnev, S. A. Malinovskaya, *Inorg. Chem.* **1992**, *31*, 4118–4123.
- [23] I. V. Ovcharenko, Y. G. Shvedenkov, R. N. Musin, V. N. Ikorskii, *J. Struct. Chem. (Engl. Edn.)* **1999**, *40*, 29–34.
- [24] A. Caneschi, P. Chiesi, L. David, D. Ferraro, D.; Gatteschi, R. Sessoli, *Inorg. Chem.* **1993**, *32*, 1445–1453.

3 Theoretical Study of the Electronic Structure and Magnetic Interactions in Purely Organic Nitronyl Nitroxide Crystals

Juan J. Novoa, Pilar Lafuente, Mercè Deumal, and Fernando Mota

3.1 Introduction

The nitronyl nitroxide radicals are a family of organic radicals giving rise to many purely organic crystals with magnetic properties, among them bulk ferromagnets [1]. Their general structure, depicted in Fig. 1, is a five-membered ring in which two NO radicals are linked to a sp^2 carbon and to a R group, where R is a substituent, which at its simplest is H, but can be a variety of groups including highly functionalized aromatic rings (Figs. 2 and 3). Each NO group is also linked to a sp^3 carbon. These carbon atoms form a C–C bond with each other and each has two methyl groups linked to it.

The magnetic properties of the purely organic crystals obtained from crystallization of the nitronyl nitroxide radicals change with the substituent. Figure 2 includes some examples of substituents the crystals of which have dominant ferromagnetic properties; examples with antiferromagnetic properties are depicted in Fig. 3 [2]. Besides the radical, the magnetic properties of the purely organic crystals grown for a given radical also depend on the polymorphic phase in which the crystal is packed. This is a clear indication of the dependence of the magnetic intermolecular interaction on the geometry of the crystal packing, i. e. intermolecular magnetic interactions in nitronyl nitroxides depend on the relative orientation of the adjacent radicals. Consequently, the rational design of purely organic crystals with dominant

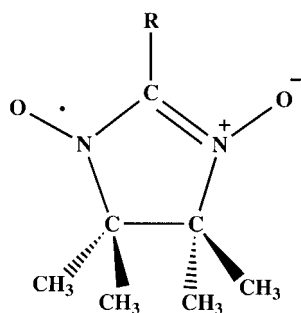


Fig. 1. General chemical structure of the members of the nitronyl nitroxide family of radicals. R is any substituent (examples of substituents furnishing crystals with dominant ferro or antiferromagnetism are given in Figs. 2 and 3).

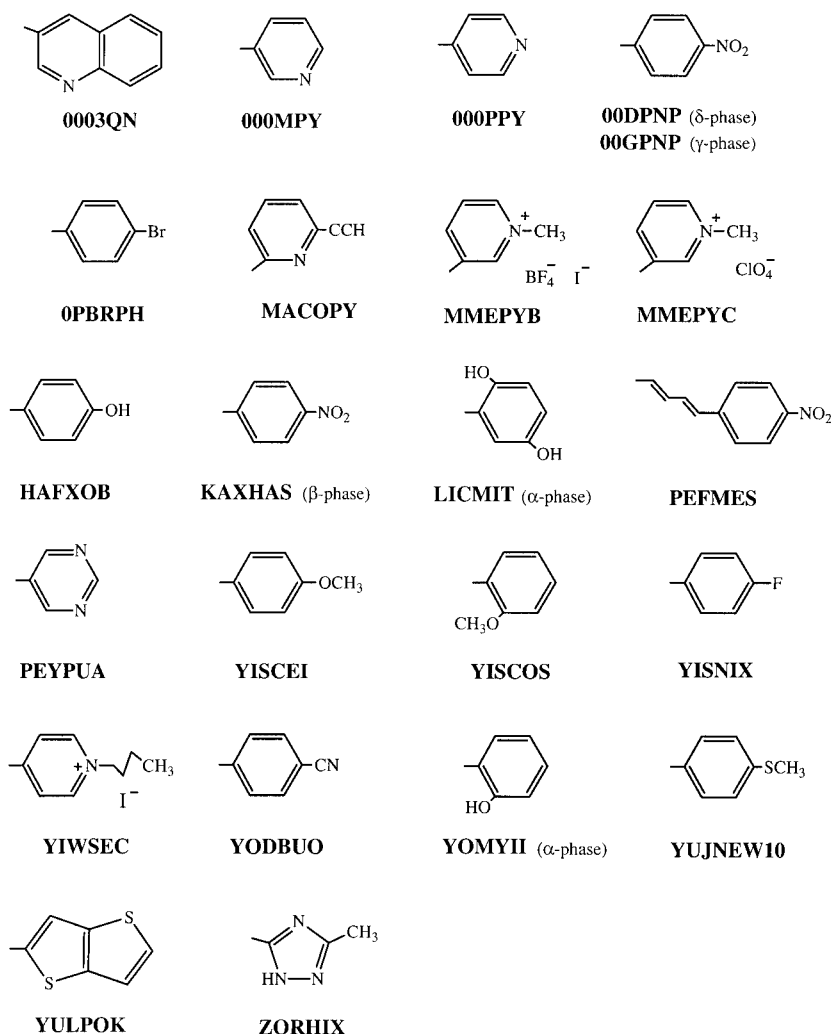


Fig. 2. Examples of substituents R for nitronyl nitroxides the crystals of which have dominant ferromagnetic interactions. Below each structure we have indicated the refcode which identifies the crystal in the Cambridge Crystallographic Database. When the crystal has not been deposited in this database we have assigned to that structure an internal name which begins with zero (details of the structures and the selection process are given elsewhere [2]).

ferro or antiferromagnetic interactions will be only possible when one has learned how to control the way the crystals pack. This is a new branch of the supramolecular chemistry called crystal engineering, which will not be treated here, despite its intrinsic interest to the field. Instead the interested reader is directed to appropriate publications describing general knowledge in that field [3], the polymorphic problem [4], and the possibility of predicting crystal packing from molecular struc-

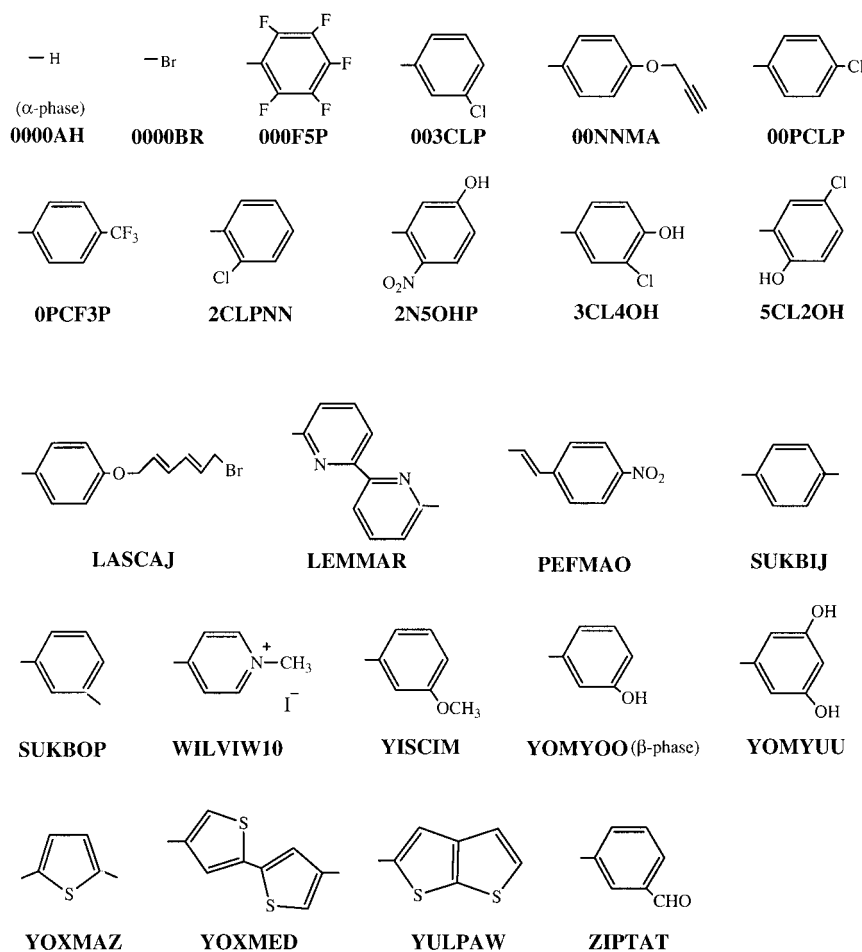


Fig. 3. As for Fig. 2, but for the substituents which give rise to crystals with dominant antiferromagnetic interactions.

ture [5]. The crystal packing polymorphs of the simplest nitronyl nitroxide (the H-substituted species) has been extensively studied [6], and many polymorphs were found, among them those known experimentally. Finally, methods have been developed to enable the rationalization of theoretically predicted or experimentally observed crystal packing, and good results have been obtained when the methods were applied to the packing of many purely organic nitronyl nitroxides [7].

Given the large number of purely organic nitronyl nitroxide crystals with well characterized structural and magnetic properties, we have selected this class of radical as prototypical for the study of the microscopic properties of the intermolecular magnetic interaction. This kind of interaction, also called “through-space”, is different from the “through-bond” interaction found in organometallic and coordination

compounds, in which the magnetic centers are the metallic atoms (sometimes with contributions from other atoms), and magnetic interaction is made possible by the bonds that the non-metallic ligands create between the metallic centers. We should point out that there have also been attempts to generate through-bond magnetism in purely organic systems, by following the so called polymeric approach. In this case, the magnetic centers would be organic radicals, which after a polymerization process would be linked by covalent bonds, thus enabling the existence of through-bond magnetic interactions between adjacent radicals. Until now this approach has not succeed in achieving its final goal, although it has produced a variety of high-spin oligomers [8].

Centering our attention on through-space magnetism, the view is far from clear in many directions. From the quantum chemical point of view the origin of this interaction is associated with the direct overlap of the orbitals of the adjacent radicals involved in the interaction, although some experimental observations have been attributed to the so-called dipolar interaction, in particular to the cooperative effect of the collective dipolar interactions in layered magnets [9]. There is, however, no well founded microscopic theoretical treatment capable of correlating the intermolecular geometry of a pair of radicals with their net magnetic behavior. As we will show later, the most popular intermolecular mechanism yet, the so called McConnell-I proposal [10], has a variety of weak points and failures when used to rationalize the experimental properties of some crystals. First, it was designed specifically for $\pi-\pi$ interactions, although it is commonly used for other types of interaction. Second, the value of the J_{ij} integrals, an important element of the McConnell-I proposal, is not normally taken into consideration, and this will give rise to serious errors, as we will discuss later. Given this situation, one can perform quantum mechanical *ab-initio* computations on model systems to obtain the value of the low-high spin energy separation, as a way of obtaining information about the nature of the through-space magnetic interaction. In the rest of this chapter we will present results from these studies that give us insight into the nature and properties of the through-space magnetic interaction.

3.2 Electronic Structure of Nitronyl Nitroxide Radicals

3.2.1 Fundamentals

Before discussing the electronic structure of these radicals, discussion of the methodology required to study the electronic properties of these radicals is required. We will do so in a descriptive manner and focus on problems found in the application of these methods to the study of nitronyl nitroxide radicals, omitting from this presentation unnecessary details of the methods; these are described in the original work, to which the reader is referred.

The description of a radical by means of *ab-initio* methods requires careful choice of the method to use. For such a task one must have a qualitative knowledge of

the types of interaction present in the electronic structure of the compound being described. These principles can be obtained by following an analysis such as that presented in the next few paragraphs for the hydro-nitronyl nitroxide (HNN) radical, the simplest member of the nitronyl nitroxide family, in which $R = H$. This radical has a five membered ring with two NO groups, two tetracoordinated $C(sp^3)$ atoms, each with two methyl groups attached to them, and a tricoordinated $C(sp^2)$ atom.

The electronic structure of this molecule can be rationalized by looking at the electronic structure of the constituting groups, and then at the ways these groups are linked. The structure of each of the groups present in the HNN radical is presented in valence bond (VB) terminology in the diagrams of Fig. 4. Thus, for instance, the $C(sp^2)$ atom forms three bonds (with the H atom, and the nearby two N atoms). Each of these bonds involves a pair of electrons, one from each of the atoms of the bond. The electrons of this pair are coupled into a closed-shell singlet (i. e., the two are in the same orbital, one with spin α and the other with spin β , graphically represented as upwards and downwards arrows). A $C(sp^2)$ atom has four valence electrons and, given its topology, they must be placed among the three sp^2 hybrids and one pure p orbital, perpendicular to the plane of the sp^2 hybrids. The three sp^2 hybrids are involved in making one C–H or two C–N bonds, thus requiring the presence of one electron in each hybrid. The remaining electron of the carbon atom must, therefore, be located in the pure p orbital, that is, the $C(sp^2)$ atom is a radical with an electron in a p orbital perpendicular to the molecular plane. Consequently, it is a π radical. Using the same arguments, the $C(sp^3)$ atoms, which form four bonds, have their four electrons involved in bond formation, so each electron is sitting in each of the sp^3 hybrids. Consequently, these atoms have no radical character. Finally, the NO groups have five valence electrons in the N atom and six in the O atom. Three of the five electrons of the N atom are involved in the sigma bonds formed by this atom (two C–N bonds and the N–O bond). They

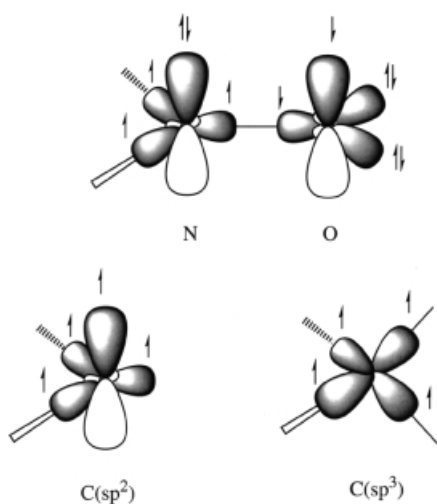


Fig. 4. Electronic structure of the fragments which constitute the HNN molecule, as analyzed using the valence bond (VB) method.

are, therefore, located in the sp^2 hybrids (defined by the geometry of the bonds). The remaining pair of electrons must necessarily go to the pure p orbitals, singlet paired (that is, one is an α electron and the other is a β electron). The topology of the bonds of the O atom is compatible with sp, sp^2 or sp^3 hybridization. We have chosen sp^2 hybridization, but we could have chosen sp hybridization and reached similar conclusions. In sp^2 hybridization the six valence electrons of the O atom are located as follows: one is placed in the sp^2 hybrid pointing to the N atom, as required for the formation of the N–O bond, and the remaining five electrons are placed in the remaining two sp^2 hybrids and the pure p orbital. One can, therefore, form two singlet pairs, leaving one orbital with a single electron. In principle, this orbital can be one of the hybrids or the p orbital, but *ab-initio* computations show that the option more stable energetically is that leaving the single electron in the pure p orbital. According to this description, therefore, the NO group is a π radical with the radical electron located on the O atom. There is, however, another way of writing this structure, in which one of the electrons of the pure p orbital of the N atom is shifted to the pure p orbital of the O atom. This alternative form (called resonant forms or structures) is quite stable energetically for the NO group. Their existence and stability gives rise to delocalization of the electron over the O and N atoms, as elaborate MCSCF *ab-initio* computations have shown [11, 12]. We must, therefore, visualize the NO groups as a π radical center in which the electron is delocalized on the two atoms of the center.

When the structure of each constituting group is known, one can rationalize the electronic structure of the HNN radical by linking each group as they are in the molecule by means of C–N or C–C bonds. Each bond involves a pair of singlet-coupled electrons, as already mentioned, thus giving rise to the formation of a closed-shell singlet. The only degrees of freedom defining the electronic structure of the HNN molecule are, therefore, the orbitals of the part with radical behavior, i. e. the two NO groups and the $C(sp^2)$ atom. We must now find the molecular orbitals of each fragment involved in the interaction between the fragments, by combining the atomic orbitals of each fragment. Thus for the NO the mixing of the two pure p orbitals which have three electrons gives rise to a bonding and antibonding combination, and the unpaired electron goes to the antibonding combination. Because of this the NO radical has no double bond. The orbitals of the $C(sp^2)$ atom are as depicted in Fig. 4. The antibonding orbital of each NO fragment and the pure p orbital of the $C(sp^2)$ atom now couple to form the molecular orbitals. This is a three orbital-three electron system within a C_2 symmetry arrangement (in the crystal geometry of the HNN molecule, this symmetry is slightly distorted). A system of this type can give rise to the formation of the three molecular orbitals depicted in Fig. 5, ordered energetically as bonding, non-bonding and antibonding, according to the number of their nodes.

The most stable ordering of the three electrons in these orbitals is that indicated in Fig. 5, which gives rise to a doublet. The quadruplet implies exciting one electron from the ϕ_1 bonding orbital to the ϕ_3 antibonding orbital. It is interesting to note that the shape of the singly occupied orbital (SOMO) has a node on the $C(sp^2)$ atom. This node has important physical consequences. One is the low delocalization of the π electrons of the ONCNO group along the atoms of the R substituent.

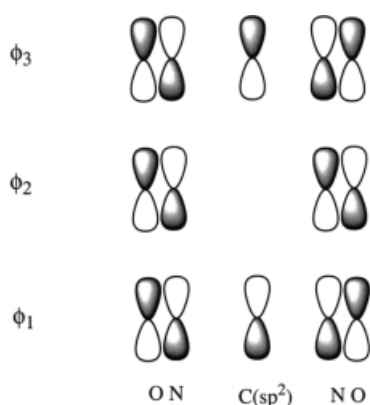


Fig. 5. Molecular orbitals of the π orbitals carrying unpaired electrons in the fragments (the two NO groups and the $C(sp^2)$ atom). This is a three orbital-three electron system, which gives rise to bonding (ϕ_1), non-bonding (ϕ_2), and antibonding (ϕ_3) molecular orbitals. Besides these orbitals, the HNN molecule has a variety of molecular orbitals associated with the formation of the σ bonds (C–N, C–C, ...), which combine among themselves to produce orbitals adapted to the symmetry of the molecule.

Another is the lack of spin on the $C(sp^2)$ atom in methods (e.g. the restricted-open Hartree–Fock – ROHF – method) in which no spin polarization is allowed. It is found experimentally that the $C(sp^2)$ atom has some spin [13–15]. One should, therefore, use methods which permit the presence of spin polarization, by allowing the mixture of the ground state wavefunction with some excited state wavefunctions of the same multiplicity, obtained by exciting the electrons from the ϕ_1 or ϕ_2 orbitals to the ϕ_3 orbital [16]. We will now focus our attention on presenting an overview of the methods which one can use for proper description of the electronic structure of the nitronyl nitroxide radicals.

The simplest could be an ROHF method [18], which computes the optimum shape of the ϕ_1 , ϕ_2 , and ϕ_3 orbitals in a single determinant wavefunction, forcing the occupation of these three orbitals to be 2, 1, and 0. As mentioned above, the ROHF method is incapable of accounting for the spin polarization of the $C(sp^2)$ atom, because this effect implies partial occupation of orbitals which have contribution in the $C(sp^2)$ atom. Such a polarization effect can be described by use of the unrestricted Hartree–Fock (UHF) method, a method which produces occupation numbers for the orbitals similar to those obtained by use of CI methods [19], i.e. it gives rise to fractional occupancies of the ϕ_1 , ϕ_2 and ϕ_3 orbitals. The wavefunction computed with the UHF method, however, is not a pure spin state. For HNN it is a mixture of doublet and quadruplet components (it is, consequently, not an eigenfunction of the \hat{S}^2 operator) [18]. This is a serious problem for the description of some properties (for instance, the spin distribution in some atoms of the nitronyl nitroxides is overestimated, or has the wrong sign [13, 20]), although some other properties are well described (the optimum geometry, for instance).

To avoid the spin contamination present in the UHF wavefunction while allowing for the presence of spin polarization, a serious alternative, albeit more costly, is the MCSCF method [18]. Unlike the different forms of the Hartree–Fock method discussed before, the MCSCF method is multi-configurational. In this method the weights of the configurations and the shapes of the orbitals are simultaneously optimized. One popular formulation of the MCSCF method employs complete active spaces (CAS(n,m)) in which the multi-configurational space is the result of placing

n electrons in m orbitals, in all possible forms. This space includes the lowest-energy configuration employed in the Hartree–Fock method, and the excited ones responsible for the spin polarization. For HNN this can be achieved by use of an orbital space which includes the ϕ_1 , ϕ_2 , and ϕ_3 orbitals and their electrons (a CAS(3,3) space). Larger spaces which include the CAS(3,3) space, e. g. the CAS(7,7) space, are also adequate. They also include the possible polarization present between the σ molecular orbitals, and/or between σ and π orbitals. The occupation of the ϕ_1 , ϕ_2 , and ϕ_3 orbitals is again fractional, with values within the 2.0–0.0 range. The MCSCF computations include only a small amount of correlation energy (that associated with the active space). To account for the remaining correlation, one can perform a second-order Moller–Plesset on the MCSCF wavefunction, a method normally known as CASPT2 [21]. This method is known to provide a very good description of the energy splitting between the ground and excited states of the same and different spin multiplicity in organic molecules and transition metal compounds [21]. Other multireference methods are the various levels of mono-reference Moller–Plesset (MP2, MP3, ...), configuration interaction (CID, CISD, ...), or coupled cluster (CCSD, CCSD(T), ...) methods [18]. These are based on the expansion up to some order of the unrestricted Hartree–Fock wavefunction. These methods suffer from the problem of the spin contamination of the expanded wavefunction. In many of these methods, in particular in expansions at low order like the MP2, the degree of spin contamination is similar to that found in the unrestricted Hartree–Fock wavefunction. These methods should, therefore, be used with caution, because physically one is describing some average of the properties of the doublet and quadruplet states, the average increasing with the amount of spin contamination.

One can eliminate the problem of spin contamination of the wavefunction by using projected methods, in which all higher multiplicity components are exactly projected out [22], or approximate projected methods, in which only a few of these components are projected out (normally the next in multiplicity, because it has been observed that this component is that inducing more spin contamination) [23]. Although the resulting projected wavefunction is not variational, when applied to nitronyl nitroxides the results seem similar to those from MCSCF or other methods of similar accuracy [24].

Besides the previous methods, one can resort to density-functional (DFT) methods [25]. These methods, based on the Hohenberg–Kohn theorems [26], enable the use of the quantum theory to compute eigenstates directly in terms of the three-dimensional single-particle monoelectronic density (ρ), instead of as a function of the wavefunction (Ψ). This speeds the computational process, the cost of which is proportional to N^3 (where N is the size of the basis set) instead of the much higher orders found in the Moller–Plesset, configuration interaction, or coupled cluster methods. The final expression for the energy obtained within the DFT methodology takes the form:

$$E_{\text{DFT}} = \text{tr}\mathbf{h}\mathbf{P} + (1/2)\text{tr}\mathbf{P}\mathbf{J}(P) + E_{\text{ex}}(P) + E_{\text{cor}}(P) + V \quad (1)$$

where \mathbf{h} is the matrix representation of the monoelectronic Hamiltonian (kinetic plus nuclear–electronic interaction), \mathbf{P} is the density matrix, tr is the trace of the

matrix, $\mathbf{J}(P)$ are the $\langle ij|ij \rangle$ Coulombic integrals, $E_{\text{ex}}(P)$ is the exchange functional, and $E_{\text{cor}}(P)$ is the correlation functional (It should be noted that the products \mathbf{hP} and $\mathbf{PJ}(P)$ both give rise to energetic contributions.) The Hartree–Fock energy can be obtained as a special case of Eq. (1) by making $E_{\text{ex}}(P) = (1/2)\text{tr}\mathbf{PK}(P)$ and $E_{\text{cor}}(P) = 0$ ($\mathbf{K}(P)$ are the $\langle ij|ji \rangle$ exchange integrals, whose values depend on \mathbf{P}). The functionals used in the exchange and correlation parts are integrals of some functions of the density and the gradient of the density. If the functional depends only on the density, it is called *local*, whereas when it depends also on the gradient of the density is called *non-local*. Many different functionals are proposed in the literature for the exchange and correlation parts. Previous experience indicates that the non-local functionals produce better results on chemical systems [27]. Among the non-local functionals, the so called BLYP [28–30] and B3LYP [31,32] functionals seem to be among the best, the second in particular.

When the UHF formulation of any of these two functionals is used to compute the properties of the HNN molecule in its doublet ground state, it produces a wavefunction which has very small spin contamination from the quadruplet [13, 17]. This gives validity to the predictions obtained with these functionals for HNN and other nitronyl nitroxide radicals. It should, however, be noticed that small spin contamination is not always observed. This has prompted some doubts on the validity of the density-functional computations where such spin contamination is found. The latest approach to this problem [21] is to accept that a single Kohn–Sham determinant might lead to spin contamination for open-shell systems and still be a proper solution, if the atomic spin density is properly described. The reason is that in the Kohn–Sham method the density, and not the orbitals, has physical meaning and the eigenvalues of the \hat{S}^2 operator for a given determinant are computed using the orbitals.

3.2.2 *Ab-initio* Computation of the Electronic Structure of Nitronyl Nitroxide Radicals

To illustrate the performance of the usual *ab-initio* methods in computing the electronic structure of the HNN molecule, and also to test the validity of the previous qualitative description, we have computed the energy of the doublet ground state at different computational levels. The quadruplet lies 81 kcal mol⁻¹ above the doublet, at the MCSCF(7,7)/6-31+G(d) level. For the HNN geometry found in the α -phase crystal [33], a UHF/6-31+G(d) calculation [34] gives a wavefunction for the doublet whose expectation value for the \hat{S}^2 operator is 1.13, compared with the 0.75 value of a pure doublet state, as obtained from direct application of the $S(S+1)$ expression when $S = 1/2$. The UHF wavefunction, therefore, has 12% quadruplet contamination. A natural orbital analysis of the UHF wavefunction [19] gives the result that all the orbitals are doubly occupied (within 0.01 error) except for three orbitals whose occupations are 1.81, 1.00, and 0.19. The shape of these three orbitals, displayed in Fig. 6, corresponds to that predicted above for the ϕ_1 , ϕ_2 , and ϕ_3 orbitals in our qualitative analysis (Fig. 5). Orbitals of the same shape are obtained after a

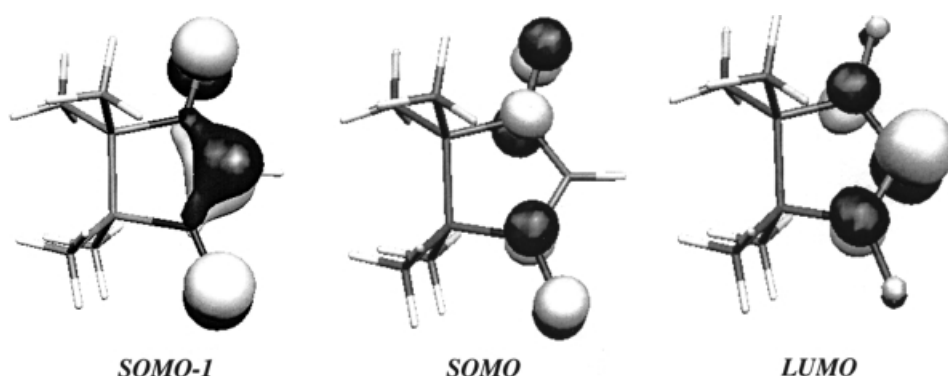


Fig. 6. Plot of the SOMO-1, SOMO, and LUMO orbitals of the HNN radical computed at the UHF/6-31+G(d) level. The contours plotted are those in which the orbital has a value of ± 0.1 atomic units. Shaded areas represent negative regions, and unshaded areas represent positive regions.

ROHF/6-31+G(d) or MCSCF(7,7)/6-31+G(d) computation [35]. The MCSCF(7,7) active space has 784 configuration state functions in it. Among these the dominating configurations are the ROHF Hartree–Fock determinant, with a coefficient of 0.96, and three configurations with coefficients 0.16, 0.15, and 0.09. All others have coefficients < 0.06 . This means that the ROHF Hartree–Fock determinant describes the basic structure of the system, and the spin polarization is introduced by these three configurations of weight approximately 0.15. The occupation of the three orbitals in the ROHF method is 2.00, 1.00, and 0.00, and in the MCSCF(7,7) computation becomes 1.91, 1.00, and 0.09. At the same time B3LYP/6-31+G(d) computations have an S^2 expectation value of 0.80, and the occupation of the ϕ_1 , ϕ_2 , and ϕ_3 orbitals is 1.98, 1.00, and 0.02 electrons. Remember that the S^2 expectation value in DFT computations has no physical significance (see comment above and Ref. [21]).

Although the overall shape of the orbitals computed by these methods seems similar, there might be changes not observed under normal inspection. These changes can, however, be quantified by computing the atomic charge on each atom; this depends on the shape of the electron density, a property which depends on the shape of the orbitals. Table 1 lists atomic charges obtained by a Mulliken population analysis of the wavefunction obtained by use of the UHF, MCSCF(7,7), and B3LYP methods, using the 6-31+G(d) and cc-pVDZ [36] basis sets, and the experimental geometry found in the α -HNN crystal. The results for UHF and MCSCF(7,7) will be compared with the charges obtained by integrating the charge density over the atomic region, defined according to Bader’s atoms-in-molecules (AIM) procedure [37]. The results show the well known difference between the Mulliken and AIM charges. They also show the dependence of the atomic charge values on the basis set. Finally, they indicate that the density in the UHF and MCSCF(7,7) methods is almost the same, but the B3LYP methods gives charges which differ from those of the previous methods, although the qualitative picture is the same for all three methods.

Table 1. First row: atomic charges for the HNN radical computed from a Mulliken population analysis of the UHF, MCSCF(7,7), and B3LYP wavefunctions, using the 6-31 + G(d) basis set. Second row: similar results obtained by use of the cc-pVDZ basis set. Third row: equivalent results from an AIM analysis of the cc-pVDZ wavefunctions. The geometry is the experimental one for the α -phase of the crystal, and the basis set is the 6-31 + G(d) basis. Values are given in atomic units.

Atom	UHF	MCSCF(7,7)	B3LYP
H	0.27	0.27	0.22
	0.08	0.08	-0.03
	0.11	0.10	
C(sp ²)	0.33	0.33	0.47
	0.35	0.35	0.32
	1.19	1.22	
N	-0.14	-0.15	-0.28
	-0.06	-0.04	0.02
	-0.62	-0.63	
O	-0.22	-0.23	-0.04
	-0.40	-0.41	-0.35
	-0.56	-0.57	
C(sp ³)	-0.30	-0.35	-0.51
	-0.23	-0.24	-0.28
	0.39	0.39	

Table 2. Values of some representative values which define the geometry of the HNN molecule. The experimental values are compared with those computed by full optimization of the geometry of the doublet state of this radical at the UHF/6-31+G(d) MCSCF(7,7)/6-31+G(d) and B3LYP/6-31+G(d) levels. Two values are given in the experimental column for all the angles except one, because the experimental geometry lacks the C₂ symmetry found in the three theoretical geometry optimizations. Values of the distances are given in Å, and those for the angles in degrees.

Parameter	Experimental	UHF	MCSCF(7,7)	B3LYP
C(sp ²)-H	0.994	1.074	1.072	1.085
C(sp ²)-N	1.337/1.329	1.349	1.341	1.345
N-O	1.279/1.289	1.240	1.238	1.267
N-C(sp ³)	1.510/1.514	1.487	1.486	1.518
H-C(sp ²)-N	122.6/127.3	124.9	124.5	123.9
C(sp ²)-N-O	125.7/125.9	126.1	127.4	127.3
N-C(sp ²)-N	110.1	110.2	111.0	112.2
O-N-C(sp ³)	122.5/122.5	122.4	122.1	122.0

The results from geometry optimization for the HNN radical in its doublet state performed at the UHF/6-31+G(d) and MCSCF(7,7)/6-31+G(d) levels are listed Table 2, together with the experimental values from the α -HNN crystal. It is clear that the UHF and MCSCF(7,7) values for this basis set are almost the same. The computed results are different from the experimental values. The first concerns the

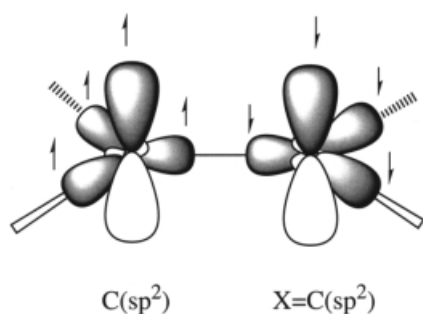


Fig. 7. Valence bond description of the electronic structure of the $C(sp^2)$ -X fragment, X being the atom of the R substituent which is linked to the $C(sp^2)$ atom of the five-membered ring of the nitronyl nitroxides. The figure shows an example in which R is a substituted aromatic ring and X is a $C(sp^2)$ atom.

symmetry, which is lost in the experimental geometry, but is preserved (C_2 group) in the UHF and MCSCF(7,7) computations. The largest differences are, furthermore, between C–H, N–O, and N– $C(sp^3)$ distances. The first discrepancy is most probably because of the well known trend of X-ray fitting to give C–H distances which are too short [38].

Let us now study the remaining members of the nitronyl nitroxide family. We can rationalize the electronic structure of any nitronyl nitroxide by starting with the electronic structure of the HNN radical and looking at the effect induced by changing the R substituent from H to that found in the radical of interest. If the atom of the R substituent linked to the $C(sp^2)$ atom (hereafter called X) has pure p orbitals of the π type (e. g. the Cl atom, or another $C(sp^2)$ atom), these orbitals can interact with the pure p orbitals of the $C(sp^2)$ atom. One ends up with the situation depicted in Fig. 7, where the R substituent is linked to the five-membered ring $C(sp^2)$ atom through another $C(sp^2)$ atom. The highest occupied orbital (which can be the bonding or antibonding orbital, depending on the number of electrons sitting on the pure p orbital of the X atom) will be that interacting with the pure p orbitals of the NO fragments. For reasons of symmetry, however, the SOMO orbital (orbital ϕ_2 in Fig. 5) will remain unchanged, because of its node on the $C(sp^2)$ atom, and the R fragment orbitals can only contribute to the SOMO-1 and LUMO orbitals (ϕ_1 and ϕ_3 in Fig. 5). This is what *ab-initio* computations also tell us, as illustrated in Fig. 8 for the phenyl-nitronyl nitroxide (PhNN) molecule. Although at the crystal geometry [13a], the five-membered and six-membered rings of the PhNN molecule are not coplanar (they are rotated 25° along the C–C bond connecting the five and six-membered rings), there is a non-negligible contribution of the ring orbitals to the SOMO-1 and LUMO orbitals. This enables the existence of spin polarization through the SOMO–LUMO monoexcitations. Because the weight of the ROHF Hartree–Fock determinant is again approximately 0.92, and those for the excited configurations are approximately 0.15, this spin polarization mechanism does not propagate the polarization very effectively, as we will discuss below. Consequently, we should expect that all the nitronyl nitroxides should have a similar electronic structure, because in the dominant determinant the distribution of the unpaired electron is always similar. The situation is similar in all other nitronyl nitroxides because of two experimental facts:

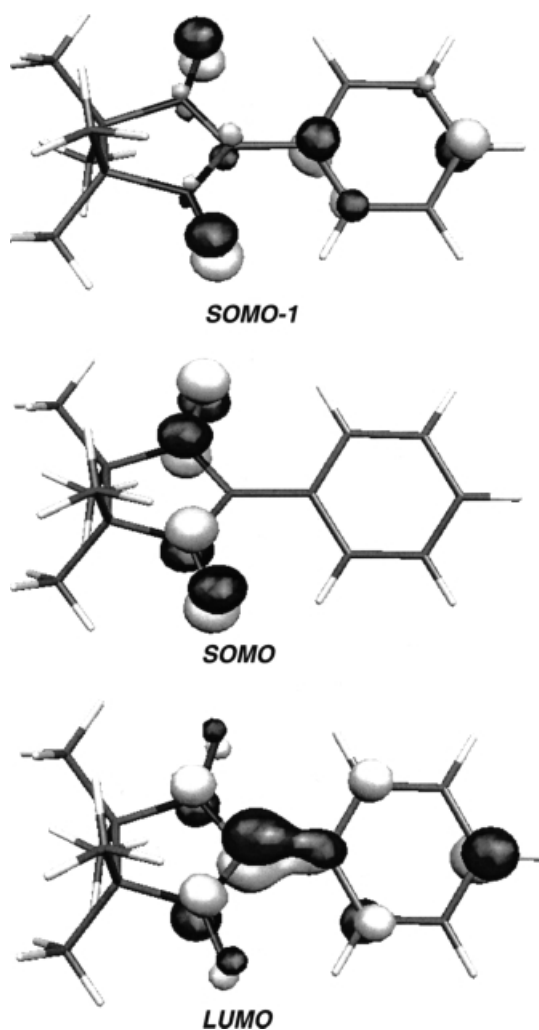


Fig. 8. Plot of the SOMO-1, SOMO, and LUMO orbitals of the phenyl-nitronyl nitroxide radical computed at the UHF/3-21G(d) level. The contours plotted are those in which the orbital has a value of ± 0.1 atomic units. Shaded areas represent negative regions and unshaded areas represent positive regions.

- the five-membered ring geometry is almost the same in all the nitronyl nitroxide radicals which crystallize as purely organic crystals and the ONCNO group is practically coplanar in that ring [39]; and
- the torsion angle between the ONCNO group and the six-membered ring in these crystals takes values between 30 and -30° [39], thus enabling some mixing between the orbitals of the $C(sp^2)$ atom of the ONCNO group and those of the six-membered ring.

3.2.3 Spin Distribution in Nitronyl Nitroxide Radicals

To understand the magnetic properties of the molecular crystals of a purely organic radical it is helpful to know how the spin is distributed along the isolated radical, to define the spin-containing regions of the radical. The magnetic interactions in monoatomic and diatomic radicals decrease exponentially with distance. At the same time the McConnell-I model bases its predictions on the atomic spin located on the atoms for which distances are shortest. For a proper control of the magnetism in the purely organic nitronyl nitroxide crystals, therefore, it seems essential to understand the form in which the spin is distributed along the atoms of the radical, for any given radical, and also the ways in which that distribution can be modified, if desired.

First we will establish some basic concepts related to the spin density. The spin density is a physically observable quantity obtained at each point by subtracting the electron density of the α electrons minus the electron density of the β electrons (it is normally assumed that the number of α electrons (n_α) is larger than the number of β electrons (n_β) in systems where these two quantities are different; in this case, the system is said to have an open shell electronic structure). As the electron density is a monoelectronic function which depends on the Cartesian coordinates, so it is the spin density. On the other hand, because the physical interpretation of the electron density is the probability of finding an electron within an element of volume dv ($dv = dx dy dz$), the spin density should be interpreted as a monoelectronic function which give us the probability of finding an excess of α electrons over β electrons in any volume element. Integrated over the whole space this should give a number equal to $n_\alpha - n_\beta$. Although the spin density is a three-dimensional property, like the orbitals, it is depicted in two-dimensional representations, in one of two forms:

- by looking at the values of the spin density in a two dimensional plane of the space – the values in this plane are then plotted as a contour map, similar to the contour maps used in geography; alternatively, they can be plotted as a hill map;
- by cutting space in parallel surfaces and then plotting in each surface the contour of the desired spin density value; this is a three dimensional map which extends over the whole space spanned by the molecule.

The two plots are complementary in some forms. The second ways gives a volume enclosing the region in which the density has a value higher than a selected cutoff, although it does not give any information on how large the density can be within that volume or about its variation from one point to another (Fig. 9). The first type of plot gives a detailed information about the variation of density on a plane, but no information of the variation in the nearby planes. One therefore chooses the representation depending on the information required. Occasionally the two representations can be used simultaneously. The two type of representations are illustrated in Fig. 9 for the HNN molecule. The spin density on the nucleus, a property of interest in NMR or ESR, is the value of the spin density at a specific point, the nucleus.

Another way of representing the distribution of spin in space is by means of the atomic spin population. This quantity is obtained by adding the spin density over

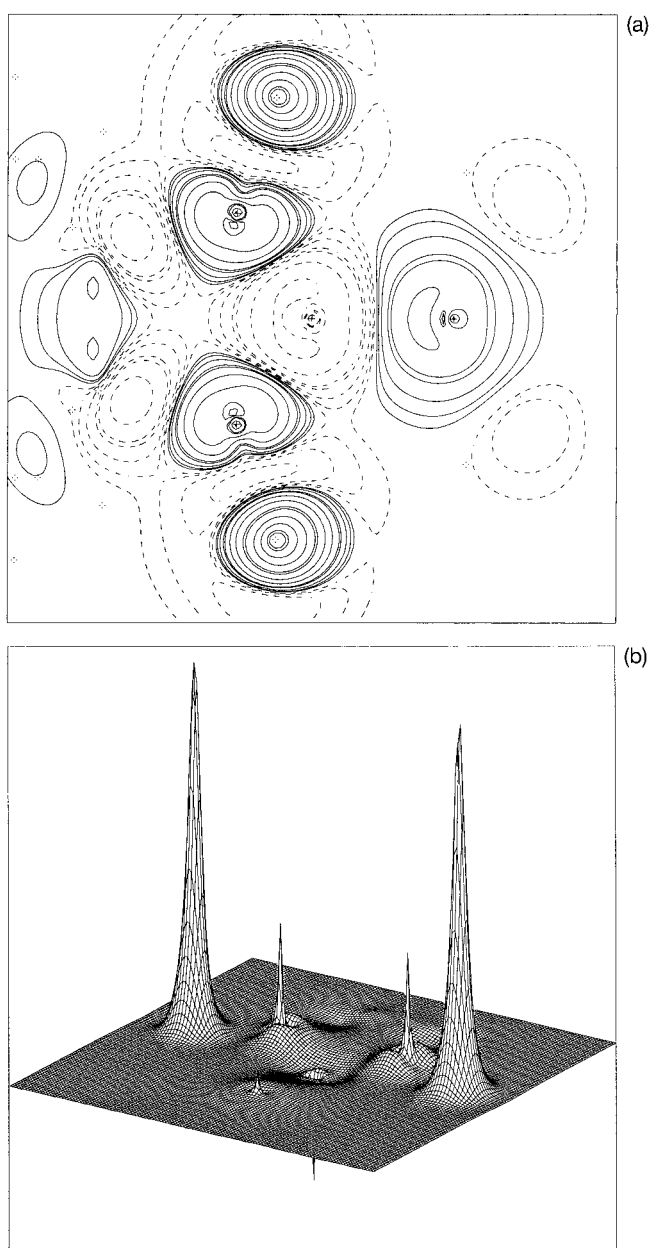


Fig. 9. Representation of the spin density of the HNN radical in its doublet state. The spin density is cut along the ONCNO plane of the molecule in two complementary forms: (a) as contour lines (solid lines are for positive contours, while broken lines are for negative values; The smallest contours correspond to a $0.001 \text{ e } \text{\AA}^{-3}$), and (b) as a 3D plot (the peaks above the plane are positive, while those below the plane are negative; The two external peaks are for the O atoms).

the region of the space associated to each atom. Such a region can only be defined in a precise way within the AIM methodology [36], although this procedure is computationally very expensive. Consequently, a much more common approach is to compute the atomic spin population on an atom by means of Mulliken population analysis, computing the atomic charges on the atom coming from the α and β electrons, and then subtracting these two values. Previous tests on the HNN molecule [17] have indicated that the atomic spin population obtained by using Mulliken population analysis is similar to that obtained by strict application of the Bader AIM model, and we will see below that this is also true for other nitronyl nitroxide radicals.

A word of caution should be introduced here when using atomic spin populations – one should keep in mind that they represent the *sum of all the values of the spin density* in a given region of the molecule. Consequently, they represent a sort of *average* value of the density on that region. When the distribution is non uniform, therefore, as for the spin distribution on atoms, there can be large variations in the magnitude and sign of the spin in that region. For this reason the value of the atomic spin on atoms with similar spin density on the nucleus can be very different, i. e. the value of the spin density on the nucleus is not always proportional to or representative of the atomic spin population on the corresponding atom. We will see some examples in the following paragraphs.

We can now analyze the shape of the electron density maps. In a ROHF wavefunction, because the doubly occupied orbitals occupy the same part of space (because of the restrictions inherent to the ROHF method), the spin density is equal to the square of the SOMO orbital (Figs. 5 and 6). Therefore, the spin density has the same shape as the SOMO orbital but without its negative regions (because corresponds to excess α electrons). It therefore has a node in the C(sp²) atom, in contrast with the experimental results, which established the existence of a region of negative density in the vicinity of the C(sp²) atom [13a, 14d, 15]. This node disappears when the UHF method is used (projected or unprojected), or also at the MCSCF or B3LYP level, because all of these methods allow the presence of spin polarization. This is clearly illustrated by looking at the spin density distributions of Fig. 9, or at the atomic spin populations of Table 3. Remarkably good agreement is obtained between the B3LYP and MCSCF(7,7) results and the experimental results obtained by projecting the spin density into atomic regions. The failure of the UHF method is because of the spin contamination of the doublet, because when that contamination was projected out the atomic spin population on the C(sp²) atom became -0.174 e. These results are basis set-dependent, but numerical tests on smaller systems indicated that they are similar when a double zeta plus polarization basis set is used [17]. These results also indicate that most of the spin distribution is located in the ONCNO group of atoms, with much smaller contribution on some of the C(sp³) atoms, and negligible contributions on all H atoms. Finally, it is also interesting to note the asymmetry of the atomic spin population, caused by the asymmetry of the geometry (the full optimized symmetric radical does not have such asymmetry in the atomic spin populations).

When the H of the HNN is replaced by another substituent, the spin distribution does not change much from that described above for the HNN radical. This is illus-

Table 3. Atomic spin population computed for the doublet state of the HNN radical (crystal geometry at the UHF/6-31 + G(d) MCSCF(7,7)/6-31 + G(d) and B3LYP/6-31 + G(d) levels. Two sets of values are given, because of the lack of symmetry of the crystal geometry of this radical. The experimental values obtained for the equivalent atoms of the phenyl-nitronyl nitroxide are also given for comparison. All the values are given in electrons.

Atom	Experimental	UHF	MCSCF(7,7)	B3LYP
H-C(sp ²)		0.057	0.012	0.011
C(sp ²)	-0.121	-0.801	-0.182	-0.238
N	0.278	0.523/0.539	0.272/0.264	0.285/0.276
O	0.262	0.388/0.352	0.304/0.297	0.335/0.321
C(sp ³)-ring	-0.025	-0.019/0.003	-0.009/0.013	-0.008/0.002
C(sp ³)-methyl		-0.019/0.001	0.012/-0.001	0.014/-0.004
H-methyl	0.009	<0.003	<0.001	<0.001

trated by comparing the spin-density map of the HNN radical (Fig. 9) and that for the PhNN radical (Fig. 10). The overall shape of the spin density distribution in the five-membered ring region is the same, and the size of the region enclosing the ± 0.01 density (in atomic units) threshold is very small on the atoms of the six-membered ring (the R substituent). The shape of the PhNN map is also nearly identical to that obtained in polarized-neutron diffraction experiments [13a], except for small details

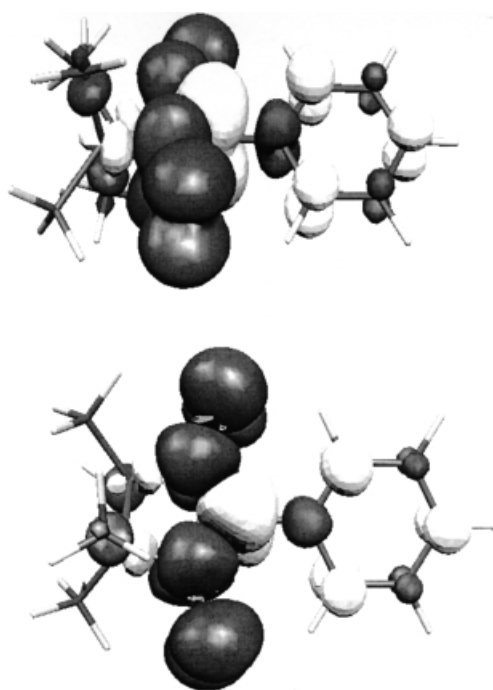


Fig. 10. Tridimensional representation of the isodensity surface whose spin density is $0.001 \text{ e } \text{\AA}^{-3}$ for the phenyl-nitronyl nitroxide radical (light: regions of negative density; dark: regions of positive density). Two views of the same spin density distribution are presented: lateral (upper diagram) and from above (lower diagram).

Table 4. Atomic spin population for some atoms of the phenyl-nitronyl nitroxide radical computed using the B3LYP functional and the following five basis sets: (a) 6-31G(d), (b) cc-pVDZ, (c) cc-pCVDZ, (d) EPR-II, and (e) IGLO-III. The Mulliken and AIM values are given. The atoms selected are the ONCNO group of the five-membered ring (the different NO groups are identified as N₁O₁ and N₂O₂), and the C atom of the six-membered ring (C-six) linked to the C(sp²) atom of the ONCNO group. The basis set size is also given in the last row.

Atom	Mulliken					Bader	
	a	b	c	d	e	b	c
C(sp ²)	-0.216	-0.203	-0.197	-0.215	-0.283	-0.154	-0.156
N1	0.295	0.285	0.284	0.291	0.340	0.270	0.276
O1	0.351	0.355	0.354	0.350	0.358	0.343	0.338
N2	0.264	0.254	0.253	0.263	0.305	0.242	0.249
O2	0.326	0.329	0.327	0.324	0.332	0.317	0.311
C-six	0.042	0.033	0.030	0.050	0.044	0.025	0.027
Size	289	323	459	408	816	323	408

in the six-membered ring region, probably associated with precision problems in that region of the experiments. The same similarity is observed when comparing the B3LYP/6-31+G(d) atomic spin populations for the HNN radical (C(sp²) = -0.238, N = 0.285/0.276, O = 0.335/0.321 e⁻) and the atomic spin populations for the same atoms in the PhNN radical (C(sp²) = -0.117, N = 0.209/0.233, O = 0.329/0.352 e⁻). The values are smaller for all the atoms of the six-membered ring (all C atoms have atomic spin populations whose absolute value is smaller than 0.017 e⁻, with sign alternation relative to the five-membered C(sp²) atom; all H atoms have atomic spin populations whose absolute values are smaller than 0.001 e⁻). These values of the atomic spin populations remain almost invariant when the number of basis sets is increased beyond the 6-31+G(d) set, as a numerical test with a variety of basis sets has manifested (see Table 4, which collects the values of the atomic spin population computed with basis sets of increasing quality on the ONCNO atoms of the five-membered ring, together with the C atom of the six-membered ring linked to the C(sp²) atom of the five-membered ring, as representative case) [40]. The quality basis set is roughly proportional to the basis set size.

For more systematic sampling we performed the same study on all the radicals of Figs. 2 and 3, i.e. the nitronyl nitroxides whose crystals are characterized by dominant ferro- or antiferromagnetic interactions (45 radicals in total). Given the large number of different radicals and the structural variety of their R substituent, we devised a method of presenting the changes in the atomic spin population of the functional groups in an unbiased form. After analyzing the results, we found that a good way of representing the atomic spin population is by quoting the value in the following four groups of atoms:

- the C(sp²) carbon of the five-membered ring;
- the whole ONCNO group;
- the remaining atoms of the five-membered ring; and
- the atoms of the R groups (see Figs. 2 and 3).

Table 5. Atomic spin population (in atomic units) on regions of the α -nitronyl nitroxide radicals included in the ferromagnetic subset. The first column lists the value on the five-membered C(sp²) atoms, the second column on the ONCNO group, the third on the remaining atoms of the five-membered ring (r(5)-ONCNO in the text), and the last column refers to the atomic spin population on the R group.

Refcode	C(sp ²)	ONCNO	r(5)-ONCNO	R
0003QN	-0.20	1.43	0.08	0.17
000MPY	-0.21	1.43	0.10	0.10
000PPY	-0.20	1.41	0.10	0.13
00DPNP	-0.22	1.46	0.09	0.21
0PBRPH	-0.21	1.42	0.10	0.15
HAFXOB	-0.21	1.43	0.08	0.17
LICMIT	-0.19	1.37	0.08	0.13
MACOPY	-0.23	1.45	0.08	0.08
MMEPYB	-0.21	1.45	0.10	0.17
PEFMES	-0.22	1.51	0.10	0.45
PEYPUA	-0.20	1.42	0.10	0.13
YISCEI	-0.19	1.40	0.10	0.15
YISCOS	-0.23	1.46	0.08	0.05
YISNIX	-0.20	1.41	0.10	0.11
YIWSEC	-0.19	1.44	0.08	0.15
YODBUO	-0.20	1.34	0.10	0.21
YOMYII	-0.17	1.34	0.08	0.09
YUJNEW	-0.20	1.43	0.08	0.17
YULPOK	-0.19	1.44	0.09	0.33
ZORHIX	-0.21	1.43	0.08	0.11
Minimum	-0.17	1.34	0.08	0.05
Maximum	-0.23	1.46	0.10	0.45
Average	-0.20	1.42	0.09	0.16
Standard deviation	0.02	0.04	0.01	0.09

Because the atomic spin population on the C(sp²) atom of the five-membered ring is always negative, and on the NO atoms of the ONCNO groups is always positive, a representative value of the amount of spin in the whole ONCNO group is obtained by adding the absolute values of the atomic spin population for all atoms of this group (from this number it is possible to obtain the NO groups population by twice subtracting the atomic population in the C(sp²) atom). For similar reasons a representative value of the spin in the remaining atoms of the five-membered ring (which we call r(5)-ONCNO), can be obtained by adding the absolute values of the atomic spin population on all participating atoms. The process was extended also to the R group. The results for these sets of atoms [40] are collected in Table 5 for the ferromagnetic subset, and in Table 6, for the antiferromagnetic subset. The total atomic spin population within the C(sp²), ONCNO and r(5)-ONCNO groups is almost invariant between radicals, the most important changes being concentrated on the R substituent. Thus, whereas the total atomic spin population on the five-membered C(sp²) atom lies within the -0.16 to -0.23 range, the values in the R

Table 6. The same data as in Table 5, but for the antiferromagnetic subset.

Refcode	C(sp ²)	ONCNO	r(5)-ONCNO	R
0000AH	-0.24	1.45	0.08	0.02
0000BR	-0.20	1.40	0.09	0.02
000F5P	-0.22	1.43	0.08	0.08
003CLP	-0.22	1.46	0.08	0.17
00NNMA	-0.20	1.41	0.08	0.17
00PCLP	-0.20	1.42	0.08	0.15
0PCF3P	-0.22	1.45	0.09	0.17
2CLPNN	-0.22	1.44	0.08	0.08
2N5OHP	-0.22	1.43	0.08	0.06
3CL4OH	-0.21	1.42	0.08	0.17
5CL2OH	-0.19	1.38	0.08	0.15
LASCAJ	-0.21	1.43	0.09	0.25
LEMMAR	-0.23	1.47	0.07	0.32
PEFMAO	-0.21	1.46	0.07	0.25
SUKBIJ	-0.20	1.43	0.08	0.08
SUKBOP	-0.22	1.46	0.07	0.33
WILVIW10	-0.20	1.46	0.08	0.13
YISCIM	-0.21	1.44	0.08	0.17
YOMYOO	-0.20	1.43	0.08	0.15
YOMYUU	-0.21	1.44	0.09	0.17
YOXMAZ	-0.18	1.39	0.08	0.11
YOXMED	-0.20	1.41	0.09	0.31
YULPAW	-0.19	1.42	0.08	0.17
ZIPTAT	-0.20	1.42	0.08	0.17
Minimum	-0.18	1.38	0.07	0.02
Maximum	-0.24	1.47	0.09	0.33
Average	-0.21	1.43	0.08	0.16
Standard deviation	0.01	0.02	0.01	0.09

substituent go from 0.05 to 0.45 electrons. At the same time each NO group has an average of 0.51 electrons, with very little change between the maximum and minimum values. So, one can safely generalize the conclusions obtained from the PhNN radical to all other nitronyl nitroxides. The main reasons for such a similar behavior are:

- the similar shape of the SOMO orbitals, which allows the presence of spin polarization only through the SOMO-LUMO and (SOMO-1)-LUMO excitations; and
- the similar energy difference between the SOMO and LUMO orbitals.

There are, however, some radicals (PEFMES, LEMMAR, SUKBOP, YOXMED and YULPOK) for which there are relatively important amounts of atomic spin populations on the atoms of the R substituent, the only reason being a change in the SOMO-LUMO energy difference.

Besides the atomic spin population, much theoretical and experimental work has been performed to obtain the amount of spin density on the atomic nucleus. The reason for such interest is the dependence of NMR and ESR spectra on that magnitude. In particular, the hyperfine coupling constants (*hfcc*, represented by the symbol a_N), which define the position of the lines in the NMR or ESR spectra, is related to the spin density at the corresponding nucleus ($\rho(r_N)$) by the equation [41]:

$$a_N = \frac{8\pi}{3} \frac{g_e}{g_0} g_N \beta_N \rho(r_N) \quad (2)$$

where g_0 is the isotropic g -value for the radical, g_e the g -value for the free electron, g_N is the gyromagnetic nuclear ratio, and β_N is the nuclear magneton of the nucleus N.

The theoretical computation of *hfcc* has been performed previously on many open-shell systems, among others on the first row atoms [42] and their hydrides [43], the hydroxyl radical and five peroxy radicals [44], a subset of π -radicals [45], and a variety of NO-containing radicals which included the HNN radical [46]. Also, there are some interesting studies covering a wide variety of radicals [47]. The first conclusion from these studies is the dependence of the computed *hfcc* on the method and the basis set employed: good results are usually obtained by use of the QCISD method [48] or the B3LYP density functional and basis set which describe well the intermediate region between the core and the valence parts of the electron density. The basis sets of the last type are the IGLO-III [49], the EPR-II and EPR-III basis sets of Barone [50], the core-valence correlation-consistent cc-pCVXZ [51], and the s-uncontracted cc-us-pVXZ basis sets [52]. Even with these basis sets and the QCSD method, however, the mean absolute deviation from the experimental values in a subset of di-, tri-, and tetra-radicals can be as large as 4.5G, and a similar value is obtained by using the B3LYP functional [47d]. Interestingly, the *hfcc* computed for these radicals at the QCISD/6-311+G(2df,p) level are better than those obtained at the QCISD/IGLO-III level; the two basis sets performed similarly at the B3LYP level [47d]. One must, however, keep in mind that part of the success of the B3LYP method in some systems has been attributed to fortuitous cancellation of errors [42a]. This explains that higher quality basis sets do not always provide *hfcc* values closer to the experimental results, as is found for the QCISD values. This is clearly illustrated in Table 7, which collects the B3LYP *hfcc* computed for the first row atoms [14d], using the same basis sets which give accurate *hfcc* results at the QCISD level [42a]. In general, the values of the *hfcc* are strongly basis-set-dependent, and large basis sets are needed to furnish, consistently, values close to the experimental results (that is, the *hfcc* converge to a limit value when the size is increased after some given quality). The EPR-II and EPR-III basis sets, considered to give accurate results for DFT computed *hfcc*, reproduce the sign and magnitude for all first row atoms, although errors of up to 5 Gauss are found in the B-O series, and even the time larger in the F atom. The errors computed with the QCISD method for these two basis sets are not much smaller. This has prompted the generation of other basis sets, specifically designed for the study of *hfcc*, although in the light of the results in Table 7 [42, 52], they are not much better than the EPR-II

Table 7. Isotropic $hfcc$ (in Gauss) computed for the first row atoms using the basis sets indicated and the unrestricted formulation of the B3LYP method. The QCISD values of Ref. [42a] are also given for comparison (second row).

Basis set	B	C	N	O	F
IGLO-III	7.1	9.2	3.6	-9.3	72.9
EPR-II	3.9	7.7	2.9	-6.9	49.1
	1.8	5.5	3.1	-8.5	84.1
EPR-III	6.2	8.2	3.5	-9.0	74.9
	1.3	3.9	2.8	-8.7	88.2
cc-pCVDZ	2.3	0.1	-1.1	5.5	-74.2
	-1.2	-2.3	-1.2	4.1	-43.9
cc-pCVTZ	3.5	5.8	2.5	-7.5	61.7
	1.7	4.5	2.5	-8.1	77.0
aug-cc-pCVDZ	4.3	3.0	0.2	2.2	-46.0
	3.7	4.2	1.6	-3.2	19.6
aug-cc-pCVTZ	4.6	7.5	3.2	-9.3	77.4
	2.9	6.6	3.6	-10.9	104.1
cc-us-pVDZ	6.1	7.4	2.7	-6.6	48.6
cc-us-pVTZ	6.0	7.9	3.1	-7.9	62.9
aug- cc-us-pVDZ	8.0	10.4	4.0	-9.8	76.8
aug- cc-us-pVTZ	8.2	10.4	4.0	-9.9	77.3
Experimental	4.1	7.0	3.7	-12.3	107.8

or EPR-III basis sets, despite their higher computational effort. More efforts are needed in the search for better basis sets for the theoretical computation of $hfcc$ at the DFT level for all atoms. The situation is not, however, as dark when compounds within the nitronyl nitroxide family are studied. Then one finds that B3LYP/EPR-II calculations reproduce well the order of magnitude and the trends in the experimental $hfcc$, when compared with values obtained from ESR experiments performed in a variety of solvents, thus enabling correction for environmental effects by means of linear correlations [14d], or against NMR values. Thus, for instance, when the B3LYP $hfcc$ results are compared with the solvent-independent experimental ESR values for the HNN radical (Table 8) one finds that the EPR-II, cc-pCVTZ, cc-uspVDZ, and cc-uspVTZ basis sets give results of similar quality, the quality of the other three basis sets being surprisingly close to the EPR-II results. In the original work [14d] it was also found that the IGLO-III, basis set provided good results, as did the aug-cc-pVDZ basis set (the $hfcc$ values computed with this basis set are approximately 2 G higher than the EPR-II, but this is the size of the recommended correction factor one should add to the B3LYP/EPR-II results to match the experimental values) [14b, 14c]. The B3LYP/EPR-II computations reproduce fairly well the main features of the solvent-independent $hfcc$ values with the exception of those for the five-membered C(sp²) nucleus. All basis sets yield good estimates of the order of magnitude of the average $hfcc$ value for the H of the CH₃ groups. Unfortunately, no experimental values are known for the O atoms, although it is again interesting to note the similarity between the EPR-II, cc-pCVTZ, cc-us-pVDZ, and cc-us-pVTZ basis sets results. We also extended our search to the B3LYP/cc-pVDZ

Table 8. Calculated B3LYP isotropic hyperfine coupling constants (in Gauss) for the optimized geometry of the HNN radical using a variety of basis sets. The basis set size is also indicated.

Atom	EPR-II	cc-pvDZ	cc-pvTZ	cc-cvpvDZ	cc-cvpvTZ	cc-us-pvDZ	cc-us-pvTZ
H	5.96	5.25	5.46	5.21	5.42	4.95	5.38
C(sp ²)	-15.05	-17.06	-10.44	-12.75	-13.75	-14.50	-14.40
N ₁	5.15	6.94	3.24	3.62	5.10	4.88	5.25
N ₂	5.15	6.94	3.24	3.62	5.10	4.88	5.25
O ₁	-9.49	-16.63	-6.04	-4.78	-9.96	-9.14	-9.96
O ₂	-9.49	-16.63	-6.04	-4.78	-9.96	-9.14	-9.96
C(sp ³)	-2.65	-2.80	-2.22	-2.50	-2.46	-2.60	-2.52
C(sp ³)	-2.65	-2.80	-2.22	-2.50	-2.46	-2.60	-2.52
C-me	3.53	3.26	3.18	3.10	3.32	3.19	3.31
C-me	1.56	1.71	1.56	1.52	1.60	1.55	1.58
C-me	3.53	3.26	3.18	3.10	3.32	3.19	3.31
C-me	1.56	1.71	1.56	1.52	1.60	1.55	1.58
H-me	-0.24	-0.21	-0.22	-0.20	-0.21	-0.21	-0.21
H-me	-0.32	-0.28	-0.31	-0.28	-0.32	-0.28	-0.32
H-me	-0.25	-0.23	-0.21	-0.22	-0.22	-0.21	-0.22
H-me	0.42	0.32	0.44	0.32	0.42	0.35	0.41
H-me	-0.67	-0.54	-0.62	-0.55	-0.63	-0.56	-0.62
H-me	-0.38	-0.31	-0.33	-0.31	-0.33	-0.30	-0.34
H-me	0.32	0.28	0.31	0.28	0.32	0.28	0.32
H-me	-0.25	-0.23	-0.21	-0.22	-0.22	-0.21	-0.22
H-me	-0.24	-0.21	-0.22	-0.20	-0.21	-0.21	-0.21
H-methyl	-0.38	-0.31	-0.33	-0.31	-0.33	-0.30	-0.34
H-methyl	0.42	0.32	0.44	0.32	0.42	0.35	0.41
H-methyl	-0.67	-0.54	-0.62	-0.55	-0.63	-0.56	-0.62
Basis Size	143	119	512	133	655	161	604

hfcc and they showed a surprising good agreement with the solvent-independent values obtained from ESR measurements [14d]. Similar conclusions can be reached when comparing the results for the PhNN radical [14d] or the values computed for a variety of phenyl-nitronyl nitroxide radicals and the experimental solid state NMR results [17]. The torsion angle between the five and six-membered rings only has a small effect on the *hfcc* values, and small changes are also found when going from one nitronyl nitroxide to another, or when changing the solvent used.

Finally, comparison of the *hfcc* values of Table 8 and the atomic spin populations of Table 3 shows that the size of the density on the nucleus is not always proportional to the atomic spin population. This is not a surprising effect in the light of the considerations above about the atomic spin populations.

3.3 Magnetic Interactions in Purely Organic Molecular Crystals

3.3.1 Basics of the Magnetism in Purely Organic Molecular Crystals

“Magnetism at its bottom is not well understood” [53]. This assertion, written some years ago, is still (at least partially) valid in relation to the mechanism of the magnetic interaction in purely organic molecular magnets, because the microscopic mechanism responsible for the presence of ferro or antiferromagnetism is not well understood in full nowadays, despite serious work performed in this field of research during recent decades.

The basic foundation of magnetism is well known – particles with a net spin tend to align in parallel or antiparallel fashion. The interaction responsible for the alignment is called magnetic interaction. In molecular systems, the electronic state of which comprises only closed-shell electrons, there is only a very small magnetic interaction, is called diamagnetism. Much more interesting, because of their strength, are the interactions present when the molecules have net spins (that is, they are radicals, biradicals, ...), in which one can distinguish two classes of magnetic interaction between a pair of molecules: *ferromagnetic interactions*, when the ground state is a triplet (the electrons are said, in a simplistic form, to order in a parallel manner, that is, both in an α or β state; note, however, that this description is only valid for two out of the three states present in the triplet state) [54], and *antiferromagnetic interactions*, in which the ground state is a singlet (the electrons are, one in an α state, and the other in a β state) [54]. Within a given crystal a molecule makes contact with nearby radicals (of the same kind in a purely organic crystal, or of different type in co-crystals). As we will see later, these interactions decrease exponentially with distance, so a common approach has been to look at the shortest contacts made by each molecule, that is, with their so-called nearest neighbors. If all these interactions are of the same type and are propagated along the three directions of space we have a three dimensional ferro or antiferromagnet (also called bulk ferro or antiferromagnets). In most of these the magnetic interactions are of different kinds. If, however, one type of interaction is much stronger than the others, one can talk about crystals having *dominant ferro* or *antiferromagnetic interactions*. These crystals can be identified, for instance, by the shape of the χT versus T curve as the temperature decreases: a continuous exponential increase of χT after some value of T is indicative of the presence of dominant ferromagnetic interactions; a continuous exponential decrease indicates the existence of dominant antiferromagnetic interactions. The presence of magnetic interactions can be noted only at low values of T , in which the separation from the magnetic ground state to the first excited state is lower than the thermal energy. Otherwise, the population in the ground state decreases while that in the first excited state (and possibly others) increases. At some given temperature there is a random number of pairs with ferro and antiferromagnetic interactions, each pair changing in a random way from one state to the other, and no net magnetic behavior can be observed. In these circumstances one talks about paramagnetism, because the macroscopic systems behave like pairs of magnetically non-interacting particles. There are many other interesting collec-

tive magnetic phenomena besides ferro and antiferromagnetism (ferrimagnetism, metamagnetism, spin glasses, ...) [1]. Their microscopic mechanism can be treated as special cases of the ferro and antiferromagnetic situations described above; for instance the two interacting spins have different S values, or are oriented in such a way that their net component is not zero, or the energetic spacing between ground and excited states enables special collective long-range behavior. Thus we will only concentrate on the ferro and antiferromagnetic cases.

The entry door to modern molecular magnetism is to understand which orientations of pairs of radicals give rise to ferromagnetic interactions and which give antiferromagnetic interactions. Of all the possible general mechanisms envisaged for magnetic interactions proposed in the literature (see Ref. [1], particularly Ref. [1b]), some have been accepted as explaining intermolecular magnetic interactions – the first mechanism or proposal of McConnell (consequently called the McConnell-I mechanism or proposal) [10], the second mechanism or proposal of McConnell (therefore called the McConnell-II mechanism or proposal) [55], and spin–dipolar interactions [56]. Besides these three mechanisms, there is strong evidence that the superexchange mechanism, originally applied to intramolecular (“through-bond”) magnetic interactions, also applies to (“through-space”) magnetic interactions [9, 57]. Other mechanisms based on orbital theories (extension of Hund rules to the intermolecular case, orthogonality of the intermolecular orbitals, ...) [1, 58] have also been proposed and applied with various amounts of success, although we will see later on that the magnetism in purely organic nitronyl nitroxide crystals usually involves more than one orbital.

Let us briefly mention the basics of the previous mechanisms. The McConnell-I mechanism is based on the sign of the atomic spin population of the atoms making the shortest contacts between the interacting molecules. The McConnell-II mechanism is based on the importance of charge-transfer configurations, and indicates that high spin multiplicity is favored by orbital degeneracy. Kollman and Kahn [59] showed that the McConnell-II mechanism fails to describe the properties of the bulk ferromagnet $\text{Fe(III)(C}_5\text{Me}_5)_2^+(\text{TCNE})^-$, and suggested that the McConnell-I mechanism or some other model should be used instead. The spin-dipolar mechanism is based on the classical view of the spin as a dipole. Here, the interaction between two spins is described, classically, as the interaction between two magnetic dipoles. Its value depends on the distance as r^{-3} [56]. It should be noticed that the classical model of the spin is included within any *ab-initio* quantum-mechanical treatment of the interaction between two spins. The dipolar interactions are said to be responsible for the presence of magnetic interactions in some layered materials with large distances between the layers [9], although Kinoshita [60] numerically dismissed its importance in nitronyl nitroxide crystals. Finally, the superexchange mechanism has been proposed for hydrogen-bonded purely organic nitronyl nitroxide crystals and co-crystals in which there are no short contacts between the spin-containing groups (the ONCNO groups) but in which magnetic interactions are observed [57]. The magnetic interaction is postulated to take place through the $\text{H}\cdots\text{O}$ hydrogen bonds, in such a way that some groups which have almost no spin on them (see above) act like carriers for the magnetic interaction (by analogy with the role played by the ligands in the magnetic metal–ligand–metal interactions) [1d].

3.3.2 The McConnell-I Mechanism: A Rigorous Theoretical Analysis

Among all models of through-space interaction, by far the most popular is the McConnell-I mechanism originally introduced by McConnell [10] in 1963 to explain intermolecular magnetic interactions between aromatic radicals. This author suggested that the magnetic interactions present between two aromatic radicals A and B could be described by the Heisenberg Hamiltonian:

$$\hat{H}^{AB} = - \sum_{i \in A, j \in B} J_{ij}^{AB} \hat{S}_i^A \hat{S}_j^B \quad (3)$$

In this expression, J_{ij}^{AB} are two-center exchange integrals of the form:

$$J_{ij}^{AB} = [ij|ij] + 2\langle i | j \rangle \langle i | h | j \rangle \quad (4)$$

that is, they depend of the bi-electronic integrals $[ij|ij]$, the overlap integrals $\langle i | j \rangle$, and the mono-electronic integrals $\langle i | h | j \rangle$ (see Ref. [18] for their analytical expression and physical meaning). $\hat{S}_i^A \hat{S}_j^B$, on the other hand, is the product of the spin operator of atoms i and j from fragments A and B, respectively [61].

Equation (3) is a particular case of the general form of a Heisenberg Hamiltonian [62], whose most general expression is of the form:

$$\hat{H}^{AB} = Q - \sum_{i,j} J_{ij} \left(2\hat{S}_i \hat{S}_j + \frac{1}{2} \hat{I}_{ij} \right) \quad (5)$$

The intra-fragment terms in this expression can be neglected making the assumption that their contribution to the expectation values is the same between states.

Equation (3) was replaced, by McConnell, by the simplified expression:

$$\hat{H}^{AB} = -\hat{S}^A \hat{S}^B \sum_{i \in A, j \in B} J_{ij}^{AB} \rho_i^A \rho_j^B \quad (6)$$

which is the equation normally employed when applying the McConnell-I mechanism. In this expression, \hat{S}^A and \hat{S}^B are the total spin operators for the fragments A and B, respectively, J_{ij}^{AB} are two-center exchange integrals defined above, and ρ_i^A and ρ_j^B are the products of the atomic spin population on atoms i and j (the first from fragment A, and the second from fragment B). We have seen that the Hamiltonian of Eq. (6) is phenomenological, because there is no strict mathematical way of deriving it from Eq. (3) [62]. Despite this, when the singlet-triplet energy difference is computed using Eqs. (6) and (5) some similarities arise. This can be illustrated for the example in which only one unpaired electron is found in fragments A and B; their interaction can give rise to a singly degenerated singlet (S) state or a triply degenerated triplet (T) state. Using the expression:

$$\langle \hat{S}^A \hat{S}^B \rangle = \frac{1}{2} [(S(S+1) - S_A(S_A+1) - S_B(S_B+1))] \quad (7)$$

it is possible to see that $\langle \hat{S}^A \hat{S}^B \rangle^T = 1/4$ and $\langle \hat{S}^A \hat{S}^B \rangle^S = -3/4$. From here, the singlet-triplet energy difference computed from Eq. (6) is:

$$E^S - E^T = \langle \hat{H}^{AB} \rangle^S - \langle \hat{H}^{AB} \rangle^T = \sum_{i \in A, j \in B} J_{ij}^{AB} \rho_i^A \rho_j^B = J \quad (8)$$

Equation (8) is the cornerstone of the McConnell-I mechanism. It predicts the relative stability of the singlet and triplet states as a function of the exchange integrals J_{ij}^{AB} and the products of the atomic spin populations (ρ_i^A and ρ_j^B). The value of the exchange integrals is not known, although, in general, their sign is negative. Consequently, it is assumed that *a triplet ground state is obtained when the products of atomic spin populations are also negative* (that is, the two atomic spin populations have opposite signs). Furthermore, not all the pairs need to be considered. If the J_{ij}^{AB} or $\rho_i^A \rho_j^B$ component of a term in the sum of Eq. (8) is negligible, this term can be discarded. This explains why normally only those terms associated with the shortest atom-atom contacts involving atoms with non-negligible atomic spin populations are considered. In practical terms, this implies making the exchange integrals for all terms zero except for the shortest contacts. This assumption is based on the fact that the exchange integrals decrease exponentially with the distance, but we will see later that, given the angular dependence of the molecular orbitals, these integrals depend on factors such as the symmetry and relative position of the atoms within the fragments.

When the singlet-triplet energy difference is computed from Eq. (5), its value is given by the equation:

$$E^S - E^T = \sum_{i,j} J_{ij} (P_{ij}^S - P_{ij}^T) \quad (9)$$

where P_{ij} are elements of the *exchange density matrix* of the singlet and triplet states, given by the expectation values (of the singlet or triplet wavefunction):

$$P_{ij} = \left\langle - \left(2\hat{S}_i \hat{S}_j + \frac{1}{2} \hat{I}_{ij} \right) \right\rangle \quad (10)$$

where \hat{I}_{ij} is the identity operator. For a single configuration of a perfectly paired valence bond wavefunction [61], P_{ij} is equal to 1 when the pair is coupled into a singlet, or -1 when the pair is coupled into a triplet. For uncoupled electrons (that is, i and j belong to different spin-paired functions) it takes a value of $-1/2$. Comparison of Eqs. (8) and (9) shows that predictions of the McConnell-I equation are only strictly valid if the following association is possible:

$$\rho_i^A \rho_j^B \Leftrightarrow P_{ij}^S - P_{ij}^T \quad (11)$$

There is no *a priori* reason why the product of atomic spin populations should be related to the difference between the singlet and triplet exchange density matrices. We have recently explored the possibility that in intermolecular interactions, at the distances found in purely organic molecular crystals, the atomic spin density of the

dimer could be approximated as a sum of that for each fragment, and that sum would be different for the singlet and triplet states. We are currently testing this possibility for several nitronyl nitroxides [63].

We can now apply the McConnell-I mechanism to nitronyl nitroxides, where 90% of the atomic spin population is located in the ONCNO groups, negative in the C(sp²) atom and positive elsewhere. A common approach has been to look at only the shortest contacts made by these groups. Usually, the McConnell-I equation (Eq. 6) is employed without computing the J_{ij}^{AB} and only taking into account the shortest contacts. This is equivalent to assuming that these integrals are equal to -1 for the shortest contacts and 0 for the remaining contacts. The equation is also extended to non- $\pi \cdots \pi$ interactions. In these situations the only magnetic interactions of importance are those in which the short contacts are between the atoms of the ONCNO groups (because those have 90% of the atomic spin population). In particular, these contacts will be antiferromagnetic when they are of the type O \cdots O, N \cdots N, O \cdots N, or C \cdots C and ferromagnetic when the shortest contacts are of the type C \cdots O or C \cdots N. The magnetic character of the remaining pairs of interactions (H \cdots O, \cdots) should be negligible.

The failure of these predictions are readily apparent for the hydrogen-bonded nitronyl nitroxides in which there are no short contacts between the ONCNO groups but for which magnetic behavior can be measured experimentally [57]. As mentioned above, the magnetism in these crystals has to be explained by use of another intermolecular mechanism (superexchange). There are also other inconsistencies between the McConnell-I predictions and the experimental behavior of nitronyl nitroxides with short ONCNO \cdots ONCNO contacts [64]. The failure of the McConnell-I mechanism can also be demonstrated by comparing its predictions with *ab-initio* results computed for simple model dimers, e.g. the H₂NO \cdots ONH₂ dimer [65]. The H₂NO \cdots ONH₂ dimer was studied by orienting the two molecules as shown in the upper part of Fig. 11, with the NO groups pointing towards each other. One of the groups was moved along the a-c plane, while preserving the four NO \cdots ON atoms in the same plane, and the H atoms are in symmetric positions relative to that plane. The O \cdots O distance was fixed at 3.0 Å. The results for the singlet-triplet energy difference computed along that surface scan, obtained by use of a variety of *ab-initio* methods, are plotted in the lower part of Fig. 11. They show that, irrespective of the method used (B3LYP, MCSCF(6,4), CASPT2(6,4), CCSD(T)), there is a change from singlet to triplet in the ground state as the dimer is moved away from its collinear (NO \cdots O angle = 180°) to a perpendicular conformation (NO \cdots O angle = 90°). This contradicts what McConnell-I predicts – according to this mechanism, the interaction should be antiferromagnetic at all the points in Fig. 11.

There is an important point about the McConnell-I mechanism which must still be addressed: why does it work in some cases but fail in others?. To answer to this question we must know the source of the failure. We addressed this question by using Eq. (9) to compute the singlet-triplet energy difference for the [2.2]paracyclophanes [66], after rigorous computation of the exchange integrals (J_{ij}^{AB}) and the exchange density matrix. We studied the *ortho*, *meta*, and *para* conformers of this radical, because they were previously used as experimental proof of the validity of

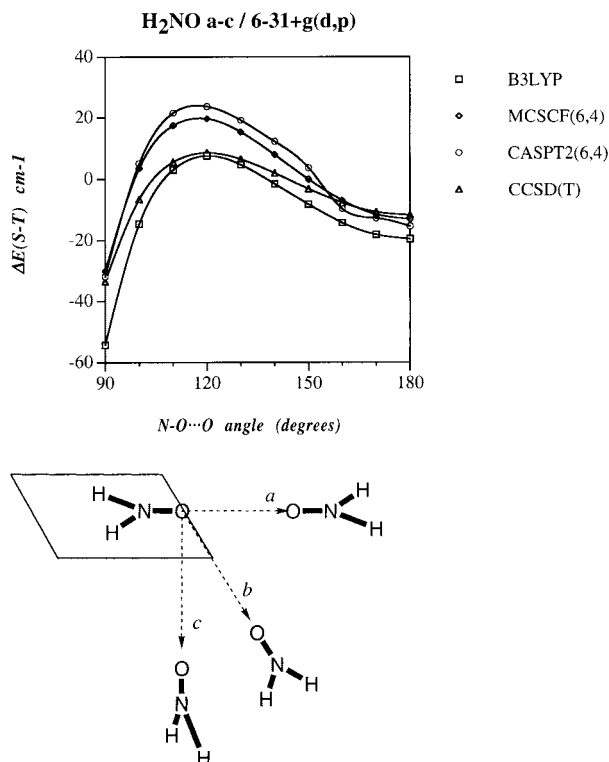


Fig. 11. *Top:* Variation of the singlet-triplet energy difference found in the H₂NO dimer as the dimer is moved along the *a-c* plane. The energy difference has been computed by subtracting the energy of the singlet and triplet states by use of the methods: MCSCF(6,4), CASPT2 on the MCSCF(6,4) computations, CCSD(T) and B3LYP. In the latter two cases the energy of the singlet was that taken from broken-symmetry computations. *Bottom:* Definition of the geometrical orientation of the molecules of the H₂NO dimer.

the McConnell-I mechanism. Although our computations correctly predict the multiplicity of the ground state, when the components of Eq. (9) are analyzed in detail one finds that the reason for the success of the McConnell-I model in this example is cancellation of many J_{ij}^{AB} ($P_{ij}^S - P_{ij}^T$) terms associated with the non-shortest contacts. This cancellation is a result of the small value of the J_{ij}^{AB} integrals, associated with the high symmetry of the [2.2]paracyclophanes; this gives rise to the direct alignment of many atoms of the nearby rings. This effect will, however, disappear when the high symmetry is lost and many other J_{ij}^{AB} integrals start to be non-negligible [62]. Interestingly enough, the association between $(P_{ij}^S - P_{ij}^T)$ and $\rho_i^A \rho_j^B$, Eq. (11), is correct for this molecule, so the biggest error seems to be the form used to evaluate the exchange integrals (as mentioned before, in the normal use of the McConnell-I mechanism, they are not evaluated).

Summarizing the previous paragraphs, one cannot usually trust results from the McConnell-I mechanism, at least without taking into account the numerical values of the J_{ij}^{AB} integrals. This is the main source of error introduced in its normal use, according to the previous considerations. When the method works is because there is a fortuitous situation which cancels many of these integrals, leaving only those terms which also appear in the normal use of the McConnell-I mechanism. A more accurate mechanism, capable of considering situations not currently properly handled by the McConnell-I mechanism, is therefore needed. For such a task, we need to obtain information about the nature of the through-space magnetic interactions in an unbiased form. We will do so in the following sections, by combination of *ab-initio* and crystallographic studies.

3.3.3 Theoretical Analysis of Through-space Intermolecular Interactions

To understand the intermolecular magnetic interaction between open-shell molecules is helpful to have a qualitative idea about the shape of the potential energy surface for the intermolecular interaction between the two radicals. The simplest example of an interaction between radicals is the interaction between two H atoms (Fig. 12). At very large distances the ground state corresponds to two isolated H atoms (the A and B atoms), each with an electron in a 1s orbital, that is, with a spatial configuration of the type $1s_A(1)1s_B(2)$. These electrons can each be in a spin configuration of the type $\alpha\alpha$, $\alpha\beta$, $\beta\alpha$ or $\beta\beta$, which gives rise to the formation of one singly degenerate singlet and a triply degenerate triplet state. Because the two atoms are too far away to interact, the two states are energetically degenerate (Fig. 12, right). If the two atoms become closer the two 1s atomic orbitals combine into bonding ϕ_1 and antibonding ϕ_2 molecular orbitals. If one electron is placed in each of these molecular orbitals ($\phi_1(1)\phi_2(2)$ configuration) and their single occupancy is preserved, the singlet and triplet states (hereafter identified as the S_1 and T_1 states) are expected to be repulsive, because the number of bonding and antibonding orbitals is the same. One can, on the other hand, allow double occupancy of the lowest energy bonding orbital, thus obtaining a $\phi_1(1)\phi_1(2)$ configuration (normally written in the compact form $\phi_1(1)^2$). At short distances, the $\phi_1(1)^2$ configuration corresponds to the formation of a H–H bond, and gives rise to a singlet state which we will identify as S_0 . The energy of the S_0 is equal to the energy of a hydrogen molecule in its ground state and, consequently, it lies below the energy of two isolated H atoms. If, however, the double occupancy is preserved, at large distances one dissociates into a $1s_A^2$ configuration, i. e. one hydrogen atom has two electrons and the other has none (this corresponds to dissociation into H^- and H^+). Such a zwitterionic state is higher in energy than dissociation into two H atoms in their 1s orbital, as shown in Fig. 12. There must, therefore, be a point at which the S_0 potential energy curve crosses the S_1 and T_1 curves, a sort of transition state, at energies above the H plus H dissociation. When the S_0 and S_1 states are allowed to mix (as in the MCSCF, CI or MP2 computations, or also partially in the UHF computation) the curves obtained after the mix (called adiabatic curves) are those indicated with broken lines. In this case, the transition state disappears, as is

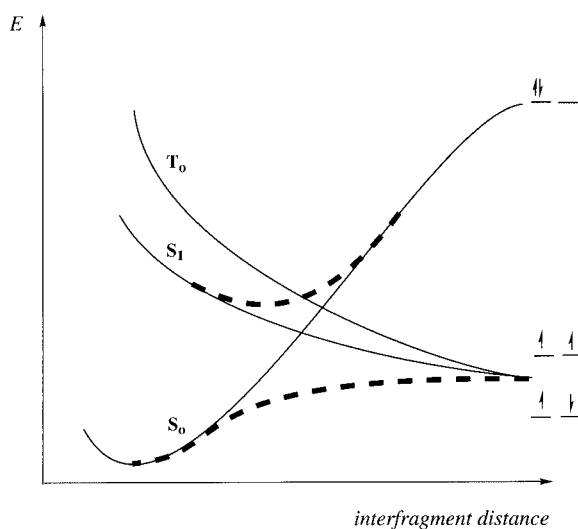


Fig. 12. Diagram showing variation of the energy with the intermolecular distance for the states generated by the interaction of two mono-electronic radicals. The continuous lines indicate the diabatic energy curves, that is, those obtained when the states are not allowed to interact with other states when computing their energy. The discontinuous curves (adiabatic curves, obtained when the diabatic states are allowed to interact) overlap the continuous curves, except in the places where they are explicitly drawn. S_0 , S_1 and T_0 identify the lowest energy singlet, first excited singlet, and ground state triplet states. No space symmetry was considered.

found experimentally. The resulting wavefunction for the singlet state is, however, a mixture of the S_0 closed shell singlet state and the open shell S_1 singlet state, with different weights. Close to the minimum of the curve the dominant component of the mixture is the closed shell component; at the S_0 - S_1 crossing point it is practically 50% of each state; at large distances, it is dominated by the S_1 state. It is easy to define the weight of each state by looking at the occupation of the natural orbitals (obtained from diagonalizing the first-order density matrix, as the eigenvalues). An RHF will give an occupation of the $\phi_1(1)\phi_2(2)$ orbitals of 2.0 and 0.0 at all the points of the S_0 curve. An UHF computation will, however, give values close to 2.0 and 0.0 near the minimum of the S_0 curve, but progressively these values will go to 1.0 and 1.0, as the H-H distance is enlarged and the S_0 and S_1 states increase their mixing.

When the H atom (the simplest radical) is substituted by more complex radicals, the process is slightly more complex, because one has to take into account the energetic effect induced by the non-bonding electrons. In such circumstances analysis of the interactions and their energetic character is easier if the electronic structure of the fragments is analyzed in valence-bond (VB) terms. We can understand the main changes by looking at the interaction between two XH_2 molecules directed in such a way that their shortest contact is the $X \cdots X$ contact. We can start our analysis with the simple case in which $X = C$. The C atom has four valence electrons which, given the geometry of the CH_2 molecule, can be placed in three sp^2 hybrids

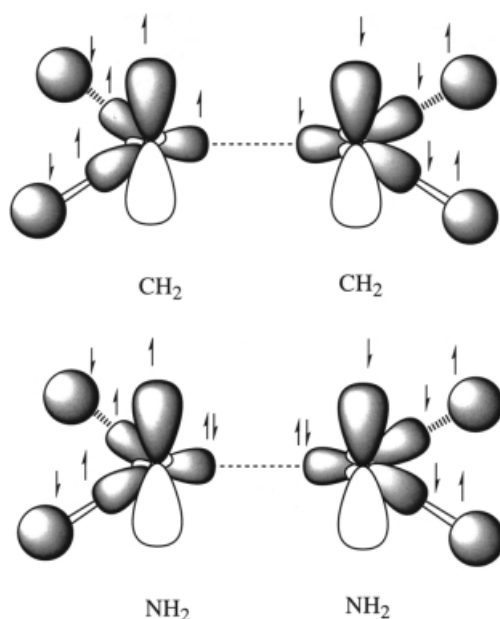


Fig. 13. Valence-bond diagram showing the distribution of the electrons in the interaction between two CH₂ or two NH₂ radicals in their ground state.

and in a pure p orbital perpendicular to these hybrids. Two of the sp² electrons form a bond against one 1s electron of an H atom. The electronic structure of the CH₂ molecule therefore contains two C–H bonds and two unpaired electrons, one in an sp² orbital and the other in a pure p orbital. This gives rise to a triplet or an open-shell singlet state, the relative stability of which is not known before performing *ab-initio* computations. Alternatively the two electrons could be located either in the sp² hybrid or in the pure p orbital, thus giving rise to a closed-shell singlet. Among all these possibilities, *ab-initio* computations tell us that the ground state is the triplet generated from the (sp²)¹p¹ configuration; this is depicted in Fig. 13.

The electronic structure of the NH₂ molecule is similar to that of CH₂, but with one more valence electron. This extra electron must go into one of the singly occupied orbitals in the CH₂. Of the two possibilities (sp² hybrid or the pure p orbital), the most stable is the sp² hybrid (Fig. 13), and the ground state of the NH₂ molecule is of the π type (²B₂). The orbitals of the H₂NO fragment were qualitatively predicted before the use of VB arguments, and are similar to those for the NH₂, with the only difference that the SOMO is the bonding combination of the pure p orbitals of the O and N atoms (Fig. 4), and in H₂NO there are two lone-pair electrons on the O atom whereas in NH₂ there is only one of these pairs.

Using the information on the electronic structure of the isolated fragments, one can rationalize the structure of the two XH₂ molecules in their ground state, as they get closer, with their X atoms facing each other. One must keep in mind that as such a decrease in distance occurs two singly occupied orbitals overlap, thus giving rise to

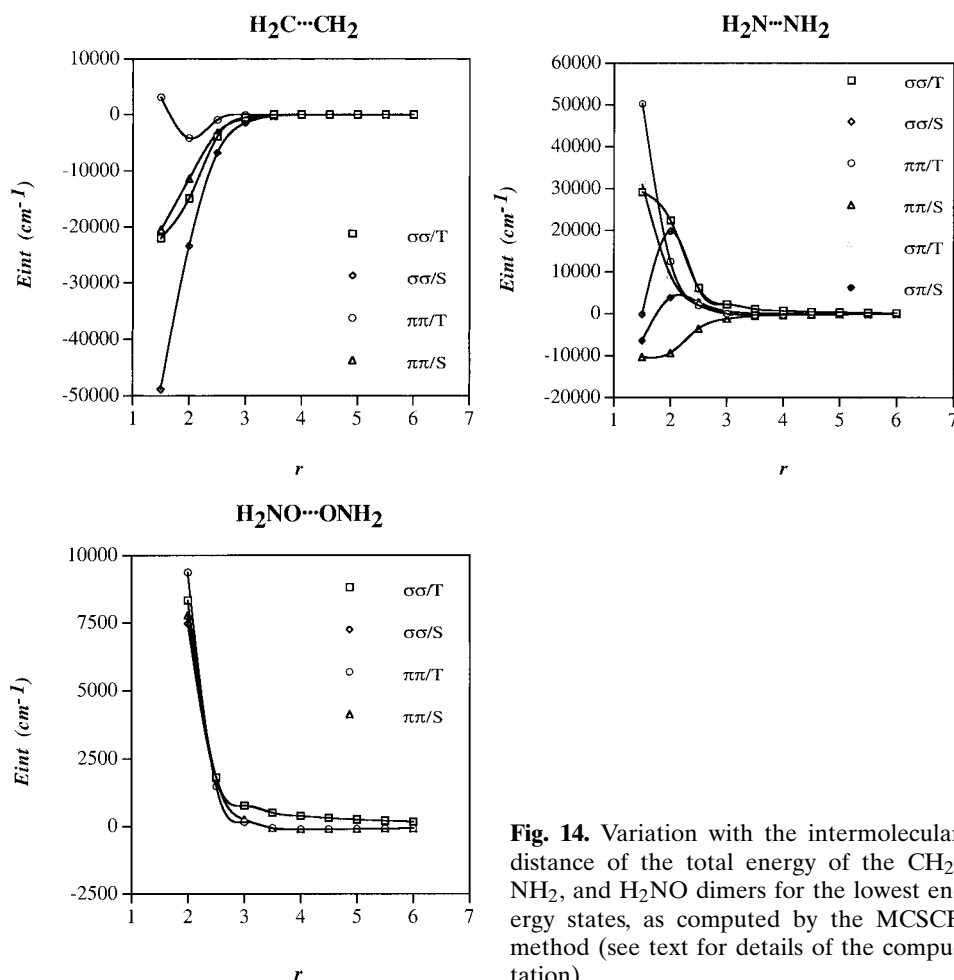


Fig. 14. Variation with the intermolecular distance of the total energy of the CH₂, NH₂, and H₂NO dimers for the lowest energy states, as computed by the MCSCF method (see text for details of the computation).

bonding (ϕ_b) and antibonding (ϕ_a) dimer orbitals. If two electrons are placed in the bonding orbitals (closed-shell singlet state) a new bond is formed whereas if the two electrons are placed one in the bonding and the other in the antibonding orbital, no new bond is formed. In the second alternative one can place the electrons in an open-shell singlet state (i. e. a $\phi_b\alpha\phi_a\beta$ configuration), or a triplet state (a $\phi_b\alpha\phi_a\alpha$ configuration). If the number of electrons in the fragment orbitals overlapping more strongly is three or four, the interaction is repulsive and no new bond is ever formed, whatever the state. This is clearly shown by study of the interaction energy curves of Fig. 14, which depict the variation of that energy as a function of the X...X distance for all or some of three orientations of the XH₂ dimers – $\sigma\sigma$ orientation, in which the two sp^2 hybrids are overlapped, $\pi\pi$ orientation, in which the two pure p orbitals of π symmetry are overlapped, and sp orientation, in which the sp^2 hybrid of one fragment overlaps the pure π orbital of the other fragment.

Figure 14 shows the interaction energy computed at the MCSCF(6,4)/6-31 + G(2d,2p) level for the CH₂, NH₂, and H₂NO dimers. It is apparent that in the singlet state of the $\sigma\sigma$ CH₂ dimer, the aggregate is more stable than at dissociation, because of the formation of two new bonds, giving rise to the H₂C=CH₂ molecule in its ground state (the equilibrium distance being 1.33 Å). If a triplet state is selected for the same dimer, one of the bonds is broken and the dimer is less stable. Parallel behavior is observed for the $\pi\pi$ CH₂ dimer, although at smaller interaction energies. In the NH₂ dimer only the singlet state of the $\pi\pi$ orientation is attractive at all distances. The other states are repulsive everywhere, or form a transition state at short distance with another state, and then become stable (the $\sigma\sigma$ /singlet and $\sigma\pi$ /singlets). The triplet states are always repulsive. Finally, in the H₂NO dimer all states of the $\sigma\sigma$ orientation are repulsive, and only a very shallow minimum is found in the $\pi\pi$ orientation at large distances (this is probably associated with the so-called basis set superposition error, shortened as BSSE [67]). All of this indicates a decrease in the tendency of the XH₂ dimers of first row atoms to form bonds between the radicals as the number of lone pairs increases. In fact, no bonds have yet been observed between the NO groups in nitronyl nitroxide crystals, in good agreement with previous considerations.

The results in Fig. 14 can now be connected with the curves of Fig. 12. The curves computed in Fig. 14 correspond to the adiabatic curves of Fig. 12 (those with broken lines), because in all cases the singlet at short distance is a closed-shell state whereas at large distances they dissociate into two neutral fragments (the diabatic curves, the solid lines in Fig. 12, will dissociate into a double charged positive-negative dimer). It is interesting to note that although the stability of the S₀ curve has changed, the physical phenomenon occurring is the same, and that depending on the inter-fragment distance, the S₀ state is a closed-shell singlet, or becomes an open-shell singlet. This is clearly shown in Fig. 15, where the variation of the occupation number of the SOMO and LUMO orbitals is shown for different distances. The distance at which this change starts to be important depends on the stability of the S₀ state – more stable means changes at larger values of the r distance. The reason for such behavior can be understood by looking at Fig. 12 – when the S₀ solid curve is deeper, the crossing of the S₀ and S₁ solid lines is shifted towards larger distances. This behavior corresponds to the results of Fig. 15 – for the H₂NO dimer, the stability of which is very small, the occupation number of the ϕ_1 and ϕ_2 SOMO orbitals of the fragments is equal to 1 up to very short distances (these distances are never reached by the dimer, because they are well within the repulsive well of the potential energy curve). In the CH₂ and NH₂ dimers, however, occupation of the SOMO orbitals (ϕ_1 and ϕ_2 , in the NH₂ dimer, and ϕ_1 , ϕ_2 , ϕ_3 , and ϕ_4 , in the CH₂ dimer) departs from 1.0 at very large distances, and becomes 1.5 at approximately 3 Å. We can, therefore, consider the CH₂ and NH₂ dimers to be dominated by their open-shell singlet component up to 3 Å, whereas the H₂NO dimer is an open-shell singlet up to 1 Å.

The change in the nature of the singlet ground state from open-shell to closed-shell has important implications for the nature of the magnetic interaction – a closed-shell singlet will induce diamagnetic behavior when propagated over all the dimers of the crystal, whereas an open-shell singlet will induce antiferromagnetic behavior.

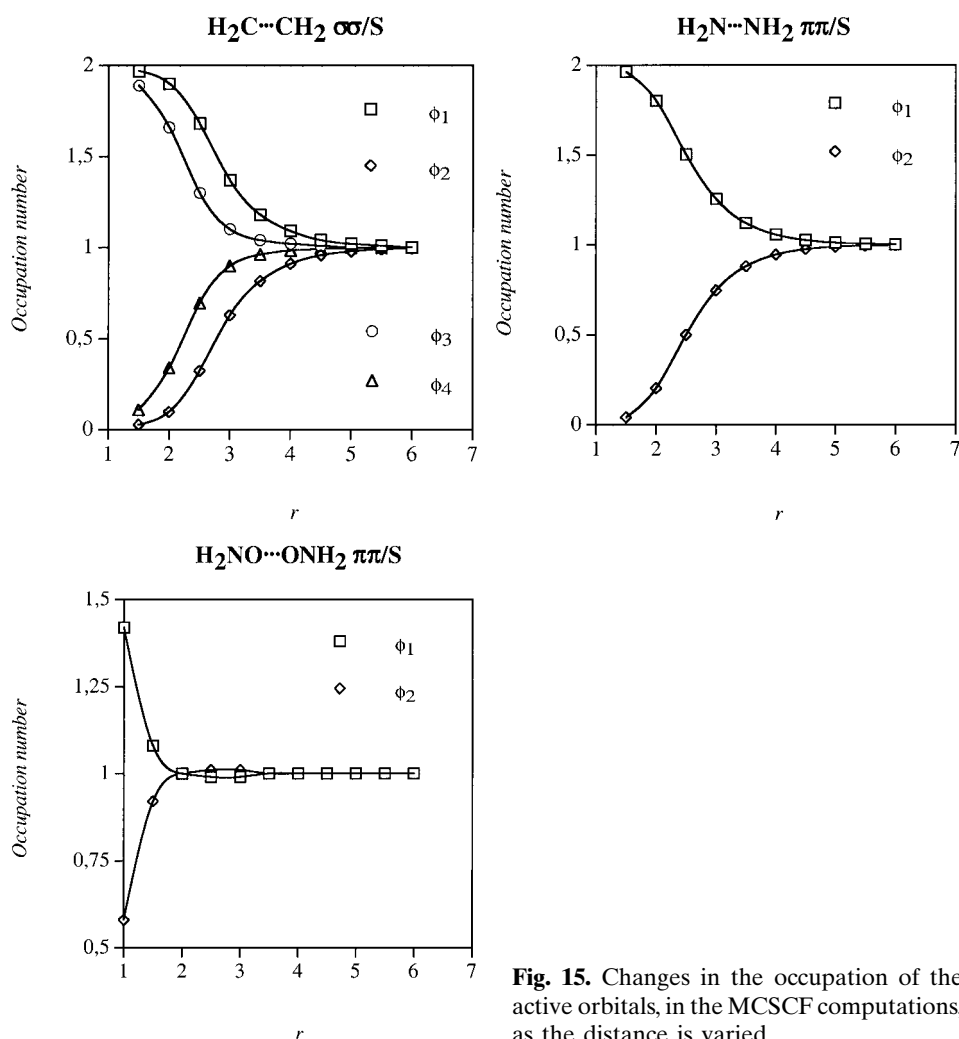


Fig. 15. Changes in the occupation of the active orbitals, in the MCSCF computations, as the distance is varied.

For a given $\text{X}\cdots\text{X}$ interaction one can adjust the character of the singlet by changing the value of the $\text{X}\cdots\text{X}$ distance found in the crystal. This can be achieved by inducing the formation of hydrogen bonds in positions near the X atoms, by placing the right functional groups in the molecule. These new hydrogen bonds will force the $\text{X}\cdots\text{X}$ distance to take the desired value. Alternatively, one can change the type of radical, thus moving the $\text{S}_0\text{-S}_1$ crossing towards the desired position.

Finally, it is necessary to mention that the previous qualitative analysis does not give us any information on the position of the triplet curve relative to the singlet curves. The T_0 triplet curve is repulsive for the $\text{H}\cdots\text{H}$ example of Fig. 12, but can be attractive in other circumstances, for instance the CH_2 dimer (Fig. 14). For the NH_2 and H_2NO dimers, more representative for intermolecular magnetic interac-

tions because no σ bond is formed, the triplets are always repulsive. Finding the regions in which their stability is greater than those of the S_0 or S_1 singlet is the aim of intermolecular magnetic studies. Unfortunately, there is currently no simple qualitative argument which can be used to find these regions.

A step towards understanding the triplet–singlet crossing responsible for the ferro–antiferro macroscopic transition can be taken by analysis at the *ab-initio* valence-bond level of the singlet–triplet crossing found in Fig. 11 for the angular displacement of the H_2NO dimer. We can do such analysis in valence-bond terms by use of Eq. (9), when an appropriate valence-bond basis set has been selected, and the values of the J_{ij} exchange integrals and the $(P_{ij}^S - P_{ij}^T)$ matrix elements have been computed on this basis. This can be achieved by using MCSCF(6,4) computations after adequate transformations to go from the molecular-orbital representation into the equivalent valence-bond form [68]. The singlet–triplet splitting can therefore be rationalized, in valence bond terms, as the result of the interactions between the three H_2NO orbitals plotted in Fig. 16 – two σ orbitals, one located in the N atom and the other in the O atom, and a π antibonding orbital, delocalized over the two atoms. The valence-bond basis set is composed of the three orbitals in each of the fragments.

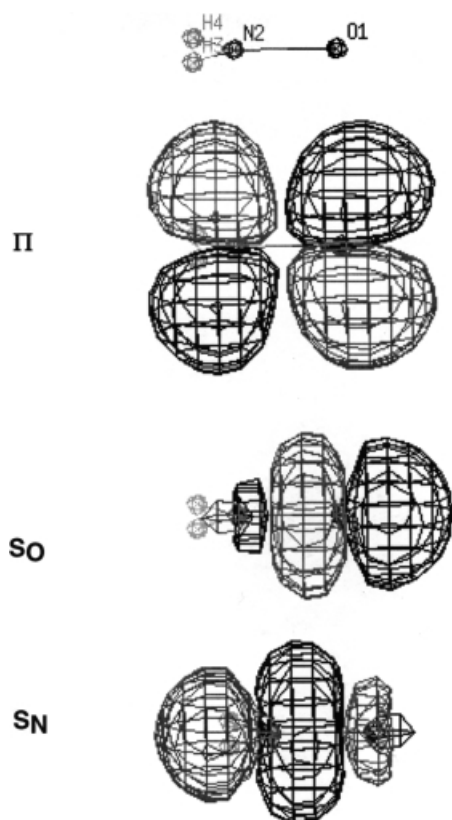


Fig. 16. Shape of the valence-bond orbitals of the H_2NO fragment employed in the analysis of Fig. 11.

Analysis of the values of the J_{ij} exchange integrals and the $(P_{ij}^S - P_{ij}^T)$ matrix elements generated by these orbitals shows that the main changes of the angle are associated with the inter-fragment elements coming from the π orbital of one fragment and the s_O orbital of the other fragment, so we will concentrate here on their values (Table 9). The variation of the $\Delta(J_{ij}P_{ij})$ π - π and s_O - π energetic components with the angle must be compared with the change reported in Fig. 11 for the $\Delta E(S - T)$ values, for which there is a maximum in the ferromagnetic properties at approximately 120° and the antiferromagnetic behavior at 180° and 90° . One should mention here that addition of the $\Delta(J_{ij}P_{ij})$ terms reproduces this variation at slightly higher energies (approx. 10 cm^{-1}). The $\Delta(J_{ij}P_{ij})$ π - π energetic components are always antiferromagnetic whereas the s_O - π energetic components are always ferromagnetic. The antiferromagnetic-ferromagnetic-antiferromagnetic change is parallel to a decrease towards zero of the intermolecular $\Delta(J_{ij}P_{ij})$ π - π elements and a simultaneous increase from zero of the intermolecular $\Delta(J_{ij}P_{ij})$ s_O - π terms. The overall result comes from addition of these two opposite terms – when the $\Delta(J_{ij}P_{ij})$ π - π elements dominate the interaction is antiferromagnetic whereas the interaction is ferromagnetic when the dominating term is the $\Delta(J_{ij}P_{ij})$ s_O - π term. As shown in Table 10, the changes in the sizes of the terms are mainly associated with changes in the values of the J_{ij} s_O - π integrals (last column of Table 10) and with the simultaneous decrease in the values of the J_{ij} π - π integrals. This variation is qualitatively similar to the change expected in the s_O - π and π - π overlap integrals. Our valence-bond analysis thus shows that the presence of ferromagnetism in the H_2NO dimer of Fig. 11 is because of a subtle balance of the SOMO-SOMO and (SOMO-1)-SOMO interactions, the first giving rise to antifer-

Table 9. Calculated values (in atomic units, and multiplied by 10^{-3}) of the $(J_{ij}P_{ij})$ terms for the π and s_N and s_O valence bond orbitals of fragments 1 and 2, when the $\text{O}\cdots\text{O-N}$ angle between the two fragments is equal to 150° .

	π	$s_O(1)$	$s_N(1)$
π	-0.0716	0.1110	0.0001
$s_O(2)$	0.0040	0.0013	-0.0002
$s_N(2)$	-0.0002	-0.0003	0.0000

Table 10. Variation with the $\text{O}\cdots\text{O-N}$ angle of the values of the inter-fragment $(J_{ij}P_{ij})$ terms, P_{ij} , and J_{ij} for the π and s_O valence-bond orbitals. The angles are given in degrees and all the other values in atomic units.

θ	$(J_{ij}P_{ij})$ π - π	$(J_{ij}P_{ij})$ s_O - π	P_{ij} π - π	P_{ij} s_O - π	J_{ij} π - π	J_{ij} s_O - π
180	-0.00011	0.00000	2.000	0.034	-0.00002	0.00000
150	-0.00007	0.00011	2.000	0.034	-0.00001	-0.00095
140	-0.00005	0.00011	2.000	-0.017	-0.00001	-0.00145
120	0.00000	0.00025	2.000	-0.017	0.00000	-0.00209
100	-0.00011	0.00020	2.000	0.035	-0.00003	-0.00164
90	-0.00033	0.00011	2.000	0.034	-0.00010	-0.00089

romagnetism, the second to ferromagnetism. This change is driven by the changes in the values of the J_{ij} integrals and the signs of the ΔP_{ij} $s_{\text{O}}-\pi$ elements.

The previous analysis has been focussed on a simple model dimer. Although this dimer is not representative of the electronic structures found in all nitronyl nitroxide radicals, or the variety of relative orientations of the NO groups, it has clarified some of the physics of the problem, namely, that the McConnell-I mechanism is an oversimplification of the real physics (it lacks sensible foundation and its normal use fails to reproduce the behavior of a simple case). It was also shown that the presence or absence of ferromagnetism in the H_2NO dimer is because of a balance between the SOMO–SOMO and (SOMO-1)–SOMO interactions, that is, does not follow a one-orbital model. Finally, we have presented a curve-crossing model which enables understanding of the basics of the intermolecular magnetic interaction in simple terms. In the following sections, we will describe how to obtain information about the nature of magnetic intermolecular interaction by combining results from analysis of the crystal packing of purely organic molecular crystals and accurate *ab-initio* computations on realistic nitronyl nitroxide aggregates.

3.3.4 Experimental Magneto-structural Correlations

The proper means of obtaining experimental magneto-structural correlations on purely organic crystals is by unbiased analysis of the packing of crystals with the same kind of *dominant* magnetic interactions over the usual range of temperatures analyzed (usually 2–300 K). The largest magnetic interactions in these crystals can be assumed to be always of the same as the dominant interactions (that is, all short nearest-neighbor contacts between radicals in the crystal can be assumed to be of the dominating type, or much smaller in size).

To obtain unbiased experimental magneto-structural correlations for nitronyl nitroxide magnetic crystals one must study the packing of all the crystals of this type with dominant ferro or antiferromagnetic properties (the FM and AFM subsets, respectively). From a combined search on the Cambridge Crystallographic Database and from crystals provided by a variety of authors it is possible to select 23 FM and 24 AFM crystals, all with R factors smaller than 0.1 or without large distortion (and thus with well refined structures), omitting also those crystals containing transition metals or which are co-crystals [2]. The radicals belonging to these two subsets are those shown in Figs. 2 and 3, which also indicate the refcode (when available, otherwise an internal refcode which begins with a zero was assigned).

When the two FM and AFM subsets are created it is possible to analyze the packing of these crystals, looking at the relative disposition of the radicals in the nearest-neighbor contacts. In accordance with previous studies of the spin distribution, most of the spin population is located on the ONCNO group of the five-membered ring. It thus seems natural to search first for magneto-structural correlations involving the relative disposition of nearby ONCNO groups. One can define the relative orientation of two ONCNO groups, given that the geometry of these groups in different crystals is almost invariant [69], by means of the six geometrical parameters of Fig. 17. The values of these parameters (Table 11 and Fig. 18) within

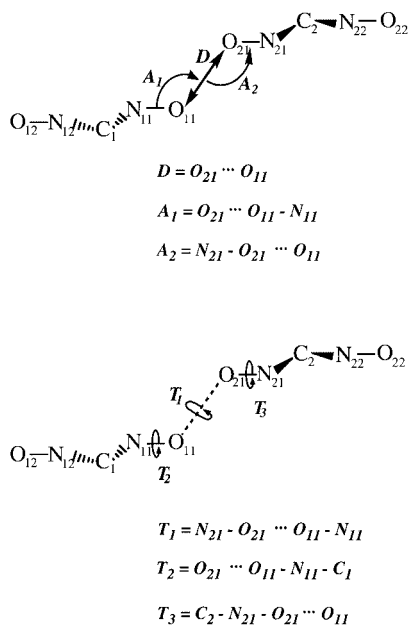


Fig. 17. Geometrical parameters used to define the relative position of two rigid ONCNO groups in space.

Table 11. List of ONCNO...ONCNO contacts for crystals of the FM and AFM subsets within the range of distances indicated. Percentages of ferro- or antiferromagnetic interactions are also given.

Range (Å)	Total contacts	FM contacts	%	AFM contacts	%
0-3	0	0	0	0	0
0-4	24	10	42	14	58
0-5	92	36	39	56	61
0-6	204	90	44	114	56
0-7	378	167	44	211	56
0-8	608	274	45	334	55
0-9	901	416	46	485	54
0-10	1312	611	47	701	53

the two subsets are distributed in a nearly uniform form over the range of values for all classes of parameter. Two important facts emerge from this distribution:

- there is no correlation between the presence of short NO...ON contacts and the presence of antiferromagnetism (Table 11), as was previously assumed; and
- there are no specific orientations of the ONCNO groups characteristic of either ferro- or antiferromagnetic interactions (Fig. 18).

Both facts contradict the normal use of the McConnell-I mechanism, which predicts that short ONCNO...ONCNO contacts should lead to antiferromagnetism,

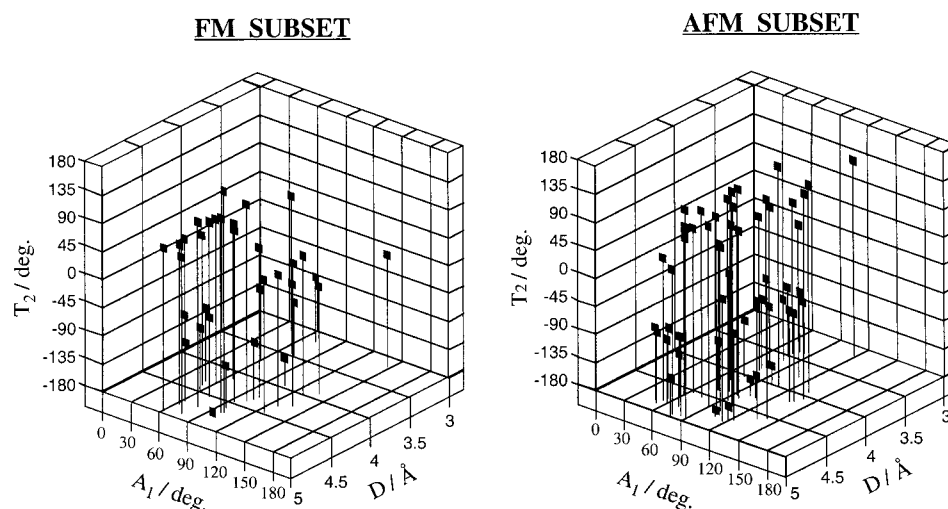


Fig. 18. Distribution of values defining the ONCNO...ONCNO orientation (intermolecular distance, D , angle A_1 , and dihedral angle T_2) in nitronyl nitroxide crystals with dominant ferro- or antiferromagnetic interactions. The parameters are defined in Fig. 17.

and the angular dependence of these interactions, as the O atom of one group gets closer to the C atom of the other.

When a similar analysis is performed for the C-H...ONCNO contacts of the FM and AFM subsets a similar conclusion is reached, i. e. *there is no statistically significant difference between the contacts found in the FM and the AFM subsets*. One can therefore conclude that no magneto-structural correlation based only on one type of contact is possible for these crystals. This result is quite surprising, because one expects that the magnetic interaction should be affected by the geometry, as shown in Fig. 11. *The most likely explanation of this result is, therefore, that more than one type of contact is playing a role in defining the nature of the dominant magnetic interaction*, i. e. it depends, for instance, on the relative geometry of the ONCNO...ONCNO and the C-H...ONCNO contacts. Such a conclusion clearly goes against normal understanding of McConnell-I predictions, because in order to exist such cooperating interactions, parts of the molecule which hold small spin populations (see above) must participate in magnetic interactions. In particular, the magnetic cooperation could occur through the hydrogen bond (C-H...ONCNO contacts), although we have already found that the spin population on the H atoms is always very small, irrespective of the H atom and radical considered (thus McConnell-I would predict a small magnetic role for these contacts, unless large J values could be attributed to such hydrogen bond interactions).

As a consequence of these facts we can rule out simple magneto-structural correlations which try to predict magnetic behavior in terms of ONCNO...ONCNO relative positions. The intermolecular interactions between nitronyl nitroxide radicals result from a combined interaction involving more than one functional group

of the molecule. This study does not, however, identify which groups participate, their importance, and the geometrical dependence of the interactions induced by each group. For such a task, we need to perform well designed theoretical studies aimed at clarifying these points.

3.3.5 Theoretical Magneto-structural Correlations

The cooperativity between all the functional groups of the radicals in defining the net character of the radical-radical magnetic interaction, reached in the previous section, requires further testing before its final acceptance. We therefore decided to perform theoretical studies aimed at establishing, without any doubt, the validity of such a conclusion. In this section we summarize these studies, after briefly presenting the methodology employed.

3.3.5.1 Theoretical Tools for the Study of Intermolecular Magnetic Interactions

The nature of the magnetic interaction between a pair of radicals can be established by use of the Heisenberg Hamiltonian, as described in detail in the previous sections. Although these methods are very efficient for analysis of the magnetic interaction, currently, however, the use of Eqs. (6)–(9) to obtain quantitative results is computationally more demanding than the use of molecular-orbital methods aimed at the computation of the energy difference between the high spin and low spin states (singlet and triplet for the interaction of doublet radicals).

The use of molecular-orbital methods to define the nature of the magnetic interactions between radicals has been covered in detail in the other chapters of this book [70], so we will only emphasize here some aspects related to the particularities of the application of these methods to intermolecular interactions. As in the study of magnetism in systems containing transition metals, two kinds of molecular-orbital method can be used to study the magnetic character of purely organic radicals. The first set of methods, which we can regard as *conventional* methods, is based on separate computation of the energy of the high spin and low spin states of interest. Here, we can, in principle, use any of the methods (HF, CI, MCSCF, MP2, CCSD, QCISD, . . .) developed over the years for the study of molecules and aggregates, and described in detail in well known texts [18]. The second kind of molecular-orbital method, the so called *dedicated* methods [71], is designed for direct computation of the energy difference between the high- and low-spin states, after obtaining the analytical expression for that energy difference. The second kind of method has not yet been applied to the study of through-space magnetic interactions, although their application to the study of through-bond interactions has resulted in very promising performance at lower cost than that of the use of the first class of methods [72]. We will, therefore, focus on summarizing the properties and problems of conventional methods, when applied to the study of through-space magnetism.

Two main problems are associated with the use of many of the conventional methods - the presence of spin contamination in some of the states and the difficulty

(or impossibility) of describing some of the states of interest in an appropriate form. The first problem is associated with the use of methods whose wavefunctions are not eigenvalues of the \hat{S}^2 operator. In general, this is true for all methods which use an UHF determinant (UHF, UMP2, ...), with the special case of the unrestricted version of the DFT functionals already mentioned. Because the UHF determinants are not always eigenfunctions of the \hat{S}^2 operator, the computed wavefunction can be an average of the wavefunction of the desired state and other states of higher or lower spin multiplicity. The wavefunction is said to be *spin contaminated*, the amount of that contamination being computed by looking at the expected value of the \hat{S}^2 operator – in a pure spin state it should be equal to $S(S+1)$, where S is the eigennumber defining the spin multiplicity of the state (defined as $2S+1$), i. e. is equal to zero for a singlet, $1/2$ for a doublet, one for a triplet, and so on. Thus, when the expectation value of the \hat{S}^2 operator for a doublet ($2S+1=2$, consequently $S=1/2$) differs from $3/4$, the doublet is contaminated by states of higher multiplicity (in this example the only possible source of contamination). The importance of this spin contamination in our high–low spin computations is that the energy computed with a spin contaminated wavefunction is an average of the energy of the pure spin states, thus making the value of the energy difference unreliable. A possible solution to the spin-contamination problem might be the use of spin-projected UHF wavefunctions, exact or approximate [23], an approach followed by Yamaguchi in the computation of the intermolecular magnetic interactions of a variety of systems [73]. The spin-contamination problem can be completely avoided by use of methods which, by construction, do not suffer from spin contamination and are capable of describing any type of spin multiplicity. One example is the MCSCF method (the name standing for multi-configurational self consistent field methods). This method is capable of properly describing the sign of the high–low spin energy differences for many intramolecular systems [20a], and it has recently been shown that it is also capable of describing the sign of the difference for model intermolecular dimers [74]. The quality of the MCSCF results can be improved to quantitative accuracy when compared with experimental values or results from full-CI computations, by including the dynamic correlation not taken into account by the MCSCF method. One efficient means of achieving this is to perform a multi-reference second order Moller-Plesset (MP2) computation on the MCSCF wavefunction, a method which has been named CASPT2 [20a].

The second type of problem is encountered in the description of the open-shell singlet state (that associated with a $\phi_1\alpha(1)\phi_2\beta(2)$ configuration), which cannot be described within the framework of the RHF method, or by all the methods which take its determinant as starting point. This configuration is, however, likely to be that associated with the ground state S_0 state, given the large distance between the radicals and the small interaction energy involved. Besides the possible spin-contamination problem described above, one must be sure the final solution has the desired spin distribution (in the example mentioned here an α spin in one of the radicals and a β spin in the other) because the UHF solution often results in no net spin density on each center (i. e. one has ended in the closed-shell state). In such circumstances one must resort to the so called *broken-symmetry approximation* [75], which enables one to end in the open-shell singlet by mixing the SOMO–LUMO

orbitals (if they are of different symmetry, otherwise the SOMO and other orbital), thus forcing a decrease in the symmetry of the Hamiltonian and wavefunction relative to the symmetry of the molecule. A broken solution of an UHF wavefunction is known to be equivalent to a small CI calculation [75]. When such a wavefunction is fed as a starting wavefunction into a coupled cluster method, e. g. the CCSD(T), and the energy is compared with that computed with the same method from the UHF triplet, it is possible to obtain reasonable results for singlet-triplet energy separation in the H₂NO dimer (Fig. 11), in contrast with accurate methods such as CASPT2, which is known to give results close to the full-CI method in simple radical dimers [74]. We will call these computations BS-CCSD(T).

The use of a broken-symmetry (BS) solution has also been found to be adequate within the density-functional (DFT) formalism [25–27]. The DFT wavefunction of many radical dimers has been found to result in small spin contamination (although this is not always so). The energy difference between the broken-symmetry singlet and the triplet wavefunctions is found to be similar to that from CASPT2 computations for the H₂NO dimer (Fig. 11), at least when the B3LYP functional is employed (BS-B3LYP computations). Similar behavior is also found in real nitronyl nitroxide dimers, as we will see later. The advantage of these BS computations is that they take only a fraction of the computational effort required for CASPT2 or BS-CCSD(T) computations. This BS-DFT approximation has been extensively used, and given experimental results with very good reproducibility, for computation of the magnetism in transition metal dimers [76]. Some controversy has, however, arisen on exact form in which the singlet-triplet energy difference should be computed when the open-shell singlet state is computed using the BS-DFT approximation [75, 72b]. Recent evidence seems to be in favor of use neither of the spin-restricted Kohn-Sham formalism or and kind of spin-correction technique [76, 77], to avoid a contaminated value of the spin for the Slater determinant. Here, in line with previous findings for inorganic compounds, we will consider the expression $\Delta E^{S-T} = E_{BS}(S) - E(T)$, which is equivalent to saying that the BS-DFT method reproduces well the energy of the open-shell singlet (the alternative solution is $\Delta E^{S-T} = 2(E_{BS}(S) - E(T))$, which is known to work better for Hartree–Fock wavefunctions, but the latest evidence seems to indicate that this is not so in the DFT formalism). Thus, we will not use such a factor in the following results. It is, in any case, worth noting that the inclusion of such a factor does not change the sign of the high-low spin energy difference.

3.3.5.2 Cooperativity in Magnetic Interactions – the LICMIT and WILVIW10 Crystals

The LICMIT [78, 79] and WILVIW10 [80, 81] crystals are the two crystals of the ferromagnetic and antiferromagnetic subsets studied in the Section 3.3.4 for which the intermolecular ONCNO...ONCNO distances are shortest (3.157 and 3.158 Å, respectively, although in the second crystal there is also another contact at 3.384 Å). Besides the similarity in the values of the distances, the two ONCNO groups separated by the shortest distances in these two crystals are distributed in a nearly

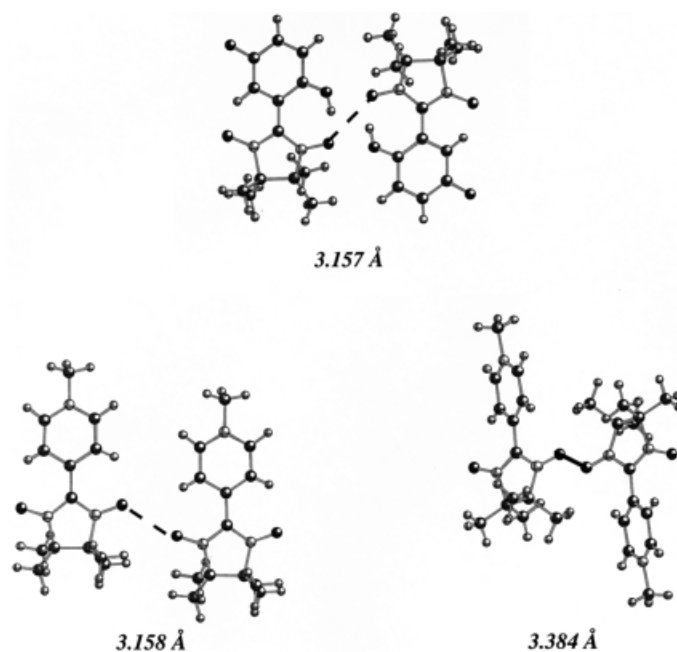


Fig. 19. Geometrical disposition of the radicals in the shortest ONCNO...ONCNO contacts found in the LICMIT and WILVIW10 crystals. The H atom of the *meta* OH group is not shown in LICMIT.

identical manner (Figs. 19 and 20). If, therefore, one assumes that the dominant magnetic interaction is determined solely by the shortest ONCNO...ONCNO interaction, it is clear that the magnetic interaction for the shortest contacts of the LICMIT and WILVIW10 crystals should be of the same type. In the WILVIW10 crystal one could argue that the second contact at 3.384 Å could have the opposite character, but, as mentioned above, if this is true one would have a crystal with competing interactions of opposite sign. This is not what is found in the experimental measurements. Furthermore, analysis of the geometry of the 3.384 Å contact indicates that the relative orientation of the ONCNO groups is similar to that found when the distance is 3.158 Å. There is, therefore, no reason to expect a different magnetic nature for the shortest (and expectedly dominating) dimers on the basis of the ONCNO groups. This is also predicted by the McConnell-I mechanism, which will predict those contacts as antiferromagnetic. Consequently, there are two possible options:

- the magnetic interactions between the ONCNO groups in these three examples are of different types, because of the small geometrical differences between these dimers; or
- other groups, besides the ONCNO groups, also play a decisive role in defining the character of the magnetic interactions in these three dimers.

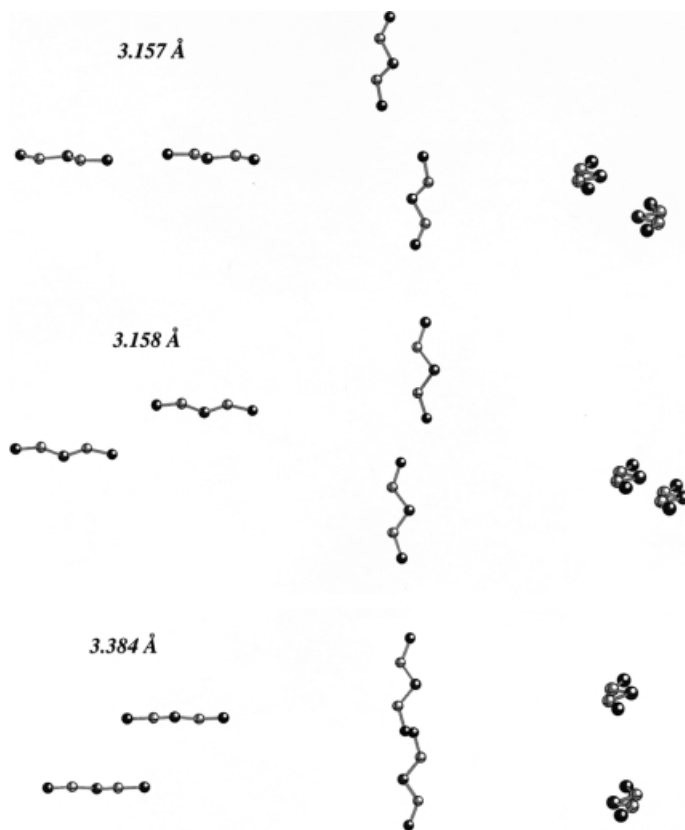


Fig. 20. Front, upper, and side view of the space disposition of the ONCNO groups in the dimers of Fig. 19.

We can investigate the validity of the first option by computing the nature of the ONCNO...ONCNO intermolecular interaction of the three dimers of Fig. 19 [82]. For this purpose one can take the real radical dimers and delete all the atoms except those in the ONCNO groups, also adding hydrogens in the places where N-C(sp³) or C(sp²)-C bonds occur in the real dimer, to preserve the oxidation state of the atoms. The directions of the new N-H and C-H bonds are the same as that of the substituted N-C(sp³) or C(sp²)-C bond, and their lengths are the optimum for each ONH-CH-HNO fragment in a B3LYP/6-31+G(2d,2p) optimization. We performed MCSCF(6,6)/6-31G and MCSCF(6,6)/6-31G(d) computations on the geometry of these three ONH-CH-HNO model dimers to calculate the singlet-triplet energy difference, after verifying that the addition of diffuse functions did not affect the sign and magnitude of the singlet-triplet energy difference on tests performed on the H₂NO dimer. One must note here that the CAS(6,6) space was used in the MCSCF computations, because each monomer requires a CAS(3,3) space to enable proper description of the spin polarization in the ONCNO group (i. e. for the presence of

Table 12. Values of the $\Delta E^{\text{S-T}}$ energy difference (cm^{-1}) computed for the (ONH-CH-HNO)₂ model dimer making the shortest contacts in the LICMIT and WILVIW10 crystals. The MCSCF method was used, with the basis set indicated. The results are compared with those from B3LYP broken-symmetry computations using the same basis set.

Crystal	Basis set	MCSCF	CASPT2	B3LYP
LICMIT	6-31G	-0.8		-2.0
	6-31G(d)	-1.0	-2.3	-1.8
WILVIW10	6-31G	-2.2 ^a		-5.4 ^a
		-16.4 ^b		-14.0 ^b
	6-31G(d)	-1.8 ^a	-0.8	-5.2 ^a
		-17.6 ^b	-9.7	-15.0 ^b

^aDimer with a ONCNO...ONCNO contact of 3.159 Å.

^bDimer with a ONCNO...ONCNO contact of 3.383 Å.

negative spin on the central C(sp²) atom and positive spin on the two atoms of the NO groups). The results of these MCSCF computations (Table 12) show that the singlet is always the ground state for all three dimers, i. e. the magnetic interaction is antiferromagnetic in character. Interestingly, for WILVIW10 the dimer with the shortest O...O distance has not the strongest antiferromagnetic interaction, clearly indicating the importance of the angular parameters in defining the strength of the antiferromagnetic interactions in ONCNO...ONCNO interactions. The basis set does not seem to have a substantial effect on the results. When the dynamic correlation is taken into account by means of CASPT2 calculations, the results are almost the same.

We repeated the previous computations at the broken-symmetry B3LYP level (see above) to test the performance of this methodology. The nature of the interaction (Table 12) is qualitatively the same as obtained previously at the MCSCF level, and the size of the interaction is also very similar, although the B3LYP results slightly exaggerate the antiferromagnetic nature of the interaction, consistent with the trend previously found in Fig. 11 for the H₂NO dimers. Taking that trend into account we can therefore feel safe when applying the broken-symmetry B3LYP methodology to the study of the magnetic character of the interaction between ONCNO-containing dimers.

The MCSCF and B3LYP results on the LICMIT and WILVIW10 dimers indicate that the three dimers of Fig. 19 have the same magnetic character. Thus, the only remaining option is the second, i. e. that groups of the LICMIT and WILVIW10 radical with much smaller spin population than the ONCNO group cooperate in establishing the nature of the magnetic interaction in the dimer. Such behavior, if confirmed, will explain the lack of correlation between the relative disposition of the ONCNO groups and the dominant magnetic character of the interactions found experimentally when analyzing the packing of crystals with dominant ferro or antiferromagnetic interactions. We therefore performed broken-symmetry B3LYP computations in the three dimers of Fig. 19, using the full geometry of these dimers and the 6-31+G(d) basis set. These computations gave a singlet-triplet energy difference of 1.3 cm⁻¹ for the LICMIT dimer, fortuitously close to the experimental

result (1.3 cm^{-1}). For the shortest and largest contact in the WILVIW10 dimers these results are -9.1 and -28.2 cm^{-1} , respectively (to be compared with an experimental average energy difference of -102.9 cm^{-1}). When these results are compared with those obtained with the isolated ONCNO groups (Table 12) one has proof of the important role that other groups, that hold approximately 10% of the spin population, play in defining the character of the magnetic interaction in these radicals. *We thus have a numerical proof of the presence of cooperativity among the spin-containing and non-spin-containing groups of these radicals in establishing the nature of the magnetic interactions between their radical dimers.*

As a final test on the validity of our analysis we computed the singlet-triplet energy difference for all the dimers of the first coordination sphere of the radicals in the LICMIT and WILVIW10 crystals (these are the dimers with the shortest contacts within the crystal). We also performed the calculations at the broken-symmetry B3LYP/6-31+G(d) level [83]. There are five different kind of dimer in the first coordination sphere of the LICMIT radical; the shortest O...O distances in these are, in increasing order, 3.158, 4.594, 5.525, 5.856, and 6.294 Å. The singlet-triplet energy difference for all these dimers in the LICMIT crystal are, in the same order, 1.34, 0.15, 0.02, -0.15 , and 0.09 cm^{-1} . The shortest contact interaction studied previously is, therefore, by far the most dominant. Interestingly, all but one of these dimers are of the ferromagnetic type. Although we will not discuss the values here, similar results were also obtained for the WILVIW10 crystal.

3.3.5.3 Magnetic Patterns

If the magnetic interactions in the dimers depend on more than one functional group, the relevant information is the number and relative disposition of these functional groups in the two molecules. This type of information is given the general name *pattern* in the field of crystal engineering [7c, 84]. When associated with magnetic properties, therefore, we decided to name it *magnetic pattern*. Different patterns can have similar or identical relative disposition of the ONCNO groups but different disposition of other groups and thus their magnetic character will be different. This is the source of the apparent inconsistencies found when analyzing the packing of the crystals with dominant ferro or antiferromagnetic interactions as a function of *one* functional group. In view of this new evidence one must learn how to perform such analysis in terms of patterns.

One can assign the magnetic character of any given pattern by direct computation of the energy difference between the high and low spin states present in that pattern. From that computation we know that the pattern for the shortest contact in the LICMIT crystal (Fig. 19) is ferromagnetic, whereas the two found in the WILVIW10 crystal are antiferromagnetic. It is, however, also useful to know the reasons for that change in behavior, i. e. to identify what groups in the molecule cooperate with the ONCNO...ONCNO magnetic interaction in each instance. To achieve this one can progressively extract groups from the full dimer and compute the resulting effect in the low-high energy difference (in this example singlet-triplet). Thus, if the LICMIT dimer is substituted by a ONH-CH-HNO...ONH-CR-HNO dimer

(R = substituent), the resulting interaction between the LICMIT radical and the ONH-CH-HNO radical is ferromagnetic, by a value of 0.31 cm^{-1} , compared with the 1.3 cm^{-1} value previously found for the full LICMIT dimer, and the -1.8 cm^{-1} value found for the $(\text{ONH-CH-HNO})_2$ dimer (all are broken-symmetry B3LYP computations). It is, therefore, the C-H and O-H groups present in the six-membered rings that make the difference. In particular, it seems likely to be the effect of the short O-H...ONCNO contacts. Such contacts are not possible in the WILVIW10 dimers, although one finds short $\text{C}(\text{sp}^2)\text{-H}\cdots\text{ONCNO}$ contacts in the shortest dimer (that with a 3.158 \AA O...O distance). Computation for the full dimer now gives a value of -9.1 cm^{-1} , that for the ONH-CH-HNO...ONH-CR-HNO dimer -5.7 cm^{-1} , and that for the $(\text{ONH-CH-HNO})_2$ dimer -5.2 cm^{-1} (all are broken-symmetry B3LYP computations). The short $\text{C}(\text{sp}^2)\text{-H}\cdots\text{ONCNO}$ contacts in WILVIW10 are, therefore, not capable of changing the nature of the antiferromagnetic interaction generated by the short ONCNO...ONCNO contacts. The same can be said about the $\text{C}(\text{sp}^2)\text{-H}\cdots\text{ONCNO}$ contacts found in the large-distance dimer of Fig. 19 (the full dimer has an interaction of -28.2 cm^{-1} whereas the WILVIW10...ONH-CH-HNO dimer interaction is -20.9 cm^{-1} , and the $(\text{ONH-CH-HNO})_2$ dimer interaction is -15.0 cm^{-1}). So, the ferromagnetic nature of the interactions found in the dimer of the LICMIT crystal shown in Fig. 19 must be attributed to the short O-H...ONCNO contacts present in that dimer.

When the character of the patterns has been properly characterized one can study the magnetic pathways within the crystal, by identifying the location in the crystal where these patterns are repeated. This will enable rationalization of the magnetism in the magnetic crystals of interest. We can apply this procedure qualitatively to the LICMIT crystal with the data given above. The data mentioned indicate the presence of strong ferromagnetic interactions between dimers, and smaller ferromagnetic interactions connecting these dimers with nearby dimers. We are currently working on procedures to determine whether these data reproduce the $\chi T - T$ behavior in the experimental range of temperatures [85].

Acknowledgments

This work was supported by DGES (Projects PB95-0848-C02-02 and PB98-1166-C02-02) and CIRIT (Projects 1997SGR-00072 and 1999SGR-00046). We are also grateful for contact with generous allocation of CPU time provided by CESCA and CEPBA on their computers, also made possible by a joint CIRIT-University of Barcelona grant. Finally, the authors also want to thank Professors J. Veciana and M. A. Robb for their invaluable support and cooperation in parts of this work.

References

- [1] For a recent reviews, see: (a) E. Coronado, P. Delhaès, D. Gatteschi, and J. S. Miller (Eds.), *Molecular Magnetism: From Molecular Assemblies to the Devices*, NATO ASI Series E, vol. 321, Kluwer Acad. Publishers, Dordrecht, **1996**; (b) J. S. Miller, A. J. Epstein, *Angew. Chem. Int. Ed. Engl.* **1994**, *33*, 385; (c) M. Kinoshita, *Jpn. J. Appl. Phys.* **1994**, *33*, 5718; (d) O. Kahn (Ed.), *Magnetism: A Supramolecular Function*, Kluwer, Dordrecht, **1996**; (e) P. M. Lahti (Ed.), *Magnetic Properties of Organic Materials*, Marcel Dekker, New York, **1999**; (f) O. Kahn (Ed.), *Mol. Cryst. Liq. Cryst.* **1999**, *334/335*, 1–712/1–706.
- [2] For details of the selection of the crystals and methodology see: (a) M. Deumal, J. Cirujeda, J. Veciana, J. J. Novoa, *Adv. Mat.* **1998**, *10*, 1461; (b) M. Deumal, J. Cirujeda, J. Veciana, J. J. Novoa, *Chem. Eur. J.* **1999**, *5*, 1631.
- [3] A. Gavezzotti, *J. Am. Chem. Soc.* **1991**, *113*, 4622; (b) A. Gavezzotti, (Ed.), *Theoretical aspects of computer modeling*, John Wiley, Chichester, **1997**.
- [4] (a) A. Gavezzotti, *Acc. Chem. Res.* **1994**, *27*, 309; (b) J. Bernstein, *J. Phys. D: Appl. Phys.* **1993**, *26*, B66; (c) J.D. Dunitz, J. Bernstein, *Acc. Chem. Res.* **1995**, *28*, 193; (d) J. Bernstein, R. J. Davey, J.-O. Henck, *Angew. Chem. Int. Ed. Engl.* **1999**, *38*, 3440.
- [5] R. J. Gdanitz, in A. Gavezzotti (Ed.) *Theoretical aspects of computer modeling*, John Wiley, Chichester, **1997**; (c) J. Perlstein, *J. Am. Chem. Soc.* **1992**, *114*, **1955**; (d) J. R. Holden, Z. Du, H. L. Ammon, *J. Comput. Chem.* **1993**, *14*, 422; (e) B. P. van Eijck, W. T. M. Mooij, J. Kroon, *Acta Crystallogr.* **1995**, *B51*, 99; (f) A. M. Chaka, R. Zaniewski, W. Youngs, C. Tessier, G. Klopman, *Acta Crystallogr.* **1996**, *B52*, 165; (g) M. U. Schmidt, U. Englert, *J. Chem. Soc., Dalton Trans.* **1996**, 2077; D. W. M. Hofmann, T. Lengauer, *Acta Crystallogr.* **1997**, *A53*, 225; P. Vermer, F. J. J. Leusen, *Rev. Comput. Chem.* **1998**, *12*, 327.
- [6] G. Filippini, A. Gavezzotti, J. J. Novoa, *Acta Crystallogr.*, **1999**, *B55*, 543.
- [7] (a) J.J. Novoa, M. Deumal, *Mol. Cryst. Liq. Cryst.* **1997**, *305*, 143. (b) M. Deumal, J. Cirujeda, J. Veciana, M. Kinoshita, Y. Hosokoshi, J.J. Novoa, *Chem. Phys. Lett.* **1997**, *265*, 190. (c) J.J. Novoa, in *Implications of Molecular and Materials Structure for New Technologies*, (J.A.K. Howard, F.H. Allen, G.P. Shields, Eds.), Kluwer Academic Publishers, Dordrecht, **1999**.
- [8] A. Rajca, *Chem. Rev.* **1994**, *94*, 871.
- [9] V.; Laget, C.; Hornick, P.; Rabu, M.; Drillon, R., Ziessel, *Coord. Chem. Rev.* **1998**, *178–180*, 1533.
- [10] H. M. McConnell, *J. Chem. Phys.* **1963**, *39*, 1910.
- [11] A. Ricca, J. Weber, M. Hanus, Y. Ellinger, *J. Chem. Phys.* **1995**, *103*, 274. MCSCF computations on the H₂NO radical. These computations also indicate that the H₂NO molecule is slightly non-planar, although when the vibrational motion is taken into account is effectively planar.
- [12] MCSCF computations performed by us using a complete active space of seven electrons and seven orbitals (CAS(7,7)) and a cc-pVDZ basis set, predict that the charge on the O atom is –0.31 atomic units, that is, has 0.31 electrons more than the six valence electrons one associates to the O atom when isolated (the charge in the N and H atoms are 0.05 and 0.13 atomic units, respectively). The atomic spin population on the O, N and H atoms is 0.68, 0.33 and 0.01 atomic units.
- [13] For neutron diffraction data on nitronyl nitroxides, see: (a) A. Zheludev, V. Barone, M. Bonnet, B. Delley, A. Grand, E. Ressouche, R. Subra, J. Schweizer, *J. Am. Chem. Soc.*

- 1994**, *116*, 2019; (b) F. M. Romero, R. Ziessel, M. Bonnet, Y. Pontillon, E. Ressouche, J. Schweizer, B. Delley, A. Grand, C. Paulsen, *J. Am. Chem. Soc.* **2000**, *122*, 1298.
- [14] Some recent articles in which the ESR and experimental results are compared are: (a) V. Barone, A. Grand, D. Luneau, P. Rey, C. Minichino, R. Subra, *New. J. Chem.* **1993**, *17*, 545; (b) V. Barone, A. Bencini, M. Cossi, A. di Mateo, M. Mattesini, F. Totti, *J. Am. Chem. Soc.* **1998**, *120*, 7069; (c) C. Adamo, A. di Mateo, P. Rey, V. Barone, *J. Phys. Chem. A*, **1999**, *103*, 3481; (d) J. Cirujeda, J. Vidal-Gancedo, O. Jürgens, F. Mota, J. J. Novoa, C. Rovira, J. Veciana, *J. Am. Chem. Soc.*, (accepted for publication).
- [15] For a recent work on NMR comparing the DFT and NMR results see, for instance: H. Heise, F. H. Köhler, F. Mota, J. J. Novoa, J. Veciana, *J. Am. Chem. Soc.* **1999**, *121*, 9659.
- [16] Notice that some methods which include spin polarization do not give the right answer to the size and sign of the atomic spin population in some of the atoms, due to the presence of spin contamination of the wavefunction by states of other multiplicity. This is the case of the UHF, UMP2, and similar methods. The problem is not present in other methods like the unrestricted formulation of the density-functional methods, among others. See, for instance, references (13a) and (17).
- [17] J. J. Novoa, F. Mota, J. Veciana, J. Cirujeda, *Mol. Cryst. Liq. Cryst.* **1995**, *271*, 79.
- [18] A. Szabo and N. S. Ostlund, *Modern Quantum Chemistry*, Macmillan, New York, **1982**.
- [19] P. Pulay, T. P. Hamilton, *J. Chem. Phys.* **1988**, *88*, 4926.
- [20] (a) B. O. Roos, K. Andersson, M.P. Fülscher, P.-A. Malmqvist, L. Serrano-Andres, K. Pierloot, M. Merchán, *Adv. Chem. Phys.* **1996**, *93*, 219; (b) J. J. McDouall, K. Peasley, M. A. Robb, *Chem. Phys. Lett.* **1988**, *148*, 183.
- [21] J. Pople, P. M. Gill, N. C. Handy, *Int. J. Quantum Chem.* **1995**, *56*, 303.
- [22] (a) P.O. Löwdin, *Phys. Rev.* **1955**, *97*, 1509; (b) I. Mayer, *Adv. Quantum Chem.* **1980**, *12*, 189.
- [23] (a) Y. G. Smeyers, L. Doreste-Suarez, *Int. J. Quantum Chem.* **1973**, *7*, 687; (b) H.B. Schelegel, *J. Chem. Phys.* **1986**, *84*, 4530; (c) S. Yamanake, T. Kawakami, K. Yamaguchi, *Chem. Phys. Lett.* **1994**, *231*, 25.
- [24] K. Yamaguchi, M. Okumura, J. Maki, T. Noro, H. Namimoto, M. Nakano, T. Fueno, K. Nakasuji, *Chem. Phys. Lett.* **1992**, *190*, 353.
- [25] R. G. Parr and W. Yang, *Density-Functional Theory of Atoms and Molecules*, Oxford University Press, Oxford, **1989**.
- [26] P. Hohenberg, W. Kohn, *Phys. Rev.* **1964**, *136*, B864.
- [27] B. B. Laird, R. B. Ross, T. Ziegler (Eds.), *Chemical Applications of Density-Functional Theory*, ACS Symposium Series 629, American Chemical Society, Washington DC, **1996**.
- [28] The BLYP functional is built by adding the non-local exchange functional of Becke (reference 29) and the non-local functional of Lee–Yang–Parr (reference 30).
- [29] A. D. Becke, *Phys. Rev. A* **1988**, *38*, 3098.
- [30] C. Lee, W. Yang, R. G. Parr, *Phys. Rev. B* **1988**, *37*, 785.
- [31] The B3LYP functional is a combination of the three parameter non-local functional of Becke (reference 32), for the exchange part, and the Lee–Yang–Parr non-local functional (reference 30), for the correlation functional.
- [32] A. D. Becke, *J. Chem. Phys.* **1993**, *98*, 5648.
- [33] Y. Hosokoshi, M. Tamura, K. Nozawa, S. Suzuki, M. Kinoshita, H. Sawa, R. Kato, *Synth. Met.* **1995**, *71*, 1795.
- [34] A UHF/6-31+G(d) calculation indicates a UHF computation using the 6-31+G(d) basis set. The same convention will be used in the rest of this work to indicate the method and mono-electronic basis set employed.

- [35] A MCSCF(7,7)/6-31+G(d) computation is a MCSCF computation using a complete active space of determinants generated by placing seven electrons in seven orbitals, in all possible forms. The 6-31+G(d) basis set is the mono-electronic basis employed.
- [36] This is a basis set in principle superior to the 6-31+G(d) basis set. See: T.H. Dunning, Jr., *J. Chem. Phys.* **1989**, *90*, 1007.
- [37] R. F. W. Bader, *Atoms in Molecules: A Quantum Theory*, Clarendon Press, Oxford, **1990**.
- [38] G. A. Jeffrey, W. Saenger, *Hydrogen bonding in biological structures*, Springer-Verlag, Berlin **1991**.
- [39] (a) M. Minguet, D. B. Amabilino, J. Cirujeda, K. Wurst, I. Mata, E. Molins, J. J. Novoa, J. Veciana, *Chem. Eur. J.* **2000**, *6*, 2350; (b) J. Cirujeda, Ph. D. Thesis, Universitat Ramon Llull (Barcelona), **1997**.
- [40] M. Deumal, P. Lafuente, F. Mota, J. J. Novoa, *Synth. Met.* (submitted). Joel Miller's ACS Award Symposium, San Francisco, **2000**.
- [41] W. Weltner, Jr. *Magnetic Atoms and Magnetic Molecules*, Dover, New York, **1989**.
- [42] I. Carmichael, *J. Phys. Chem. A* **1997**, *101*, 4633. (b) V. Barone, *Chem. Phys. Lett.*, **1994**, *226*, 392.
- [43] D. M. Chipman, *J. Chem. Phys.* **1989**, *91*, 5455.
- [44] (a) S. D. Wetmore, R. J. Boyd, L. A. Eriksson, *J. Chem. Phys.* **1997**, *106*, 7738; (b) S.D. Wetmore, L. A. Eriksson, R. J. Boyd, *J. Chem. Phys.* **1998**, *109*, 9451.
- [45] C. Adamo, V. Barone, A. Fortunelli, *J. Chem. Phys.* **1995**, *102*, 384.
- [46] (a) C. Adamo, A. di Matteo, P. Rey, V. Barone, *J. Phys. Chem. A* **1999**, *103*, 3481; (b) V. Barone, A. Bencini, M. Cossi, A. di Matteo, M. Mattesini, F. Totti, *J. Am. Chem. Soc.* **1998**, *120*, 7069.
- [47] (a) L. A. Eriksson, V. G. Malkin, O. I. Malkina, D. R. Salahub, *J. Chem. Phys.* **1963**, *99*, 9756; (b) L. A. Eriksson, V. G. Malkin, O. I. Malkina, D. R. Salahub, *Int. J. Quantum Chem.* **1994**, *52*, 879; (c) J. Wang, B. G. Johnson, R. J. Boyd, L. A. Eriksson, *J. Phys. Chem.* **1996**, *100*, 6317; (d) J. W. Gauld, L. A. Eriksson, L. Radom, *J. Phys. Chem. A* **1997**, *101*, 1352.
- [48] Quadratic Configuration Interaction including single and double excitations from the Hartree-Fock determinant. This method is one of the most accurate ab initio methods, giving for many properties results close to the full-CI method. See J.A. Pople, M. Head-Gordon, K. Raghavachari, *J. Chem. Phys.* **1987**, *85*, 7382.
- [49] W. Kutzelnigg, U. Fleischer, M. Schindler, *NMR-Basic Principles and Progress*, Springer, Heidelberg, vol. 23, p. 165, **1990**.
- [50] V. Barone, *Recent Advances in Density Functional Theory*, Part 1, (D. P. Cong, Ed.), World Scientific Publishing Co., Singapore, p. 287, **1995**.
- [51] D. E. Woon, T. H. Dunning, *J. Chem. Phys.* **1995**, *103*, 4572.
- [52] Obtained by fully decontracting the inner *s* component of the cc-pVXZ basis sets. See: T. Helgaker, M. Jaszunski, K. Ruud, A. Górska, *Theor. Chem. Acc.*, **1998**, *99*, 175.
- [53] The New Encyclopaedia Britannica, 15 ed., Chicago, **1986**.
- [54] This is a simplistic but visual representation of the state in a pair of electrons, as the electrons are antisymmetric, according to the Pauli Principle. According to it, there are four possible spin configurations, $\alpha\alpha$, $\alpha\beta$, $\beta\alpha$, and $\beta\beta$, but the wavefunction is the antisymmetric solution associated to each configuration which is eigenvector of the \hat{S}^2 operator. The determinant associated to $\alpha\alpha$ will be represented as the $|\alpha\alpha\rangle$ determinant. Among these four determinants, those associated to the $\alpha\alpha$ and $\beta\beta$ spin-configurations are eigenfunctions for the triplet. The other two configurations are not eigenfunctions of the \hat{S}^2 operator. However, the combination of determinants $|\alpha\alpha\rangle - |\beta\beta\rangle$ is eigenfunction of the triplet, while the $|\alpha\alpha\rangle + |\beta\beta\rangle$ is eigenfunction of the singlet. This is what is meant

in a strict way, when one talks about spin alignments in a pair of electrons. One has to keep in mind this, when graphically representing the triplet and singlet states by two arrows in the same direction and in opposite directions, respectively.

- [55] H. M. McConnell, *Proc. Robert A. Welch Found. Conf. Chem. Res.* **1967**, *11*, 144.
- [56] (a) R. S. Drago, *Physical Methods for Chemists*, 2nd edition, Saunders College Publishing, Ft. Worth, **1992**, chapter 9; (b) N.W. Ashcroft, N.D. Mermin, *Solid State Physics*, Hold-Saunders Int. Ed., **1981**.
- [57] (a) J. Veciana, J. Cirujeda, C. Rovira, J. Vidal-Gancedo, *Adv. Mater.* **1994**, *4*, 1377; (b) T. Akita, Y. Mazaki, K. Kobayashi, *Chem. Commun.* **1995**, 1861; (c) T. Kawakami, S. Takeda, W. Mori, K. Yamaguchi, *Chem. Phys. Lett.* **1996**, *261*, 129.
- [58] An excellent overview of the orbital mechanisms has been given by J. Veciana in a chapter of reference [1a] (pages 425-448).
- [59] (a) C. Kollmar, M. Couty, O. Kahn, *J. Am. Chem. Soc.* **1991**, *113*, 7994; (b) C. Kollmar, O. Kahn, *Acc. Chem. Res.* **1993**, *26*, 259.
- [60] K. Takeda, K. Konishi, M. Tamura, M. Kinoshita, *Mol. Cryst. Liq. Cryst.* **1995**, *273*, 57. See also pages 463-464 of reference [1a], from a review of M. Kinoshita.
- [61] Their general expression is given in: R. Pauncz, *Spin Eigenfunctions*, Plenum Press, New York, **1979**.
- [62] M. Deumal, J. J. Novoa, M. J. Bearpark, P. Celani, M. Olivucci, M. A. Robb, *J. Phys. Chem. A*, **1998**, *102*, 8404.
- [63] P. Lafuente and J. J. Novoa, work in progress.
- [64] M. Deumal, Ph. D. Thesis, Universitat de Barcelona, **1999**.
- [65] J. J. Novoa, M. Deumal, P. Lafuente, M. A. Robb, *Mol. Cryst. Liq. Cryst.* **1999**, *335*, 603.
- [66] (a) A. Izuoka, S. Murata, T. Sugawara, H. Iwamura, *J. Am. Chem. Soc.* **1985**, *107*, 1786; (b) A. Izuoka, S. Murata, T. Sugawara, H. Iwamura, *J. Am. Chem. Soc.* **1987**, *109*, 2631.
- [67] (a) S. F. Boys, F. Bernardi, *Mol. Phys.* **1970**, *19*, 553; (b) F. B. van Duijneveldt, J. G. C. M. van Duijneveldt-van de Rijdt, J. H. van Lenthe, *Chem. Rev.* **1994**, *94*, 1873; (c) J. J. Novoa, M. Planas, M.-H. Whangbo, *Chem. Phys. Lett.* **1994**, *225*, 240; (d) J. J. Novoa, M. Planas, M. C. Rovira, *Chem. Phys. Lett.* **1996**, *251*, 33; (e) J. J. Novoa and M. Planas, *Chem. Phys. Lett.*, **1998**, *285*, 186.
- [68] J. P. Malrieu et al, *J. Phys. Chem.* **1995**, *99*, 6417, as implemented by M. A. Robb and M. Bearpark, (to be published).
- [69] A detailed analysis of the intramolecular geometry of many nitronyl nitroxide radicals has shown that the internal geometry of the ONCNO group is nearly invariant (see reference 39).
- [70] E. Ruiz et al. in J. S. Miller, M. Drillon (Eds.): *Magnetism: From Molecules to Materials*, Vol. 2, Wiley-VCH, Weinheim **2001**.
- [71] J. Miralles, O. Castell, R. Caballol, J. P. Malrieu, *Chem. Phys.* **1993**, *172*, 33.
- [72] See, for instance: (a) O. Castell, R. Caballol, R. Subra, A. Grand, *J. Phys. Chem.* **1995**, *99*, 154; (b) R. Caballol, F. Illas, I. De, P. R. Moreira, J. P. Malrieu, *J. Phys. Chem. A* **1997**, *101*, 7860.
- [73] See, for instance: (a) K. Yamaguchi, Y. Toyoda, T. Fueno, *Chem. Phys. Lett.* **1989**, *159*, 459; (b) K. Yamaguchi, M. Okumura, J. Maki, T. Noro, H. Namimoto, M. Nakano, T. Fueno, K. Nakasuji, *Chem. Phys. Lett.* **1992**, *190*, 353.
- [74] S. Yamanaka, M. Okumura, K. Yamaguchi, K. Hirao, *Chem. Phys. Lett.* **1994**, *225*, 213.
- [75] (a) L. Noodleman, *J. Chem. Phys.* **1981**, *74*, 5737; (b) L. Noodleman, E. Davidson, *Chem. Phys.* **1986**, *109*, 131; (c) L. Noodleman, D. A. Case, *Adv. Inorg. Chem.* **1992**, *38*, 423.

- [76] See, for instance: (a) J. Cano, P. Alemany, S. Alvarez, M. Verdaguer, E. Ruiz, *Chem. Eur. J.* **1998**, *4*, 476; (b) E. Ruiz, J. Cano, S. Alvarez, P. Alemany, *J. Am. Chem. Soc.* **1998**, *120*, 11122; (c) E. Ruiz, J. Cano, S. Alvarez, P. Alemany, *J. Comput. Chem.* **1999**, *20*, 1391.
- [77] See the extensive and detailed discussion in the work of: J. Gräfenstein, A. M. Hjerpe, E. Kraka, D. Cramer, *J. Phys. Chem. A* **2000**, *104*, 1758. See also J. Pople, P. M. Gill, N. C. Handy, *Int. J. Quantum Chem.* **1995**, *56*, 303.
- [78] The LICMIT crystal belongs to the $P2_1/n$ spatial group, with cell parameters $a = 15.142 \text{ \AA}$, $b = 12.320 \text{ \AA}$, $c = 7.196 \text{ \AA}$, and $\beta = 99.18^\circ$. It has four molecules per unit cell, packed forming parallel strips along the c direction, in which the molecules are ordered in an up-up disposition (primary structure). The strips form planes (secondary structure), ordered in a T-shaped disposition among themselves (tertiary structure). The shortest $\text{ONCNO} \cdots \text{ONCNO}$ contacts are found between molecules of parallel strips, connecting radicals in one strip with these in the nearby parallel strip (these molecules present an up-down disposition). It presents ferromagnetic properties up to 0.5 K, and a J/k_B value +0.93 K. See reference [79].
- [79] (a) T. Sugawara, M. M. Matsushita, A. Izuoka, N. Wada, N. Takeda, M. Ishiwara, *J. Chem. Soc. Chem. Commun.* **1994**, 1723; (b) M. M. Matsushita, A. Izuoka, T. Sugawara, T. Kobayashi, N. Wada, N. Takeda, M. Ishiwara, *J. Am. Chem. Soc.* **1997**, *119*, 4369.
- [80] The WILVIW10 crystal belongs to the $P-1$ space group, with cell parameters $a = 11.843 \text{ \AA}$, $b = 12.695 \text{ \AA}$, $c = 9.532 \text{ \AA}$, $\alpha = 95.53^\circ$, $\beta = 90.55^\circ$, and $\gamma = 146.89^\circ$. This crystal has two molecules per unit cell, packed forming planes along the b - c directions. Each plane is made by replicating a strip of molecules, ordered within the strip in an up-up disposition. The strips are the primary structure, and the plane is the secondary structure. These planes then pile up to form the crystal (tertiary structure). The shortest $\text{ONCNO} \cdots \text{ONCNO}$ contacts are found within the planes, between adjacent molecules of the same strip. It shows dominant antiferromagnetism, being its J/k_B constant -74 K . See reference [81].
- [81] K. Awaga, A. Yamaguchi, T. Okuno, T. Inabe, T. Nakamura, M. Matsumoto, Y. Maruyama, *J. Mater. Chem.* **1994**, *4*, 1377.
- [82] M. Deumal, J. J. Novoa, *J. Mol. Struct. Theochem.* **2000**, *506*, 287.
- [83] M. Deumal and J. J. Novoa, Preliminary results computed using the Broken-symmetry approach.
- [84] (a) A. I. Kitaigorodsky, *Molecular crystals and molecules*, Academic Press, New York, **1973**; (b) G. R. Desiraju, *Crystal engineering. The design of organic solids*, Elsevier, Amsterdam, **1989**; (c) M. C. Etter, *Acc. Chem. Res.* **1990**, *23*, 120; (d) J. Bernstein, R. E. Davis, L. Shimoni, N.-L. Chang, *Angew. Chem. Int. Ed. Engl.* **1995**, *34*, 1555; (e) G. R. Desiraju, *Angew. Chem. Int. Ed. Engl.* **1995**, *34*, 2311.
- [85] M. Deumal, M. A. Robb, J. J. Novoa, (to be published).

4 Exact and Approximate Theoretical Techniques for Quantum Magnetism in Low Dimensions

Swapan K. Pati, S. Ramasesha, and Diptiman Sen

4.1 Introduction

The non-relativistic Schrödinger equation of a system of electrons is spin-independent. It therefore seems at first glance that the solutions of the Schrödinger equation should also be spin-independent. Because the electrons are indistinguishable, however, forces the total wave function, a product of the spin wave function and the spatial wave function, to be antisymmetric. This in turn implies that for two electrons, a spatially symmetric wave function should be associated with an antisymmetric spin wave function and vice versa. The different charge distribution in the spatially symmetric and antisymmetric wave functions leads to different coulomb repulsions by virtue of which the spin states which are symmetric and antisymmetric have different energies [1]. Dirac represented the splitting between the energies of the two spin states by the spin operator $-2J\hat{S}_i \cdot \hat{S}_j$, where J is the exchange integral involving the two spatial orbitals in which the two electrons are singly occupied. In most open-shell atomic systems the exchange integral J is large enough to force the total spin of the ground-state configuration to be the largest permissible value. This in essence is Hund's rule of maximum multiplicity and is also the reason why we find transition and rare earth metal ions in high spin states in nature.

In solids containing transition metal or rare earth ions surrounded by ligands, the relative alignment of the unpaired spins at the metal site is not at all obvious. To understand this we should examine the possible pathways for the delocalization of the valence electrons in the system. If the favorable delocalization pathways involve antiparallel alignment of the metal-ion spins the nature of the exchange interaction between the metal-ion spins is antiferromagnetic; otherwise it is ferromagnetic. This is because delocalization of electrons reduces their kinetic energy and the ground state therefore corresponds to an alignment of spins that enables maximum delocalization. This is indeed the reason why the ground state of a hydrogen molecule is a spin singlet. In a system with degenerate partially occupied orbitals Hund's coupling favors high-spin alignment of the electrons on an ion. If delocalization pathways exist that allow for these high-spin states in the process of delocalization, alignment of the spins on two neighboring centers will be ferromagnetic. If delocalization pathways exist only when these high-spin states are aligned antiparallel, one would have an antiferromagnetic alignment of the spin. Thus, the overall nature of

the spin alignment is governed by competition between the Hund's coupling and electron delocalization [2, 3].

Given a collection of spins, the exchange Hamiltonian for the system is written:

$$H = \sum_{ij} J_{ij} \hat{\mathbf{S}}_i \cdot \hat{\mathbf{S}}_j \quad (1)$$

where J_{ij} is the effective exchange integral for the interaction between the spins at sites “ i ” and “ j ”. Because the spins in the cluster arise from unpaired electrons of a transition metal ion in a crystal field, it is natural to expect that the spin-orbit and spin-spin interactions of the electrons in the ion could alter the nature of the total spin on the ion by giving the net spin a preferred direction of orientation. Such a situation can be easily handled by treating each J_{ij} as a vector and generalizing the exchange Hamiltonian as:

$$H = \sum \left(J_{ij}^x \hat{S}_i^x \hat{S}_j^x + J_{ij}^y \hat{S}_i^y \hat{S}_j^y + J_{ij}^z \hat{S}_i^z \hat{S}_j^z \right) \quad (2)$$

Such a model is often referred to as the *XYZ* spin model [2]. Two extreme cases are often studied:

- the spin is assumed to have no projection on the X - Y plane, in which case the resulting model is the Ising model and corresponds to scalar spins; and
- the spin is assumed to have no projection on the z -axis, in which case we have an *XY* model or a planar spin model.

The Ising model is a discrete classical model, because it consists of no non-commuting operators in its Hamiltonian, whereas the *XY* model could be classical or quantum mechanical. Usually, when dealing with large site spin systems, it is not uncommon to assume that the spins are classical, in the spirit of Bohr's correspondence principle.

In the crystalline state, the spins in the solid would be arranged on a lattice. If the exchange interaction is predominant between spins along a single crystalline direction, the model could be treated as a one dimensional array of spins. There are many examples of solids for which this is true [4]. Likewise, it is also possible that the interactions amongst spins is large along two crystallographic directions and weak along a third direction; this would result in two-dimensional spin system [5].

In this review article, we will mainly concern ourselves with the study of isotropic spin clusters and one-dimensional spin systems, sometimes in the presence of an external magnetic field. We will be mostly interested in properties of the ground state and low-lying excitations, because these are the states which govern the low-temperature properties of systems such as the specific heat and magnetic susceptibility. The symmetries of a system often enable us to characterize the energy eigenstates in terms of quantum numbers such as the total spin, S_{tot} , the component of the total spin along some particular direction, say, $S_{\text{tot},z}$, spin parity (which is a symmetry for states with $S_{\text{tot},z} = 0$), the wave number, k , for a translation-invariant system, and possibly other spatial symmetries depending on the structure. We will discuss

below how the use of symmetries can help to reduce the numerical effort required to study the low-energy states.

In the next two sections we introduce some exact numerical methods and describe the application of these methods to magnetic clusters. In Section 4.4, we discuss two analytical methods which use field theoretic approximations. In Section 4.5, we describe an innovative way of solving the spin Hamiltonians, which goes beyond the conventional techniques and is based on the density matrix renormalization group (DMRG) theory. Various applications of DMRG to the properties of low-dimensional extended chains are described in Sections 4.6 to 4.8.

4.2 Exact Calculations

The properties of a spin Hamiltonian can be computed from the eigenstates of the Hamiltonian, which are in turn obtained by setting up the Hamiltonian matrix in a suitable basis and diagonalizing it thereafter. Although the procedure itself is quite straightforward, the space spanned by the Hamiltonian rapidly increases with the number of the spins in the system. The Fock space dimensionality of a system of n spins with spin s_i is given by:

$$D_F = \prod_{i=1}^n (2s_i + 1) \quad (3)$$

The Hamiltonian matrix is block-diagonal in structure with each block corresponding to specified values of the quantities conserved by the Hamiltonian. Thus, for an isotropic spin system, the z -component of the total spin, M_S , and the total spin S are conserved. Restricting the Fock space to specified values of M_S and S gives Hilbert spaces whose dimensionalities are smaller than the Fock space dimensionality.

Whereas constructing spin basis functions which are eigenstates of the total \hat{S}^z operator is quite simple, construction of spin-adapted functions (SAF, eigenstates of the total \hat{S}^2 operator) is not direct. Perhaps the simplest and chemically most appealing way of constructing SAF is by the valence bond (VB) method which uses the Rumer–Pauling rules. This method is best illustrated by applying it to a system of $2n$ spins, each possessing a spin of half, in the total spin $S = 0$ sector. A total spin singlet can be formed by choosing pairs of sites and spin-coupling each of these obtain a singlet. The product of these singlet pairs will be a spin eigenstate of the operator \hat{S}_{total}^2 . This is illustrated in Fig. 1. There are, however, more ways to spin-couple in pairs than the number of linearly independent singlet states, e. g. the state $|3\rangle$ in Fig. 1 can be expressed as a linear combination of the states $|1\rangle$ and $|2\rangle$. The overcompleteness can be avoided by resorting to the Rumer–Pauling rules. To implement this rule we arrange the $2n$ spins at the vertices of a regular $2n$ -gon and draw lines between pairs of sites that are singlet-paired. According to the Rumer–Pauling rule the subset of these encompassing all diagrams (to be called

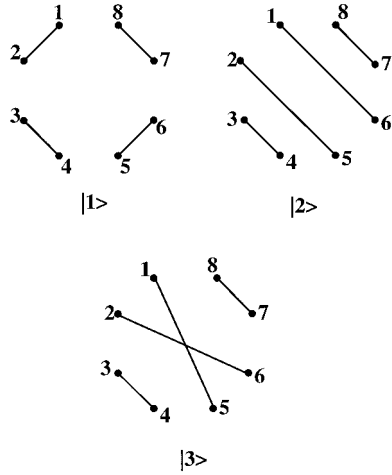


Fig. 1. A schematic representation of the VB diagrams for eight spin-1/2 objects. States $|1\rangle$ and $|2\rangle$ are legal VB diagrams and $|3\rangle$ is an illegal VB diagram.

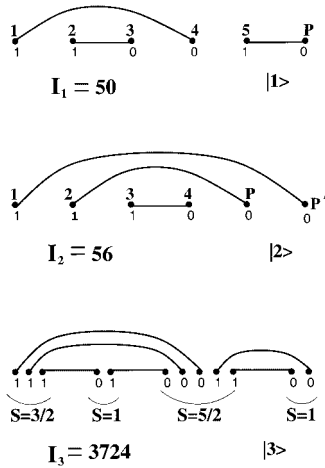


Fig. 2. VB diagram for spin-1/2 objects with total spin 1/2 ($|1\rangle$) and total spin 1 ($|2\rangle$). Their bit representations (0 and 1) and the unique integer I_k representing them are shown. P and P' are the phantom sites. $|3\rangle$ is a singlet VB diagram corresponding to two spin-1, a spin-5/2, and a spin-3/2 object.

“legal” diagrams) with no crossing lines forms a complete and linearly independent set of states [6].

The Rumer–Pauling rules can be easily extended to construct complete and linearly independent basis sets in higher-spin Hilbert spaces involving spin-1/2 objects. This is done most easily with the help of phantom sites. If we wish to construct VB diagrams for total spin S subspace involving n spin-1/2 objects we introduce $2S$ additional sites to be called phantom sites. Besides imposing the Rumer–Pauling rules on the diagrams with $n + 2S$ sites, we impose the additional constraint that there should be no singlet lines amongst the $2S$ phantom sites. In Fig. 2 we show a few examples of VB diagrams with higher total spin.

It is also quite simple to extend the VB rules to spin clusters made up of different site spins [7]. If the spin at a site is s_i , then we replace this site by a set of $2s_i$ sites,

each with spin-1/2. We then proceed with constructing the VB basis, as though the system is made up entirely of spin-1/2 objects, with one difference – we impose the additional constraint that there should be no singlet lines within the subset of $2s_i$ sites which replace the spin s_i at site i . The VB diagrams with total spin $S > 1/2$ are constructed as before with the help of phantom sites. An example of a legal VB diagram involving higher site spins is shown in Fig. 2.

Generating and storing the VB diagrams on a computer is also quite simple. We associate one bit with every site. The state of the bit is “1” if, in the VB diagram, a line begins at the site; the state is “0” if a line ends at the site. Thus, we can associate an integer of n bits with every VB diagram involving n spin-1/2 objects. This association is unique if we decipher the bit pattern of the integer corresponding to the diagram from inside-out, much like expanding an algebraic expression with multiple parentheses. In Fig. 2 we have also shown the bit pattern and the associated integer for each VB diagram. The VB diagrams are generated on a computer by checking the bit pattern in all n -bit integers to see if they satisfy the criterion for representing the desired VB diagram. This also enables us to generate the VB diagrams as an ordered sequence of the integers that represent them, a fact that helps in rapid generation of the Hamiltonian matrix.

The Hamiltonian matrix in the VB basis can be easily constructed by knowing the action of the operator $\hat{S}_i \cdot \hat{S}_j$ for spin-1/2 particles (i) on a singlet line joining sites i and j and (ii) on the pair of sites i and j singlet paired to two different sites i' and j' (Fig. 3). For Hilbert spaces with non-zero total S , the Hamiltonian involves spin exchange between the real sites only. These exchange operators could, however, lead to VB diagrams in which the phantom sites are interconnected. In this event, simply neglecting these resultant states is sufficient to ensure we are dealing exactly with the spin S Hilbert space. The Hamiltonian for spin clusters with arbitrary spins can be treated as consisting of operators with only spin-1/2 objects. This is done by replacing the spin-exchange operator between sites i and j , $\hat{S}_i \cdot \hat{S}_j$, by the operator $(\sum_{k=1}^{2s_i} \hat{\tau}_k) \cdot (\sum_{l=1}^{2s_j} \hat{\tau}_l)$, where the operators $\hat{\tau}_k$ and $\hat{\tau}_l$ are the usual spin-1/2 operators.

The matrix representing the Hamiltonian in the VB basis is, in general, non-symmetric, because the VB basis is non-orthogonal. The matrix itself is sparse, however. There are efficient numerical algorithms [8] for obtaining the low-lying eigenstates of sparse non-symmetric matrixes, and it is possible to solve a non-symmetric matrix eigenvalue problem for a million by million matrix with approximately 100 million non-zero matrix elements on a powerful PC-based workstation.

$$\begin{aligned}
 (\hat{S}_i \cdot \hat{S}_j - \frac{1}{4}) |i \text{---} j\rangle &= - |i \text{---} j\rangle \\
 (\hat{S}_i \cdot \hat{S}_j - \frac{1}{4}) |i \text{---} i' \quad j \text{---} j'\rangle &= \frac{1}{2} |i \text{---} i' \quad j \text{---} j'\rangle
 \end{aligned}$$

Fig. 3. Effect of operation by the operator $(\hat{S}_i \cdot \hat{S}_j - 1/4)$ on a state with a singlet line between sites i and j and on a state with sites i and j singlet paired with two different sites i' and j' .

Although VB theory guarantees spin purity in the computed eigenstates of the spin-conserving Hamiltonians, it has several drawbacks. Computation of quantities such as spin-spin correlation functions and spin densities is not easy, because a site-spin operator operating on a VB diagram spoils the spin purity of the diagram. This could be overcome by converting the eigenstate of the Hamiltonian in the VB basis to the constant M_S basis. Another difficulty with the VB procedure is exploiting the spatial symmetries of the problem. Operation by a spatial symmetry operator on a legal VB diagram could lead to illegal VB diagrams. Disentangling these illegal diagrams into legal diagrams can be computationally prohibitive [9].

In more general spin problems, it is often advantageous to use the constant M_S basis and exploit all the spatial symmetries. Partial spin symmetry adaptation in these cases is also possible by using the spin-parity operator. The effect of the spin-parity operator on a basis state is to flip all the spins in the state. In the $M_S = 0$ sector, it is possible to factor the Hilbert space into odd and even parity Hilbert spaces. The odd (even) parity Hilbert space is spanned by basis vectors with odd (even) total spin. This also has the effect of reducing the dimensionality of the Hilbert space and providing partial spin symmetry adaptation. It is rather simple to set up the Hamiltonian matrix in the symmetry-adapted basis. The Hamiltonian matrix is symmetric and usually very sparse. The lowest few eigenstates can be easily computed by employing the Davidson algorithm. Given these eigenstates, the computation of properties can proceed by converting an eigenstate in the symmetrized basis into that in the unsymmetrized basis. The orthogonality of the basis states and the simple rules involved in obtaining the resultant when a basis state is operated upon by any type of spin operator in any combination affords easy computation of a variety of properties of a magnetic system.

The exact diagonalization techniques discussed above are, in general, applicable to systems whose Hilbert space dimensionality is approximately 10 million. The major problem with exact diagonalization methods is the exponential increase in the dimensionality of the Hilbert space with increasing system size. Thus, the study of larger systems becomes not only CPU-intensive but also memory-intensive as the number of non-zero elements of the matrix increases rapidly with system size. With increasing computer power, slightly larger problems have been solved every few years. To illustrate this trend, we consider the spin-1 Heisenberg chain. In 1973, ten years before the Haldane conjecture, De Neef [10] used the exact diagonalization procedure to solve an eight-site spin-1/2 chain. In 1977 Blote [11] diagonalized the Hamiltonian of a chain of ten sites. In 1982 Botet and Jullien [12] increased this to twelve sites. In 1984 Parkinson and Bonner [13] solved the 14-site spin-1 problem and in the same year Moreo [14] solved the sixteen-site spin-1 chain. In 1990 Takahashi [15] pushed this up to eighteen sites and in 1994 Golinelli et al. [16] produced a solution for the low-lying states of a twenty-two-site spin-1 chain. The growth in chain length of the longest spin-1 chain solved is almost linear with time, increasing by approximately two sites every three years. Just to remind ourselves, the Fock space dimensionality in this case increases as 3^N with chain length N . The size of the matrix also increases similarly and the CPU and storage scales quadratically with the size of the matrix, if we are targeting only a few eigenstates. For this reason, for systems which span much larger spaces, the focus has shifted to approximate techniques.

4.3 Applications to Spin Clusters

Some of the magnetic clusters that have been studied extensively in recent years are the Mn_{12} [17], Fe_8 [18], and V_{15} [19] clusters. These clusters are characterized by many interesting phenomena, e. g. quantum resonant tunneling and quantum interference [20]. Fundamental to a proper understanding of these phenomena is a knowledge of the low-energy excitation spectrum in these systems. The methods discussed under exact diagonalization schemes enable us to calculate the low-energy excitation spectrum, given a set of exchange constants. The exchange constants themselves are not known with any certainty, however. It is, therefore, all the more important to be able to perform exact diagonalization studies of low-lying states to infer the possible sign and magnitude of the exchange constants [7].

The geometry and exchange parameters for the Mn_{12} cluster are shown in Fig. 4. The crystal structure suggests that the exchange constant J_1 is largest and antiferromagnetic in nature [21]. On the basis of magnetic measurements it has been suggested that J_1 has a magnitude of 215 K. The magnitude and sign of the other exchange constants are based on comparisons with manganese systems in smaller clusters. It has been suggested that the exchange constant J_2 and J_3 are antiferromagnetic and have a magnitude of approximately 85 K. For the exchange constant J_4 , however, there is no concrete estimate, either of the sign or of the magnitude. In an earlier study the $\text{Mn}^{\text{III}}\text{-Mn}^{\text{IV}}$ pair with the strongest antiferromagnetic exchange constant was replaced by a composite spin-1/2 object [22] and the exchange Hamiltonian of the cluster solved for three different sets of parameters. It was found that the ordering of the energy levels was very sensitive to the relative strengths of the exchange constants. In these studies, J_4 was set to zero and the low-lying excited states were computed. Only states with spin S up to ten could be obtained because of the replacement of the higher-spin ion pairs by the composite spin-1/2 objects.

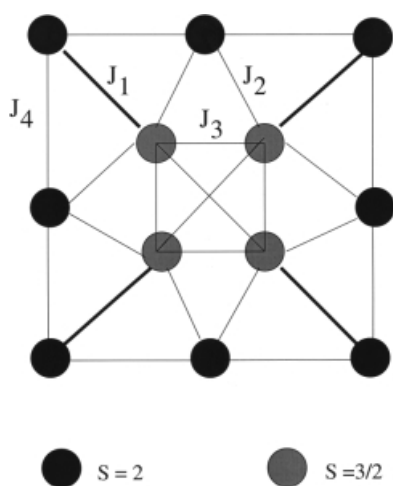


Fig. 4. Schematic diagram of the exchange interactions between the Mn ions in the Mn_{12}Ac molecule.

The technique described earlier, however, enables exact computation of the low-lying states of Mn_{12} . The results of the exact calculations are presented in Table 1. We note that none of the three sets of parameters studied using an effective Hamiltonian gives the correct ground and excited states when an exact calculation is performed. It seems that setting the exchange constant J_4 to zero cannot yield an $S = 10$ ground state (Table 1, Cases A, B, and C). When J_3 is equal to or slightly larger than J_2 (Table 1, Cases A and B), we find a singlet ground state, unlike the result of the effective Hamiltonian in which the ground state has $S = 8$ and $S = 0$ respectively. The ground state has spin $S = 6$ when J_3 is slightly smaller than J_2 (Table 1, Case C). In all these cases the first few low-lying states are found to lie within 20 K of the ground state.

When we use the parameters suggested by Chudnovsky [17] (Table 1, case D), we obtain an $S = 10$ ground state separated from an $S = 9$ first excited state by 223 K. This is followed by another $S = 9$ excited state at 421 K. Only when the exchange constant J_4 is sufficiently strongly ferromagnetic (Table 1, case E) do we find an $S = 10$ ground state with an $S = 9$ excited state separated from it by a gap of 35 K, which is close to the experimental value [23]. The second higher excited state has $S = 8$, and is separated from the ground state by 62 K.

In Fig. 5 we show the spin density [24] for the Mn_{12} cluster in the ground state for the $S = 10$, $M_S = 10$ state. Although the manganese ions connected by the strong antiferromagnetic exchange have opposite spin densities, it is worth noting that the total spin density on these two ions is 0.69, very different from the value of 0.5 expected if these ions were indeed to form a spin-1/2 object.

The Fe_8 cluster is shown in Fig. 6. Each of the Fe ions has a spin of 2 and the ground state of the system has a total spin $S = 10$, with the $S = 9$ excited state separated from it by approximately 20 K. All the exchange interactions in this system are expected to be antiferromagnetic. Although the structure of the complex dictates that the exchange interaction J_2 along the back of the butterfly should be small in comparison with the interaction J_1 across the wing [25]. It has previously been

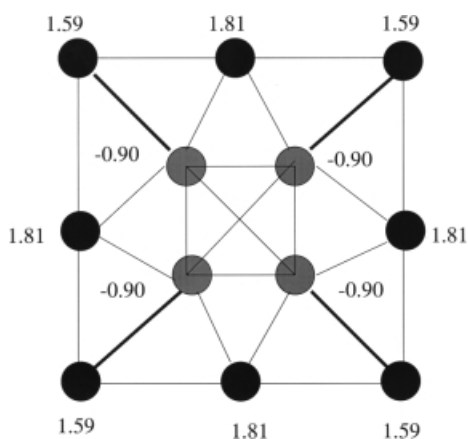


Fig. 5. Spin densities in the ground state ($S = 10$, $M_S = 10$) of Mn_{12}Ac for parameter values $J_1 = 215$ K, $J_2 = 85$ K, $J_3 = 85$ K, and $J_4 = -64.5$ K.

Table 1. Low-lying states of $Mn_{12}Ac$, relative to the ground state for the parameter in question. Entries in parentheses in cases A, B, and C correspond to the effective Hamiltonian results of Sessoli et al. [22]. Case D corresponds to the parameters suggested by Chudnovsky [17]. The parameters corresponding to different cases are: Case A. $J_1 = 225$ K, $J_2 = 90$ K, $J_3 = 90$ K, $J_4 = 0$ K; Case B. $J_1 = 225$ K, $J_2 = 90$ K, $J_3 = 93.8$ K, $J_4 = 0$ K; Case C. $J_1 = 225$ K, $J_2 = 90$ K, $J_3 = 86.2$ K, $J_4 = 0$ K; Case D. $J_1 = 215$ K, $J_2 = 85$ K, $J_3 = -85$ K, $J_4 = -45$ K; Case E. $J_1 = 215$ K, $J_2 = 85$ K, $J_3 = 85$ K, $J_4 = -64.5$ K. All energies are in K.

Case A		Case B		Case C		Case D		Case E			
State	S	E (K)	State	S	E (K)	State	S	E (K)	State	S	E (K)
eB	0	0.0	eB	0	0.0	eB	6	0.0	eB	10	0.0
	(8)		(0)		(10)						
oE	1	10.8	oE	1	16.2	oE	1	15.5	oE	9	223
	(9)	(6.4)	(8)		(1.4)		(8)	(2.7)			35.1
	(10)	(6.4)									
oB	1	19.8	oB	1	20.0	oB	1	19.6	oB	9	421.2
	(0)	(6.8)			(9)		(9)	(5.0)			62.1
eA	2	24.7	eA	2	30.5	eA	2	23.8	oB	9	425.1
oE	3	39.0	eB	4	58.4	oE	1	28.8	eB	8	439.5
eE	2	49.9	eE	2	60.9	eB	6	53.6	eB	8	443.7
eB	4	57.1	oA	3	64.3	eB	6	54.4	eB	8	458.1
eB	8	57.8	eE	2	80.0	eB	8	57.2	oA	11	573.4
oB	2	57.8	oA	3	88.1	eE	2	63.0	eE	9	583.8
oB	3	78.4	eA	6	88.3	oA	3	77.0	oA	8	632.8
oB	3	86.8	oB	3	112.8	oB	3	85.3	oA	9	640.5
eA	6	105.7	oB	5	114.6	eE	2	86.1	eE	8	658.3
oB	3	113.4	oB	5	158.4	eA	6	97.1	eA	8	767.1
eE	4	117.3	oA	1	165.2	eA	6	98.2	eB	8	807.6
oB	5	154.2	oA	1	181.6	oB	3	112.2	oA	8	815.8

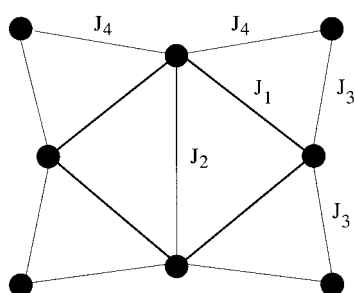


Fig. 6. Schematic diagram of the exchange interactions between the Fe ions in the Fe_8 molecule.

Table 2. Energies of a few low lying states in Fe_8 . The exchange constants corresponding to the different cases are: Case 1. $J_1 = 150 \text{ K}$, $J_2 = 25 \text{ K}$, $J_3 = 30 \text{ K}$, $J_4 = 50 \text{ K}$; Case 2. $J_1 = 180 \text{ K}$, $J_2 = 153 \text{ K}$, $J_3 = 22.5 \text{ K}$, $J_4 = 52.5 \text{ K}$; Case 3. $J_1 = 195 \text{ K}$, $J_2 = 30 \text{ K}$, $J_3 = 52.5 \text{ K}$, $J_4 = 22.5 \text{ K}$. All energies are in K.

Case 1		Case 2		Case 3	
S	$E \text{ (K)}$	S	$E \text{ (K)}$	S	$E \text{ (K)}$
10	0.0	10	0.0	10	0.0
9	13.1	9	3.4	9	39.6
8	27.3	8	10.2	9	54.2
9	41.7	7	20.1	9	62.4

reported that such a choice of interaction parameters would not provide an $S = 10$ ground state [26].

Results from exact calculation of the eigenstates of the Fe_8 cluster using three sets of parameters is shown in Table 2. In two of these cases J_2 is very much smaller than J_1 . We find that in all these cases, the ground state has spin $S = 10$ and the lowest excited state has spin $S = 9$. One of the main differences among the three sets of parameters is in the energy gap to the lowest excited state (Table 2). For the set of parameters used in the earlier study, this gap is the lowest at 3.4 K. For the parameter sets 1 and 3 [27] this gap is, respectively, 13.1 K and 39.6 K. Whereas in cases 1 and 2 the second excited state is an $S = 8$ state, in case 3 this state also has spin 9.

The spin densities in all the three cases for the ground state are shown in Fig. 7. The spin densities are always positive at the corners. In cases 1 and 2, the spin density on the Fe ion on the backbone is positive and negative on the remaining two Fe sites [28]. In case 3, however, the negative and positive spin density sites for Fe ions in the middle of the edges are interchanged. This is, perhaps, because in cases 1 and 2 the exchange constant J_3 is less than J_4 whereas in case 3 the opposite is true. Thus a spin-density measurement can provide relative strengths of these two exchange constants. In all three case the difference between the spin densities in the ground and excited states is that the decrease in the spin density in the excited state is mainly confined to the corner Fe sites.

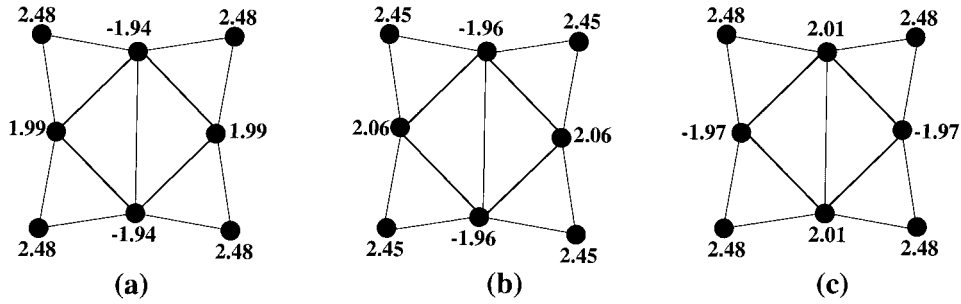


Fig. 7. Spin density in the ground state ($S = 10$, $M_S = 10$) of Fe_8 for three different parameter values: (a) $J_1 = 150$ K, $J_2 = 25$ K, $J_3 = 30$ K, $J_4 = 50$ K; (b) $J_1 = 180$ K, $J_2 = 153$ K, $J_3 = 22.5$ K, $J_4 = 52.5$ K; (c) $J_1 = 195$ K, $J_2 = 30$ K, $J_3 = 52.5$ K, $J_4 = 22.5$ K.

4.4 Field Theoretic Studies of Spin Chains

One-dimensional and quasi-one-dimensional quantum spin systems have been studied extensively in recent years for several reasons. Many such systems have been realized experimentally, and a variety of theoretical techniques, both analytical and numerical, is available to study the relevant models. Because of large quantum fluctuations in low dimensions, such systems often have unusual properties such as a gap between the ground state and the excited states. The most famous example of this is the Haldane gap which was predicted theoretically in integer spin Heisenberg antiferromagnetic chains [29], and then observed experimentally in a spin-1 system $\text{Ni}(\text{C}_2\text{H}_8\text{N}_2)_2\text{NO}_2(\text{ClO}_4)$ [30]. Other examples include the spin ladder systems in which a small number of one-dimensional spin-1/2 chains interact among each other [31]. It has been observed that if the number of chains is even, i. e. if each rung of the ladder (which is the unit cell for the system) contains an even number of spin-1/2 sites the system effectively behaves like an integer spin chain with a gap in the low-energy spectrum. Some two-chain ladders which have a gap are $(\text{VO})_2\text{P}_2\text{O}_7$ [32], SrCu_2O_3 [33], and $\text{Cu}_2(\text{C}_5\text{H}_{12}\text{N}_2)_2\text{Cl}_4$ [34]. Conversely, a three-chain ladder which effectively behaves like a half-odd-integer spin chain and does not have a gap is $\text{Sr}_2\text{Cu}_3\text{O}_5$ [33]. A related observation is that the quasi-one-dimensional system CuGeO_3 spontaneously dimerizes below a spin-Peierls transition temperature [35]; the unit cell then contains two spin-1/2 sites and the system is gapped.

The results for the gaps discussed above are all in the absence of an external magnetic field. The situation becomes more interesting in the presence of a magnetic field [36]. It is then possible for an integer spin chain to be gapless and a half-odd-integer spin chain to have a gap above the ground state for appropriate values of the field [37–45]. This has been demonstrated in several models by use of a variety of methods such as exact diagonalization of small systems and bosonization [46, 47]. It has, in particular, been shown that the magnetization of the system can have plateaus at certain non-zero values for some finite ranges of the magnetic field. Further, for a Hamiltonian which is invariant under translation by one unit cell,

the value of the magnetization per unit cell is quantized to be a rational number at each plateau [37]. In Section 4.8, we will study the magnetization plateau which can occur in a three-chain ladder.

In the next two subsections we will discuss some field theoretic methods which can be used for studying spin chains and ladders. These methods rely on the idea that the low-energy and long-wavelength modes of a system (i. e. wavelengths much longer than the lattice spacing, a , if the system is defined on a lattice at the microscopic level) can often be described by a continuum field theory.

4.4.1 Nonlinear σ -model

The nonlinear σ -model (NLSM) analysis of antiferromagnetic spin chains with the inclusion of J_2 (next-nearest neighbor coupling) and δ (dimerization) proceeds as follows [48]. The Hamiltonian for the frustrated and dimerized spin chain can be written as:

$$\hat{H} = J_1 \sum_i \left[1 - (-1)^i \delta \right] \hat{\mathbf{S}}_i \cdot \hat{\mathbf{S}}_{i+1} + J_2 \sum_i \hat{\mathbf{S}}_i \cdot \hat{\mathbf{S}}_{i+2} \quad (4)$$

The interactions are shown schematically in Fig. 8. The region of interest is defined by $J_2 \geq 0$ and $0 \leq \delta \leq 1$. We first do a classical analysis in the $S \rightarrow \infty$ to find the ground state configuration of the spins. Let us make the general *ansatz* that the ground state is a coplanar configuration of spins with the energy per spin being equal to:

$$e_0 = S^2 \left[\frac{J_1}{2} (1 + \delta) \cos \theta_1 + \frac{J_1}{2} (1 - \delta) \cos \theta_2 + J_2 \cos(\theta_1 + \theta_2) \right] \quad (5)$$

where θ_1 is the angle between the spins \mathbf{S}_{2i} and \mathbf{S}_{2i+1} and θ_2 is the angle between the spins \mathbf{S}_{2i} and \mathbf{S}_{2i-1} .

Minimization of the classical energy with respect to θ_i yields the following three phases:

- Néel phase: This phase has $\theta_1 = \theta_2 = \pi$; hence all the spins point along the same line and they go $\dots \uparrow \downarrow \uparrow \downarrow \dots$ along the chain. This phase is stable for $1 - \delta^2 > 4J_2/J_1$

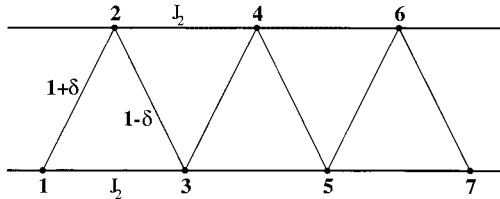


Fig. 8. Schematic picture of the frustrated and dimerized spin chain.

- Spiral phase: Here, the angles θ_1 and θ_2 are given by:

$$\cos \theta_1 = -\frac{1}{1+\delta} \left[\frac{1-\delta^2}{4J_2/J_1} + \frac{\delta}{1+\delta^2} \frac{4J_2}{J_1} \right]$$

and

$$\cos \theta_2 = -\frac{1}{1-\delta} \left[\frac{1-\delta^2}{4J_2/J_1} + \frac{\delta}{1-\delta^2} \frac{4J_2}{J_1} \right] \quad (6)$$

where $\pi/2 < \theta_1 < \pi$ and $0 < \theta_2 < \theta_1$. Thus the spins lie on a plane. This phase is stable for $(1-\delta^2) < 4J_2/J_1 < (1-\delta^2)/\delta$.

- Colinear phase: This phase (which needs both dimerization and frustration) is defined as having $\theta_1 = \pi$ and $\theta_2 = 0$; hence all the spins again point along the same line and they go ... $\uparrow\downarrow\uparrow\downarrow$... along the chain. This phase is stable for $(1-\delta^2)/\delta < 4J_2/J_1$.

These phases and their boundaries are depicted in Fig. 9. Thus even in the classical limit $S \rightarrow \infty$, the system has a rich ground state “phase diagram” [49].

We can now go to the next order in $1/S$, and study the spin wave spectrum about the ground state in each of the phases. The main results are: In the Néel phase, we find two zero modes, i. e. modes for which the energy ω_k vanishes linearly at certain values of the momentum, k , with the slope $d\omega_k/dk$ at those points (the velocity) being the same for the two modes. In the spiral phase we have three zero modes, two with the same velocity describing out-of-plane fluctuations and one with a higher velocity describing in-plane fluctuations. In the colinear phase we get two zero modes with

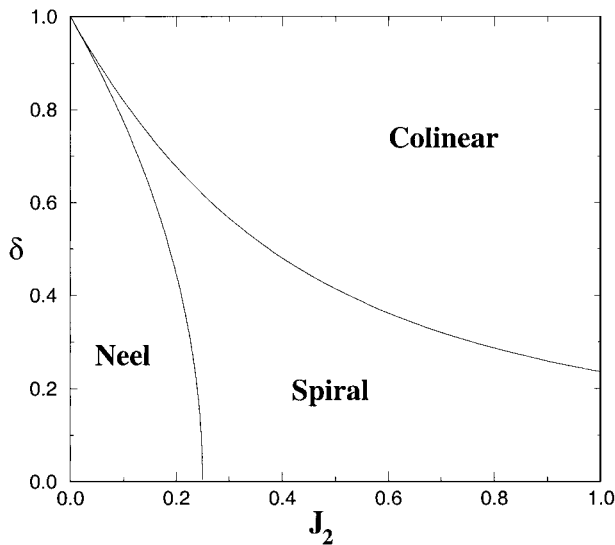


Fig. 9. Classical phase diagram of the spin chain in the $J_2 - \delta$ plane.

equal velocities just as in the Néel phase. The three phases also differ in the behavior of the spin–spin correlation function $S(q) = \sum_n \langle S_0 \cdot S_n \rangle \exp(-iqn)$ in the classical limit. $S(q)$ is peaked at $q = (\theta_1 + \theta_2)/2$, i. e. at $q = \pi$ in the Néel phase, at $\pi/2 < q < \pi$ in the spiral phase, and at $q = \pi/2$ in the colinear phase.

To study the interactions between the spin waves it is convenient to derive a semi-classical NLSM field theory which can describe the low-energy and long-wavelength excitations. The field theory in the Néel phase is given by an $O(3)$ NLSM with a topological term [29, 47]. The field variable is a unit vector with the Lagrangian density:

$$\mathcal{L} = \frac{1}{2cg^2} \dot{\vec{\phi}}^2 - \frac{c}{2g^2} \vec{\phi}'^2 + \frac{\theta}{4\pi} \vec{\phi} \cdot \vec{\phi}' \times \dot{\vec{\phi}}, \quad (7)$$

where $c = 2S(1 - 4J_2 - \delta^2)^{1/2}$ is the spin wave velocity, $g^2 = 2/[S(1 - 4J_2 - \delta^2)^{1/2}]$ is the coupling constant (which describes the strength of the interactions between the spin waves), and $\theta = 2\pi S(1 - \delta)$ is the coefficient of the topological term (the integral of this term is an integer which defines the winding number of a field configuration $\vec{\phi}(x, t)$). Note that θ is independent of J_2 in the NLSM. (Time and space derivatives are denoted by a dot and a prime, respectively). For $\theta \pmod{2\pi} = \pi$ and g^2 less than a critical value it is known that the system is gapless [47, 50]. For any other value of θ , the system is gapped. For $J_2 = \delta = 0$ one therefore expects that integer spin chains should have a gap whereas half-odd-integer spin chains should be gapless. This is known to be true even for small values of S like $1/2$ (analytically) and 1 (numerically) although the field theory is derived for large S only. In the presence of dimerization one expects a gapless system at certain special values of δ . For $S = 1$, the special value is predicted to be $\theta_c = 0.5$. We see that the *existence* of a gapless point is correctly predicted by the NLSM. As we will see later, however, according to reliable numerical results from DMRG δ_c is 0.25 for $J_2 = 0$ [51] and decreases with J_2 as shown in Fig. 10. These deviations from field theory are probably because of higher-order corrections in $1/S$ which have not yet been studied analytically.

In the spiral phase it is necessary to use a different NLSM which is known for $\delta = 0$ [52, 53]. The field variable is now an $SO(3)$ matrix \mathbf{R} . The Lagrangian density is:

$$\mathcal{L} = \frac{1}{2cg^2} \text{Tr}(\dot{\mathbf{R}}^T \mathbf{R} \mathbf{P}_0) - \frac{c}{2g^2} \text{Tr}(\mathbf{R}'^T \mathbf{R} \mathbf{P}_1), \quad (8)$$

where $c = S(1 + y)\sqrt{1 - y^2}$, $g^2 = 2\sqrt{(1 + y)/1 - y}/S$ with $1/y = 4J_2$, and \mathbf{P}_0 and \mathbf{P}_1 are diagonal matrixes with diagonal elements $(1, 1, 2y(1 - y)/(2y^2 - 2y + 1))$ and $(1, 1, 0)$, respectively. Note that there is no topological term. Hence there is no apparent difference between integer and half-odd-integer spin chains in the spiral phase. A one-loop renormalization group [52] and large N analysis [53] indicate that the system should have a gap for all values of J_2 and S , and that there is no reason for a particularly small gap at any special value of J_2 .

Finally, in the colinear phase, the NLSM is known for $\delta = 1$, i. e. for the spin ladder. The Lagrangian is the same as in Eq. (7), with $c = 4S\sqrt{J_2(J_2 + 1)}$,

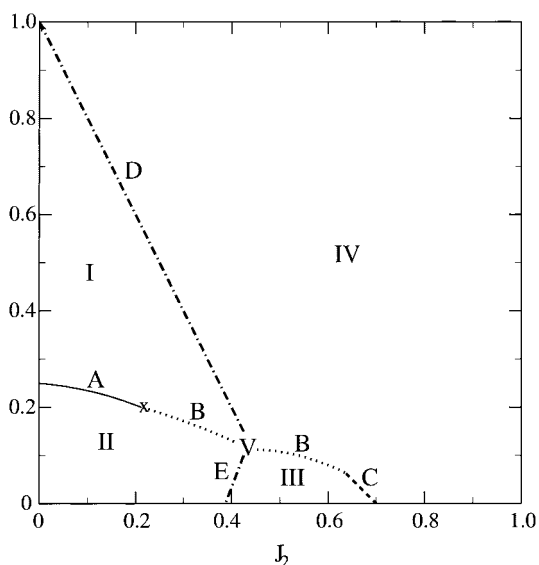


Fig. 10. “Phase” diagram for the spin-1 chain in the $J_2 - \delta$ plane.

$g^2 = \sqrt{1 + 1/J_2}/S$, and $\theta = 0$. There is no topological term for any value of S , and the model is therefore gapped [54].

The field theories for general δ in both the spiral and colinear phases are still not known. Although the results are qualitatively expected to be similar to the $\delta = 0$ case in the spiral phase and the $\delta = 1$ case in the colinear phase, quantitative features such as the dependence of the gap on the coupling strengths will require the explicit form of the field theory.

4.4.2 Bosonization

Another field theoretic method for studying spin systems in one dimension is the technique of bosonization [46, 47, 55–57]. This technique consists of mapping bosonic operators into fermionic ones, and then using whichever set of operators is easier to compute with. For instance, consider a model with a single species of fermion with a linear dispersion relation $E(k) = \pm v_k$, where the \pm denotes the right- and left-moving fermions, respectively (with the corresponding fields being denoted by $\hat{\psi}_R$ and $\hat{\psi}_L$), and v denotes the velocity. Similarly, consider a model with a single species of boson with the dispersion relationship $E(k) = v|k|$; the right- and left-moving fields are denoted by $\hat{\psi}_R$ and $\hat{\psi}_L$ respectively. Then it can be shown that these operators are related to each other as:

$$\hat{\psi}_R \approx \frac{1}{\sqrt{2\pi\alpha}} e^{-i2\sqrt{\pi}\hat{\phi}_R} \quad \text{and} \quad \hat{\psi}_L \approx \frac{1}{\sqrt{2\pi\alpha}} e^{+i2\sqrt{\pi}\hat{\phi}_L} \quad (9)$$

The length parameter α is a cut-off which is required to ensure that the contribution from high-momentum modes do not produce divergences when computing

correlation functions. It is convenient to define the two bosonic fields:

$$\hat{\phi} = \hat{\phi}_R + \hat{\phi}_L \quad \text{and} \quad \hat{\theta} = -\hat{\phi}_R + \hat{\phi}_L \quad (10)$$

Then the fermionic density is given by:

$$\hat{\rho} - \rho_0 = \hat{\psi}_R^+ \hat{\psi}_R + \hat{\psi}_L^+ \hat{\psi}_L = -\frac{1}{\sqrt{\pi}} \frac{\partial \hat{\phi}}{\partial x} \quad (11)$$

where ρ_0 is the background density; fluctuations around this density are described by the quantum fields $\hat{\psi}$ or $\hat{\phi}$.

Although the dispersion relationship is generally not linear for all the modes of a given system, it often happens that the low-energy and long-wavelength modes can be studied using bosonization. For a fermionic system in one dimension these modes are usually the ones lying close to the two Fermi points with momenta $\pm k_F$, respectively. One can define right- and left-moving fields $\hat{\psi}_R$ and $\hat{\psi}_L$ which vary slowly on the scale length a :

$$\hat{\psi}(x) = \hat{\psi}_R(x) e^{ik_F x} + \hat{\psi}_L(x) e^{-ik_F x} \quad (12)$$

Quantities such as the density will generally contain terms which vary slowly as well as terms varying rapidly on the scale of a :

$$\begin{aligned} \hat{\rho} - \rho_0 &= \hat{\psi}^+ \hat{\psi} = \hat{\psi}_R^+ \hat{\psi}_R + \hat{\psi}_L^+ \hat{\psi}_L + e^{-i2k_F x} \hat{\psi}_R^+ \hat{\psi}_L + e^{+i2k_F x} \hat{\psi}_L^+ \hat{\psi}_R \\ &= -\frac{1}{\sqrt{\pi}} \frac{\partial \hat{\phi}}{\partial x} + \frac{1}{2\pi\alpha} \left[e^{i(2\sqrt{\pi}\hat{\phi}-2k_F x)} + e^{-i(2\sqrt{\pi}\hat{\phi}-2k_F x)} \right] \end{aligned} \quad (13)$$

One can compute various correlation functions in the bosonic language. Consider an operator of the form:

$$\hat{O}_{m,n} = e^{i2\sqrt{\pi}(m\hat{\phi}+n\hat{\theta})} \quad (14)$$

we find the following result for the two-point equal-time correlation function at spatial separations which are much larger than the microscopic lattice spacing, a :

$$\langle 0|T \hat{O}_{m,n}(x) \hat{O}_{m',n'}^+(0)|0\rangle \approx \delta_{mm'} \delta_{nn'} \left(\frac{\alpha}{x}\right)^{2(m^2 K + n^2/K)} \quad (15)$$

where K denotes an interaction parameter which will be described below. Note that the correlation function decays as a power law. In the language of the renormalization group, the scaling dimension of $\hat{O}_{m,n}$ is given by $m^2 K + n^2/K$.

We can now study a quantum spin chain using bosonization. To be specific, let us consider a spin-1/2 chain described by the anisotropic Hamiltonian:

$$\hat{H} = \sum_{i=1}^N \left[\frac{J}{2} (\hat{S}_i^+ \hat{S}_{i+1}^- + \hat{S}_i^- \hat{S}_{i+1}^+) + J_z \hat{S}_i^z \hat{S}_{i+1}^z - h \hat{S}_i^z \right] \quad (16)$$

where the interactions are between nearest-neighbor spins only and $J > 0$. $\hat{S}_i^+ = \hat{S}_i^x + i\hat{S}_i^y$ and $\hat{S}_i^- = \hat{S}_i^x - i\hat{S}_i^y$ are the spin raising and lowering operators and h denotes a magnetic field. Note that the model has a $U(1)$ invariance, namely, rotations about the S^z axis. When $J_z = J$ and $h = 0$ the $U(1)$ invariance is enhanced to an $SU(2)$ invariance, because at this point the model can be written simply as $\hat{H} = J \sum_i \hat{S}_i \cdot \hat{S}_{i+1}$. Although the model in Eq. (16) can be solved exactly by use of the Bethe *ansatz*, and one has the explicit result that the model is gapless for a certain range of values of J_z/J and h/J (see Ref. [39]), it is not easy to compute explicit correlation functions in that approach. We therefore use bosonization to study this model.

We first use the Jordan–Wigner transformation to map the spin model to a model of spinless fermions. We map a \uparrow spin or a \downarrow spin at any site to the presence or absence of a fermion at that site. We introduce a fermion annihilation operator ψ_i at each site, and write the spin at the site as:

$$\hat{S}_i^z = \hat{\psi}_i^+ \hat{\psi}_i - 1/2 = \hat{n}_i - 1/2$$

and

$$\hat{S}_i^- = (-1)^i \hat{\psi}_i e^{i\pi \sum_j \hat{n}_j} \quad (17)$$

where the sum runs from one boundary of the chain up to the $(i - 1)$ th site (we assume open boundary conditions here for convenience), $n_i = 0$ or 1 is the fermion occupation number at site i , and the expression for \hat{S}_i^+ is obtained by taking the Hermitian conjugate of \hat{S}_i^- . The string factor in the definition of \hat{S}_i^- is added to ensure the correct statistics for different sites; the fermion operators at different sites anticommute, whereas the spin operators commute.

We now find that:

$$\hat{H} = - \sum_i \left[\frac{J}{2} (\hat{\psi}_i^+ \hat{\psi}_{i+1} + h.c.) - J_z (\hat{n}_i - 1/2) (\hat{n}_{i+1} - 1/2) + h (\hat{n}_i - 1/2) \right] \quad (18)$$

We see that the spin-flip operators C lead to hopping terms in the fermion Hamiltonian, whereas the interaction term leads to an interaction between fermions on adjacent sites.

Let us first consider the non-interacting case given by $J_z = 0$. By Fourier transforming the fermions $\hat{\psi}_k = \sum_j \hat{\psi}_j e^{-ikja} / \sqrt{N}$, where a is the lattice spacing and the momentum, k , lies in the first Brillouin zone $-\pi/a < k < \pi/a$, we find that the Hamiltonian is given by:

$$\hat{H} = \sum_k \omega_k \hat{\psi}_k^+ \hat{\psi}_k \quad (19)$$

where

$$\omega_k = -J \cos(ka) - h \quad (20)$$

The non-interacting ground state is the one in which all the single-particle states with $\omega_k < 0$ are occupied and all the states with $\omega_k > 0$ are empty. If we set the magnetic field $h = 0$ the magnetization per site $m \equiv \sum_i S_i^z / N$ will be zero in the

ground state; equivalently, in the fermionic language, the ground state is precisely half-filled. Thus, for $m = 0$, the Fermi points ($\omega_k = 0$) lie at $ka = \pm\pi/2 k_F a$. Let us now add the magnetic field term. In the fermionic language, this is equivalent to adding a chemical potential term (which couples to \hat{n}_i or \hat{S}_i^z). In that case, the ground state no longer has $m = 0$ and the fermion model is no longer half-filled.

The Fermi points are then given by $\pm k_F$, where:

$$k_F a = \pi(m + 1/2) \quad (21)$$

It turns out that this relationship between k_F (which governs the oscillations in the correlation functions as discussed below) and the magnetization m continues to hold even if we turn on the interaction J_z , although now the simple picture of the ground state (with states filled below some energy and empty above some energy) is no longer valid.

In the linearized approximation, the modes near the two Fermi points have the velocities ($\partial\omega_k/\partial k = \pm v$, where v is some function of J , J_z , and h). Next, we introduce the slowly varying fermionic fields $\hat{\psi}_R$ and $\hat{\psi}_L$ as indicated above; these are functions of a coordinate, x , which must be an integer multiple of a . Finally, we bosonize these fields. The spin fields can be written in terms of either the fermionic or the bosonic fields. For instance, \hat{S}^z is given by the fermion density as in Eq. (17) which then has a bosonized form given in Eq. (13). Similarly:

$$\begin{aligned} \hat{S}^+(x) = & (-1)^{x/a} \left[e^{+ik_F x/a} \hat{\psi}_R^+(x) + e^{-ik_F x/a} \hat{\psi}_L^+(x) \right] \\ & \times \left[e^{-i\pi \int_{-\infty}^x dx (\hat{\psi}^+(x') \hat{\psi}(x') + 1/2a)} + h.c. \right] \end{aligned} \quad (22)$$

where $(-1)^{x/a} = \pm 1$, because x/a is an integer. This can now be written entirely in the bosonic language. the term in the exponential is given by:

$$\int_{-\infty}^x dx' \hat{\psi}^+(x') \hat{\psi}(x') = -\frac{1}{\sqrt{\pi}} \int_{-\infty}^x dx' \frac{\partial \hat{\psi}}{\partial x'} = -\frac{1}{\sqrt{\pi}} \left[\hat{\phi}_R(x) + \hat{\phi}_L(x) \right] \quad (23)$$

where we have ignored the contribution from the lower limit at $x = -\infty$.

We can now use these bosonic expressions to compute the two-spin, equal-time correlation functions $G^{ab}(x) \equiv \langle 0 | T \hat{S}^a(x) \hat{S}^b(0) | 0 \rangle$. We find that:

$$G^{zz}(x) = m^2 + \frac{c_1}{x^2} + c_2 \frac{\cos(2k_F x)}{x^{2K}}$$

and

$$G^{+-}(x) + G^{-+}(x) = c_3 \frac{(-1)^{x/a}}{x^{1/2K}} + c_4 \frac{(-1)^{x/a} \cos(2k_F x)}{x^{2K+1/2K}} \quad (24)$$

where $c_1 \dots c_4$ are constants. K and ν are functions of J_z/J and h/J ; the exact dependence can be found elsewhere [39]. For $h = 0$, K is given by the analytical expression:

$$\frac{1}{K} = 1 + \frac{2}{\pi} \sin^{-1} \left(\frac{J_z}{J} \right) \quad (25)$$

Note that at the $SU(2)$ invariant point $J_z = J$ and $h = 0$, we have $K = 1/2$, and the two correlations G^{zz} and G^{+-} have the same forms.

In addition to providing a convenient way of computing correlation functions, bosonization also enables us to study the effects of small perturbations. For instance, a physically important perturbation is the dimerizing term:

$$V = \delta \sum_i (-1)^i \left[\frac{J}{2} (\hat{S}_i^+ \hat{S}_{i+1}^- + \hat{S}_i^- \hat{S}_{i+1}^+) + J_z \hat{S}_i^z \hat{S}_{i+1}^z \right] \quad (26)$$

where δ is the strength of the perturbation. On bosonizing we find that the scaling dimension of this term is K . Hence it is relevant if $K < 2$; it then produces an energy gap in the system which scales with δ as:

$$\Delta E \sim \delta^{1/(2-K)} \quad (27)$$

This kind of phenomenon occurs in spin-Peierls systems such as CuGeO_3 ; below a transition temperature T_{sp} they go into a dimerized phase which has a gap [58].

4.5 Density Matrix Renormalization Group Method

One method which held promise for overcoming the difficulty of exploding dimensionalities is the renormalization group (RG) technique in which one systematically eliminates the degrees of freedom of a many-body system. Although this technique found dramatic success in the Kondo problem [59], its straightforward extension to interacting lattice models was quite inaccurate [60].

In early 1992 the key problems associated with the failure of the old RG method were identified and a different renormalization procedure based on the eigenvalues of the many-body density matrix of proper subsystems was developed [61, 62]. This method has come to be known as the density matrix renormalization group (DMRG) method and has found dramatic success in solving quasi-one-dimensional many-body Hamiltonians.

In a real-space RG approach, one begins by subdividing the total system into several blocks A_n and proceeds to build effective blocks iteratively so that at each iteration each effective block represents two or more blocks of the previous iteration, without increasing the Fock space dimensionality of the blocks from that which existed at the previous iteration. Usually, one starts with each A_n consisting of a single site. Because the Hilbert space grows exponentially with increasing system size, one truncates the number of states kept at each iteration.

The main reason for the failure of the old RG methods is the choice of the states retained at each stage of the iteration [61]. White [62], recognized that the weakness of the old RG procedure was in the truncation of the Fock space of a block on the basis of the eigenvalues of the block Hamiltonian being re-normalized. He replaced this choice by introducing a truncation scheme completely different from

that was used in the old quantum RG procedures. The choice is the eigenvalues of the reduced density matrix of the block constructed from the desired state of the full Hamiltonian. The truncated Fock space is now spanned by the m eigenvectors of the reduced density matrix of order $l \times l$ ($m \leq l$) corresponding to the m highest eigenvalues of the reduced many-body density matrix. The reason for choosing the eigenvalues of the reduced density matrix as a criterion for implementing a cut-off is that, the larger the density matrix eigenvalue, the larger is the weight of the eigenstate of the density matrix in the expectation value of any property of the system. This result becomes evident when all the dynamic operators are expressed as matrixes on the basis of the eigenvectors of the density matrix. The expectation value of any operator \hat{A} is simply:

$$\langle \hat{A} \rangle = \frac{\sum_i A_{ii} \rho_i}{\sum_i \rho_i} \quad (28)$$

where ρ_i is the density matrix eigenvalue. The larger the value of a particular ρ_i , the larger is its contribution to the expectation value, for a physically reasonable spread in the diagonal matrix elements A_{ii} .

The many-body density matrix of a part of the system can be easily constructed as follows. Let us begin with given state $|\psi\rangle_S$ of S , which is called the *universe* or *superblock*, consisting of the system (which we call a block) A and its *environment* A' . Let us assume that the Fock space of A and A' are known, and can be labeled $|i\rangle_A$ and $|j\rangle_{A'}$, respectively. The representation of $|\psi\rangle_S$ in the product basis of i_A and $j_{A'}$ can be written as:

$$|\psi\rangle_S = \sum_{ij} \psi_{ij} |i\rangle_A \times |j\rangle_{A'} \quad (29)$$

where we assume the coefficients ψ_{ij} to be real, without loss of generality. Then the reduced many-body density matrix for block A is defined as:

$$\rho_{kl} = \sum_j \psi_{kj} \psi_{lj} \quad (30)$$

The eigenvalue ρ_i of the density matrix ρ gives the probability of finding the corresponding eigenstate $|\mu_i\rangle_A$ in the projection of $|\psi\rangle_S$ on block A . It therefore follows that the eigenvectors with the highest eigenvalues of the density matrix of A are the optimum or most probable states to be retained while the system is augmented.

In the early literature on quantum chemistry the eigenvectors corresponding to large eigenvalues of one-particle density matrixes were employed as the orbital basis for performing a configuration interaction (CI) calculation. The eigenvectors of the density matrix were called the “natural” orbitals and it was observed that the CI procedure converged rapidly when the “natural” orbitals were employed in setting up the Slater determinants [63].

The DMRG scheme differs from the “natural” orbital scheme in two important respects:

- the reduced density matrixes are many-body density matrixes, and
- the size of the system in terms of the number of sites being studied at each iteration is usually augmented by two sites.

The Hamiltonian matrix that one encounters from iteration to iteration, however, remains roughly of the same order while the matrix elements keep changing (re-normalized). In this sense the procedure can be called a renormalization procedure. The coupling constants (the Hamiltonian matrix elements) keep changing while the system size increases, as in the RG procedure performed within a blocking technique.

4.5.1 Implementation of the DMRG Method

We now describe the procedure to carry out the computations. One starts the computation with a small size system, $2n$, which can be solved exactly, $1 \leq n \leq 4$, depending on the degree of freedom at each site. By exact diagonalization, one gets the desired eigenstate of that system. The density matrixes of the left and right blocks, each consisting of n sites (in principle it is not necessary to have the same number of sites for the two blocks, although in practice this is what is most generally used) are obtained from the desired eigenstate. The density matrixes are diagonalized and at the first iteration usually all the density matrix eigenvectors (DMEV) are retained. The Hamiltonian matrix of the left and right blocks (denoted A and A') obtained in any convenient basis are transformed into the density matrix eigenvector basis. So also are the matrixes corresponding to the relevant site operators in both blocks. Now, the iterative procedure proceeds as follows.

1. Construct a superblock $S = A \bullet \bullet A'$, consisting of the block A , two additional sites σ , and σ' and the block A' . Thus, at the first iteration, the system S has $n + 1 + 1 + n = 2n + 2$ sites.
2. Set up the matrixes for the total Hamiltonian of the superblock S in the direct product basis of the DMEV of the blocks A and A' and the Fock space states of the new sites. Considering that the new sites are spin- S sites with $(2S + 1)$ Fock states each, the order of the total Hamiltonian matrix will be $m^2(2S + 1)^2 \times m^2(2S + 1)^2$, where m is the dimension of the block DMEV basis.
3. Diagonalize the Hamiltonian of the superblock $S = 2n + 2$ to find the desired eigenstate $|\psi\rangle$. Using the state $|\psi\rangle$, evaluate all the properties of the superblock of interest.
4. Construct the reduced many-body density matrix, ρ , for the new block $A \bullet$. If the system does not have reflection symmetry, construct the density matrix, ρ' , for the new right block $\bullet A'$ also.
5. Diagonalize the density matrix, ρ , and if necessary ρ' . Usually, the density matrix is block-diagonal in the z -component of the total spin of the block, and it becomes computationally efficient to exploit such quantum numbers. Construct a non-square matrix \mathbf{O} , with m columns, each column being an eigenvector of the density matrix corresponding to one of the m largest eigenvalues. The number of rows in the matrix \mathbf{O} corresponds to the order of the density matrix.

6. Construct the matrixes corresponding to the Hamiltonian, $H_{A\bullet}$, of the new left block $A\bullet$, and the site spin operators (\hat{S}^z and \hat{S}^+) of all the necessary sites. The \hat{S}^- operators are simply the adjoints of the \hat{S}^+ operators.
7. Re-normalize all the matrixes corresponding to the block and site operators by using the RG transformation matrix \mathbf{O} , e. g. $\tilde{H}_{A\bullet} = \mathbf{O}H_{A\bullet}\mathbf{O}^+$. The resulting re-normalized matrixes are of order $m \times m$ and the procedure amounts to a simultaneous change of basis and a truncation.
8. Replace the A by $A\bullet$. If the system does not have reflection symmetry replace A' by $\tilde{A}'\bullet$.
9. Go to step 1.

Use of the block-diagonal nature of the density matrix, besides reducing the CPU time requirement, also enables one to label the DMEV with the appropriate z -component of the total spin of the block ($M_{s,A}$). The Fock space of the individual sites that are added at each iteration are eigenstates of the site spin and number operators. This enables us to target a definite projected spin (M_s) state of the total system.

We now briefly describe the mathematical notation we have used so far for various states. A state of $A\bullet$ is given by the tensor product of a state of A with quantum number q , and an index i , and a state σ , of the additional site. Thus:

$$|q, i, \sigma\rangle_{A\bullet} = |q, i\rangle_A \times |\sigma\rangle \quad (31)$$

A state of a superblock $S = A\bullet\bullet A'$ is given by:

$$|q_A, \mu, \sigma, q_{A'}, \nu, \tau\rangle_S = |q_A, \mu, \sigma\rangle_{A\bullet} \times |q_{A'}, \nu, \tau\rangle_{\bullet A'} \quad (32)$$

The eigenstate of the Hamiltonian of the super-block can be written as:

$$|\psi\rangle_S = \sum_{q_{A'}, \mu', \tau} \psi_{\mu, \nu}^{q_A, q_{A'}, \sigma, \tau} |q_A, \mu, \sigma, q_{A'}, \nu, \tau\rangle_S \quad (33)$$

The density matrix for $A\bullet$ then will have a block structure and can be expressed as

$$\rho_{\mu, \nu}^{q_A, \sigma} = \sum_{q_{A'}, \mu', \tau} \psi_{\mu, \mu'}^{q_A, q_{A'}, \sigma, \tau} \psi_{\nu, \mu'}^{q_A, q_{A'}, \sigma, \tau} \quad (34)$$

This algorithm is called the infinite lattice DMRG algorithm because this procedure is best suited for the system in the thermodynamic limit, i. e. when the properties of the system are extrapolated to the infinite system size limit.

4.5.2 Finite Size DMRG Algorithm

If we are interested in accurate properties of the system at a required size it is possible to improve on the accuracies obtainable from the infinite DMRG procedure. This involves recognizing that the reduced many-body density matrixes at each iteration correspond to a different system size. For example, when we are performing

the DMRG procedure to obtain the properties of a system of $2M$ sites, at an iteration corresponding to $2p$ sites ($n \leq p \leq M$), the reduced density matrix we construct is that of a block of p sites in a system of $2p$ sites. If, however, our interest is in the $2M$ -site system we should employ the density matrix of the block of p sites in a $2M$ -site system. It is possible to construct, iteratively, the p -site reduced density matrix of the $2M$ -site system. This is achieved by the so called finite-size algorithm [62]. This method provides highly accurate solutions even when the states of the full Hamiltonian have inhomogeneous (symmetry breaking) properties.

To obtain the $2M$ -site result we should perform the infinite lattice algorithm up to $p = (M - 1)$ sites first storing all operators in each iteration. Now the algorithm for finite lattices with reflection symmetry (left block = right block), proceeds as follows.

1. On reaching a system size of $2M$ sites, obtain the density matrix of the block of M sites.
2. Use the density matrix of M sites on the left and that of $(M - 2)$ sites on the right, add two new sites as in the infinite DMRG procedure, and obtain the desired eigenstate of the $2M$ system.
3. Now obtain the reduced density matrix of the $(M + 1)$ sites from the eigenstate of the previous iteration obtained in the direct product basis of the DMEV of the M -site, $(M - 2)$ -site density matrixes, and the Fock space states of the individual sites.
4. Go back to step 2, replacing M by $(M + 1)$ and $(M - 2)$ by $(M - 3)$ and iterate until a single site results on the right and $(2M - 3)$ sites result on the left.
5. Because the system has reflection symmetry, use the density matrix of the $(2M - 3)$ sites on the right and construct the $2M$ system as built-up from three individual sites on the left and $(2M - 3)$ sites on the right. Obtain the desired eigenstate of the $2M$ system in this basis.
6. Now obtain the new 2-site density matrix on the left and $(2M - 4)$ site density matrix on the right. Replace the single-site on the left by two sites and $(2M - 3)$ sites on the right by $(2M - 4)$ sites in step 5.
7. Repeat steps 5 and 6 until $(M - 1)$ sites are obtained both on the left and right. The properties of the $2M$ system obtained from the eigenstates at this stage corresponds to the first iteration of the finite-size algorithm. We can now go back to step 1 and carry through the steps to obtain properties at later iterations of the finite-size DMRG algorithm.

In systems without reflection symmetry, the DMEV of the right and left parts are not identical even if the sizes of the reduced systems are the same. The finite-DMRG algorithm in this case involves first constructing the density matrixes of the left part for sizes greater than M and on reaching the density matrix of $(2M - 3)$ sites, reducing the size of the left-part and increasing that of the right, from one site to $(M - 1)$. This will result in the refined density matrixes of both the right and the left blocks of the total system, for block sizes of $(M - 1)$. At this stage, we can compute all the properties and continue the reverse sweep until the right block is of size $(2M - 3)$ and the left block is of size 1. The forward sweep that follows will increase the block size on the left and reduce that on the right. We would have

completed the second iteration when the two block sizes are equal. The forward and reverse sweeps can be continued until we reach the desired convergence in the properties of the whole system.

4.5.3 Calculation of Properties in the DMRG Basis

At the end of each iteration, one can calculate the properties of the targeted state [64]. The reduced many-body density matrix computed at each iteration can be used to calculate the static expectation values of any site operator or their products. Care should be taken to use the density matrixes appropriate to the iteration. The expectation value of a site property corresponding to the operator \hat{A}_i can be written:

$$\langle \hat{A}_i \rangle = \text{Tr}(\rho \mathbf{A}_i) \quad (35)$$

where ρ is the density matrix of the block in which the site i is situated and \mathbf{A}_i is the matrix of the re-normalized site operator at site i . For calculating correlation functions, one can use a similar equation. The correlation function between two site operators belonging to separate blocks can be written as:

$$\langle \hat{A}_i \hat{A}_j \rangle = \text{Tr}(\rho \mathbf{A}_i \mathbf{A}_j) \quad (36)$$

The accuracy of this procedure turns out to be very poor, however, if the sites i and j belong to the same block [62]. The reason is that one feature implicit in the above procedure is the resolution of identity by expansion in terms of the complete basis. Unfortunately, the basis in which the site operators are represented is incomplete and such an expansion is therefore error-prone. To circumvent this difficulty it has been suggested [62] that one obtains the matrix representation of the products of the site operators from the first occurrence of the product pair $\langle ij \rangle$ and, by re-normalizing the product operator $\hat{B}_{ij} = \hat{A}_i \hat{A}_j$, at every subsequent iteration until the end of the RG procedure. Then, the correlation function between \hat{A}_i and \hat{A}_j (where i and j belong to the same block) can be evaluated as:

$$\langle \hat{A}_i \hat{A}_j \rangle = \text{Tr}(\rho \mathbf{B}_{ij}) \quad (37)$$

This procedure is usually found to be more accurate.

4.5.4 Remarks on the Applications of DMRG

The DMRG method is currently the most accurate method for large quantum lattice models in one dimension. It can be applied to interacting bosonic, fermionic, or spin models and to models which have interactions among them. The overall accuracy of the DMRG method is exceptionally high for one-dimensional systems with only nearest neighbor interactions. For a spin-1/2 chain where exact Bethe *ansatz* ground-state energy is available the DMRG ground state energy per site in units of the

exchange constant J is found to be accurate to seven decimal places with a cut-off $m = 100$ [62]. The method is found to be almost as accurate for the one-dimensional Hubbard model, where again the DMRG results are comparable with exact results obtained from the exact analytical Bethe *ansatz* solution [65].

Because higher dimensionality is equivalent to longer-range interactions within one dimension, the model also restricts the range of interactions in one dimension. It has been noted that the number of DMEV that should be retained in a calculation on higher dimensional systems, for accuracies comparable with that in one dimension, scales exponentially with dimensionality. Thus, to obtain accuracy comparable with that obtained in a chain of L -sites for a cut-off m , in a $L \times L$ square lattice, the number of DMEV that must be retained for the corresponding two-dimensional lattice is $\sim m^2$.

Extending the range of interactions to next-nearest neighbors does not significantly reduce the accuracy [66]. Inclusion of cyclic boundary conditions, however, reduces the accuracy of the method significantly – although in one-dimension the DMRG method still would outperform any other method for the same system size. In the DMRG procedure the most accurate quantity computed is the total energy. In dealing with other quantities, e. g. correlation functions, caution must be exercised in interpreting the results.

The density matrix eigenvalues sum to unity and the truncation error, which is defined as the sum of the density matrix eigenvalues corresponding to the discarded DMEV, gives a qualitative estimate of the accuracy of the calculation and provides a framework for extrapolation to the $m \rightarrow \infty$ limit. The accuracy of the results obtained in this way is unprecedented [67, 68]. The accuracy of the ground state energy per site for the spin-1 chain is limited by the precision of machine arithmetic, e. g. $e_o = 1.401484038971(4)$. Similarly, the accuracy persists even when calculating for the Haldane gap – e. g. the gap is evaluated to be $0.41050(2)$.

Another aspect of the DMRG technique worth noting is that the method is best suited for targeting one eigenstate at a time, although it is possible to obtain reasonable results for a set of states by using an average many-body reduced density matrix constructed as a weighted sum of the density matrixes corresponding to each of the states in question. One way of constructing the average density matrix is by using a statistical weight for the chosen set of states; the averaged density matrix in this instance is given by:

$$\rho_{\beta;kl} = \sum_{ij} \psi_{i;kj} \psi_{i;lj} \exp[-\beta \varepsilon_i] / \sum_i \exp[-\beta \varepsilon_i] \quad (38)$$

where $\beta = 1/k_B T$ and k_B and T are the Boltzmann constant and temperature, respectively. One can thus extend the DMRG method to finite temperatures.

Finite size algorithms have been used extensively to study edge states and systems with impurities, where substantial improvement of the accuracy is needed to characterize the various properties of a finite system. The DMRG method has been applied to diverse problems in magnetism: study of spin chains with $S > 1/2$ [69], chains with dimerization and/or frustration [51, 66, 70, 71], and coupled spin chains [66, 72, 73], to list a few. Highly accurate studies have been performed of the structure factor

and string-order parameter (topological long-range order) [67] and edge states in Haldane phase systems [74]. Dynamic properties for both spin and fermionic systems with DMRG have also been reported within the maximum entropy method [75] and the continued fraction [76] and correction vector [77] approaches. DMRG has also been successfully formulated to obtain low-temperature thermodynamic properties for a variety of spin systems [78, 79], and the solution of models of spin chains dynamically coupled to dispersionless phonons [80]. Nishino and Okunishi have also derived two re-formulations of DMRG – the product wave function renormalization group (PWFRG) [81], and the corner transfer matrix renormalization group (CTMRG) [82] methods. These methods are a means of calculating dynamic correlation functions in spin chains and obtaining highly accurate results for the two-dimensional Ising model at criticality.

4.6 Frustrated and Dimerized Spin Chains

It is well known that the one-dimensional XY chain can be mapped on to a one-dimensional non-interacting spinless fermion model. The isotropic spin chain will then map on to a chain of interacting spinless fermions. According to the Peierls theorem a partly filled one-dimensional band of non-interacting fermions is unstable with respect to a lattice distortion that results in an insulating ground state. It has been shown that introduction of interactions in the Peierls system leads to greater instability. The mapping between the Heisenberg spin chains with equal nearest-neighbor exchange interactions (uniform spin chain) and the spinless fermion model suggests that such a spin chain is also unstable with regard to a lattice distortion leading to alternately strong and weak nearest-neighbor exchange constants, i. e. a dimerized spin chain. What is of importance is that such dimerization is unconditional – no matter how strong the lattice is, the lattice dimerizes, because the exchange energy gained as a result of dimerization always exceeds the strain energy. This is because the gain in exchange energy varies as $\delta^2 \ln \delta$ whereas the strain energy loss varies as δ^2 , where δ is the magnitude of dimerization that leads to the nearest neighbor exchange constants alternating as $J(1 \pm \delta)$.

In recent years, many systems which closely approximate the one-dimensional spin chain have been synthesized. What has been observed in these experimental systems is that besides the nearest-neighbor antiferromagnetic exchange there is also a second neighbor exchange J_2 of the same sign and comparable magnitude. Such a second neighbor interaction has the effect of frustrating the spin alignment favored by the nearest-neighbor interaction. Realistic study of these systems therefore requires modeling them using both dimerization and frustration. Theoretically, spin chains with frustration only ($J - J_2$ model) were studied by Majumdar and Ghosh. Interestingly, they showed that for $J_2 = J/2$, the ground state is doubly degenerate and is spanned by the two possible Kekulé structures (Fig. 11). It is quite gratifying to note that a century after the Kekulé structure for benzene was proposed there is actually a Hamiltonian for which the Kekulé structure happens to be the ground state!

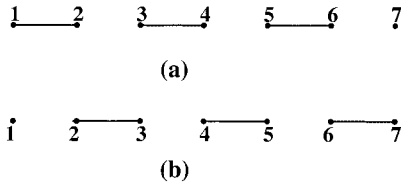


Fig. 11. Doubly degenerate ground states (a) and (b) of the $J - J_2$ chain (see Fig. 8 for $\delta = 0$) at $J_2 = J/2$. The solid line between sites i and j represents a singlet, $[|\uparrow_i \downarrow_j\rangle - |\downarrow_i \uparrow_j\rangle]/\sqrt{2}$.

Although most of the discussion above is restricted to spin-1/2 chains, there has been much interest in the higher-spin chains after the conjecture of Haldane which predicts that for uniform spin chains the excitation spectrum of integer spin chains is qualitatively different from that of half-odd-integer spin chains. The latter have a gapless excitation spectrum whereas the excitation spectrum of the former is gapped. The synthesis and study of integer spin chains have indeed confirmed this conjecture.

Notwithstanding many interesting exact analytical solutions for spin chains, there are still many situations for which such solutions have been elusive. The exact solutions are basically confined to the uniform Heisenberg model and the frustrated and dimerized model along the line $2J_2 + \delta = 1$ in the $J_2 - \delta$ plane, with $J = 1$. Reliable numerical study of these models therefore requires the development of techniques which are highly accurate so that the results of large finite systems can be scaled or extrapolated to the thermodynamic limit. As has already been discussed, the DMRG technique is ideally suited, because of its high accuracy for quasi-one-dimensional systems.

The Hamiltonian for the frustrated and dimerized spin chain is given in Eq. (4) and is shown schematically in Fig. 8. A few low-lying states in a sector with a given value of the total spin component, M_S are obtained at representative points in the $J_2 - \delta$ plane, using the DMRG method. The ground state is always the first (lowest energy) state in the $M_S = 0$ sector. The accuracy of the DMRG method depends crucially on the number of eigenstates of the density matrix, m , which are retained. Working with $m = 100$ to 120 over the entire $J_2 - \delta$ plane gives accurate results. This can be verified by comparing the DMRG results for these m values with exact numerical diagonalizations of chains with up to 16 sites for spin-1 systems [83] and 22 sites for spin-1/2 systems [84]. The chain lengths studied vary from 150 sites for $J_2 > 0$ to 200 sites for $J_2 = 0$. The DMRG results are also tracked as a function of N , the chain length, to verify that convergence is always reached well before 150 sites. The numerical results are much better convergent for open chains than for periodic chains, a feature generic to the DMRG technique [62, 68].

The quantum phase diagrams obtained for a spin-1/2 chain is shown in Fig. 12. The system is gapless on the line A running from $J_2 = 0$ to $J_{2c} = 0.241$ for $\delta = 0$, and is gapped everywhere else in the $J_2 - \delta$ plane. There is a disorder line B given by $2J_2 + \delta = 1$; the peak in the structure factor $S(q)$ is at $q_{\max} = \pi$ to the left of B (region I), decreases from π to $\pi/2$ as we go from B up to line C (region II), and is at $q_{\max} = \pi/2$ to the right of C (region III). This is in agreement with the results obtained in Section 4.4 by use of the NLSM approach. The correlation length goes through a minimum on line B.

In the spin-1 case (Fig. 10), the phase diagram is more complex. There is a solid line marked A which runs from $(0, 0.25)$ to approximately $(0.22 \pm 0.02, 0.20 \pm 0.02)$,

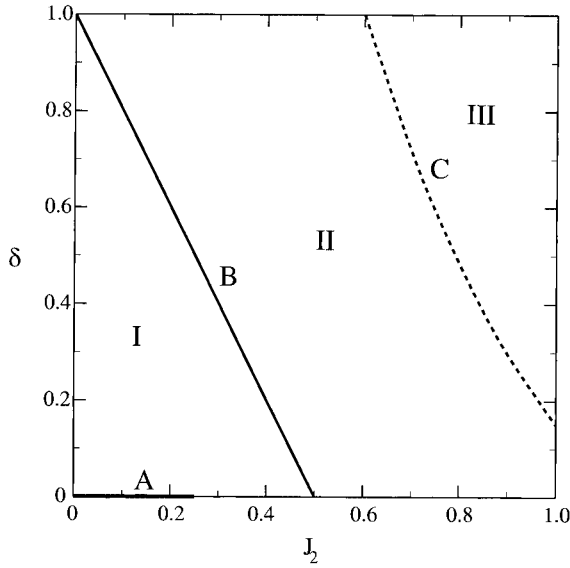


Fig. 12. “Phase” diagram for the spin-1/2 chain in the $J_2 - \delta$ plane.

shown by a cross. To within numerical accuracy the gap is zero on this line and the correlation length ξ is as large as the system size N . The rest of the “phase” diagram is gapped. The gapped portion can, however, be divided into different regions characterized by other interesting features. On the dotted lines marked B, the gap is finite. Although ξ goes through a maximum when we cross B in going from region II to region I or from region III to region IV, its value is much smaller than N . There is a dashed line C extending from $(0.65, 0.05)$ to about $(0.73, 0)$ on which the gap seems to be zero (to numerical accuracy), and ξ is very large, but not as large as N . The straight line D satisfying $2J_2 + \delta = 1$ extends from $(0, 1)$ to approximately $(0.432, 0.136)$. Regions II and III are separated by line E which goes down to about $(0.39, 0)$. Across D and E the peak in the structure factor decreases from π (Néel) in regions I and II to less than π (spiral) in regions III and IV. In regions II and III the ground state for an open chain has a fourfold degeneracy (consisting of states with $S = 0$ and $S = 1$), whereas it is non-degenerate in regions I and IV with $S = 0$. The regions II and III, where the ground state is fourfold degenerate for an open chain, can be identified with the Haldane phase; the regions I and IV correspond to a non-Haldane singlet phase. The lines B, D, and E meet in a small region V where the ground state of the system is numerically very difficult to find. Note that the numerically zero gap at $(0.73, 0)$ is unexpected from either bosonic mean-field theory [85] or the NLSM approach discussed earlier.

For the spin-1 system, there is a striking similarity between the ground state properties of the dimerized and frustrated model (Eq. 4) as a function of J_2 (with $\delta = 0$) and the biquadratic model:

$$\hat{H} = \sum_i \left[\hat{\mathbf{S}}_i \cdot \hat{\mathbf{S}}_{i+1} + \beta (\hat{\mathbf{S}}_i \cdot \hat{\mathbf{S}}_{i+1})^2 \right] \quad (39)$$

as a function of (positive) β [70]. For $J_2 < 0.39$ and $\beta < 1/3$ both models are in the Néel phase and are gapped. For $J_2 > 0.39$ and $\beta > 1/3$, the two models are in the spiral phase and are generally gapped, although the model represented by Eq. (4) is “gapless” for $J_2 = 0.73$ and the model represented by Eq. (39) is gapless for $\beta = 1$. Qualitatively, the cross-over from the Néel to the spiral phase (but not the gaplessness at a particular value of J_2 or β) can be understood by means of the following classical argument. Let us set the magnitudes of the spins equal to 1 and define the angle between spins S_i and S_{i+n} to be $n\theta$. The angle θ can be obtained by minimizing $\cos \theta + J_2 \cos 2\theta$ in Eq. (4), and $\cos \theta + \theta \cos^2 \theta$ in Eq. (39). This gives us a Néel phase ($\theta = \pi$) if $J_2 \leq 1/4$ and $\beta \leq 1/2$ in the two models, and a spiral phase for larger values of J_2 and β with $\theta = \cos^{-1}(-1/4J_2)$ and $\theta = \cos^{-1}(-1/2\beta)$, respectively. The actual crossover points from Néel to spiral are different from these classical values for spin-1. In the classical limit $S \rightarrow \infty$ the ground state of the model is in the Néel phase for $4J_2 < 1 - \delta^2$, in a spiral phase for $1 - \delta^2 < 4J_2 < (1 - \delta^2)/\delta$, and in the colinear phase for $(1 - \delta^2)/\delta < 4J_2$ (Fig. 9).

As is apparent from Fig. 8, $\delta = 1$ results in two coupled spin chains wherein the inter-chain coupling is 2 and the intrachain coupling is J_2 . By use of DMRG one can study the dependence of the gap Δ and the two-spin correlation function $C(r)$ on the inter-chain coupling J . In Fig. 13 Δ is plotted against J for spin-1/2 and spin-1 systems. For spin-1/2 the system is gapped for any non-zero value of the inter-chain coupling J , although the gap vanishes as $J \rightarrow 0$. The gap increases and correspondingly the correlation length decreases with increasing J . For coupled spin-1 chains one obtains the somewhat surprising result that both the gap and the correlation length ξ are fairly large for moderate values of J . Note that the variation

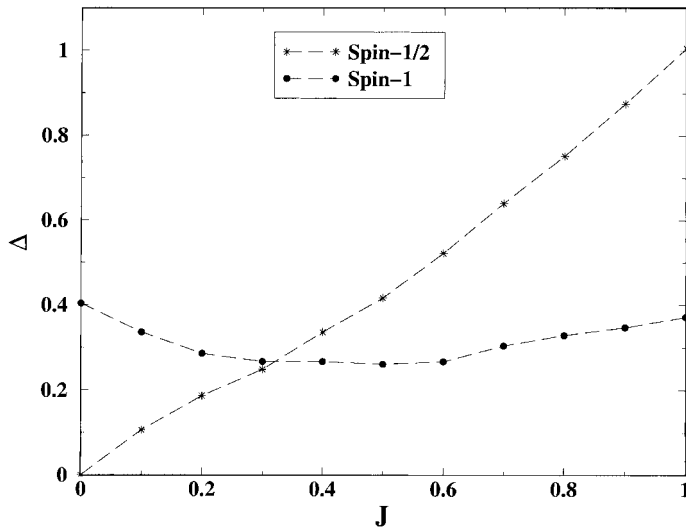


Fig. 13. Gap Δ vs J for coupled spin chains ($\delta = 1$). Spin-1/2 and spin-1 data are indicated by crosses and circles, respectively.

of the gap with J for spin-1 (shown as circles) is much less than that for spin-1/2 (crosses).

The NLSM derived in Section 4.4 can be expected to be accurate only for large values of the spin S . It is interesting to note that the numerically obtained “phase” boundary between the Néel and spiral phases for spin-1 is closer to the classical ($S \rightarrow \infty$) boundary $4J_2 = 1 - \delta^2$ than for spin-1/2. For instance, the crossover from Néel to spiral occurs, for $\delta = 0$, at $J_2 = 0.5$ for spin-1/2, at 0.39 for spin-1, and at 0.25 classically.

To conclude this section, we have studied a two-parameter “phase” diagram for the ground state of isotropic antiferromagnetic spin-1/2 and spin-1 chains. The spin-1 diagram is considerably more complex than the corresponding spin-1/2 chain, with surprising features like a “gapless” point inside the spiral “phase”; this point could be close to a critical point discussed earlier in the literature [50, 86]. It would be interesting to establish this more definitively. Our results show that frustrated spin chains with small values of S have features not expected from large S field theories.

4.7 Alternating (S_1, S_2) Ferrimagnetic Spin Chains

Ferrimagnets belong to a class of magnet with spontaneous magnetization below a certain critical temperature. Several attempts have been made to synthesize molecular materials with spontaneous magnetization at low temperatures [87, 88]. These are quasi-one-dimensional bimetallic molecular magnets in which each unit cell contains two spins with different spin values, with the general formula $ACu(pbaOH)(H_2O)_3 \cdot 2H_2O$, where pbaOH is 2-hydroxy-1,3-propylenebis(oxamato) and $A = Mn, Fe, Co, \text{ or } Ni$; they belong to the alternating or mixed spin chain family [88, 89]. These alternating spin compounds have been seen to have ferrimagnetic behavior. It is important that there are many other classes of ferrimagnetic system – homometallic chains with different Lande factors [90] and topological ferrimagnets [91, 92], with behavior very similar to that of mixed-spin systems.

The thermodynamic behavior of these ferrimagnetic spin compounds is very interesting [89, 93]. In very low magnetic fields these systems have one-dimensional ferrimagnetic behavior. Plots of χT against T (where χ is the magnetic susceptibility and T the temperature) have a rounded minimum – as the temperature is increased χT decreases sharply and goes through a minimum before increasing gradually. The temperature at which this minimum occurs differs from system to system and depends on the site spins of the chain. The variation of the field-induced magnetization with temperature is also interesting because the ground state is a magnetic state. These exciting observations have motivated us to study ferrimagnetic systems with arbitrary spins s_1 and s_2 alternating from site to site. It would also be of interest to know the thermodynamic properties of systems with varying s_1 and s_2 .

4.7.1 Ground State and Excitation Spectrum

We start our discussion with the Hamiltonian for a chain with spins s_1 and s_2 on alternating sites (with $s_1 > s_2$, without loss of generality):

$$\hat{H} = J \sum_n \left[(1 + \delta) \hat{\mathbf{S}}_{1,n} \cdot \hat{\mathbf{S}}_{2,n} + (1 - \delta) \hat{\mathbf{S}}_{2,n} \cdot \hat{\mathbf{S}}_{1,n+1} \right] \quad (40)$$

where the total number of sites is $2N$ and the sum is over the total number of unit cells N . $\hat{\mathbf{S}}_{i,n}$ corresponds to the spin operator for the site spin s_i in the n th unit cell. The exchange integral J is taken to be positive for all our calculations; δ is the dimerization parameter and lies in the range $\{0, 1\}$.

Before describing our numerical results, we briefly summarize the results of a spin-wave analysis for the purposes of comparison [79]. We will first state the results for $\delta = 0$. According to spin-wave theory, the ground state has total spin $S_G = N(s_1 - s_2)$. Let us define a function:

$$\omega(k) = J \sqrt{(s_1 - s_2)^2 + 4s_1s_2 \sin^2(k/2)} \quad (41)$$

where k denotes the wave number. The ground state energy per site is given by:

$$\varepsilon_0 = \frac{E_0}{2N} = -Js_1s_2 + \frac{1}{2} \int_0^\pi \frac{dk}{\pi} [-J(s_1 + s_2) + \omega(k)] \quad (42)$$

The lowest branch of excitations is to states with spin $S = S_G - 1$, with the dispersion:

$$\omega_1(k) = J(-s_1 + s_2) + \omega(k) \quad (43)$$

the gap vanishes at $k = 0$. There is a gapped branch of excitations to states with spin $S = S_G + 1$, with the dispersion:

$$\omega_2(k) = J(s_1 - s_2) + \omega(k) \quad (44)$$

the minimum gap occurs at $k = 0$ and is given by $\Delta = 2J(s_1 - s_2)$. In the ground state with $S^z = S_G$ the sublattice magnetizations are given by the expectation values:

$$\langle \hat{S}_{1,n}^z \rangle = \left(s_1 + \frac{1}{2} \right) - \frac{1}{2} \int_0^\pi \frac{dk}{\pi} \frac{J(s_1 + s_2)}{\omega(k)}$$

and

$$\langle \hat{S}_{2,n}^z \rangle = (s_1 - s_2) - \langle \hat{S}_{1,n}^z \rangle \quad (45)$$

The various two-spin correlation functions decay exponentially with distance; the inverse correlation length is given by $\xi^{-1} = \ln(s_1/s_2)$. The results with dimerization ($\delta > 0$) are very similar. In fact, within spin-wave theory the minimum gap Δ to states with spin $S = S_G + 1$ is independent of δ .

We now use the powerful DMRG method to study the system defined by Eq. (40) both with and without dimerization $-\delta \neq 0$ and $\delta = 0$ respectively. We have considered alternating spin-3/2/spin-1 (hereafter denoted $(3/2, 1)$), spin-3/2/spin-1/2 (denoted $(3/2, 1/2)$), and spin-1/spin-1/2 (denoted $(1, 1/2)$) chains with open boundary condition for the Hamiltonian given by Eq. (40). We compute the ground-state properties for these three systems by studying chains with 80 to 100 sites. The number of dominant density matrix eigenstates, m , that we have retained at each DMRG iteration also varies between 80 to 100. With increasing Fock space dimensionality of the site spins, we increase m to obtain more accurate results. We follow the usual steps for the “infinite system” DMRG method discussed above [62, 66, 94], except that the alternating chains studied here are not symmetric between the left and right halves; hence the density matrixes for these two halves must be separately constructed at every iteration of the calculations. We have also verified the convergence of our results by varying the values of m and the system size.

The ground states of all the systems lie in the $S^z = N(s_1 - s_2)$ sector, as verified from extensive checks performed by obtaining the low-energy eigenstates in different S^z sectors of a 20-site chain. A state corresponding to the lowest energy in $S^z = N(s_1 - s_2)$ is found in all subspaces with $|S^z| \leq N(s_1 - s_2)$, and is absent in subspaces with $|S^z| > N(s_1 - s_2)$. This shows that the spin in the ground state is $S_G = N(s_1 - s_2)$. (Actually, the lowest energy states in the different S^z sectors are found to be degenerate only up to $10^{-5}J$. Such small errors are negligible when studying thermodynamics at temperatures higher than, say, $10^{-2}J$).

In Fig. 14, we show the expectation value of site-spin operator $\hat{S}_{i,n}^z$ (spin density) at all the sites for the $(3/2, 1)$, $(3/2, 1/2)$, and $(1, 1/2)$ chains. The spin densities are uniform on each of the sublattices in the chain for all three systems. For the $(3/2, 1)$ chain the spin density at a spin-3/2 is 1.14427 (the classical value is $3/2$), whereas at spin-1 site it is -0.64427 (classical value 1). For the $(3/2, 1/2)$ chain the spin density at a spin-3/2 site is 1.35742 and at a spin-1/2 site it is -0.35742 . For the $(1, 1/2)$ chain the value at a spin-1 site is 0.79248 and at a spin-1/2 site it is -0.29248 . These can be compared with the spin-wave values of 1.040 and -0.540 ; 1.314 and -0.314 ; and 0.695 and -0.195 for the spin- s_1 and spin- s_2 sites of the $(3/2, 1)$, $(3/2, 1/2)$, and $(1, 1/2)$ systems, respectively. We note that the spin-wave analysis overestimates the quantum fluctuations for systems with small site-spin values. We also notice that there is a greater quantum fluctuation when the difference between site spins, $|s_1 - s_2|$ is larger. This is also seen in spin-wave theory. The spin density distribution in an alternating (s_1, s_2) chain is more similar to that of a ferromagnetic chain than to that of an antiferromagnet, with the net spin of each unit cell perfectly aligned (but with small quantum fluctuations on the individual sublattices). In a ferromagnetic ground state, the spin density at each site has the classical value appropriate to the site spin, whereas for an antiferromagnet this averages out to zero at each site, because the ground state is non-magnetic. From this standpoint the ferrimagnet is similar to a ferromagnet and is quite unlike an antiferromagnet. The spin-wave analysis also yields the same physical picture.

Because of the alternation of spin- s_1 and spin- s_2 sites along the chain, one must distinguish between three different types of pair correlation, $\langle \hat{S}_{1,0}^z \hat{S}_{1,n}^z \rangle$, $\langle \hat{S}_{2,0}^z \hat{S}_{2,n}^z \rangle$ and $\langle \hat{S}_{1,0}^z \hat{S}_{2,n}^z \rangle$. We calculate all the three correlation functions with the mean val-

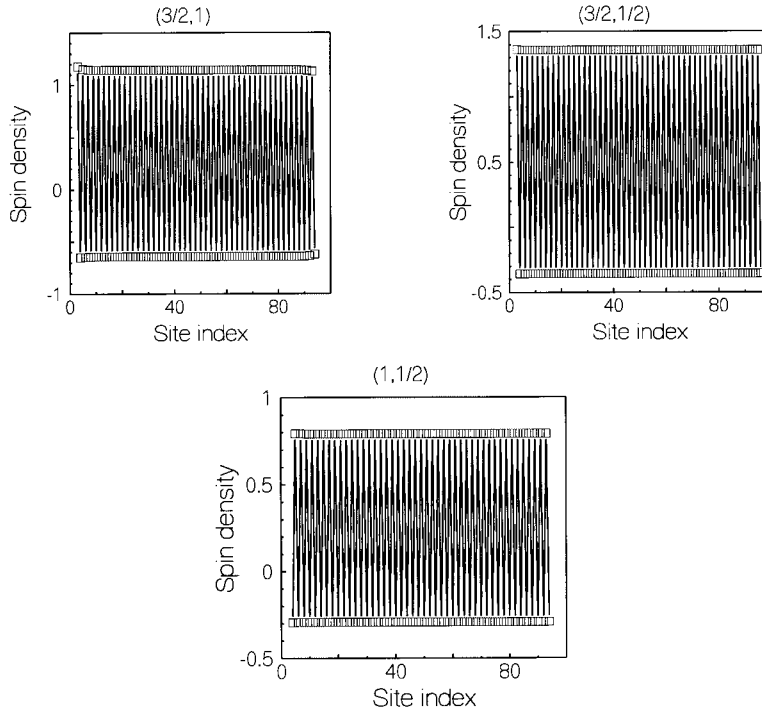


Fig. 14. Expectation values of the z-components of the two spins vs the unit cell index, n , for an alternating spin chain. The upper and lower points are for the spin- s_1 and the spin- s_2 sites respectively.

ues removed by subtraction, because the mean values are non-zero in all these three systems, in contrast with pure antiferromagnetic spin chains. In the DMRG procedure we have computed these correlation functions from the sites inserted at the last iteration, to minimize numerical errors. In Fig. 15, we plot the two-spin correlation functions in the ground state as a function of the distance between the spins for an open chain of 100 sites for all three cases. All three correlation functions decay rapidly with distance for each of the three systems. From the figure it is clear that, except for the $\langle \hat{S}_{1,0}^z \hat{S}_{2,n}^z \rangle$ correlation, the correlations are all almost zero, even for the shortest possible distances. The $\langle \hat{S}_{1,0}^z \hat{S}_{2,n}^z \rangle$ correlation has an appreciable value [-0.2 for $(3/2, 1)$, -0.07 for $(3/2, 1/2)$, and -0.094 for $(1, 1/2)$] only for the nearest neighbors. This rapid decay of the correlation functions makes it difficult to find the exact correlation length ξ for a lattice model, although it is clear that ξ is very small (less than one unit cell) for the $(3/2, 1/2)$ and $(1, 1/2)$ cases, and a little larger ($1 < \xi < 2$) for the $(3/2, 1)$ system. Spin-wave theory gives $\xi = 2.47$ for $(3/2, 1)$, $\xi = 0.91$ for $(3/2, 1/2)$, and $\sim \xi 1.44$ for $(1, 1/2)$ cases. (We should remark here that our ξ is not to be confused with the conventional definition of the correlation length; the latter is actually infinite in these systems, because of the long-range ferrimagnetic order).

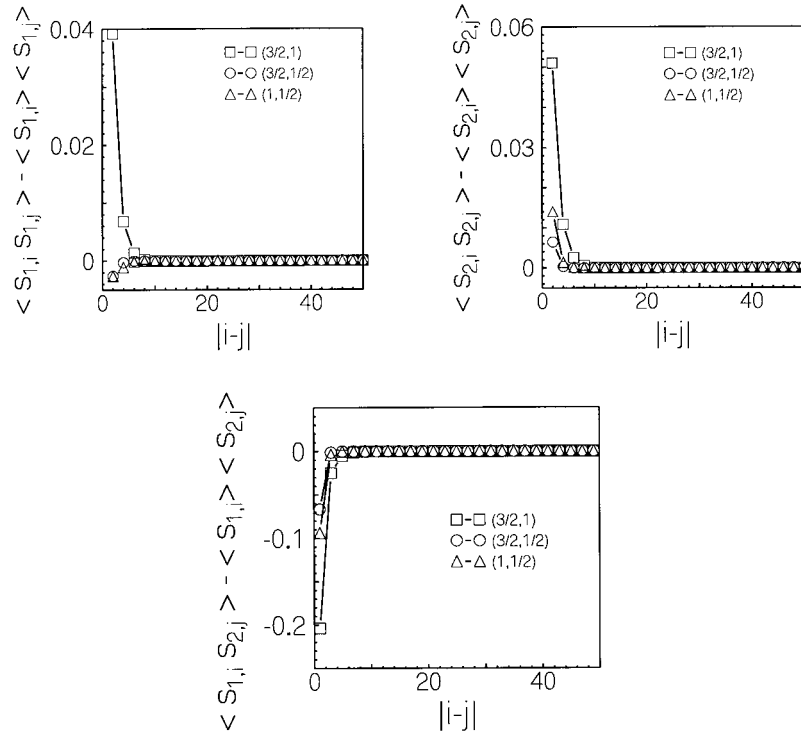


Fig. 15. Subtracted two-spin correlation functions as a function of distance between the two spins. (a) spin- s_1 -spin- s_1 correlations, (b) spin- s_2 -spin- s_2 correlations, and (c) spin- s_1 -spin- s_2 correlations. In each figure, squares correspond to $(3/2, 1)$, circles to $(3/2, 1/2)$, and triangles to $(1, 1/2)$ systems.

The lowest spin excitation of all three chains is to a state with $S = S_G - 1$. To study this state we target the 2nd state in the $S^z = S_G - 1$ sector of the chain. To confirm that this state is a $S = S_G - 1$ state we have computed the 2nd state in the $S^z = 0$ sector and find that it also has the same energy. The corresponding state is, however, absent in S^z sectors with $|S^z| > S^G - 1$. Also, from exact diagonalization of all the states of all the $s_1 - s_2$ alternating spin chains with eight sites we find that the energy ordering of the states is such that the lowest excitation is to a state with spin $S = S_G - 1$. We have obtained the excitation gaps for all three alternating spin chains in the limit of infinite chain length by extrapolating from the plot of spin gap against the inverse of the chain length (Fig. 16). We find that this excitation is gapless in the infinite chain limit for all three cases.

To characterize the lowest spin excitations completely, we also have computed the energy of the $S = S_G + 1$ state by targeting the lowest state in the $S^z = S_G + 1$ sector. In Fig. 17 we have plotted the excitation gaps to the $S = S_G + 1$ state from the ground state for all three systems as a function of the inverse of the chain length. The gap saturates to a finite value of $(1.0221 \pm 0.0001)J$ for the $(3/2, 1)$ case,

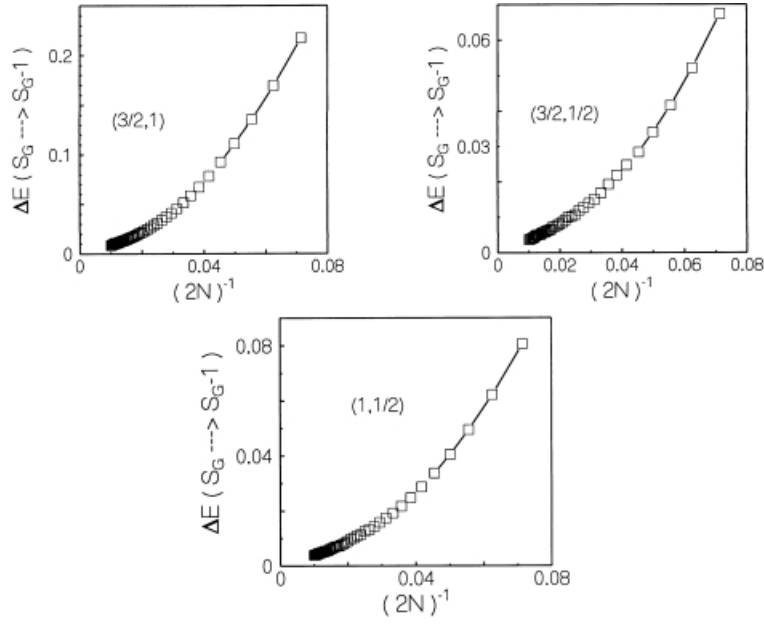


Fig. 16. Energy difference (units of J) between the ground state and the lowest energy state with spin $S = S_G - 1$ as a function of inverse system size. S_G is the total spin of the ground state.

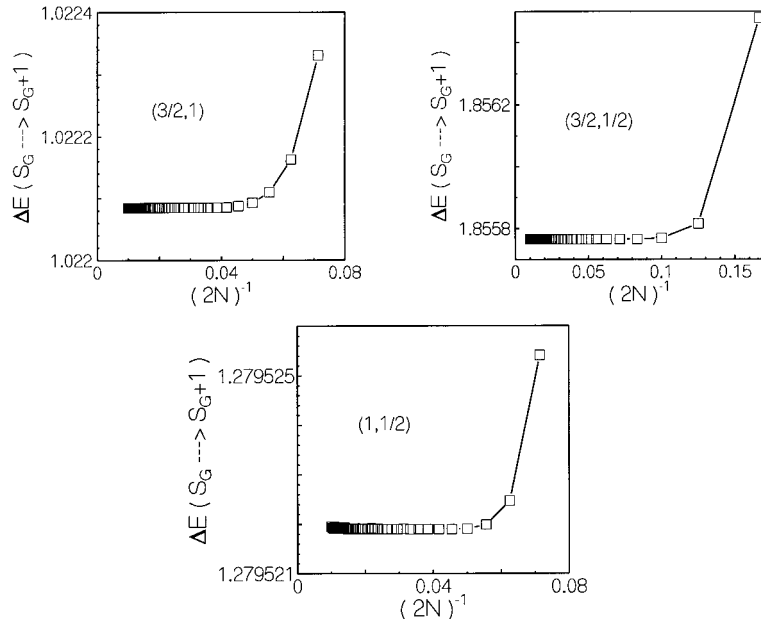


Fig. 17. Excitation gap (units of J) from the ground state (spin $S = S_G$) to the state with spin $S = S_G + 1$, as a function of the inverse system size.

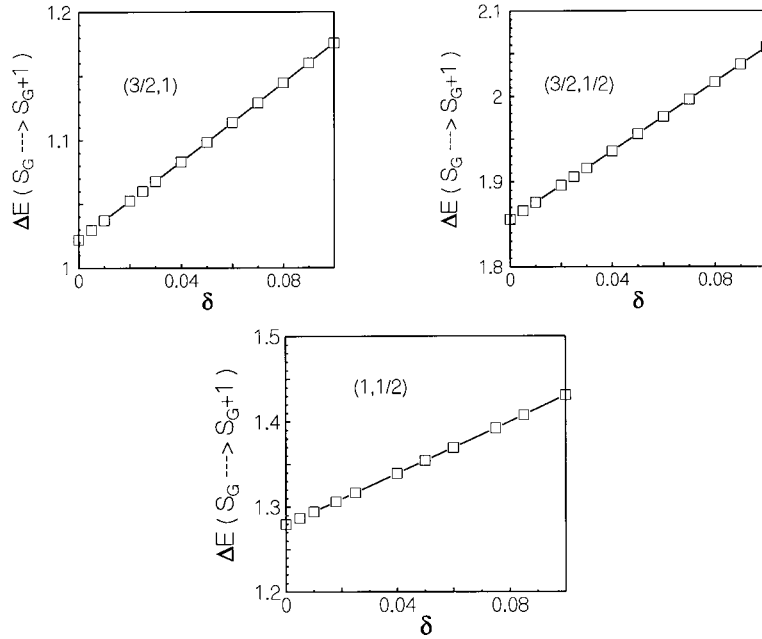


Fig. 18. Excitation gap (units of J) to the state with spin $S = S_G + 1$ from the ground state ($S = S_G$) as a function of δ for the dimerized alternating chain. The exponent is 1.0 ± 0.01 for all three systems.

$(1.8558 \pm 0.0001)J$ for $(3/2, 1/2)$, and $(1.2795 \pm 0.0001)J$ for $(1, 1/2)$. It seems that the gap is also higher when the difference in site spins, $|s_1 - s_2|$, is larger. The site spin densities expectation values computed in this state for all three cases are found to be uniform (i. e. independent of the site) on each of the sublattices. This leads us to believe that this excitation cannot be characterized as the states of a magnon confined in a box, as has been observed for a spin-1 chain in the Haldane phase [67].

We have also studied the spin excitations in the dimerized alternating (s_1, s_2) chains, defined in Eq. (40). We calculate the lowest spin excitation to the $S = S_G - 1$ state from the ground state. We find that the $S = S_G - 1$ state is gapless from the ground state for all values of δ . This result agrees with the spin-wave analysis of the general (s_1, s_2) chain. The systems remain gapless even while dimerized unlike the pure antiferromagnetic dimerized spin chains. There is a smooth increase of the spin excitation gap from the ground state to the $S = S_G + 1$ state with increasing δ for all three systems studied here. We have plotted this gap against δ in Fig. 18. The gap has almost linear behavior as a function of δ , with an exponent of 1.0 ± 0.01 for all three systems. This seems to be an interesting feature of all ferrimagnets. The spin-wave analysis shows, however, that this excitation gap is independent of δ for the general (s_1, s_2) chain. The similar behavior of these three alternating spin systems suggests that a ferrimagnet can be considered as a ferromagnet with small quantum fluctuations.

4.7.2 Low-temperature Thermodynamic Properties

We have varied the size of the system from 8 to 20 sites to calculate the thermodynamic properties. We imposed periodic boundary conditions to minimize finite size effects with $\hat{S}_{1,N+1} = \hat{S}_{1,1}$, so that the number of sites is equal to the number of bonds. We set up the Hamiltonian matrixes in the DMRG basis for all allowed S^z sectors for a ring of $2N$ sites. We can diagonalize these matrixes completely to obtain all the eigenvalues in each of the S^z sectors. As the number of DMRG basis states increases rapidly with increasing m , we retain a smaller number of dominant density matrix eigenvectors in the DMRG procedure, i. e. $50 \leq m \leq 65$, depending on the S^z sector and the size of the system. We have checked the dependence of properties (with m in the range $50 \leq m \leq 65$) for the system sizes we have studied ($8 \leq 2N \leq 20$), and have confirmed that the properties do not vary significantly for the temperatures at which they are computed; this is true for all three systems.

It might appear surprising that the DMRG technique which essentially targets a single state, usually the lowest energy state in a chosen S^z sector, should provide accurate thermodynamic properties, because these properties are governed by the energy level spacings and not by the absolute energy of the ground state. There are, however, two reasons why the DMRG procedure yields reasonable thermodynamic properties at low temperatures. First, the projection of the low-lying excited state eigenfunctions on the DMRG space which contains the ground state is substantial; hence these excited states are well described in the chosen DMRG space. Second, the low-lying excitations of the full system are often the lowest energy states in different sectors in the DMRG procedure; hence their energies are quite accurate even on an absolute scale.

The canonical partition function Z for the $2N$ site ring can be written as:

$$Z = \sum_j e^{-\beta(E_j - B(M)_j)} \quad (46)$$

where the sum is over all the DMRG energy levels of the $2N$ site system in all the S^z sectors. E_j and $(M)_j$ denote the energy and the \hat{z} -component of the total spin of the state j , and B is the strength of the magnetic field in units of $1/g\mu_B$ (g is the gyromagnetic ratio and μ_B is the Bohr magneton) along the \hat{z} direction. The field-induced magnetization $\langle M \rangle$ is defined as:

$$\langle M \rangle = \frac{\sum_j (M)_j e^{-\beta(E_j - B(M)_j)}}{Z} \quad (47)$$

The magnetic susceptibility χ is related to the fluctuation in magnetization:

$$\chi = \beta[\langle M^2 \rangle - \langle M \rangle^2] \quad (48)$$

Similarly, the specific heat C_V is related to the fluctuation in the energy and can be written as:

$$\frac{C_V}{k_B} = \beta^2[\langle E^2 \rangle - \langle E \rangle^2] \quad (49)$$

In the discussion to follow we present results on the 20-site ring, although all calculations have been performed for system sizes from 8 to 20 sites. This is because the qualitative behavior of the properties we have studied are similar for all the ring sizes in this range for all three systems.

The dependence of magnetization on temperature for different magnetic field strengths is shown in Fig. 19 for all three systems. At low magnetic fields the magnetization decreases sharply at low temperatures and has paramagnetic behavior at high temperatures. As the field strength is increased, the magnetization decreases more slowly with temperature, and for high field strengths the magnetization has a broad maximum. This behavior can be understood from the type of spin excitations present in these systems. The lowest energy excitation at low magnetic fields is to a state with spin s less than S_G , so the magnetization initially decreases at low temperatures. As the field strength is increased the gap to spin states with $S > S_G$ decreases as the Zeeman coupling to these states is stronger than to states with $S \leq S_G$. The critical field strengths at which the magnetization increases with temperature varies from system to system, because this corresponds to the lowest spin gap of the corresponding system. The behavior of the system at even stronger fields turns out to be remarkable. The magnetization in the ground state ($T = 0$) increases abruptly, signalling that the ground state at this field strength has $S^z > S_G$. The temperature-

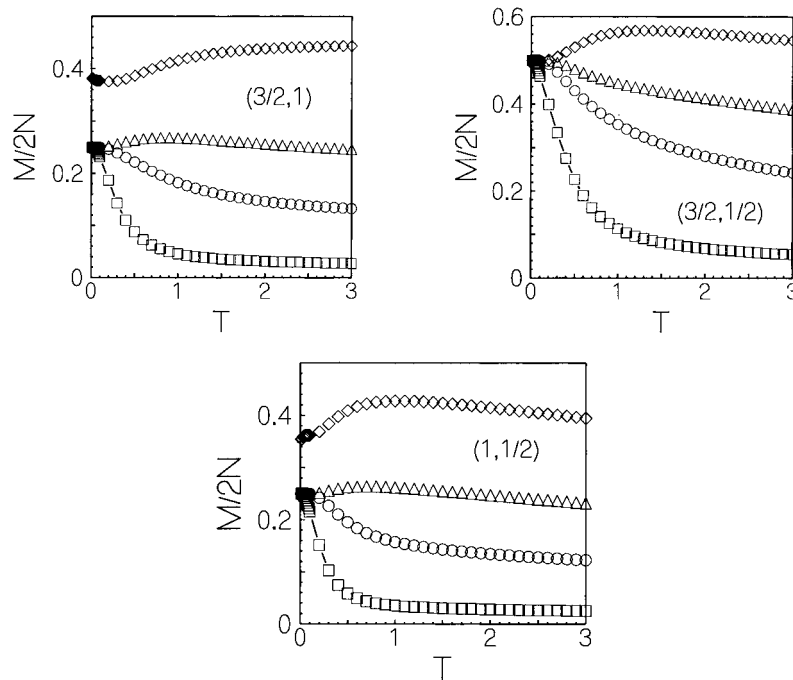


Fig. 19. Plot of magnetization per site as a function of temperature, T , for four different values of the magnetic field B . Squares are for $B = 0.1J/g\mu_B$, circles for $B = 0.5J/g\mu_B$, triangles for $B = J/g\mu_B$, and diamonds for $B = 2J/g\mu_B$.

dependence of the magnetization has a broad maximum, indicating the presence of states with even higher spin values lying above the ground state in the presence of this strong field. In all three cases, the ground state at very high field strengths should be ferromagnetic. For the systems at such high fields, the magnetization decreases slowly with increasing temperature because no other higher spin states lies above the ground state. Although we have not studied such high-field behavior, we find that the field strength corresponding to switching the spin of the ground state s_G to $s_G + 1$ is higher for the $(3/2, 1/2)$ system compared with the $(3/2, 1)$ and $(1, 1/2)$ systems. The switching field seems to depend on the value of $|s_1 - s_2|$. We see in Fig. 19 that for the $(3/2, 1)$ and $(1, 1/2)$ cases the ground state has switched to the higher spin state at the highest magnetic field strength we have studied but that in the $(3/2, 1/2)$ case the ground state has not switched even at the field strength, indicating that the excitation gap for this system is larger than for the other two. For the $(3/2, 1/2)$ case the same situation should occur at very high magnetic fields. Thus, we predict that the highest S^z is attained in the ground state at high magnetic field and that this field strength increases with increasing site-spin difference $|s_1 - s_2|$.

The dependence of $\chi T/2N$ on temperature for different field strengths is shown in Fig. 20 for all three systems. For zero field the zero temperature value of χT is infinite in the thermodynamic limit; for finite rings it is finite and equal to the av-

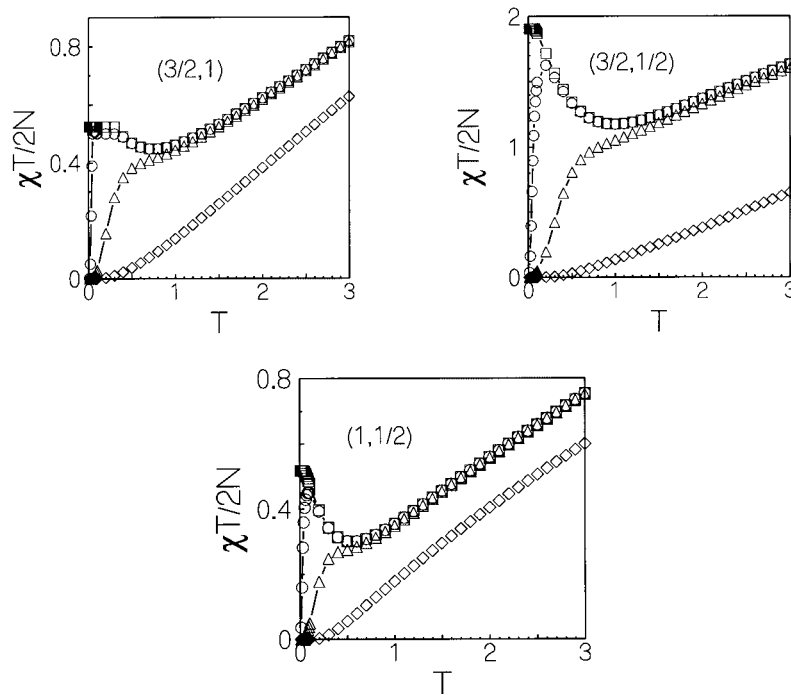


Fig. 20. χT (defined in the text) per site as a function of temperature T for different magnetic fields B . Zero field results are shown by squares, $B = 0.01J/g\mu_B$ by circles, $B = 0.1J/g\mu_B$ by triangles, and $B = J/g\mu_B$ by diamonds.

erage of the square of the magnetization in the ground state. For the ferrimagnetic ground state $\chi T/2N$, as $T \rightarrow 0$, is given by $S_G(S_G + 1)/6N$. As the temperature increases this product decreases and passes through a minimum before increasing again. For the three systems studied here the minimum occurs at different temperatures depending on the system. For the $(3/2, 1)$ alternating-spin system it is at $k_B T = (0.8 \pm 0.1)J$, whereas for the $(3/2, 1/2)$ and $(1, 1/2)$ systems it occurs at $k_B T = (1.0 \pm 0.1)J$ and $k_B T = (0.5 \pm 0.1)J$, respectively. These results agree well with previous numerical calculations on small system sizes [95]. The minimum occurs because states with $S^z < S_G$ become populated at low temperatures. In the infinite chain limit, these states turn out to be the gapless excitations of the system. The subsequent increase in the product χT is because of the higher energy-higher spin states being accessed with further increase in temperature. This increase is slow for the $(3/2, 1/2)$ case, because in this system very high spin states are not accessible within the chosen temperature range. It has been found experimentally in the bimetallic chain compounds that the temperature at which the minimum occurs in the χT product depends on the magnitudes of the spins s_1 and s_2 [93]. The $\text{Ni}^{II}-\text{Cu}^{II}$ bimetallic chain has a minimum in $\chi T/2N$ at a temperature corresponding to 55 cm^{-1} (80 K); an independent estimate of the exchange constant in this system is 100 cm^{-1} [96]. This is in very good agreement with the minimum theoretically found at the temperature $(0.5 \pm 0.1)J$ for the $(1, 1/2)$ case. Drillon et al. also found the minimum to be at $T = 0.5J$ for the $(1, 1/2)$ system [97]. The minimum in $\chi T/2N$ vanishes at $B = 0.1J/g\mu_B$ which corresponds to approximately $10T$ for all three systems. It would be interesting to study the magnetic susceptibility of these systems experimentally under the action of such high fields. The low-temperature zero-field behavior of our systems can be compared with that of the one-dimensional ferromagnet. In the latter the spin-wave analysis shows that the product χT increases in proportion to $1/T$ at low temperatures [98].

In finite but weak fields, the behavior of χT is different. The magnetic field opens up a gap and χT falls exponentially to zero for temperatures less than the gap in the applied field for all three systems. Even in this case a minimum is found at the same temperature as in the zero-field case for the corresponding system, for the same reason as discussed in the zero field case.

In stronger magnetic fields, the behavior of χT from zero temperature up to $k_B T = J_{\min}$ (J_{\min} is the temperature at which the minimum in χT is observed) is qualitatively different. The minimum in this case vanishes for all three systems. At these field strengths the states with higher S^z values are accessed even below $k_B T = J_{\min}$. The dependence of χT above $k_B T = J_{\min}$ at all field strengths is the same in all three systems. In even stronger magnetic fields, the initial sharp increase is suppressed. At very low temperature the product χT is nearly zero and increases almost linearly with T over the temperature range we have studied. This can be attributed to a switch in the ground state at this field strength. The very-high-temperature behavior of χT should be independent of field strength and should saturate to the Curie law value corresponding to the mean of magnetic moments due to spin- s_1 and spin- s_2 .

The temperature dependence of specific heat is also markedly dependent on the magnetic field at strong fields. This dependence is shown in Fig. 21 for a variety

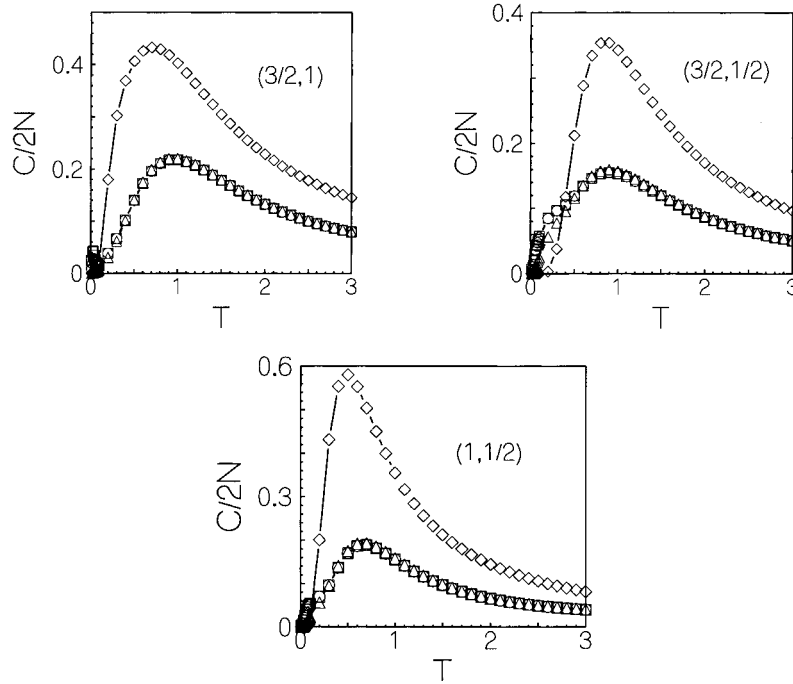


Fig. 21. Specific heat per site as a function of temperature T for four different values of the magnetic field B . Zero field data are shown by squares, $B = 0.01J/g\mu_B$ by circles, $B = 0.1J/g\mu_B$ by triangles, and $B = J/g\mu_B$ by diamonds.

of field strengths and for all three systems. In zero and weak magnetic fields the specific heat has a broad maximum at different temperatures which are specific to the system. Interestingly, the temperature at which the specific heat is maximum corresponds closely to the temperature where the low-field χT is minimum for the corresponding system. For a strong magnetic field ($B \approx J$), there is a dramatic increase in the peak height at approximately the same temperature corresponding to the specific system, although the qualitative dependence is still the same as at low magnetic fields in all three cases. This phenomenon indicates that the higher-energy high-spin states are brought to within $k_B T$ of the ground state at this magnetic field strength for all three cases.

Studies of the thermodynamic properties of the dimerized alternating spin chains in these three cases reveal trends qualitatively similar to that of the corresponding uniform systems; this is because the low-energy spectrum does not change qualitatively upon dimerization.

4.8 Magnetization Properties of a Spin Ladder

As mentioned above, a quantum spin system are sometimes characterized by magnetization plateaus as a function of an applied magnetic field [37–45]. In this section, we will use the finite system DMRG method to study the magnetic properties of a three-legged spin-1/2 ladder [99]. We consider the Hamiltonian:

$$\hat{H} = J' \sum_a \sum_n \hat{S}_{a,n} \cdot \hat{S}_{a+1,n} + J \sum_{a=1}^3 \sum_n \hat{S}_{a,n} \cdot \hat{S}_{a,n+1} - h \sum_{a=1}^3 \sum_n \hat{S}_{a,n}^z \quad (50)$$

where a denotes the chain index, n denotes the rung index, h denotes the magnetic field (we have absorbed the gyromagnetic ratio g and the Bohr magneton μ_B in the definition of h), and $J, J' > 0$. It is convenient to scale out the parameter J , and quote all results in terms of the two dimensionless quantities J'/J and h/J . If the length of each chain is L , the total number of sites is $N = 3L$. Because the total \hat{S}^z is a good quantum number, it is more convenient to perform the numerical computations without including the magnetic-field term in Eq. (50), and then to add the effect of the field at the end of the computation. For the ground-state properties we have only considered an open boundary condition (OBC) in the rung direction, namely summation over a in the first term of Eq. (50) runs over 1, 2. For low-temperature properties, however, we have studied both OBC and a periodic boundary condition (PBC) in the rung direction in which we sum over $a = 1, 2, 3$ in the first term.

We have performed DMRG calculations (using the finite system algorithm [62]) with open boundary conditions in the chain direction. We have gone up to 120 sites, i. e. a chain length of 40. The number of dominant density matrix eigenstates, corresponding to the m largest eigenvalues of the density matrix, that we retained at each DMRG iteration was $m = 80$. We varied the value of m from 60 to 100 and found that $m = 80$ gives satisfactory results in terms of agreement with exact diagonalization for small systems and good numerical convergence for large systems. For inputting the values of the couplings into the numerical programs, it is more convenient to think of the system as a single chain (rather than as three chains) with the Hamiltonian:

$$\hat{H} = \frac{2}{3} J' \sum_i \left[1 - \cos\left(\frac{2\pi i}{3}\right) \right] \hat{S}_i \cdot \hat{S}_{i+1} + J \sum_i \hat{S}_i \cdot \hat{S}_{i+3} \quad (51)$$

The system is grown by adding two new sites at each iteration. Note that our method of construction ensures that we obtain the three-chain ladder structure after every third iteration when the total number of sites becomes a multiple of 6. For different system sizes, starting from 48 sites and going up to 120 sites in multiples of 6 sites, we computed the energies after doing three finite system iterations; we found that the energy converges very well after three iterations. The energy data are used in Figs. 22 and 23 below. After reaching 120 sites we computed the spin correlations after doing three finite system iterations. This data are used in Figs. 24

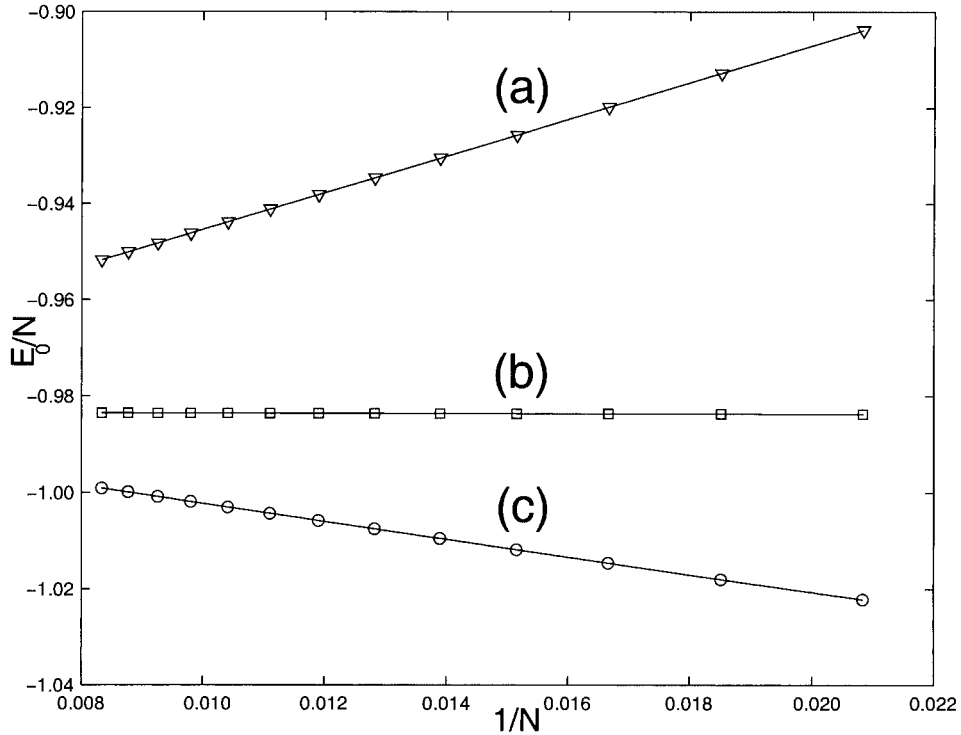


Fig. 22. The energy/site in units of J against $1/N$ at the $m_s = 1/2$ plateau, for the three-chain ladder with $J/J' = 1/3$. The curves indicate quadratic fits for (a) $E_0(M + 1, N)$, (b) $E_0(M, N)$, and (c) $E_0(M - 1, N)$.

and 25. All our numerical results quoted below are for $J/J' = 1/3$. We chose this particular value of the ratio because there is a particularly broad magnetization plateau at $m_s = 1/2$ which can be easily found numerically.

We now describe the variety of ground-state properties we have found with OBC along the rungs. We looked for magnetization plateaus at $m_s = 0, 1/2$, and 1. For a system with N sites, a given value of magnetization per rung m_s corresponds to a sector with total S^z equal to $M = m_s N/3$. By use of the infinite system algorithm we found the lowest energies $E_0(S^z, N)$ in the three sectors $S^z = M + 1, M$, and $M - 1$. Then we examined the three plots of E_0/NJ against $1/N$ and extrapolated the results to the thermodynamic limit $N \rightarrow \infty$. We fitted these plots with the formula $E_0/NJ = e_i + a_i/N + b_i/N^2$ where the label $i = 1, 2, 3$ denotes the S^z sectors $M + 1, M$, and $M - 1$. In the thermodynamic limit the values of the three intercepts e_i should match, because those are just the energy per site for the three states whose S^z values differ by only unity. However, the three slopes a_i are not equal in general. We now show that there is a magnetization plateau if $a_1 + a_3 - 2a_2$ has a non-zero value. Because the three energies E_0 are computed without including the magnetic field term, the upper critical field h_{c+} where the states with $S^z = M + 1$ and M

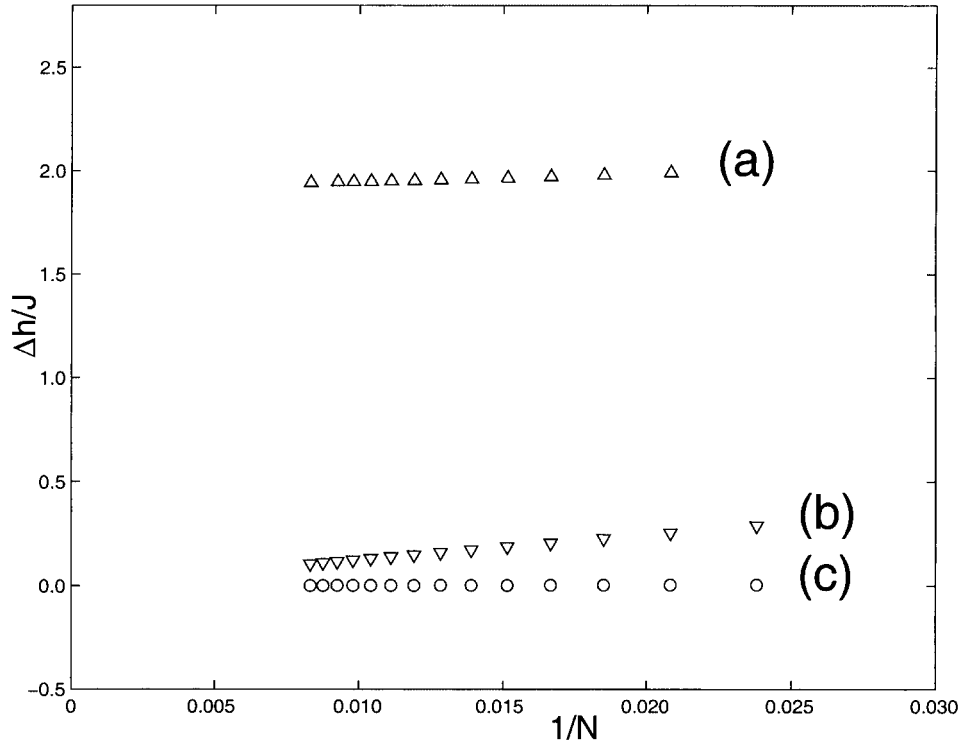


Fig. 23. Dependence of plateau widths on $1/N$ for (a) $m_s = 1/2$, (b) $m_s = 0$, and (c) $m_s = 1$.

become degenerate is given by:

$$h_{c+}(N) = E_0(M + 1, N) - E_0(M, N) \quad (52)$$

Similarly, the lower critical field h_{c-} where the states with $S^z = M$ and $M - 1$ become degenerate is given by:

$$h_{c-}(N) = E_0(M, N) - E_0(M - 1, N) \quad (53)$$

We therefore have a finite interval $\Delta h(N) = h_{c+}(N) - h_{c-}(N)$ in which the lowest energy state with $S^z = M$ is the ground state of the system with N sites in the presence of a field h . If this interval has a non-zero limit as $N \rightarrow \infty$ we have a magnetization plateau. Thus, in the thermodynamic limit, the plateau width $\Delta h/J$ is equal to $a_1 + a_3 - 2a_2$.

We will now quote our numerical results for $J/J' = 1/3$. For a rung magnetization of $m_s = 1/2$, i. e. $M = N/6$, we found the three slopes a_i to be equal to 3.77, -0.02 , and -1.93 (Fig. 22). This gives the upper and lower critical fields as:

$$\begin{aligned} h_{c+}/J &= a_1 - a - 2 = 3.79, \quad h_{c-}/J = a_2 - a_3 = 1.91, \\ h/J &= (h_{c+} + h_{c-})/J = 1.88 \end{aligned} \quad (54)$$

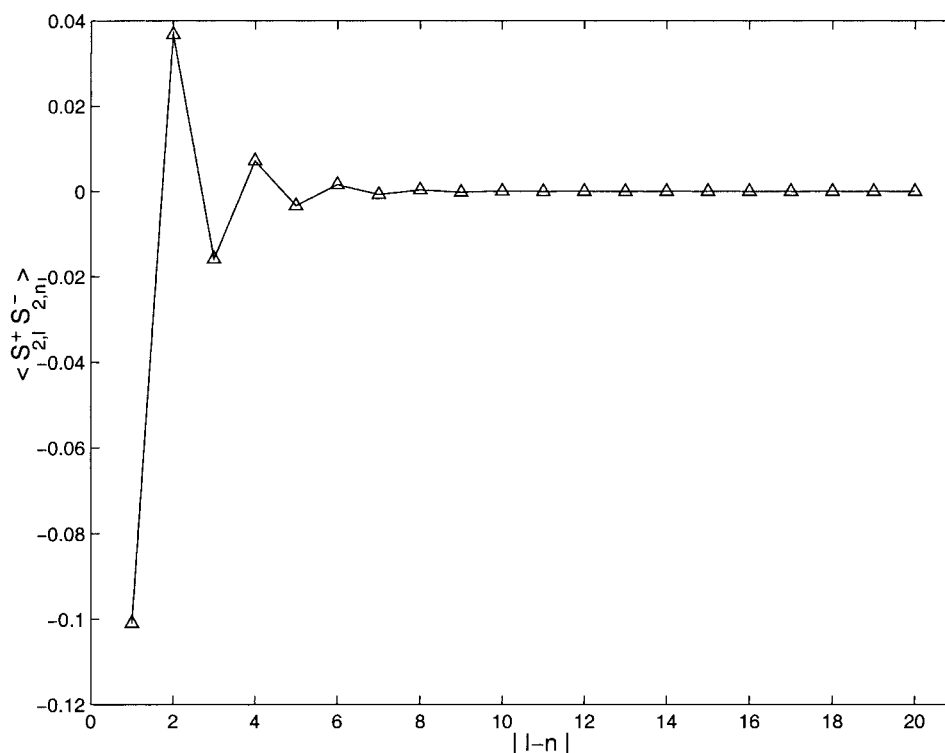


Fig. 24. Correlation function $\langle \hat{S}_{2,l}^+ \hat{S}_{2,n}^- \rangle$ at the $m_s = 1/2$ plateau for $J/J' = 1/3$.

This is a sizeable plateau width. For a rung magnetization of $m_s = 1$ we found the a_i to be equal to 4.97, -0.24 , and -5.43 . Thus the upper and lower critical fields are:

$$h_{c+}/J = 5.21, \quad h_{c-}/J = 5.19, \quad h/J = 0.02 \quad (55)$$

Finally, for a rung magnetization of $m_s = 0$, we need the energies of states with $M = 0$ and $M = \pm 1$. Because the last two states must have the same energy, we have $a_1 = a_3$ and it is sufficient to plot only $E_0(0, N)$ and $E_0(1, N)$ against $1/N$. We found a_1 and a_2 to be equal to 0.39 and 0.34. Thus the upper and lower critical fields are:

$$h_{c+}/J = 0.05, \quad h_{c-}/J = -0.05, \quad h/J = 0.10 \quad (56)$$

The plateau widths given in Eqs. (55) and (56) are rather small. In Fig. 23 we give the plateau widths $\Delta h(N)/J$ as a function of $1/N$ for $m_s = 1/2, 0$ and 1 .

Next, we computed various two-spin correlations for the 120-site system. These are denoted by $\langle \hat{S}_{a,l}^z \hat{S}_{b,n}^z \rangle$ and $\langle \hat{S}_{a,l}^+ \hat{S}_{b,n}^- \rangle$. For the zz correlations it is convenient to subtract the product of the two separate spin densities. At $m_s = 1/2$ we found that

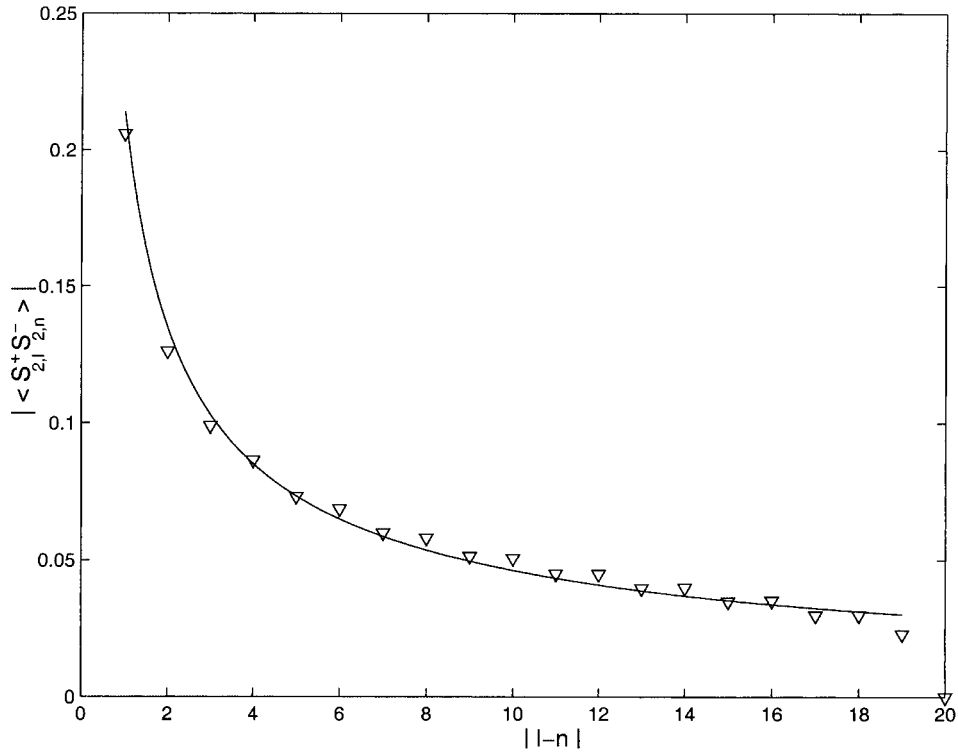


Fig. 25. Correlation functions $\langle \hat{S}_{1,l}^+ \hat{S}_{2,n}^- \rangle$ in the $m_s = 1$ state for $J/J' = 1/3$.

all these correlations decay very rapidly to zero as the rung separation $|l-n|$ grows. In fact, the fall offs were so fast that we were unable to compute sensible correlation lengths. The correlation lengths are of the order of one or two rungs, as is apparent from Fig. 24.

For the state at $m_s = 0$, on the other hand, we found that all the correlations decay quite slowly. The decays are consistent with power law fall offs of the form $A(-1)^{|l-n|}/|l-n|^\eta$. It is difficult to find η very accurately because the maximum value of $|l-n|$ is only 20; this is because we fixed one site to be in the middle of the chain (to minimize edge effects), and the maximum chain length is 40 for our DMRG calculations. For $m_s = 0$ the exponent η for all the correlations was found to be around 1. There was no difference in the behavior of the zz and $+-$ correlations, because this was an isotropic system; $m_s = 0$ is the ground state if the magnetic field is zero.

For the state at $m_s = 1$ (which is the ground state for a substantial value of the magnetic field only), we found that the $+-$ correlations again decay quite slowly consistent with a power law. The exponents η for the different $+-$ correlations varied from 0.61 to 0.70 with an average value of 0.66; an example is given in Fig. 25.

We now describe some low-temperature thermodynamic properties of the three-chain system obtained using DMRG. Although DMRG is normally expected to be

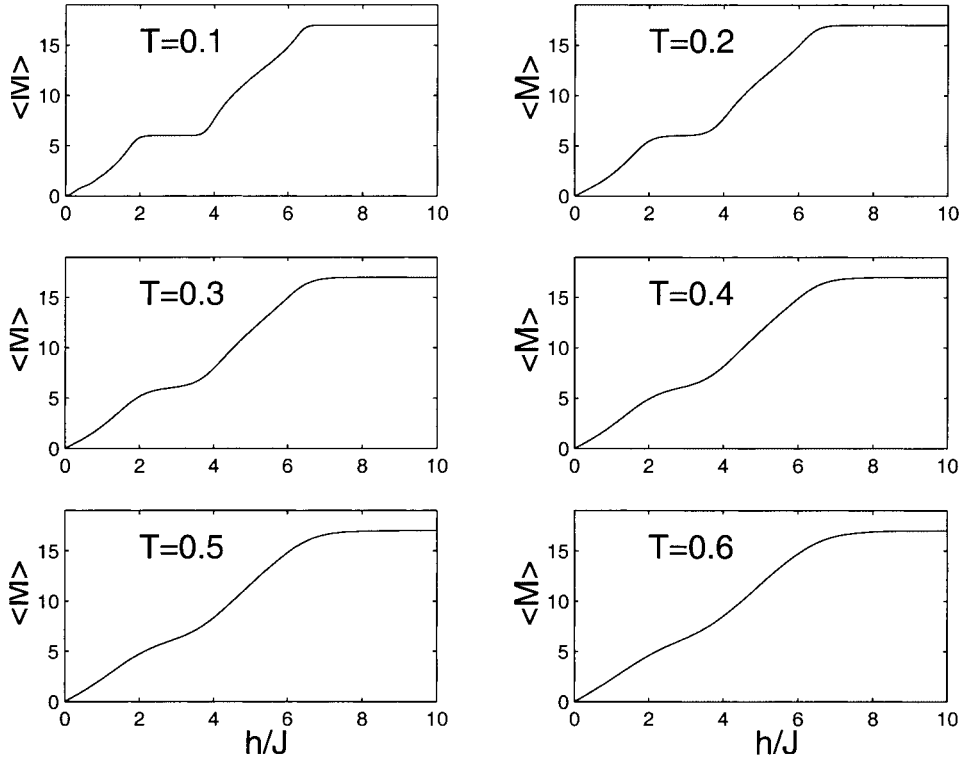


Fig. 26. Dependence of magnetization on magnetic field, at six different temperatures, for a 36-site system with OBC along the rungs and $J/J' = 1/3$.

most accurate for targeting the lowest states in different S^z sectors, earlier studies of mixed spin chains have shown that DMRG is quite reliable for computing low-temperature properties also [79]. There are two reasons for this; the low-lying excited states generally have a large projection on to the space of DMRG states which contains the ground state, and the low-lying excitations in one sector are usually the lowest states in nearby S^z sectors.

We first checked that for systems with 12 sites the results obtained by use of DMRG agree well with those obtained by exact diagonalization. We then used DMRG to study the magnetization, susceptibility, and specific heat of 36-site systems with both OBC and PBC along the rungs. We computed these quantities using the techniques described in Eqs. (46)–(49). The plots of magnetization against magnetic field for different temperatures are shown in Fig. 26 for OBC along the rungs. The temperature T is measured in units of J/k_B . We see that the plateau at $m_s = 1/2$ disappears quite rapidly as we increase the temperature. The plateau has almost disappeared at $T = 0.4$ which is substantially lower than the width $\Delta h/J = 1.88$. The magnetic susceptibility is (exponentially) small at low temperatures in the region of the plateau, because the magnetic excitations there are separated from the

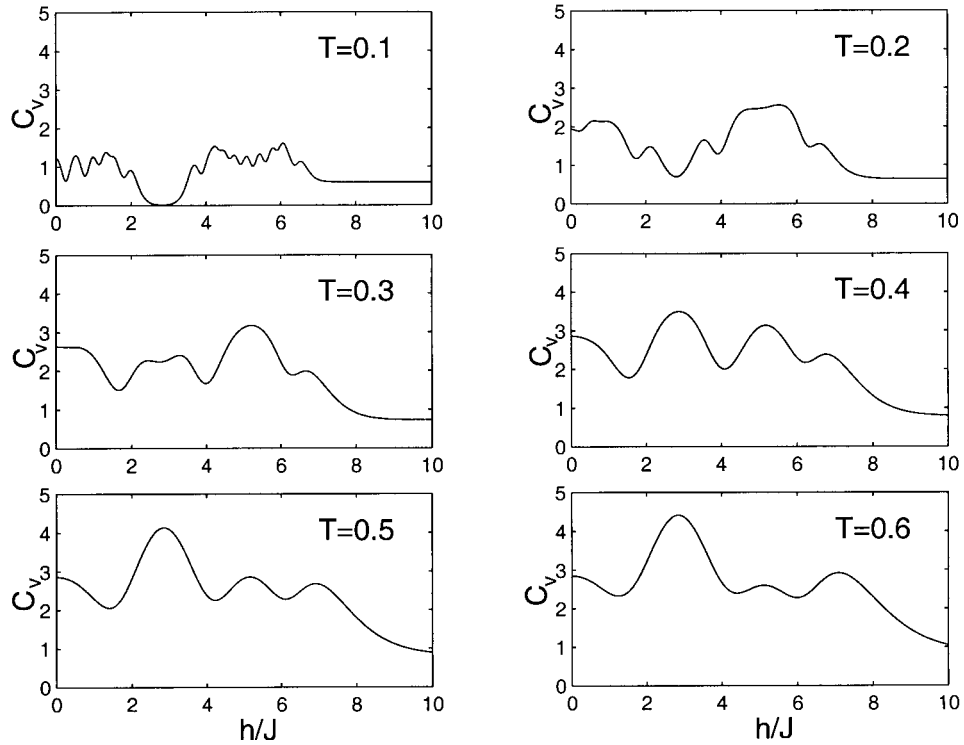


Fig. 27. Dependence of specific heat, in units of k_B , on magnetic field, at six different temperatures, for a 36-site system with OBC along the rungs and $J/J' = 1/3$.

ground state by a gap. Similar results for the magnetization and susceptibility are found for PBC along the rungs.

The specific heats at the $m_s = 1/2$ plateau, however, reveal an interesting difference between OBC and PBC along the rungs. Whereas it is very small at low temperatures for OBC (Fig. 27), it is not small for PBC, although a plateau is observed in the same range of magnetic fields as the magnetization itself. This observation strongly suggests that the system with PBC along the rungs has non-magnetic excitations which do not contribute to the magnetization or susceptibility, but do contribute to the specific heat. A more direct comparison between OBC and PBC along the rungs is shown in Fig. 28. Although these non-magnetic excitations have been studied by previous authors [38, 39, 100], we believe that our specific heat plots are the best physical evidence for their existence. To show these excitations even more explicitly, we present in Fig. 29 all the energy levels for a 12-site chain in the sector $S^z = 2$ (i. e. $m_s = 1/2$), using exact diagonalization. It is clear that the ground state is well separated from the excited states for OBC, but it is at the bottom of a band of excitations for PBC; these excitations are non-magnetic, because they have the same value of S^z as the ground state.

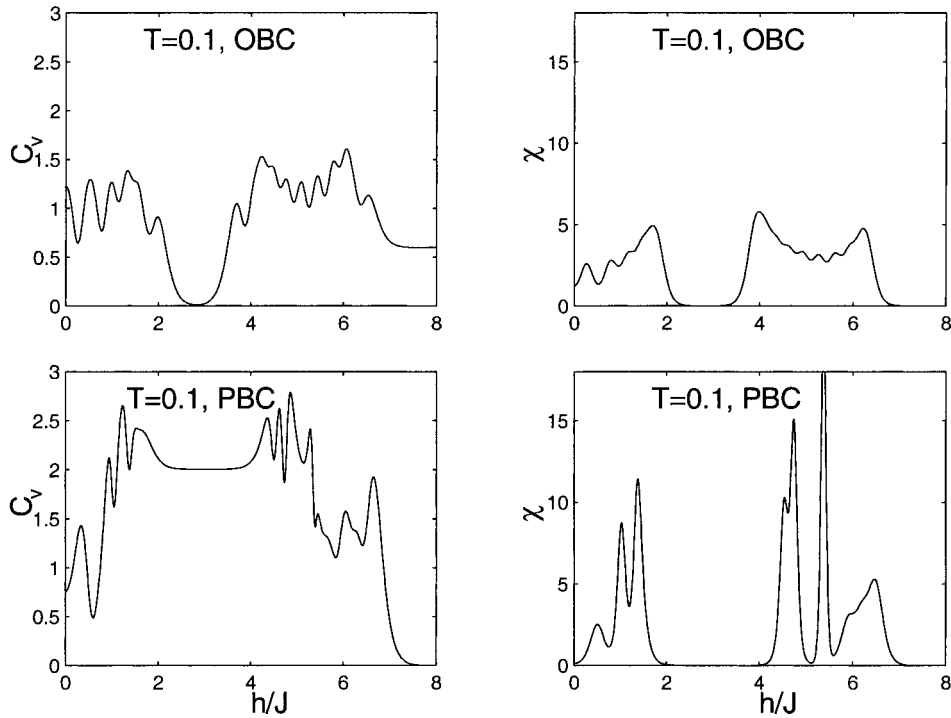


Fig. 28. Comparison of the dependence of specific heat and susceptibility on the magnetic field for a 36-site systems with OBC and PBC along the rungs.

We summarize our results for a three-chain spin-1/2 ladder with a large ratio of inter-chain coupling to intra-chain coupling. There is a wide plateau with rung magnetization given by $m_s = 1/2$ for both OBC and PBC along the rungs. For OBC the two-spin correlations are extremely short-ranged, and the magnetic susceptibility and specific heat are very small at low temperature in the plateau. All these are consistent with the large magnetic gap. At other values of m_s the two-spin correlations fall off as power laws. For PBC, the magnetic susceptibility is again very small at low temperature in the plateau. The specific heat, however, goes to zero much more slowly; this dramatically shows the presence of non-magnetic excitations.

To summarize this review, we have discussed a variety of numerical and analytical methods for studying spin clusters and quasi-one-dimensional spin systems. The methods discussed for spin clusters are directly relevant to areas of current interest, e. g. quantum tunneling in the presence of time-dependent magnetic fields [17–20, 95]. One-dimensional spin systems sometimes have unusual properties (e. g. a disordered ground state with an excitation gap above it) which are not observed in similar models in higher dimensions. The techniques described here, particularly the DMRG method, are well-suited to the study of extended systems in one dimension.

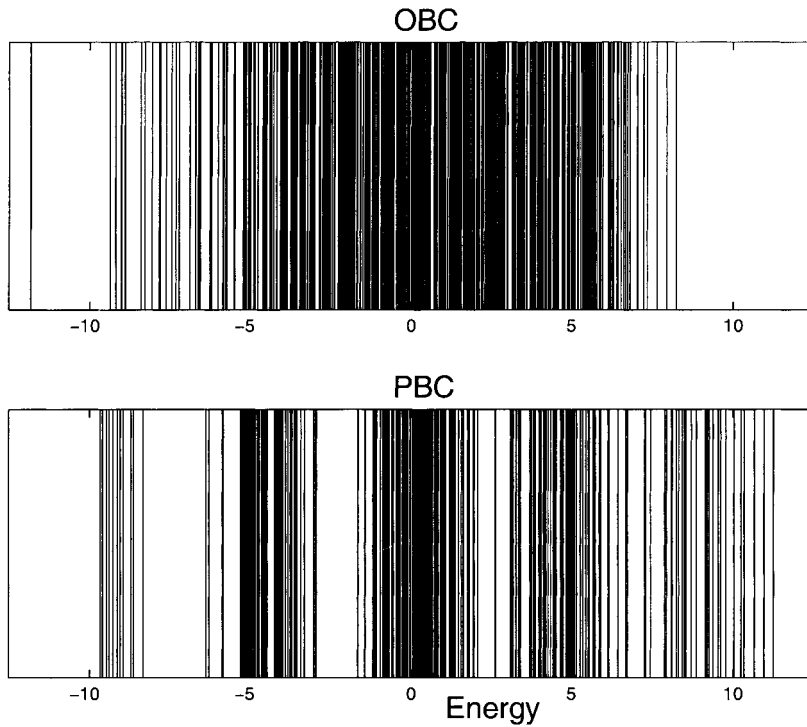


Fig. 29. Comparison of the energy spectra, in units of J , for the 12-site system with OBC and PBC along the rungs. The energies in the $S^z = 2$ sector are shown for $J/J' = 1/3$.

Acknowledgments

We thank H. R. Krishnamurthy, Sumathi Rao, R. Chitra, Y. Anusooya, Kunj Tandon, Siddhartha Lal, C. Raghu, and Indranil Rudra for several collaborations over the years. The work on mixed spin systems was motivated by discussions with the late Professor Olivier Kahn.

References

- [1] L.D. Landau, E.M. Lifshitz, *Quantum Mechanics: Non-Relativistic Theory*, 3rd edn., Pergamon, **1977**.
- [2] D.C. Mattis, *The Theory of Magnetism*, Vol. 1, Springer, Berlin, **1987**; R.M. White, *Quantum Theory of Magnetism*, 2nd edn., Springer, Berlin, **1983**.
- [3] B. Sinha, S. Ramasesha, *Phys. Rev. B* **1993**, *48*, 16410.
- [4] J.N. Bray, L.V. Interrante, J.S. Jacobs, J. C. Bonner. In: J.S. Miller (Ed.) *Extended Linear Chain Compounds*, Vol. III, Plenum, New York, **1982**.
- [5] G.T. Rado, H. Suhl (Eds) *Magnetism*, Academic Press, New York, **1963**.

- [6] Z.G. Soos, S. Ramasesha. In: D.J. Klein, N. Trinajstić (Eds.) *Valence Bond Theory and Chemical Structure*, Elsevier, Amsterdam, **1990**, p. 81.
- [7] C. Raghu, I. Rudra, D. Sen, S. Ramasesha, *Phys. Rev. B* **2001**, 64, 064419.
- [8] S. Rettrup, *J. Comput. Phys.* **1982**, 45, 100.
- [9] S. Ramasesha, Z.G. Soos, *J. Chem. Phys.* **1993**, 98, 4015.
- [10] T. De Neef, *Phys. Lett. A* **1974**, 47, 51.
- [11] H.J. Blote, *Physica B* **1978**, 93, 93.
- [12] R. Botet, R. Jullien, *Phys. Rev. B* **1983**, 27, 613; R. Botet, R. Jullien, M. Kolb, *Phys. Rev. B* **1983**, 28, 3914.
- [13] J.B. Parkinson, J.C. Bonner, *Phys. Rev. B* **1985**, 32, 4703.
- [14] A. Moreo, *Phys. Rev. B* **1987**, 35, 8562.
- [15] M. Takahashi, *Phys. Rev. Lett.* **1989**, 62, 2313; *Phys. Rev. B* **1993**, 48, 311.
- [16] O. Golinelli, Th. Jolicoeur, R. Racaze, *Phys. Rev. B* **1994**, 50, 3037.
- [17] E.M. Chudnovsky, *Science* **1996**, 274, 938.
- [18] W. Wernsdorfer, R. Sessoli, *Science* **1999**, 284, 133.
- [19] I. Chioresu, W. Wernsdorfer, A. Miffier, H. Bögge, B. Barbara, *Phys. Rev. Lett.* **2000**, 84, 15.
- [20] L. Gunther, B. Barbara (Eds.) *Quantum Tunneling of Magnetization – QTM'94*, NATO ASI Ser. E, Vol. 301, Kluwer, Dordrecht, **1995**; J.R. Friedman, M.P. Sarachik, J. Tejada, R. Ziolo, *Phys. Rev. Lett.* **1996**, 76, 3830; L. Thomas, F. Lioni, R. Ballou, D. Gatteschi, R. Sessoli, B. Barbara, *Nature* **1996**, 383, 145 and references cited therein; W. Wernsdorfer, R. Sessoli, *Science* **1999**, 284, 133.
- [21] D.N. Hendrickson, G. Christou, E.A. Schmitt, B. Libby, J.S. Baskin, S. Wang, H.L. Tsai, J.B. Vincent, W.P.D. Boyd, J.C. Haftman, K. Folting, Q. Li, W.E. Streib, *J. Am. Chem. Soc.* **1992**, 114, 2455 and references cited therein.
- [22] R. Sessoli, H.-L. Tsai, A.R. Schake, S. Wang, J.B. Vincent, K. Folting, D. Gatteschi, G. Christou and D.N. Hendrickson, *J. Am. Chem. Soc.* **1993**, 115, 1804.
- [23] M. Hennion, L. Pardi, I. Mirebeau, E. Surad, R. Sessoli, A. Caneschi, *Phys. Rev. B* **1997**, 56, 8819; A.A. Mukhin, V.D. Travkin, A.K. Zvezdin, S.P. Lebedev, A. Caneschi, D. Gatteschi, *Europhys. Lett.* **1998**, 44, 778.
- [24] P.A. Reynolds, E.P. Gilbert, B.N. Figgis, *Inorg. Chem.* **1996**, 35, 545.
- [25] S.M. Gorun, S.J. Lippard, *Inorg. Chem.* **1988**, 27, 149; W.H. Armstrong, M.E. Roth, S.J. Lippard, *J. Am. Chem. Soc.* **1987**, 109, 6318.
- [26] C.D. Delfs, D. Gatteschi, L. Pardi, R. Sessoli, K. Weighardt, D. Hanke, *Inorg. Chem.* **1993**, 32, 3099.
- [27] I. Tupitsyn, B. Barbara in: J. Miller, M. Drillon (Eds.), *Magnetism – From Molecules to Materials, Volume 3*, Wiley-VCH, **2001**.
- [28] Y. Pontillon, A. Caneschi, D. Gatteschi, R. Sessoli, E. Ressouche, J. Schweizer and E. Lelievre-Berna, *J. Am. Chem. Soc.* **1999**, 121, 5342.
- [29] F.D.M. Haldane, *Phys. Lett.* **1983**, 93A, 464; *Phys. Rev. Lett.* **1983**, 50, 1153.
- [30] W.J.L. Buyers, R.M. Morra, R.L. Armstrong, M.J. Hogan, P. Gerlach, K. Hirakawa, *Phys. Rev. Lett.* **1986**, 56, 371; J.P. Renard, M. Verdaguer, L.P. Regnault, W.A.C. Erkelens, J. Rossat-Mignod, W.G. Stirling, *Europhys. Lett.* **1987**, 3, 945; S. Ma, C. Broholm, D.H. Reich, B.J. Sternlieb, R.W. Erwin, *Phys. Rev. Lett.* **1992**, 69, 3571.
- [31] E. Dagotto, T.M. Rice, *Science* **1996**, 271, 618.
- [32] R.S. Eccleston, T. Barnes, J. Brody, J.W. Johnson, *Phys. Rev. Lett.* **1994**, 73, 2626.
- [33] M. Azurna, Z. Hiroi, M. Takano, K. Ishida, Y. Kitaoka, *Phys. Rev. Lett.* **1994**, 73, 3463.
- [34] G. Chaboussant, P.A. Crowell, L.P. Levy, O. Piovesana, A. Madouri, D. Mailly, *Phys. Rev. B* **1997**, 55, 3046.

- [35] M. Hase, I. Terasaki, K. Uchinokura, *Phys. Rev. Lett.* **1993**, 70, 3651; M. Nishi, O. Fujita, J. Akimitsu, *Phys. Rev. B* **1994**, 50, 6508; G. Castilla, S. Chakravarty, V.J. Emery, *Phys. Rev. Lett.* **1995**, 75, 1823.
- [36] G. Chaboussant, Y. Fagot-Revurat, M.-H. Julien, M.E. Hanson, C. Berthier, M. Horvatic, L.P. Levy, O. Piovesana, *Phys. Rev. Lett.* **1998**, 80, 2713.
- [37] M. Oshikawa, M. Yamanaka, I. Affleck, *Phys. Rev. Lett.* **1997**, 78, 1984.
- [38] D.C. Cabra, A. Honecker, P. Pujol, *Phys. Rev. Lett.* **1997**, 79, 5126.
- [39] D.C. Cabra, A. Honecker, P. Pujol, *Phys. Rev. B* **1998**, 58, 6241; see also the web site <http://thew02.physik.uni-bonn.de/~honecker/troc.html>.
- [40] K. Hida, *J. Phys. Soc. Jpn.* **1994**, 63, 2359.
- [41] T. Kuramoto, *J. Phys. Soc. Jpn.* **1998**, 67, 1762.
- [42] K. Totsuka, *Phys. Lett. A* **1997**, 228, 103; *Phys. Rev. B* **1998**, 57, 3454.
- [43] T. Tonegawa, T. Nishida, M. Kaburagi, *cond-mat/9712297*.
- [44] K. Sakai, M. Takahashi, *Phys. Rev. B* **1998**, 57, R3201; *Phys. Rev. B* **1998**, 57, R8091.
- [45] R. Chitra, T. Giamarchi, *Phys. Rev. B* **1997**, 55, 5816.
- [46] H.J. Schulz, G. Cuniberti, P. Pieri in: G. Morandi, A. Tagliacozzo, P. Sodano (Eds.) *Field Theories for Low Dimensional Condensed Matter Systems*, Springer, Berlin, **2000**; H.J. Schulz in: E. Akkermans, G. Montambaux, J. Pichard, J. Zinn-Justin (Eds.) *Proc. Les Houches Summer School LXI*, Elsevier, Amsterdam, **1995**.
- [47] I. Affleck. In: E. Brezin, J. Zinn-Justin (Eds.) *Fields, Strings and Critical Phenomena*, North-Holland, Amsterdam, **1989**; I. Affleck, F.D.M. Haldane, *Phys. Rev. B* **1987**, 36, 5291.
- [48] S. Rao, D. Sen, *J. Phys. Condens. Matter* **1997**, 9, 1831.
- [49] We use the word 'phase' only for convenience to distinguish between regions with different modulations of the two-spin correlation functions. Our model actually has no phase transition from Néel to spiral, even at zero temperature.
- [50] I. Affleck, *Nucl. Phys. B* **1986**, 265, 409.
- [51] Y. Kato, A. Tanaka, *J. Phys. Soc. Jpn.* **1994**, 63, 1277; K. Totsuka, Y. Nishiyama, N. Hatano, M. Suzuki, *J. Phys. Condens. Matter* **1995**, 7, 4895.
- [52] S. Rao, D. Sen, *Nucl. Phys. B* **1994**, 424, 547.
- [53] D. Allen, D. Senechal, *Phys. Rev. B* **1995**, 51, 6394.
- [54] G. Sierra in: G. Sierra, M. A. Martin-Delgado (Eds.) *Strongly Correlated Magnetic and Superconducting Systems*, Lecture Notes in Physics 478, Springer, Berlin, **1997**.
- [55] A.O. Gogolin, A.A. Nersesyan, A. M. Tsvelik, *Bosonization and Strongly Correlated Systems*, Cambridge University Press, Cambridge, **1998**.
- [56] R. Shankar, Lectures given at the BCSPIN School, Kathmandu, 1991. In Y. Lu, J. Pati, Q. Shafi (Eds.) *Condensed Matter and Particle Physics*, World Scientific, Singapore, **1993**.
- [57] J. von Delft, H. Schoeller, *Arm. der Physik* **1998**, 4, 225.
- [58] J.P. Boucher, L.P. Regnault, *J. de Phys.* **1996**, 16, 1939.
- [59] K.G. Wilson, *Rev. Mod. Phys.* **1975**, 47, 773.
- [60] J.W. Bray, S.T. Chui, *Phys. Rev. B* **1979**, 19, 4876; J.E. Hirsch, *Phys. Rev. B* **1980**, 22, 5259.
- [61] S.R. White, R.M. Noack, *Phys. Rev. Lett.* **1992**, 68, 3487.
- [62] S.R. White, *Phys. Rev. Lett.* **1992**, 69, 2863; *Phys. Rev. B* **1993**, 48, 10345.
- [63] R. McWeeny, B.T. Sutcliffe, *Methods of Molecular Quantum Mechanics*, Academic Press, London, **1969**.
- [64] Y. Anusooya, S.K. Pati, S. Ramasesha, *J. Chem. Phys.* **1997**, 106, 1.
- [65] S.R. White, *Phys. Rev. Lett.* **1992**, 45, 5752.

- [66] R. Chitra, S.K. Pati, H.R. Krishnamurthy, D. Sen, S. Ramasesha, *Phys. Rev. B* **1995**, 52, 6581; S.K. Pati, R. Chitra, D. Sen, H.R. Krishnamurthy, S. Ramasesha, *Europhys. Lett.* **1996**, 33, 707.
- [67] S.R. White, D.A. Huse, *Phys. Rev. B* **1993**, 48, 3844; E.S. Sorensen, I. Affleck, *Phys. Rev. Lett.* **1993**, 71, 1633.
- [68] E.S. Sorensen, I. Affleck, *Phys. Rev. B* **1994**, 49, 13235; *Phys. Rev. B* **1994**, 49, 15771.
- [69] U. Schollwöck, Th. Jolicoeur, *Europhys. Lett.* **1995**, 30, 493; Y. Nishiyama, K. Totsuka, N. Hatano, M. Suzuki, *J. Phys. Soc. Jpn.* **1995**, 64, 414.
- [70] U. Schollwöck, Th. Jolicoeur, T. Garel, *Phys. Rev. B* **1996**, 53, 3304.
- [71] R.J. Bursill, T. Xiang, G.A. Gehring, *J. Phys. A* **1994**, 28, 2109; R.J. Bursill, G.A. Gehring, D.J. Farnell, J.B. Parkinson, T. Xiang, C. Zeng, *J. Phys. C* **1995**, 7, 8605.
- [72] S.R. White, R.M. Noack, D.J. Scalapino, *Phys. Rev. Lett.* **1994**, 73, 886; M. Azzouz, L. Chen, S. Moukouri, *Phys. Rev. B* **1994**, 50, 6223.
- [73] T. Narushima, T. Nakamura, S. Takada, *J. Phys. Soc. Jpn.* **1995**, 64, 4322; U. Schollwöck, D. Ko, *Phys. Rev. B* **1996**, 53, 240.
- [74] S.J. Qin, T.K. Ng, Z.B. Su, *Phys. Rev. B* **1995**, 52, 12844.
- [75] H.B. Pang, H. Akhlaghpour, M. Jarrel, *Phys. Rev. B* **1996**, 53, 5086.
- [76] K.A. Hallberg, *Phys. Rev. B* **1995**, 52, R9827.
- [77] S.K. Pati, S. Ramasesha, Z. Shuai, J.L. Brédas, *Phys. Rev. B* **1999**, 59, 14827.
- [78] L.J. Caron, S. Moukouri, *Phys. Rev. Lett.* **1996**, 77, 4640.
- [79] S.K. Pati, S. Ramasesha, D. Sen, *Phys. Rev. B* **1997**, 55, 8894; *J. Phys. Condens. Matter* **1997**, 9, 8707.
- [80] L.G. Caron, S. Moukouri, *Phys. Rev. Lett.* **1996**, 76, 4050.
- [81] T. Nishino, K. Okunishi, *J. Phys. Soc. Jpn.* **1995**, 64, 4084.
- [82] T. Nishino, K. Okunishi, *J. Phys. Soc. Jpn.* **1996**, 65, 891.
- [83] T. Tonegawa, M. Kaburagi, N. Ichikawa, I. Harada, *J. Phys. Soc. Jpn.* **1992**, 61, 2890.
- [84] S. Ramasesha, Z.G. Soos, *Solid State Commun.* **1983**, 46, 509.
- [85] S. Rao, D. Sen, *Phys. Rev. B* **1993**, 48, 12763.
- [86] B. Sutherland, *Phys. Rev. B* **1975**, 12, 3795.
- [87] For a review, see M. Steiner, J. Villain, C.G. Windsor, *Adv. Phys.* **1976**, 25, 88.
- [88] O. Kahn, *Struct. Bond. (Berlin)* **1987**, 68, 89.
- [89] O. Kahn, Y. Pei, M. Verdagner, J.P. Renard, J. Sletten, *J. Am. Chem. Soc.* **1988**, 110, 782; P. Van Koningsbruggen, O. Kahn, K. Nakatani, Y. Pei, J.P. Renard, M. Drillon, P. Leggol, *Inorg. Chem.* **1990**, 29, 3325.
- [90] J. Curely, R. Georges, M. Drillon, *Phys. Rev. B* **1986**, 33, 6243.
- [91] M. Drillon, E. Coronado, N. Belaiche, R. Carlin, *J. Appl. Phys.* **1986**, 63, 3551.
- [92] M. Drillon, M. Belaiche, P. Leggol, J. Aride, A. Boukhari, A. Moqine, *J. Magn. Magn. Mat.* **1993**, 83, 128.
- [93] O. Kahn, *Adv. Inorg. Chem.* **1995**, 43, 179.
- [94] K.A. Hallberg, P. Horsch, G. Martinez, *Phys. Rev. B* **1995**, 52, R719; R.J. Bursill, T. Xiang, G.A. Gehring, *J. Phys. A* **1994**, 28, 2109; Y. Kato, A. Tanaka, *J. Phys. Soc. Jpn.* **1994**, 63, 1277.
- [95] M. Drillon, E. Coronado, R. Georges, J. Gianduzzo, J. Curely, *Phys. Rev. B* **1989**, 40, 10992.
- [96] O. Kahn, *Molecular Magnetism*, VCH, New York, **1993**.
- [97] M. Drillon, J. Gianduzzo, R. Georges, *Phys. Lett. A* **1983**, 96, 413.
- [98] M. Takahashi, *Phys. Rev. B* **1987**, 36, 3791.
- [99] K. Tandon, S. Lal, S.K. Pati, S. Ramasesha, D. Sen, *Phys. Rev. B* **1999**, 59, 396.
- [100] K. Kawano, M. Takahashi, *J. Phys. Soc. Jpn.* **1997**, 66, 4001.
- [101] I. Rudra, S. Ramasesha, D. Sen, *Phys. Rev. B* **2001**, 64, 014408.

5 Magnetic Properties of Self-assembled [2 × 2] and [3 × 3] Grids

Laurence K. Thompson, Oliver Waldmann, and Zhiqiang Xu

5.1 Introduction

An euphoric view of the future of *chip* technology expressed by Gordon Moore in the nineteen-sixties indicated that “The complexity [of cheap integrated circuits] has increased at a rate of roughly a factor of two per year” [1]. The view was held for quite a few years, until it became revised to a doubling every one and a half years. The explosion in computer power in the nineteen-eighties and beyond hinged dramatically on the ability of industry to miniaturize chips, and it appeared that there was no limit (e. g. 64 transistors per chip in 1965 versus 28 million transistors in a Pentium III processor). In recent years the realization that Moore’s Law would finally fail has led to the search for new devices not constrained by the physical limitations of chip size. Current chip “pitches” in the 150 nm range can lead to electron tunneling through the chip “gates”, and so a realistic size limit is fast approaching. Magnetic data storage faces similar scaling problems, although at a lower dimension. It is estimated that magnetic grain size cannot be scaled below 10 nm without the occurrence of thermal self-erasure problems. Thus in both areas the time is ripe for new approaches or even “new physics” [1–3].

Paramagnetic metal ions with covalent radii of the order of 1 Å (0.1 nm) can be brought into close proximity with suitable diamagnetic, single atom bridging ligands, and with appropriate magnetic orbital overlap situations can produce parallel or antiparallel alignment of the metal centered spins (ferromagnetic or antiferromagnetic behavior respectively). For simple dinuclear systems many examples of such spin coupled systems are known, but most are antiferromagnetically coupled. Increasing the number of spin centers in a polynuclear, bridged arrangement is more of a challenge, but can be achieved using polydentate ligands of various types. One approach uses well-defined, polydentate ligands to impose specific geometries on the resulting arrays, while another approach uses simple ligands, and essentially is controlled by properties of the metal ion (e. g. in cyanide or carbonyl clusters). An intermediate approach uses coordinatively flexible ligands.

Grid-like two-dimensional arrangements of spin centers offer significant benefits to random clusters, in that flat surface arrays are possible (*vide infra*), and so the prospects for addressing individual molecules or even metal atoms are enhanced. The organization of paramagnetic metal centers into regular grid-like arrangements has been achieved using the ligand directed, self-assembly approach [4], and examples of [2 × 2] and [3 × 3] grid structures have been produced. The success of this

approach relies on the fact that the structural attributes necessary for the formation of a specific grid arrangement are pre-programmed into the ligand itself, and the grid forms by a self assembly process in which the donor groupings of the ligand are read by the metal ions in terms of their *coordination algorithms* as the polynuclear structure is built [5].

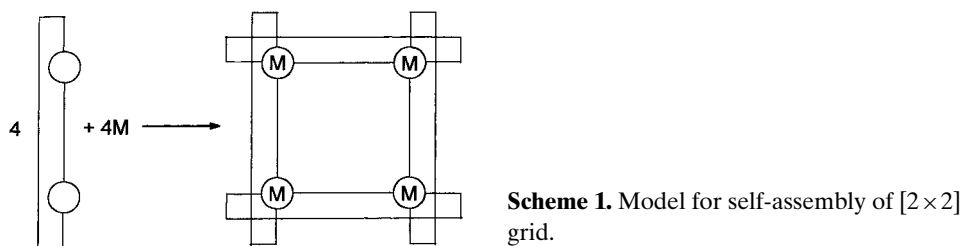
A number of these $[2 \times 2]$ and $[3 \times 3]$ grid structures have shown a remarkable variety of magnetic properties, with isotropic coupling characterized by examples of both antiferromagnetic and ferromagnetic exchange. Evidence for anisotropic and biquadratic exchange couplings has been reported, systems with pronounced magnetic anisotropy and/or strong interplay between ligand-field and exchange interactions have been identified, and even cooperative spin-crossover effects have been observed. In this review, the structural and magnetic properties of such systems will be described with a focus on the isotropic coupling situation. A brief theoretical treatment of the magnetism will be presented.

Section 5.2 deals with a survey of the ligands and ligand types found to be suitable for self-assembly into grids, with examples of structures of typical complexes. Section 5.3 examines the magnetic properties, in relation to structure, and Section 5.4 examines possible applications of such systems to information storage, and the problem of addressing such systems in the nanoscale realm.

5.2 Polytopic Ligands and Grid Complexes

The complexes described in this chapter will be based on the definition of a metallic coordination grid as an “array of metal centers positioned at the vertices of a (approximate) square lattice”, with the number of occupied rows and columns greater than one. This implies a two-dimensional flat or close to flat polynuclear array. From the magnetic perspective only systems with paramagnetic metal centers that are linked by diamagnetic monatomic or poly-atomic bridges, with metal–metal separations $<10 \text{ \AA}$, will be discussed. The characteristic feature of such structures is the parallel ligand groupings connecting the metal centers.

Regular grids have been successfully produced from polytopic ligands with “n” coordination pockets, which self-assemble with metal ions to form $[n \times n]$ grids [5]. The smallest members of such a series would be $[2 \times 2]$ tetranuclear complexes (Scheme 1). The distinction between grids, squares and small metalla-cycles in this class is essentially semantic, and from a magnetic perspective there is no symmetric difference (vide infra). Systems with higher nuclearity will be restricted to grids, as formerly defined, with single metal ion periodicities, and so will not include metalla-cyclic rings *per se*. The definition does not require that all vertices of a $[n \times m]$ grid have to be occupied by a metal ion, and so incomplete grid structures, e. g. with a “pin wheel” shape, are also included. An extensive review of “self-assembled structural motifs in coordination chemistry” [6] highlights the structural features of some examples of “grids” and “squares” in this class.



5.2.1 $[2 \times 2]$ Ligands

Building grids of nanoscopic dimensions from individual subunits using sequential bond formation methodologies is time-consuming and results in low yields. Supramolecular architectures can conveniently be approached using self assembly chemistry by including key design elements in the ligands that allow the metal ions to read the ultimate structural outcome as the system builds [4, 5]. Typical ligands that produce $[2 \times 2]$ square grids are shown in Fig. 1, with examples of their primary coordination modes. They all have two potential coordination pockets (ditopic) and involve monatomic, diatomic, tri-atomic and tetra-atomic bridging groups. In each example $[2 \times 2]$, thermodynamically favored, grid complexes are formed by self assembly processes in high yield, with homoleptic and non-homoleptic examples.

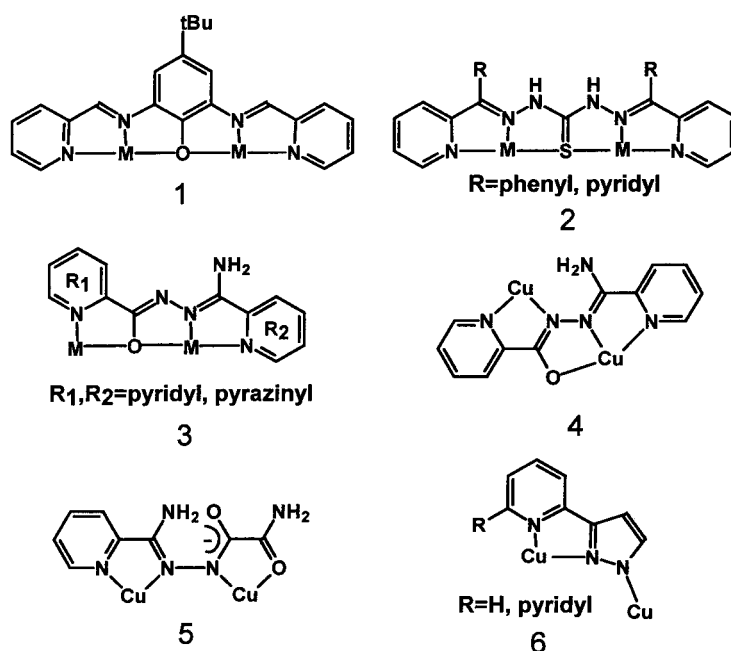


Fig. 1. Polytopic ligands and their coordination modes.

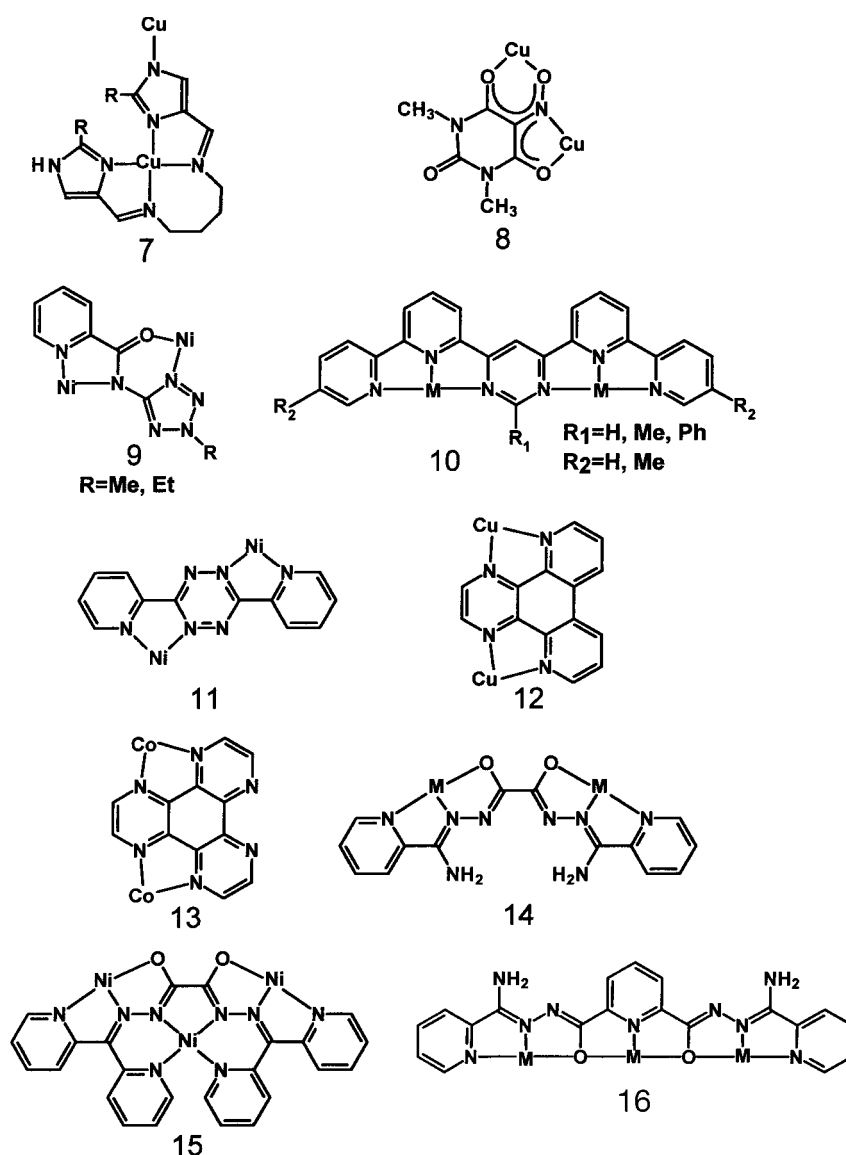


Fig. 1. Continued

5.2.2 Representative $[2 \times 2]$ Complexes

Ligand **1** has a linear arrangement of coordination pockets, and forms five-membered chelate rings on coordination. The complex $[\text{Cu}(\text{L1})_4(\text{PF}_6)_4]$ (**17**) [7] (Fig. 2) forms in 80% yield and has a $[2 \times 2]$ square grid structure with two pairs of parallel ligands above and below the $[\text{Cu}_4(\mu\text{-O})_4]$ plane. The copper atoms are sep-

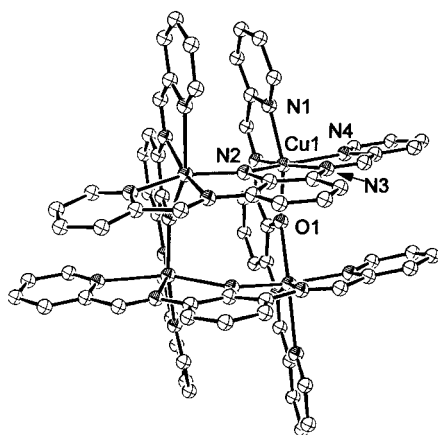


Fig. 2. Structural representation of $[\text{Cu}(\text{L}1)]_4(\text{PF}_6)_4$ (**17**).

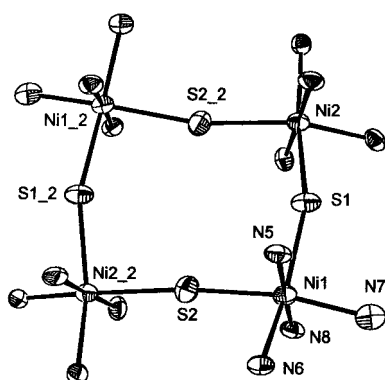


Fig. 3. Structural representation of the core in $[\text{Ni}(\text{L}2)]_4(\text{PF}_6)_4 \cdot 4\text{EtOH} \cdot \text{H}_2\text{O}$ (**18**).

arated by 4.04 Å, with Cu–O–Cu angles of 140.6°. Ligands of type **2** have a similar arrangement of coordination pockets, and self assemble in the presence of Ni(II) and Co(II) ions to produce $[\text{Ni}(\text{L}2)]_4(\text{PF}_6)_4 \cdot 4\text{EtOH} \cdot \text{H}_2\text{O}$ (**18**) (R = phenyl) [8] and $[\text{Co}(\text{L}2)]_4(\text{CH}_3\text{COO})_4 \cdot \text{H}_2\text{O}$ (**19**) (R = pyridyl) [9] (Fig. 3 shows the core structure only for **18**; **19** has an identical core), with square $[\text{M}_4(\mu\text{-S})_4]$ cores, and two pairs of parallel ligands above and below the metal plane. The M–M distances are 4.8 Å and 4.43 Å, respectively, and the M–S–M angles are 163° and 151° respectively.

Ligands of type **3** have produced numerous $[2 \times 2]$, $[\text{M}_4(\mu\text{-O})_4]$ grids (M = Cu(II), Ni(II), Mn(II), Co(II)) in high yield with similar dimensions. Figure 4 shows the structure of the cation in $[\text{Cu}_4(\text{L}_3)_4(\text{H}_2\text{O})](\text{NO}_3)_4 \cdot 3\text{H}_2\text{O}$ (**20**) (R₁ = pyridine; R₂ = pyrazine) [10a], with Cu–Cu distances of 4.01–4.05 Å, and Cu–O–Cu angles 139.8–141.0°. A striking feature of this and related Cu₄ grid complexes is the strictly orthogonal bridging arrangement between the $d_{x^2-y^2}$ ground state copper centers (*vide infra*). Figure 5 shows the structure of the cation in $[\text{Ni}_4(\text{L}_3)_4(\text{H}_2\text{O})_4](\text{NO}_3)_4 \cdot 8\text{H}_2\text{O}$ (**21**) (R₁ = R₂ = pyridine), with Ni–Ni distances in the range 3.95–3.98 Å, and Ni–O–Ni angles in the range 136.2–140.1° [10a]. Figure 6 shows the structure of the cation in $[\text{Mn}_4(\text{L}_3)_4(\text{H}_2\text{O})_4](\text{NO}_3)_4 \cdot \text{H}_2\text{O}$ (**22**)

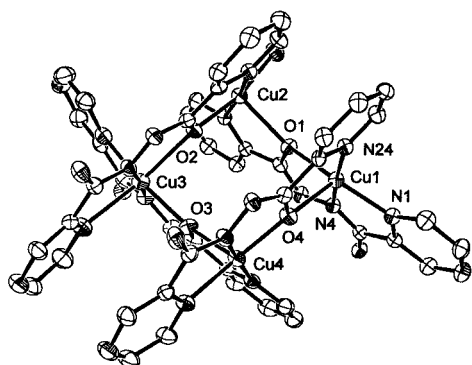


Fig. 4. Structural representation of $[\text{Cu}_4(\text{L}_3)_4(\text{H}_2\text{O})](\text{NO}_3)_4 \cdot 3\text{H}_2\text{O}$ (**20**) ($\text{R}_1 = \text{pyridine}$; $\text{R}_2 = \text{pyrazine}$).

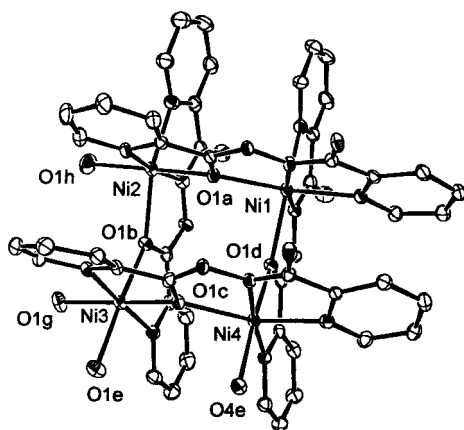


Fig. 5. Structural representation of $[\text{Ni}_4(\text{L}_3)_4(\text{H}_2\text{O})_4](\text{NO}_3)_4 \cdot 8\text{H}_2\text{O}$ (**21**) ($\text{R}_1 = \text{R}_2 = \text{pyridine}$).

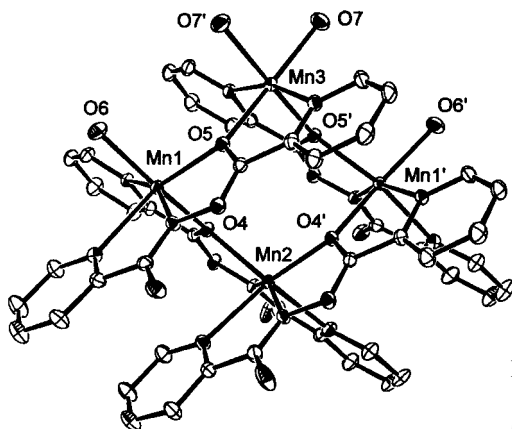


Fig. 6. Structural representation of $[\text{Mn}_4(\text{L}_3)_4(\text{H}_2\text{O})_4](\text{NO}_3)_4 \cdot \text{H}_2\text{O}$ (**22**) ($\text{R}_1 = \text{pyridine}$; $\text{R}_2 = \text{pyrazine}$).

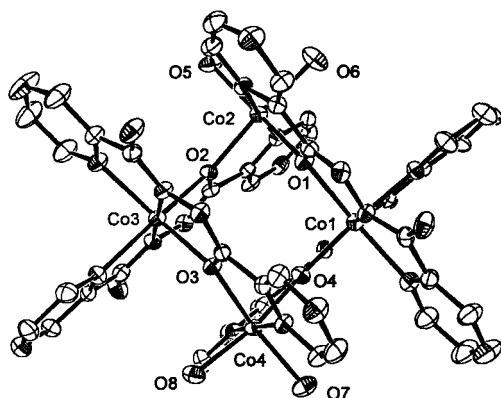


Fig. 7. Structural representation of $[\text{Co}_4(\text{L}_3)_4(\text{H}_2\text{O})_4](\text{ClO}_4)_4 \cdot 3\text{H}_2\text{O}$ (**23**) ($\text{R}_1 = \text{R}_2 = \text{pyrazine}$).

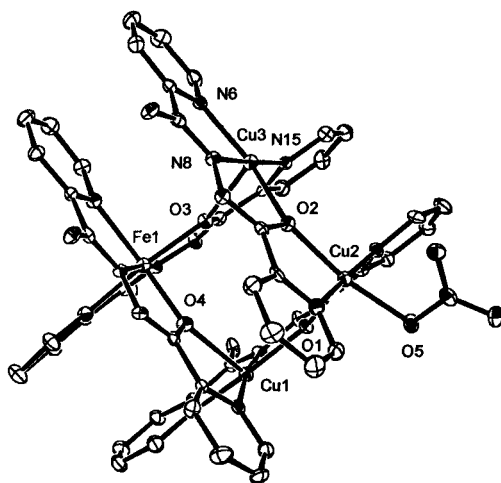


Fig. 8. Structural representation of $[\text{Cu}_3\text{Fe}(\text{L}_3)_4(\text{NO}_3)]_2(\text{ClO}_4)_4(\text{NO}_3)_4$ (**24**) ($\text{R}_1 = \text{R}_2 = \text{pyridine}$).

($\text{R}_1 = \text{pyridine}$; $\text{R}_2 = \text{pyrazine}$), with Mn–Mn distances in the range 3.91–3.97 Å and Mn–O–Mn angles in the range 127.9–129.3° [10b]. Figure 7 shows the structure of the cation in $[\text{Co}_4(\text{L}_3)_4(\text{H}_2\text{O})_4](\text{ClO}_4)_4 \cdot 3\text{H}_2\text{O}$ (**23**) ($\text{R}_1 = \text{R}_2 = \text{pyrazine}$), with Co–Co distances in the range 3.88–3.95 Å, and Co–O–Co angles in the range 133.5–136.0° [10b]. Mixed metal grids of this ligand type can also be produced, and the related structure of a $[\text{Fe}(\text{III})\text{Cu}_3(\mu\text{-O})_4]$ square grid cation in the complex $[\text{Cu}_3\text{Fe}(\text{L}_3)_4(\text{NO}_3)]_2(\text{ClO}_4)_4(\text{NO}_3)_4$ (**24**) ($\text{R}_1 = \text{R}_2 = \text{pyridine}$) is shown in Fig. 8 [10c]. Ligands of type **3** exist in a number of different conformational forms e. g. **4**, and can accordingly coordinate in a number of different ways. In the complex $[\text{Cu}_4(\text{L}_4)_4(\text{H}_2\text{O})_2](\text{NO}_3)_4 \cdot 4\text{H}_2\text{O}$ (**25**) (Fig. 9) [10a] a flat rectangular grid is observed involving two pairs of ligands with different coordination modes, one pair bridging by their alkoxide oxygen atoms, and the other pair via the N–N diazine single bonds. Cu–Cu distances are 4.097 Å and 4.759 Å, with a Cu–O–Cu angle of 139.9°. Cu(1) and Cu(2) are disposed in an almost *trans* arrangement around the N–N bonds (Cu–N–N–Cu torsional angle 158.8°).

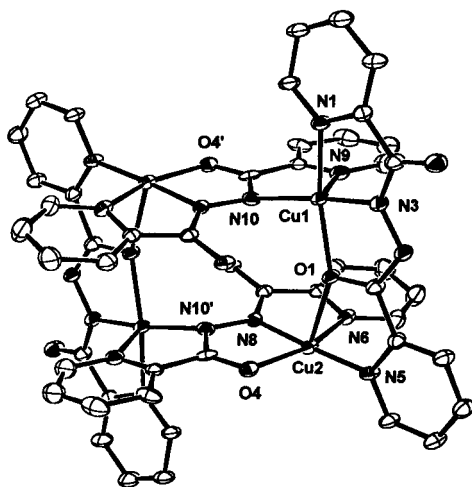


Fig. 9. Structural representation of $[\text{Cu}_4(\text{L}4)_4(\text{H}_2\text{O})_2](\text{NO}_3)_4 \cdot 4\text{H}_2\text{O}$ (**25**).

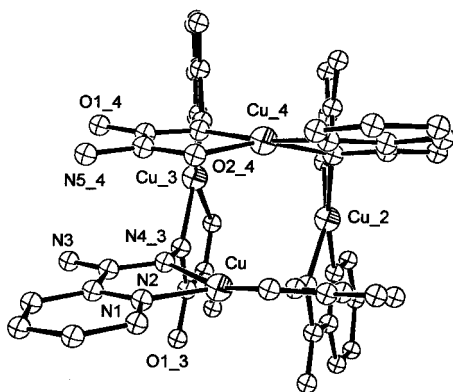


Fig. 10. Structural representation of $[\text{Cu}(\text{L}5)]_4(\text{NO}_3)_4 \cdot 8\text{H}_2\text{O}$ (**26**).

Ligand **5** contains a rotationally flexible N–N bond, and self assembles to produce the $[\text{Cu}_4(\mu\text{-N-N})_4]$ homoleptic $[2 \times 2]$ grid complex $[\text{Cu}(\text{L}5)]_4(\text{NO}_3)_4 \cdot 8\text{H}_2\text{O}$ (**26**) [11]. Figure 10 shows the structure of the cation. An interesting 90° twist of the ligand around the N–N bond leads to effective magnetic isolation of the Cu(II) centers (*vide infra*), but this produces a significant tetrahedral distortion of the cluster. Ligand types **6** combine terminating pyridine and bridging pyrazole groups, and self assemble to form $[2 \times 2]$ grids with pyrazolate N–N bridges. With **6** (R = pyridyl) the complex $[\text{Cu}_4(\text{L}6)_6(\text{MeOH})_2](\text{PF}_6)_2 \cdot 2\text{MeOH}$ (**27**) [12] (Fig. 11) is formed and involves six pyrazole bridges with two pairs bridging Cu(1) and Cu(2) equatorially, and the other pair bridging Cu(1) and Cu(2a) axially. This leads to an essentially square grid with Cu–Cu separations of 3.939 Å and 3.984 Å. Ligand **6** (R = H) behaves differently, and forms $[\text{Cu}_4(\text{L}6)_4(\text{dmf})_4](\text{PF}_6)_4 \cdot 6\text{dmf}$ (**28**) [12]. Figure 12 shows that the $[2 \times 2]$ grid has two pairs of parallel, mutually perpendicular ligands arranged above and below the Cu_4 grid, as in the earlier examples. Each adjacent pair of copper centers is bridged equatorially by one pyrazole N–N linkage. Terminal copper sites are occupied by solvent molecules in both cases.

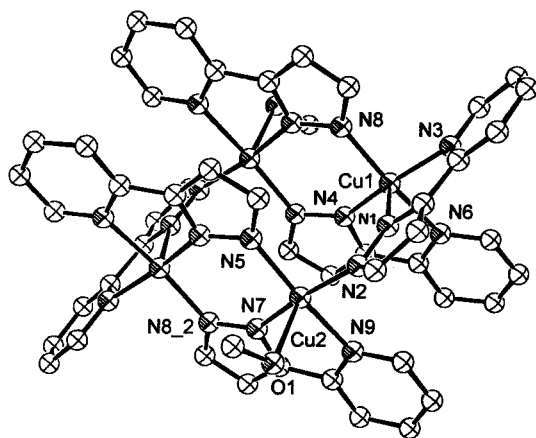


Fig. 11. Structural representation of $[\text{Cu}_4(\text{L6})_6(\text{MeOH})_2](\text{PF}_6)_2 \cdot 2\text{MeOH}$ (**27**) (R = pyridyl).

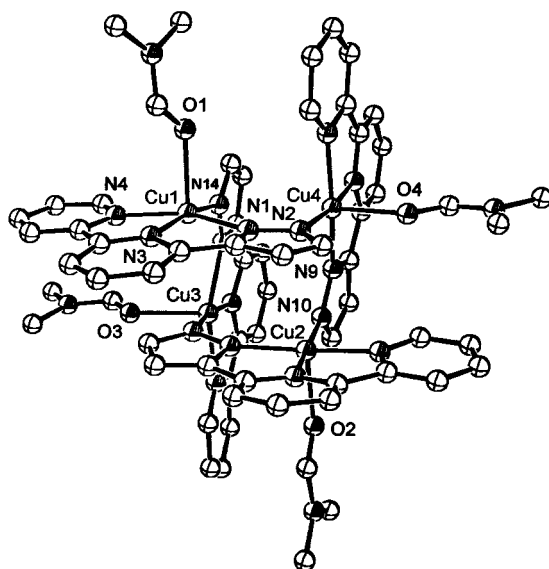


Fig. 12. Structural representation of $[\text{Cu}_4(\text{L6})_4(\text{dmf})_4](\text{PF}_6)_4 \cdot 6\text{dmf}$ (**28**) (R = H).

Ligand **7** self assembles in the presence of Cu(II) ions to produce square $[2 \times 2]$ grids with one terminal and one bridging imidazolate group per copper center. Figure 13 shows the structure of the cation in $[\text{Cu}(\text{L7})_4(\text{NO}_3)_2\text{Cl}_2 \cdot 1.25\text{H}_2\text{O}$ (**29**) [13]. Cu–Cu distances are in the range 6.10–6.15 Å. The four copper centers are connected equatorially by the imidazolate bridges in a flat array (Cu–Cu–Cu–Cu torsional angle 18.3°). Ligand **8** (1,3-dimethylvioluric acid) acts in a bis-bidentate fashion and forms a flat, square $[\text{Cu}_4(\mu\text{-NO})_4]$ “oximate” bridged $[2 \times 2]$ grid complex $[\text{Cu}(\text{L8})(\text{H}_2\text{O})_2]_4(\text{ClO}_4)_4 \cdot 2\text{H}_2\text{O}$ (**30**) [14] (Fig. 14; bridging oximate groups are disordered over two positions) with Cu–Cu distances of 4.764(3) Å, and the copper centers all linked equatorially.

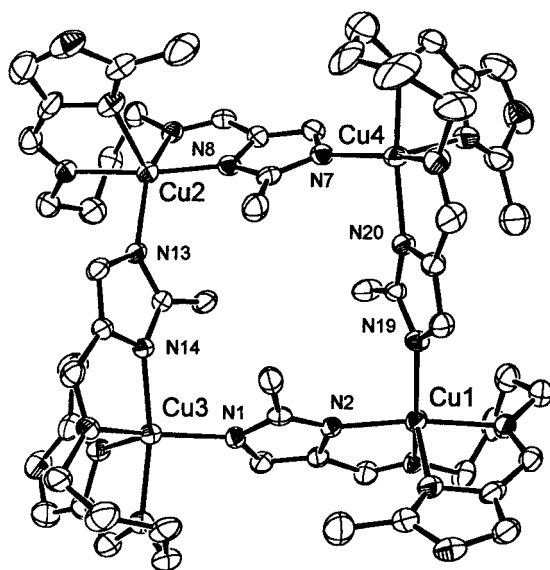


Fig. 13. Structural representation of $[\text{Cu}(\text{L}7)]_4(\text{NO}_3)_2\text{Cl}_2 \cdot 1.25\text{H}_2\text{O}$ (**29**).

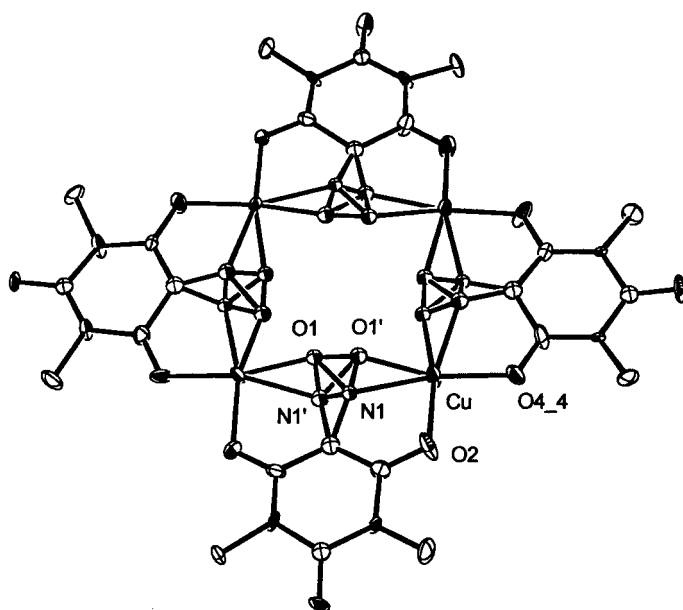


Fig. 14. Structural representation of $[\text{Cu}(\text{L}8)(\text{H}_2\text{O})_2]_4(\text{ClO}_4)_4 \cdot 2\text{H}_2\text{O}$ (**30**).

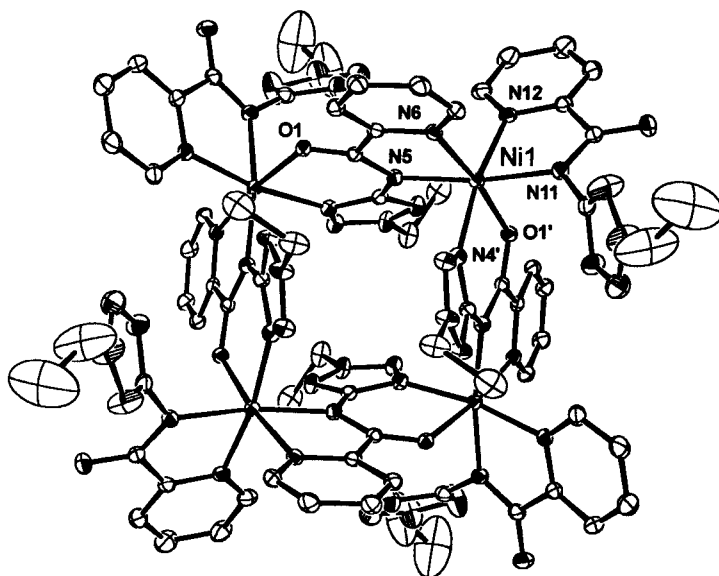


Fig. 15. Structural representation of $[\text{Ni}_4(\text{L9Et})_8] \cdot 4\text{CH}_2\text{Cl}_2$ (**31**).

Ligands of type **9** can act in a bis-bidentate bridging mode, and with Ni(II) self assemble to produce a $[2 \times 2]$ distorted square grid complex $[\text{Ni}_4(\text{L9Et})_8] \cdot 4\text{CH}_2\text{Cl}_2$ (**31**) [15] (Fig. 15). The six-coordinate nickel(II) centers are linked by three atom bridges, and as a consequence Ni–Ni distances are quite long (5.567 Å). Ligands of type **10** create a linear array of coordination pockets, as in **1–3**, leading to ideal geometric conditions for self-assembly into square grids. Ligand **10** ($R_1 = \text{phenyl}$; $R_2 = \text{H}$) reacts with $\text{Co}(\text{BF}_4)_2$ to produce $[\text{Co}(\text{L10})_4(\text{BF}_4)_8]$ (**32**) [16] in high yield. Figure 16 shows the cationic structure with four distorted octahedral Co(II) centers bridged by four pyrimidine groups, and two pairs of parallel ligands above and below the metal plane. Co–Co distances are quite long (6.453–6.570 Å), as would be expected, because of the three atom bridges. A corresponding Fe(II) complex $[\text{Fe}(\text{L10})_4(\text{ClO}_4)_8]$ (**33**) was obtained with ligand **10** ($R_1 = \text{phenyl}$; $R_2 = \text{H}$) with an iso-structural, homoleptic pyrimidine bridged Fe_4 cation. Structural studies at 100 K and 293 K reveal significant differences in Fe–N bond distances, some of which are intermediate between those expected for LS and HS Fe(II) systems. This is related to the demonstrated spin crossover behavior (*vide infra*) [17].

The bis-bidentate ligand **11** undergoes self-assembly in the presence of Ni(II) ions to produce a $[2 \times 2]$ square grid complex $[\text{Ni}_4(\text{L11})_4(\text{CH}_3\text{CN})_8](\text{BF}_4)_8$ (**34**) [18] (Fig. 17), with the four octahedral Ni(II) centers bridged on opposite sides of each ligand through the tetrazine subunit, with remaining coordination sites filled by acetonitrile molecules. The inclusion of a BF_4^- ion in the grid cavity is viewed as evidence of an anion cyclization templating effect. The four atom bridging connection between Ni(II) centers leads to quite long Ni–Ni separations (6.84–6.89 Å). An equivalent bridging situation exists in **12** and **13**, which both bridge through

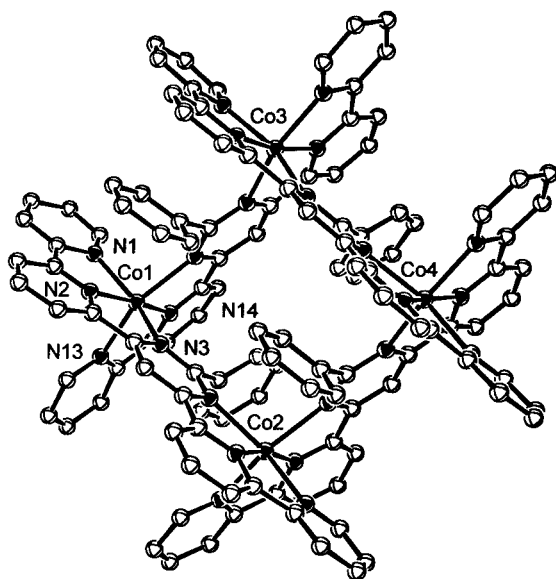


Fig. 16. Structural representation of $[\text{Co}(\text{L10})_4](\text{BF}_4)_8$ (**32**).

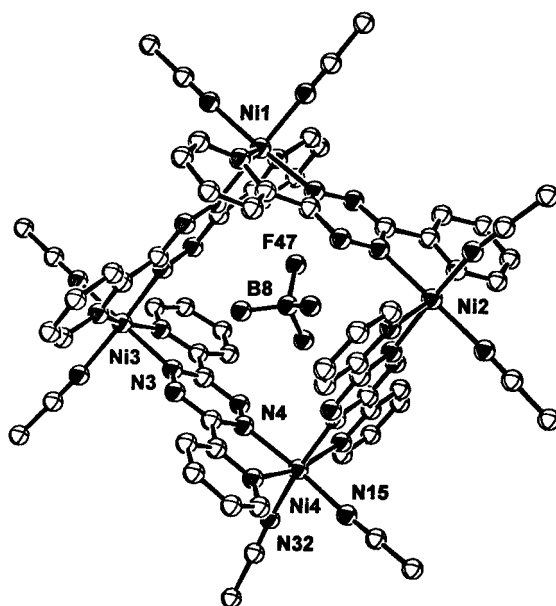


Fig. 17. Structural representation of $[\text{Ni}_4(\text{L11})_4(\text{CH}_3\text{CN})_8](\text{BF}_4)_8$ (**34**).

the pyrazine fragments of the ligands. The complex $[\text{Cu}_4(\text{L12})_4\text{Cl}_7]_n\text{Cl}_n \cdot 15n\text{H}_2\text{O}$ (**35**) [19] (Fig. 18) has a $[2 \times 2]$ almost square grid structure with four ligands arranged in two parallel pairs connecting Cu(1) and Cu(2) axially, and Cu(2) and Cu(1a) equatorially. Cu–Cu distances are long (6.89–7.30 Å), due to the four atom pyrazine bridge connections. Cu(1) and Cu(2) form axial bonds to N(6) and N(7)

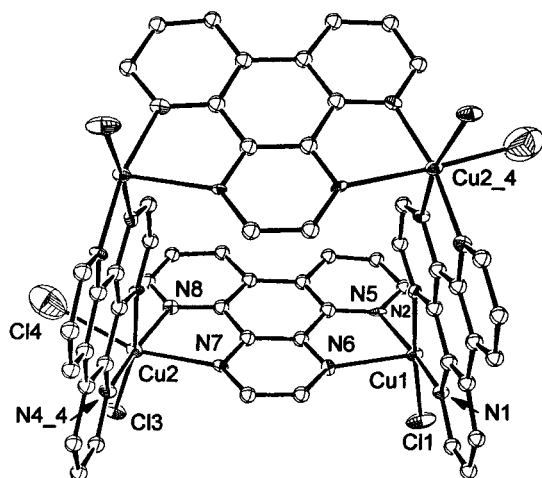


Fig. 18. Structural representation of $[\text{Cu}_4(\text{L12})_4\text{Cl}_7]_n \cdot 15n\text{H}_2\text{O}$ (**35**).

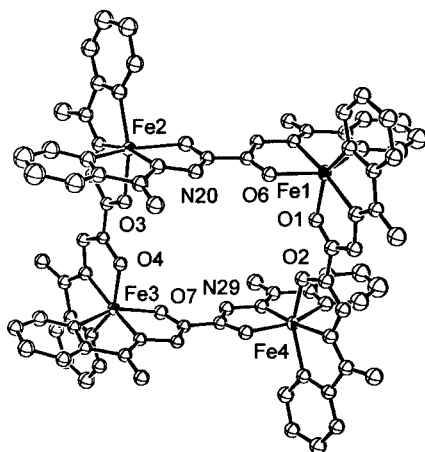


Fig. 19. Structural representation of $[\text{Fe}_4(\text{L14})_4](\text{ClO}_4)_6 \cdot 7\text{H}_2\text{O}$ (**37**).

respectively, while the connection between Cu(1) and Cu(2–4) links the $d_{x^2-y^2}$ copper centers equatorially, resulting in a “dimer of dimers” system (*vide infra*). The complex $[\text{Co}(\text{L13})\text{Cl}_2]_4 \cdot 27\text{H}_2\text{O}$ (**36**) [20] has a similar structure with the ligands bridging through the pyrazine subunits in exactly the same way. Co–Co distances (7.1 Å) are long, as would be expected.

Ligand **14** has two fairly widely spaced N_2O coordination pockets, and self assembles with e. g. $\text{Fe}(\text{ClO}_4)_2$ to produce a square $[2 \times 2]$ grid with oxalyl hydrazide bridges between the metal centers. Figure 19 shows the cation structure in the complex $[\text{Fe}_4(\text{L14})_4](\text{ClO}_4)_6 \cdot 7\text{H}_2\text{O}$ (**37**) [21]. Fe(II)–Fe(II) distances fall in the range 6.75–7.25 Å, and two oxalyl–hydrazide bridges have a *trans* configuration, while the other two are *cis*. Extension of this ligand to include two additional pyridine rings in place of the NH_2 groups (**15**) allows for a highly novel self assembly situation where

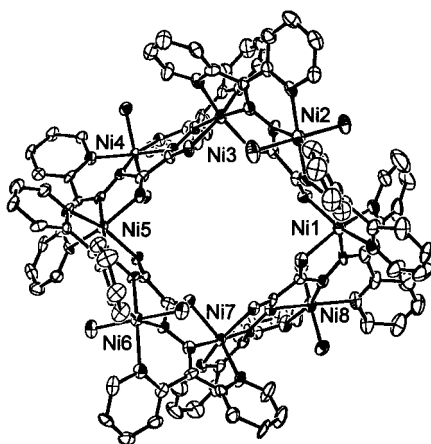


Fig. 20. Structural representation of $[\text{Ni}_8(\text{L15})_4(\text{H}_2\text{O})_8](\text{BF}_4)_8 \cdot 16\text{H}_2\text{O}$ (**38**).

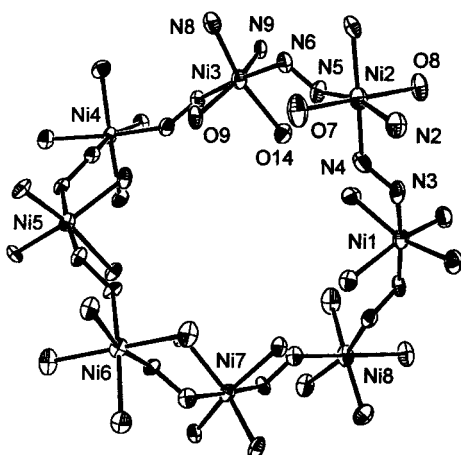


Fig. 21. Structural representation of the octanuclear core in $[\text{Ni}_8(\text{L15})_4(\text{H}_2\text{O})_8](\text{BF}_4)_8 \cdot 16\text{H}_2\text{O}$ (**38**).

the same primary square grid arrangement can be produced, with additional metal centers attached to the sides of the $[2 \times 2]$ grid. **15** self assembles in high yield in the presence of $\text{Ni}(\text{BF}_4)_2$ to produce an expanded octanuclear grid [22]. The structure of $[\text{Ni}_8(\text{L15})_4(\text{H}_2\text{O})_8](\text{BF}_4)_8 \cdot 16\text{H}_2\text{O}$ (**38**) is shown in Fig. 20, revealing the oxalyl-hydrazide bridged square $\text{Ni}(\text{II})_4$ $[2 \times 2]$ grid core (Fig. 21; Ni1–Ni3–Ni5–Ni7), with appended Ni(II) centers (Ni2–Ni4–Ni6–Ni8) attached to the external coordination pockets. This effectively creates a large octanuclear ring with almost *trans* N–N single bond bridges linking adjacent Ni(II) centers (Ni–N–N–Ni torsional angles 152.0 – 161.0°).

5.2.3 $[3 \times 3]$ Ligands and their Complexes

Extensions of the geometric features that successfully led to $[2 \times 2]$ grids with the ligand **3** systems have been programmed into ligand **16** (Fig. 1). The linear arrangement of three contiguous coordination pockets with the formation of five-membered chelate rings leads successfully to $[3 \times 3]$ square grids in high yields. The complex $[\text{Mn}_9(\text{L16})_6](\text{ClO}_4)_6 \cdot 18\text{H}_2\text{O}$ (**39**) (Fig. 22) involves a homoleptic structure with six parallel ligands, arranged in two groups of three, above and below the pseudo-planar grid of nine alkoxide bridged Mn(II) centers. The central $[\text{Mn}_9(\mu_2\text{-O})_{12}]$ core is shown in Fig. 23 [23, 24]. The Mn(II) centers are closely spaced (Mn–Mn

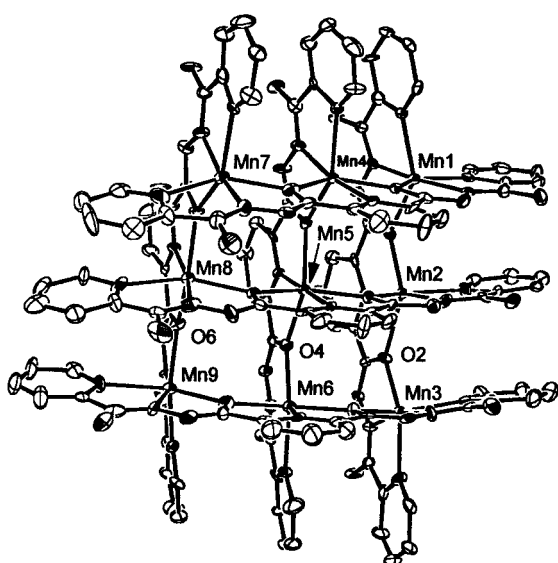


Fig. 22. Structural representation of $[\text{Mn}_9(\text{L16})_6](\text{ClO}_4)_6 \cdot 18\text{H}_2\text{O}$ (**39**).

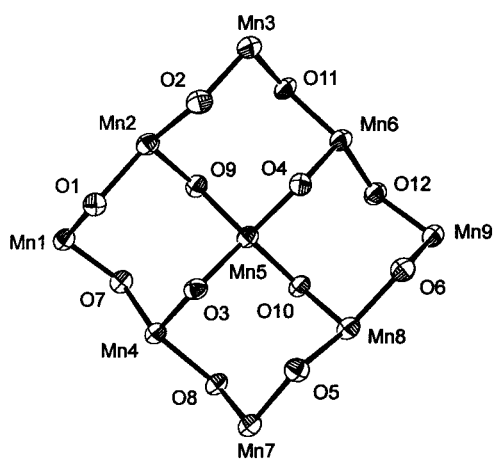


Fig. 23. Structural representation of the core in $[\text{Mn}_9(\text{L16})_6](\text{ClO}_4)_6 \cdot 18\text{H}_2\text{O}$ (**39**).

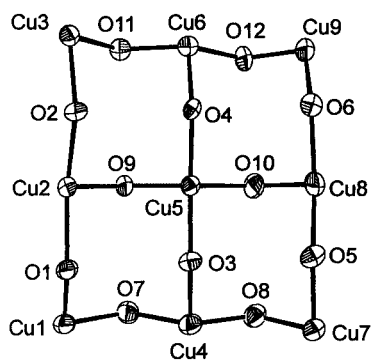


Fig. 24. Structural representation of the core in $[\text{Cu}_9(\text{L16})_6](\text{NO}_3)_{12} \cdot 9\text{H}_2\text{O}$ (**40**).

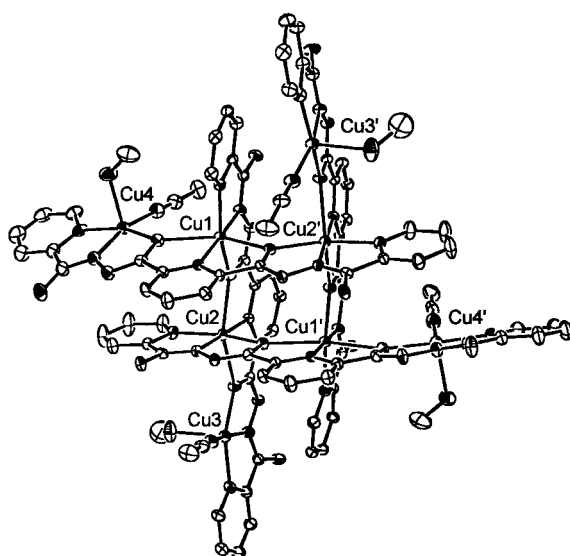


Fig. 25. Structural representation of the Cu_8 fragment in $[\text{Cu}_8(\text{L16})_4(\text{CH}_3\text{OH})_4(\text{CH}_3\text{CN})_4][\text{Gd}(\text{NO}_3)_4(\text{H}_2\text{O})_2]_2(\text{NO}_3)_6 \cdot 1.3\text{Cu}(\text{NO}_3)_2 \cdot 10\text{H}_2\text{O}$ (**41**).

3.9–4.0 Å), with Mn–O–Mn angles in the range 126.6–130.0°. An analogous $[\text{Cu}_9(\mu_2\text{-O})_{12}]$ square grid is found in the complex $[\text{Cu}_9(\text{L16})_6](\text{NO}_3)_{12} \cdot 9\text{H}_2\text{O}$ (**40**) [24, 25]. The core (Fig. 24) has similar dimensions (Cu–Cu 4.03–4.17 Å; Cu–O–Cu 136.5–143.6°), and all copper centers are connected orthogonally to neighboring metal sites.

In an attempt to introduce lanthanide ions into a nine metal grid assembly **16** was reacted sequentially with $\text{Gd}(\text{NO}_3)_3$ and $\text{Cu}(\text{NO}_3)_2$, with the formation of an unusual octanuclear grid-like cluster (Fig. 25) in the complex $[\text{Cu}_8(\text{L16})_4(\text{CH}_3\text{OH})_4(\text{CH}_3\text{CN})_4][\text{Gd}(\text{NO}_3)_4(\text{H}_2\text{O})_2]_2(\text{NO}_3)_6 \cdot 1.3\text{Cu}(\text{NO}_3)_2 \cdot 10\text{H}_2\text{O}$ (**41**), with a “pinwheel” arrangement of four peripheral Cu(II) centers attached by alkoxide bridges to a typical $[\text{Cu}_4(\mu\text{-O})_4]$ central core [26]. Figure 26 shows the core structure. As

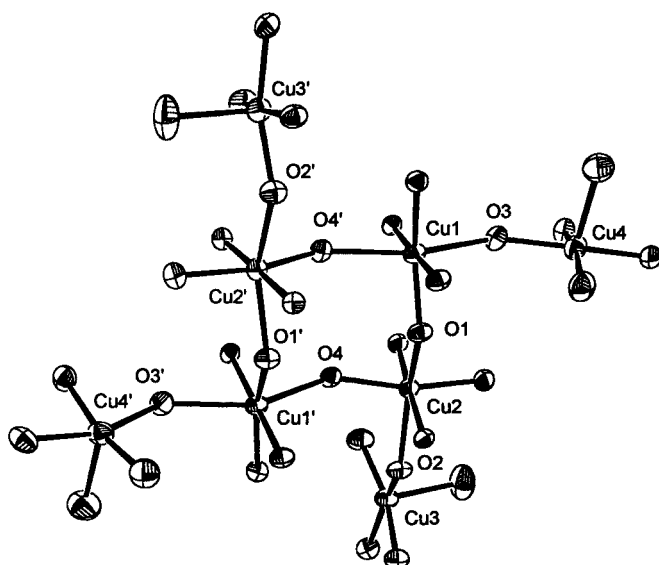


Fig. 26. Structural representation of the octanuclear core in $[\text{Cu}_8(\text{L16})_4(\text{CH}_3\text{OH})_4(\text{CH}_3\text{CN})_4][\text{Gd}(\text{NO}_3)_4(\text{H}_2\text{O})_2]_2(\text{NO}_3)_6 \cdot 1.3\text{Cu}(\text{NO}_3)_2 \cdot 10\text{H}_2\text{O}$ (**41**).

in previous copper examples of alkoxide bridged grids in this class all bridging connections between adjacent Cu(II) centers are strictly orthogonal, as a result of a twisting of the copper magnetic planes relative to neighboring magnetic planes.

5.3 Magnetic Properties of Grid Complexes

The proximity of the paramagnetic metal ion centers in these grid complexes can lead to spin exchange interactions through the intervening diamagnetic bridge groups. Representative examples of exchange coupling schemes will be described, and related to the symmetry properties of the particular grid arrangement.

5.3.1 $[2 \times 2]$ Complexes

In a general case the square (D_{4h}) or distorted square (D_{2d}) $[2 \times 2]$ grid can be described by an exchange coupling scheme involving two exchange integrals (J_1 , J_2) according to the appropriate Hamiltonian expression (Eq. 1) (Fig. 27):

$$H_{\text{ex}} = -2J_1\{S_2 \cdot S_3 + S_1 \cdot S_4\} - 2J_2\{S_1 \cdot S_2 + S_3 \cdot S_4\} - 2J_3\{S_1 \cdot S_3 + S_2 \cdot S_4\} \quad (1)$$

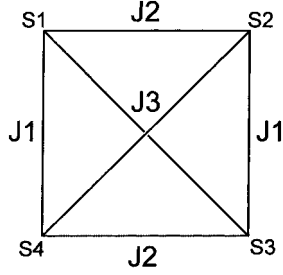


Fig. 27. Magnetic model for a $[2 \times 2]$ grid.

where $J1$ is the exchange along the vertical sides and $J2$ along the horizontal sides of the square. Diagonal terms ($J3$) can be set to zero because cross-coupling terms are assumed to be insignificant. Using the conventional spin-vector coupling model [27, 28] eigenvalues of Eq. (1) can be obtained analytically for a D4h $[2 \times 2]$ grid with $J = J1 = J2$. The eigenvalues are then given by

$$E(S', S_{13}, S_{24}) = -J[S'(S' + 1) - S_{13}(S_{13} + 1) - S_{24}(S_{24} + 1)] \\ - J3[S_{13}(S_{13} + 1) + S_{24}(S_{24} + 1)]$$

where $S_{13} = S_1 + S_3$; $S_{24} = S_2 + S_4$; and $S' = S_1 + S_2 + S_3 + S_4$.

Another coupling situation which arises in the limit $J1 = J3 = 0$ is that of a “dimer of dimers” (see Fig. 27 for model), corresponding to the general Hamiltonian

$$H_{ex} = -2J2S_1 \cdot S_2 - 2J2'S_3 \cdot S_4$$

where the horizontal coupling strengths might assume different values $J2$ and $J2'$. Using the same method the eigenvalues are obtained as:

$$E(S', S_{12}, S_{34}) = -J2[S_{12}(S_{12} + 1)] - J2'[S_{34}(S_{34} + 1)]$$

where $S_{12} = S_1 + S_2$; $S_{34} = S_3 + S_4$, and $S' = S_{12} + S_{34}$. All these results are valid for arbitrary values of the spin quantum numbers S_i ($i = 1 \dots 4$)

$$\chi_{M'} = \frac{N\beta^2 g^2}{3k(T - \theta)} \frac{\sum S'(S' + 1)(2S' + 1)E^{-E(S')/kT}}{\sum S'(2S' + 1)E^{-E(S')/kT}} \quad (2)$$

$$\chi_M = \chi_{M'}(1 - \rho) + \frac{2N\beta^2 g^2 \rho}{3kT} + TIP \quad (3)$$

Using the addition rules for spin vectors the allowed values for S' , and S_{13} , S_{24} , or S_{12} , S_{34} respectively can be obtained. Substituting the appropriate energy terms into the van Vleck equation (Eq. 2), the susceptibility values can be computed for a particular temperature range. In practice this can be achieved by the use of simple programming techniques whereby iterative procedures span the required S' values for fitted values of J , in routines that allow regression of the experimental data against

Eq. (3) [29]. Best fit values of g and J are thus obtained, allowing for paramagnetic impurity (fraction ρ), *TIP* (temperature independent paramagnetism), and a Weiss-like corrective term (θ) to deal with small intermolecular exchange effects. A review by Murray [30] deals more generally with the magnetic properties of tetranuclear complexes.

5.3.2 $[3 \times 3]$ Complexes

A similar approach can be adopted to deal with the $[3 \times 3]$ grid cases using an expanded Hamiltonian expression (Eq. 4) that assumes different J values for the interactions within the external ring of eight metal ions ($J1$), and for the interaction between the central metal and its immediate neighbors ($J2$) (model based on Fig. 28).

$$H_{\text{ex}} = -J1\{S_1 \cdot S_2 + S_2 \cdot S_3 + S_3 \cdot S_6 + S_6 \cdot S_9 + S_8 \cdot S_9 + S_7 \cdot S_8 + S_4 \cdot S_7 + S_1 \cdot S_4\} - J2\{S_2 \cdot S_5 + S_5 \cdot S_6 + S_5 \cdot S_8 + S_4 \cdot S_5\} \quad (4)$$

However, the energy eigenvalues cannot be obtained analytically as for the $[2 \times 2]$ grid examples described in the previous section. Their calculation requires the machinery of irreducible tensor operators [31, 32] and numerical diagonalization routines.

Dealing with such a complex system leads to a situation where, depending on the metal ion spin state, matrix dimensions quickly exceed the capacity of most computers. In the case of Cu(II) ($S = 1/2$) this is not a problem, but for Mn(II) ($S = 5/2$) calculations of the spin state ladder cannot be completed on a Pentium III based computer, even if all symmetries of the Hamiltonian (Eq. 4) are considered [32]. Simplification of Eq. (4) assuming $J1 = J2$ does enable fitting of the experimental data in an acceptable timeframe, since in this case the energy spectrum needs to be calculated numerically only once. We have developed the MAGMUN/ow0L program package, which handles such a situation. It is freely available on request from the authors [33]. In an initial step the energy spectrum is calculated with ow0L and stored as a ".spk" file. This file is then opened with MAGMUN, which performs the

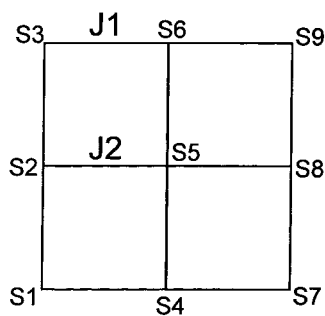


Fig. 28. Magnetic model for a $[3 \times 3]$ grid.

fitting according to Eqs. (2) and (3). If not otherwise stated the theoretical curves presented in this review were obtained with these programs.

5.3.3 Magnetic Properties of [2 × 2] and [3 × 3] Grids

Complex **17** (Fig. 2) appears to be coupled very weakly antiferromagnetically, with a slight drop in χT below 25 K, associated with $J = -0.24 \text{ cm}^{-1}$ [7], as determined by data fitting to Eqs. (1)–(3) for $J = J1 = J2$. The very weak coupling is consistent with the orthogonal arrangement of the magnetic d orbitals relative to the phenoxide bridging connections, despite the large Cu–O–Cu angles ($>140.0^\circ$), but surprisingly inconsistent with the properties observed for e. g. **20** and related compounds (*vide infra*). **18** (Fig. 3) appears to exhibit strong intra-molecular anti-ferromagnetic coupling, but the magnetic results are somewhat inconclusive. No magnetic properties are reported for **19** [8, 9].

Complex **20** (Fig. 4) has a similar orthogonal arrangement to **17** in which the metal ion $d_{x^2-y^2}$ orbitals are twisted relative to their neighbors, with short/long axial/equatorial contacts through the alkoxide bridges. **20** displays magnetic properties typical of an intra-molecular ferromagnet [10a]. Figure 29 shows the variation of μ (mol) as a function of temperature, with an increase in moment with decreasing temperature to a maximum of $4.8 \mu_B$ at 5 K. The data were fitted to Eq. (3) ($S_i = 1/2$) to give $g = 2.119(7)$, $J = 9.8(4) \text{ cm}^{-1}$, $\rho = 0.00002$, $\theta = -0.5 \text{ K}$, $TIP = 0.000234 \text{ cm}^3 \text{ mol}^{-1}$, $10^2 R = 0.48$ ($R = [\sum(\chi_{\text{obs}} - \chi_{\text{calc}})^2 / \sum \chi_{\text{obs}}^2]^{1/2}$). The solid line in Fig. 29 was calculated with these parameters. Magnetization data as a function of field at 2 K (Fig. 30) can be fitted successfully to the appropriate Brillouin function for $g = 2.119$, $S = 4/2$, thus confirming the ferromagnetic ground state. The remarkable feature of this compound, and several others like it [10a, b], is the ferromagnetic behavior. The close spacing of the metal centers, and the very large Cu–O–Cu bridge angles, would normally have dictated strong anti-ferromagnetic exchange, as a result of the usually efficient overlap situation between the copper magnetic orbitals via the alkoxide bridges, if they were connected equatorially [34–36]. However the orthogonal bridging interactions in this case clearly impede this

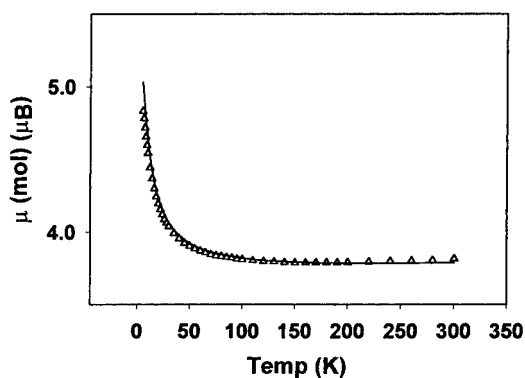


Fig. 29. Magnetic data (μ mol versus temperature) for $[\text{Cu}_4(\text{L}_3)_4(\text{H}_2\text{O})](\text{NO}_3)_4 \cdot 3\text{H}_2\text{O}$ (**20**) (see text for fitted parameters).

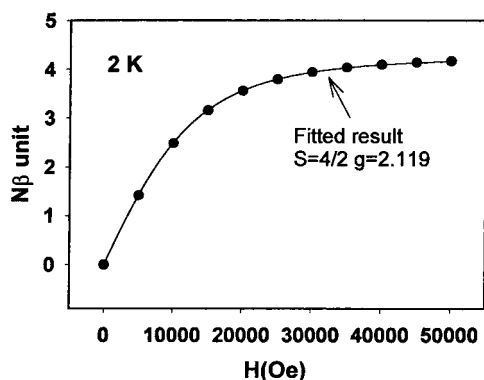


Fig. 30. Magnetization versus field data for $[\text{Cu}_4(\text{L}_3)_4(\text{H}_2\text{O})](\text{NO}_3)_4 \cdot 3\text{H}_2\text{O}$ (**20**) at 2 K.

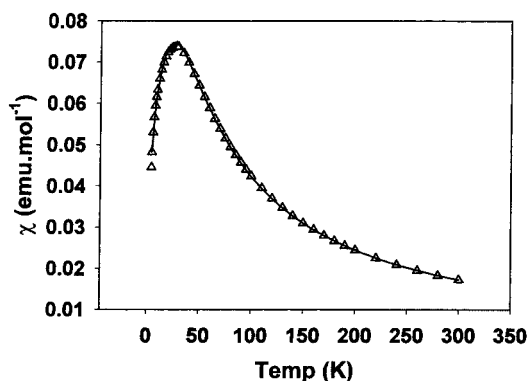


Fig. 31. Magnetic data (χ_{mol} versus temperature) for $[\text{Ni}_4(\text{L}_3)_4(\text{H}_2\text{O})_4](\text{NO}_3)_4 \cdot 8\text{H}_2\text{O}$ (**21**) (see text for fitted parameters).

process, as the copper magnetic orbitals orient themselves at right angles to those in neighboring atoms, leading to the ferromagnetic behavior.

Complex **21** (Fig. 5) has a similar square alkoxide bridged structure, but orbital orthogonality is not an issue in the nickel case. Figure 31 clearly shows that the intra-molecular exchange coupling is anti-ferromagnetic, and a data fitting to Eq. (3) ($S_i = 1$) gives $g = 2.29(1)$, $J = -13.6(2) \text{ cm}^{-1}$, $\rho = 0.012$, $\theta = 0 \text{ K}$, $TIP = 0.000800 \text{ cm}^3 \text{ mol}^{-1}$, $10^2 R = 0.70$. The solid line in Fig. 31 was calculated with these parameters. The moderate anti-ferromagnetic exchange is entirely consistent with the large Ni–O–Ni angles [10a, 37]. **22** (Fig. 6) displays similar anti-ferromagnetic properties with a magnetic moment per mole dropping from $11.4 \mu_{\text{B}}$ at 300 K to $3.5 \mu_{\text{B}}$ at 4.5 K. A similar data treatment using Eq. (3) ($S_i = 5/2$) gave $g = 1.99(1)$, $J = -2.85(4) \text{ cm}^{-1}$, $\rho = 0.014$, $\theta = 0 \text{ K}$, $TIP = 0 \text{ cm}^3 \text{ mol}^{-1}$ ($10^2 R = 1.0$). Such behavior is again consistent with the large Mn–O–Mn bridge angles [10b]. **23** (Fig. 7) has a similar drop in moment ($9.4 \mu_{\text{B}}$ at 300 K, $3.5 \mu_{\text{B}}$ at 5 K), and surprisingly gave a good fit to Eq. (3) ($S_1 = 3/2$) for $g = 2.42(1)$, $J = -6.95(4) \text{ cm}^{-1}$, $\rho = 0.004$, $TIP = 0.001200 \text{ cm}^3 \text{ mol}^{-1}$ ($10^2 R = 1.2$). The intra-molecular anti-ferromagnetic coupling is again consistent with the alkoxide bridged square structure, and the large Co–O–Co angles [10b].

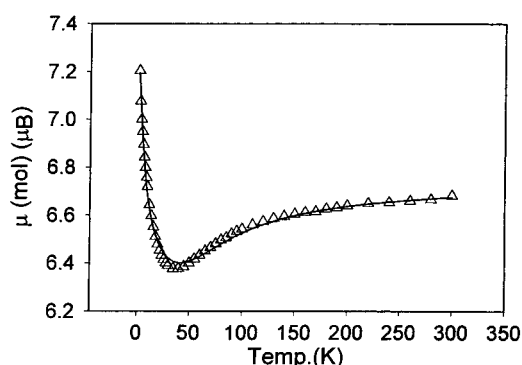


Fig. 32. Magnetic data (μmol versus temperature) for $[\text{Cu}_3\text{Fe}(\text{L}_3)_4(\text{NO}_3)_2](\text{ClO}_4)_4(\text{NO}_3)_4$ (**24**) (see text for fitted parameters).

Complex **24** (Fig. 8) has a unique structural arrangement in which axial connections between both Cu(3) and Cu(1) and Fe(1), and between Cu(2) and Cu(1), and an equatorial connection between Cu(2) and Cu(3) (Cu(2)–O(2)–Cu(3) 142.0°) would suggest a combination of ferromagnetic and anti-ferromagnetic interactions. The plot of μ (mol) as a function of temperature (Fig. 32) shows a drop from $6.68 \mu_B$ at 300 K to $6.38 \mu_B$ at 35 K followed by a rise to $7.20 \mu_B$ at 2 K, suggesting that this is the case. The magnetic data were fitted to an exchange expression based on the Hamiltonian (Eq. 5).

$$H_{\text{ex}} = J_1 S_{\text{Cu}2} S_{\text{Cu}3} - J_2 S_{\text{Fe}1} S_{\text{Cu}1} - J_3 S_{\text{Fe}1} S_{\text{Cu}3} - J_4 S_{\text{Cu}1} S_{\text{Cu}2} \quad (5)$$

The best fit was obtained when J_3 and J_4 were set to zero, corresponding to a “dimer of dimers” situation, with $g_{\text{av.}} = 2.04$, $J_1 = -61.5 \text{ cm}^{-1}$, $J_2 = 1.1 \text{ cm}^{-1}$, $TIP = 0.000150 \text{ cm}^3 \text{ mol}^{-1}$. The solid line in Fig. 32 was calculated with these values. This is reasonable given the orthogonal Cu–Fe and Cu–Cu connections. The significant anti-ferromagnetic coupling between Cu(2) and Cu(3), in combination with the ferromagnetic interaction between Fe(1) and Cu(1) would of necessity lead to a $S = 3$ ground state. Magnetization versus field data at 2 K (0–5 T) (Fig. 33) confirm this [10c] (solid line calculated from the appropriate Brillouin function with $S = 3$, $g = 2.04$).

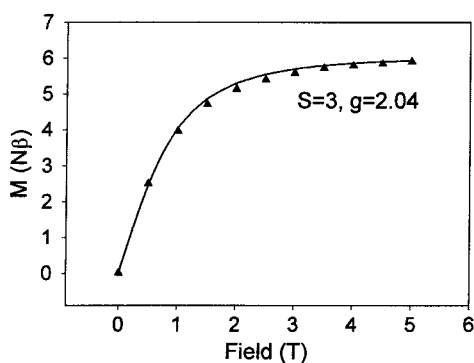


Fig. 33. Magnetization versus field data for $[\text{Cu}_3\text{Fe}(\text{L}_3)_4(\text{NO}_3)_2](\text{ClO}_4)_4(\text{NO}_3)_4$ (**24**).

Complex **25** (Fig. 9) has an unusual rectangular structure with both alkoxide and diazine bridges. The alkoxide bridges connect adjacent pairs of copper centers orthogonally, while the diazine groups bridge equatorially. The χ (mol)/T profile shows a maximum at 150 K, and a fit of the data to Eq. (3) ($S_i = 1/2$) gives an excellent fit with $g = 2.18(1)$, $J_1 = -168(1) \text{ cm}^{-1}$, $J_2 = 0 \text{ cm}^{-1}$, $\rho = 0.029$, $TIP = 0.000240 \text{ cm}^3 \text{ mol}^{-1}$ ($10^2 R = 0.29$). The strong anti-ferromagnetic component is clearly associated with the almost *trans* N–N bridges [38–40], while $J_2 = 0 \text{ cm}^{-1}$ is in complete agreement with the orthogonal alkoxide bridges. χT for **26** (Fig. 10) is almost constant in the range 6.5–280 K indicating no significant interaction between the copper(II) centers. Cu–N–N–Cu torsion angles of 97° are consistent with this behavior, but somewhat larger than anticipated for orthogonal overlap of the copper magnetic orbitals via the N–N single bond connection [38–40].

Magnetic data for **27** and **28** (Figs. 11 and 12) indicate intramolecular antiferromagnetic coupling within the square grids, with $J \approx -170$ and -63.5 cm^{-1} respectively. The orthogonality between Cu(1) and Cu(2) in **27** suggests that a dimer model is more appropriate with Cu(1) and Cu(1') bridged by two pyrazole groups. In **28** all four copper centers are linked equatorially with a single pyrazole bridge. **29** (Fig. 13) has a clearly defined square arrangement of four copper centers bridged by single imidazolate linkages. Variable temperature magnetic data are interpreted with a square model (Eq. 3; $S_i = 1/2$; $J = J_1 = J_2$) to give $g = 2.062(4)$, $J = -97.6 \text{ cm}^{-1}$. These results are consistent with previous studies involving pyrazole and imidazole bridged complexes [38, 41, 42].

Complex **30** (Fig. 14) has a square arrangement of four copper ions bridged equatorially by single N–O linkages. Variable temperature magnetic data indicated strong antiferromagnetic coupling, and a data fit to Eq. (3) ($S_i = 1/2$; $J = J_1 = J_2$) gave $g = 2.15(3)$, $J = -349(5) \text{ cm}^{-1}$, consistent with related aldoxime bridged dicopper(II) complexes [43]. Complex **31** (Fig. 15) has four octahedral Ni(II) centers bridged directly by a bifurcated bridge involving two four bond pathways (Ni–N–C–N–Ni and Ni–N–C–O–Ni). The grid is slightly distorted (Ni–Ni–Ni–Ni torsional angle 34.8° , with long Ni–Ni distances (5.567 \AA), but exhibits a crystallographically imposed S_4 symmetry axis. Variable temperature magnetic data have been interpreted according to Eq. (3) ($S_i = 1$; $J = J_1 = J_2$) to give $g = 2.24$, $J \approx 0.75 \text{ K}$, with inclusion of a uniaxial zero field splitting term $|D| = 3 \text{ K}$ [15]. Given the long distance between the Ni centers the positive J value, indicating ferromagnetic coupling, is quite surprising. Complex **32** (Fig. 16) involves pyrimidine bridges between Co(II) centers, creating even larger Co–Co separations ($6.4\text{--}6.6 \text{ \AA}$). The magnetic properties of a related, and structurally similar complex $[\text{Co}(\text{L10})]_4(\text{PF}_6)_8$ (L10; $R_1 = \text{H}$, $R_2 = \text{Me}$) [44] are interpreted in terms of a quantum spin system of four antiferromagnetically coupled high spin Co(II) centers with effective spin $S_i = 1/2$. This is confirmed by magnetization studies at 2 K as a function of field. The quantitative analysis of the magnetic properties is impeded in this case by the orbital contribution of the high spin Co(II) ions to the magnetism. The effective exchange integral was estimated to be $J' \approx -13.5 \text{ K}$, corresponding to a microscopic exchange coupling of $J \approx -1.5 \text{ K}$. The magnetism of the isomorphous $[\text{Ni}(\text{L10})]_4(\text{PF}_6)_8$ complex has been carefully examined by variable temperature magnetic measurements on single crystals [45]. The data have been analyzed with Eq. (3) ($S_i = 1$; $J = J_1 = J_2$),

expanded by uniaxial zero field splitting terms and anisotropic g -factors ($g = 2.10$, $g = 2.02$, $J = -4.2$ K, $D = -8.0$ K). Strong evidence for a sizeable biquadratic exchange contribution ($J' = 0.5$ K) has also been found.

The related iso-structural iron(II) complex **33** is an example of an unusual spin-crossover grid system. Room temperature magnetization data at 1 T suggest three HS Fe(II) ions and one LS Fe(II) ion. χT values drop gradually from $2.5 \text{ cm}^3 \text{ K mol}^{-1}$ at 300 K to $1.4 \text{ cm}^3 \text{ K mol}^{-1}$ at 30 K, followed by a further drop towards 4.2 K attributable to zero-field splitting. The gradual decrease in χT on lowering the temperature is interpreted in terms of a “practically non-cooperative spin crossover situation”, with a residual HS fraction at low temperature. At 4.2 K both HS and LS Fe(II) forms are confirmed by Mössbauer spectroscopy, with a population of 46% and 54% respectively. At 300 K the HS state has a population of 80% [17].

Complex **34** (Fig. 17) involves five bond pathways between Ni(II) centers, and not surprisingly exchange coupling is essentially non-existent [18]. **35** (Fig. 18) has a similar five bond pyrazine bridging connection between Cu(II) centers, and good fitting of the variable temperature magnetic data to Eq. (3) ($S_i = 1/2$) gave $g = 2.09$, $J_1 = -2.5 \text{ cm}^{-1}$, $J_2 = -0.2 \text{ cm}^{-1}$ [19]. Given the long copper–copper distances and the effective “dimer of dimers” magnetic structure in **35** this result is very reasonable. **36** has a similar structure and magnetic data are interpreted in terms of ZFS effects only, with insignificant intra-molecular spin exchange [20].

37 (Fig. 19) involves a similar sized asymmetric grid to **34–36**, with five bond bridges between Fe(II) centers. μ (mol) drops slightly from $11.5 \mu_B$ at 300 K to $11.0 \mu_B$ at 30 K, and then drops precipitously to $6.1 \mu_B$ at 2 K. These data are consistent with HS Fe(II) and insignificant exchange coupling, with the low temperature drop in μ_B associated with zero-field splitting [21]. Complex **38** (Figs. 20 and 21) is a novel expanded square grid with a ring of eight Ni(II) centers linked by *trans* N–N bond bridges [22]. μ (mol) shows a dramatic drop from $8.2 \mu_B$ at room temperature to $2 \mu_B$ at 2 K, indicative of substantial intra-molecular anti-ferromagnetic exchange (Fig. 34). The data were fitted, as described earlier [33], to an isotropic exchange expression based on an exchange Hamiltonian (Eq. 6) that assumes a ring

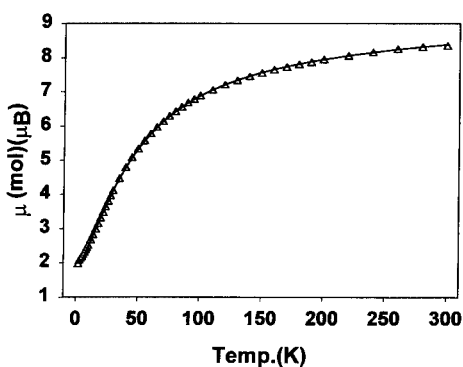


Fig. 34. Magnetic data (μ mol versus temperature) for $[\text{Ni}_8(\text{L15})_4(\text{H}_2\text{O})_8](\text{BF}_4)_8 \cdot 16\text{H}_2\text{O}$ (**38**) (see text for fitted parameters).

of eight Ni(II) centers connected by equivalent bridging groups.

$$H_{\text{ex}} = -J \{ S_1 \cdot S_2 + S_2 \cdot S_3 + S_3 \cdot S_4 + S_4 \cdot S_5 \\ + S_5 \cdot S_6 + S_6 \cdot S_7 + S_7 \cdot S_8 + S_1 \cdot S_8 \} \quad (6)$$

A good data fit to adapted Eq. (3) gave $g = 2.250(5)$, $J = -15.0(4) \text{ cm}^{-1}$, $TIP = 0.00150 \text{ cm}^3 \text{ mol}^{-1}$. The moderately strong anti-ferromagnetic exchange is associated with the almost *trans* bridging arrangement of the Ni(II) centers around the N–N single bonds, in complete agreement with earlier studies [38–40]. The solid line in Fig. 34 is calculated with these parameters.

Complex **39** (Figs. 22 and 23) corresponds to a fusion of four square subunits like **22**, and as such would be expected to display similar magnetic properties. Figure 35 shows a pronounced drop in magnetic moment (per mole) from $16.9 \mu_{\text{B}}$ at 300 K to $5.0 \mu_{\text{B}}$ at 1.8 K, clearly indicating the presence of nine HS Mn(II) centers experiencing intra-molecular anti-ferromagnetic exchange. The low temperature value suggests an $S = 5/2$ ground state with a sizeable magnetic anisotropy due to zero field splitting. This is corroborated by field dependent studies at 1.8 K (Fig. 36; solid line calculated from the appropriate Brillouin function with $g = 2$, $S = 5/2$). The increase of magnetic moment at higher fields reflects the presence of low-lying excited states. Quantifying the exchange integral using Eq. (4) has proved to be difficult since, even if all symmetries of Eq. (4) are exploited [32, 46], the dimension of the largest matrix to be solved is still as large as 22 210 [47]. This exceeds by far the capacity of today's PCs. However, the somewhat simpler system of a ring of eight $S_i = 5/2$ ions has been solved recently [46]. These results could be used to calculate the susceptibility of Eq. (4) in the limit $|J_1| > |J_2|$. With $J_1 = -3.8 \text{ cm}^{-1}$ a reasonable fit could be obtained (Fig. 35; $g = 2.0$). This value is comparable with that observed for the square $[2 \times 2]$ analog **22** ($J = -2.85 \text{ cm}^{-1}$) [10b].

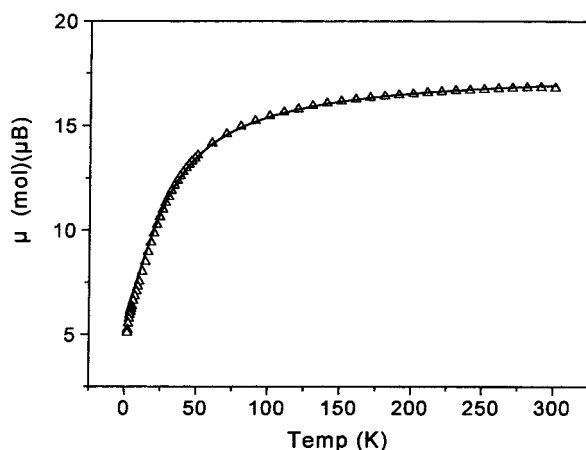


Fig. 35. Magnetic data (μ_{mol} versus temperature) for $[\text{Mn}_9(\text{L16})_6](\text{ClO}_4)_6 \cdot 18\text{H}_2\text{O}$ (**39**) (see text for fitted parameters).

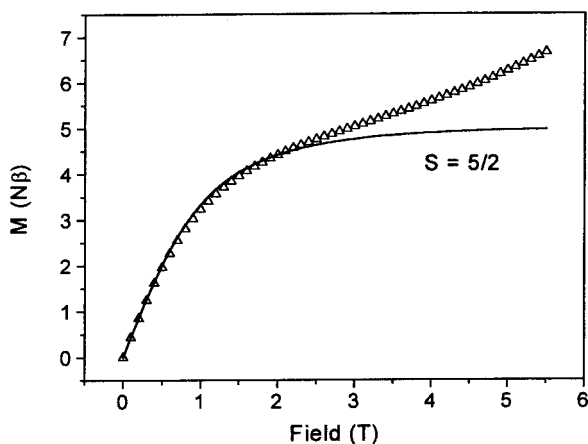


Fig. 36. Magnetization versus field data for $[\text{Mn}_9(\text{L16})_6](\text{ClO}_4)_6 \cdot 18\text{H}_2\text{O}$ (**39**) at 1.8 K.

Complex **40** has an analogous structure (Fig. 24 illustrates the core), with a similar disposition of the copper(II) magnetic orbitals to those found in related Cu_4 square grids [10, 25]. In the outer ring the eight copper centers are linked with alternating axial/equatorial connections between the copper $d_{x^2-y^2}$ orbitals leading to a situation of strict magnetic orbital orthogonality. $\text{Cu}(5)$ has an unusual tetragonally compressed six-coordinate geometry, and nominally a d_{z^2} ground state. This suggests orthogonality between $\text{Cu}(5)$ and its neighbors as well. The profile of magnetic moment per mole as a function of temperature (Fig. 37) shows a drop from $6.4 \mu_{\text{B}}$ at 300 K to $5.5 \mu_{\text{B}}$ at 25 K, followed by a sharp rise to $6.9 \mu_{\text{B}}$ at 2 K, indicating the presence of fairly strong anti-ferromagnetic exchange, but also ferromagnetic exchange as well. The data were fitted to Eq. (4) to give $g = 2.30$, $J1 = 0.52 \text{ cm}^{-1}$,

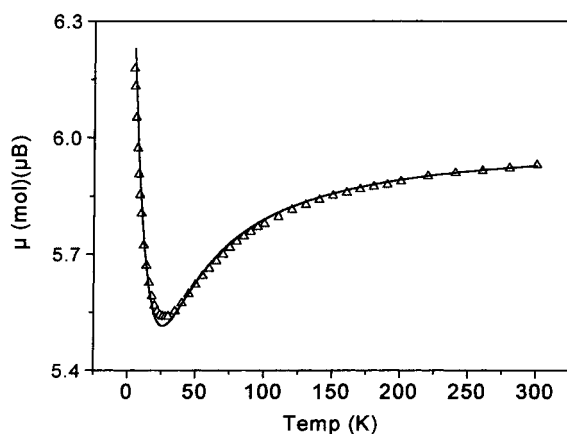


Fig. 37. Magnetic data (μmol versus temperature) for $[\text{Cu}_9(\text{L16})_6](\text{NO}_3)_{12} \cdot 9\text{H}_2\text{O}$ (**40**) (see text for fitted parameters).

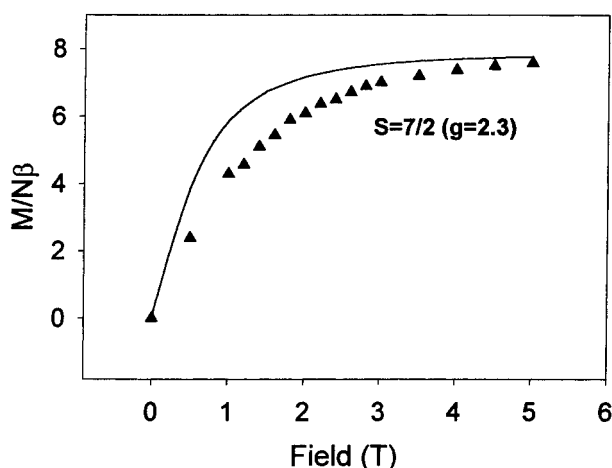


Fig. 38. Magnetization versus field data for $[\text{Cu}_9(\text{L16})_6](\text{NO}_3)_{12} \cdot 9\text{H}_2\text{O}$ (**40**) at 2 K.

$J_2 = -24.3 \text{ cm}^{-1}$ [48]. The solid line in Fig. 37 is calculated with these parameters. Since J_1 (ferromagnetic) dominates at low temperature this leads to an effective $S = 7/2$ low temperature ground state [48], in agreement with magnetization versus field data at 2 K (Fig. 38). The dominant exchange term is between Cu(5) and its neighbors, and combined with the nominal S_4 molecular symmetry, it reveals what can only be described as a fluxional ground state for Cu(5). While Cu(5) appears to have a d_{z^2} ground state according to the structure it must undergo a dynamic Jahn–Teller distortion effect, where in its relationship with one equivalent neighboring copper center it appears to be $d_{x^2-y^2}$, and is anti-ferromagnetically coupled ($J_2 = -24.3 \text{ cm}^{-1}$). A detailed study of the magnetic anisotropy has provided further strong evidence for a complicated ground state of the Cu(II) ions [48]. The thermodynamic spectroscopy of the ground state, obtained by means of high-field torque magnetometry, gave a g-factor anisotropy of $\Delta g \equiv g_{\parallel} - g_{\perp} = -0.14(2)$ [48]. If the Cu(II) ions assume pure $d_{x^2-y^2}$ or d_{z^2} ground states as suggested by the structure, one would expect $\Delta g > 0$ in striking contrast to the experimental finding. The zero field splitting factor was also determined to be $D = 0.009(1) \text{ K}$. Since the dipole–dipole interaction between the nine Cu(II) ions contributes only $D^{\text{dip}} = 0.012 \text{ K}$ to this splitting, the presence of an anisotropic exchange interaction must be assumed, adding an additional splitting of $D^{\text{ex}} = -0.003(1) \text{ K}$. Because $|J_1| \ll |J_2|$ one expects that only the couplings involving Cu(5) contribute to the anisotropic exchange, with a strength which could be estimated to be $J^{\text{aniso}} = 0.11(3) \text{ K}$, in satisfying agreement with theoretical expectation [48].

Complex **41** (Fig. 25) has an orthogonally bridged expanded $[2 \times 2]$ grid structure in the shape of a “pin-wheel” of eight Cu(II) centers, with two isolated Gd(III) ions and 1.3 Cu(II) ions in the lattice structure, according to the X-ray structural analysis. Magnetic moments (per mole) rise with decreasing temperature from $13.1 \mu_{\text{B}}$ at 300 K to $14.5 \mu_{\text{B}}$ at 2 K (Fig. 39), exceeding the spin only value sum associated with

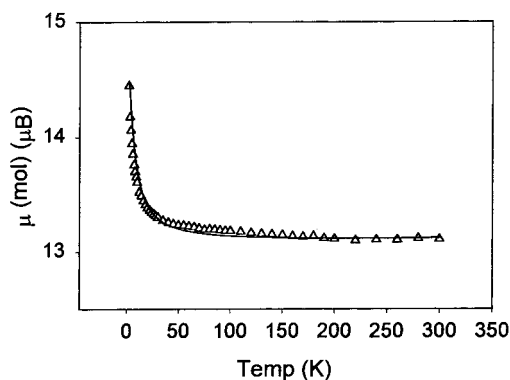


Fig. 39. Magnetic data (μ mol versus temperature) for $[\text{Cu}_8(\text{L16})_4(\text{CH}_3\text{OH})_4(\text{CH}_3\text{CN})_4][\text{Gd}(\text{NO}_3)_4(\text{H}_2\text{O})_2]_2(\text{NO}_3)_6 \cdot 1.3\text{Cu}(\text{NO}_3)_2 \cdot 10\text{H}_2\text{O}$ (41) (see text for fitted parameters).

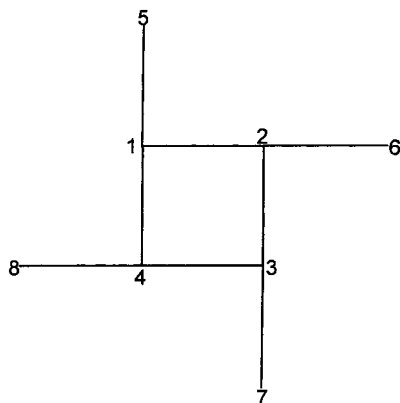


Fig. 40. Magnetic model for “pin-wheel” cluster.

two isolated Gd(III) centers and 9.3 isolated Cu(II) centers. This suggests intramolecular ferromagnetic behavior within the cluster. The magnetic data were fitted to an isotropic exchange expression based on the Hamiltonian (Eq. 7) for a “pin-wheel” arrangement of eight copper centers (Fig. 40), with terms to include two Curie-like Gd(III) centers, and 1.3 isolated Curie-like Cu(II) centers.

$$H_{\text{ex}} = -J \{ S_1 \cdot S_2 + S_2 \cdot S_3 + S_3 \cdot S_4 + S_4 \cdot S_1 + S_1 \cdot S_5 + S_2 \cdot S_6 + S_3 \cdot S_7 + S_4 \cdot S_8 \} \quad (7)$$

A good data fit was obtained with $g_{\text{av.}} = 2.113(2)$, $J = 5.0(2) \text{ cm}^{-1}$, $TIP = 0.000500 \text{ cm}^3 \text{ mol}^{-1}$, $\theta = -0.10 \text{ K}$, ($10^2 R = 1.0$). The solid line in Fig. 39 was calculated with these parameters. Magnetization versus field data at 2 K show that at 5 T the system approaches an $S = 23/2$ ground state, in agreement with the total spin situation. The dominant intramolecular ferromagnetic exchange is consistent with

previous Cu₄ and Cu₉ square grids with orthogonally arranged Cu(II) centers, and highlights the fact that systems of this sort are important models for higher order ferromagnetic grids.

5.3.4 Potential Applications of Magnetic Grids to Nanoscale Technology

It has been demonstrated that self-assembly procedures can produce ordered grid-like arrays of paramagnetic transition metal ions in close proximity, with magnetic interactions between the spin centers, and in some cases ferromagnetic behavior. Fabricating devices such that individual magnetic subunits can be addressed is a challenge, but could be approached in a number of ways; e. g. chemical incorporation into polymeric substrates, dispersion within a polymer matrix, surface deposition etc. It has recently been demonstrated that grids of type **10**, (e. g. [Co₄(L10)₄](PF₆)₈ (R₁ = H, R₂ = Me) can be deposited from solution in highly ordered monolayers on a pyrolytic graphite surface, and addressed using STM techniques [49], which is a clear indication of the potential in this area. Single grid cations could be addressed and extracted with a -0.5 V pulse at the STM probe. Monolayer deposition of such systems using vacuum technology has not been tried, but recent MALDI–TOF experiments with **39** and **40** indicate prominent molecular species corresponding to the molecular cations, indicative of the high gas phase stability of grids of this sort [50].

The successful use of magnetic grids will depend on many factors, in particular their ability to retain data bits of information once addressed and perturbed at room temperature. We are perhaps a long way from this goal, but the new physics that this type of system may present is as yet largely unexplored, and intensive activity will doubtless follow to e. g. increase grid dimensions by expanding the polytopic nature of the ligands, link magnetic grids together into chains and interlocked 2D and 3D arrays, add redox probes to the magnetic grids such that magnetic properties can be turned on and off by external electrochemical perturbations etc. These possibilities present exciting opportunities to address e. g. the failure of Moore's law, the thermal erasure problems with current magnetic data storage media, and the apparent insatiable desire of computer consumers to have faster and larger machines.

Acknowledgments

We thank the Cambridge Crystallographic Data Center for structural data.

References

- [1] C.C. Mann, *Technology Review* **2000**, May/June, 44–48.
- [2] D.A. Thompson and J.S. Best, *IBM J. Res. Develop.* **2000**, *44*, 311–322.
- [3] P. Vettiger, M. Despont, U. Drechsler, U. Drig, W. Hberle, M.I. Lutwyche, H.E. Rothuizen, R. Stutz, R. Widmer and G.K. Binning, *IBM J. Res. Develop.* **2000**, *44*, 323–340.
- [4] J.-M. Lehn, *Supramolecular Chemistry – Concepts and Perspectives*; VCH; Weinheim, **1995**.
- [5] P.N.W. Baxter, J.-M. Lehn, J. Fischer and M.-T. Youinou, *Angew. Chem. Int. Ed. Engl.* **1994**, *33*, 2284–2287.
- [6] G.F. Swiegers and T.J. Malefeste, *Chem. Rev.* **2000**, *100*, 3483–3537.
- [7] J. Rojo, J.-M. Lehn, G. Baum, D. Fenske, O. Waldmann and P. Müller, *Eur. J. Inorg. Chem.* **1999**, 517–522.
- [8] H. Cheng, D. Chun-ying, F. Chen-jie, L. Yong-jiang and M. Qing-jin, *J. Chem. Soc., Dalton Trans.* **2000**, 1207–1212.
- [9] C-y Duan, Z-h Liu, X-z You, F. Xue and T.W.C. Mak, *Chem. Commun.* **1997**, 381–382.
- [10] (a) C.J. Matthews, K. Avery, Z. Xu, L.K. Thompson, L. Zhao, D.O. Miller, K. Biradha, K. Poirier, M.J. Zaworotko, C. Wilson, A. Goeta and J.A.K. Howard, *Inorg. Chem.* **1999**, *38*, 5266–5276. (b) L.K. Thompson, C.J. Matthews, L. Zhao, Z. Xu, D.O. Miller, C. Wilson, M.A. Leech, J.A.K. Howard, S.L. Heath, A.G. Whittaker and R.E.P. Winpenny, *J. Solid State Chem.* **2001**, *159*, 308–320. (c) Z. Xu, L.K. Thompson, C.J. Matthews, D.O. Miller, A.E. Goeta and J.A.K. Howard, *Inorg. Chem.* **2001**, *40*, 2446–2449.
- [11] P.J. van Koningsbruggen, E. Müller, J.G. Haasnoot and J. Reedijk, *Inorg. Chim. Acta* **1993**, *208*, 37–42.
- [12] K.L.V. Mann, E. Psillakis, J.C. Jeffery, L.H. Rees, N.M. Harden, J.A. McCleverty, M.D. Ward, D. Gatteschi, F. Totti, F.E. Mabbs, E.J.L. McInnes, P.C. Riedi and G.M. Smith, *J. Chem. Soc., Dalton Trans.* **1999**, 339–348.
- [13] M. Mimura, T. Matsuo, T. Nakashima and N. Matsumoto, *Inorg. Chem.* **1998**, *37*, 3553–3560.
- [14] E. Colacio, C. López-Magaña, V. McKee and A. Romerosa, *J. Chem. Soc. Dalton Trans.* **1999**, 2923–2926.
- [15] R.W. Saalfrank, S. Trummer, U. Reimann, M.M. Chowdhry, F. Hampel and O. Waldmann, *Angew. Chem., Int. Ed. Engl.* **2000**, *39*, 3492–3494.
- [16] J. Rojo, F.J. Romero-Salguero, J.-M. Lehn, G. Baum and D. Fenske, *Eur. J. Inorg. Chem.* **1999**, 1421–1428.
- [17] E. Breuning, M. Ruben, J.-M. Lehn, F. Renz, Y. Garcia, V. Ksenofontov, P. Gütllich, E. Wegelius and K. Rissanen, *Angew. Chem. Int. Ed. Engl.* **2000**, *39*, 2504–2507.
- [18] C.S. Campos-Fernández, R. Clérac and K.R. Dunbar, *Angew. Chem. Int. Ed. Engl.* **1999**, *38*, 3477–3479.
- [19] H. Grove, J. Sletten, M. Julve, F. Lloret and J. Cano, *J. Chem. Soc., Dalton Trans.* **2001**, 259–265.
- [20] J. R. Galán-Mascarós and K. R. Dunbar, *Chem. Commun.* **2001**, 217–218.
- [21] L.K. Thompson, C. Wilson and J.A.K. Howard, unpublished results.
- [22] Z. Xu, L.K. Thompson, V.A. Milway, L. Zhao, T. Kelly and D.O. Miller, *Inorg. Chem.* (submitted for publication).
- [23] L. Zhao, C.J. Matthews, L.K. Thompson and S.L. Heath, *Chem. Commun.* **2000**, 265–266.
- [24] L. Zhao, Z. Xu, L.K. Thompson and D.O. Miller, *Polyhedron*, **2001**, *20*, 1359–1364.

- [25] L. Zhao, Z. Xu, L.K. Thompson, S.L. Heath, D.O. Miller and M. Ohba, *Angew. Chem. Int. Ed. Engl.* **2000**, *39*, 3114–3116.
- [26] Z. Xu, L.K. Thompson and D.O. Miller, *Chem. Commun.* **2001**, 1170–1171.
- [27] K. Kambe, *J. Phys. Soc. Jpn.* **1950**, *5*, 48.
- [28] R.L. Martin, In “*New Pathways in Inorganic Chemistry*”, E.A.V. Ebsworth, A.G. Maddock, A.G. Sharpe, Eds.; Cambridge University Press, Cambridge, **1978**, Chap. 9.
- [29] R.G. Dugleby, *Anal. Biochem.* **1981**, *110*, 9.
- [30] K.S. Murray, *Advances in Inorganic Chemistry*, **1995**, *43*, 261–356.
- [31] D. Gatteschi and L. Pardi, *Gazz. Chim. Ital.* **1993**, *123*, 231.
- [32] O. Waldmann, *Phys. Rev. B* **2000**, *61*, 6138.
- [33] MAGMUN/ow0L is available as a combined package free of charge from the authors (lthomp@mun.ca; waldmann@physik.uni-erlangen.de). MAGMUN has been developed by Dr. Zhiqiang Xu (Memorial University), and ow01.exe by Dr. O. Waldmann. We do not distribute the source code. The programs may be used only for scientific purposes, and economic utilization is not allowed. If either routine is used to obtain scientific results, which are published, the origin of the programs should be quoted together with a reference to this review.
- [34] V.H. Crawford, H.W. Richardson, J.R. Wasson, D.J. Hodgson and W.E. Hatfield, *Inorg. Chem.* **1976**, *15*, 2107.
- [35] L. Merz and W. Haase, *J. Chem. Soc., Dalton Trans.* **1980**, 875.
- [36] H. Astheimer and W. Haase, *J. Chem. Phys.* **1986**, *85*, 1427.
- [37] K.K. Nanda, L.K. Thompson, J.N. Bridson and K. Nag, *Chem. Commun.* **1994**, 1337–1338.
- [38] Z. Xu, L.K. Thompson and D.O. Miller, *Inorg. Chem.* **1997**, *36*, 3985–3995.
- [39] Z. Xu, L.K. Thompson, D.O. Miller, H.J. Clase, J.A.K. Howard and A.E. Goeta, *Inorg. Chem.* **1998**, *37*, 3620–3627.
- [40] L.K. Thompson, Z. Xu, A.E. Goeta, J.A.K. Howard, H.J. Clase and D.O. Miller, *Inorg. Chem.* **1998**, *37*, 3217–3229.
- [41] M.S. Haddad, E.N. Duesler and D.N. Hendrickson, *Inorg. Chem.* **1979**, *18*, 141–148.
- [42] C-L. O’Young, J.C. Dewan, H.R. Lillienthal and S.J. Lippard, *J. Amer. Chem. Soc.* **1978**, *100*, 7291.
- [43] P. Chaudhuri, M. Winter, U. Flörke and H-J. Haupt, *Inorg. Chim. Acta* **1995**, *232*, 125.
- [44] O. Waldmann, P. Müller, G.S. Hannan, D. Volkmer, U.S. Schubert and J-M. Lehn, *Phys. Rev. Lett.* **1997**, *78*, 3390–3393.
- [45] O. Waldmann, J. Hassmann, P. Müller, D. Volkmer, U.S. Schubert and J-M. Lehn, *Phys. Rev. B* **1998**, *58*, 3277–3285.
- [46] (a) O. Waldmann, *Phys. Rev. B* **2000**, *61*, 6138. (b) O. Waldmann, R. Koch, S. Schromm, J. Schülein, P. Müller, I. Bernt, R.W. Saalfrank, F. Hampel and A.E. Balthes, *Inorg. Chem.* **2001**, *40*, 2986–2995.
- [47] O. Waldmann, L. Zhao and L.K. Thompson, *Phys. Rev. Lett.* **2002**, *88*, 066401-1.
- [48] O. Waldmann, R. Koch, S. Schromm, P. Müller, L. Zhao and L.K. Thompson, *Chem. Phys. Lett.* **2000**, *332*, 73–78.
- [49] A. Semenov, J.P. Spatz, M. Möller, J-M. Lehn, B. Sell, D. Schubert, C.H. Weidl and U.S. Schubert, *Angew. Chem. Int. Ed. Engl.* **1999**, *38*, 2547–2550.
- [50] L.K. Thompson and R. Helleur, unpublished results.

6 Biogenic Magnets

Richard B. Frankel and Bruce M. Moskowitz

6.1 Introduction

Biogenic iron minerals are formed by many organisms for a number of physiological functions [1, 2], form as a result of bacterial metabolic activities such as Fe(II)-oxidation or Fe(III)-respiration [3], or deposit on bacterial surfaces [4]. The most widely occurring biogenic iron minerals are amorphous or quasi-crystalline ferric oxyhydroxides, related to the mineral ferrihydrite ($\text{Fe}_2\text{O}_3 \cdot 9\text{H}_2\text{O}$). Some organisms form more crystalline minerals such as lepidocrocite ($\gamma\text{-FeOOH}$) and goethite ($\alpha\text{-FeOOH}$) [5]. These minerals are all weakly magnetic at ambient temperature and while their magnetic properties have been exploited in certain medical diagnostic and imaging technologies, their magnetism has no known physiological function.

Other important biogenic iron minerals are the structurally isomorphous, inverse spinel ferrimagnets magnetite (Fe_3O_4) and greigite (Fe_3S_4). Magnetite occurs in a number of organisms including vertebrates [6], invertebrates [5], and bacteria [2] while greigite occurs in bacteria [7–9] and is reportedly associated with some plants [10]. Bacteria mineralize nanocrystalline magnetic iron minerals either directly by processes known as biologically controlled mineralization (BCM) or indirectly by processes known as biologically-induced mineralization (BIM) [11]. Examples of BCM and BIM of magnetic iron minerals are afforded by magnetotactic bacteria [12, 13] and dissimilatory iron-reducing bacteria [3, 14], respectively.

While all the physiological functions of magnetite and greigite in all organisms are not completely known, in some organisms magnetism per se is thought to play a role in behavioral responses to the direction and/or intensity of the geomagnetic field [15–18]. This role places certain restraints on the structure of the iron mineral grains and their spatial organization. The most studied connection between structure, organization, magnetic properties and function of magnetic iron minerals is in the magnetotactic bacteria [19]. These organisms will be the primary focus of this review.

6.1.1 Magnetotactic Bacteria

The ability of some motile, aquatic bacteria to orient and migrate along magnetic field lines is known as magnetotaxis [19]. Killed cells orient but do not migrate along the field lines, indicating that each cell has a permanent magnetic dipole that is oriented by the torque exerted by the local magnetic field. Cellular motility results in migration along the magnetic field lines [20]. Thus magnetotactic bacteria are essentially self-propelled magnetic dipoles.

Magnetotactic bacteria are indigenous in chemically stratified water columns or sediments where they occur predominantly at the microaerobic and the anoxic regions of the habitat or both [21]. The diversity of magnetotactic bacteria is reflected by the large number of different morphotypes found in environmental samples of water or sediment as well as by the phylogenetic analysis of cultured and uncultured magnetotactic bacteria [22]. Commonly observed morphotypes include coccoid to ovoid cells, rods, vibrios and spirilla of various dimensions and an apparently multicellular bacterium referred to as the many-celled magnetotactic prokaryote (MMP) [23]. All magnetotactic bacteria are motile by means of flagella and have a cell wall structure characteristic of Gram-negative bacteria. The arrangement of flagella varies between species/strains and can be either polar, bipolar, or in tufts.

6.1.2 Magnetosomes

All magnetotactic bacteria contain magnetosomes [24], intracellular structures that are responsible for the cellular magnetic dipole and magnetotaxis. The magnetosomes comprise magnetite or greigite crystals enveloped by phospholipid membranes [25, 26]. The magnetosome membrane is presumably a structural entity that is the locus of biological control over the nucleation and growth of the mineral crystal. Each magnetotactic species or strain exclusively produces either magnetite or greigite magnetosomes, except for one marine organism that produces magnetosomes of both kinds [21]. With few exceptions, the magnetosome crystals are of order 35 to 120 nm in length [27], which is within the permanent single-magnetic-domain (SD) size range for both minerals (Section 6.2.2). In the majority of magnetotactic bacteria, the magnetosomes are organized in one or more straight chains of various lengths parallel to the long axis of the cell (Fig. 1). There is evidence from Mössbauer spectroscopy of whole cells that the magnetosome chain is fixed within



Fig. 1. Transmission electron micrograph of *Magnetospirillum magnetotacticum* showing the chain of magnetosomes inside the cell. The magnetite crystals incorporated in the magnetosomes have cuboctahedral morphology and are ca. 42 nm long. The magnetosome chain is fixed in the cell and the interaction between the magnetic dipole moment associated with the chain and the local magnetic field causes the cell to be oriented along magnetic field lines. Rotation of the cellular flagella (not shown) causes the cell to migrate along the field lines. Bar equals 1 micron.

the cell [28], presumably by the magnetosome membrane. Dispersed aggregates or clusters of magnetosomes occur in some magnetotactic bacteria, usually at one side of the cell, which often corresponds to the site of flagellar insertion [29].

6.1.3 Magnetite Magnetosomes

Magnetite and other cubic spinel minerals are described in the $Fd\bar{3}m$ space group. Macroscopic crystals display octahedral $\{111\}$, more rarely dodecahedral $\{110\}$ or cubic $\{100\}$ habits. High resolution transmission electron microscopy and selected area electron diffraction have revealed that the magnetite grains within magnetosomes are single crystals of relatively high structural perfection [27, 30]. A striking feature of magnetosome magnetite crystals is that different bacterial species or strains can have different projected shapes when observed by transmission electron microscopy [12, 13, 27] (Fig. 2). In addition to roughly equidimensional shapes, several non-equidimensional shapes have been described [31, 32]; these include pseudo-prismatic and tooth-, bullet-, or arrowhead shapes [27, 32, 33], although some variations of shape and size can occur within single magnetosome chains [32]. Idealized habits of magnetosome magnetite crystals in a number of magnetotactic bacteria have been inferred from 2D high resolution lattice images, assuming low index faces [31, 34–37] (Fig. 3). In magnetotactic spirilla, such as *Magnetospirillum magnetotacticum*, the idealized crystal habits are equidimensional cuboctahedra comprising $\{100\}$ and $\{111\}$ forms [38]. In a number of other magnetotactic bacterial morphotypes, including cocci and vibrios, the crystals are elongated along a $[111]$ axis parallel to the magnetosome chain direction and the projected shapes are pseudo-prismatic. The idealized habits for the latter crystals comprise $\{100\}$, $\{111\}$, and $\{110\}$ forms with a total of 26 possible faces. The elongation along $[111]$ breaks the symmetry between the twelve $\{110\}$ faces into two groups of six symmetry-related faces, and between the eight possible $\{111\}$ faces into two groups of two and six faces. The six

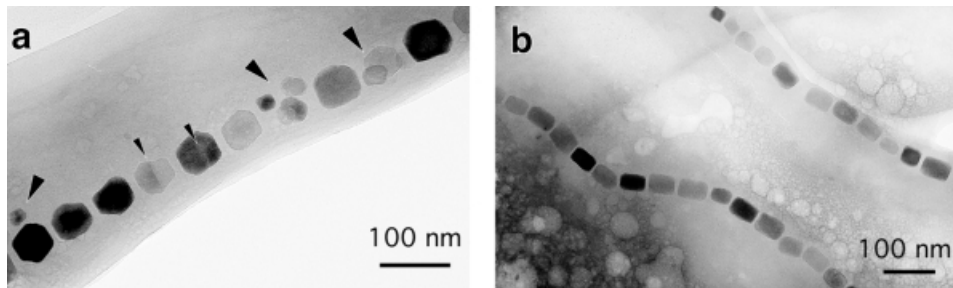


Fig. 2. Electron micrographs of magnetosome magnetite crystals in two cultured magnetotactic bacteria. (a) Cuboctahedral crystals in *Magnetospirillum magnetotacticum* (Fig. 1). Small arrows indicate twinned crystals and large arrows indicate clusters of small crystals. (b) Elongated crystals in magnetotactic bacterium strain MV-1. There are two cells, each with one chain of magnetosomes.

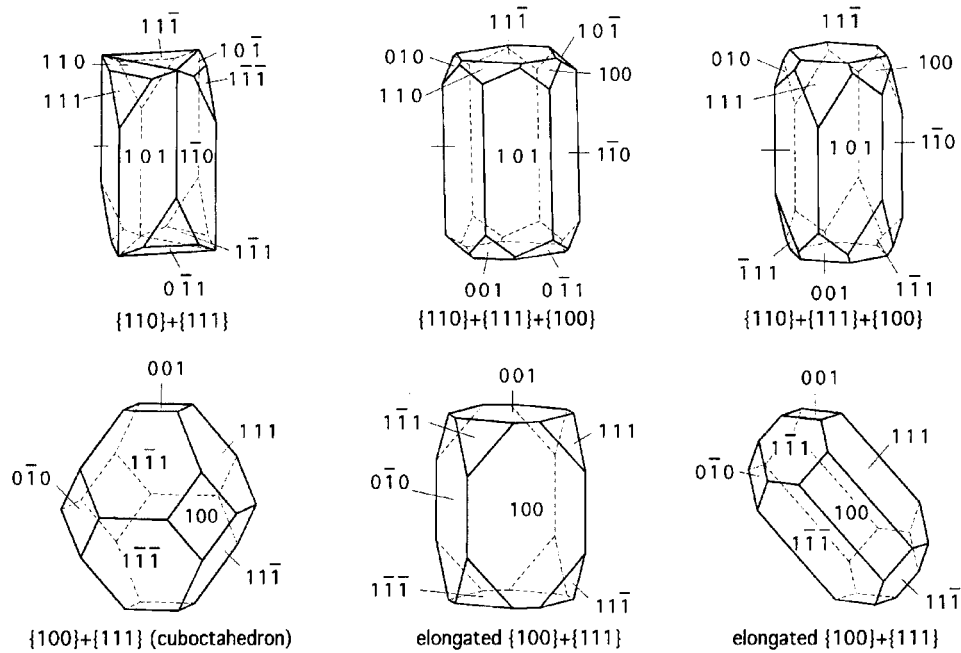


Fig. 3. Idealized crystal habits comprising $\{100\}$, $\{111\}$ and $\{110\}$ forms inferred from high resolution transmission electron microscopy of several different strains of magnetotactic bacteria.

$\{100\}$ faces remain symmetrically related. The result is a pseudo prism in which the $[111]$ axis of elongation is a threefold axis of symmetry. Six $\{110\}$ faces, parallel to $[111]$, form the body of the prism and two $\{111\}$ faces perpendicular to $[111]$ the end-caps [31]. The remaining six $\{100\}$, six $\{111\}$ and six $\{110\}$ planes form corner faces at the intersections between the body $\{110\}$ and end-cap $\{111\}$ faces. The overall size of the crystals, the width to length ratio, and the relative sizes of the corner faces of different form can vary from one bacterial species or strain to another, resulting in the distinctive projected shapes.

Statistical analysis of magnetosome magnetite crystals show narrow, asymmetric, size distributions and consistent W/L ratios within individual species, whereas synthetic magnetite crystals and BIM magnetite of similar mean size are distinctively different and have a lognormal size distribution that extends to relatively large crystals [27, 39].

6.1.4 Greigite Magnetosomes

Whereas all freshwater, magnetotactic bacteria have been found to contain magnetite magnetosomes, many marine, estuarine, and salt marsh species produce iron sulfide magnetosomes [7, 40] consisting primarily of the magnetic iron sulfide, greigite

ite. While none of the bacteria with greigite magnetosomes are available in pure culture, recognized greigite-producing magnetotactic bacteria includes the MMP and a variety of relatively large, rod-shaped bacteria. Like magnetite crystals in magnetosomes, the morphologies of the greigite crystals also appear to be species- and/or strain-specific [41].

The structures and compositions of intracellular Fe sulfides produced by magnetotactic bacteria have been studied by transmission electron microscopy [8, 9]. Greigite is common in all magnetotactic bacteria with iron sulfide magnetosomes. In addition, mackinawite (tetragonal FeS) and, tentatively, sphalerite-type cubic FeS were identified. Mackinawite converts to greigite over time. Orientation relationships between the two minerals indicate that the cubic close-packed S substructure remains unchanged during the transformation; only the Fe atoms rearrange. Planar defects typically occur along the close-packed layers of greigite crystals. Such defects are probably remnants of precursor structures and could indicate that all greigite crystals formed by solid-state transformation from mackinawite or cubic FeS. Neither mackinawite nor cubic FeS are magnetic; yet they are aligned in chains such that when converted to greigite, [100], probably the easy axis of magnetization in greigite, is parallel to the chain direction. It is perhaps kinetically easier for the bacterium to grow mackinawite or cubic FeS first; these then convert to greigite. A similar process occurs abiotically in sulfidic marine sediments, with greigite eventually converting to non-magnetic pyrite.

6.2 Magnetic Properties of Magnetosomes

The following sections summarize the physical principles that underlie the permanent cellular dipole in magnetotactic bacteria, including the roles of grain size, crystallographic orientation and organization of magnetosomes in chains. This will be followed by experimental studies of magnetosomes and the mechanism and function of magnetotaxis (Section 6.3). Some bulk physical and magnetic properties of magnetite and greigite are presented in Table 1.

6.2.1 Magnetic Microstates and Crystal Size

Ferrimagnetic materials are composed of small regions of uniform magnetization, magnetic domains, separated by domain walls, narrow transition regions of rapidly varying spin orientation. Domains are small in size (one to hundreds of micrometers), but much larger than atomic distances. The width of domain walls is typically 10 to 500 nm depending on the magnetic exchange and anisotropy energies of the material. The main driving force for domain formation is the minimization of magnetostatic energy through various types of flux closure configurations. In a uniformly magnetized grain (Fig. 4), uncompensated magnetic poles will form on the surfaces due to the magnetization (M_s) and is a potent source of magnetostatic

Table 1. Some magnetic and physical properties for magnetite and greigite [42].

Property	Fe ₃ O ₄	Fe ₃ S ₄
Crystal type	Cubic (Fd3m), $T > 125$ K Monoclinic, $T < 125$ K	Cubic (Fd3m)
Lattice parameter (300 K)	0.8396 nm	0.9881 nm
Density	5197 kg m ⁻³	4097 kg m ⁻³
Magnetic ordering	Ferrimagnetic	Ferrimagnetic
M_s (300 K)	480 kA m ⁻¹	80–125 kA m ⁻¹
Magnetic moment per formula unit (0 K)	4.1 μ_B	2.2 μ_B
Curie temperature	853 K	~603 K
Magnetic easy axis	$\langle 111 \rangle$, $T > 131$ K $\langle 100 \rangle$, 125 K $< T < 131$ K c -axis, $T < 125$ K	$\langle 100 \rangle$
K_1 (300 K)	-1.35×10^4 J m ⁻³	N/A
Crystallographic transition	$T = 125$ K	None
Magnetic isotropic point	$T = 131$ K	None

Notes: There is uncertainty in the value of the Curie temperature for greigite because its thermal decomposition temperature (starting around 573 K) is below the Curie temperature; M_s = saturation magnetization; μ_B = Bohr magneton, K_1 = magnetocrystalline anisotropy constant.

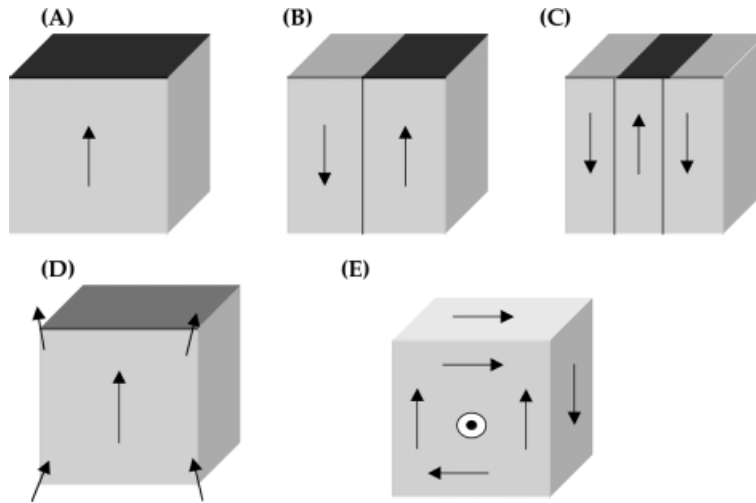


Fig. 4. Idealized domain states showing (A) uniform single domain state, (B) two and (C) three domain states with domain walls separating oppositely magnetized domains, (D) flower state, and (E) vortex state. The flower and vortex states are spin configurations predicted from three-dimensional micromagnetics models. The arrows show the direction of magnetization and dark and light shading on top surfaces indicate surface N or S poles. The flower state is an SD state but with lower energy than (A) due to the fanning out of the magnetization near the cube corners. The vortex state replaces the flower state above the SD limit and has lower energy than (B) due to the closed-flux configurations in three dimensions.

energy. Spin configurations that tend to form flux closure on surfaces or within the volume of the grain are preferred. The magnetostatic energy is long-ranged and also anisotropic due to the shape of the grain and leads to a grain-size dependence of microstates. Domains and domain walls in magnetite can be directly observed using various magnetic imaging techniques [43, 44].

6.2.2 Single-domain (SD) and Multi-domain (MD) States

A SD grain is uniformly magnetized with M_s along an easy axis, thus minimizing exchange and anisotropy energies (Fig. 4A). However, depending on the grain volume, the magnetostatic energy of this configuration may not be minimal. The magnetostatic energy can be reduced if the grain divides into two domains each magnetized with M_s in opposite directions (Fig. 4B), thus reducing the remanent moment of the grain. This subdivision into more and more domains (Fig. 4C) cannot continue indefinitely because the domain walls separating domains require additional exchange and magnetocrystalline energy to be produced. Eventually, an equilibrium number of domains will be reached which reflects the balance between the decrease in magnetostatic energy and the increase in wall energy, for a given grain size. Therefore, unlike SD grains, a multidomain (MD) grain is not uniformly magnetized. Inside each domain, the magnetization $M_i = M_s$ but the direction of M_i varies between different domains resulting in the grain as a whole having a small net remanence $\Sigma M_i \ll M_s$. On average, as the grain size increases, the number of domains also increases.

6.2.3 Superparamagnetic (SPM) State

The SD state is not the only important microstate for biogenic magnetic minerals. As grain size continues to decrease within the SD range, another critical threshold is reached, at which M_r (remanent magnetization) and H_c (coercive force) go to zero. When this happens, the grain becomes superparamagnetic (SPM). For magnetite, the SPM transition size at room temperature is about 30 nm [42]. In SPM grains, the magnetization, although uniform, is not constant in direction. Thermal energy causes spontaneous transitions of the magnetization over anisotropy barriers between energetically equivalent easy axis directions in the grain resulting in a time-average remanent moment of zero; thus, SPM grains do not exhibit remanence.

An SPM grain with volume V will approach an equilibrium value of magnetization in zero field with a characteristic relaxation time given by:

$$1/\tau = f_0 \exp(KV/kT) \quad (1)$$

where f_0 is the frequency factor ($\sim 10^9 \text{ s}^{-1}$; [45]), KV is the anisotropy energy, and T is absolute temperature. Because of the exponential dependence of the relaxation time on V and T , grains display sharp blocking transitions between stable SD with long relaxation times ($\tau \gg$ measurement time), and magnetically unstable SPM

with very short relaxation times ($\tau \ll$ measurement time). At a particular temperature (the blocking temperature), the measurement time equals the relaxation time (τ) and the grains become superparamagnetic and no longer carry remanence. At sufficiently low temperature, SPM grains block and exhibit stable SD behavior. The relaxation behavior of SPM grains as a function of temperature can be used to detect the presence of these particularly small grains (<30 nm) in biological and geological samples by measuring the temperature dependence of magnetic remanence (Fig. 5) or using variable temperature Mössbauer spectroscopy [45–47].

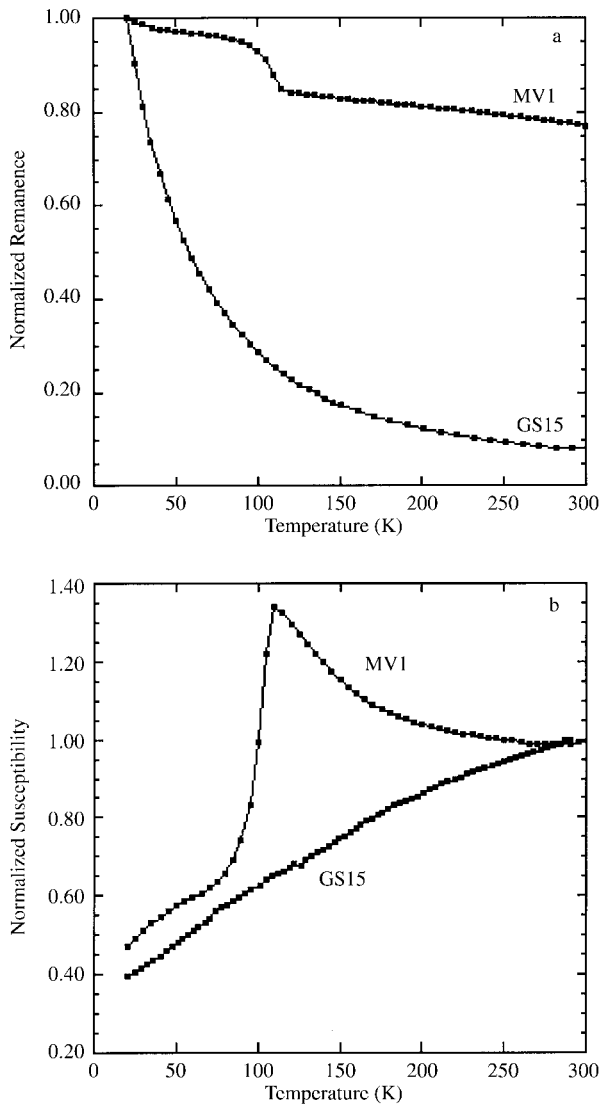


Fig. 5. Normalized (a) thermal demagnetization of saturation remanent magnetization and (b) magnetic initial AC susceptibility for two types of biogenic magnetites. Magnetite from magnetotactic bacteria (strain MV-1) shows the characteristic magnetite transition near 110 K, expected for grain sizes greater than 30 nm. Magnetite produced by *Geobacter* (GS-15) shows typical superparamagnetic behavior expected for magnetite grain sizes less than 30 nm.

6.2.4 Theoretical Domain Calculations: Butler–Banerjee Model

As the MD grain size decreases, a critical size (d_0) will be reached where the grain can no longer accommodate a domain wall. Below this critical size, the single domain structure is the lowest energy microstate. The critical size for the SD state depends on several parameters (M_s , magnetocrystalline anisotropy, exchange energy, grain shape). Theoretical estimates of size and shape ranges of single-domain, two-domain (TD), and superparamagnetic states for magnetite at 290 K were calculated by Butler and Banerjee [48] and are shown in Fig. 6. The model makes two main predictions:

- for an equidimensional cube, the SD–TD threshold size is 76 nm; and
- with increasing grain elongation, d_0 increases and becomes greater than 1000 nm for an axial ratio (width/length) <0.2 .

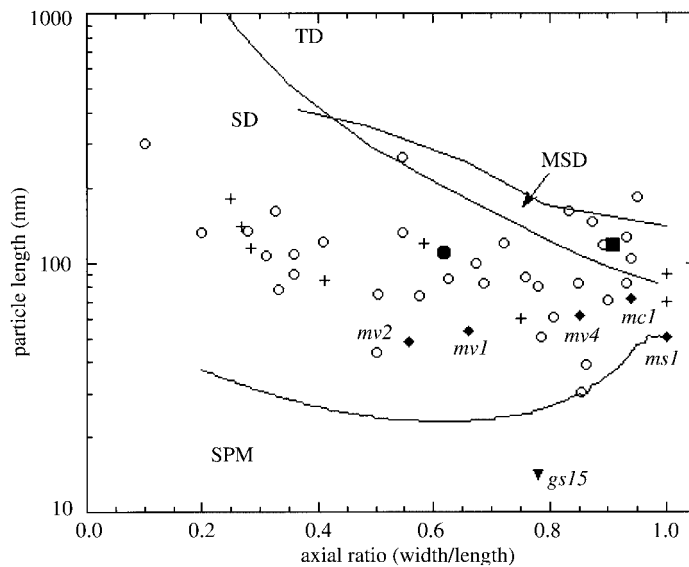


Fig. 6. Theoretical domain state diagram for magnetite showing the superparamagnetic (SPM), single domain (SD), two domain (TD), and metastable single domain (MSD) stability ranges for parallelepiped-shaped grains. Cubic-shaped grains correspond to an axial ratio of 1.0 and elongated grains have axial ratios (width/length) <1.0 . The SPM–SD and SD–TD curves are from Butler and Banerjee [48] and the MSD curve is from Fabian et al. [50]. The symbols represent the size and shape distributions of magnetite grains from magnetotactic bacteria and dissimilatory iron-reducing bacteria. Open circles: uncultured magnetotactic bacteria from lake sediments from Germany [33, 51]; crosses: uncultured magnetotactic bacteria from marine, brackish and freshwater environments in an around Moreton Bay, Australia [30]; solid diamonds: cultured strains of magnetotactic bacteria (*M. magnetotacticum*, MV-1, MV-2, MV-4, MC-1); solid square: Itaipu-1 magnetosome; solid circle: Itaipu-3 magnetosome (both Itaipu-1 and -3 are from uncultured magnetotactic bacteria from Brazil [52–54]; solid inverted triangle: extracellular magnetite from *Geobacter* (GS-15 [3, 47]). (After Bazylnski and Moskowitz, 1997 [55]).

Because of shape anisotropy, the SD threshold increases with decreasing axial ratio for non-equidimensional grains. A similar calculation has also been carried out for the SD–TD transition size for greigite and shows that greigite magnetosomes fall within the predicted SD stability field [49]. However, many of the magnetic parameters for greigite needed for the domain calculations are poorly known.

Experimental confirmation for these numerical predictions are difficult because the predicted SD threshold size in magnetite and greigite are below 1000 nm and direct domain observations are limited at this length scale. Instead of domain observations, remanence and coercivity data obtained from sized dispersions of natural and synthetic magnetites that span the predicted SD threshold are used to infer the actual SD size range. Results from these types of experiments are generally consistent with the theoretical predictions that the critical threshold size for SD behavior is <1000 nm [42, 56].

Originally, the Butler–Banerjee calculations were used to confirm that magnetosomes were indeed uniformly magnetized, SD grains [57, 58, 59], as would be required for optimizing magnetotaxis in the geomagnetic field. Almost all magnetite magnetosomes from both cultured and uncultured bacteria that have been characterized by TEM fall within the theoretical SD size range (Fig. 6). Because there are biological arguments for magnetosomes to be SD as well as independent experimental evidence for the SD nature of magnetosomes from magnetic measurements on bulk samples of freeze-dried cells [60] and on individual cells [61, 62], the best evidence for the general validity of the Butler–Banerjee model in fact comes from the size and shape distributions of magnetosomes found in magnetotactic bacteria.

6.2.5 Local Energy Minima and Metastable SD States: Micromagnetic Models

One significant shortcoming with the Butler–Banerjee model is that it is a one-dimensional model constrained by the assumptions that the magnetization is uniform within domain walls and that the SD state transforms into a simple two-domain (TD) state with a planar wall separating the domains (Fig. 4A, B). In fact the simple TD state may not be lowest energy ground state configuration for grains sizes larger than SD. More recent micromagnetic calculations in three dimensions remove many of the constraints necessitated by earlier modeling techniques and allow other spin configurations with more efficient magnetostatic energy minimization to form [42]. These micromagnetic calculations predict that a variety of other microstates (flower and vortex states, Fig. 4D, E) with lower energy configurations than the simple uniform SD and TD states can develop in cubic grains with low anisotropy such as magnetite [50, 63]. Furthermore, these alternative microstates can be local energy minima (LEM) rather than global energy minima or ground states. This means that grains can be trapped in higher energy LEM states until perturbed by magnetic fields which subsequently initiate the transformation to a lower energy state. An important LEM state is the metastable SD state, in which the nearly uniformly magnetized SD state (flower state) metastably persists in larger sized grains

whose ground state configurations are predicted to be a non-SD vortex configuration. Metastable SD states and alternative LEM states for the same grain have been experimentally observed in magnetite, titanomagnetite, and pyrrhotite for grain sizes >1000 nm, well above their equilibrium values for d_0 (a recent review is available elsewhere [42]).

While three-dimensional micromagnetic calculations have predicted a variety of non-SD structures forming just above the SD transition size, the equilibrium, ground state transition size d_0 does not change significantly from the original Butler–Banerjee calculations. For an equidimensional cube of magnetite, $d_0 \approx 80$ nm. However, the fundamental new insight obtained from the micromagnetic models is the existence of a metastable SD region that effectively extends the grain size range for SD states (in this case the flower state). At the metastable SD boundary, the grain will spontaneously transform into a non-SD state, either by nucleating a domain wall or transforming into a vortex-like state. The metastable SD transition boundary for magnetite as a function of axial ratio, obtained from a recent unconstrained three-dimensional micromagnetic model [50], is shown in Fig. 6. For an equidimensional cube of magnetite, a metastable SD state can exist in grain sizes up to 140 nm, significantly higher than the ground state value of 80 nm. Application of a magnetic field can transform the metastable SD state into lower energy vortex states.

In summary, although variations exist between species, almost all magnetite and greigite magnetosomes fall within a narrow size range of about 35–120 nm when measured along their long axes [27, 30, 32, 33, 41]. This size range is significant because it places these grains within the stable magnetic single domain (SD) size range for magnetite and greigite [42]. Grains within the SD size range are uniformly magnetized, which means their magnetic dipole moment is maximum, that is, equal to the saturation moment M_s . Grains larger than about 100 to 120 nm are non-uniformly magnetized because of the formation of multiple magnetic domains, domain walls, or vortex configurations (Section 6.3.10); this has the effect of making their magnetic moments significantly smaller than in SD grains. At the other extreme, SD grains smaller than about 30 nm are superparamagnetic (SPM) at ambient temperature. Although SPM grains are still uniformly magnetized, their moments are not constant in direction because of thermally induced spontaneous reversals which produce a time-averaged moment of zero. Therefore, magnetotactic bacteria produce the optimum grain size for maximum moment per magnetosome. In contrast, BIM magnetite, greigite, and other magnetic iron sulfide minerals produced extracellularly by dissimilatory iron-reducing bacteria are mostly in the superparamagnetic state at ambient temperatures [46, 64]. Crystal size distributions for BIM and BCM magnetite grains are shown in Fig. 7.

6.2.6 Magnetic Anisotropy of Magnetosomes

In addition to crystal habit and size, the crystallographic orientation of each individual magnetosome along a magnetosome chain is also determined in most magnetotactic bacteria. Magnetite magnetosomes are almost exclusively oriented with a [111] crystallographic axis aligned along the magnetosome chain axis [31]. For

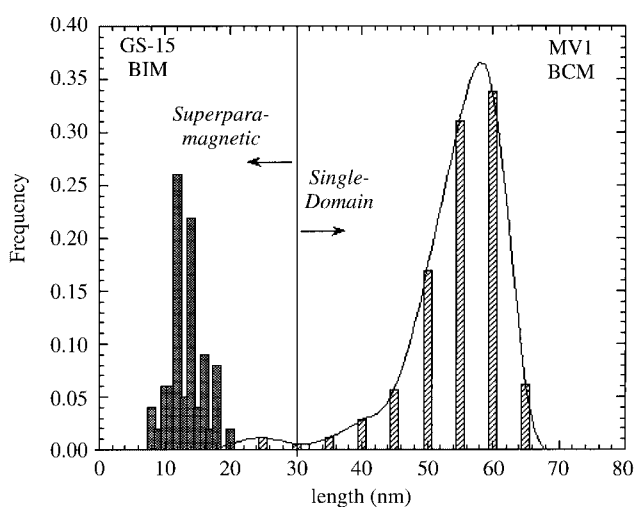


Fig. 7. Crystal size distributions for magnetite grains produced by magnetotactic bacterium strain MV-1 (BCM type) and *Geobacter metallireducens* GS-15 (BIM type) [27, 47]. The two modes of biomineralization produces grains with two distinct magnetic microstates: single domain (SD) and superparamagnetic (SPM).

elongated crystal morphologies, the [111] crystallographic axis aligned along the chain is the elongation axis. In contrast, greigite magnetosomes are aligned with a [100] crystallographic axis direction parallel to the chain axis [41]. The significance of the [111] direction in magnetite is that it corresponds to the magnetic easy axis (defined below). Similarly, the [100] direction is probably the magnetic easy axis in greigite. No direct determination of easy axis orientation in greigite has yet been made, primarily because of the difficulty of synthesizing high quality, large single crystals of this mineral usually required for magnetic anisotropy measurements.

The magnetic easy (i. e., low energy) axes arise from anisotropy in the magnetocrystalline energy resulting from the interaction of spin magnetic moments with the crystalline structure. This spin-orbit coupling determines the crystallographic directions along which M_s prefers or avoids being directed. In magnetite above 120 K, the {111} directions are the magnetic easy axes and the {100} directions are the hard (i. e., high energy) axes. To reverse the magnetization by an applied field from one easy axis to another requires rotation through a hard axis. The magnetocrystalline anisotropy thus creates an energy barrier that pins M_s along one easy axis until a large enough magnetic field is applied to cause an irreversible jump of M_s over the anisotropy barrier. This field is related to the coercivity H_c and is a measure of the stability of remanence against remagnetization by time, temperature or magnetic fields. However, if a grain is elongated, it is shape anisotropy rather than magnetocrystalline anisotropy that inhibits remagnetization during a hysteresis cycle and is another source of coercivity in materials with high M_s such as magnetite. Shape anisotropy is primarily responsible for the coercivity observed in magnetosomes.

6.2.7 Magnetosome Chains

The arrangement of the single-magnetic-domain magnetosomes in chains maximizes the dipole moment of the cell because magnetic interactions between the magnetosomes cause each magnetosome moment to spontaneously orient parallel to the others along the chain axis by minimizing the magnetostatic energy. Thus the total dipole moment of the chain, M , is the algebraic sum of the moments of the individual magnetosomes in the chain. However this is true only because the magnetosomes are physically constrained by the magnetosome membranes in the chain configuration. If free to float in the cytoplasm, magnetosomes would likely clump, resulting in a smaller net dipole moment than in the chain. For organisms such as *Magnetospirillum magnetotacticum*, the remanent moment is the maximum possible moment of the chain.

6.2.8 Magnetic Properties of Magnetosomes at Ambient Temperatures

The SD nature of magnetosomes has been confirmed by various magnetic measurements. A room temperature hysteresis loop for a bulk magnetotactic bacterial sample is shown in Fig. 8. The sample exhibits classical SD behavior. The saturation remanence to saturation magnetization ratio, M_r/M_s , is approximately 0.5, which is the theoretical value for a randomly oriented assemblage of SD grains with uniaxial anisotropy [42]. The chain structure effectively removes the equivalence among the different $\{111\}$ easy directions and produces a unique easy axis coinciding with the particular $[111]$ axis aligned along the chain axis.

Hysteresis measurements from a number of different cultured strains of magnetotactic bacteria yield coercivities (H_c) between 20–50 mT, which are larger than the expected theoretical coercivity (~ 11 mT) for randomly oriented SD magnetite grains with magnetocrystalline easy axes along $[111]$ directions [65]. This indicates that the intrinsic magnetocrystalline anisotropy is not the main source of the coer-

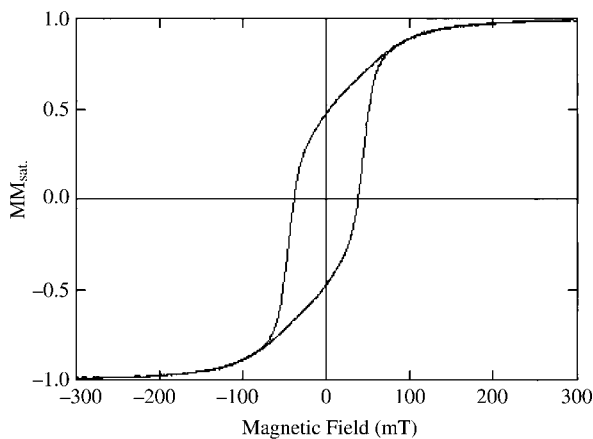


Fig. 8. Magnetic hysteresis loop for a sample consisting of freeze-dried cells of magnetotactic bacterium (strain MV-1).

civity but instead a combination of grain elongations along [111] (giving rise to shape anisotropy) and their linear arrangements in chains (producing positive magnetostatic interaction between grains) controls the remagnetization process and pins the magnetization along the chain direction. More significantly, the observed coercivities are much larger than the geomagnetic field (0.05 mT) and demonstrates that changes in the geomagnetic field, even polarity reversals in the geologic past, are not sufficient to remagnetize the polarity of the magnetosome chains. This has been confirmed by magnetic measurements of individual magnetotactic bacteria with single magnetosome chains which show square hysteresis loops with coercive forces of the order of 30 mT [62] and on isolated magnetosomes arranged in chain segments of up to 14 grains [66]. Additional results on room temperature remanence, hysteresis, and demagnetization behavior of whole cells and extracted magnetosomes can be found elsewhere [46, 49, 60, 64, 67, 68].

6.2.9 Low-temperature (<300 K) Magnetic Properties

Moskowitz et al. have shown that low-temperature remanence measurements provide a method to identify and quantify magnetosome magnetite produced by magnetotactic bacteria in pure culture, bulk sediment, soil or water samples and extraterrestrial materials [46, 64]. Remanence measurements can be 100–1000 times more sensitive for the detection of minute amounts of magnetite in natural or biological samples than using other traditional techniques such as X-ray diffraction or Mössbauer spectroscopy.

The magnetic behavior of magnetite below room temperature has been extensively studied because it exhibits both a structural phase transition at $T = 125$ K, called the Verwey transition (T_v), and a magnetic isotropic point (T_i) at $T = 130$ K [42]. At the Verwey transition, stoichiometric magnetite undergoes a first-order crystallographic transition, in which the lattice structure changes from an inverse cubic spinel ($T > T_v$) to monoclinic ($T < T_v$) symmetry [69]. At the magnetic isotropic point, which occurs at a temperature slightly above T_v , the first order cubic magnetocrystalline anisotropy constant (K_1) becomes zero as it changes sign and the easy directions of magnetization change their orientation from [111] above T_i to [100] below T_i . Both critical transitions produce a distinctive magnetic signature in remanence or magnetic susceptibility. For example, remanence given above or below T_v or T_i will be partially demagnetized upon cycling through these transitions. Likewise, magnetic susceptibility is a maximum at T_i , where the anisotropy energy is a minimum, and drops sharply below T_v as the anisotropy of monoclinic magnetite markedly increases. A typical example of low-temperature magnetic behavior for magnetite produced by magnetotactic bacteria is shown in Fig. 5. This remanence behavior provides a diagnostic signature for stoichiometric magnetite. Slight deviations from stoichiometry or minor amounts of cation substitution (e. g. Ti^{4+} or Al^{3+}), typical of naturally occurring, inorganic magnetites, can reduce the Verwey transition below 100 K or suppress it entirely [70–72].

Unlike magnetite, greigite lacks low-temperature remanence transitions [73] and therefore greigite magnetosomes should not display marked changes in remanence

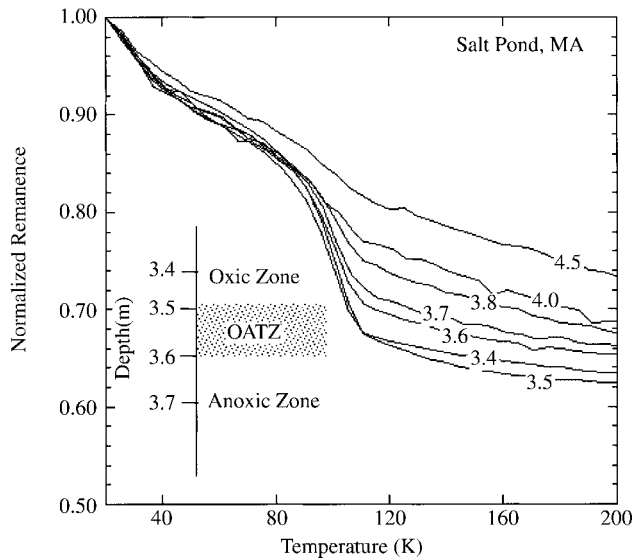


Fig. 9. Normalized thermal demagnetization of saturation remanent magnetization for filtered water samples collected at Salt Pond (MA) in July 1997. The series of curves show a magnetization profile through the oxic–anoxic transition zone (OATZ), where each individual curve represents a sample collected at a specific depth from the surface (noted on each curve). The OATZ interface is approximately located at a depth of 3.5–3.6 m (insert). The results above but near the OATZ indicate a strong magnetite contribution from magnetite producing magnetotactic bacteria, whereas below the OATZ the data indicate a greater contribution from greigite-producing magnetotactic bacteria.

or susceptibility below 300 K. Although no axenic cultures of greigite magnetosomes are currently available, natural populations of greigite- and magnetite-producing magnetotactic bacteria from aquatic habitats can be collected and studied. An example of low-temperature measurements for samples collected from a coastal pond at different water depths above and below the OATZ (3.5–3.6 m), where different types of magnetotactic bacteria are dominant, is shown in Fig. 9. In samples from 3.4–3.5 m depth, the magnetite transition is well developed and coincides with the presence of high concentrations of magnetite-producing magnetotactic bacteria. Upon passing through the OATZ into the anoxic zone, the amount of remanence lost at the transition progressively decreases with water depth, indicating a greater contribution from greigite producers in the anoxic zone.

Another useful feature of LT measurements is that they can be used to discriminate superparamagnetic (<30 nm) grains of iron oxides and iron sulfides from stable single domain (ca. 30 to 100 nm) and larger multi-domain grains (>100 nm). In biogenic samples, the superparamagnetic behavior would be indicative of BIM magnetic grains produced by dissimilatory iron- and sulfate-reducing bacteria whereas single domain behavior would be indicative of SD magnetosome grains produced by magnetotactic bacteria [46, 64] as shown in Fig. 5. The shape of the SPM re-

manence or susceptibility curves reflect the lognormal grain size distribution produced by BIM process and is typical of relaxation behavior in nanophase magnetic materials. A lognormal grain size distribution produces a distribution of magnetic blocking temperatures and results in the progressive unblocking of magnetization as SD grains become SPM with increasing temperature.

6.2.10 Magnetosomes and Micromagnetism

While the dimensions of most magnetite magnetosomes place them within the theoretical SD size range, some appear to be much larger than SD and plot within the theoretical TD size range. In some cases, the grain dimensions may be just an experimental artifact resulting from the determination of three-dimensional shape from a two-dimensional projection on a TEM photomicrograph. Other examples are more unambiguous, such as the large magnetosomes found in coccoid cells from Lagoa de Itaipu, near Rio de Janeiro [52, 53] and plotted in Fig. 6.

The existence of the metastable SD state provides a possible explanation for the grain dimensions of the anomalously large magnetosomes [50, 74]. As initially uniformly magnetized magnetosomes nucleate and grow in size from the SPM state to the stable SD state and beyond, it may be energetically favorable for the grains to retain a near uniform SD state (flower state) into the metastable SD range instead of reverting to a non-SD state because the additional activation energy needed for the transformation is not available. Magnetic interactions between magnetosomes along a chain may also help to stabilize the SD structure [50]. If this speculation is true, bacteria that make metastable SD magnetosomes can provide critical confirmation of micro-magnetic models as well as provide a source of metastable SD magnetite grains for study.

Using the results from three-dimensional micromagnetic models, the magnetosomes in the coccoid cells from Brazil as well as large magnetosomes in other organisms fall within the predicted metastable SD range and therefore can quite naturally possess an SD structure. This hypothesis has recently been tested using the technique of off-axis electron holography in a transmission electron microscope. This technique allows the visualization of magnetic structure and correlation with physical structure [75, 76] as discussed below.

6.2.11 Magnetosome Magnetization from Electron Holography

In off-axis electron holography, the sample is positioned in the transmission electron microscope so that it covers approximately half the field of view and a charged electrostatic biprism causes the electron wave that has passed through the specimen to overlap with a reference wave that has only passed through vacuum. The resulting hologram is an interference pattern in which amplitude information is contained in the relative amplitude of the cosine-like fringes and information about the phase shift of the electron wave is contained in the fringe positions. The holographic phase

data can be decomposed into electrostatic and magnetic contributions and displayed as thickness contours and magnetic field lines, respectively [76].

Superposition of contours of the magnetic contribution to the holographic phase on the electrostatic contribution to the phase allows correlation of the magnetic flux lines with the positions of the magnetosomes. Contours of spacing 0.064 radians are overlaid on the magnetosomes in Fig. 10 for a cell of the magnetotactic bacterium *Magnetospirillum magnetotacticum* [75, 76]. The contours provide a semi-quantitative map of the magnetic field in the sample; the direction of the field at each point is tangential to the contour. All the magnetosomes in *M. magnetotacticum* are single magnetic domains magnetized parallel to the axis of the magnetosome chain, in confirmation of the discussion in Sections 6.2.4–6.2.7. For a magnetosome at the

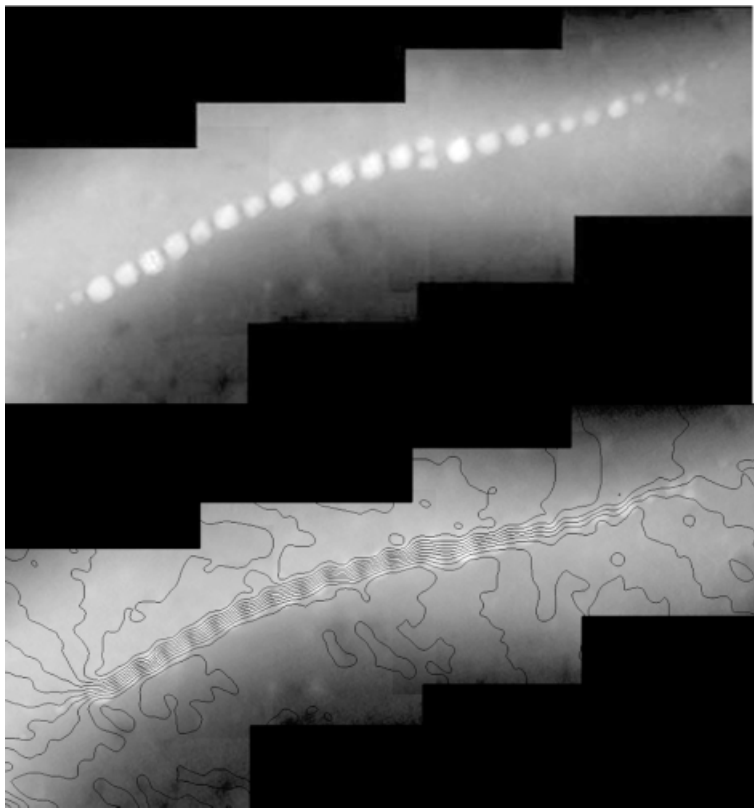


Fig. 10. (Top): Mean inner potential contributions to the electron holographic phase indicating the position of the magnetosomes in a cell of *Magnetospirillum magnetotacticum*. (Bottom): Contours derived from the magnetic contribution to the electron holographic phase overlaid onto positions of the magnetosomes. The contours provide a map of the local magnetic field in the cell. The confinement of the magnetic flux within the magnetosomes shows that all the magnetite crystals are single magnetic domains magnetized approximately parallel to the axis of the chain.

end of the chain, the contours “fan out” suggesting a flower state configuration as predicted by micromagnetic models. At one point in the chain there is a “defect” in which two small magnetosomes have mineralized in place of a larger one, resulting in a slightly poorer, but detectable, confinement of the magnetic field at that point. Smaller crystals at the right end of the chain are in the SPM size range, yet they are also magnetized parallel to the chain axis, presumably by interactions with the magnetic field of the larger crystals in the chain. Finally, the magnetic dipole moment of the magnetosome chain can be obtained from the magnetic contribution to the phase, giving $5 \times 10^{-16} \text{ Am}^2$ ($5 \times 10^{-13} \text{ emu}$), which is consistent with the value predicted for a chain of twenty-two 45 nm diameter spheres of magnetite, using the bulk magnetization 480 kA m^{-1} (Table 1).

Similar measurements have been made with the large (up to 200 nm) magnetosomes with roughly square projected shapes in uncultured bacteria (Itaipu-1) collected at Itaipu, Brazil [52, 53]). The sample also contained bacteria with smaller, more elongated magnetosomes (Itaipu-3). Preparation of the TEM grids resulted in mixing of the two magnetosome types. Although a significant amount of flux could be seen emerging from the sides of the larger magnetosomes, the concentration of flux lines within the crystals showed that the Itaipu-1 magnetosomes in the chain configuration are SD [54].

A fortuitous arrangement of magnetosomes comprising three large crystals forming a right angle and three elongated crystals showed containment of the magnetic flux lines parallel to the long axes of the elongated magnetosomes, suggesting that these latter crystals are SD. On the other hand, the magnetic field pattern in the large crystals suggested that these crystals contain domain walls and therefore are not SD in the non-chain configuration (Fig. 11). Thus it appears that the large magnetosomes are SD only in the chain configuration where they are magnetized by

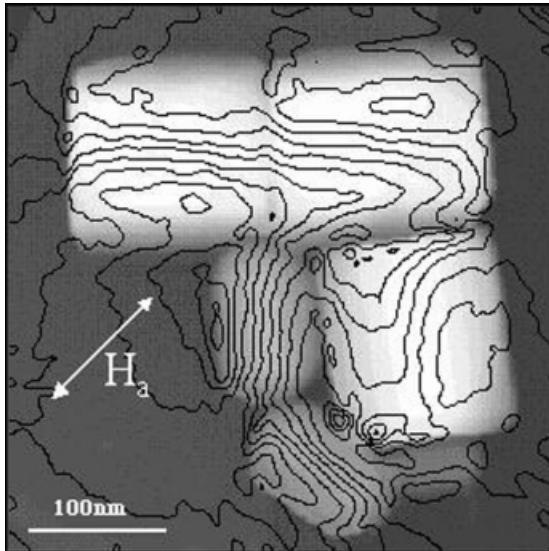


Fig. 11. Magnetic field contours for a non-linear configuration of three large Itaipu-1 magnetosomes and three elongated Itaipu-3 magnetosomes derived from the difference in holographic phase images after application of applied fields as indicated by the arrow. The field contours in the elongated magnetosomes are consistent with single domain behavior, whereas the contours in the large magnetosomes are consistent with the presence of domain walls [54].

the neighboring crystals [54]. Figure 6 shows a theoretical domain-state diagram for magnetite with calculated SPM, SD, TD and MSD size ranges [55], with solid square and circle indicating large and elongated magnetosomes, respectively. According to Fig. 6, the elongated magnetosomes lie in the SD region, in agreement with the numerical results. In contrast, the large magnetosomes are predicted to lie in the MSD region where the SD size range is extended for materials of low anisotropy by the existence of the metastable SD state [50]. The curvature of the field lines emerging from the sides of the large crystals is typical of the “flower-like” state predicted by micromagnetic models. This illustrates the power of electron holography to determine the magnetic microstructure of crystals with sizes close to the domain-state transition dimension for comparison with theoretical calculations.

6.3 Mechanism of Bacterial Magnetotaxis

6.3.1 Passive Orientation by the Geomagnetic Field

Magnetotaxis results from the passive orientation of magnetotactic bacteria along the local vertical direction of the geomagnetic field by the torque exerted by the field (B) on the cellular dipole moment (M) [20]. The potential energy of the cellular moment in the magnetic field is given by:

$$E_m = -MB \cos \theta \quad (2)$$

where θ is the angle between M and B . Thermal energy at ambient temperatures will tend to misalign the swimming bacterium. In a state of thermal equilibrium at temperature T , the probability of the moment having energy E_m is proportional to the Boltzmann factor, $\exp(-E_m/kT)$, where k is Boltzmann’s constant. The thermally averaged projection of the dipole moment on the magnetic field can be determined from the Langevin theory of paramagnetism and is given by the Langevin function

$$\langle \cos \theta \rangle = L(\alpha) = \coth(\alpha) - 1/\alpha \quad (3)$$

where $\alpha = MB/kT$. The Langevin function is plotted in Fig. 12 and asymptotically approaches 1 for large α .

For example, experimental determination of the dipole moment per cell using electron holography for *Magnetospirillum magnetotacticum* and the cultured marine vibrioid strain MV-1 gave values of $5 \times 10^{-16} \text{ Am}^2$ and $7 \times 10^{-16} \text{ Am}^2$, respectively [75]. In a geomagnetic field of $50 \mu\text{T}$ at room temperature, $L(\alpha)$ is greater than 0.8 for both cells, meaning that cells would swim approximately parallel to the local direction of the geomagnetic field. If the number of magnetosomes is too low, then the alignment of the cell and its migration along the field is inefficient. On the other hand, increasing the number of magnetosomes beyond a certain value will not significantly improve the alignment of the cell in the field because of the asymptotic

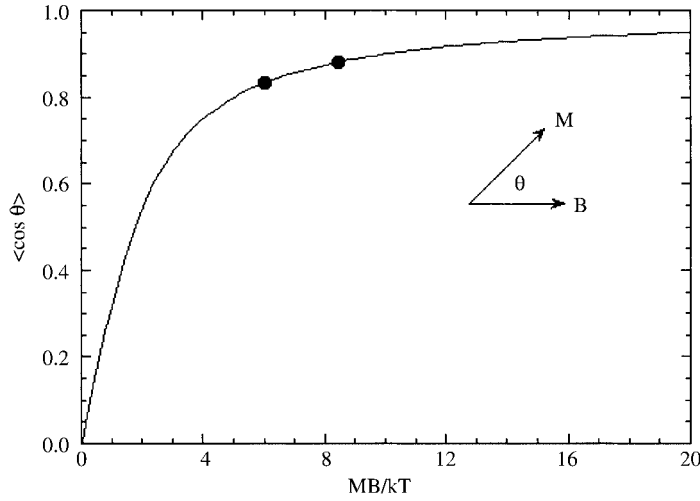


Fig. 12. The Langevin function plotted as a function of MB/kT . This function gives the average alignment of a magnetotactic cell with magnetic moment (M) in a magnetic field (B). The solid symbol represents the average orientation of magnetotactic bacteria (*M. magnetotacticum* and strain MV-1) in a $50\text{-}\mu\text{T}$ field at 300 K. The magnetic moment per cell was determined by electron holography.

nature of the Langevin function. Magnetotactic bacteria have optimized the biomineralization process to produce just the right number of grains for efficient magnetic navigation in the geomagnetic field.

The migration velocity v_m of the bacterium in the direction of B is given by the component of the forward swimming velocity v_0 along the direction of the field, $v_m = v_0 L(a)$. For magnetotactic bacteria, migration velocities can be $>80\%$ of their forward velocities and are significantly faster than other motile bacteria that may use only chemotaxis or aerotaxis [20]. Magnetotactic bacteria have effectively turned a three-dimensional biased random walk problem along a chemical concentration gradient into a one-dimensional biased random walk along the geomagnetic field.

In addition to the requirement that the magnetic energy be greater than thermal energy, another condition for magnetotaxis is that the characteristic time scale for re-orientation in the field direction after the cell is perturbed must be comparable to the time required to swim several body lengths [20]. Otherwise, magnetotaxis would lose its adaptive advantage. The re-orientation time, t_0 , is given approximately by [78, 79]:

$$t_0 = 8\pi\eta R^3 / MB \quad (4)$$

where η is the dynamic viscosity of water ($\eta = 1 \times 10^{-6} \text{ m}^2 \text{ s}^{-1}$) and R is the hydrodynamic radius of the bacterium. Typical re-orientation times are <1 s, and meet the condition for fast alignment time [78]. This equation also forms the basis for measuring the magnetic moment of individual cells in the laboratory by either measuring

the time required for a cell to rotate into the new field direction after an instantaneous field reversal, or in a rotating field, or the width of a “U-turn” executed by the cell after a field reversal [62, 78, 79]. Estimates of the cellular dipole moments obtained from these methods for a variety of different magnetotactic bacteria yield values of $0.3\text{--}54 \times 10^{-15} \text{ Am}^2$.

Equation (3) also shows that the critical dipole moment of the cell scales as R^3 and predicts that as the hydrodynamic radius of the bacterium increases, additional magnetosomes are required to overcome rotational viscous drag than would be necessary for passive alignment according to the Langevin function. There are examples of magnetotactic bacteria that contain hundreds of magnetosomes [33, 79], many more than required to overcome the thermal energy. One large, rod-shaped organism, *Magnetobacterium bavaricum*, contains up to 1000 bullet-shaped magnetosomes arranged in several chains traversing the cell [80]. This arrangement of magnetosomes into multiple chains provides an additional means to enhance the dipole moment of the cell. Furthermore, due to mutual magnetostatic repulsion of such chains, the multiple chain design may provide additional mechanical stability and more effective coupling of the magnetic torque to the cell by forcing the chains outward toward the cell envelope [81].

6.3.2 Magneto-aerotaxis

As discussed above, the permanent magnetic dipole moment of a cell is generally large enough so that its interaction with the geomagnetic field overcomes the thermal forces tending to randomize the orientation of the magnetic dipole in its aqueous surroundings. Since the dipole is fixed in the cell, orientation of the dipole results in orientation of the cell. Magnetotaxis results as the oriented cell swims along the magnetic field lines (B). Magnetotactic bacteria, like most free-swimming bacteria, swim by rotating their helical flagella. The direction of migration, parallel or antiparallel to the magnetic field, is determined by the direction of flagellar rotation (clockwise (cw) or counter-clockwise (ccw)) which in turn is determined by a second sensory system, the aerotactic response of the cell [82]. Thus magnetotaxis works in conjunction with aerotaxis, i. e., magneto-aerotaxis.

Some magnetotactic spirilla, such as *Magnetospirillum magnetotacticum*, swim parallel or antiparallel to B and form aerotactic bands [83] at a preferred oxygen concentration $[\text{O}_2]$ in oxygen gradient cultures or in suspensions of living cells. In a homogeneous medium, roughly equal numbers of cells swim in either direction along B [19]. Most microaerophilic bacteria form aerotactic bands at a preferred or optimal $[\text{O}_2]$ where the proton motive force is maximal [84], using a temporal sensory mechanism [85] that samples the local environment as they swim and compares the present $[\text{O}_2]$ with that in the recent past. The change in $[\text{O}_2]$ with time determines the sense of flagellar rotation [86]. The behavior of individual cells of *M. magnetotacticum* in aerotactic bands, termed axial magnetoaerotaxis, is consistent with the temporal sensory mechanism [82]. For these cells, the magnetic field axis is important, but the field direction is not. Thus the axial magneto-aerotactic response is invariant with respect to magnetic field reversal.

In contrast, the ubiquitous freshwater and marine magnetotactic cocci and some other magnetotactic strains swim persistently in a preferred direction relative to B when examined microscopically in aerated water drops [19, 87]. In oxygen gradients they can, like the spirilla, swim in both directions along B without turning around and form aerotactic bands at a preferred $[O_2]$ along the concentration gradient. However, unlike the spirilla, the aerotactic behavior of the cocci is not consistent with the temporal sensory mechanism. Instead their behavior is described by a two-state aerotactic sensory model in which the $[O_2]$ determines the sense of the flagellar rotation and hence the swimming direction relative to B , a model termed polar magneto-aerotaxis [82] (Fig. 13). Under higher than optimal $[O_2]$, a cell is presumably in an “oxidized state” and ccw flagellar rotation causes the cell to migrate persistently parallel to B , that is, downward in the Northern hemisphere. Under reducing conditions, or sub-optimal oxygen concentrations, the cell switches to a “reduced state”, in which cw flagellar rotation causes the cell to migrate anti-parallel to B , that is, upward in the Northern Hemisphere. The two-state sensing mechanism results in an efficient aerotactic response, provided that the oxygen-gradient is oriented vertically so that it is more or less anti-parallel to B , guiding the cell back toward the optimal oxygen concentration from either reducing or oxidizing conditions. Note that polar magnetoaerotaxis is not invariant to reversal of the magnetic field. An assay using chemical gradients in thin capillaries has been developed that distinguishes between axial and polar magneto-aerotaxis [88].

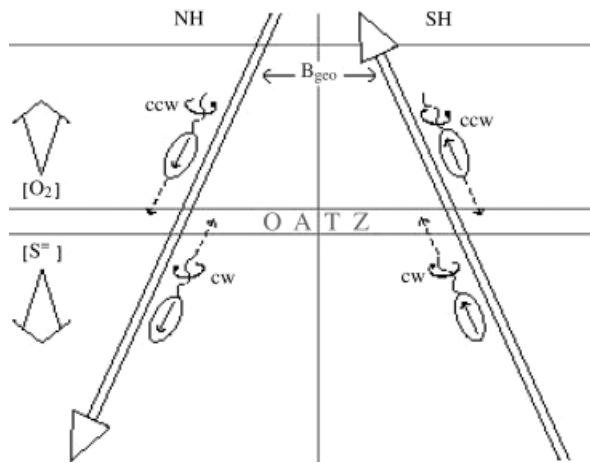


Fig. 13. Schematic diagram showing how polar magneto-aerotaxis keeps cells at the preferred oxygen concentration in the oxic–anoxic transition zone (OATZ) in chemically stratified water columns and sediments (NH, Northern hemisphere; SH, Southern hemisphere; B_{geo} , geomagnetic field). In both hemispheres, cells at higher than optimal oxygen concentration in the “oxidized state” swim forward by rotating their flagella counter clockwise (ccw), whereas cells at lower than optimal oxygen concentration in the “reduced state” rotate their flagella clockwise (cw) and swim backward without turning around. Note that the geomagnetic field selects for cells with polarity such that ccw flagellar rotation causes cells to swim downward along the magnetic field lines in both hemispheres.

For both aerotactic mechanisms, migration along magnetic field lines reduces a three-dimensional search problem to a one-dimensional search problem. Thus, magnetotaxis is presumably advantageous to motile microorganisms in locales with horizontal chemical stratification because it increases the efficiency of finding and maintaining an optimal position in vertical concentration gradients, in this case, vertical oxygen gradients [89]. It is possible that there are other forms of magnetically-assisted chemotaxis to molecules or ions other than oxygen, such as sulfide, or magnetically-assisted redox- or phototaxis in bacteria that inhabit the anoxic zone below the microaerobic zone.

6.4 Conclusion

The grain size, crystallographic orientation and chain assembly of magnetosomes in magnetotactic bacteria are all highly significant for the function of magnetotaxis in the geomagnetic field. In fact, the magnetosome chain is a masterpiece of permanent magnet design that makes each cell, in effect, a self-propelled magnetic dipole. It solves the problem of designing a permanent magnetic compass needle that is sufficiently magnetic to be oriented in the geomagnetic field in the face of buffeting by thermal (Brownian) noise, yet fits into a one micron diameter cell and can be assembled *in situ*. The cells migrate along magnetic field lines and use aerotaxis to efficiently locate and remain at an optimal oxygen concentration in the vertical oxygen concentration gradient in a water column or sediments with horizontal chemical stratification.

Magnetically sensitive behavior, including orientation and homing, have been reported in a number of higher organisms [15, 16, 18, 90, 91]. Magnetite crystals with morphologies and sizes similar to those produced by some magnetotactic bacteria have been found in the ethmoid tissues of salmon [92], trout [6], and pigeons [17], and in the human brain [93]. The fact that these and possibly other organisms biomineralize SD magnetite crystals suggests that magnetoreception in these and possibly other organisms is based on SD magnetite. It has been suggested that the as yet unknown genes responsible for magnetite biomineralization in higher organisms could have originated in the magnetotactic bacteria [94]. However, it should be noted that models for magnetoreception have been proposed that do not involve magnetic minerals [95]. Ritz et al., for example, have proposed a photoreceptor-based model for magnetoreception in birds in which anisotropic hyperfine interactions in oriented radical pairs produced by photon absorption influence the visual transduction pathway in a manner that depends on the orientation of the bird in the geomagnetic field [91].

Finally, magnetite crystals with morphologies and sizes similar to those in magnetotactic bacteria have been reported in the Martian meteorite ALH84001 [37]. Whether or not these crystals are evidence for life on ancient Mars is still under discussion [96, 97, 98] but their discovery has raised the possibility that nanophase magnetite could serve as a biomarker for life beyond the earth.

Acknowledgments

We thank D. A. Bazylinski for ongoing collaboration. We also gratefully acknowledge support from the US National Science Foundation grant CHE-971404. The Institute for Rock Magnetism is supported by the NSF Instrumentation and Facilities Program, Earth Science Division. This is IRM contribution 0110.

References

- [1] Mann, S., Webb, J., Williams, R. J. P. (Eds.), *Biom mineralization: Chemical and Biochemical Perspectives*, VCH, Weinheim, Germany, **1989**.
- [2] Frankel, R. B., Blakemore, R. P. (Eds.), *Iron Biom minerals*, Plenum, New York, **1990**.
- [3] Lovley, D.R., *Fe(III) and Mn(IV) Reduction*, In *Environmental Microbe–Metal Interactions*, D.R. Lovley (Ed.), ASM Press, American Society for Microbiology, Washington, D.C., 3-30p, **2000**.
- [4] Fortin, D., Beveridge, T. J., *Mechanistic Routes to Biom mineral Surface Development In Biom mineralization: From Biology to Biotechnology and Medical Application*, Baeuerlein, E. (Ed.), Wiley-VCH, Weinheim, Germany, **2000**.
- [5] Webb, J., St. Pierre, T. G., Macey, D. J., *Iron Biom mineralization In Invertebrates in Iron Biom minerals*, R. B. Frankel, R. P. Blakemore (Eds.), Plenum, New York, **1990**.
- [6] Diebel, C. E., Proksch, R., Green, C. R., Neilson, P., Walker, M. M., *Nature* **2000**, *406*, 299–302.
- [7] Mann, S., Sparks, N. H. C., Frankel, R. B., Bazylinski, D. A., Jannasch, H. W., *Nature* **1990**, *343*, 258–260.
- [8] Pósfai, M., Buseck, P. R., Bazylinski, D. A., Frankel, R. B., *Science* **1998**, *280*, 880–883.
- [9] Pósfai, M., Buseck, P. R., Bazylinski, D. A., Frankel, R. B., *Am. Mineral.* **1998**, *83*, 1469–1481.
- [10] Stanjek, H., Fassbinder, J. W. E., Vali, H., Waegele, H., Graf, W., *Eur. J. Soil Sci.* **1994**, *45*, 97–103.
- [11] Lowenstam, H. A., Weiner, S., *On Biom mineralization*, Oxford, New York, **1989**.
- [12] Bazylinski, D. A., Frankel, R. B., *Biologically Controlled Mineralization of Magnetic Iron Minerals by Magnetotactic Bacteria In Environmental Microbe–Metal Interactions*, D. R. Lovley (Ed.), ASM Press, Washington, D.C., **2000**, 109–144.
- [13] Bazylinski, D. A., Frankel, R. B., *Magnetic iron oxide and iron sulfide minerals within organisms In Biom mineralization: From biology to biotechnology and medical application*, E. Baeuerlein (Ed.), Wiley-VCH, Weinheim, Germany, **2000**, 25–46.
- [14] Lovley, D. R. *Microbiol. Rev.* **1991**, *55*, 259–287.
- [15] Kirschvink, J. L., Jones, D. S., MacFadden, B. J. (Eds.), *Magnetite Biom mineralization and Magnetoreception in Organisms*, J. L. Plenum, New York, **1985**.
- [16] Walker, M. M., Diebel, C. E., Haugh, C.V., Pankhurst, P. M., Montgomery, J. C., *Nature* **1997**, *390*, 371–373.
- [17] Winklhofer, M., Holtzkaemp-Rotzler, Hanzlik, M., Fleissner, G., Petersen, N., *Eur. J. Mineral.* **2001**, *13*, 659–670.
- [18] Lohmann, K. J., Cain, S. D., Dodge, S. A., Lohmann, C. M. F., *Science* **2001**, *294*, 364–366.

- [19] Blakemore, R. P., *Annu. Rev. Microbiol.* **1982**, *36*, 217–238.
- [20] Frankel, R. B., *Annu. Rev. Biophys. Bioeng.* **1984**, *13*, 85–103.
- [21] Bazylinski, D. A., Frankel, R. B., Heywood, B. R., Mann, S., King, J. W., Donaghy, P. L., Hanson, A. K., *Appl. Environ. Microbiol.* **1995**, *61*, 3232–3239.
- [22] Spring, S., Amann, R., Ludwig, W., Schleifer, K.-H., Petersen, N., *Syst. Appl. Microbiol.*, **1992**, *15*, 116–122.
- [23] DeLong, E. F., Frankel, R. B., Bazylinski, D. A., *Science* **1993**, *259*, 803–806.
- [24] Balkwill, D. L., Maratea, D., Blakemore, R. P., *J. Bacteriol.* **1980**, *141*, 1399–1408.
- [25] Baeuerlein, E. (Ed.), *Biomining: From Biology to Biotechnology and Medical Application*, Wiley-VCH, Weinheim, Germany, **2000**.
- [26] Gorby, Y. A., Beveridge, T. J., Blakemore, R. P., *J. Bacteriol.* **1988**, *170*, 834–841.
- [27] Devouard, B., Pósfai, M., Hua, X., Bazylinski, D.A., Frankel, R.B., Buseck, P. R., *Am. Mineral.* **1998**, *83*, 1387–1398.
- [28] Ofer, S., Nowik, I., Bauminger, E. R., Papaefthymiou, G. C., Frankel, R. B., Blakemore, R. P., *Biophys. J.* **1984**, *46*, 57–64.
- [29] Towe, K. M., Moench, T. T., *Earth. Planet. Sci. Lett.* **1981**, *52*, 213–220.
- [30] Taylor, A.P., Barry, J.C., Webb, R.I., *J. Micro.* **2001**, *201*, 84–106.
- [31] Mann, S., Frankel, R. B. Magnetite biomineralization in unicellular organisms. In *Biomining: Chemical and Biochemical Perspectives*, S. Mann, J. Webb, R. J. P. Williams (Eds.), VCH, New York, **1989**.
- [32] Bazylinski, D. A., Garratt-Reed, A. J., Frankel, R. B., *Microsc. Res. Tech.* **1994**, *27*, 389–401.
- [33] Vali, H., Kirschvink, J. L., *Observations of magnetosome organization, surface structure, and iron biomineralization of undescribed magnetic bacteria: evolutionary speculations in iron biominerals*, R. B. Frankel, R. P. Blakemore (Eds.), Plenum, New York, **1990**.
- [34] Matsuda, T., Endo, J., Osakabe, N., Tonomura, A., Arai, T., *Nature* **1983**, *302*, 411–412.
- [35] Meldrum, F. C., Heywood, B. R., Mann, S., Frankel, R. B., Bazylinski, D. A., *Proc. R. Soc. London B* **1993**, *251*, 231–236.
- [36] Meldrum, F. C., Heywood, B. R., Mann, S., Frankel, R. B., Bazylinski, D. A., *Proc. R. Soc. London B* **1993**, *251*, 237–242.
- [37] Thomas-Keprta, K. L., Clemett, S. J., Bazylinski, D. A., Kirschvink, J. L., McKay, D. S., Vali, H., Gibson, E. K., Jr., Romanek, C. S., *Proc. Natl. Acad. Sci. USA* **2001**, *98*, 2164–2169.
- [38] Mann, S., Frankel, R. B., Blakemore, R. P., *Nature* **1984**, *310*, 405–407.
- [39] Eberl, D. D., Frankel, R. B., *Annu. Meeting of the Geol. Soc. Am. Abstracts* **1999**, *31*, A379.
- [40] Farina, M., Esquivel, D. M. S., Lins de Barros, H. G. P., *Nature (London)* **1990**, *343*, 256–258.
- [41] Heywood, B. R., Mann, S., Frankel, R. B., *Structure, Morphology and Growth of Biogenic Greigite (Fe₃S₄) in Materials Synthesis Based on Biological Processes*, M. Alpert, P. Calvert, R. B. Frankel, P. Rieke, D. Tirrell, (Eds.), Materials Research Society, Pittsburgh, Pennsylvania, **1991**.
- [42] Dunlop, D. J., Özdemir, Ö., *Rock Magnetism: Fundamentals and Frontiers*, Cambridge University Press, Cambridge, U.K., **1997**.
- [43] Özdemir, Ö., Xu, S., Dunlop, D. J., *J. Geophys. Res.* **1995**, *100*, 2193–2209.
- [44] Pokhil, T. G., Moskowitz, B. M., *J. Geophys. Res.* **1997**, *102*, 22,681–22,694.
- [45] Moskowitz, B. M., Frankel, R.B., Walton, S. A., Dickson, D. P. E., Wong, K. K. W., Douglas, T., Mann, S., *J. Geophys. Res.* **1997**, *102*, 22671–22680.
- [46] Moskowitz, B. M., Frankel, R. B., Bazylinski, D. A., Jannasch, H. W., Lovley, D. R., *Geophys. Res. Lett.* **1989**, *16*, 665–668.

- [47] Sparks, N.H.C., Mann, S., Bazylinski, D. A., Lovley, D. R., Jannasch, H. W., Frankel, R. B., *Earth. Planet. Sci. Lett.* **1990**, 98, 14–22.
- [48] Butler, R. F., Banerjee, S. K., *J. Geophys. Res.* **1975**, 80, 4049–4058.
- [49] Diaz Ricci, J. C., Kirschvink, J. L., *J. Geophys. Res.*, **1992**, 97, 17309–17315.
- [50] Fabian, K., Kirchner, A., Williams, W., Heider, F., Leibl, T., Huber, A., *Geophys. J. Int'l.* **1996**, 124, 89–104.
- [51] Petersen, N., Weiss, D.G., and Vali, H., *Magnetic bacteria in lake sediments in geomagnetism and paleomagnetism*, F. J. Lowes, J. H. Parry, S. K. Runcorn, A. M. Soward, D. W. Collinson, D. C. Tozer (Eds.), Kluwer Academic, Dordrecht, Netherlands, **1989**, 231–241.
- [52] Farina, M., Kachar, B., Lins, U., Broderick, R., Lins de Barros, H., *J. Microsc.* **1994**, 173, 1–8.
- [53] Lins, U., Solórzano, G., Farina, M., *Bull. Instit. Océanograph. Monaco* (no. spécial, 14), **1994**, 1, 95–104.
- [54] McCartney, M. R., Lins, U., Farina, M., Buseck, P.R., Frankel, R.B. *Eur. J. Mineral.* **2001**, 13, 685–689.
- [55] Bazylinski, D. A., Moskowitz, B. M., *Microbial biomineralization of magnetic iron minerals: microbiology, magnetism and environmental significance in geomicrobiology: interactions between microbes and minerals*, J. F. Banfield, K. H. Nealson (Eds.), *Rev. Mineral.* **1997**, 35, 181–223. Mineralogical Society of America, Washington, D.C.
- [56] Merrill, R. T., Halgedahl, S. L., *Rev. Geophys. Supp.* **1995**, 137–144.
- [57] Frankel, R. B., *Comments Mol. Cell. Biophys.* **1982**, 1, 293–310.
- [58] Kirschvink, J. L., Lowenstam, H. A., *Earth Planet. Sci. Lett.* **1979**, 44, 193–204.
- [59] Frankel, R. B., Blakemore, R. P., *J. Magn. Magn. Mater.* **1980**, 15–18, 1562–1564.
- [60] Moskowitz, B. M., Frankel, R. B., Flanders, P. J., Blakemore, R. P., Schwartz, B. B., *J. Magn. Magn. Mater.* **1988**, 73, 273–288.
- [61] Proksch, R., Moskowitz, B. M., Dahlberg, E. D., Bazylinski, D. A., Frankel, R. B., *Appl. Phys. Lett.* **1995**, 66, 2582–2584.
- [62] Penninga, I., deWaard, H., Moskowitz, B. M., Bazylinski, D. A., Frankel, R. B., *J. Magn. Magn. Mater.* **1995**, 149, 279–286.
- [63] Williams, W., Dunlop, D. J., *Nature* **1989**, 337, 634–637.
- [64] Moskowitz, B. M., Frankel, R.B., Bazylinski, D. A., *Earth. Planet. Sci. Lett.* **1993**, 120, 283–300.
- [65] Walker, M., Mayo, P. I., O'Grady, K., Charles, S. W., Chantrell, R. W., *J. Phys. Condens. Matter* **1993**, 5, 2779–2792.
- [66] Wittborn, J. Rao, K. V., Proksch, R., Revenko, I., Dahlberg, E. D., Bazylinski, D. A., *Nanostructured Materials* **1999**, 12, 1149–1152.
- [67] Proksch, R., Moskowitz, B. M., *J. Appl. Phys.* **1994**, 75, 5894–5896.
- [68] Carter-Stiglitz, B., Moskowitz, B.M., Jackson, M., *J. Geophys. Res.* **2001**, 106, 26297–26412.
- [69] Otsuka, N., Sato, H., *J. Solid State Chem.* **1986**, 61, 212–222.
- [70] Özdemir, Ö., Dunlop, D. J., Moskowitz, B. M., *Geophys. Res. Lett.* **1993**, 20, 1671–1674.
- [71] Moskowitz, B.M., Jackson, M., Kissel, C., *Earth Planet. Sci. Lett.* **1998**, 157, 141–149.
- [72] Muxworthy, A.R., McClelland, E., *Geophys.J. Int.* **2000**, 140, 101–114.
- [73] Roberts, A. P., *Earth Planet. Sci. Lett.* **1995**, 134, 227–236.
- [74] Moskowitz, B. M., *Rev. Geophys. Supp.* **1995**, 123–128.
- [75] Dunin-Borkowski, R. E., McCartney, M. R., Frankel, R. B., Bazylinski, D. A., Posfai, M., Buseck, P. R., *Science* **1998**, 282, 2868–1870.
- [76] Dunin-Borkowski, R. E., McCartney, M. R., Posfai, M., Frankel, R. B., Bazylinski, D. A., Buseck, P. R. *Eur. J. Mineral.* **2001**, 13, 671–684.

- [77] Torres de Araujo, F. F., Pires, M. A., Frankel, R. B., Bicudo, C. E. M., *Biophys. J.* **1986**, *50*, 375–378.
- [78] Lins de Barros, H. G. P., Esquivel, D. M. S., Magnetotactic microorganisms found in muds from Rio de Janeiro: a general view in magnetite biomineralization and magnetoreception in organisms, J. L. Kirschvink, D. S. Jones, B. J. MacFadden (Eds.), Plenum Press, New York, **1985**.
- [79] Thornhill, R. H., Burgess, J. G., T. Sakaguchi, T., Matsunaga, T., *FEMS Microbiol. Lett.*, **1994**, *115*, 169–176.
- [80] Spring, S., Amann, R., Ludwig, W., Schleifer, K-H., van Germerden, H., Petersen, N., *Appl. Environ. Microbiol.*, **1993**, *59*, 2397–2403.
- [81] Hanzlik, M. M., Winklhofer, M., Petersen, N., *Earth. Planet. Sci. Lett.* **1996**, *145*, 125–134.
- [82] Frankel, R. B., Bazylinski, D. A., Johnson, M., Taylor, B. L., *Biophys. J.* **1997**, *73*, 994–1000.
- [83] Spormann, A. M., Wolfe, R. S., *FEMS Lett.* **1984**, *22*, 171–177.
- [84] Zhulin, I. B., Besselov, V. A., Johnson, M. S., Taylor, B. L., *J. Bacteriol.* **1996**, *178*, 5199–5204.
- [85] Segall, J. E., Block, S. M., Berg, H. C., *Proc. Natl. Acad. Sci. USA* **1986**, *83*, 8987–8991.
- [86] Taylor, B. L., *Trends Bioch. Sci.* **1983**, *8*, 438–441.
- [87] Blakemore, R. P., Frankel, R. B., Kalmijn, A. J., *Nature* **1980**, *236*, 384–385.
- [88] Frankel, R. B., Bazylinski, D. A., Schüler, D., *Supramol. Sci.* **1998**, *5*, 383–390.
- [89] Frankel, R. B., Bazylinski, D. A., *Hyperfine Interactions* **1994**, *90*, 135–142.
- [90] Wiltshko, R., Wiltshko, W., *Magnetic Orientation in Animals*, Springer, Berlin, **1995**.
- [91] Ritz, T., Adern, S., Schulten, K., *Biophys. J.* **2000**, 707–718.
- [92] Mann, S., Sparks, N. H. C., Walker, M. M., Kirschvink, J. L., *J. Exp. Biol.* **1988**, *140*, 35–49.
- [93] Kirschvink, J. L., Kobayashi-Kirschvink, A., Woodford, B. J., *Proc. Natl. Acad. Sci. USA* **1992**, *89*, 7683–7687.
- [94] Kirschvink, J. L., Hagadorn, J. W., *A grand unified theory of biomineralization in biomineralization: From biology to biotechnology and medical application*, E. Baeuerlein (Ed.), Wiley-VCH, Weinheim, Germany, **2000**.
- [95] Weaver, J. C., Vaughan, T. E., Astumian, R. D., *Nature* **2000**, *405*, 707–709.
- [96] Buseck, P. R., Dunin-Borkowski, R. E., Devouard, B., Frankel, R. B., McCartney, M. R., Midgley, P. A., Posfai, M., Weyland, M., *Proc. Natl. Acad. Sci. USA* **2001**, *98*, 13490–13495.
- [97] Golden, D. C., Ming, D., Schwandt, C. S., Lauer, H., Socki, D. J. Morris, R. V., Lofgren, G. E., McKay, G. A., *Amer. Mineral.* **2001**, *86*, 370–375.
- [98] Barber, D. J., Scott, E. R. D., *Proc. Natl. Acad. Sci. USA* **2002**, *99*, 6556–6561.

7 Magnetic Ordering due to Dipolar Interaction in Low Dimensional Materials

Pierre Panissod and Marc Drillon

7.1 Introduction

In the quest towards the development of new materials, in which the dimensions of the building units do not exceed a few atoms in at least one direction of the space – organic magnets built of spin chains or lamellae, for instance, or magnetic dots, wires and multilayers – the scientists are currently facing the influence of through-space interactions of dipolar origin. Basically, the concept of dipolar interaction is very familiar in solid state physics, and its manifestations at the macroscopic scale are well described in many textbooks [1], and actually used for magnetic applications. However, at the atomic scale, this interaction is mostly negligible and, when it occurs, the magnetic ordering is controlled by the quantum exchange mechanism which usually prevails in 3D networks.

In this chapter, we demonstrate that the dipole–dipole interaction may have a foremost importance when considering low dimensional magnetic materials, made of strongly correlated objects of dimensionality zero (0D), one (1D) or two (2D) interacting through a weak interaction of dipolar origin. The aim is not to provide an exhaustive review on the dipolar interaction effects in magnetic materials but rather an outlook, both theoretical and experimental, on the magnetic ordering of 0D to 2D units embedded in higher dimensionality systems.

From a fundamental viewpoint, magnetic ordering due to pure dipole–dipole interaction is a clean phase transition problem since the related Hamiltonian does not involve any adjustable parameter: unlike the exchange-coupled systems, one cannot change the form and the magnitude of the interaction in order to improve the agreement between theory and experiment. Therefore, experimental observations provide a direct answer for testing the models used to predict the magnetic structure and the ordering temperature, if observed.

From the applied physics viewpoint, the pure dipole–dipole interaction is essentially an academic problem as long as only ionic/atomic moments are involved. Indeed the expected dipolar ordering temperature is of the order of $\mu M_s / k_B$ (M_s is the saturation magnetization and μ the individual moment) that is at most a few Kelvin for rare earth compounds. Nevertheless, there is nowadays a large renaissance of interest for pure dipole systems that involve not individual atomic moments but magnetic assemblies comprising a large number of strongly exchange coupled atomic moments. Indeed the magnetic ordering temperature for such systems can be much higher than in classical dipole systems because the magnetic moment μ of the objects

is several order of magnitude larger than the atomic ones, whereas the magnetization M is only slightly reduced. Such a situation may be realized in an assembly of 1D or 2D arrays of single-domain ferromagnetic dots, or arrays of magnetic nanowires. Another situation where the dipolar interaction might play a significant part in the magnetic ordering is the case of materials composed of ferro- or ferrimagnetic chains with large intra-chain exchange coupling, connected to each other by a weak inter-chain exchange coupling. Such situation extends to materials composed of magnetic planes separated by bulky diamagnetic spacers although, unlike the 1D chain case, 2D magnetic ordering might also take place due to in-plane exchange coupling.

It is, of course, well known that the dipolar effects can change the critical properties of three-dimensional ferromagnets where the exchange interaction largely dominates [2]. This is due to the long range character of the interaction. One immediate consequence of which is that the magnetostatic energy is very significant in real – finite size – samples, and depends on the shape and size of the sample. However, since the focus is on the dipolar interaction *between magnetic objects*, the effects of this interaction *inside a single object*, in particular the most obvious ones (magnetic domain patterns, shape dependent anisotropy and magnetization reversal modes) are beyond the scope of this chapter.

For 2D systems the presence of dipolar interaction has even more striking consequences. Indeed, while a 2D arrays of spins coupled by isotropic exchange cannot sustain long-range order, it has been demonstrated that dipole–dipole interaction induces an in-plane anisotropy that stabilizes long range magnetic order, namely ferromagnetic-like if the exchange coupling is ferromagnetic [3–5]. The dipolar interaction also can give rise to a rich variety of spatially modulated phases in 2D systems [6–11] and the competition between magnetic surface anisotropy and magnetostatic dipolar energy can lead to the existence of a reorientation transition. This is evidenced in magnetic films such that the surface and bulk magneto-crystalline anisotropy favor an easy magnetization axis perpendicular to the film [11–15].

The outline of the chapter is as follows. After a short recall of the peculiarities of the dipole–dipole interaction, Section 7.2 is devoted to magnetic ordering in pure (point) dipole systems. Section 7.3 covers arrays of single domain ferromagnetic or superparamagnetic objects. Finally, Section 7.4 deals with the occurrence of 3D ferromagnetism in molecular compounds due to the dipolar interaction between chain or layer units, where no long range magnetic order is expected.

7.2 Magnetic Ordering in Pure Dipole Systems

7.2.1 The Dipole–Dipole Interaction – A Well Known Hamiltonian?

The energy associated with the dipole–dipole interaction between two magnetic moments $\boldsymbol{\mu}_i$ and $\boldsymbol{\mu}_j$ is:

$$E_{\text{dip}} = - \left\{ \frac{\mu_0}{4\pi} \right\} \frac{1}{r_{ij}^3} [3(\boldsymbol{\mu}_i \cdot \mathbf{u}_{ij})\mathbf{u}_{ij} - \boldsymbol{\mu}_i] \cdot \boldsymbol{\mu}_j = -\mathbf{B}_{d,ij} \cdot \boldsymbol{\mu}_j \quad (1)$$

where \mathbf{u}_{ij} is the unit vector along the bond between the moments and r_{ij} the length of this bond. Note that here, and throughout this chapter, the equations are written for the international unit system (SI). If the CGS–emu unit system were used the term $\{\mu_0/4\pi\}$ between the curly braces should be omitted. For instance in the CGS system the dipolar field arising from $\boldsymbol{\mu}_i$ at the moment $\boldsymbol{\mu}_j$ is:

$$\mathbf{B}_{d,ij} = \frac{1}{r_{ij}^3} [3(\boldsymbol{\mu}_i \cdot \mathbf{u}_{ij})\mathbf{u}_{ij} - \boldsymbol{\mu}_i] \text{ [Gauss]} \quad (2)$$

whereas in the international system (SI) it is:

$$\mathbf{B}_{d,ij} = \frac{\mu_0}{4\pi} \frac{1}{r_{ij}^3} [3(\boldsymbol{\mu}_i \cdot \mathbf{u}_{ij})\mathbf{u}_{ij} - \boldsymbol{\mu}_i] \text{ [Tesla]} \quad (2')$$

Considering the case of parallel moments for simplicity, the dipolar energy of the moment pair can be re-written as:

$$E_{\text{dip}} = - \left\{ \frac{\mu_0}{4\pi} \right\} \frac{\mu_i \mu_j}{r^3} [3 \cos^2(\theta) - 1] \quad (1')$$

where θ is the angle between the moment orientation and the bonding vector between the moments. This expression shows immediately the intricate character of the dipolar interaction as being:

- long ranged: for a 3D assembly of dipoles one has to sum up over all pair energies and this summation (or integration) is not absolutely convergent – the sum $\sum n(r)/(r^3)$ or the integral $\int r^2 dr/r^3$ do not converge [$n(r) \approx r^2 dr$ is the number of moment pairs separated by the distance r],
- strongly anisotropic – leading to ferromagnetic coupling for $\cos^2(\theta) > 1/3$ ($\theta < 54.75^\circ$) or antiferromagnetic coupling for $\cos^2(\theta) < 1/3$ ($\theta > 54.75^\circ$).

These properties make it usually impossible to handle the problem analytically. Moreover:

- the first property makes the boundary conditions (finite size sample) a crucial ingredient of the problem (i. e. the dipolar energy is not only a property of the material but also of the object shape); and
- beyond the simple case of a single pair of moments, the second property makes the prediction of the actual kind of ordering not intuitive, as it is strongly dependent on the locations of the moments on a lattice.

7.2.2 Ordering Temperature – The Mean-field Approach

The possibility, type and magnitude of the magnetic order that should occur in a lattice of interacting magnetic dipoles has been studied by a number of investigators over the past century, beginning with the original work of Onsager [16] who treated the problem classically in a high-temperature approximation. A consistent quantum

mechanical theory was subsequently developed by Van Vleck [17] who expands the partition sum of the crystal in decreasing powers of the temperature. Both found that “dipolar ferromagnetism” is impossible. However, such calculations fail at low temperatures where the dipole interactions becomes important.

The simplest way to tackle the question of dipole ordering, and, more particularly, the question of dipole ferromagnetism is the mean field approach. This approximation is rather crude in terms of the existence of magnetic ordering, of the nature of the ordering and, if any ordering, it overestimates the critical temperature as compared to exact calculations or better approximations [18–20]. However, it is very instructive about the effects of the long range character of the dipolar interaction.

7.2.2.1 The Local-field Approximation

Basically a local field approach consists in solving a self-consistent set of two $3N$ -equations (where N is the number of moments):

$$\mathbf{B}_i = F(\langle \boldsymbol{\mu}_{j \neq i} \rangle) \quad (3)$$

and

$$\langle \boldsymbol{\mu}_i \rangle = \boldsymbol{\mu}_i G(\boldsymbol{\mu}_i \mathbf{B}_i / k_B T) \quad (4)$$

Equation (3) yields the local field acting on the moment $\boldsymbol{\mu}_i$ as a function F of – a summation over – all the other moments $\langle \boldsymbol{\mu}_{j \neq i} \rangle$, while Eq. (4) yields the expectation value $\langle \boldsymbol{\mu}_i \rangle$ of each moment at thermal equilibrium in its local field \mathbf{B}_i and along this field. The function G can be the Langevin function for freely rotating classical spins, a hyperbolic tangent if the orientation of the classical spins is fixed, or the Brillouin function for a quantum spin. The main approximation of the approach is to neglect any temporal and spatial correlation between the moments.

Finding the critical temperature T_C , for magnetic ordering within such approximation consists merely in looking for the largest T for which there exists a non-zero solution of $\langle \boldsymbol{\mu}_i \rangle$. For the purpose Eq. (4) can be linearized around T_C where \mathbf{B}_i and $\langle \boldsymbol{\mu}_i \rangle$ are vanishing and becomes

$$\langle \boldsymbol{\mu}_i \rangle = (\mu_i \mathbf{B}_i / nk_B T) \mu_i \quad (4')$$

where n is the number of degrees of freedom per spin ($n = 3$ for isotropic spins; for classical moments with uniaxial anisotropy $n = 3$ if the anisotropy axis are random or 1 if they are parallel).

7.2.2.2 The Mean-field Approximation

To look for the possibility of ferromagnetic order a second approximation step consists in assuming that all moments experience the same – mean – field B_0 that takes the average value of the local fields \mathbf{B}_i over all magnetic sites. This second step obviously neglects all spatial fluctuations of the local field.

In the simplest case of identical moments μ Eq. (4') becomes:

$$\langle \mu \rangle = (\mu B_0 / nk_B T) \mu \quad (5)$$

where n takes the value 1 for uniaxial moments or 3 for freely rotating moments or quantum spins.

As to the mean dipole field, Eq. (3) can be integrated over the sample within a continuous approximation, which yields

$$B_0 = \{\mu_0/4\pi\}(4\pi/3 - N_M)\rho\langle\mu\rangle = \{\mu_0/4\pi\}(4\pi/3 - N_M)M(T) \quad (6)$$

where ρ is the moment density, $M(T)$ is the spontaneous magnetization and $M_s = \rho\mu$ is the saturation magnetization at 0 K. The influence of the sample shapes appears in Eq. (6) as the demagnetizing factor N_M that takes the value $4\pi/3$ for a sphere, 0 or 4π for a film when M is in plane or perpendicular to it, respectively, and 0 or 2π for a thin wire when M is along its long axis or transverse to it, respectively.

Equation (6) can be re-written:

$$B_0 = B_{\text{Lor}} - B_{\text{dem}}$$

where $B_{\text{Lor}} = \{\mu_0/4\pi\}4\pi M/3$ is the Lorentz cavity field, and $B_{\text{dem}} = N_M\{\mu_0/4\pi\} \cdot 4\pi M/3$ is the demagnetizing field.

Combining Eqs. (5) and (6) yield the critical temperature:

$$nk_B T_C = \{\mu_0/4\pi\}(4\pi/3 - N_M)\mu M_s = \{\mu_0/4\pi\}(4\pi/3 - N_M)\rho\mu^2 \quad (7)$$

This leads to two important conclusions. First, the ferromagnetic ordering temperature, if any, depends on both the value of magnetization and that of the moment: the typical dipolar energy is $\{\mu_0/4\pi\}\mu M_s = \{\mu_0/4\pi\}\rho\mu^2$. The immediate consequence is that the ordering temperature $T_C \approx \{\mu_0/4\pi\}\rho\mu^2/k_B$ for systems built of individual atomic moments shall never exceed a few K. However systems composed of larger moments $N\mu$, comprising a large number N of strongly exchange coupled atomic moments μ , may order at much higher temperature since $\rho'(N\mu)^2 \gg \rho\mu^2$ even though their magnetization may be lower than that of the first ones ($\rho' < \rho/N$). This opens the possibility to obtain "dipolar" magnets at room temperature.

Second, the long range character of the dipolar interaction emphasizes boundary effects even for an arbitrary large sample: while an infinite, boundary free sample ($N_M = 0$, $B_{\text{dem}} = 0$) is predicted to order ferromagnetically for any magnetization (density), the Curie temperature of a real, bounded sample, depends on its shape. In particular a spherical sample ($N_M = 4\pi/3$ in Eq. 7) should not order, regardless of its size and magnetization, because of the demagnetizing field arising from the discontinuity on the surface. It must be noted however, that this conclusion only holds for a uniformly magnetized, single domain, sample. Indeed, from the point of view of domain theory, in 1951 C. Kittel [21] has argued that, if ferromagnetism is possible for a boundary free sample, it should occur for all specimen sizes and shapes provided the sample can minimize its demagnetizing energy by breaking into domains. This simple example stresses the tricky effects of the long range character

of the dipolar interaction. One must always pay attention to whether calculations reported in the literature are for a sample without an external surface (using periodic replicas) or for a sample with an external surface (even if it is infinite). Theoretical investigations generally favor the former case because it is independent of the sample shape and also because accurate calculations of the dipolar energy can be performed by taking advantage of the periodic character. Oppositely real samples are obviously bounded.

The approximation in the simplest mean field approach neglects the spatial fluctuations of the moments. Therefore, even if the ferromagnetic state may be more stable than the paramagnetic one, at least in the absence of demagnetizing field, it does not mean that another type of spin ordering is not more stable. Indeed, the magnetization is not the only factor in determining the local internal field as shown first by Sauer [22] who computed the energies of certain intuitively selected dipole arrays and found that ordered arrays of zero net magnetization (antiferromagnets) may have widely different energies, some of them lower than that due to the Lorentz field. The question then arose of identifying the actual magnetic order in the ground state of a pure dipole system for a given network (periodic or random) of moments (single- or multi-valued).

7.2.3 Dipolar Ordering in 3D Systems

Actually the exact prediction of the ordered structures arising in a system of interacting moments is still an unsolved problem. A prediction of such structures can be made only through approximate methods whose validity must be tested by experiment. As to moments interacting through the dipole force, because of its intricate angular dependence and long range nature, and despite the exact knowledge of the Hamiltonian, the more general theoretical approaches limit themselves to a calculation of the interaction energy of periodically ordered arrays of dipoles at zero Kelvin. In the general case, the type of magnetic order predicted by these theories depends critically on the details of the lattice parameters, and the anisotropy of the magnetic moments, or g tensor.

7.2.3.1 Crystalline 3D Systems – The Cubic Case

That the dipolar interaction could be responsible for the ordering has been suggested by a number of experiments, mostly in rare earth based compounds. For example, the magnetic ordering EuSO_4 , near 1 K, is because of dipolar interactions [23, 24].

Actually, as early as 1946, Luttinger and Tisza [25] made the prediction that the ground state of an assembly of freely rotating magnetic dipoles sitting on either a face centered cubic (*fcc*) or a body centered cubic (*bcc*) lattice *without boundaries* would be *ferromagnetic* even in the absence of exchange interaction. On the contrary, for dipoles on a simple cubic lattice (*sc*) the ground state would be *antiferromagnetic*.

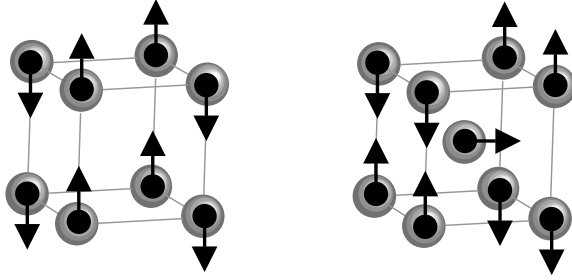


Fig. 1. Ground state AF spin configurations for a sphere of point dipoles on a *simple cubic* (left) and *body centered cubic* (right) lattices (after Luttinger and Tisza [25]). For boundary free samples – no demagnetizing energy coming from the surface – the simple cubic lattice is still antiferromagnetic but the body centered and face centered lattices are ferromagnetic.

The Luttinger method uses the fact that, within the local field approximation, the dipolar interaction is quadratic in the components of the moments which can be diagonalized. The diagonalization yields base dipole arrays (spin arrangements on the lattice) as eigenvectors and the associated dipolar energy as eigenvalues. Arbitrary spin arrays are linear combinations of the base arrays so that their free energy at 0 K is easily calculated (since moments take their full value) and the one with the lowest energy is considered as the ground state.

In fact, for the *fcc*, *bcc*, and *sc* lattices, the minimum energy configuration for a spherical sample has been found antiferromagnetic (Fig. 1). Indeed the lowest energy constants of the non-polarized arrays are for *sc* $-2.675\{\mu_0/4\pi\}\rho\mu^2$, for *bcc* $-1.986\{\mu_0/4\pi\}\rho\mu^2$, and for *fcc* $-1.808\{\mu_0/4\pi\}\rho\mu^2$ while the energy of the ferromagnetic array is 0 for all three cubic types, as expected for sites of cubic symmetry in a spherical sample. However, if the demagnetizing energy $1/2(4\pi/3)\{\mu_0/4\pi\}\rho\mu^2$ is subtracted from the energy of the ferromagnetic array, as it should be for a boundaryless sample or a very long thin needle, the energy constant of the ferromagnetic array becomes $-(2\pi/3)\{\mu_0/4\pi\}\rho\mu^2 = -2.094\{\mu_0/4\pi\}\rho\mu^2$. Thus the *sc* array is always non-ferromagnetic, while *bcc* and *fcc* cases predict ferromagnetism for long thin needles.

The method of Luttinger and Tisza to determine the kind of magnetic ordering in a crystal is one of the two attempts (to our knowledge) towards a general solution of the problem. The other one, proposed by Villain, was initially used to investigate ordering in spin systems with short-range interactions, and led to the prediction of helical structures [26]. It has also proved very successful in the prediction of the dipolar magnetic ordering of nuclei [27–29]. Both methods are similar in that they use the same local field approximation (Eqs. 3 and 4). The difference is that where Villain considers the vicinity of the transition temperature when the magnetization is infinitely small (Eq. 4'), Luttinger and Tisza look for the stable structures in the low temperature limit ($\langle \mu_i \rangle = \mu_i \mathbf{B}_i / B_i$). The methods are shown to yield the same stable magnetic structure at $T = 0$ for the former and at T_C for the latter [29] so that presumably the same structure holds between the two, at least for the local approach.

Extensions of the Luttinger method have been devised and applied to less symmetrical cases [30] but it was shown that it cannot be applied for systems where more than two equivalent spins per unit cell are present [31]. Presently, thanks to the easy access to fast computing systems, it is rather easy to search for the stable dipolar structures within the local field approach at 0 K by numerically performing the energy minimization as a function of the orientation of the spins for periodically ordered arrays. The calculations are performed in the reciprocal space, which enables to perform energy minimization for one or several continuous wave vectors thus minimizing the chances to omit some structures. However, it is always possible that a complicated magnetic structure is missed. More exact numerical simulations using the Monte-Carlo method are now preferred, as they also yield the thermodynamics information (see below), but they have also some intrinsic problem of finite site effects. In addition, such simulations are quite time demanding and may get stuck in a local energy minimum that can be misinterpreted as the final state.

Since Luttinger and Tisza treated the magnetic spins as classical quantities, the question arose as to the validity of their conclusions in the presence of quantum fluctuations. Cohen and Keffer [32] examined the quantum-mechanical conditions of stability and calculated the zero-point energy of ferromagnetic arrays of point dipoles in the three primitive cubic lattices. They used a linearized spin-wave approximation, modified to include dipole–dipole interactions. They found that the quantum-mechanical energy of the ferromagnetic state is sufficiently less than the classical energies of other arrays to suggest that ferromagnetism will occur for spins greater than $5/2$ in the *fcc* and 6 in the *bcc* lattice. Later quantum calculations [33–35] confirmed the predictions of the classical theory.

Although a number of experiments in less symmetrical systems suggested the veracity of Luttinger’s prediction [30], it has been only very recently investigated for a true *fcc* lattice. Experiments by Roser et al. [36] were performed on *fcc* rare-earth (R) salts $\text{Cs}_2\text{NaR}(\text{NO}_2)_6$. The compounds have perfect tetrahedral symmetry at the rare-earth site and the magnetic ions are sufficiently far apart so that the exchange interaction through the R-O-N-Na-N-O-R path is less (10 mK) than the dipolar energy (100 mK). As noted above the demagnetizing field prevents the spontaneous appearance of a non-zero magnetization for spherical samples. Because of the demagnetizing factor N_M the measured (apparent) sample susceptibility $\chi_{\text{ext}} = \chi/(1 + \chi N_M)$ reaches the limit value $1/N_M$ at T_C when the intrinsic susceptibility χ diverges. Experimentally, χ_{ext} has indeed been found to saturate at low temperatures to a value close to $1/N_M$. This was interpreted as a dipolar ferromagnetic transition, which occurs at a temperature comparable to the dipolar energy scale (approximately 0.1 K). The results appear to hold for four members of the series $\text{Cs}_2\text{NaR}(\text{NO}_2)_6$ (R = Nd, Gd, Dy and Er). No magnetic transition was observed above 6.5 mK for the other rare earths.

More recently Bouchaud and Zérah [37] have investigated the dipolar induced ferromagnetic transition on a *fcc* lattice using a Monte-Carlo technique. The dipolar field acting on a given dipole was calculated using the Ewald’s sum procedure for fast convergence with a sample periodically replicated in the three directions [38, 39]. This ensures that the system is free of a demagnetizing field from the surface. The

ferromagnetic T_C and the critical exponents in three dimensions were deduced from the simulation. The Curie temperature was found at $k_B T_C = 0.43\{\mu_0/4\pi\}\rho\mu^2$, half of the experimental result [36] while the mean field prediction is 1.5 larger than the experimental result. An interesting finding of the study is that the ferromagnetic low-temperature phase exhibits a reorientation transition (roughly at $T_C/2$) to a phase with a (100) easy magnetization axis from a phase with a (111) easy axis. Note that the Luttinger approach predicts an isotropic ferromagnet for a cubic system (the easy magnetization axis being determined only by the shape of the sample). The anisotropy evidenced by the Monte-Carlo simulation is probably a thermally induced anisotropy on the spin-wave spectrum as it has been demonstrated in two dimensional cases (see below). Another result of the study is that a weak disorder would not destroy the order so that one can think of a model system of spherical superparamagnetic particles arranged regularly in a suitable diamagnetic matrix like zeolites or a polymer exhibiting ordered mesophases [40]. The authors show that, indeed, such a lattice of spherical particles of permalloy, of diameter 10 nm, volume fraction 10%, would exhibit a Curie temperature at about 550 K. However a strong disorder, where the dipole positions are completely random, has been shown to destroy the long-range order [41, 42] since, due to the r^{-3} dependence of the dipolar energy, the coupling constant is so strongly fluctuating that its variance and mean value diverges (although hard cores will in practice introduce a cutoff – see below).

7.2.3.2 Random 3D Systems

Although the case of randomly dispersed magnetic particles is a topic of large interest, it will only be shortly introduced here since a full chapter, at least, would be needed to survey reasonably the topic [43, 44].

The magnetic properties of small spherical ferromagnetic particles (diameter in the 1–100 nm range) are governed by their single domain character (when their size is smaller than the exchange correlation length) and their magnetic anisotropy, magneto-crystalline (single ion) and/or shape anisotropy. Non-interacting particles are “superparamagnetic” as first introduced by Néel in 1949, i. e. above a certain temperature, called the blocking temperature, T_B , they behave as paramagnetic molecules with giant magnetic moment. This behavior results from the spontaneous reversal of their magnetization through a thermally activated process over the anisotropy energy barrier, even in the absence of an externally applied field. The average time for the particles to reverse their magnetic moment is given by $\tau = \tau_0 \exp(KV/k_B T)$, where τ_0^{-1} is a characteristic attempt frequency of the order of 10^{10} Hz, and KV is the effective energy barrier between equilibrium orientations defined by the magnetic anisotropy (V is the particle volume and K the anisotropy energy density of the particle). Below T_B the single-domain particles are in the “blocked” state where they behave as a “normal” ferromagnet showing hysteretic magnetization loops and remanence. The complexity of the problem makes exact solutions possible only in few limiting cases, at $T = 0$ K for fully blocked particles [45], or $T \gg T_B$ in the fully super-paramagnetic limit [46, 47]. It is worth noting

that there is no phase transition between the superparamagnetic regime and the blocked one, but merely a freezing of the magnetization for a time-scale τ in one of the orientations permitted by the magnetic anisotropy. As a consequence the blocking temperature T_B depends on the characteristic time of the measurement technique τ_m from minutes in standard magnetometric measurement to 10^{-9} s in Mössbauer spectroscopy, for example. For a given measurement time τ_m , T_B will be the temperature such that $\tau(T_B) = \tau_m$, i. e. $k_B T_B = K V / \ln(\tau_m/\tau_0)$.

In real systems the problem becomes even more complicated because of the presence of a distribution of the particle sizes and, of course, that of unavoidable interactions between the particles. The first problem has been solved with the synthesis of the so-called “single molecule magnets” [48], $[\text{Mn}_{12}\text{O}_{12}(\text{OAc})_{16}(\text{H}_2\text{O})_4] \cdot 2\text{AcOH} \cdot 4\text{H}_2\text{O}$ and $[\text{Fe}_8(\text{N}_3\text{C}_6\text{H}_{15})_6\text{O}_2(\text{OH})_{12}] \cdot [\text{Br}_8 \cdot 9\text{H}_2\text{O}]$ which are intrinsically mono-disperse [49, 50]. These systems have been extensively studied in order to unravel the question of magnetic quantum tunneling [51].

As to the role of the dipolar interactions in fine particle systems, many theoretical and experimental efforts have focused recently on their understanding of [52]. Granular metal solids and frozen ferrofluids have been used to investigate the role of dipolar interactions. In the latter the concentration of magnetic particles in the liquid makes it easy to control the average particle distance and, therefore, the strength of the interactions [53–55]. Evidence for interactions among the magnetic entities have been undoubtedly found by using several experimental techniques and in different physical systems [56–65].

Because of the complexity of the fundamental problem and, also, of the real experimental systems, most attempts to treat quantitatively the dipolar interactions use phenomenological approaches involving merely an adjustable mean field $\langle B_0 \rangle$ or interaction energy $\langle B_0^2 \rangle$. Thanks to recent advances of numerical calculations, realistic multiparticle systems could be reliably simulated using Monte-Carlo techniques where the exact dipolar Hamiltonian is explicitly taken into account [66–71]. Most of the simulations and the experimental results agree that the magnetostatic interaction results in an increase of T_B – with a noticeable exception [61] – and a slower decay of the remanence and of the coercivity with increasing temperature. Although no long range ferromagnetic order has been demonstrated, the existence of a short range ferromagnetic correlation [67] or vortices (flux closing patterns) [70] could be responsible for the effects.

As to the question of long range magnetic ordering, both the long range character of the dipolar interaction and the randomness of the systems makes it unlikely, as noted at the end of the previous section. However, the mean field approximation results have been recently revisited by taking into account the fact that dipoles cannot be closer than a minimum “hard core” distance thus eliminating the $1/r^3$ divergence of the fluctuations [72]. The conclusion drawn out of this analytical calculation is that magnetic ordering may exist, *above some critical volume fraction* ρ_c , $\rho_c = 3/(10a^3)$ for freely rotating dipoles and $\rho_c = 9/(16a^3)$ for oriented uniaxial moments. In contrast, an assembly of randomly oriented uniaxial particles, which is the most investigated case, would not order. Note that the usual mean field approximation (Section 7.2.2.2) does not distinguish between freely rotating moments and randomly oriented uniaxial moments.

It is worth noting that spin glass-like properties are often invoked to describe the properties of randomly positioned, interacting, dipoles [56, 57] and recent experiments points towards the existence of a true magnetic transition in some systems where the blocking (critical ?) temperature takes very close values for characteristic measurement times as different as 100s and 10^{-9} s [63].

7.2.4 Dipolar Ordering in 2D Systems

A rapid examination of the interaction energy between nearest neighbors dipoles for a planar system suggests immediately that the ground state of the system is antiferromagnetic. However it was realized in the nineteen-eighties that the situation is more subtle than this intuitive conclusion in several aspects. First, in the case of the square and honeycomb lattices, it can be shown that the ground state is highly degenerate and defines a continuous manifold of spin configurations. Second, for the rhombic lattice and in particular for the triangular lattice it was shown that the ground state is ferromagnetic.

7.2.4.1 The Square and Honeycomb Lattice

In 1983 Belobrov et al. [73] showed that the ground state spin configuration of a square planar lattice of dipoles exhibits a continuous degeneracy, i. e. all configurations where the two spins on one side of the unit square make an angle $0 + \alpha$ and $0 - \alpha$, respectively, with the a axis and $180^\circ + \alpha$ and $180^\circ - \alpha$, respectively, on the other side have the same energy (Fig. 2a). Since α is an arbitrary angle the degeneracy of the ground state would imply the existence of a gapless excitation at zero Kelvin in spite of the fact that the dipolar interaction does not exhibit a continuous symmetry with respect to rotation of the spins. In both the Heisenberg and XY ferromagnetic exchange models the existence of gapless spin-wave excitations destroys long-range order at any finite temperature in the thermodynamic limit [74]. However, in the present case the degeneracy of the ground state is accidental, not a property of the Hamiltonian. This led to question the suppression of the long-range magnetic order

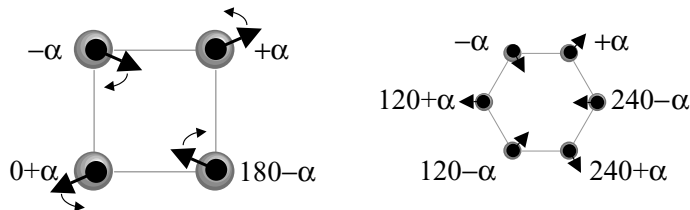


Fig. 2. “Spin rotator” ground states – continuously degenerated – antiferromagnetic order of the *planar square* (left – after Belobrov et al. [73]) and the *honeycomb* (right – after Ibrahim and Zimmerman [76]) lattices of point dipoles. The dipolar free energy is independent of the – arbitrary – value of α .

at finite temperature. Indeed, in 1987, Monte-Carlo simulation for the same system showed [75] that this degeneracy is removed at finite temperature where a columnar antiferromagnetic configuration along the a axis is preferred. The same kind of continuous degeneracy was found by Zimmermann et al. for the honeycomb lattice [76] (Fig. 2b) in their attempt to explain the magnetic susceptibility measured in the plane of FeCl_3 graphite intercalation compounds. The susceptibility measurement in the compounds show a maximum around 2 K and a power law temperature dependence with a critical exponent of approximately 2, greater than that of a 2D Ising system [77]. These results suggested a second order magnetic transition that they attributed to the dipolar interaction between the Fe(III) ions. Both systems were revisited by Prakash and Henley [78] using a linearized spin wave calculation. They showed that, despite the fact that the ground state exhibits a continuous degeneracy, the effects of thermal fluctuations, dilution, and a uniform external field induce an effective potential in the free energy that selects particular orientations of the spins. They concluded that the systems are likely to order magnetically at low temperature. Similar effects of fluctuations, named “ordering due to disorder”, have been studied in various Ising systems called “spin rotators” with an infinite ground-state entropy like the frustrated Ising antiferromagnet on a fcc lattice [79–81]. Prakash and Henley used a model where the interaction had the same form as dipoles but limited to nearest neighbors. The full dipolar Hamiltonian was investigated in the case of the square lattice by De’Bell et al. who solved the problem in the linearized spin wave approximation and through Monte-Carlo simulations [82]. They showed that comparison of the Monte-Carlo results with those from spin-wave theory indicate that the system orders at a finite critical temperature. The results were confirmed by Rastelli et al. [83]. Potential systems where this ordering might take place are some high- T_C superconducting copper oxides where the rare earth ions form a quasi-two-dimensional, square lattice [84–87] but the question of long range magnetic ordering in these systems is still open.

7.2.4.2 The More General Rhombic Case

The square planar lattice of dipoles, as a spin rotator, is an interesting fundamental problem but the degeneracy of its ground state is lifted as soon as it undergoes a rhombic distortion. The more general case of the rhombic planar lattice has been examined by Rosenbaum et al. [88–90]. They have shown that for a small distortion of the square lattice – rhombic angle $78^\circ < \varphi < 90^\circ$ – the ground state is *antiferromagnetic* with moments parallel to the a axis. However, the ground state is *ferromagnetic* for $\varphi < 78^\circ$. The easy magnetization axis is along the long diagonal (counter-intuitive) for $78^\circ > \varphi > 60^\circ$, and along the short diagonal for $\varphi < 60^\circ$. It is isotropic in plane for the triangular lattice ($\varphi = 60^\circ$) – Fig. 3.

Since the phases with ferromagnetic and antiferromagnetic long-range order have different symmetries, the phase transition between them must be of first order. This means also that the ferromagnetic state may be metastable for a slightly distorted square lattice ($\varphi > 78^\circ$). This question and the mechanisms of the magnetization reversal have been analyzed by Fraerman and Sapozhnikov [91]. They found that

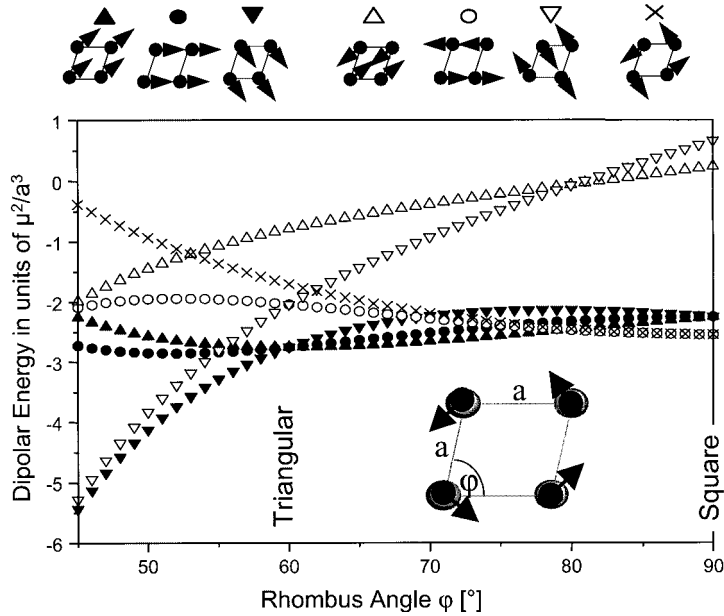


Fig. 3. Dipolar free energy at 0 K of selected spin configurations (top) on a *planar rhombic* lattice as a function of the rhombus angle φ (after Rosenbaum et al. [88–90]). The ground state is ferromagnetic (full symbols) for $\varphi < 78^\circ$ and, in particular for the triangular hexagonal lattice. For $78^\circ < \varphi < 90^\circ$ the ground state is antiferromagnetic (open symbols) but the ferromagnetic order is still metastable [91]. The square lattice shows a “mini-vortex”, “spin rotator state” (Fig. 2). For small angles, dipoles are ferromagnetically aligned along the dense rows, but the ferromagnetic and antiferromagnetic alignment between dense rows are nearly degenerated.

the ferromagnetic state is metastable in zero field except for the square lattice. This implies that a metamagnetic transition should be observed on a virgin sample and the system may exhibit hysteresis and remanence as a ferromagnet. Owing to the weakness of the energy difference between the two states, the presence of magnetic anisotropy, even moderate, may also easily favor local energy minima for the ferromagnetic alignment.

The magnetic properties of the square and triangular systems have also been investigated at 0 K by Russier [92], who confirms the antiferromagnetic and the ferromagnetic state of the pure dipole square and triangular lattice, respectively. When a random uniaxial anisotropy is introduced in the system, the long-range order is lost but the local ordering (correlation function) is still reminiscent of the pure dipole case. It must be stressed, though, that the response of the system to an external field (magnetization loops, coercive fields) is nearly independent of the lattice symmetry, which is certainly due to the metastable character of the local ferromagnetic order in the presence of anisotropy.

7.2.4.3 Random 2D Systems

Cases of planar random dipole systems were studied by Monte-Carlo simulations [70, 71] together with the 3D cases. These studies aimed to explain the magnetic properties of granular layers. The results are essentially similar to the 3D case. One interest of the studies is the possibility to visualize more easily snapshots of the spin arrangement at equilibrium as well as some stages during a magnetization reversal. Figure 4 illustrates the kind of short range ferromagnetic correlation that can be found in the simulation and the snapshot corresponding to the spatial correlation function. However, at longer distances, the correlation is antiferromagnetic (negative).

7.3 Strongly Correlated Extended Objects

This section deals now with finite magnetic objects interacting only through magnetic dipole interaction. Within individual objects the exchange interaction dominates and is much greater than the thermal energy so that, as far as a single object is concerned, it is either ferromagnetic or superparamagnetic depending on the strength of its magnetic anisotropy energy with respect to $k_B T$.

Below are examples that have been treated as arrays of point dipoles, as they illustrate the theoretical predictions of the previous section. Simple calculations of the dipolar interaction energy (or average field) between two spheres or two cubes [70] show that it is quite close to that of point dipoles with the same moment as soon as the distance between the centers is larger than 1.5 times their diameter (or side length). However, for objects whose shape is far from a sphere or a cube, the stray fields are very different in strength and geometry from that of a point dipole, even for distances larger than noted above. In addition the shape anisotropy of the objects must be taken into account. It must be stressed that, while the exchange interaction is usually much larger than the magneto-crystalline or single ion anisotropy energy, this is not the case for the dipolar coupling. Therefore, it is expected that in many cases the anisotropy will play a significant part in determining or selecting the ground state configuration. More generally, even if a ground state is antiferromagnetic, the anisotropy energy may maintain the system in a ferromagnetic metastable state even in zero field leading to magnetization loops similar to that of ferromagnetic material (see the first example in Section 7.3.2).

7.3.1 Stacking of Magnetic Planes

The dipolar interaction between infinite and uniformly ferromagnetic planes is vanishingly small (per unit area). Therefore the question of its effects arises only for stacked or lamellar systems of finite lateral size. As far as uniformly magnetized planes are concerned, the problem is trivial, close to that of the 1D dipole array.

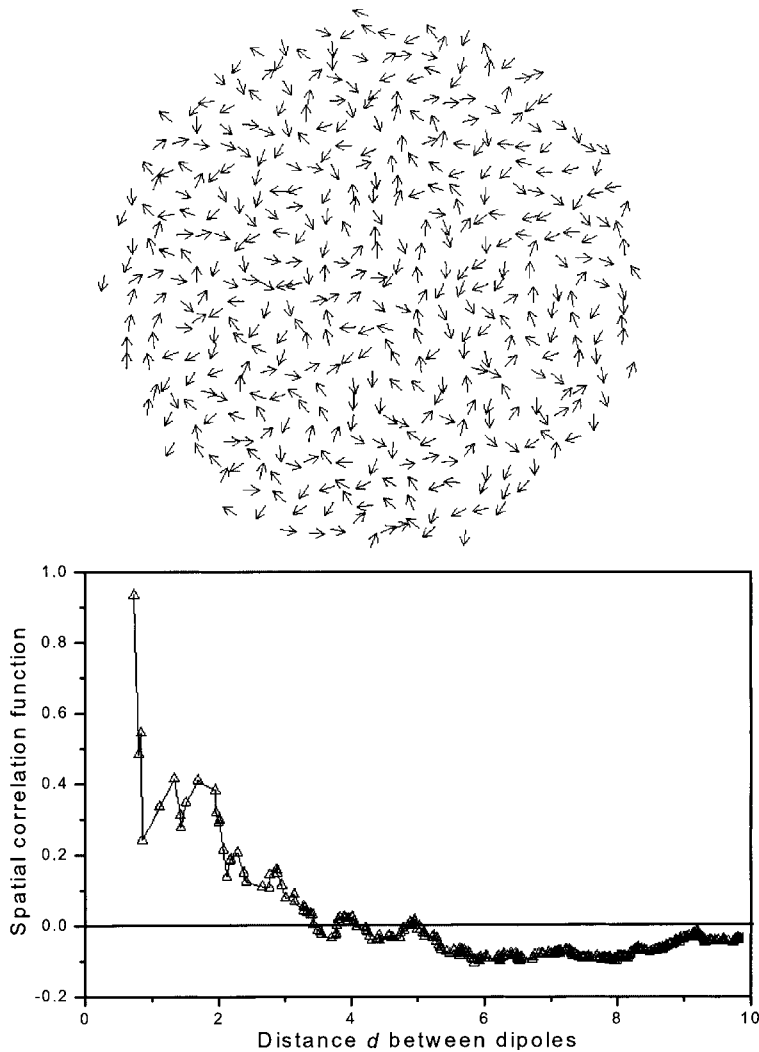


Fig. 4. A Monte-Carlo snapshot of the spin configuration of a *planar random array* of point dipoles (top) showing short ferromagnetic queues of dipoles and flux closing patterns (vortices) (after Altbir et al. [70]). The bottom pane shows the spatial correlation function $\langle \mathbf{S}_i(r) \mathbf{S}_j(r+d) \rangle$ computed for this snapshot showing ferromagnetic correlation (positive) at short distances and antiferromagnetic correlation (negative) at long distances. d is in units of the average nearest neighbor distance.

The coupling which arises from the stray fields is antiferromagnetic when the magnetization is in the planes (the most common case) and ferromagnetic when the magnetization is perpendicular to the plane. A number of studies of the magnetostatic coupling between ferromagnetic ultrathin films have been performed [93] because it is a concern for applications where a good decoupling is sought for (the

opposite of the main topic of this chapter). Beside the stray fields at the edges of a finite plane, the most common source of coupling are the stray fields originating in the roughness of the surface (Néel's "orange peel" mechanism) [94, 95]. The cases where domains and domain walls are present in the planes is an even larger concern for applications, since the stray fields can be several orders of magnitude larger than in the uniform ferromagnet case [96].

The question will be re-examined in the last section for planes where 3D ordering due to the dipolar interaction might occur before 2D ordering.

7.3.2 3D of 1D – Bunching of Wires or Chains

The study of the rhombic lattice of point dipoles presented above can be easily extended to that of magnetic lines perpendicular to the xy plane. The dipolar interaction energy between two parallel lines can be analytically calculated within a continuous approximation. It yields the average field – tensor – on a line due to the other one:

$$[\mathbf{B}] = \left\{ \frac{\mu_0}{4\pi} \right\} \frac{\sigma}{al} \cdot 2(\alpha - 1) \cdot \begin{bmatrix} (2 + 1/\alpha) \cos^2(\varphi) - 1 & (2 + 1/\alpha) \sin(\varphi) \cos(\varphi) & 0 \\ (2 + 1/\alpha) \sin(\varphi) \cos(\varphi) & (2 + 1/\alpha) \sin^2(\varphi) - 1 & 0 \\ 0 & 0 & -1/\alpha \end{bmatrix} \quad (8)$$

where σ is the linear magnetization density in the line, l the line length, a their distance and $\alpha = \sqrt{1 + (l/a)^2}$. The angle φ is that of the vector bonding the two lines in the xy plane. φ could be set to 0, but it is convenient to keep it explicitly for calculations on a lattice. This expression reduces, of course, to the usual Eq. (1) for $l = 0$ (using $\sigma = \mu/l$).

For an infinite length l it reduces to:

$$[\mathbf{B}] = \left\{ \frac{\mu_0}{4\pi} \right\} \frac{2\sigma}{a^2} \begin{bmatrix} (2 \cos^2(\varphi) - 1) & (2 \sin(\varphi) \cos(\varphi)) & 0 \\ (2 \sin(\varphi) \cos(\varphi)) & (2 \sin^2(\varphi) - 1) & 0 \\ 0 & 0 & 0 \end{bmatrix} \quad (9)$$

which corresponds to the true 2D dipole case.

For *longitudinal magnetization* (along the z axis) the dipolar coupling is anti-ferromagnetic, as expected, and it vanishes when the length tends toward infinity. However the magneto-crystalline anisotropy, and, particularly in this case, the demagnetizing energy of a single wire, may be much larger than the interaction between wires. As a consequence, after saturation in an external field, the wires may remain in a metastable ferromagnetic arrangement even in zero field. In such a case the magnetization reversal of a pair of wires takes place in two steps:

- the magnetization reversal of a first wire takes place in a *smaller* field than its intrinsic coercive field because the stray field of the second one adds to the reverse external field, and

- after this first reversal the second wire reverses its magnetization in a *larger* field than its intrinsic coercive field because the stray field of the first one now subtracts from the reverse external field (or in other words the first reversal leaves the system in the more stable antiferromagnetic state).

The argument extends to larger arrays of wires, which are expected to show jumps and plateaus in the demagnetization curve, where each step corresponds to the magnetization reversal of an individual wire (see Section 7.3.3). For very large arrays, the magnetostatic interaction between the wires should produce two effects: reducing the overall coercive field compared to the one of a single nanowire) and increasing the saturation field. These effects have indeed been observed by Raposo et al. [97] for random bunches of cobalt nanowires ($0.2\ \mu\text{m}$ in diameter) electrodeposited into the pores of alumina membranes (thickness $60\ \mu\text{m}$). Realistic Monte-Carlo and micromagnetic simulations have also been performed by the same authors leading to qualitatively similar hysteresis loops as those obtained experimentally.

For *transverse magnetization* (in the xy plane), the dipolar free energy of a rhombic lattice of infinite lines has been computed for different spin configurations as shown in Fig. 5. In contrast with 2D arrays of point dipoles, the ground state is antiferromagnetic for any angle φ of the rhombus for a cylindrical sample. As com-

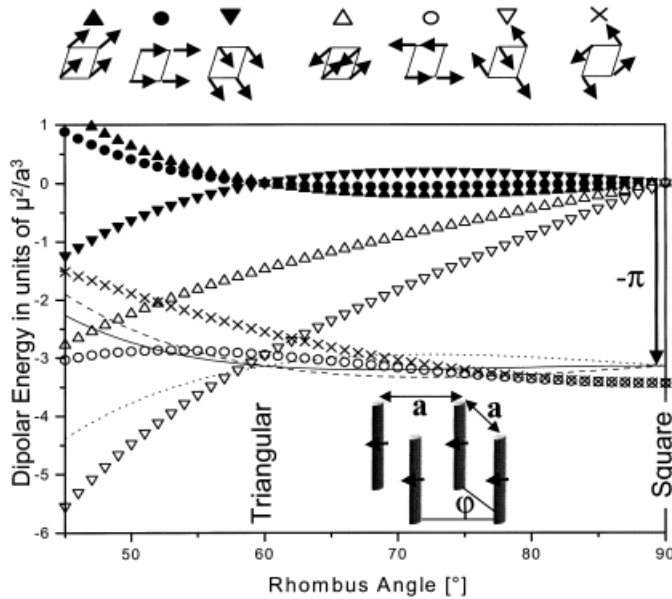


Fig. 5. Dipolar free energy at 0K of selected spin configurations (top) for a *rhombic lattice of infinite wires* as a function of the rhombus angle φ . In contrast with the point dipole the ground state is always antiferromagnetic (open symbols) for a bounded cylinder. However if the demagnetizing energy $(-\pi)$ is subtracted from that of the ferromagnetic states (down arrow), a ferromagnetic order is predicted for $59^\circ < \varphi < 75^\circ$ (the full, dashed, and dotted lines). This will be the case if the system can break into ferromagnetic domains.

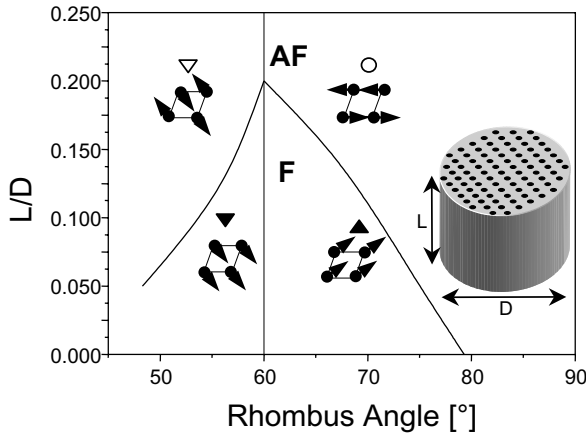


Fig. 6. Effect of the aspect ratio – controlling the demagnetizing energy – of a cylinder cut out of a *rhombic lattice of wires*. Ground state spin configurations as a function of the rhombus angle and the length/diameter ratio.

pared to the point dipole cases the destabilization of the ferromagnetic state is due to the demagnetizing energy due to the discontinuity at the surface of the cylinder. If this demagnetizing energy ($1/2N_M = \pi$) is subtracted, the ferromagnetic state is still marginally stable for $59^\circ < \varphi < 75^\circ$. Due to the intrinsic cylindrical symmetry of the problem, the aspect ratio of the sample (length/diameter, L/D) determines the relative stability of the polarized and not polarized spin configurations, which results in the phase diagram shown in Fig. 6 as a function of the rhombus angle and the aspect ratio L/D .

Experimentally, wires with a transverse magnetization are rather difficult to obtain because the shape anisotropy, which favors longitudinal magnetization, usually dominates. Some cases have been reported, though, [98] but, as far as we are aware, there is no report about the dipolar interaction between bunches of such wires. The theoretical results should also apply to the case of molecule-based magnets built out of spin chains where the interchain separation is much larger than the spin–spin distance in the chain (see Section 7.4.3).

7.3.3 2D of 1D – Planar Arrays of Magnetic Wires

The case of 2D arrays of wires with a *longitudinal magnetization* have been studied by Sampaio et al. [99]. The experimental study has been performed at room temperature for arrays of 2, 3, 4 and 5 microwires of glass-coated amorphous FeSiB with a diameter of $5\ \mu\text{m}$ and lengths from 5 to 60 mm. For such small arrays the magnetization loops show very clearly the expected jumps and plateaus (Fig. 7). Monte-Carlo simulations have been performed, which agree well with the experiment.

The case of 2D arrays of wires with a *transverse magnetization* has been studied mostly on nanostripes. Regular systems of parallel metallic nanostripes can be

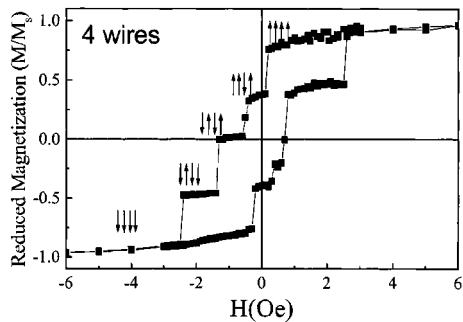


Fig. 7. Magnetization loop of a *planar array of microwires* (glass coated FeSiB amorphous alloy) with easy longitudinal magnetization axis showing the steps associated with the successive reversal of the individual wires (after Sampaio et al. [99]). Although the ground state is antiferromagnetic, the anisotropy/coercivity of the wires keeps the system in successive, polarized, metastable states.

prepared by deposition and growth of atomic thick layers onto a stepped (vicinal) substrate made by miscleaving a single crystal at some small angle with respect to one of the crystal axis [100, 101]. The easy magnetization axis is determined by the preparation conditions, by the substrate and growth orientations and by the thickness of the layers. By epitaxial growth of Fe on a vicinal W(110) substrate, Gradmann and coworkers prepared densely spaced and continuous monolayer and bilayer stripes of Fe(110), directed along (001) [102, 103]. In this system the magnetic easy axis switches from being in-plane for a monolayer to being perpendicular for bilayer stripes. Therefore, it is expected that monolayer stripes for which the magnetization points towards the adjacent stripe interact ferromagnetically through the dipolar interaction while bilayer stripes, for which the magnetization points in the orthogonal direction, should be antiferromagnetically coupled.

Indeed, in case of *transverse and out-of-plane magnetization* (bilayer thick stripes), the magnetization loops show the absence of hysteresis in combination with a low saturation field, which strongly suggests that the magnetostatic interactions induce *antiferromagnetic* order in the nanostripe array [102]. The dipolar nature of the antiferromagnetic coupling is confirmed by the order of magnitude of the saturation field that compares well with the dipolar stray field that one stripe feels by interaction with all other stripes. The antiferromagnetic order between the stripes has been confirmed by direct local measurements using spin-polarized scanning tunneling spectroscopy [104].

The case of *transverse and in-plane magnetization* (monolayer thick stripes) has also been investigated [103]. In this case the coupling is expected to be ferromagnetic. However, unlike bilayer and thicker stripes, isolated monolayer stripes do not order magnetically. Yet, arrays of such stripes do exhibit a sharp phase transition at $T_{Cexp} \approx 180$ K to ferromagnetic order, free from relaxation, i. e. it is not a mere freezing of superparamagnetic objects (Fig. 8). The resulting ferromagnetic phase transition is therefore driven by the dipolar interaction between the stripes. The onset of the ferromagnetic ordering can be summarized as follows. Even though a

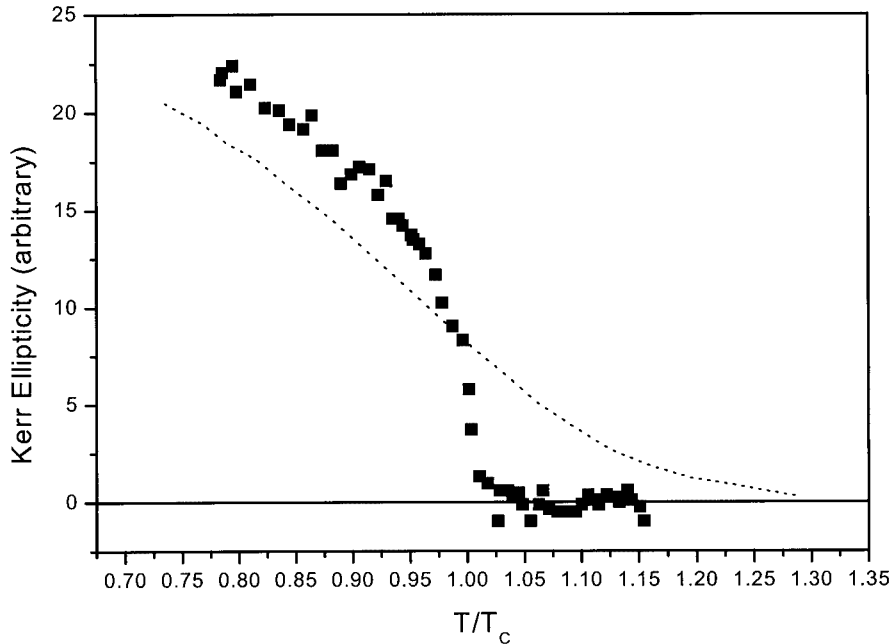


Fig. 8. The sharp ferromagnetic transition observed in a *planar array of stripes* (Fe on a vicinal W substrate) with in-plane and transverse easy magnetization axis (after Hauschild et al. [103]). Isolated stripes do not show long range magnetic order. The long-range ordering is because of the dipolar coupling (ferromagnetic in this case) between the stripes. Symbols show the temperature dependence of the magnetization measured by Kerr effect and the dotted curve show what would be the result of a mere freezing of the magnetization in an assembly of non-interacting stripes.

single stripe does not order at finite temperature, the exchange interaction is responsible for the formation of correlated spin blocks the size of which diverges exponentially with decreasing temperature [105]. The dipolar interaction between such spin blocks in adjacent stripes also diverges exponentially and the phase transition takes place when the block length reaches some critical length. Following this idea, the authors have computed T_C within a mean field approximation, which they have found to agree quite well with the experimental observation ($T_{Cth} \approx 1.1T_{Cexp}$). This situation will be treated in more details in the last section of the chapter (Section 7.4.3).

7.3.4 2D of 0D – Planar Arrays of Magnetic Dots

As indicated above planar arrays of point dipoles exhibit in plane ferromagnetic order for compact structures ($\varphi < 78^\circ$) and antiferromagnetism (or a spin rotator state) for the less compact ones (and the square lattice). This theoretical re-

sult must obviously be re-considered for objects (or moments) where either shape or magneto-crystalline anisotropy is present. Particularly if the anisotropy favors a magnetization perpendicular to the plane of the lattice it is easy to understand that the dipolar interaction favors an antiferromagnetic configuration for the square lattice and that it is frustrated in case of triangular lattice.

Arrays of micron size perpendicularly magnetized ultrathin cobalt dots with 20 nm separation were obtained by etching a Co/Pt multilayered thin film with a focused ion beam. The surface magnetic anisotropy at the Co/Pt interfaces of these multilayers favors an easy axis perpendicular to the plane of the square dots. It is sufficiently large to overcome the shape anisotropy (demagnetizing energy) that would favor an in-plane easy axis. The magnetic state of this regular square lattice of squares has been studied by Ferré and co-workers using polar magneto-optical microscopy [106]. Frustrated checkerboard patterns are observed in the demagnetized state (Fig. 9). The checkerboard patterns agree with the expected antiferromagnetic order. The regions of frustration are actually antiphase boundaries which are formed where two antiferromagnetic domains of opposite phase merge during the demagnetization process, in agreement with numerical simulations performed in the same study.

The magnetic order in 2D arrays of nanometer-sized superparamagnets has also been studied by Scheinfein and co-workers [107]. In this study random two-dimensional island assemblies have been grown on an insulating CaF_2 substrate with a variable coverage. Despite some degree of randomness, the islands exhibit a narrow distribution of sizes and the arrays are rather compact. For low coverage the aspect ratio of the island ($L/D > 0.75$) and, therefore, the shape anisotropy are such that the easy magnetization is perpendicular to plane. In such a case a random, frustrated, antiferromagnet is expected although no direct evidence has been given except the absence of hysteresis in the magnetization loops. For large coverage the islands become flatter, the easy magnetization axis switches to being

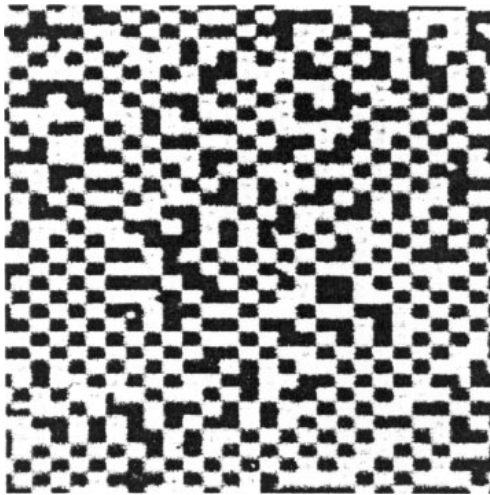


Fig. 9. Magnetic pattern observed by magneto-optic microscopy on a demagnetized *square planar array of dots* (Co/Pt multilayers) with easy magnetization axis perpendicular to the plane (after Aign et al. [106]). The checkerboard patterns are characteristic of the antiferromagnetic dipolar coupling between the dots. The frustrated regions between them are antiphase boundaries that form when domains out of registry merge during the demagnetization process.

in-plane and eventually the array becomes ferromagnetic at room temperature despite the fact that isolated islands should still be superparamagnetic. Mean field calculations and Monte-Carlo simulations have been performed using a fully featured dipolar Hamiltonian – including all the geometrical aspects – which are in agreement with the experimental observations. As usual the critical temperature estimated within the mean field approximation is about twice that determined by the Monte-Carlo simulations. However, the simulations show that the ferromagnetic order is not long-range as the correlation length is still finite below the “ordering” temperature because of the disorder and the average magnetization decreases when increasing the number of islands over which the average is taken (see also Fig. 4).

7.3.5 1D of 0D – Lines of Magnetic Dots

The possibility to achieve room temperature dipolar ferromagnetism has also been demonstrated by Sugarawa and Scheinfein [108] for linear arrays of Fe particles with radii larger than 2.5 nm. Quasi 1D Fe particle arrays have been prepared by self-organized shadow growth on regularly faceted NaCl (110) surfaces. Surface magneto-optic Kerr magnetization curves indicate easy-axis alignment along the rows of particles. Remanence and coercivity have been found to depend strongly on the particle diameter and linear island density. It is clear, however, that closely packed linear arrays can exhibit remanence and coercivity at temperatures where the isolated particles are superparamagnetic with a relaxation time shorter than microseconds. The experimental observations have been compared to those predicted by a Monte-Carlo simulation with no free parameters. The computed hysteresis loops accurately reproduce the results of the experiment (Fig. 10). Despite the disorder and unlike in the 2D array case (Section 7.3.4) the computation predicts

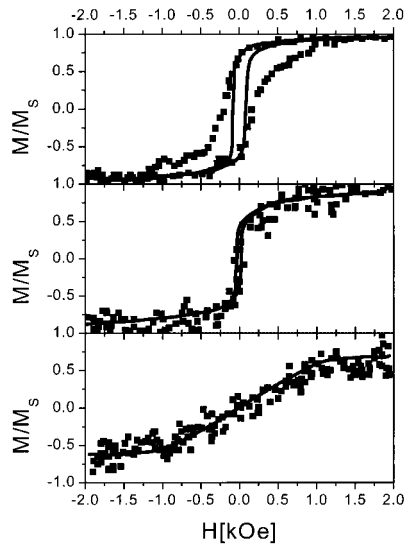


Fig. 10. Magnetization loops observed at room temperature for *parallel arrays of dotted lines* (Fe on a faceted NaCl substrate) with different sizes and densities (after Sugarawa and Scheinfein [108]). Average dot diameter/height/spacing, from top to bottom: 70/10/90, 50/6/90, 30/3/70 in Å. For the larger and denser dots (top) a dipolar ferromagnetic order is observed at room temperature. The full lines are the strikingly similar results of *parameter free* Monte-Carlo simulations, taking into account the actual geometry of the samples.

global ordering along the rows through the dipolar interaction. This is attributed to the strong symmetry breaking in the plane. Except for the distribution of sizes and distances this ordering is understood in the frame of the rhombic lattice for small angle values (Section 7.2.4.2 and Fig. 3).

7.4 Weakly Correlated Extended Systems

This section addresses the question of ferromagnetic 3D ordering in systems exhibiting ferromagnetically exchange-coupled sub-networks – chains or layers – only interacting through dipolar coupling. A similar problem has already been sketched in Section 7.3.3 for planar arrays of nanostripes but here the focus will be put on molecule-based magnets, usually characterized by magnetic interactions of the order or less than $k_B T$ in the temperature range of interest, so that temperature dependent dipolar effects must be considered. The possibilities to achieve in such systems high temperature ferromagnetic ordering will be demonstrated.

7.4.1 Low Dimensional Molecular-based Magnets

Molecule-based or polymeric magnetic materials are of great interest from a magnetic point of view even if the spatial extension of molecules induces low spin density, typically a few percent of that of metal-based magnets. The assembling of molecular species in a controllable fashion offers the opportunity to prospect new extended systems with predictable properties [109].

Ferromagnetic coupling is significantly less prevalent in nature than the antiferromagnetic one – unpaired electrons in orthogonal orbitals, residing in the same spatial region, are required – so that research on fully ferromagnetic compounds remains challenging [110]. The occurrence of a net moment necessitates significant interactions between neighboring molecules (0D) in all three directions of the solid. This is a major hurdle for compounds whose cohesion arises from weak intermolecular interactions, such as van der Waals or hydrogen bonds. As a result, many studies have been devoted to units of higher dimensionality (1D or 2D) characterized by a ferro- or ferrimagnetic exchange coupling, with the aim of constructing, through a self assembling of the exchange-coupled units, a 3D hopefully ferro- or ferrimagnetic network. This strategy has led to significant increase of the ordering temperatures, but the real mechanism of the long-range order is not always well established. A net moment may also be observed when interchain or interlayer interactions compete with non-collinear single ion anisotropies, giving rise to a canted antiferromagnetic structure. Of course, in that case, the net magnetic moment will be of reduced magnitude, as compared to that of the ferromagnetic chains or layers.

Another approach, albeit counterintuitive, is to minimize the antiferromagnetic interchain or interlayer exchange to the point of being negligible, leading to the coupling being dominated by the weaker – but potentially ferromagnetic – dipole–

dipole interactions. As will be seen, by incorporating large exchange in one or two directions, sizeable T_C values can be achieved despite the weakness of the dipole–dipole interactions between chains or layers.

Note that as early as 1970, thorough investigations of the TMMC-based linear compounds (TMMC = $(\text{CH}_3)_4\text{NMnCl}_3$) have pointed out a 3D antiferromagnetic order near 1 K, likely due to the dipole interactions between radical chains [111]. Similarly, the long-range ordering around 8 K in $\text{Mn}^{\text{II}}(\text{hfac})_2\text{NITR}$ (hfac = hexafluoroacetylacetonate; NITR = 2-R-4,4,5,5-tetramethylimidazoline-1-oxyl-3-oxide, R = ethyl, isopropyl, *n*-propyl), consisting of spin-5/2 manganese(II) ions alternating with spin-1/2 radicals, was ascribed to the same mechanism [112]. The authors have calculated the interchain dipolar interaction from the point dipole approximation, by neglecting thermal effects which induce a reduction of the magnetic moment. Considering the crude nature of the model, a quite good agreement between theoretical and experimental T_C values was obtained for spins orientated perpendicular to the chain axis.

7.4.1.1 Mn-porphyrin-based 1D Systems

An important class of 1D molecular compounds is the family of charge-transfer complexes based on metalloporphyrin and TCNE (TCNE = tetracyanoethylene) reported by Miller et al. [113, 114]. It is exemplified by $[\text{MnTPP}]^+[\text{TCNE}]^- \cdot 2\text{PhMe}$ (TPP = tetraphenylporphyrin) which has a chain structure, with Mn(III)-porphyrin cations (donors, D) bonded to $[\text{TCNE}]^-$ anions (acceptors, A), according to $\dots\text{D}^+\text{A}^-\text{D}^+\text{A}^-\dots$. The $S = 2$ Mn(III) is in axially distorted octahedral environment, with $S = 1/2$ $[\text{TCNE}]^-$ being located on each side, around 2.30 Å apart (Fig. 11). Because of the covalent bonding between the two spin-carrying units ($S_{\text{Mn}} = 2$ and $S_{\text{rad}} = 1/2$) along the chain axis, this class of compounds magnetically order with $T_C \leq 28$ K. Hence, $[\text{MnTPP}]^+[\text{TCNE}]^- \cdot$ is a prototype for studying 1D magnetism and related phenomena.

The magnetic properties are well dominated, over a wide temperature range, by the antiferromagnetic coupling between Mn(III) and $[\text{TCNE}]^-$ radical giving 1D ferrimagnetism, but low temperature investigations show intriguing behavior. Unlike the behavior expected for isolated chains, which only order at absolute zero, a metamagnetic ground-state and a transition towards a long range ferromagnetic state, with a net magnetic moment, are observed below a critical temperature $T_C = 13$ K [113].

Because of the relative ease of modifying the porphyrin structure, series of substituted tetraporphyrin TCNE electron transfer salts have been investigated to analyze the structure–property relationship and the mechanism of the magnetic ordering. Several papers have appeared reporting how T_C and the magnetic properties change when using:

- other cyanocarbon acceptors connecting the Mn(III) ions [115, 116];
- bulky substituents at the periphery of the porphyrin cation keeping the chains apart [117].

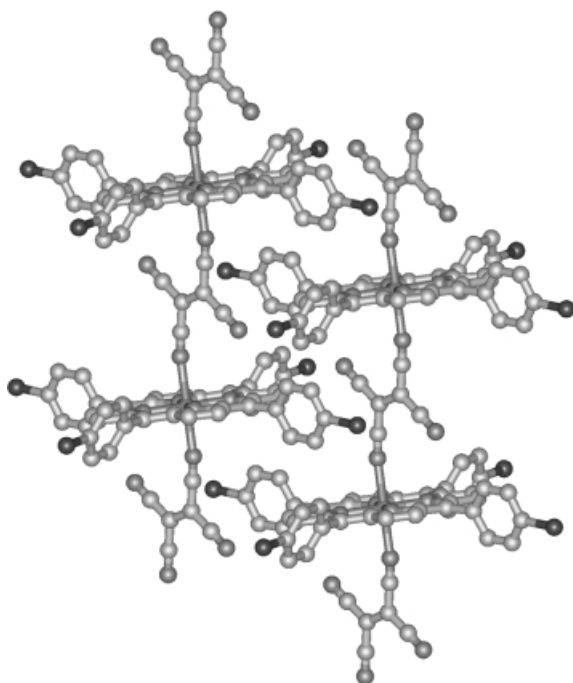


Fig. 11. Schematic structure of the charge transfer complex $[\text{MnTPP}][\text{TCNE}].2\text{PhMe}$ where TPP = tetraphenylporphyrin, TCNE = tetracyanoethylene. The Mn–Mn distance along the chain (repeat unit) is 10.12 \AA , while the distances between parallel chains along the two other crystallographic directions are 11.01 and 12.50 \AA . These distances increase up to 31.2 \AA when long chains $\text{R} = \text{OC}_n\text{H}_{2n+1}$ are grafted at the periphery of the porphyrin disk.

At high temperatures, all these compounds exhibit 1D ferrimagnetism with $\chi T(T)$ well described by a classical-quantum spin model [118]. The temperature at which the characteristic minimum of $\chi T(T)$ occurs -80 K to more than 300 K – indicates unambiguously that the in-chain interaction is strong, typically -115 K for the non-substituted compound up to -225 K for the fluorine derivative [119]. Upon cooling down, the magnetic susceptibility, and also $\chi T(T)$, shows a steep raise which in fact deviates from the isolated chain prediction, then a sudden drop pointing to a phase transition towards a 3D state. The observed T_C (or T_N) values are closely related to small changes in the $[\text{MnTPP}]^+$ species and the nature of crystallization solvent. For example, in $[\text{MnTPP}][\text{TCNE}](\text{solvent})$, the interchain interactions are ferromagnetic with T_C ranging from 13 to 8.5 K for toluene, o-xylene and o-dichlorobenzene solvents, while for $[\text{MnOEP}][\text{C}_4(\text{CN})_6]$ (OEP = octaethylporphyrinato) the interchain coupling is antiferromagnetic with $T_N = 22 \text{ K}$ [115].

Using a different strategy, Haase and coworkers have attempted to minimize the interchain exchange interactions by linking long alkoxy chains $\text{R} = \text{OC}_n\text{H}_{2n+1}$, with $n = 10-14$, to the phenyl groups of porphyrins (Fig. 11). Although the distance between magnetic chains is increased up to 31.2 \AA , the ordering temperature is not significantly affected, T_C varying from 21.7 K for $n = 10$ to 20.5 K for $n = 14$ [120]. The AC susceptibility data, characterized by an out-of-phase signal at T_C , and the large coercive fields observed at lower temperature – up to 3600 Oe at 5 K – confirm the stabilization of a ferromagnetic state (Fig. 12).

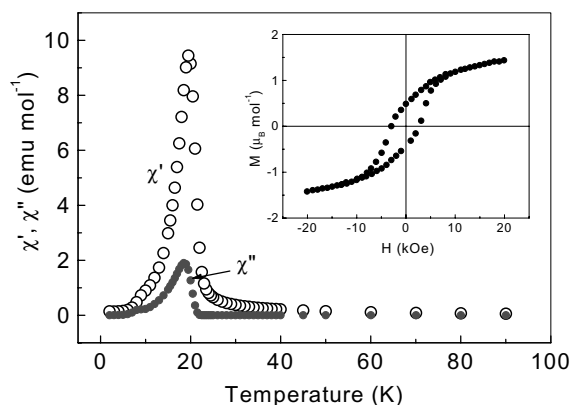


Fig. 12. Temperature-dependence of the AC susceptibility of the [MnTPP][TCNE]-based complex with OC₁₄H₂₉ substituted in the p position on each phenyl group to favor large separation between magnetic chains. The observed out-of-phase signal, and the large coercive field observed at 5 K demonstrate the ferromagnetic 3D character of the transition.

Remarkable results on the magnetic properties of Mn-porphyrin-based complexes were further reported by Wynnet al. [121–123]. Assuming that the quantum “through bond” exchange between neighboring chains is negligible – this is supported by distances larger than 9 Å – the authors proposed a mechanism of “through-space” dipolar interaction together with single ion anisotropy as being responsible for bulk magnetism at low temperature. The interchain dipolar interaction is estimated from the point dipole model with spins in registry between neighboring chains. The interaction strength is typically a few mK for the most favorable cases. Due to the presence of two interchain separations, the authors deduced that the interaction is ferromagnetic in one direction (along the shortest interchain distance) and antiferromagnetic in the second direction. Hence, in the absence of local anisotropy, the resulting system would be antiferromagnetic. In order to explain the existence of a net magnetic moment in the system they invoked a canting of the spins due to the presence of Mn(III) single ion anisotropy resulting in a *canted antiferromagnet* (or *weak ferromagnet*) [24]. The ordering temperatures have been calculated from estimated values of the dipolar interaction and the relationship developed for anisotropic exchange interaction [124]:

$$k_B T_C = 4S(S + 1)[J_{\text{intra}} J_{\text{inter}}]^{1/2} \quad (10)$$

where S is the net spin of a repeat unit ($S = 3/2$), J_{intra} the in-chain exchange interaction and J_{inter} the dipolar interaction along the transversal directions. The resulting T_C values (~ 8 K) compare favorably with those observed experimentally. This model clearly emphasizes that bulk magnetic ordering with substantial T_C values can be achieved in chain systems, resulting from dipole–dipole interactions.

It should be noted that:

- The presence of single ion anisotropy is not needed to obtain a net magnetic moment in such systems. As shown in Section 7.3.2, there exists a range of angles of the chain lattice (i. e. of the ratio between the short and long distance between chains) for which the ground state is ferromagnetic (at least multi-domain).

This implies that a large net moment may also be obtained, although the on-site anisotropy can lead to a *canted ferromagnet*.

- The J_{inter} value has been calculated for individual spins, neglecting collective effects arising from the intra-chain correlation on the magnitude of the inter-chain dipolar coupling. A mean field-type argument for estimating the 3D ordering temperature for weakly coupled systems provides insight into the interchain or interlayer interactions. According to Villain and Loveluck [125], long-range ordering is achieved when the thermal energy is comparable to the interaction energy between correlated spin blocks of size η namely:

$$k_{\text{B}}T_{\text{C}} = z|j|S(S+1)\eta(T_{\text{C}}) \quad (11)$$

As will be seen in Section 7.4.2, this mechanism reinforces the influence of the dipolar effects and can explain the high T_{C} values observed in low dimensional systems with very large separations between magnetic species.

7.4.1.2 Hydroxide-based 2D Systems

The metal hydroxides made of regular 2D arrays of metal ions coordinated by hydroxyl groups are considered as good prototypes of layered magnetic systems. The parent compounds $\text{M}_2(\text{OH})_3\text{A}$ ($\text{M} = \text{Co}, \text{Cu}$), involving the coordinating species $\text{A} = \text{NO}_3^-$ or OAc^- , exhibit a similar structure with the $\text{M}_2(\text{OH})_3$ layers separated by A^- anions and held together through hydrogen bonds [126]. The in-plane metal-metal separations remain close to that of hydroxides ($\sim 3.15 \text{ \AA}$), whereas the substitution of OH^- by larger anions induces a significant increase of the interlayer spacing (from 4.6 \AA for the hydroxide up to 9.3 \AA for the acetate). Ferromagnetic in-plane interactions dominate the high temperature behavior, while in turn 3D antiferromagnetism is stabilized at low temperature, due to small interlayer exchange involving hydrogen bonds [127].

Significant progress in the understanding of the low temperature properties has been achieved by studying the series of n -alkyl carboxylates $\text{Cu}_2(\text{OH})_3(\text{C}_m\text{H}_{2m+1}\text{COO})$ ($m = 1$ to 12) [128–130]. The distance between layers is mediated by the length of the n -alkyl chains, according to the relation $d(\text{\AA}) = d_0 + 2.54m \cos(\theta)$ available for double organic layers (Fig. 13). The tilt angle of the chains θ with respect to the normal to the layers is 22° , while the interlayer spacing increases from 28.8 to 40.7 \AA , for $m = 7$ to 12 , respectively.

The magnetic behavior of $\text{Cu}(\text{II})$ n -alkyl carboxylate compounds, illustrated in Fig. 14 for $n = 10$, is representative of the long-chain compounds. The AC and DC ($H = 10 \text{ Oe}$) susceptibilities increase strongly on decreasing temperature, and reaches a sharp maximum and a plateau, respectively, limited by demagnetizing effects, near $T_{\text{C}} = 20.5 \text{ K}$ where ferromagnetic order sets in. The occurrence of a long range magnetic state is confirmed by an out-of-phase (χ'') signal, and at lower temperature a hysteretic effect ($H_{\text{c}} = 1500 \text{ Oe}$ at 2 K). Both the magnitude of the net magnetization and its variation in high fields point towards a ferrimagnetic or a

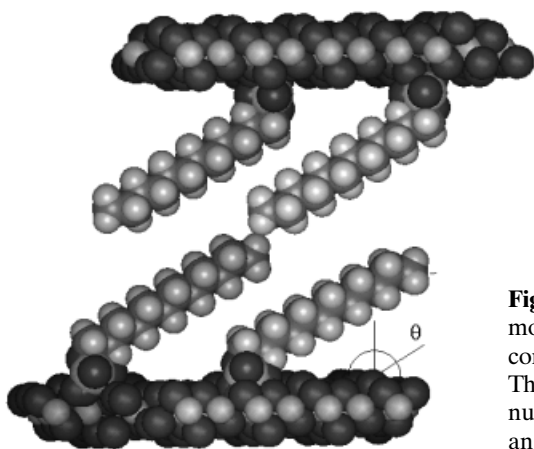


Fig. 13. Packing of the metal hydroxide monolayers and organic chains in the hybrid compounds $\text{Cu}_2(\text{OH})_3(\text{C}_m\text{H}_{2m+1}\text{COO})$. The interlayer spacing is mediated by the number of carbon atoms (m) and the tilt angle of the chains.

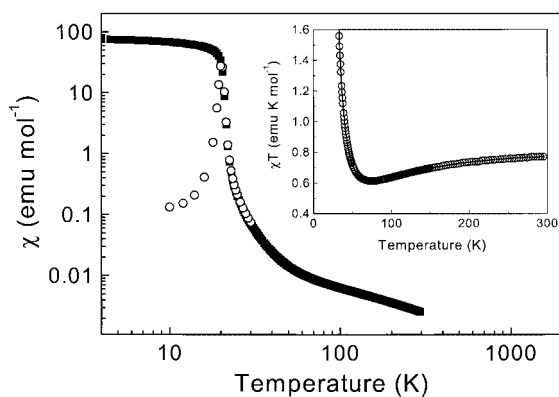


Fig. 14. Temperature dependence of the AC (open circles) and DC (squares) susceptibilities for the layered organic-inorganic compound $\text{Cu}_2(\text{OH})_3(\text{C}_{10}\text{H}_{21}\text{COO})$. The broad minimum of $\chi T(T)$ observed in the inset is the signature of a ferrimagnetic or non-collinear spin configuration within copper(II) layers. The full line represents the best fit from the sum of two Arrhenius-like contributions (see text).

non-collinear spin configuration. Such systems show similarities with the copper(II) weak ferromagnets, $\text{CuCl}_4(\text{C}_m\text{H}_{2m+1}\text{NH}_3)_2$ ($m = 1$ to 16) [131].

Another characteristic feature is the presence of a broad minimum in the temperature dependence of $\chi T(T)$, well above T_C (inset in Fig. 14). This thermal behavior is very well approximated by a double exponential law $C_1 \exp(\alpha J/k_B T) + C_2 \exp(\beta J/k_B T)$ [132]. The driving interaction, responsible of the initial high temperature decay of χT is antiferromagnetic ($\alpha J/k_B = -40.47$ K). It is attributed to the dominant in-plane interaction. Conversely, the low temperature behavior of χT is dominated by the second term ($\beta J/k_B = 126.8$ K) that is appropriate for a 2D Heisenberg ferromagnet [133]. Note that, in the above expression, the sum

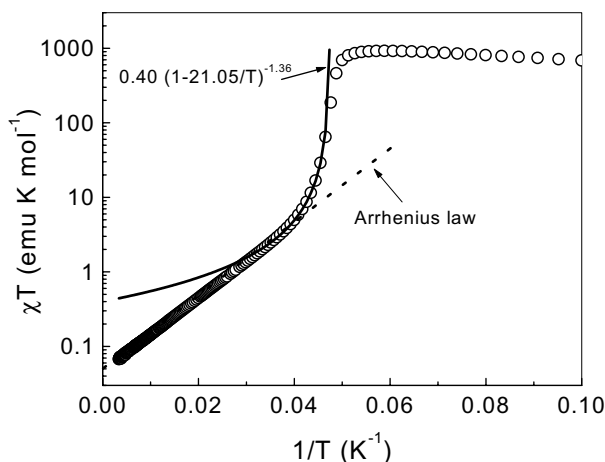


Fig. 15. Variation of $(\chi T)_F$ vs $1/T$ for $\text{Cu}_2(\text{OH})_3(\text{C}_{10}\text{H}_{21}\text{COO})$ showing the departure from the high temperature Arrhenius law (2D regime) below 30 K. The low temperature behavior is well fitted by the power law $\chi T = 0.40(1 - 21.05/T)^{-1.36}$ indicating a transition to a 3D state.

$C_1 + C_2 = 0.807$ is the high temperature Curie constant for two Cu(II) ions ($S = 1/2$) per formula. The same conclusion can be drawn for the other members of the copper(II) series with large m values.

In order to know more about the nature of the phase transition, these systems have been studied in the framework of a “generalized scaling” theory [132]. A spectacular crossover of the ferromagnetic component to the susceptibility from a 2D to a 3D regime is evidenced by the Arrhenius plot $\log(\chi T)$ vs $1/T$ (Fig. 15). At high temperature, the exponential variation characteristic of a 2D Heisenberg system is evidenced by a straight line down to $T \approx 30$ K, then upon further reduction of the temperature a sudden departure from linearity occurs and the system obeys the power law $\chi T = 0.40(1 - 21.05/T)^{-1.36}$ characteristic of a 3D regime with $T_C = 21.05$ K.

Finally, these layered compounds are noteworthy at least from two points of view:

- as model systems for elucidating the key role of organic spacers on the magnetic properties; the through-bond interlayer interactions being negligible for $d > 10$ Å, a model of dipolar interactions must be considered; and
- for the development of what is called multi-property materials, namely systems in which at least two basic properties coexist, and possibly interact [134].

7.4.2 3D Ordering Due to Dipolar Interaction – A Model

The kind of dipolar ordering that may occur in widely spaced layered or chain compounds is formally understood along the lines discussed in Sections 7.3.1 (planes) and 7.3.2 (wires). However, the formal calculation of the ordering temperature is

still in its infancy. As compared to the cases treated in Section 7.3, an additional difficulty arises, namely, the chains or planes, are not fully magnetized, i. e. they are not even superparamagnetic. They are composed of correlated spin blocks (SB) whose correlation length is temperature dependent. Following the above mentioned work of Villain and Loveluck [125] long range 3D ordering can be expected when the thermal energy is comparable to the dipolar energy between these spin blocks. To our knowledge the problem has only been treated within a modified version of the mean field approximation independently by Gradmann and coworkers [103] for 2D arrays of nanostripes (Section 7.3.3) and Drillon and Panissod [135] for layered hybrid organic–inorganic compounds. More recently the ordering of chain compounds has also been understood within the same approach [136]. The case of layered compounds is examined herein as an example of the approach.

Consider a 2D square lattice of spins $S = 1/2$ coupled by an isotropic ferromagnetic exchange interaction. At absolute zero the magnetic layer exhibits a fully ferromagnetic alignment of the spins but upon increasing temperature, the spins become only correlated at a finite distance ξ . For such a 2D Heisenberg ferromagnet, ξ is related to the exchange constant J and the spin value S by the relationship [133]:

$$\xi^2 = (JS/k_B T) \exp(4\pi JS^2/k_B T) \quad (12)$$

Despite the fact that the dipole interaction between individual spins lying in different layers is very small, the dipole interaction between correlated spins of size ξ^2 becomes sizeable as the temperature decreases and that it leads to 3D order when the in-plane correlation length reaches a threshold value.

To model its spin block structure each plane is considered at a non-zero temperature as a checkerboard made of square blocks containing ξ^2 parallel – correlated – spins S . The net moment of each spin block is $\xi^2 g S \mu_B = \xi^2 \mu$ and is assumed oriented anti-parallel to its neighbors thus prefiguring a multidomain structure in the 3D ordered state. It must be emphasized that the finite size of these domains is essential since the dipole–dipole interaction between uniformly magnetized infinite planes is virtually zero. Accordingly, the expected transition is not towards a uniform ferromagnet but a multidomain one (unless the size of the sample grains is small).

The average dipolar field acting on a spin block and arising from adjacent layers (AL) is then calculated as follows:

$$B_{\text{dip}} = \{\mu_0/4\pi\} \langle \mu \rangle_T (1/\xi^2) \sum_{i \in \text{SB}} \sum_{j \in \text{AL}} [3 \cos^2(\theta_{ij}) - 1]/r_{ij}^3 \quad (13)$$

which takes into account the spin fluctuations through the thermal average of the moment, $\langle \mu \rangle_T$ and the spatial extension of the spin block through the first sum over its ξ^2 individual spins. In the frame of the mean field approximation, this dipolar field acts on the moment $\xi^2 \mu$ of the spin block as a whole and the linearized Eq. (5) is:

$$\langle \mu \rangle_T / \mu = \xi^2 \mu B_{\text{dip}} / 3k_B T \quad (14)$$

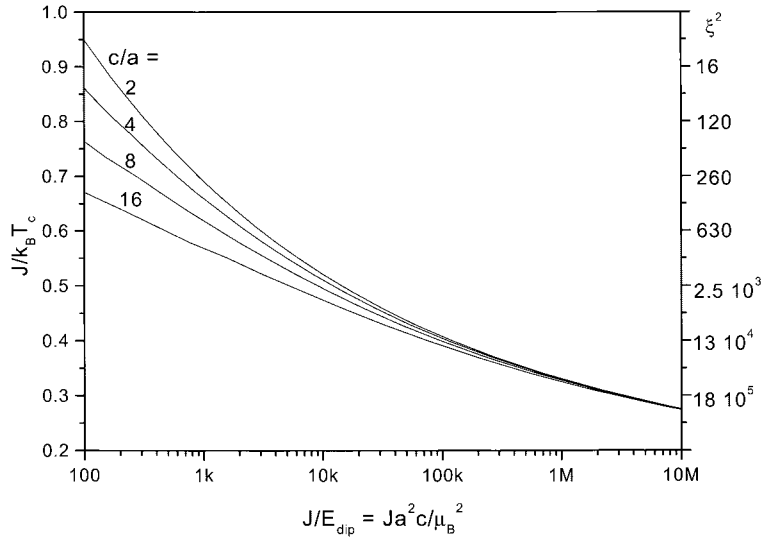


Fig. 16. Mean field calculation of the 3D ordering temperature for a *tetragonal lattice of spins* 1/2 where the intralayer exchange coupling is ferromagnetic and the interlayer coupling is purely dipolar. The ordering temperature depends mostly on the intralayer exchange strength J and only logarithmically on the dipolar energy μ^2/a^2c . The reason is the exponential divergence at $T = 0$ of the in-plane coherence length $\xi \approx \exp(J/k_B T)$ which makes the effective interacting moments to diverge also exponentially [135]. A similar behavior is expected for 3D chain compounds in the presence of magnetic anisotropy (Ising-like spins). For Heisenberg spin chains the power law divergence of the coherence length results in much lower ordering temperatures (typically 0.1 J) [136].

Equations (13) and (14) are solved self-consistent for a layered tetragonal system, using the thermal evolution of ξ given by Eq. (12). This yields the $J/k_B T_C$ plot as a function of the intra-plane exchange constant J and the lattice parameters a and c (Fig. 16).

Hence:

- For reasonable values of the exchange interaction and lattice constants, the ratio $J/E_{\text{dip}} = Ja^2c/\mu_B^2$ lies in the range 10^3 – 10^6 , and the critical temperature ranges from $0.7 J/k_B$ to $0.3 J/k_B$. The model predicts 3D ordering temperatures close to the intra-layer exchange energy even though the base interlayer dipolar energy is orders of magnitude lower. Such a behavior is very similar to that found for 2D systems with a weak interlayer exchange coupling j , the transition temperature of which is given by $k_B T_C/J = 4/\ln(J/j)$ [137].
- It may be argued that the mean field approximation overestimates quite generally the ordering temperature by a factor up to 2. However, the proposed model differs substantially from the standard mean field approximation in that the thermal variation of the interaction energy $\xi^2 \mu B_{\text{dip}}$ is largely dominated by the exponentially diverging size of the effective interacting moments $\xi^2(T)\mu$ and depends only

marginally on the thermal variation of $\langle\mu\rangle_T$. Therefore, the critical temperature is mostly determined by the intralayer exchange constant through the rate of divergence of ξ , while it varies only as the logarithm of the other parameters – the lattice constants, the moment of the ions. Therefore the way B_{dip} is actually estimated should not affect much the estimated value of T_C and one can assume that better approximations would yield very similar results.

- The calculation has been performed for a preferred orientation of the moments perpendicular to the layers, which corresponds to the lowest dipolar energy and favors a ferromagnetic order. In case of an in-plane preferred orientation, due to single ion anisotropy, the ordered state is antiferromagnetic, B_{dip} is coarsely divided by 2 but the T_C is reduced by less than 10%.
- For Ising-like spins, the reduction of the degrees of freedom increases the calculated T_C only by about 10%, whereas it would be multiplied by 3 in the standard mean field approach.

The model has been used with success to explain the magnetic ordering of *n*-alkyl copper(II) *layered compounds* with an interlayer spacing ranging from 28.8 to 40.7 Å and T_C values in the range 20 ± 1 K, respectively. The number of correlated spins at T_C is of the order of $\xi^2 \approx 10^4$. The weak dependence of T_C upon the interlayer spacing observed in these compounds is well explained by the weak influence of the moment density. However, this weak dependence could also be considered as an evidence for 2D ordering expected to occur for Ising-like systems [138]. Actually, the analysis of the critical behavior of the magnetic susceptibility suggests, as seen above, that the magnetic ordering is three-dimensional [132].

There is no such ambiguity in *chain compounds* since 1D ordering cannot be stabilized, except at absolute zero. Recently the same model, adapted for chains, has been used to explain the ferromagnetic ordering observed in Mn-porphyrin-based magnets exhibiting ferrimagnetic chains well separated in space (up to 31.2 Å apart) and arranged on a triangular lattice [136]. The case of chains system calls for two remarks, though:

- As shown above (Section 7.3.2) the dipolar interaction favors uniform ferromagnetic ordering only for chains of limited length. Therefore, when the coherence length diverges within the chains, the dipolar coupling becomes antiferromagnetic (or multidomain ferromagnetic).
- The divergence of the coherence length in 1D systems obeys an exponential law only if some anisotropy is present. For 1D Heisenberg systems, the coherence length is rather described by the power law $|J|S(S+1)/k_B T$ [138].

Hence, the calculation of the ordering temperature has been performed for both ferromagnetic and antiferromagnetic inter-chain configurations and for both Heisenberg and Ising exchange coupling within the chains. In all cases the ordering occurs when the coherence length reaches $\xi \approx 10^4$ repeat units. Owing to the number of correlated spins at T_C , it results that the interaction between strongly correlated spin blocks is essential to promote 3D ordering. The calculated T_C is five times larger in the Ising model than in the Heisenberg model because of the much slower divergence of ξ in the latter case. In fact, the calculated T_C agrees with the

experiment only for Ising-like spins, which is not surprising for Mn(III) ions because of the Jahn–Teller effect and which is also in agreement with the rather large coercive field observed on the magnetization loops [136].

As to the type of magnetic order below T_C the experiments point towards a ferromagnetic ground state whereas energy minimization at T_C suggests that the ordered state is antiferromagnetic, because the length of the spin blocks is about 2000 times the interchain spacing (Section 7.3.2). This discrepancy can be explained either because the system remains in a metastable ferromagnetic state favored by the single ion anisotropy or because the system is actually in a multidomain ferromagnetic state (weak demagnetizing energy). It was shown in the same study that a multidomain ferromagnetic spin configuration is even more stable than the antiferromagnetic configuration.

Despite its crudeness, the proposed model shows that:

- 3D dipolar induced ordering can take place between chains or layers at temperatures that depend essentially upon the in-chain or in-plane exchange interaction; and
- a long range ferromagnetic order below a quite high T_C can be stabilized.

It follows from these studies of chain or layered systems that the 3D magnetic ordering is basically driven by the divergence of the correlation length (in 1D or 2D) as the temperature is lowered. From the same argument, it can be inferred that an in plane long-range order, as for quasi 2D Ising systems, will automatically entail a 3D ordering as soon as *the inter-plane interaction j cannot be neglected*; the critical temperature for the 3D order will always be slightly larger than the critical temperature for 2D ordering ($j = 0$). More refined theories or simulations are needed, though, to confirm these findings.

7.5 Conclusion

Although the dipolar interaction is usually ignored as exchange-coupling usually dominates, it is shown in this review that it may have a key role in the nature of the magnetic ordering in low dimensional systems, in particular for the design of high T_C molecular-based ferromagnets. This includes magnetic molecular materials made of chains or layers, where the through space interactions are usually neglected, and dense arrays of nanosized objects such as metal-based dots, wires or layers which are in the forefront in the development of spin electronics, magnetic sensors and magnetic recording media.

Unlike the exchange coupling, the dipolar interaction has a long range effect, and an anisotropic character which in some cases makes difficult an accurate prediction of the bulk properties. In addition, its influence over very large distances is a limiting factor for investigating the fundamental aspects of individual magnetic objects where a weak interaction is usually sought for.

In regard to molecule-based magnets, the reported substantial T_C values may be ascribed to dipolar interactions, thus adding another paradigm in addition to the

overlap of magnetic orbitals, to design new molecule-based magnets. Unlike the metal-based materials, the exchange interaction within molecular clusters, chains or layers is relatively small so that the individual units are not fully magnetized at a non-zero temperature. Nonetheless, the divergence of the coherence length as the temperature decreases makes dipolar interactions much stronger than expected on an isolated spin basis, this is essential to explain the observed 3D ferromagnetic order in chain or layer systems. As a result, the T_C values depend weakly on the strength of the base (isolated spins) dipolar interaction, but essentially – and quasi linearly – on that of the exchange coupling within the low dimensional units. Hence significant progress can be made in the improvement of “molecule-based magnets” and the physics of related systems.

References

- [1] For example: *Ferromagnetic Materials*, Ed. E.P. Wohlfarth (North Holland Publishing Company, Amsterdam) 1998; *Introduction to Solid State Physics*, Ed. C. Kittel (John Wiley and Sons, New York) 1986, p. 423.
- [2] A. Aharony, in *Phase Transitions and Critical Phenomena*, Eds. C. Domb and M.S. Green (Academic, New York) **1976**, Vol. 6, p. 357.
- [3] Y. Yafet, J. Kwo and E.M. Gyorgy, *Phys. Rev. B* **1986**, 33, 6519.
- [4] P. Bruno *Phys. Rev. B* **1991**, 43, 6015.
- [5] C. Pich and F. Schwabl *Phys. Rev. B* **1993**, 47, 7957.
- [6] D. Pescia and V.L. Pokrovsky, *Phys. Rev. Lett.* **1990**, 65, 2599.
- [7] M. Seul and R. Wolfe, *Phys. Rev. Lett.* **1992**, 68, 2460.
- [8] A.P. Levanyuk, N. Garcia, D. Pescia, V.L. Pokrovsky, *Phys. Rev. Lett.* **1993**, 70, 1184.
- [9] M. Seul and D. Andelman, *Science* **1995**, 267, 476.
- [10] J. Arlett, J.P. Whitehead, A.B. MacIsaac, and K. De’Bell, *Phys. Rev. B* **1996**, 54, 3394.
- [11] See K. De’Bell, A.B. MacIsaac, J.P. Whitehead, *Rev. Mod. Phys.* **2000**, 72, 225.
- [12] J. Gay and R. Richter, *Phys. Rev. Lett.* **1986**, 56, 2728.
- [13] A. Abanov, V. Kalatsky, V. L. Pokrovsky, and W. M. Saslow, *Phys. Rev. B* **1995**, 51, 1023.
- [14] J. A.C. Bland, C. Daboo, G.A. Gehring, B. Kaplan, A.J.R. Ives, R.J. Hicken, and A.D. Johnson, *J. Phys. Cond. Mat.* **1995**, 7, 6467.
- [15] A.B. MacIsaac, J.P. Whitehead, K. De’Bell and P.H. Poole, *Phys. Rev. Lett.* **1996**, 77, 739.
- [16] L. Onsager, *J. Am. Chem. Soc.* **1936**, 58, 1486.
- [17] J.H. Van Vleck, *J. Chem. Phys.* **1937**, 5, 320.
- [18] H.E. Stanley, *Introduction to Phase Transitions and Critical Phenomena* (Oxford University Press, London) **1971**.
- [19] D.C. Mattis, *The Theory of Magnetism II* (Springer-Verlag, Berlin) **1985**.
- [20] J.J. Binney, N.J. Dowrick, A.J. Fisher, and M.E.J. Newman, *The Theory of Critical Phenomena* (Oxford Science Publications, London) **1993**.
- [21] C. Kittel, *Phys. Rev.* **1951**, 82, 965.
- [22] J.A. Sauer, *Phys. Rev.* **1940**, 57, 142.
- [23] G.J. Ehnholm, T.E. Katila, O.V. Lounasmaa, P. Reivari, G.M. Kalvius, O.K. Shenoy, *Z. Physik* **1970**, 235, 289.

- [24] R.L. Carlin, *Magnetochemistry* (Springer-Verlag, New York) **1986**.
- [25] J.M. Luttinger, L. Tisza, *Phys. Rev.* **1946**, *70*, 954; *Phys. Rev.* **1947**, *72*, 257.
- [26] J. Villain, *J. Phys. Chem. Solids* **1959**, *11*, 303.
- [27] M. Goldman, M. Chapellier, Vu Hoang Chau, and A. Abragam, *Phys.Rev.B* **1974**, *10*, 226.
- [28] M. Goldman, *Phys. Rep.* **1977**, 32G, 1.
- [29] A. Abragam and M. Goldman, *Nuclear Magnetism: Order and Disorder* (Clarendon, Oxford) **1982**.
- [30] J. Felsteiner, S.K. Misra, *Phys. Rev. B* **1973**, *8*, 253.
- [31] S.K. Misra, *Phys. Rev. B* **1973**, *8*, 2026.
- [32] M.H. Cohen and F. Keffer, *Phys. Rev.* **1955**, *99*, 1135.
- [33] T. Niemeyer, *Physica* **1972**, *57*, 281.
- [34] T. Niemeyer and H.W.J. Bibte, *Physica* **1973**, *67*, 125.
- [35] T. Niemeyer and P.H.E. Meijer, *Phys. Rev. B* **1974**, *10*, 2962.
- [36] M.R. Roser, L.R. Corruccini, *Phys. Rev. Lett.* **1990**, *65*, 1064.
- [37] J.P. Bouchaud and P.G. Zérah, *Phys. Rev. B* **1993**, *47*; 9095.
- [38] G.N. Patey, D. Levesque, and S.S. Weiss, *Mol. Phys.* **1982**, *45*, 733.
- [39] S.W. de Leeuw, S.W. Perram, and E.R. Smith, *Proc. R. Soc. Lond. A* **1980**, *373*, 27.
- [40] R.F. Ziolo, E.P. Giannelis, B.A. Weinstein, M.P. O'Horo, B.N. Ganguly, V. Mehrotra, M.N. Russel, and D.R. Hoffman, *Science* **1992**, *257*, 219.
- [41] B.E. Vugmeister, M.D. Glinchuk, *Rev. Mod. Phys.* **1990**, *62* 993.
- [42] H. Zhang, M. Widom, *J. Magn. Magn. Mater.* **1993**, *122* 119.
- [43] See *Magnetic Properties of Fine Particles*, Eds. J.L. Dormann and D. Fiorani (North-Holland, Amsterdam) **1992**.
- [44] J.L. Dormann, D. Fiorani, and E. Tronc, *Adv. Chem. Phys.* **1997**, *98*, 283.
- [45] E.C. Stoner and E.P. Wohlfarth, *Phil. Trans. R. Soc. London, Ser. A* **1948**, *240*, 599.
- [46] D.A. Dimitrov and G.M. Wysin, *Phys. Rev. B* **1996**, *54*, 9237.
- [47] J. Garcia-Otero, A.J. Garcia-Bastida, and J. Rivas, *J. Magn. Magn. Mater.* **1998**, *189*, 377.
- [48] G. Christou, D. Gatteschi, D. N. Hendrickson, R. Sessoli, *MRS Bulletin* **2000**, *25*, 66.
- [49] M. A. Novak, R. Sessoli, A. Caneschi, D. Gatteschi, *J. Magn. Magn. Mater.* **1995**, *146*, 211.
- [50] A. L. Barra, P. Debrunner, D. Gatteschi, C. E. Schulz, R. Sessoli, *Europhys. Lett.* **1996**, *35*, 133.
- [51] L. Thomas, F. Lioni, R. Ballou, D. Gatteschi, R. Sessoli, B. Barbara, *Nature* **1996**, *383*, 145.
- [52] J.L. Dormann, D. Fiorani and E. Tronc, *J. Magn. Magn. Mater.* **1999**, *202*, 251.
- [53] C.L. Chien, *J. Appl. Phys.* **1991**, *69*, 5267.
- [54] F.J. Lopez, R. Lazaro, J.L. Von Helmlolt, J.Garcia-Palacios, J. Wecker, H. Cerva, *J. Magn. Magn. Mater.* **1998**, *187*, 221.
- [55] J.L. Dormann, R. Cherkaoui, L. Spinu, M. Nogués, F. Lucari, F. D'Orazio, D. Fiorani, A. Garcia, E. Tronc, and J.P. Jolivet, *J. Magn. Magn. Mater.* **1998**, *187*, L139.
- [56] J.L. Dormann, L.Bessais, and D.Fiorani, *J. Phys. C* **1988**, *21*, 2015.
- [57] R.W. Chantrell, M. El-Hilo, and K.O'Grady, *IEEE Trans. Magn.* **1991**, *27*, 3570.
- [58] W. Luo, S.R. Nagel, T.F. Rosenbaum, and R.E. Rosensweig, *Phys. Rev. Lett.* **1991**, *67*, 2721.
- [59] M. El-Hilo, K.O'Grady, and R.W. Chantrell, *J. Magn. Magn. Mater.* **1992**, *114*, 295.
- [60] K.O'Grady, M El-Hilo, and R.W. Chantrell, *IEEE Trans. Magn.* **1993**, *29*, 2608.
- [61] S. Mørup and E. Tronc, *Phys. Rev. Lett.* **1994**, *72*, 3278.
- [62] P. Allia, M. Knobel, P. Tiberto, and F. Vinai, *Phys. Rev. B* **1995**, *52*, 15398.

- [63] S. Mørup, F. Bodker, P.V. Hendriksen, and S. Linderoth, *Phys. Rev. B* **1995**, **G2**, 287.
- [64] J.L. Dormann, F. D’Orazio, F. Lucari, E. Tronc, P. Prené, J.P. Jolivet, D. Fiorani, R. Cherkaoui, and M. Nogués, *Phys. Rev. B* **1996**, *53*, 14291.
- [65] R.W. Chantrell, in *Magnetic Hysteresis in Novel Magnetic Materials*, Vol. 338 of *NATO Advanced Study Institute, Series E: Applied Sciences*, Ed. G. C. Hadjipanayis (Kluwer, Dordrecht) **1997**, p. 21.
- [66] M. El-Hilo, R.W. Chantrell, and K.O’Grady, *J. Appl. Phys.* **1998**, *84*, 5114.
- [67] D. Kechrakos and K.N. Trohidou, *Phys. Rev. B* **1998**, *58*, 12169.
- [68] M. Knobel, E.F. Ferrari, and F.C.S. da Silva, *Mater. Sci. Forum* **1999**, *169–178*, 302.
- [69] R. Iglesias, H. Rubio, and S. Suárez, *Appl. Phys. Lett.* **1998**, *73*, 2503.
- [70] D. Altbir, P. Vargas, J. d’Albuquerque J.D.E. Castro, U. Raff, *Phys. Rev. B* **1998**, *57* 13604; *J. Phys. Cond. Mat.* **1997**, *9*, 9931.
- [71] P. Vargas, J. d’Albuquerque J.D.E. Castro, D. Altbir, *Phys. Rev. B* **1999**, *60*, 6541.
- [72] H. Zhang and M. Widom, *Phys. Rev. B* **1995**, *51*, 8951.
- [73] P.I. Belobrov, R.S. Gekhtch, V.A. Ignatchenko, *Sov. Phys. JETP* **1983**, *57*, 636.
- [74] N.D. Mermin and H. Wagner, *Phys. Rev. Lett.* **1966**, *17*, 1133.
- [75] S. Romano, *Nuovo Cimento* **1987**, *9D*, 409.
- [76] G.O. Zimmerman, A.K. Ibrahim, F.Y. Wu, *Phys. Rev. B* **1988**, *37*, 2059.
- [77] K. Ibrahim, G.O. Zimmerman, *Phys. Rev. B* **1987**, *35*, 1860.
- [78] S. Prakash and C.L. Henley, *Phys. Rev. B* **1990**, *42*, 6574.
- [79] J. Villain, *J. Phys. C* **1977**, *10*, 1717; *J. Phys. C* **1977**, *10*, 4793.
- [80] V.I. Lebedev, Zh. Vychisl. Mat. Mat. Fiz. **1975**, *15*, 48; *Zh. Vychisl. Mat. Mat. Fiz.* **1976**, *16*, 293.
- [81] J. Villain, R. Bidaux, J-P. Carton and R. Conte, *J. Phys. (Paris)* **1980**, *41*, 1263.
- [82] K. De’Bell, A. B. MacIsaac. I. N. Booth and J. P. Whitehead, *Phys. Rev. B* **1997**, *55*, 15108.
- [83] E. Rastelli, A. Carbognani, S. Regina and A. Tassi, *Eur. Phys. J. B* **1999**, *9*, 641.
- [84] T. Chattopadhyay, P.J. Brown, B.C. Sales, L.A. Boatner, H.A. Mook, and H. Maletta, *Phys. Rev.* **1989**, *40*, 2624.
- [85] P. Furrer, P. Allenspach, J. Mesot, U. Staub, H. Blank, H. Mutka. C. Vettier, E. Kaldis, J. Karpinski, S. Rusiecki, and A. Mirmelstein, *Eur. J. Solid State Inorg. Chem.* **1991**, *28*, 627.
- [86] S K. Misra, J. Felsteiner, *Phys. Rev. B* **1992**, *46*, 11033.
- [87] A.B. MacIsaac, J.P. Whitehead, K. De’Bell and K. S. Narayanan, *Phys. Rev. B* **1992**, *46*, 6387.
- [88] U.M. Malozovsky. V.M. Rosenbaum, *Zh. Exp. Teor. Fiz.* **1990**, *98*, 265.
- [89] V.M. Rosenbaum. V.M. Ogenko. A.A. Chuiko, *Uspekhi Fiz. Nauk* **1991**, *161*, 79.
- [90] V.M. Rosenbaum, *Zh. Exp. Teor. Fiz.* **1991**, *99*, 1836; and *Zh. Exp. Teor. Fiz.* **1997**, *11*, 669.
- [91] A.A. Fraerman, M.V. Sapozhnikov, *J. Magn. Magn. Mater.* **1999**, *192*, 200.
- [92] J. Russier, *J. App. Phys.* **2001**, *89*, 1287.
- [93] B.D. Schrag, A. Anguelouch, G. Xiao, P. Trouilloud, Y. Lu, J. Gallagher, S.S.P. Parkin, *J. App. Phys.* **2000**, *87*, 4682.
- [94] B.D. Schrag, A. Anguelouch, S. Ingvarsson, Gang Xiao, Yu Lu, P. Trouilloud, A. Gupta, R.A. Wagner, J. Gallagher, P. M. Rice, S.S.P. Parkin, *App. Phys. Lett.* **2000**, *77*, 2373.
- [95] S. Demokritov, E. Tsymbal, P. Grünberg, W. Zinn, I.K. Schuller, *Phys. Rev. B* **1994**, *49*, 720.
- [96] L. Thomas, M. G. Samant, S. S. P. Parkin, *Phys. Rev. Lett.* **2000**, *84*, 1816.

- [97] V. Raposo, J.M. Garcia, J.M. González, M. Vázquez, *J. Magn. Magn. Mater.* **2000**, 222, 227.
- [98] Y. Henry, K. Ounadjela, L. Piraux, S. Dubois, J.M. George and J.L. Duvail, *Eur. Phys. J. B* **2001**, 20, 35.
- [99] L.C. Sampaio, E.H.C.P. Sinnecker, G.R.C. Cernicchiaro, M. Knobel, M. Vázquez and J. Velázquez, *Phys. Rev. B* **2000**, 61, 8976.
- [100] T. Jung, R. Schlittler, J.K. Gimzewski, F. Himpsel, *J. Appl. Phys.* **1995**, 61, 467.
- [101] J. Shen, R. Skomski, M. Klaua, H. Jenniches, S.S. Manoharan, J. Kirschner, *J. Appl. Phys.* **1997**, 81, 3901.
- [102] J. Hauschild, U. Gradmann, H.J. Elmers, *App. Phys. Lett.* **1998**, 72, 3211.
- [103] J. Hauschild, H.J. Elmers, U. Gradmann, *Phys. Rev. B* **1998**, 57, R677.
- [104] O. Pietzsch, A. Kubetzka, M. Bode, and R. Wiesendanger, *Phys. Rev. Lett.* **2000**, 84, 5212.
- [105] E.V. Albano, K. Binder, D.W. Heermann, W. Paul, *Z. Phys. B* **1989**, 77, 445.
- [106] T. Aign, P. Meyer, S. Lemerle, J. P. Jamet, J. Ferré, V. Mathet, C. Chappert, J. Gierak, C. Vieu, F. Rousseaux, H. Launois, and H. Bernas, *Phys. Rev. Lett.* **1998**, 81, 5656.
- [107] M.R. Scheinfein, K.E. Schmidt, K.R. Heim, and G.G. Hembree, *Phys. Rev. Lett.* **1996**, 76, 1541.
- [108] A. Sugarawa and M.R. Scheinfein, *J. App. Phys.* **1993**, 73, 4516.
- [109] J.S. Miller and M. Drillon (Eds) *Magnetism – From Molecules to Materials, Volume 2*, Wiley-VCH, Weinheim, **2001**.
- [110] J.S. Miller and A.J. Epstein, *Angew. Chem.* **1994**, 33, 385.
- [111] R. Dingle, M.E. Lines, S.L. Holt, *Phys. Rev.* **1969**, 187, 643.
- [112] A. Caneschi, D. Gatteschi, J.P. Renard, P. Rey, R. Sessoli, *Inorg. Chem.* **1989**, 28, 2940; A. Caneschi, D. Gatteschi, P. Rey, R. Sessoli, *Inorg. Chem.* **1991**, 30, 3936.
- [113] J.S. Miller, J.C. Calabrese, R.S. McLean, A.J. Epstein, *Adv. Mater.* **1992**, 4, 490.
- [114] J.S. Miller and A.J. Epstein, *J. Chem. Soc., Chem. Comm.* **1998**, 1319.
- [115] A.J. Epstein, C.M. Wynn, M.A. Girtu, W.B. Brinckerhoff, K.I. Sugiura and J.S. Miller, *Mol. Cryst. Liq. Cryst.* **1997**, 305, 321.
- [116] M. Kelemen, Ch. Wachter, H. Winter, E. Dormann, R. Gompper and D. Hermann, *Mol. Phys.* **1997**, 90, 407.
- [117] K. Griesar, M. Athanassopoulou, E. Soto Bustamante, Z. Tomkowicz, A. Zaleski and W. Haase, *Adv. Mater.* **1997**, 9, 45; M. Balanda, K. Falk, K. Griesar, Z. Tomkowicz and W. Haase, *J. Magn. Magn. Mater.* **1999**, 205, 14.
- [118] J. Seiden, *J. Phys. (Paris) Lett.* **1983**, 44, 947.
- [119] D.K. Rittenberg and J.S. Miller, *Inorg. Chem.* **1999**, 38, 4838.
- [120] K. Falk, R. Werner, Z. Tomkowicz, M. Balanda and W. Haase, *J. Magn. Magn. Mater.* **1999**, 196–197, 564.
- [121] C.M. Wynn, M.A. Girtu, J.S. Miller and A.J. Epstein, *Phys. Rev. B* **1997**, 56, 315; M.A. Girtu, C.M. Wynn, K.I. Sugiura, J.S. Miller, A.J. Epstein, *J. Appl. Phys.* **1997**, 81, 1.
- [122] C.M. Wynn, M.A. Girtu, K.I. Sugiura, E.J. Brandon, J.L. Manson, J.S. Miller and A.J. Epstein, *Synth. Metals* **1997**, 85, 1695.
- [123] C.M. Wynn, M.A. Girtu, W.B. Brinckerhoff, K.I. Sugiura, J.S. Miller and A.J. Epstein, *Chem. Mat.* **1997**, 9, 2156.
- [124] P.M. Richards, *Phys. Rev. B* **1974**, 10, 4687.
- [125] J. Villain and J.M. Loveluck, *J. Phys. Lett. (Paris)* **1977**, 38, 77.
- [126] S. Yamanaka, T. Sako, K. Seki and M. Hattori, *Sol. State Ionics* **1992**, 53, 527.
- [127] P. Rabu, S. Angelov, P. Legoll, M. Belaiiche and M. Drillon, *Inorg. Chem.* **1993**, 32, 2463.

- [128] P. Rabu, S. Rouba, V. Laget, C. Hornick and M. Drillon, *J. Chem. Soc., Chem. Comm.* **1996**, 1107.
- [129] W. Fujita and K. Awaga, *Inorg. Chem.* **1996**, 35, 1915.
- [130] V. Laget, C. Hornick, P. Rabu, M. Drillon and R. Ziessel, *Coord. Chem. Rev.* **1998**, 178, 1533.
- [131] L.J. de Jongh and A.R. Miedema, *Adv. Phys.* **1974**, 23, 1.
- [132] M. Drillon, P. Panissod, P. Rabu, J. Souletie, V. Ksenofontov and P. Gütlich, *Phys. Rev. B* **2002**, 65.
- [133] F. Suzuki, N. Shibata and C. Ishii, *J. Phys. Soc. Jpn.* **1994**, 63, 1539.
- [134] P. Rabu, M. Drillon, K. Awaga, W. Fujita and T. Sekine, in: J.S. Miller and M. Drillon (Eds.) *Magnetism – From Molecules to Materials, Volume 2*, Wiley-VCH, Weinheim, **2001**, p 357.
- [135] M. Drillon and P. Panissod, *J. Magn. Magn. Mat.* **1998**, 188, 93.
- [136] S. Ostrovsky, W. Haase, M. Drillon and P. Panissod, *Phys. Rev. B* **2001**, 64, 134418.
- [137] V.I. Pokrovsky, G.V. Uimin, in: L. J. de Jongh (Ed.) *Magnetic Properties of Layered Transition Metal Compounds*, Kluwer Academic Publishers, Dordrecht, **1990**, p 53.
- [138] L. Onsager, *Phys. Rev.* **1944**, 65, 117.
- [139] M. Steiner, J. Villain and C.G. Windsor, *Adv. Phys.* **1976**, 25, 87.

8 Spin Transition Phenomena

Philipp Gütlich, Yann Garcia, and Hartmut Spiering

Dedicated to Professor Karl Heinrich Lieser on occasion of his 80th birthday.

8.1 Introduction

The phenomenon of thermal spin transition (spin crossover) was first reported in the literature some seventy years ago. Around 1930, Cambi and his coworkers examined the magnetic properties of a series of iron(III) dithiocarbamate complexes and found that some of them showed a dramatic change of the magnetic moment, from a value corresponding to five unpaired electrons near room temperature to one corresponding to only one unpaired electron on lowering the temperature [1]. It took then more than thirty years until, in the early sixties, the first iron(II) coordination compound, viz. *cis*-[Fe(phen)₂(NCS)₂] (phen = 1,10-phenanthroline) became known also to exhibit temperature dependent spin transition (ST) between high spin (HS) and low spin (LS) states near 175 K [2]. Many more examples of iron(II) spin crossover (SC) compounds have been communicated soon after [3–22], and other coordination compounds of 3d transition elements such as cobalt(II) [23–28], and to a lesser extent cobalt (III) [29], chromium (II) [30, 31], manganese (II) [32–34], manganese (III) [35–37], and nickel [38–40] were found to show similar thermal ST phenomena. As is known from basic ligand field theory [41], complexes of 3d⁴ up to 3d⁷ electron configuration in the approximation of O_h symmetry are capable of undergoing thermal spin transition. Such complexes may adopt HS ground states with weak field ligands (such as halogens, water, ammonia, etc.) or LS ground states with strong field ligands (such as CN⁻, phen, etc.); for critical ligand field strengths comparable to the spin pairing energy the spin state becomes temperature dependent as a result of the Boltzmann distribution over all populated spin states. Thermal ST is not expected for compounds of 4d and 5d transition elements, as the ligand field strength increases markedly in comparison with analogous 3d compounds and is generally much larger than the spin pairing energy; thus practically all 4d and 5d transition metal complexes show LS behavior.

Looking back over four decades of SC research we notice that by far most of the work was done with compounds of iron(II) [3–22] and to a lesser extent with iron(III) and cobalt(II). The reason is mainly that with the development of ⁵⁷Fe Mössbauer spectroscopy a powerful technique has become available for the characterization of the valence states [42], particularly for iron(II) compounds, where the rates of spin state transitions are generally slower and thus relaxation times longer than the Mössbauer time scale (~10⁻⁷ s) such that the characteristic “fingerprint” signals referring to the different spin states appear well resolved in the spectrum. This is not the case in many iron(III) SC systems, where shorter spin state relaxation

times fall into the Mössbauer “time window” and therefore broaden considerably the resonance lines and make the analysis more difficult and less conclusive.

Research activities in the area of iron(II) SC systems have enormously increased in recent years, stimulated by both the eagerness to explore more deeply the microscopic spin state switching processes and the hope of eventually applying such materials in technical devices. The present review article is supposed to serve two purposes, casting light on (i) cornerstones of the past and (ii) on new trends of SC research in the forefront of present activities. We shall commence with a section on physical characterization, where the specific information content of standard methods as well as of new techniques employed in studies of iron(II) ST phenomena will be briefly reviewed.

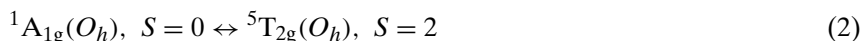
8.2 Physical Characterization

8.2.1 Occurrence of Thermal Spin Transition

A transition metal compound exhibiting thermally induced ST necessarily undergoes a drastic change in electronic configuration, favoring the HS states with increasing and the LS state with decreasing temperature. For iron(II) complexes with six 3d electrons in the valence shell of the metal center, thermal ST is denoted, in the “strong field approach” of ligand field theory [41, 43], as



where t_{2g} and e_g refer to the two subsets of d-orbitals split by a ligand field of O_h symmetry. Within the “weak field approach” of ligand field theory, preferentially used to interpret optical spectra, LS \leftrightarrow HS transition in iron(II) complexes is denoted as:



where ${}^1A_{1g}$ and ${}^5T_{2g}$ refer to the Mulliken ligand field terms under O_h symmetry, and S to the total spin quantum number. It should be mentioned that the spin triplet states ($S = 1$) are thermally not accessible, which is clearly seen in the Tanabe–Sugano diagram for d^6 complexes (Fig. 1).

On thermodynamic grounds, thermal spin transition LS \leftrightarrow HS in a $3d^6$ complex is expected, if the energy difference between the lowest vibronic levels of the 1A_1 state, and that of the 5T_2 manifold are comparable to thermal energy: ΔE_{HL}^0 , cf. Fig. 2.

It is noteworthy in this context that in the SC literature one often finds the statement that thermal ST occurs if the difference between the ligand field strength and the mean spin pairing energy is on the order of thermal energy. At a critical value of $(10Dq)_{crit}$ the Tanabe–Sugano diagram shows the crossover of the 1A_1 and 5T_2

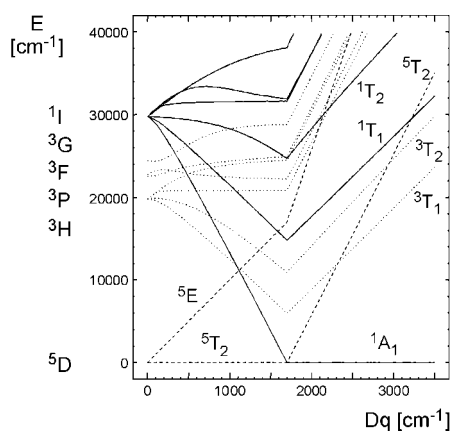


Fig. 1. Tanabe–Sugano diagram for an octahedral d^6 complex, calculated [17] with the Racah parameters [43] of the free iron(II) according to Tanabe and Sugano [48].

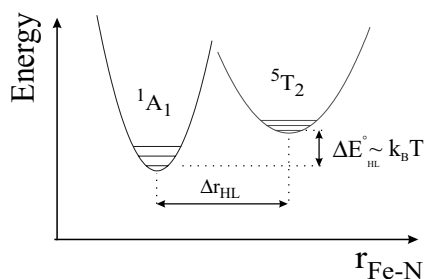


Fig. 2. Schematic representation of the potential wells for the 1A_1 and the 5T_2 states of an iron(II) SC complex. The condition for a thermal ST is $\Delta E_{HL}^0 \approx k_B T$. The nuclear coordinate $r(\text{Fe-N})$ refers to the Fe–ligand bond distance.

state. This value, which corresponds to a certain metal–ligand distance r_{crit} , however, is never met in a molecule. Instead, the bonding effects lead to a much higher (by $\sim 0.2 \text{ \AA}$) metal–ligand bond length in the HS state than in the LS state and correspondingly lower $10Dq$ of ca. 12000 cm^{-1} in the HS state and ca. 20000 cm^{-1} in the LS state [41]. The bond length r_{crit} at which the adiabatic oscillator potentials of the HS and LS state cross provides no direct information on the energy separation of the minima of the two potentials. This energy separation has to be compared with kT in order to observe thermal spin crossover. Therefore the ligand field picture is not adequate to describe the requirements for spin crossover. Thus $(10Dq)_{\text{crit}}$ is a fictitious quantity of a non-existent compound. We can only say that $(10Dq)_{\text{LS}} > (10Dq)_{\text{crit}} > (10Dq)_{\text{HS}}$, where $(10Dq)_{\text{crit}}$ changes with r^{-6} [43]. A deeper account of such ligand field considerations can be found elsewhere [17].

Thermal SC occurs in liquid solution as well as in the solid state. In liquids there are practically no interactions between the spin state changing molecules. As a result, a plot of the molar fraction of the HS molecules as a function of temperature, $\gamma_{\text{HS}}(T)$, which can be recorded for example by magnetic or optical measurements (see Sections 8.2.2, 8.2.3), can be described by a Boltzmann population of the molecular states. Considering only the electronic degeneracies, i. e. 15 for the $^5T_{2g}$ HS state and 1 for the $^1A_{1g}$ state, this would result in a “saturation” molar fraction γ_{HS} of

15/16 = 94% in the high temperature limit. In fact, in many SC compounds the ST is practically complete, which is expected from a distribution over the vibronic manifolds. Clearly, thermal ST is a molecular process and needs no cooperative interactions. The driving force is the considerable entropy gain of ca. 50 to 80 J mol⁻¹ K⁻¹ on going from the LS to the HS state [44]. The total entropy change contains a spin part, $\Delta S_{\text{spin}} = R[\ln(2S + 1)_{\text{HS}} - \ln(2S + 1)_{\text{LS}}]$, which is ca. 13 J mol⁻¹ K⁻¹ on going from the LS ($S = 0$) to the HS ($S = 2$) state; this part contributes only 15 to 25% to the total entropy gain. The main portion stems from the intramolecular vibrations because of the much higher densities in the HS than in the LS state. The enthalpy change of ST from the LS to the HS state in iron(II) compounds is typically 6 to 15 kJ mol⁻¹ [14]. The difference in Gibbs free energy $\Delta G = \Delta H - T\Delta S$ becomes zero at the temperature $T_{1/2}$, where HS and LS molecules are present to 50% each.

In the solid state, there is coupling of elastic origin between the spin state changing molecules resulting into more or less strong cooperative interactions. Such interactions are responsible for the appearance of different shapes of transition curves $\gamma_{\text{HS}}(T)$ as depicted in Fig. 3. They may be as gradual as in the liquid state, where cooperative interactions hardly play a role. They may be very abrupt, or exhibit hysteresis or steps, and finally they may be incomplete in both high and low temperature regions. More or less gradual transition curves are classified as “continuous” and those exhibiting hysteresis as “discontinuous” spin transitions. The examination of the shape of these curves is of the utmost importance in a SC study as they can bear information on the existence of cooperative effects, the occurrence of hysteresis being the prerequisite for bistability and thus for eventual application of the material in display or switching devices. Thermal ST in iron(II) compounds is always accompanied by changes of magnetic, optical, and structural properties. In the following we shall describe briefly how these changes can be followed using a variety of standard methods and special techniques.

8.2.2 Magnetic Susceptibility Measurements

Measuring the magnetic susceptibility of a sample as a function of temperature, $\chi(T)$, has always been the main characterization method from the very beginning of SC research up to now. The transition from the strongly paramagnetic HS state with four unpaired electrons in case of iron(II) to the (nearly) diamagnetic LS state with no unpaired electron is readily reflected in a dramatic change of the measured magnetic susceptibility. $\chi(T)$ is then determined by the temperature-dependent fractional contributions of the susceptibilities of the molecules in different spin states:

$$\chi(T) = \gamma_{\text{HS}}(T) \cdot \chi_{\text{HS}} + (1 - \gamma_{\text{HS}}(T)) \cdot \chi_{\text{LS}} \quad (3)$$

where γ_{HS} is the molar fraction of HS molecules as plotted in Fig. 3 as function of temperature. χ_{HS} and χ_{LS} refer to the magnetic susceptibilities of the sample in the pure HS and LS states (at sufficiently high and low temperatures of a complete spin state transition), respectively. Only if these quantities are known, a ST curve

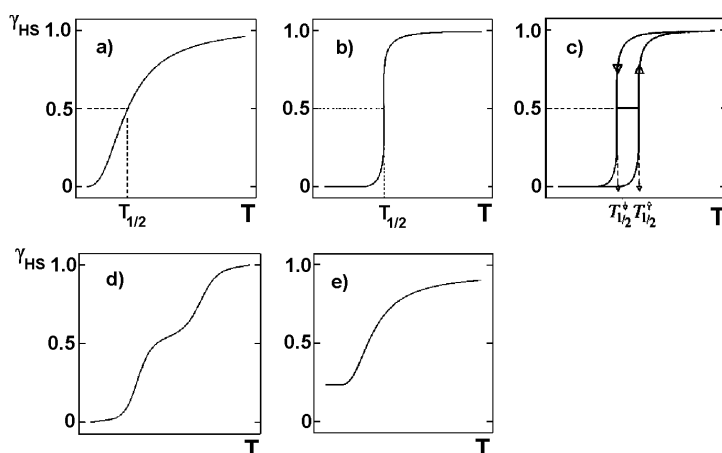


Fig. 3. Schematic representation of the ST types: (a) gradual, (b) steep or abrupt, (c) with hysteresis, (d) with steps, (e) incomplete. $\gamma_{\text{HS}}(T)$ represents the fraction of complex molecules in the HS state ($\gamma_{\text{HS}}(T_{1/2}) = 0.5$) [17].

$\gamma_{\text{HS}}(T)$ can be readily obtained. Otherwise the ST behavior can be followed quantitatively by plotting the product χT as function of temperature, which deviates more or less drastically from Curie law behavior in the ST region and may also unravel special features like those exemplified in Fig. 3. Alternatively, one can also derive the effective magnetic moment $\mu_{\text{eff}} = 2.83\sqrt{\chi T}$ [45] and plot it as a function of temperature. The expected spin-only moment $\mu_{\text{s.o.}} = \sqrt{4S(S+1)}$ of the pure HS state with $S = 2$ should level off at 4.9 B.M., while that of the LS state with $S = 0$ should be close to 0 B.M. The measured μ_{eff} values are often higher than the expected ones at both ends of the ST due to orbital contributions and zero-field splitting [45]. Because of these complications it has become more preferable to study the ST behavior by plotting the $\gamma_{\text{HS}}(T)$ function rather than the magnetic moment $\mu_{\text{eff}}(T)$.

In practice, a variety of methods are being used to measure $\chi(T)$ data: Faraday balance, Foner vibrating sample magnetometer, AC and SQUID devices in solid state studies, and Evans' NMR method for solution studies. Techniques for studying magnetic properties are described in [46]. The possibility of measuring $\chi(T)$ data down to 2 K under applied hydrostatic pressure up to 15 kbar has recently been installed in a Foner magnetometer [47]; results from such measurements will be alluded in Section 8.4.2.4.

8.2.3 Optical Spectroscopy

Thermal ST is always accompanied by a color change (thermochromism), e. g. iron(II) complexes generally change from weakly colored in the HS state to more deeply colored in the LS state. For example, tetrazole and triazole complexes of

iron(II) are nearly white in the HS state and purple in the LS state. Therefore, the optical spectrum in the UV/visible region differs drastically for the two spin states and proves to be well suited to follow the ST qualitatively and quantitatively, provided the absorption bands of interest are sufficiently resolved and not hidden under more intense “spin crossover inactive” bands.

If a suitable single crystal of a SC complex is available, it is highly desirable to run the optical spectra as a function of temperature in the UV/visible range between 300 and 1000 nm, where one usually observes the spin-allowed but parity-forbidden d–d transitions (*ligand-field bands*), if they are not hidden by metal-to-ligand charge transfer bands, which are spin- and parity-allowed and therefore much more intense (by ca. 3 orders of magnitude) than the d–d bands. From the Tanabe–Sugano diagram [48] for an octahedral d⁶ complex (in the approximation of O_h symmetry) as shown in Fig. 1 one sees that the lowest ligand field term 1A_1 arising from the 1I Russell–Saunders term of the free ion crosses the 5T_2 term, which arises from the 5D Russell–Saunders term, at $Dq \approx 1700 \text{ cm}^{-1}$. In the region left of this crossover point, the 5T_2 term is the ground state, only one spin-allowed transition, namely $^5T_2 \rightarrow ^5E$, can be expected here. To the right of the crossover point, 1A_1 is the ground state term; two spin-allowed transitions, *viz.* $^1A_1 \rightarrow ^1T_1$ and $^1A_1 \rightarrow ^1T_2$, are predicted to appear in the UV/visible region at considerably higher energies (wave numbers) than that of the HS absorption band. From the temperature dependent area fractions of a well resolved absorption band one can easily construct the ST curve. Examples will be given below. One can also perform reflectivity measurements to follow the ST optically [49, 50] knowing that this technique provides only qualitative results.

8.2.4 Vibrational Spectroscopy

In all SC complexes of $3d^4$ up to $3d^7$ transition metal ions, there is a depletion of charge in the antibonding e_g orbitals and simultaneous increase of charge in the slightly bonding t_{2g} orbitals on going from the HS state to the LS state. As a consequence, a strengthening of the metal-donor atom bonds occur, and this should be observable in the vibrational spectrum in the region between ~ 250 and $\sim 500 \text{ cm}^{-1}$, where the metal-donor atom stretching frequencies of transition metal compounds usually appear [51]. This energy change has been reinvestigated by new measurements in this region and as a result, a new assignment could be proposed [52]. In a series of temperature dependent far infrared or Raman spectra, one can readily recognize the vibrational bands belonging to the HS and the LS species as those decreasing and increasing in intensity, respectively, on lowering the temperature. Of course, one can also derive the spin state conversion curve $\gamma_{\text{HS}}(T)$ by plotting the normalized area fractions of characteristic HS or LS bands. Many examples have been reported in the literature [53–56].

Vibrational spectroscopy has not only been employed to probe the metal donor atom stretching frequencies during spin transition. Certain ligand vibrations have also been found to be susceptible to change of spin state at the metal center. Typical examples are the N-coordinated ligands NCS^- and NCSe^- , which are widely

used in the synthesis of iron(II) SC complexes to complete the FeN_6 core like in the “classical” system $[\text{Fe}(\text{phen})_2(\text{NCS})_2]$. The C–N stretching bands of NCS^- and NCSe^- are found in the HS state as a strong doublet near $2060\text{--}2070\text{ cm}^{-1}$. On cooling below the transition temperature (176 K), the intensity of this doublet decreases in favor of a new doublet appearing at $2100\text{--}2110\text{ cm}^{-1}$, which evidently arises from the LS state [51]. This observation was interpreted as being due to increased metal-to-ligand $d_\pi\text{--}p_\pi$ back donation during HS \rightarrow LS transition, which however seems to be more pronounced for the Fe–N(phen) bonds than for the Fe–N(NCS) bonds, because the bond lengths were found by X-ray diffraction on $[\text{Fe}(\text{bipy})_2(\text{NCS})_2]$ (bipy = 2,2'-bipyridyl) to shorten by ca. 0.15 \AA in Fe–N (bipy), but only by ca. 0.08 \AA in Fe–N(NCS) [57]. Electron delocalization from the antibonding C–N bond occurs to make up for the t_{2g} electron deficiency at the LS iron center caused by the enhanced metal \rightarrow ligand back donation in the Fe–N(phen) bond; this explains the shift of the C–N stretching vibrations by ca. 40 cm^{-1} to higher energy in the LS state. Such a strategy was recently applied to monitor the hysteresis loop of $[\text{Fe}(\text{btr})_2(\text{NCS})_2]\cdot\text{H}_2\text{O}$ (btr = 4,4'-bis-1,2,4-triazole) [58].

Often the lattice constituents (cationic complexes, non-coordinated anions and crystal solvent molecules) are all interconnected through hydrogen bonds, van der Waals or other interactions. It is therefore conceivable that characteristic anion or solvent molecule bands “feel” the spin state changes in the metal centers; they gradually disappear at the favor of new bands growing in at different energy positions. It has, for instance, been observed for $[\text{Fe}(\text{ptz})_6](\text{BF}_4)_2$ (ptz = 1-propyltetrazole) focusing on the B–F vibration of the tetrafluoroborate anion [54]. Also recently, the ST of $[\text{Fe}(\text{Htrz})_3](\text{NO}_3)_2$ (Htrz = 4-H-1,2,4-triazole) and $[\text{Fe}\{\text{HB}(\text{trz})_3\}]$ (HB(trz)₃ = hydrotris(1,2,4-triazolyl)borate) were detected following the variation of the torsional and stretching deformation vibrations of the triazole ligands [59, 60].

8.2.5 ^{57}Fe Mössbauer Spectroscopy

^{57}Fe Mössbauer spectroscopy is a particularly elegant and powerful tool in probing the valence states (oxidation and spin states) of iron compounds [42]. The isomer shift δ and the quadrupole splitting ΔE_Q , two of the most important parameters derived from a Mössbauer spectrum, differ significantly between iron(II)-HS and iron(II)-LS. The isomer shift δ is proportional to the s-electron density at the nucleus, $|\Phi_s(0)|^2$, and the difference $R_e^2 - R_g^2$ of the mean squared radius of the excited (e) and the ground (g) state of the Mössbauer nucleus:

$$\delta = \frac{2}{5}\pi Z e^2 \left(|\Phi_A(0)|^2 - |\Phi_S(0)|^2 \right) (R_e^2 - R_g^2) \quad (4)$$

where $|\Phi(0)|^2$ denotes the charge density which is predominantly of s-character in the absorber (A) and the source (S), respectively. In the case of iron(II), δ is more positive for the HS state ($\sim 1\text{ mm s}^{-1}$) than for the LS state ($0\text{--}0.3\text{ mm s}^{-1}$) for the following reason: due to the π -back donation of charge from the filled t_{2g} orbitals of iron(II) in the LS state into the ligand π^* -orbitals, the 3d electron density decreases.

As a consequence, the shielding effect of the d-electrons for s-electrons (mainly 3s) towards the nuclear charge decreases, which in turn increases the s-electron density $|\Phi_S(0)|^2$ at the nucleus. As the relative change of the nuclear volume on going from the excited to the ground state of ^{57}Fe , $R_c^2 - R_g^2$, is negative, the higher electron density at the nucleus causes a more negative shift of δ in the LS state compared to the HS state. π -back donation from the HS configuration is not as effective, hence the shielding effect of 3d electrons is greater and the s-electron density at the nucleus decreases, which in turn causes a more positive isomer shift. Similar arguments hold to explain the less positive isomer shift values ($\sim 0\text{--}0.5 \text{ mm s}^{-1}$) observed for HS iron(III) as compared to HS iron(II) compounds: the lower d-electron population in iron(III) causes less shielding and thus higher s-electron density at the nucleus and consequently more negative shift of δ . Similarly, an iron(III) LS state gives rise to a more negative δ value than iron(III) HS state because of enhanced $d_{\pi}\text{--}p_{\pi}$ back bonding effect yielding less shielding and therefore higher s-electron density $|\Phi(0)|^2$.

An additional extremely helpful Mössbauer parameter for the characterization of valence states is the *electric quadrupole splitting* ΔE_Q . Electric quadrupole interaction arises only if there is a nuclear quadrupole moment $eQ \neq 0$ and an electric field gradient (EFG) $q \neq 0$ [42c]. ^{57}Fe possesses a quadrupole moment in the first excited state ($I = 3/2$), but not in the ground state ($I = 1/2$). Therefore, in the presence of an EFG $q \neq 0$, the excited nuclear level splits into two sublevels, with quantum numbers $m_I = \pm 3/2$ and $m_I = \pm 1/2$ in axial symmetry. This is the origin of a quadrupole doublet in a ^{57}Fe Mössbauer spectrum. The EFG may have contributions from a non-cubic arrangement of the ligand molecules (“lattice contribution” to the EFG) and non-cubic distribution of the valence electrons (“valence electron contribution”). Iron(II) HS compounds usually have a large quadrupole splitting (near 3 mm s^{-1}) due to a large valence electron contribution to the EFG; this arises from a non-cubic distribution of the four 3d electrons over the t_{2g} orbitals which are split (e.g. into b_{2g} and e_g orbitals in a ligand field of D_{4h} symmetry) due to the Jahn–Teller distortion or non-cubic coordination of the ligands. The lattice contribution arising from such an axial distortion is usually smaller than the valence electron contribution (and often has opposite sign). The quadrupole splitting of iron(II)-LS compounds is generally considerably smaller than that of iron(II)-HS compounds, because the t_{2g} orbitals, whether split or unsplit, are fully occupied by the six 3d electrons; the partial contributions from each orbital add up to a vanishing valence electron contribution, and what remains, for example in iron compounds with ligands of different kinds or with bi- or multidentate ligand molecules, is a lattice contribution to the EFG.

These typical Mössbauer parameters effectively give a fingerprint to each spin state and enable one to distinguish between the spin states. When a thermally induced SC in an iron(II) compound occurs, the intensity of the HS quadrupole doublet decreases and that of the LS doublet increases as the temperature is lowered. As an example, selected ^{57}Fe Mössbauer spectra of $[\text{Fe}(\text{ptz})_6](\text{BF}_4)_2$ recorded as a function of temperature are shown in Fig. 4 [54]. The outer two resonance lines of each spectrum with decreasing intensity on lowering the temperature refer to the iron(II) HS doublet. The signal in the middle represents the poorly resolved

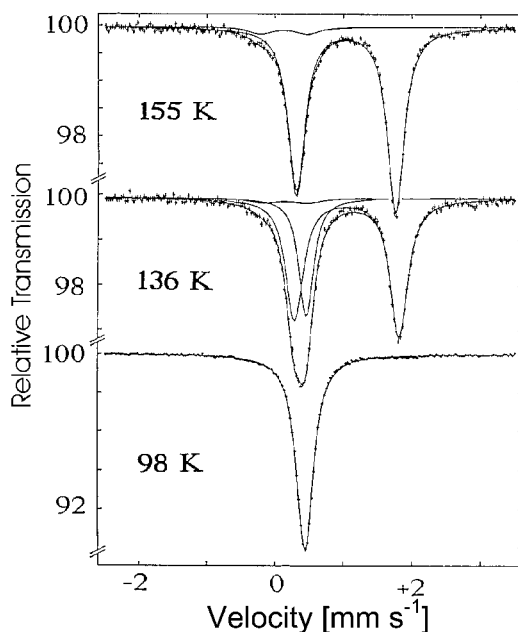


Fig. 4. Selected ^{57}Fe Mössbauer spectra of $[\text{Fe}(\text{ptz})_6](\text{BF}_4)_2$ as a function of temperature [54].

quadrupole doublet of the LS state, with increasing intensity on lowering the temperature. The quantitative determination of the ST curve from a series of Mössbauer spectra recorded over a certain temperature range is based on the evaluation of the area fractions t_{HS} and t_{LS} of the resonance lines. The area fractions are proportional to the products $f_{\text{HS}} \cdot \gamma_{\text{HS}}$ and $f_{\text{LS}} \cdot \gamma_{\text{LS}}$, respectively, where f_{HS} and f_{LS} refer to the so-called Lamb–Mössbauer factors (LMF) of the HS and the LS states, respectively. Only for $f_{\text{HS}} = f_{\text{LS}}$ can the area fractions of the HS and the LS resonance lines be taken directly as a measure of the fractions of complex molecules in the HS and the LS states, respectively:

$$\text{For } f_{\text{HS}} = f_{\text{LS}} \rightarrow t_{\text{HS}}/(t_{\text{HS}} + t_{\text{LS}}) = \gamma_{\text{HS}} \quad (5)$$

The approximation of $f_{\text{HS}} \approx f_{\text{LS}}$ generally holds for SC compounds with continuous spin transition. In case of discontinuous ST, f_{LS} may be larger than f_{HS} and underestimates $\gamma_{\text{HS}}(T)$, particularly towards lower temperatures [61]; corrections are then necessary.

8.2.6 Calorimetry

As with studies of phase transitions in general, calorimetric measurements (DSC or $C_p(T)$) on SC compounds deliver important thermodynamic quantities and information such as enthalpy and entropy changes accompanying a ST process, the transition temperature and the order of the transition. The ST can be considered as a phase

transition associated with a change of the Gibbs free energy $\Delta G = \Delta H - T\Delta S$. The enthalpy change $\Delta H = H_{\text{HS}} - H_{\text{LS}}$ is typically 10 to 20 kJ mol⁻¹, and the entropy change $\Delta S = S_{\text{HS}} - S_{\text{LS}}$ is of the order of 50 to 80 J mol⁻¹ K⁻¹ [14]. The thermally induced ST is an entropy-driven process; the degree of freedom is much higher in the HS state than in the LS state. Approximately 25% of the total entropy gain on going from LS to HS arises from the change in spin multiplicity:

$$\Delta S_{\text{mag}} = R \ln \frac{(2S + 1)_{\text{HS}}}{(2S + 1)_{\text{LS}}}$$

and the major part originates from changes in the intramolecular vibrations [44].

The first precise heat capacity measurements were performed by Sorai and Seki on [Fe(phen)₂(NCX)₂] with X = S, Se [44]. A few other SC compounds of Fe^{II} [62, 63], Fe^{III} [64] and Mn^{III} [35b] have been studied quantitatively down to very low (liquid helium) temperatures. For quick, and only qualitative, information on ΔH , ΔS , the transition temperature, and the occurrence of hysteresis, DSC measurements, although mostly accessible only down to liquid nitrogen temperatures, are useful and easy to perform [65].

8.2.7 Diffraction Methods

Thermal ST in solid transition metal compounds is always accompanied by more or less drastic positional changes in the crystal lattice. Continuous spin transitions always go along with changes in metal–ligand bond lengths and angles only (so-called *displacive* transitions), but do not undergo changes in space groups. Discontinuous spin transitions with hysteresis in the $\chi_{\text{HS}}(T)$ curves are generally accompanied by a change in space groups, that is show a first order crystallographic phase change with major lattice reorganization (so-called *reconstructive* transitions). A crystal structure determination at variable temperatures above and below the ST temperature is highly desirable when studying ST phenomena in solids. Even if a suitable single crystal is not available for a complete structure determination, recording the temperature-dependent X-ray powder diffraction data can be extremely helpful in characterizing the type of ST (continuous or discontinuous), and determining changes of the lattice parameters, which are needed for example to understand pressure effects on spin transition [9]; in favorable cases one may even derive the crystal structure from powder diffraction data using the Rietveld method [66].

Structural investigations have been carried out on many SC compounds mostly by X-ray diffraction [10, 14]. One important finding in all cases is that the metal–ligand bond length is longer in the HS state than in the LS state as is expected from the depletion of charge in the antibonding e_g orbitals and a simultaneous filling of the slightly bonding t_{2g} orbitals. In the case of iron(II) SC compounds this bond length change is particularly large and amounts to ca. 10% ($\Delta r_{\text{HL}} = r_{\text{HS}} - r_{\text{LS}} \approx 200\text{--}220$ pm), which may cause a 3–4% change in elementary cell volumes [14], as a consequence of moving two electrons from e_g* to t_{2g} orbitals. The bond length change in iron(III) SC compounds, also with $\Delta S = 2$ transitions, are less

dramatic with only $\Delta r_{\text{HL}} = 10\text{--}13$ pm, because of an electron hole remaining in t_{2g} orbitals in the LS state. Δr_{HL} is even less pronounced in cobalt(II) SC systems ($\Delta r_{\text{HL}} \leq 10$ pm), because only one electron is transferred from e_g^* to t_{2g} orbitals in the $\Delta S = 1$ transitions. The size of Δr_{HL} has important consequences for the build-up of cooperative interactions which in turn influence decisively the spin state relaxation kinetics (Section 8.3.8).

EXAFS (extended X-ray absorption fine structure) measurements have also been successfully applied to the determination of the metal–donor atom bond length changes in SC systems [67]. This method is increasingly applied in those cases where X-ray diffraction becomes difficult or impossible because of highly dispersed particles or amorphous polymeric materials (see next section).

Another aspect of structural investigations relates to the bonding properties of the SC molecules in the lattice. For example, single crystal X-ray diffraction can reveal the pathways of existing hydrogen bonding networks or specific π -stacking orderings. Such features, although not being a prerequisite for thermal ST to occur, take part or even assist in the cooperative interactions involved in the spin transition. This can be proven experimentally by studying the effect of deuteration or $^{14}\text{N}/^{15}\text{N}$ isotope exchange on the $\gamma_{\text{HS}}(T)$ conversion curves (Section 8.3.1).

8.2.8 X-ray Absorption Spectroscopy

X-ray absorption spectroscopy (XAS) can be divided into X-ray absorption near edge structure (XANES), which provides information essentially about geometry and oxidation states, and extended X-ray absorption fine structure (EXAFS) which provides information about metal site ligation [68, 69]. Although, XAS has not been widely applied to follow spin state transitions, this technique is nevertheless ideally suited, as it is sensitive to both the electronic and the local structure around the metal ion undergoing the SC phenomena. Metal K-edges X-ray absorption fine-structure spectroscopy (XAFS) has been used to study the structural and electronic changes occurring during SC in iron(II) complexes [70–73], iron(III) complexes [74, 75], cobalt(II) complexes [67, 76, 77] and iron haem model compounds [78, 79]. In addition, a few reports on the use of iron L-edge and cobalt L-edge XAFS are available (Section 8.4.2.1) [80, 81]. The direct analysis of the near-edge structure can afford the LS–HS composition ratios as a function of temperature and thus the ST curve $\gamma_{\text{HS}}(T)$. Not only XANES spectra can be used to follow the electronic modification occurring during SC, but also EXAFS can provide information about the contraction of the first coordination shell around the active SC center. It is also possible to obtain the HS and LS fractions as function of temperature [82].

The Debye–Waller factor σ plays an important role in EXAFS spectroscopy. It is divided in two components σ_{stat} and σ_{vib} due to static disorder and thermal vibrations, respectively. For a SC compound, σ is a measure of the vibrations of the Fe^{II} ions with respect to the six donor atoms of the ligands around the metal ion. It can also be used to monitor the ST curve as exemplified for $[\text{Fe}(\text{bpp})_2](\text{BF}_4)_2$ with $\text{bpp} = 2,6\text{-bis}(\text{pyrazol-3-yl})\text{pyridine}$ [72].

Several structures have been derived from EXAFS spectroscopy. This is the case for instance for the iron(II)-1,2,4-triazole polymeric chain compounds (see Section 8.4.1) [83–88]. Particular attention has been devoted to a peak situated at 7 Å in the Fourier transform, which has been assigned to a multiple scattering double metal–metal distance assuming an aligned polymeric structure [83]. This has been convincingly proved by the observation of this peak for a Cu^{II} analog for which the aligned crystal structure was known [85]. Later, this peak was observed at low temperature in the LS and in the HS state for a SC compound [87] whereas it always vanished at higher temperature [83]. Actually, a local Jahn–Teller distortion may be present together with an aligned metallic long chain, and the corresponding EXAFS multiple scattering signal which is observed at low temperature, can vanish just by an increase of its Debye–Waller factor [85, 87]. This does not confirm the recent results obtained by wide-angle X-ray scattering (WAXS) supporting a *zigzag* chain structure in the HS state for these materials [89].

EXAFS information is restricted to the first or second coordination sphere around a central atom whereas WAXS can afford information on short and medium range order up to 20 Å. It has been, for instance, applied to the polymeric chain ST material [Fe(Htrz)₂trz](BF₄) with trz = 1,2,4-triazolato, in the LS and HS state. It was found that the tetrafluoroborate anion may be bonded by hydrogen bonding to the hydrogen in 4- position of the triazole ring [89]. However, no interaction between the polymeric chains could be detected using this technique.

It is worthwhile mentioning that X-ray absorption spectroscopy has recently been used to examine the LIESST phenomenon for some iron(II) complexes [90, 91]

8.2.9 Positron-annihilation Spectroscopy

Positron annihilation spectroscopy (PAS) was first applied to investigate the iron(II) SC compound [Fe(phen)₂(NCS)₂] [92], soon after one found that the so-called Doppler broadened energy distribution of the 0.511 keV annihilation γ -peak and the lifetime of the *ortho*-positronium (*o*-Ps) atom changed upon adding ligand molecules of different field strength to an aqueous solution of iron and cobalt ions and thereby altering the spin state of the transition metal ion [93]. This technique was later successfully applied to study the SC behavior in single crystals of [Fe(ptz)₆](BF₄)₂ and zinc diluted mixed crystals thereof [94].

PAS is a nuclear technique, which usually uses ²²Na as a positron (β^+) source “sandwiched” between two samples (e. g. single crystals) of the material under study. This source/sample package can be mounted in a cryostat for temperature dependent measurements. The emitted positrons of ca. 300 keV average energy enter the material and are quickly slowed down to reach thermal energy. They collide with electrons and will have a certain annihilation probability depending on the relative orientations of the spins of the positron and of the electron. The formation of the singlet state (opposed spins) is several hundred times more probable than that of the triplet state (parallel spins). This relation obviously holds true also for the relative occurrence of the decay of these states via 2-gamma- and 3-gamma-annihilation, respectively. It is also possible that a thermalized positron forms a (H-like) tran-

sient bound system with an electron called a positronium (Ps) atom (e^+e^-), before annihilation occurs. The lifetime of the singlet Ps (called parapositronium p -Ps) is so short that no information can be extracted about interactions with the surroundings. Instead, the lifetime of o -Ps is much longer even in condensed media (ca. 500–1500 ps) and can be shortened by several processes such as:

- electron pick off with an alien electron;
- spin conversion from o -Ps to p -Ps in the presence of magnetic fields or paramagnetic species; and
- chemical reactions with the substrate molecules and phase transformations.

The most important chemical information comes from the o -Ps lifetime as determined by the electron density in the medium. It has been demonstrated that PAS spectroscopy can be used to signalize changes in electron density going along for instance with ST or a thermally induced lattice deformation, which could actually trigger a ST phenomenon [94, 95].

8.2.10 Nuclear Resonant Scattering of Synchrotron Radiation

Synchrotron radiation (SR) has in recent years developed to one of the most important tools in solid state research. It is polarized electromagnetic radiation of unusually high brilliance and intensity, with frequencies ranging from infrared to hard X-rays. Synchrotron radiation is produced in particle accelerators or storage rings, when relativistic electrons are deflected in magnetic fields.

Beginning with the first successful observation of a resonant signal in a nuclear scattering experiment with synchrotron radiation by Gerdau et al. in 1985 [96], the so-called nuclear forward scattering (NFS) technique has been established as a powerful tool to probe hyperfine interactions in condensed matter [97]. This technique is related to conventional Mössbauer spectroscopy and even proves to have its outstanding merits when the traditional Mössbauer effect experiments reach their limits. As an example, the high brilliance of SR allows to perform NFS studies on very small samples or substances with extremely small contents of resonating nuclei, where conventional Mössbauer experiments are no more feasible.

NFS measurements have been carried out on iron(II) SC complexes with amazing success [98]. The time dependence of the NFS intensities yield typical “quantum beat structures” for the HS and the LS states, the quantum beat frequency being considerably higher in the HS state due to the larger quadrupole splitting than in the LS state. The temperature dependent transition between the two spin states yields complicated interference NFS spectra, from which the molar fractions of HS and LS molecules, respectively, can be extracted using special computer programs. A comparison of the results with the data from conventional Mössbauer measurements on the same sample gave excellent agreement between the hyperfine interaction parameters. Admittedly, conventional Mössbauer spectra are easier to analyze and read at first glance, but NFS measurements have their particular merits for example in the more precise determination of the so-called Lamb–Mössbauer factor, which is necessary for accurate determination of the molar fractions of HS and LS

molecules. Furthermore, NFS measurements can be combined with simultaneous “nuclear inelastic scattering” (NIS) of synchrotron radiation, which bears valuable information on the vibrational properties of the different spin states of a SC compound [99] and thus complements conventional infrared and Raman spectroscopic studies.

Detailed information on anisotropic properties and their temperature and pressure dependent changes will be expected from studies with synchrotron radiation in angular dependent measurements.

8.2.11 Magnetic Resonance Studies (NMR, EPR)

Proton NMR measurements have proven to be an elegant and easy method to follow a temperature dependent ST phenomenon in solution (Evans method) [29b, 100, 101]. The thermally induced change of the paramagnetic peak relative to the signal of a standard component, which in favorable cases can even be part of the SC compound (e. g. the anion) [29b, 102], reflects the ST process. In solid state studies, however, the NMR spectrum of SC compounds has been of little value in learning much about this phenomenon, except to detect the transition itself from the line width change. The numerous different protons in the ligands studied lead to broad lines, which are difficult or impossible to analyze regarding details of the transition. A way out of it would be choosing a simpler system with a small number of distinct protons in the ligand sphere [103]. More interesting and promising regarding detailed information of the ST mechanism seem to be the results of T_1 relaxation time measurements. First attempts were reported by McGarvey et al. [103], who observed for example that in iron(II) compounds T_1 decreases with increasing distance of protons from the paramagnetic iron center. A comparative detailed proton relaxation time study on $[\text{Fe}(\text{ptz})_6](\text{BF}_4)_2$ and its zinc analog was reported later by Bokor et al. [104]. The authors plotted the measured T_1 relaxation times as a function of $1/T$ and found several minima, which they assigned to tunneling (at low temperatures) and classical group rotations (at higher temperatures). The corresponding activation energies were derived from the temperature dependence of the NMR spectrum. In a later similar NMR study the same research group measured the ^{19}F and ^{11}B relaxation times T_1 on the same ion and zinc compounds [105] and again found characteristic minima in different temperature regions of the $\ln T_1$ versus $1/T$ plot. They concluded that the SC takes place in a dynamic surrounding and not in a static crystal lattice.

EPR spectroscopy has much more often been employed in SC research than the NMR technique. The reason is that for all three classes of SC compounds of iron(III), iron(II), and cobalt(II), which are the most actively studied ones, sufficiently well resolved characteristic spectra can be obtained in both HS and LS states. In the case of iron(III) SC compounds there is no spin-orbit coupling in the HS (^6S) state and thus the relaxation times are long. EPR signals appear at characteristic g values yielding characteristic ZFS parameters, D for axial and E for rhombic distortions. In the LS state of iron(III) ($^2\text{T}_2$) spin-orbit coupling does occur, but due to the low temperature the vibrations are slowed down and electron-phonon coupling becomes weak

and therefore relaxation times are long. The result is that the EPR spectrum of the LS state of iron(III) exhibits a single line near to $g \approx 2$ for a polycrystalline sample; in a single-crystal study anisotropy effects can be observed *via* g_x , g_y , g_z . Thus, it is obvious that EPR spectroscopy is an extremely valuable tool to unravel structural information of a SC system, which is otherwise not accessible. Many examples have been reported, for instance, by Hendrickson et al. and Maeda et al.; their work and other ST studies by EPR has recently been reviewed elsewhere [106]. Direct EPR studies on neat SC compounds of cobalt(II) are also very informative as has been demonstrated by Zarembowitch [26]. As spin-orbit coupling in the HS state (4T_1) shortens the spin-lattice relaxation times and makes signal recording difficult in the room temperature region, good EPR spectra of cobalt(II) SC complexes in the HS state are usually obtained at lowest possible temperatures, i. e. just above the transition temperature. No problem arises in the recording of the LS spectrum, even with an anisotropic g -pattern reflecting axial and rhombic distortion.

EPR spectroscopy of paramagnetic iron(II) is not possible at higher temperatures. Spin-orbit coupling within the 5T_2 state leads to so short a spin-lattice relaxation time that EPR spectra can only be observed at 20 K or lower. The Fe^{II} ion is coupled to its environment more strongly than any other 3d ion. However, doping the Fe^{II} SC complex with suitable EPR probes like Mn^{II} or Cu^{II} , as was done first by McGarvey et al. [107] with $[Fe(phen)_2(NCS)_2]$ and $[Fe(2-pic)_3]Cl_2 \cdot EtOH$ (2-pic = 2-picolyamine) doped with 1% Mn^{II} and later by Haasnoot et al. [108] with $[Fe(btr)_2(NCS)_2] \cdot H_2O$ doped with ca. 10% Cu^{II} , can improve the resolution of the EPR signals considerably. If the dopant concentration, however, is too high (as was the case in the work of Vreugdenhil et al. [108]), the EPR spectrum of the paramagnetic HS phase becomes poorly resolved due to spin-spin interaction and exchange broadening. McGarvey et al. have recorded EPR spectra of excellent quality of single crystals of $[Fe(ptz)_6](BF_4)_2$ doped with 1% Mn^{II} [109]. They determined the D and E values in both spin states and confirmed the existence of two structurally different LS phases which are formed by fast and slow cooling, respectively. The above mentioned strategy of using Cu^{II} or Mn^{II} as local probe was also recently applied to other compounds [110, 111].

It is worth mentioning that a small amount of Fe^{III} ions, sometimes being present as an impurity, can be used as an EPR probe to follow the ST in an Fe^{II} SC compound [112].

8.3 Highlights of Past Research

8.3.1 Chemical Influence on Spin-crossover Behavior

Already in the early stage of SC research one has learned that various chemical alterations of the coordination compound such as ligand replacement or exchange of substituents in certain ligand positions can influence the ligand field strength at the metal center. Well known examples are the phenanthroline complexes of iron(II)

[7]. $[\text{Fe}(\text{phen})_3]\text{X}_2$ is a LS complex at all temperatures irrespective of the nature of the anion X, but $[\text{Fe}(\text{phen})_2(\text{NCS})_2]$ is a HS complex at room temperature which converts to the LS state near 185 K due to the fact that two *cis* NCS groups coordinated through N, replacing one bidentate phen, sufficiently weaken the average field strength in order to compete with the spin pairing energy [2]. In the case of the substituted $[\text{Fe}(2\text{-Y-phen})_3]\text{X}_2$ complexes the ligand field strength is controlled by the Y-substituent in 2 or 9 position of the phen ligand, whereby two factors are operative simultaneously:

- an electronic push/pull effect influencing the basicity of the coordinating nitrogen atom; and
- a steric hindrance effect caused by the rotating Y-substituent, which in turn lengthens more or less the metal–ligand bond distance R and consequently changes the cubic ligand field parameter through $10Dq \approx 1/R^5$ [17].

This way one has explained qualitatively, and confirmed by CNDO/2-MO calculations [113], that the tendency to stabilize the HS state in $[\text{Fe}(2\text{-Y-phen})_3]\text{X}_2$ at a given temperature increases in the series $\text{Y} = \text{H} < \text{CH}_3\text{O} < \text{CH}_3 < \text{Cl}$ [17], where the H and the Cl substituents causes HS behavior at all temperatures, whereas the CH_3O and CH_3 derivatives exhibit thermal spin transition. It is tempting to conclude that the ligand field strength may be “fine-tuned” via the electronic influence and the steric hindrance effect and thereby shifting “at will” the ST up or downwards the temperature scale. This may indeed be the case in liquid solutions, where no other perturbation except these two influences play a significant role. In the solid state, however, cooperative interactions primarily due to the volume change as a consequence of the ST, but also due to hydrogen bonding, π -stacking, crystal packing effects, to name the most essential ones, come into play and can alter the SC behavior. And yet, the ligand replacement effect mostly introducing the NCS groups as the new ligand, and more importantly the exchange of specific substituents has always been a powerful strategy in order to influence the ST behavior in a kind of controlled manner [7, 18, 22]. The most attractive goal is, in view of eventual technical applications, in displays and switching devices, synthesizing SC complexes exhibiting ST with hysteresis near to room temperature [114].

The most extensively studied SC systems, both from the chemical and physical point of view, are the picolylamine complexes $[\text{Fe}(2\text{-pic})_3]\text{X}_2 \cdot \text{Sol}$, for which the occurrence of thermal ST was first reported by Renovitch and Baker [115]. This system appeared to be very favorable in the sense that it could be chemically altered in many ways and then examined by ^{57}Fe Mössbauer spectroscopy, which deliver well resolved signals unambiguously attributable to the two spin states (HS and LS) involved [116, 117]. This way the effect of metal dilution on the SC behavior was studied for the first time in the mixed crystal series $[\text{Fe}_x\text{Zn}_{1-x}(2\text{-pic})_3]\text{Cl}_2 \cdot \text{EtOH}$, with x ranging from 1 down to 0.007 [116, 118]. As is seen from Fig. 5, the ST curve given as the HS fraction as a function of temperature, $\gamma_{\text{HS}}(T)$, which is still rather steep in the neat compound ($x = 1.0$), becomes more and more gradual and shifted to lower temperatures, reflecting increasing stabilization of the HS state, upon lowering the iron concentration. The shape of the $\gamma_{\text{HS}}(T)$ function approaches more and more that of a Boltzmann distribution over all spin states, as is generally found for thermal

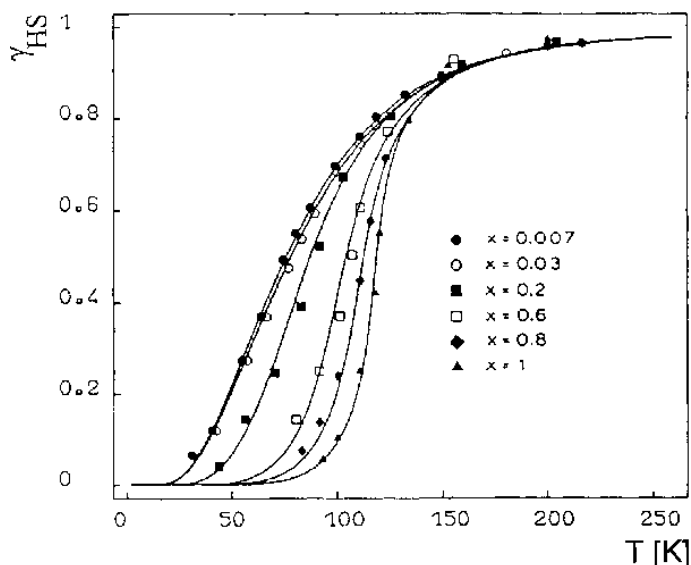


Fig. 5. ST curves $\gamma_{HS}(T)$ of the mixed crystals $[Fe_xZn_{1-x}(2-pic)_3]Cl_2 \cdot EtOH$ for different concentrations [116, 118].

ST in liquid solutions. The metal dilution effect in the solid state seen in Fig. 5 was later on observed in other SC complexes of iron(II) [119–124]. It clearly reflects the existence of cooperative elastic interactions between the spin state changing metal centers. The nature of such cooperative interactions is purely mechanical. In a crude description, if the spin state in a particular metal center changes say from LS to HS, driven by the entropy gain of $40\text{--}80\text{ J mol}^{-1}\text{ K}^{-1}$, the molecular volume increases (by $\sim 3\text{--}5\%$) leading to an expansion of the lattice which causes a change of the “chemical pressure” acting on all complex molecules in the crystal. This facilitates further spin state changes in other centers. With decreasing iron concentration in a crystal diluted for instance with Zn complex molecules, however, the crystal volume change per iron complex and thus the chemical pressure decrease. Finally, in the highly diluted mixed crystal, with distances of $>50\text{ \AA}$ between the iron centers, cooperative interactions are practically vanishing and the $\gamma_{HS}(T)$ curve adopts a Boltzmann like shape as in a liquid solution where cooperative interactions are absent. A model has been developed, based on elasticity theory, which accounts properly for the changes of chemical pressure as the origin of cooperative elastic interactions in solid SC systems [117, 125]. This model, which will be described in Section 8.3.4.8, was used to fit the experimental data in Fig. 5.

The nature of the non-coordinating anion has also shown to affect the ST behavior in solid SC systems. Detailed examination by Mössbauer spectroscopy and magnetic susceptibility measurements [117, 126] of the transition region near $T_{1/2}$ in $[Fe(2-pic)_3]X_2 \cdot EtOH$ ($X = Cl, Br$) have yielded most interesting features, which have been observed for the first time in a SC complex (see Fig. 6). The chloride system undergoes a stepwise ST with a plateau at $\gamma_{HS} \approx 0.5$ extending over nearly 10 K

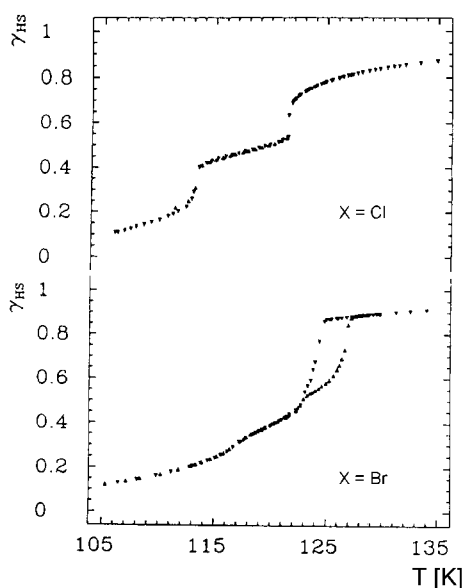


Fig. 6. ST curves $\gamma_{\text{HS}}(T)$ of $[\text{Fe}(2\text{-pic})_3]\text{X}_2 \cdot \text{EtOH}$ ($\text{X} = \text{Cl}, \text{Br}$) [117, 126].

around $T_{1/2}$ [117]. As will be discussed in more detail in Section 8.3.4.8, the plateau in this case arises from short-range interactions which are dominating in the transition region and lead to domains of ...HS-LS... next neighbor arrangements like in a chess board.

Like the anions, the solvent molecules incorporated into the crystals of $[\text{Fe}(2\text{-pic})_3]\text{X}_2 \cdot \text{Sol}$ during the preparation are not coordinated to the iron(II) centers as seen by X-ray diffraction studies of the different solvates with Sol = EtOH [127, 128], MeOH [129, 130], $2\text{H}_2\text{O}$ [130, 131], but nevertheless their influence on the ST behavior is quite enormous [132, 133]. The methanolate is more gradual than the ethanolate, with higher $T_{1/2} \approx 150$ K and no step, the monohydrate shows very large hysteresis with $T_{1/2} \downarrow \approx 200$ K and $T_{1/2} \uparrow \approx 290$ K, and the dihydrate remains in the LS state up to the highest temperature under study of ca. 300 K. The crystal structures of these solvates are all different from one another [128, 129], but there is no doubt that hydrogen bonding being also quite different in the four solvates, influences the ST behavior. This was supported by examining the effect of isotopic exchange (H/D and $^{14}\text{N}/^{15}\text{N}$) in various positions of the picolylamine ligand and the solvent molecules [42b, 133]. One observed drastic changes in the ST curves only when the substitution took place in positions directly built in the hydrogen bonding network interconnecting the iron(II) complex molecules. An example is the picolylamine complex with $\text{C}_2\text{H}_5\text{OD}/\text{ND}_2$ where the ST curve is shifted by ca. 15 K to higher temperatures and shows no longer a plateau as compared to the non-deuterated system with $\text{C}_2\text{H}_5\text{OH}/\text{NH}_2$. The deuterated hydrogen positions are in this case constituents of the hydrogen bonding network. On the other hand, the ST curve of the deuterated system with $\text{C}_2\text{D}_5\text{OH}/\text{NH}_2$ is hardly changed, because in this case the deuterated positions are located in the ethyl substituent, which is only attached to the hydrogen bonding pathway. Hydrogen bonding has been found later

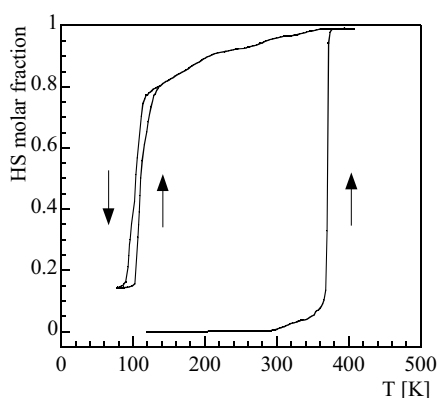


Fig. 7. Optical detection of the spin state as a function of temperature for $[\text{Fe}(\text{hyetrz})_3](3\text{-nitrophenylsulfonate})_2 \cdot x\text{H}_2\text{O}$ [149].

in other SC complexes to be an important “communication link” between the spin state changing centers [22, 134–138]. The presence of hydrogen bonding is not a prerequisite for thermal ST to occur, but where it exists, it generally greatly assists in the cooperative interactions.

The influence of crystal solvent molecules on the ST behavior was first studied by the Mainz group [132]. Numerous studies followed later [49, 139–151]. A prominent example, which was recently reported in the literature, is $[\text{Fe}(\text{hyetrz})_3](3\text{-nitrophenylsulfonate})_2 \cdot \text{Sol}$ (hyetrz = 4-2'-hydroxyethyl-1,2,4-triazole) [148]. This compound contains three non-coordinated water molecules and exhibits LS behavior up to ca. 370 K (Fig. 7). Heating the material above this temperature releases the water molecules from the crystal lattice and the spin state jumps from LS (pink) to HS (white). Upon cooling the water-free substance, the HS state is retained down to ca. 100 K, where thermal SC occurs with hysteresis. The particularity of this material is that the dehydration process is irreversible in a normal atmosphere and is accompanied by a color change. It has been suggested that this material is well suited for applications such as single use displays or temperature threshold indicators [114c, 148, 149, 152].

8.3.2 Structural Insights

The crystal structure of $[\text{Fe}(2\text{-pic})_3]\text{Cl}_2 \cdot \text{EtOH}$ was solved at two temperatures corresponding to the LS and HS states by Mikami and Konno [127] (Fig. 8). The Fe–N distances were found to decrease by 10% on going from the HS to the LS state, a result which can be extended to the majority of iron(II) SC compounds. No change of space group was observed for $[\text{Fe}(2\text{-pic})_3]\text{Cl}_2 \cdot \text{EtOH}$, which is not surprising as no hysteresis loop could be detected in the SC curve.

This is not the case for $[\text{Fe}(\text{ptz})_6](\text{BF}_4)_2$ which undergoes a ST with a thermal hysteresis of about 7 K [54]. The ST is accompanied by a structural phase transition from $\bar{R}\bar{3}$ in the HS phase to $\bar{P}\bar{1}$ in the LS phase as deduced from powder diffraction experiments [153]. If the compound is rapidly cooled, the formation of the $\bar{R}\bar{3}$

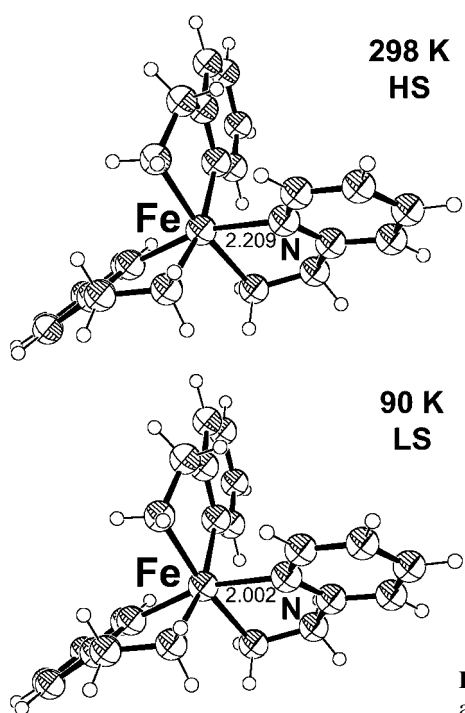


Fig. 8. Crystal structure of $[\text{Fe}(\text{2-pic})_3]\text{Cl}_2 \cdot \text{EtOH}$ at two temperatures [127].

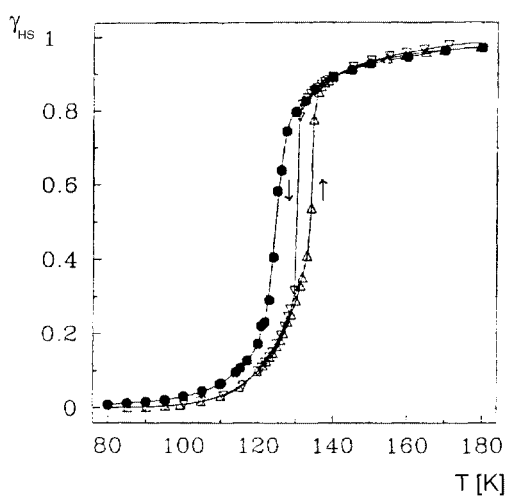


Fig. 9. Temperature dependence of the HS molar fraction of $[\text{Fe}(\text{ptz})_6](\text{BF}_4)_2$: (●) in the supercooled $R\bar{3}$ phase, (▽, △) accompanied by the structural phase transition $R\bar{3} \leftrightarrow P\bar{1}$ on slowly cooling and warming [122].

phase is preserved, but a ST without hysteresis is still observed (see Fig. 9) [122]. This proves, at least in this case, that the occurrence of ST does not depend on the occurrence of the crystal structure change. On the other hand, the crystal structure change may very likely be induced by the spin transition.

In 1986 it was first observed with $[\text{Fe}(\text{2-pic})_3]\text{Br}_2 \cdot \text{EtOH}$ that a ST occurs with hysteresis but without space group change [126]. Later on, the same behavior was found for $[\text{Fe}(\text{phen})_2(\text{NCS})_2]$. This SC compound shows a small hysteresis [154], but no space group change [155]. A more recent example with similar behavior is $[\text{Fe}(\text{pmbia})_2(\text{NCS})_2]$ with $\text{pmbia} = N\text{-(2-pyridylmethylene)aminobiphenyl}$ [156]. Only in these cases, one can affirm that the observed hysteresis is only due to cooperative effects as it is well known that a first order phase transition is generally accompanied by a hysteresis loop. Structural insights can also be gained under perturbation conditions such as pressure and light as will be discussed in Section 8.4.2.4.

8.3.3 Influence of Crystal Quality

Sample preparation through mechanical treatment or different synthetic procedures have been shown to influence strongly the ST behavior of coordination compounds. The very first observation of such effects was made by Hendrickson et al. on an iron(III) SC complex [157]. Grinding the sample resulted in the flattening of the ST curve with an increase of the residual HS fraction at low temperatures. The same effect was later observed on the iron(II) complexes $[\text{FeL}_2(\text{NCS})_2]$ ($\text{L} = \text{phen, bpy}$) [154] as well as for a cobalt(II) compound [158]. In the case of these ferrous compounds, the very narrow hysteresis in addition becomes broader and gradual. The SC characteristics may be also highly susceptible to the synthetic method. A typical example is given by $[\text{Fe}(\text{phen})_2(\text{NCS})_2]$, which can be prepared in two ways: by precipitation in MeOH or by extraction of a phen group from $[\text{Fe}(\text{phen})_3](\text{NCS})_2 \cdot \text{H}_2\text{O}$ using acetone [159]. Both compounds have the same chemical formula, but undergo different SC behavior. The compound obtained by the first method shows a smooth ST with a noticeable HS fraction at low temperature, whereas the second compound undergoes a sharp and complete spin transition [154]. Similar effects were also found later for the linear chain compound $[\text{Fe}(\text{Htrz})_2\text{trz}](\text{BF}_4)$ using different solvents in the synthetic procedure [160]. In this case, the width of the hysteresis loop is greatly altered on going from ≈ 40 K, for the compound prepared in an EtOH–H₂O mixture, to 20 K for the compound obtained in MeOH.

The origin of the effects mentioned above stems from crystal quality considerations, in particular crystal defects introduced during sample preparation either by milling (sheared deformations) or rapid precipitation, the size of the particles playing a minor role. In some cases, polymorphism can also be invoked to account a difference in the observed magnetic properties. It was assumed to be relevant for $[\text{FeL}_2(\text{NCS})_2]$ ($\text{L} = \text{phen, bpy}$) [161] and later clearly demonstrated for $[\text{Fe}(\text{dppa})_2(\text{NCS})_2]$ ($\text{dppa} = (3\text{-aminopropyl})\text{bis}(2\text{-pyridylmethyl})\text{amine}$) [162], three polymorphic modifications being identified by X-ray analysis.

Thus, this section points out the extreme sensitivity of SC complexes to sample preparation that is for the synthetic procedure or prior to physical measurements. This aspect should not be neglected when considering a new SC problem.

8.3.4 Theoretical Approaches to Spin Transition Phenomena

8.3.4.1 General Remarks

The experimentally determined ST curve $\gamma_{\text{HS}}(T)$, i. e. the fraction of HS molecules as a function of temperature as the natural order parameter, may have different shapes for spin transitions in solid state (Fig. 3), whereas in a liquid solution of a SC complex the $\gamma_{\text{HS}}(T)$ curve always follows the gradual Boltzmann distribution function. Thermal populations of all electronic levels of the HS and LS states are, of course, also the decisive factor in solid state, but it is obvious that extra features must be present which are responsible for the fact that the $\gamma_{\text{HS}}(T)$ curve in a solid SC compound may be abrupt, or incomplete, or occur with hysteresis or with steps. From the early stage of SC research, it has been one of the main concerns trying to understand the nature of such extra features and to develop physically meaningful theoretical descriptions incorporating these features.

Already Ewald et al. in their review article [163] pointed out that a difference in the molecular frequencies of the HS and LS states, might be important for the ST behavior. König et al. attempted to understand quantitatively the measured ST curves of Schiff base complexes of iron(II) [53b, 164] by taking the vibrational part of the partition function into account with different frequencies in the two spin states and also paying attention to the fact that the ${}^5\text{T}_2$ and ${}^1\text{A}_1$ states differ in the ligand field strength and consequently in the metal–ligand bond distances of ca. 0.2 Å. And yet the agreement between the measured and calculated magnetic moments as function of temperature was not satisfactory. But from the present point of view it is fair to state that key features such as changes of the molecular dimension and frequencies accompanying the ST had already been recognized as such even in their “local picture” interpretation of ST, which in fact paid no attention to differences between solid and liquid state spin transitions. The breakthrough, however, came later when one recognized that SC molecules “communicate with other” during ST in the crystalline state by virtue of the above mentioned changes of molecular properties, thereby setting up cooperative interactions, which do not exist in liquid state. It is by now commonly accepted among the researchers in the field that the presence of short-range and long-range cooperative interactions are responsible for any significant deviation from a Boltzmann like ST curve $\gamma_{\text{HS}}(T)$, irrespective of the dimensionality (mononuclear, chains, layers, or 3D) of the lattice and special bonding properties like hydrogen bonding and π – π stacking. Thus it is generally agreed that any theory describing successfully ST phenomena in solid state must take cooperativity into account.

In the following we shall review, in chronological order, the various efforts that have been undertaken to describe theoretically ST phenomena.

8.3.4.2 The Chesnut Model

The earliest theoretical treatment was published by Chesnut [165] already in 1964 for a singlet–triplet system attempting to understand the magnetic excitations in the linear chain compounds of tetracyanoquinodimethane–ion–radical salts. Ches-

nut's model considers N molecules, a fraction γ_{HS} is excited from a singlet ground state to a $g = 2S + 1$ -fold degenerate excited state separated by an energy Δ . To account for cooperative effects, an energy term quadratic in γ_{HS} is added. The shape of the free energy is now familiar (with the notation used up to now in SC research):

$$F/N = \gamma_{\text{HS}}\Delta - \Gamma\gamma_{\text{HS}}^2 - Tk_{\text{B}} \ln g - T\sigma_{\text{mix}} \quad (6)$$

where $\sigma_{\text{mix}} = -k_{\text{B}}\{\gamma_{\text{HS}} \ln \gamma_{\text{HS}} + (1 - \gamma_{\text{HS}}) \ln(1 - \gamma_{\text{HS}})\}$, Γ denotes the interaction between the excited state molecules, $k_{\text{B}} \ln g$ is the entropy gain of an excitation, k_{B} is the Boltzmann constant, and σ_{mix} is the mixing entropy of a random distribution of excited states. Δ is the elastic energy difference between excited state and ground state. It depends on the size of the particle, which is considered different in the two states. The merit of the paper by Chesnut is that it allowed a prediction of the sign of the interaction constant Γ to be made considering the effect of lattice strain. It took eight years that this paper was rediscovered for the iron(II) SC community by Bari and Sivardière [166].

8.3.4.3 The Wajnflasz Model

The first theoretical paper, which refers to experimental facts from ST studies, was that of Wajnflasz [167]. Wajnflasz introduced an interaction constant (he called it J) between the spin changing molecules and considered the ST as a cooperative phenomenon. He used the picture of the molecule with a LS ground state and a HS excited state which has a bond length r_{LS} , and vice versa a HS ground state and a LS excited state at bond length r_{HS} with a temperature independent energy separation $\Delta E = E_{\text{HS}}(\text{ground state}) - E_{\text{LS}}(\text{ground state}) > 0$. The two molecular states are mapped onto a two-valued fictitious spin $\sigma = \pm 1$ with +1 for the HS and -1 for the LS state. The Hamiltonian then adopts the shape of an Ising Hamiltonian in an applied field. The interaction Hamiltonian between site i and j is written as $\sum_i J_{ij}\sigma_i\sigma_j$. This means that the interaction energy between two neighboring HS or LS molecules is $+J_{ij}$ and between a HS and a LS molecule $-J_{ij}$. The Hamiltonian of the interacting system of molecules is solved by the molecular field approximation with only nearest neighbor interactions. The different multiplicities of the spin levels was taken into account by a degeneracy ratio $g_{\text{HS}}/g_{\text{LS}} = 15$. Wajnflasz pointed out that a negative value of the interaction J , which increases the energy of the system by the number of HS-LS pairs, qualitatively reproduces the steep transitions as in $[\text{Fe}(\text{phen})_2(\text{NCS})_2]$. The unrealistic model Hamiltonian for the molecule with the extra excited states at the same bond lengths may be the reason why the paper was not adequately received. Nevertheless, this Hamiltonian yielded a formal solution for the deviation from Boltzmann population and removed the unrealistic temperature dependence of the energy separation between the spin states introduced by Jesson et al. [168].

8.3.4.4 The approach of Drickamer and Slichter

Slichter and Drickamer [169] introduced an interaction term and discussed in great detail the consequences of the cooperativity for the spin transition behavior. They followed the conjecture of König and Madeja [53b, 164] who proposed the possible existence of cooperative phenomena and took, as the simplest form of the Gibbs free energy, a linear interpolation with HS fraction γ_{HS} between the value $G_{\text{HS}}(T)$ of the unconverted material and the corresponding quantity $G_{\text{LS}}(T)$ of the completely converted material (we drop here a consideration of the pressure dependence). An interaction is introduced by a term $\gamma_{\text{HS}}(1 - \gamma_{\text{HS}})$ which they viewed as the next term in a power series of expansion in the two variables γ_{HS} and $(1 - \gamma_{\text{HS}})$. This way they obtained for the Gibbs free energy:

$$G/N_0 = (1 - \gamma_{\text{HS}})G_{\text{LS}}(T) + \gamma_{\text{HS}}G_{\text{HS}}(T) + \Gamma\gamma_{\text{HS}}(1 - \gamma_{\text{HS}}) - T\sigma_{\text{mix}} \quad (7)$$

where N_0 is the total number of molecules. This equation connects thermodynamic quantities and avoids a detailed model for the isolated SC molecules. The non-interacting molecules as for example in a low concentration liquid solution are described by $\Gamma = 0$. For different values of Γ the so far known transition curves could be reproduced, especially for $\Gamma > 0$ the observed steep transition. For sufficiently large $\Gamma > 0$ values spin transitions with hysteresis are predicted.

The first comparison between theory and experiment was done by König and Ritter on the SC compound $[\text{Fe}(4,7\text{-}(\text{CH}_3)_2\text{-phen})_2(\text{NCS})_2]$ [170]. They found a hysteresis width of 3.1 K with a transition temperature of 118.6 K for lowering of temperature and could qualitatively reproduce the observed transition curve with the theory of Slichter and Drickamer. The mean field interaction parameter was determined to be $\Gamma = 192 \text{ cm}^{-1}$, the origin of which, however, was not discussed.

8.3.4.5 The Theory of Bari and Sivardière

Bari and Sivardière [166] published a pure theoretical contribution independent of Slichter and Drickamer. They paid attention to the theoretical works of Chesnut [165] and Wajnflasz [167] and extended the theory of Chesnut by magnetic exchange interactions and discussed also the possible existence of two-sublattice-spin-structures. The theoretical results were not applied to any of the numerous experimental results known at that time. The extension to long range magnetic exchange was mathematically appealing but was not applicable to the large molecular crystals where magnetic ordering was never observed down to low temperatures.

8.3.4.6 The Model of Zimmermann and König

The first step towards better understanding the interaction constant in terms of the properties of the SC compound was done by Zimmermann and König [171]. They tried to explore the consequences of the decrease of the lattice vibrational frequencies on going from the LS to the HS state. This decrease was carefully studied by

the Mössbauer effect by Ritter and König [172]. The observed decrease of the Debye temperature θ leads to a higher density of states of lattice phonons in the HS state. Employing the experimentally derived Debye temperatures $\theta_{LS} = 140$ K and $\theta_{HS} = 130$ K, they calculated a contribution to the interaction constant Γ of only 40 cm^{-1} . The actual interaction constant, however, which is needed to fit the ST curves $\gamma_{HS}(T)$ of $[\text{Fe}(4,7\text{-}(\text{CH}_3)_2\text{-phen})_2(\text{NCS})_2]$ is about five times larger. Also, about one third of the total entropy change observed at the transition temperature was explained on this basis. This is particularly rewarding in view of the fact that measurements of the specific heat have shown that the entropy change at the transition temperature may be more than three times as large as would be expected from the electronic entropy difference between HS and LS states, which is for iron(II) SC complexes with low local symmetry (orbital coupling quenched) $\Delta S_{\text{el}} = R[\ln(2S + 1)_{\text{HS}} - \ln(2S + 1)_{\text{LS}}] \approx 13 \text{ J mol K}^{-1}$ [44]. The major part of the entropy change is to be accounted for by contributions from lattice and molecular vibrations.

8.3.4.7 The Cluster Model of Sorai and Seki

Sorai and Seki [44b] suggested a cluster model based on the Frenkel theory of heterophase fluctuations in a liquid. Clusters of n molecules assumed to be completely in the LS or in the HS state are considered in thermal equilibrium without interactions between the clusters. The cluster size n is treated as a measure for the steepness of the ST curve $\gamma_{HS}(T)$: the larger n , the steeper the transition curves.

The model was applied to reproduce the ST functions of the zinc diluted mixed crystal series of $[\text{Fe}_x\text{Zn}_{1-x}(2\text{-pic})_3]\text{Cl}_2 \cdot \text{EtOH}$ where it was found by Mössbauer spectroscopy that the $\gamma_{HS}(T)$ functions became increasingly gradual and shifted to lower temperatures with decreasing iron concentration (see Fig. 5) [116, 117]. The data were parameterized by a modification of the cluster model of Sorai and Seki and it was found that the cluster size n decreased with decreasing iron concentration and the concomitant decrease of the steepness of $\gamma_{HS}(T)$.

The drawback of the cluster model of Sorai and Seki, however, was readily apparent in view of these results of metal dilution studies: there is no physical background built in the model which could explain the effect of metal dilution on the ST curves, that is the fact that, with decreasing iron concentration, and thereby increasing distances between the spin state changing centers, the apparent cooperative interactions are gradually weakened, which more and more stabilizes the entropy-favored HS state. The wealth of such metal dilution studies first carried out in a systematic manner by the Mainz group [116, 117] was evident: it is the best choice to prove the existence of cooperative interactions in solid SC complexes. But a new theory was badly needed to incorporate specifically the role of cooperative interactions. Such a theory was later developed by H. Spiering of the Mainz group [117, 125]. Their model is based on changes of volume, shape, and elasticity of the lattice as the main factors influencing the cooperative interactions. The essential features of this “model of lattice expansion and elastic interactions” are outlined in the next section.

8.3.4.8 The Mainz Model of Lattice Expansion and Elastic Interactions

Knowing about the experimental facts from (i) metal dilution studies [116, 117] and (ii) the volume change upon ST from temperature dependent crystal structure determination on the $[\text{Fe}(\text{2-pic})_3]\text{Cl}_2 \cdot \text{EtOH}$ [126, 127], Spiering et al. [117, 125] attempted to interpret quantitatively all parameters with a new model featured by lattice expansion and elastic interactions upon spin transition. The authors divided the task into two parts:

- high dilution with practically no interactions, and
- highly concentrated mixed crystals with cooperative interactions.

As any interaction is assumed to be zero in the first case, the fraction of molecules in the HS state is solely determined by the Boltzmann population according to the free energy difference $\Delta f_{\text{HL}}(T)$ between HS and LS states. The resulting molar fraction of HS molecules as function of temperature is:

$$\gamma_{\text{HS}}(T) = \frac{\exp(-\Delta f_{\text{HL}}(T)/k_{\text{B}}T)}{1 + \exp(-\Delta f_{\text{HL}}(T)/k_{\text{B}}T)} \quad (8)$$

Knowing $\gamma_{\text{HS}}(T)$ means that $\Delta f_{\text{HL}}(T)$ is also known. The free energy difference has been parameterized by an electronic part taking the ligand field parameters from a fit of the temperature dependence of the quadrupole splitting of the Mössbauer doublet, by a vibrational part with two frequencies of degeneracy 6 and 9 being different in the HS and LS states following Ewald et al. [163], and a small temperature dependence of the energy difference between the lowest vibrational HS and LS states due to the thermal lattice expansion. This way the experimental data of the highly diluted compound $[\text{Fe}_x\text{Zn}_{1-x}(\text{2-pic})_3]\text{Cl}_2 \cdot \text{EtOH}$ ($x = 0.0009$) with practically isolated $[\text{Fe}(\text{2-pic})_3]^{2+}$ SC centers in the corresponding Zn matrix could be well reproduced [116, 118].

For the case of highly concentrated mixed crystal systems cooperative interactions come into play, for which an extra term $w(\gamma_{\text{HS}}, x, T)$ has to be included in the expression for the free energy per complex molecule:

$$f_x = x[\gamma_{\text{HS}}f_{\text{HS}} + (1 - \gamma_{\text{HS}})f_{\text{LS}} - T S_{\text{mix}}(\gamma_{\text{HS}})] \\ + (1 - x)f_{\text{Zn}} + x \cdot w(\gamma_{\text{HS}}, x, T) + f_{\text{G}} \quad (9)$$

where f_{G} is the free energy per complex molecule of the residual lattice, taken independent of the HS fraction γ_{HS} ;

$$S_{\text{mix}} = -k_{\text{B}}[\gamma_{\text{HS}} \ln \gamma_{\text{HS}} + (1 - \gamma_{\text{HS}}) \ln(1 - \gamma_{\text{HS}})] \quad (10)$$

is the mixing entropy between HS and LS molecules. As the interaction energy per complex molecule vanishes at infinite dilution, $w(\gamma_{\text{HS}}, x \rightarrow 0, T) \rightarrow 0$, the equilibrium condition $\partial f_x / \partial \gamma_{\text{HS}} = 0$ yields the Boltzmann type population as given in Eq. (8) for “isolated” non-interacting complex molecules:

$$\gamma_{\text{HS}}(T) = \frac{Z_{\text{HS}}(T)}{Z_{\text{HS}}(T) + Z_{\text{LS}}(T)} = \frac{\exp(-\Delta f_{\text{HL}}(T)/k_{\text{B}}T)}{1 + \exp(-\Delta f_{\text{HL}}(T)/k_{\text{B}}T)} \quad (11)$$

$Z_{\text{HS}}(T)$ and $Z_{\text{LS}}(T)$ are the partition functions of the molecules in the HS and LS states. For concentrated systems with non-vanishing interactions the equilibrium condition ($\partial f_x / \partial \gamma_{\text{HS}} = 0$) yields:

$$\left(\frac{\partial w}{\partial \gamma_{\text{HS}}} \right)_T = -k_{\text{B}}T \ln [\gamma_{\text{HS}}(T)/(1 - \gamma_{\text{HS}}(T))] - \Delta f_{\text{HL}} \quad (12)$$

which can be calculated as function of T and x using experimental data of Δf_{HL} of highly diluted systems and the measured $\gamma_{\text{HS}}(T)$ curves at different concentrations x . Plotting ($\partial f_x / \partial \gamma_{\text{HS}}$) as function of γ_{HS} for different x yields, as a good approximation, linear functions which may be expressed as:

$$\left(\frac{\partial w}{\partial \gamma_{\text{HS}}} \right)_x = \Delta - 2\Gamma \gamma_{\text{HS}} \quad (13)$$

where $\Delta(x)$ and $\Gamma(x)$ also turn out to be linear functions of x . Integration of Eq. (13) gives the following expression for the interaction energy:

$$w(\gamma_{\text{HS}}, x) = \Delta(x)\gamma_{\text{HS}} - \Gamma(x)\gamma_{\text{HS}}^2 \quad (14)$$

where the formal integration constant is included in the lattice contribution $f_{\text{G}}(x, T)$. The linear dependence of $\partial w / \partial \gamma_{\text{HS}}$ on x as well as on γ_{HS} was verified in several mixed crystal series [125a, 125b, 173, 174].

The interaction term $w(\gamma_{\text{HS}}, x, T)$ is interpreted as has been described in review articles of Gütlich et al. [17, 18b, 21]. Following Eshelby [175] the HS, LS, and other metal M complex molecules are defects in their own crystal which is approximated by a homogeneous, isotropic elastic medium characterized by a bulk modulus, K and a Poisson ratio, σ . The matrix provides a stress-free volume v_0 for a molecule that may be occupied by volumes v_{HS} , v_{LS} and v_{M} in case of HS, LS, and metal complex molecules, respectively. These volumes can be larger or smaller than v_0 and for simplicity are considered to be incompressible. The incompressibility is justified in the case of a soft matrix (small bulk modulus, K) as compared to large intramolecular force constants (frequencies) of the oscillator potentials especially the A_1 breathing mode frequency. The misfit of the volume v ($v = v_{\text{HS}}, v_{\text{LS}}, v_{\text{M}}$) builds up a strain field, which has an elastic energy [175]:

$$E_{\text{el}} = 1/2K(\gamma_0 - 1)(v - v_0)^2/v_0 - 1/2K\gamma_0(\gamma_0 - 1)(v - v_0)^2/V \quad (15)$$

V is the volume of the crystal and the Eshelby constant γ_0 is related to the Poisson ratio σ by $0 \leq \gamma_0 = 3(1 - \sigma)/(1 + \sigma) \leq 3$. The second term in Eq. (15) which is very small for an isolated defect, since V/v_0 is of the order of Avogadro's number, refers to an interaction between the defects. This term attains a finite value if the number of defects N is of the same order, this means each lattice site acts as a defect due to its misfit to v_0 . The negative second term is understood by the image pressure on the free surface, which builds up by adjusting the volume v_0 to the size of v .

Eshelby has shown that the crystal volume V changes by more than just $v - v_0$, namely by δv

$$\delta v = \gamma_0(v - v_0) \quad (16)$$

This additional crystal volume change $\delta v - (v - v_0) = (\gamma_0 - 1)(v - v_0)$ is formally attributed to a pressure $p_I = -K(\gamma_0 - 1)(v - v_0)/V$, such that the second term in Eq. (15) being equal to $1/2 p_I \delta v$ is interpreted as volume work against this pressure, which is called *image pressure*. Although a homogeneous stress field (due to pressure) only applies for one defect if centered in a matrix of spherical shape, this solution can be generalized by two facts. First, Eshelby has shown that the volume excess remains valid irrespective of the shape of V and the location of the defect. Second, the distribution of defects is assumed to be homogeneous which results again in a homogeneous stress field. For N defects with volume v_i the volume excess is $\delta V = (\gamma_0 - 1)\sum_i (v_i - v_0)$ and the *image pressure* $p_I = -K_V/V$ so that the total elastic energy is given by:

$$E_{\text{total}} = \frac{1}{2}K(\gamma_0 - 1)\sum_{i=1}^N (v_i - v_0)^2/v_0 - \frac{1}{2}K\gamma_0(\delta V)^2/V \quad (17)$$

The volume excess per defect $\delta V/N$ is expressed by the fraction of x of SC molecules in a mixed crystal and γ_{HS} of HS molecules:

$$\delta V/N = x[\gamma_{\text{HS}}(v_{\text{HS}} - v_0) + (1 - \gamma_{\text{HS}})(v_{\text{LS}} - v_0)] + (1 - x)(v_{\text{M}} - v_0) \quad (18)$$

Inserting δV into Eq. (17) an interpretation of $\Delta(x)$ and $\Gamma(x)$ is obtained. E_{total} has to be divided by xN to get the energy per iron ion:

$$\Gamma(x) = x1/2K\gamma_0(\gamma_0 - 1)(v_{\text{HS}} - v_{\text{LS}})^2/v_c \quad (19)$$

$$\Delta(x) = 2\Gamma(x)\frac{v_{\text{M}} - v_{\text{LS}}}{v_{\text{HS}} - v_{\text{LS}}} \quad (20)$$

The volume $v_c = V/N$ is the volume per complex molecule. Note that v_0 does not enter these formula, so that all quantities are experimentally accessible. The volume changes per molecule $\gamma_0(v_{\text{HS}} - v_{\text{LS}})$ and $\gamma_0(v_{\text{M}} - v_{\text{LS}})$ are obtained by comparing the unit cell volumes $v_{c,\text{HS}}$, $v_{c,\text{LS}}$, and $v_{c,\text{M}}$ of the crystal in the HS and LS states and the isomorphous metal compound, respectively, measured by X-ray diffraction. Because of the temperature dependence of the unit cell volume, which takes place without ST, the volumes have to be taken at the same temperature by extrapolation. The elastic constants K and γ_0 can be measured for example by Brillouin scattering.

This model so far described for spherical defects was later on extended for anisotropic defects [125b, 125c].

8.3.5 Influence of a Magnetic Field

Knowing the free energy of the system, thermodynamics predicts the transition behavior in an applied magnetic field if the magnetic response of the molecules is known, which is the susceptibility of the two spin states. A decrease of the transition temperature in an applied magnetic field B is expected because of the decrease in energy of the molecules in the HS state by its magnetic moment $\mu_{\text{H}}S = \chi B$. Adding the energy shift $-1/2\chi B^2$ to the free energy, the shift of the transition temperature $\Delta T_{1/2}$ can be calculated:

$$\Delta T_{1/2} = -\chi B^2 / 2\Delta S_{\text{HL}}(T_{1/2}) \quad (21)$$

where $\Delta S_{\text{HL}}(T_{1/2})$ is the entropy difference between HS and LS states at the transition temperature.

Qi et al. [176] were the first to measure the shift of the transition curve of the compound $[\text{Fe}(\text{phen})_2(\text{NCS})_2]$ in an applied magnetic field of 5.5 T. The compound is well suited for measuring small shifts as the transition at $T_{1/2} = 178$ K with a hysteresis widths of <0.5 K is very steep. The transition shifts by $-0.10(4)$ K compared with the calculated value of -0.06 K (which is half of the value given by Qi et al. because the integration factor 1/2 is missing in their article).

Later Bousseksou et al. [177] repeated the measurement in a large pulsed magnetic field of 32 T, which corresponds to an expected temperature shift at $T_{1/2}$ of 2.0 K. The HS fraction was determined by optical reflectivity. The pulsed field has a rise time of 75 ms and a decay time of about 0.5 s. The hysteresis leads to a complex response of the HS fraction versus time. An increase of the HS fraction is obtained with an irreversible (reversible) character in the ascending (descending) branch of the hysteresis loop. The time dependence of the HS fraction provides information on the kinetics of the SC process, which has been qualitatively discussed. Independently, magnetic field experiments were also performed on a Co^{III} complex [178] and a Mn^{III} SC complex [35b].

8.3.6 Two-step Spin Transition

8.3.6.1 First Observations in Mononuclear Complexes

The first observation of an anomaly of the ST behavior of a step near $T_{1/2}$ in the compound $[\text{Fe}(\text{2-pic})_3]\text{Cl}_2 \cdot \text{EtOH}$ in 1982 by Köppen et al. [117] has led to many speculations about the origin of the so-called “two step spin transition”. The structure of this compound remains the same during the ST and shows no peculiarities [126]. Based on the ideas of the lattice expansion model an anomalous behavior of the elastic properties was first discussed. It turned out that a few percent variation of the bulk modulus easily leads to deviations from the “normal” transition curves. This procedure, which tended to trace back the anomaly of the transition curve to an anomaly of the bulk modulus, was unsatisfactory and was not followed further. Later it was found that the step in $[\text{Fe}(\text{2-pic})_3]\text{Cl}_2 \cdot \text{EtOH}$ most likely arises from

short range interactions, whereby ...-HS-LS-HS-LS-... formation appears to be energetically favored (see below).

The second anomalous transition with a pronounced step, a plateau of ca. 40 K, was observed by Petrouleas and Tuchagues in 1987 by Mössbauer spectroscopy and magnetic susceptibility measurements on the compound Fe[(5NO₂-sal-N(1,4,7,10))] (5-NO₂-sal-N(1,4,7,10) = 2,2'-(2,5,8,11-tetraazadodeca-1,11-diene-1,12-diyl)4-nitrophenolato [179]. In 1989, Sasaki and Kambara proposed a two-sublattice-model with a “ferromagnetic” type of interaction inside a sublattice and an “antiferromagnetic” type of interaction between the sublattices [180] and could show, that such an interaction scheme produces steps without special assumption concerning elastic properties. The fact that Kambara considered a Jahn–Teller interaction to be responsible for the cooperativity is not important in this context. The consequences of sublattice structure formation were explored in the theory of magnetism. By mapping the ST energy expressions to an Ising Hamiltonian as was done by Wajnflasz [167] the solutions obtained in magnetism could be reinterpreted in the context of spin crossover. This way complete phase diagrams were worked out for two-sublattice-models and the region of existence of two-step-transitions was given [181, 182]. The sublattice picture seemed to be supported by an X-ray diffraction study of [Fe(5NO₂-sal-N(1,4,7,10))] showing different lattice sites for HS and LS complexes inside the step region [183]. It was proved later with a new crystallographic data set that all sites are equivalent [184].

8.3.6.2 Specific Heat Measurement on a Two-step Spin Transition

The free energy, which was successfully used to describe gradual spin transitions, predicts the specific heat associated with the ST of the compound. A test of the generalized free energy equation of Slichter and Drickamer [169] was first undertaken on the gradual ST of the deuterated compound [Fe_xZn_{1-x}(2-pic-ND₂)₃]Cl₂ · EtOD for a series of concentrations x [184]. It was shown that the specific heat is adequately described by a sum of the specific heat of the lattice and the contribution from the inner degrees of freedom of the SC molecules. Differentiating the Gibbs free energy ($C_p(T) = -T\partial^2 G/\partial T^2$)

$$G(x, \gamma_{\text{HS}}, T) = x(\gamma_{\text{HS}}\Delta G_{\text{HL}}(T) - TS_{\text{mix}} + G_{\text{I}}(x, \gamma_{\text{HS}})) + xG_{\text{LS}}(T) + (1-x)G_{\text{Zn}}(T) \quad (22)$$

$$G_{\text{I}}(x, \gamma_{\text{HS}}) = x\Delta\gamma_{\text{HS}} - x\Gamma\gamma_{\text{HS}}^2$$

where the interaction term G_{I} is assumed to be independent of temperature, one obtains:

$$C_p(x, \gamma_{\text{HS}}, T) = xC_p^{\text{HL}}(\gamma_{\text{HS}}, T) + xC_p^{\text{LS}}(T) + (1-x)C_p^{\text{Zn}}(T) \quad (23)$$

$$C_p^{\text{HL}}(\gamma_{\text{HS}}, T) = -T \left[\gamma_{\text{HS}} \frac{\partial^2 \Delta G_{\text{HL}}}{\partial T^2} + \frac{\partial \gamma_{\text{HS}}}{\partial T} \left(\frac{\partial \Delta G_{\text{HL}}}{\partial T} - \frac{\partial S_{\text{mix}}}{\partial \gamma_{\text{HS}}} \right) \right]$$

The shape of the formula of the specific heat $C_p^{\text{HL}}(\gamma_{\text{HS}}, T)$ of an ensemble of SC molecules is derived by use of the equilibrium condition $(\partial G/\partial \gamma_{\text{HS}}) = 0$. C_p^{HL} leads to a pronounced peak in the transition region mainly determined by the derivative of the HS fraction $\partial \gamma_{\text{HS}}/\partial T$. This peak, the area of which is proportional to the concentration x of iron molecules, superimposes the monotonically increasing heat capacity $x C_p^{\text{LS}}(T) + (1-x) C_p^{\text{Zn}}(T)$ of the lattice. The shape of the peak was well reproduced and the quantitative analysis fits 95% of the area for all concentrations x [185].

The heat capacity of the two-step ST $[\text{Fe}(2\text{-pic})_3]\text{Cl}_2 \cdot \text{EtOH}$ was already measured by Kaji and Sorai [62] in 1985. The specific heat curve has two narrow peaks at both sides of the step as is expected from the term proportional to $\partial \gamma_{\text{HS}}/\partial T$ in C_p^{HL} . Jakobi et al. re-measured this curve together with the pure zinc compound and zinc diluted mixed crystal $[\text{Fe}_{0.73}\text{Zn}_{0.27}(2\text{-pic})_3]\text{Cl}_2 \cdot \text{EtOH}$ in order to get access to all three terms of $C_p(T)$. While the gradual transition of the $\text{Fe}_{0.73}\text{Zn}_{0.27}$ compound was perfectly fitted, the two-step-transition at $x = 1$ showed significant deviations of the measured entropy of the ensemble of SC molecules:

$$S(T) - S_{\text{LS}}(T) = \int_0^T \frac{C_p(T) - C_p^{\text{LS}}(T)}{T} dT \quad (24)$$

from the calculated entropy ($S = -\partial G/\partial T$):

$$S(T) - S_{\text{LS}}(T) = \gamma_{\text{HS}} \Delta S_{\text{HS}}(T) + S_{\text{mix}}(\gamma_{\text{HS}}) \quad (25)$$

in the temperature region of the step. In Fig. 10 the difference $S(T) - S_{\text{LS}}(T) - \gamma_{\text{HS}} \Delta S_{\text{HL}}(T)$ is plotted against the HS fraction γ_{HS} [186] (smooth curve), such that the S_{mix} is the theoretical value of the mean field theory according to Eq. (24). Taking the experimental values $S(T) - S_{\text{LS}}(T)$ from the integration of the specific heat data (Eq. 24) and subtracting the entropy contribution of non interacting molecules $\gamma_{\text{HS}} \Delta S_{\text{HL}}(T)$ an experimental mixing entropy is obtained which in the step region is much less than the theoretical one (Fig. 10).

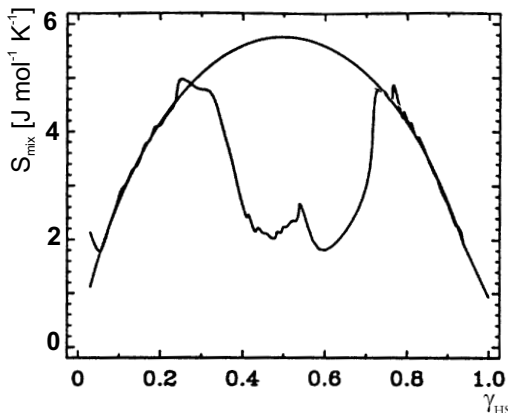


Fig. 10. The entropy difference $S - S_{\text{LS}} - \gamma_{\text{HS}} \Delta S_{\text{HL}}$ as function of the HS fraction γ_{HS} obtained by Eqs. (24) and (25) from the experimental data $C_p(T)$ and $\gamma_{\text{HS}}(T)$ (experimental points connected by a solid line). In mean field theory the entropy difference is equal to the mixing entropy S_{mix} (solid line) [186].

The deviation from a random mixture of molecules in HS and LS state causes the decrease in entropy in the step region. The reason for such a deviation is, of course, the cooperative interaction, which deviates from the mean field **interaction term** G_I in Eq. (22). Thermodynamically a “loss” of entropy leads to a destabilization, which must be compensated by a decrease in enthalpy as a result of the interaction between the spin changing molecules. As done for the entropy the difference of enthalpies $H(T) - H_{LS}(T)$ can be obtained by integration of the specific heat curves:

$$H(T) - H_{LS}(T) = \int_0^T (C_p(T) - C_p^{LS})dT \quad (26)$$

The interaction term is obtained from the Gibbs free energy of Eq. (22) calculating $H = G + TS$ which leads to:

$$G_I = H(T) - H_{LS}(T) - \gamma_{HS}\Delta H_{HL} \quad (27)$$

In Fig. 11, the interaction G_I is plotted versus the HS fraction γ_{HS} . The G_I values obtained by integration of $\int_0^T (C_p(T) - C_p^{LS})$ minus $\gamma_{HS}(T)\Delta H_{HL}$ are the experimental points (+), which are significantly lower around $\gamma_{HS} = 0.5$ in the step region from the mean field interaction term $G_I = \Delta\gamma_{HS} - \Gamma\gamma_{HS}^2$ (solid line). Obviously, the decrease in entropy reflects a partial arrangement of HS and LS molecules being not at random but showing some ordering which is stabilized by a further decrease of the energy as compared to the mean field energy which favors a random distribution.

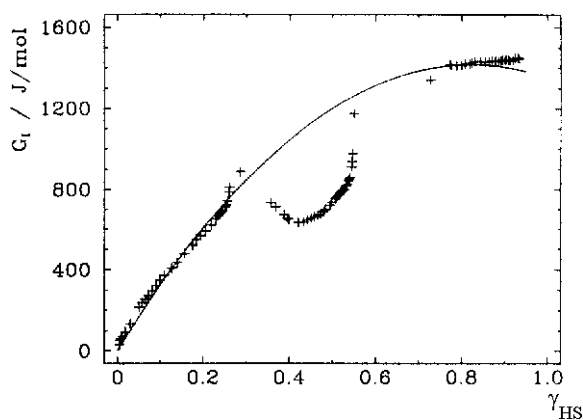


Fig. 11. The interaction Gibbs free energy G_I as function of the HS fraction γ_{HS} (+) obtained by use of Eqs. (26) and (27) from the experimental data $C_p(T)$ and $\gamma_{HS}(T)$. The solid line is the calculated mean field contribution $G_I = \Delta\gamma_{HS} - \Gamma\gamma_{HS}^2$ to the interaction term [174].

8.3.6.3 Two-step Transition of a Dinuclear Complex

The two-step transition curve of a dinuclear iron(II) complex $[\text{Fe}(\text{bt})(\text{NCS})_2]_2\text{bpym}$, where bt denotes 2,2'-bi-2-thiazoline and bpym for 2,2'-bipyrimidine, observed by Real et al. [187] was simulated in quite a different way. The simple assumptions of an asymmetric energy level scheme of the dinuclear molecule and an attractive

interaction between molecules with one iron in the HS and the other in the LS state, (HS,LS) and (LS,HS) molecules, were successful. The excitation enthalpy of the LS molecule (LS,LS) with both sites in the LS state to a (LS,HS) or (HS,LS) molecule was assumed to be different by a value W from half the enthalpy ΔH needed for the conversion of both LS states to the HS molecule (HS,HS). For negative values of W a number of N (HS,LS) and (LS,HS) molecules are lower in energy by NW than N (LS,LS) and (HS,HS) molecules, so that HS,LS pairs are favored in thermodynamic equilibrium. With the fractions x, y, z ($x + y + z = 1$) for (LS,LS), (HS,LS) or (LS,HS), and (HS,HS) molecules, respectively, and the entropy difference $\Delta S/2$ between the HS and LS state of one site, and taking into account only mean field interaction between sites in LS and HS states of iron(II) in different dimers the authors obtained the following free energy [187]:

$$F = y(\Delta H/2 + W) + z\Delta H + \Gamma(xy + yz + 2xz) - (y/2 + z)T\Delta S - TS_{\text{mix}} \quad (28)$$

where $S_{\text{mix}} = -R(x \ln x + y \ln y + z \ln z)$ is the mixing entropy of the three species. Rewriting Eq. (28) using the HS fraction $\gamma_{\text{HS}} = y/2 + z$ and dropping constant energies the equation obtains a shape similar to the mean field free energy equation of Slichter and Drickamer [169] for the first two terms, an attractive interaction between y molecules and the energy shift W concerning these molecules:

$$F = (\Delta H - T\Delta S)\gamma_{\text{HS}} - \Gamma\gamma_{\text{HS}}^2 - 1/2\Gamma y^2 + Wy - TS_{\text{mix}} \quad (29)$$

The interaction scheme implicitly favors y -type dinuclear molecules by the interaction term $-1/2\Gamma y^2$ even if the energy levels are equidistant ($W = 0$) and this way causes already a small step in the transition curve. Such a term cannot be justified by molecular properties and represents an undesirable term inherently introduced by the Ansatz of Eq. (28). A positive energy W decreases this step and, more importantly, by a negative W pronounced steps can be simulated. This work has shown that short range correlation (preference of (HS, LS) pairs) of the distribution of the spin states gives rise to step transitions so that HS and LS sublattices are not necessarily a prerequisite for stepwise spin transition.

8.3.6.4 Monte Carlo Simulation of Two-step Transitions

A great success was the simulation of the two step transition in $[\text{Fe}(2\text{-pic})_3]\text{Cl}_2 \cdot \text{EtOH}$, the transition curves of the $(\text{Fe}_x\text{Zn}_{1-x})$ dilution series and the anomalous relaxation curves of the LIESST state (Section 8.3.7). The insight gained by the simulation results of the dinuclear compound encouraged to start Monte Carlo simulations based on a very simple picture, which does not start out from any correlations from the beginning, like the presence of sublattices or dimers. The interaction scheme is given as simple as possible with a minimum of parameters and entirely equivalent lattice sites. Kohlhaas et al. [188] have treated successfully the thermal ST in the system $[\text{Fe}_x\text{Zn}_{1-x}(2\text{-pic})_3]\text{Cl}_2 \cdot \text{EtOH}$, and Romstedt et al. [189] have also reproduced successfully the anomalous relaxation curves recorded after LIESST. At that time the behavior of the step in a metal dilution series and

under small pressure (~ 1 kbar) was already known from experiment [190]. The step was found to vanish already for small Zn concentrations ($x \approx 0.9$) such that the transitions in mixed crystals with $x < 0.9$ can be described as gradual ones. The mean field interaction energy of the crystal of N sites with xN SC molecules, is the starting point (Eq. 14),

$$E_I = x^2 N \Delta \gamma_{HS} - x^2 N \Gamma \gamma_{HS}^2 \quad (30)$$

with well defined values for Δ and Γ . Note that Γ and Δ are defined such that $\Gamma(x)$ now equals $x\Gamma$ and $\Delta(x)$ equals $x\Delta$. The short-range interaction is introduced by only one parameter for nearest and next nearest neighbor interactions, such that their mean field sum vanishes at every site. Such a minimal extension of the theory preserves the mean field interaction constant. The interaction energy of Eq. (30) is extended by a sum over all lattice sites in the HS state. Interaction constants between only one type of spin states and other metal centers are sufficient to describe the mutual interaction between all types of sites [184]. If the two center interaction can be expressed by the properties P (i. e. \vec{P} stands for an elastic dipole tensor) of the centers, the total sum of interaction energies was rearranged in such a way that not the property (\mathbf{P}_{HS} , \mathbf{P}_{LS} and \mathbf{P}_M) of the sites but the differences $\mathbf{P}_{HS} - \mathbf{P}_{LS}$ and $\mathbf{P}_M - \mathbf{P}_{LS}$ are attributed to the HS and M sites, respectively. The sum collecting the contributions of short range interactions:

$$\Delta E_I = - \sum_{\substack{r_i=n,nn, \\ i=i_H}} \vec{J}_{HH}^{r_i} v_H^{r_i} + \vec{J}_{HM}^{r_i} v_M^{r_i} \quad (31)$$

runs over all sites $i = i_{HS}$ in the HS state. $v_H^{r_i}$ and $v_M^{r_i}$ are the numbers of next ($r_i = n$) and next nearest ($r_i = nn$) molecules in the HS state and metal sites M, respectively. The four interaction constants $\vec{J}_{SS}^{r_i}$ ($SS = HH, HM$) are reduced to two constants by the requirement that ΔE_I vanishes. If v^n and v^{nn} are the number of next and next nearest neighbors, respectively, then there are $v^n \gamma_{HS}$ and $v^{nn} \gamma_{HS}$ sites in the HS state. The mean field interaction energy ΔE_m with the central HS site:

$$\Delta e_m = - \left(\vec{J}_{HH}^n v^n + \vec{J}_{HH}^{nn} v^{nn} \right) \gamma_{HS} \quad (32)$$

vanishes for $\vec{J}_{HH}^{nn} = \vec{J}_{HH}^n v^n / v^{nn}$. The molecules with metal centers $M = \text{Zn}$ are very similar to the molecules in the HS state, so that the same ratio between the two neighboring shells are imposed. The ratio of the HM and HH interaction constants $\vec{J}_{HM}^r \vec{J}_{HH}^r = 0.8$ ($r = n, nn$) is also taken from the mean field evaluation [125c], so that only one fit parameter is left.

For the Monte Carlo simulations the free energy difference $\Delta f_{HL}(T)$ and the values $\Delta = 275 \text{ cm}^{-1}$ and $\Gamma = 175 \text{ cm}^{-1}$ from the calculation of the transition curves of the diluted series ($x \leq 8$) [188] were used.

In Fig. 12, the experimental and the simulated data of the metal ($M = \text{Zn}$) dilution series are plotted. The step of the transition curve is very sensitive to the concentration of Zn and vanishes already at $x = 0.9$. The simulated curves in Fig. 12 were calculated with the parameter $J^n = -17.4 \text{ cm}^{-1}$ fitted to the $x = 1$ transition curve.

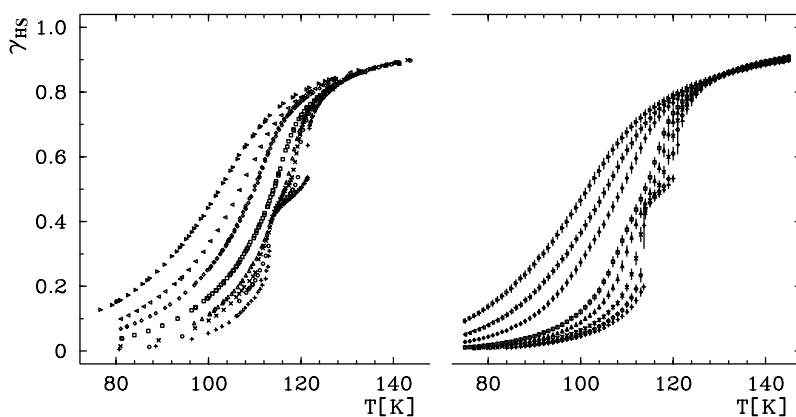


Fig. 12. The effect of metal dilution on the ST curve of $[\text{Fe}_x\text{Zn}_{1-x}(\text{2-pic})_3]\text{Cl}_2 \cdot \text{EtOH}$ ($x = 1; 0.98; 0.94; 0.89; 0.86; 0.70; 0.60; 0.50$, from right to left). The transition temperatures increase with increasing iron concentrations x . The Monte Carlo simulations on the right side fit with the experimental data [190] on the left side.

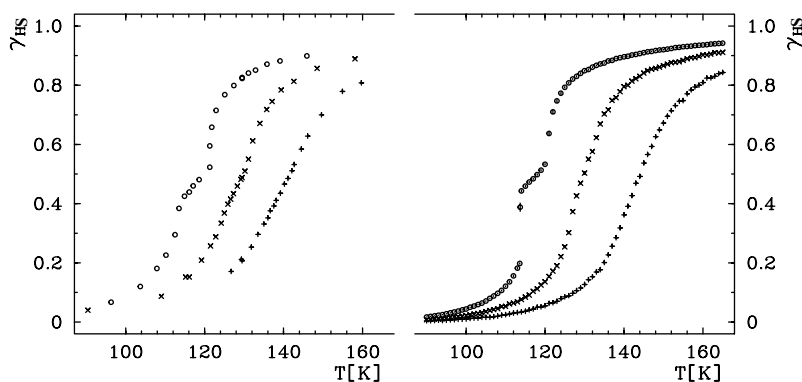


Fig. 13. The effect of pressure on the ST curve of $[\text{Fe}(\text{2-pic})_3]\text{Cl}_2 \cdot \text{EtOH}$ ($p = 1, 600, 1350$ bar, from left to right). The transition temperatures increase with increasing pressure. The Monte Carlo simulation on the right side fit with the experimental data [190] on the left side.

J^n , the sign of which is opposite to the long-range interactions and J^{nn} , refers to an antiferromagnetic type of interaction in accordance to a preferred $\dots\text{HS}\text{--}\text{LS}\text{--}\text{HS}\text{--}\text{LS}\text{--}\dots$ formation.

The absolute value of the interactions with the nearest neighbor molecules is of comparable size with that of the long range interactions. For $\nu^n = 6$ neighbors the interaction energy is approximately -105 cm^{-1} . Nevertheless, the appearance of a step in the transition curve sensitively depends on other parameters involved. Small applied pressures on the order of $p = 1$ kbar already suppresses the step in the transition curve as shown in Fig. 13.

The energy shift of the HS state is equal to $p\delta v_{\text{HL}}$, where $\delta v_{\text{HL}} = 14 \text{ \AA}^3$ is the volume increase of the unit cell for each molecule changing spin from LS to HS [191]. These shifts of $p\delta v_{\text{HL}} = 42 \text{ cm}^{-1}$ and 95 cm^{-1} for $p = 600 \text{ bar}$ and 1350 bar , respectively, are small energies as compared to the range of energy separations in SC molecules. The simulated transition curves in Fig. 13 again reproduce the observed behavior of the transition curves.

Correlations between spin states can be analyzed from the Monte Carlo samples in thermal equilibrium. The correlation length of an antiferromagnetic order has been estimated to be very short (for details see [192]), not larger than the next nearest neighbor distance and is therefore not observable by X-ray diffraction.

8.3.7 LIESST Experiments

The most striking result of the last twenty years of SC research is certainly the discovery of the photo-switching of spin states in Fe^{II} coordination compounds in 1984 [193, 194]. This effect was actually accidentally first observed on a single crystal of the SC complex $[\text{Fe}(\text{ptz})_6](\text{BF}_4)_2$. Irradiating the compound with green light into the ${}^1\text{A}_1 \rightarrow {}^1\text{T}_{1,2}$ absorption bands at 20 K, that is in the LS region, resulted in the population of a metastable HS state with a virtually infinite lifetime at this temperature. This phenomenon became known as the LIESST effect (light-induced excited spin state trapping). Thermal relaxation to the thermodynamically stable LS state was observed by warming the compound up to $\sim 50 \text{ K}$. This relaxation occurs by non adiabatic tunneling through the energy barrier between the potential wells of the two states, whereby the observed temperature dependence of the relaxation rate is due to thermal population of the vibronic levels of the ${}^5\text{T}_2$ manifold [195]. It was also possible to directly come back to the LS state by irradiating into the ${}^5\text{T}_2 \rightarrow {}^5\text{E}$ absorption band with red light for the initial excitation followed by two inter-system crossing (ISC) processes ${}^5\text{T}_2 \rightarrow {}^3\text{T}_{1,2} \rightarrow {}^1\text{A}_1$. This back switching has been termed “reverse-LIESST” [196]. The mechanism of these photo-switching processes is depicted in Fig. 14.

Excitation with green light at low temperature affords the ${}^1\text{A}_1 \rightarrow {}^1\text{T}_{1,2}$ transitions which is followed by a fast relaxation cascading over two successive ISC steps, ${}^1\text{T}_{1,2} \rightarrow {}^3\text{T}_{1,2} \rightarrow {}^5\text{T}_2$ populating thereby the metastable ${}^5\text{T}_2$ state. As radiative relaxation ${}^5\text{T}_2 \rightarrow {}^1\text{A}_1$ is spin and parity forbidden and decay by thermal tunneling to the ground state ${}^1\text{A}_1$ very slow, the lifetime of the ${}^5\text{T}_2$ state is found to be practically infinite at sufficiently low temperature, for example weeks at 20 K in case of $[\text{Fe}(\text{ptz})_6](\text{BF}_4)_2$. Fig. 14 also shows that red light irradiation into the spin and parity forbidden ${}^1\text{A}_1 \rightarrow {}^3\text{T}_1$ band should also lead to a population of the metastable ${}^5\text{T}_2$ state, provided the excitation wavelength is sufficiently separated from that affording the back switching of the LIESST state [196].

Fig. 15 shows the single-crystal absorption spectra of $[\text{Fe}(\text{ptz})_6](\text{BF}_4)_2$ recorded at 20 K after irradiation at 514 nm affording the double ISC process ${}^1\text{A}_1 \rightarrow {}^1\text{T}_{1,2} \rightarrow {}^3\text{T}_{1,2} \rightarrow {}^5\text{T}_2$ (Fig. 15b), and at 980 nm affording the single ISC process ${}^1\text{A}_1 \rightarrow {}^3\text{T}_{1,2} \rightarrow {}^5\text{T}_2$ (Fig. 15d), both populating the long-lived metastable LIESST state and the reverse-LIESST effect by irradiation at 820 nm (Fig. 15c) [21].

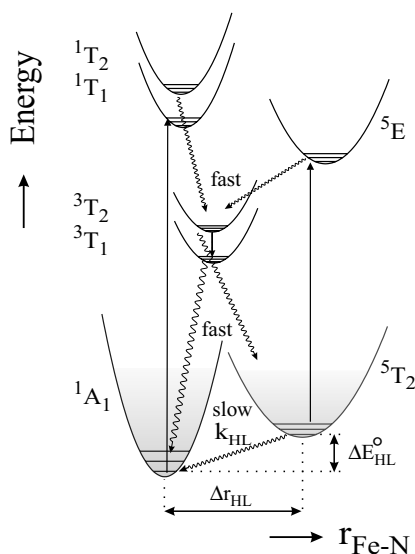


Fig. 14. Schematic illustration of LIESST and reverse LIESST of a d^6 complex in the SC range. Spin allowed d–d transitions are denoted by arrows and the radiationless relaxation processes by wavy lines [17].

The LIESST effect was also observed on other compounds [17, 18, 20] and appeared actually to be a common phenomenon for Fe(II) complexes exhibiting thermal SC [197]. A major difference, however, is the lifetime of the LIESST state at a given temperature, which depends strongly on the ligand field strength, viz. the weaker the ligand field strength, the smaller the difference ΔE_{HL}^0 between the lowest vibronic levels of the HS and LS states, the longer the lifetime of the LIESST state. The difference Δr_{HL} in the metal–ligand bond distance between HS and LS state (Fig. 2) is also to be considered: the larger this quantity, the longer the lifetime of the LIESST state.

Although LIESST was first discovered on a single crystal, it can also occur for SC molecules embedded in polymer films, Langmuir Blodgett films or in KBr pellets [198–201]. LIESST is not restricted to compounds with FeN_6 cores as the phenomenon was also observed for compounds of the FeP_4Cl_2 type with phosphorus coordinating ligands [202]. Recently the effect was even reported for an Fe^{III} complex [203] contrary to the previous expectations [17]. In this case the trapping of the metastable state might be assisted by a photo-induced crystallographic phase transition.

Another appealing aspect of the LIESST effect concerns the possibility of probing cooperative effects of the spin transition by analyzing the shape of the HS \rightarrow LS relaxation curves. For non cooperative compounds such as for instance diluted systems, single exponential relaxation curves are always observed. Cooperative effects, however, give rise to strong deviations from first-order kinetics [195, 204] with sigmoidal curves. This shape must be interpreted as a self-acceleration of the HS \rightarrow LS relaxation with increasing proportions of LS fraction. The acceleration stems from the build-up of an internal pressure (image pressure) with increasing LS proportions, which in turn is caused by the volume change of the complexes associated with the spin transition.

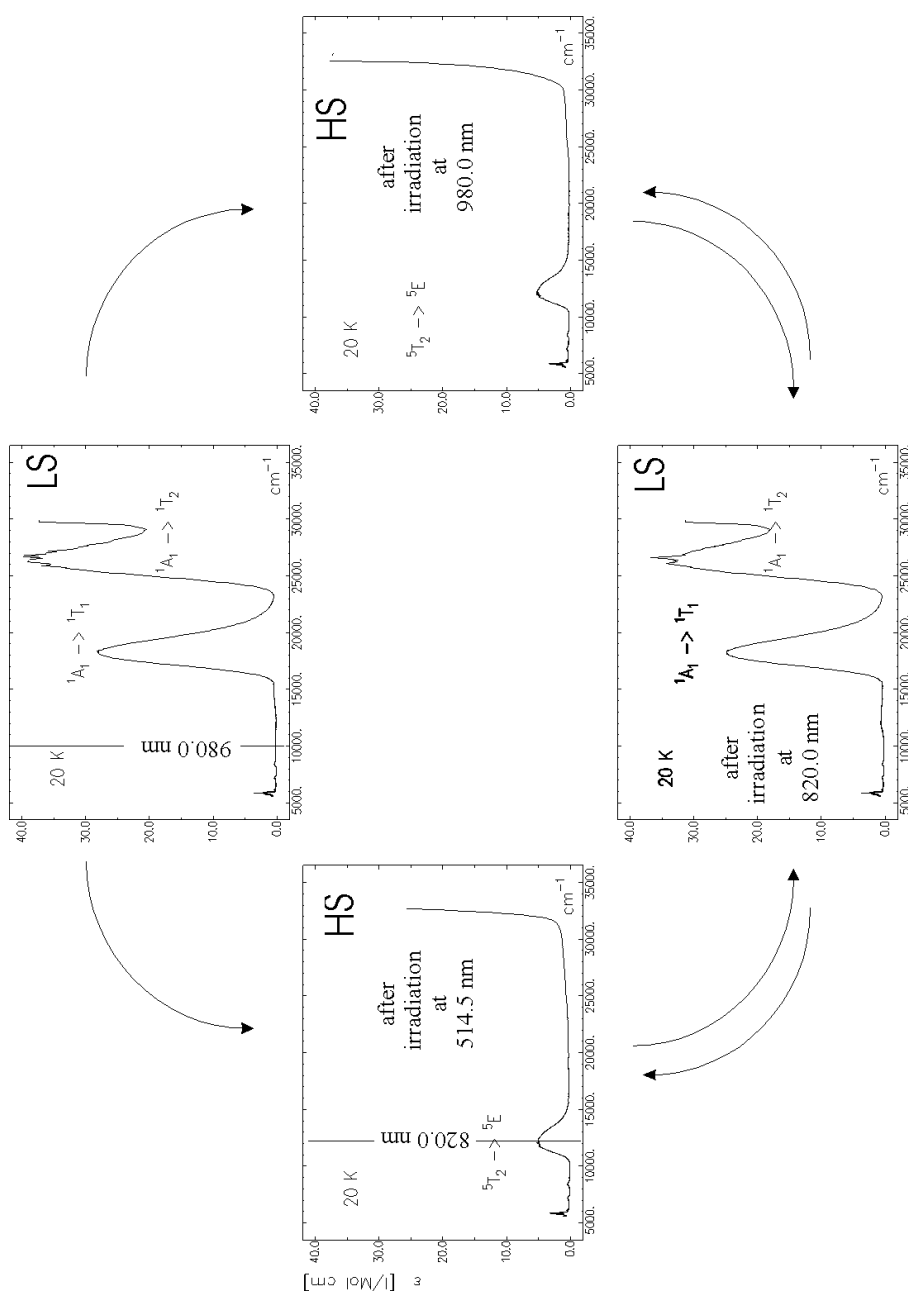


Fig. 15. Single-crystal absorption spectra of $[\text{Fe}(\text{ptz})_6](\text{BF}_4)_2$ at 20 K: a) normal spectrum before irradiation, b) after irradiation into the spin-allowed transition of the LS state, ${}^1\text{A}_1 \rightarrow {}^1\text{T}_1$, at 514.5 nm, c) after subsequent irradiation into the maximum of the spin-allowed transition of the HS species, ${}^5\text{T}_2 \rightarrow {}^5\text{E}$, at 820 nm, and d) after irradiation into the spin-forbidden transition, ${}^1\text{A}_1 \rightarrow {}^3\text{T}_1$, at 980 nm [17, 21, 216].

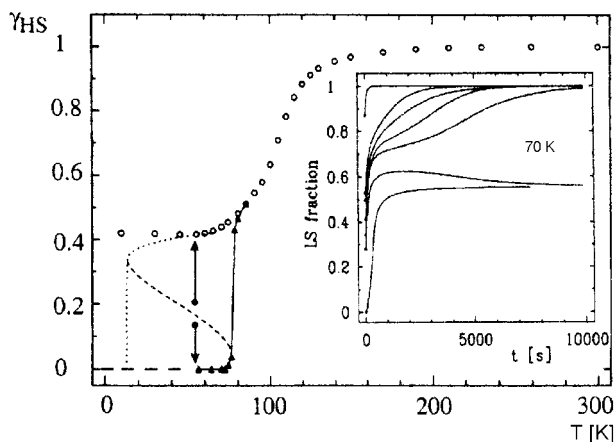


Fig. 16. Spin transition in $[\text{Fe}(\text{etz})_6](\text{BF}_4)_2$: (\circ) normal cooling mode; (\times) heating mode after irradiation at 820 nm. The arrows indicate relaxation processes which are possible inside the hysteresis subsequent to irradiation. The relaxation direction inside the hysteresis is determined by the existence of a critical LS concentration at a given temperature, as visualized by the sigmoidal curve inside the loop [205b].

Light-induced bistability was observed for the first time for $[\text{Fe}(\text{etz})_6](\text{BF}_4)_2$ with $\text{etz} = 1\text{-ethyltetrazole}$ [205] opening a new area of photo-magnetic investigations (Section 8.4.2.3). In this system, two inequivalent lattice sites in a ratio of 2:1 were detected by X-ray analysis. Site A reveals a thermal HS \rightarrow LS transition around 105 K whereas site B remains in the HS state down to liquid helium temperatures as we can see in Fig. 16. Irradiation with red light affords first the population of the metastable LS state, which becomes after reaching some critical LS fraction the ground state of the system. As the temperature is raised to above 80 K, site B goes back to the HS state (Fig. 16). This can be regarded as a thermal ST in the heating mode with a very large hysteresis. The corresponding branch in the cooling mode is not accessible in a simple temperature cycle, because of the macroscopic nature of the energy barrier between the HS and LS state of the whole crystal.

8.3.8 Formation of Correlations During HS \rightarrow LS relaxation

Relaxation measurements following laser excitation of the metastable HS state (LIESST) under different irradiation conditions provided a direct proof of the formation of correlations in the SC compound $[\text{Fe}(\text{2-pic})_3]\text{Cl}_2 \cdot \text{EtOH}$. For infinite (long) range interactions, the decay rate depends only on the fraction of molecules in the HS state:

$$\frac{d\gamma_{\text{HS}}}{dt} = -k_{\text{HL}}(\gamma_{\text{HS}})\gamma_{\text{HS}} \quad (33)$$

The system $[\text{Fe}(\text{ptz})_6](\text{BF}_4)_2$ and its $(\text{Fe}_x\text{Zn}_{1-x})$ mixed crystals was the first system where the decay rates were measured in detail [204]. The rate k_{HL} was found to depend exponentially on the HS fraction γ_{HS} according to $k_{\text{HL}} = k_{\text{HL}}^0 \exp(-\alpha\gamma_{\text{HS}})$ leading to self-accelerated sigmoidal relaxation curves. In systems with strong short range interactions the decay probability of each individual complex will also depend on the spin state of the neighboring molecules. As a result correlations may build up during the decay, and these, in turn, may change the decay probability of the whole system.

In SC systems there is the unique possibility to prepare metastable HS states with a random distribution of spin states of any HS fraction γ_{HS} employing the LIESST effect. The preparation of such a random distribution of spin states makes use of the fact that the excitation of a LS molecule by a photon is a random process. As long as the optical density at the irradiation wavelength is low enough so that there are no large intensity gradients of the exciting light inside the crystal, concentration gradients during the light induced $\text{HS} \rightarrow \text{LS}$ conversion are negligible.

Figure 17 shows the single crystal spectra of $[\text{Fe}(\text{2-pic})_3]\text{Cl}_2 \cdot \text{EtOH}$ before and after irradiation at 647 nm ($15\,456\text{ cm}^{-1}$), that is into the tail of the MLCT transition, using a Kr^+ laser. For this irradiation wavelength, the light induced $\text{LS} \rightarrow \text{HS}$ conversion takes only a short time (<1 min), as was confirmed by comparison of the HS bands after irradiation and at temperatures above the transition at 200 K (details are given elsewhere [189]). From the spectra recorded at constant time intervals of 5 min at 23 K included in Fig. 17, the full $\text{HS} \rightarrow \text{LS}$ relaxation curve shown in Fig. 18a was extracted. The decay deviates strongly from single exponential with the rate increasing with increasing fraction of LS molecules at the beginning. The self-acceleration region extends to $\gamma_{\text{HS}} > 0.5$, at lower HS fractions the decay slows down considerably but the rate is still not constant. The dashed line represents the

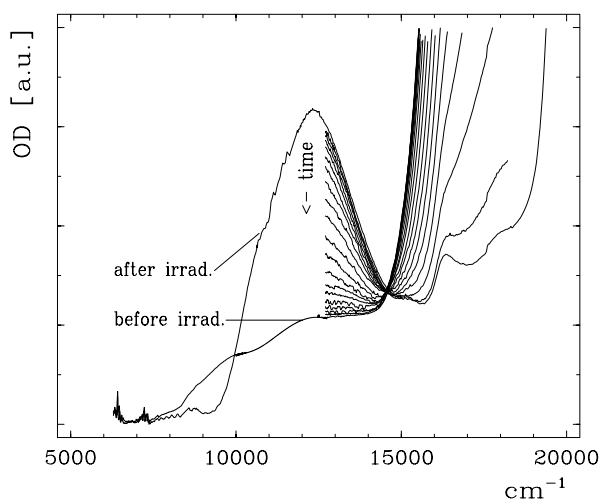


Fig. 17. Single-crystal absorption spectra of $[\text{Fe}(\text{2-pic})_3]\text{Cl}_2 \cdot \text{EtOH}$ at 23 K before and after irradiation with light at $15\,500\text{ cm}^{-1}$ and $\text{HS} \rightarrow \text{LS}$ relaxation spectra in time intervals of 5 min (\rightarrow increasing time of intervals) following irradiation [189].

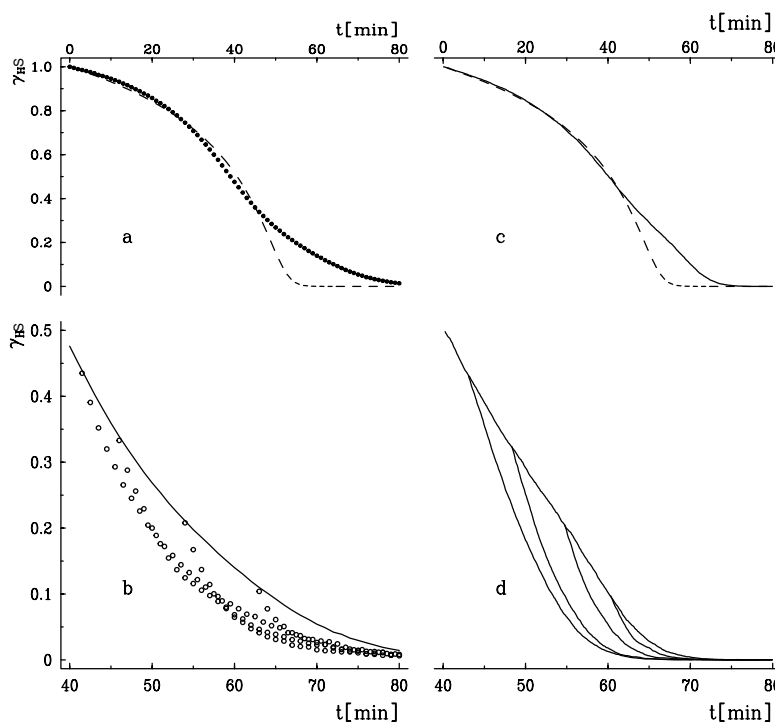


Fig. 18. HS \rightarrow LS relaxation curves $\gamma_{\text{HS}}(t)$ at 23 K for various starting values of the HS content $\gamma_{\text{HS}}(t = 0)$ for $[\text{Fe}(2\text{-pic})_3]\text{Cl}_2 \cdot \text{EtOH}$. (a) The relaxation curve starting at $\gamma_{\text{HS}}(t = 0) = 1$ (full circles). The dashed curve is calculated using mean field approximation. (b) Time shifted relaxation curves for $\gamma_{\text{HS}}(t = 0) < 0.5$ (open circles) together with the decay curve $\gamma_{\text{HS}}(t = 0) = 1$ from (a) as a reference represented by a spline function. The corresponding simulated relaxation curves are plotted in (c), (b) [189]. The dashed line in (c) is the same as in (a).

theoretical decay curve calculated in mean field theory as described below. The deviations from mean field theory becomes obvious at HS fractions $\gamma_{\text{HS}} < 0.4$. There the actually observed decay of the metastable HS molecules is slower than predicted by mean field theory. The reason is that $\dots\text{HS-LS-HS-LS}\dots$ correlations are developing in the course of the decay, which stabilize the HS state. Mean field theory does not take into account such correlations. In order to prepare starting values lower than $\gamma_{\text{HS}}(t = 0) = 1$, irradiation at 676 nm ($14\,793\text{ cm}^{-1}$) close to the minimum optical density of the isosbestic point at $14\,400\text{ cm}^{-1}$ was carried out. By varying the irradiation time (typically 5–15 min at 5 mW laser power) $\gamma_{\text{HS}}(t = 0)$ could be adjusted from 0.1 up to 1.0.

In Fig. 18b, the relaxation curves for $\gamma_{\text{HS}}(t = 0) < 0.5$ are plotted together with the $\gamma_{\text{HS}}(t = 0) = 1$ curve Fig. 18a as reference curve. The decay curves are shifted in time such that the $t = 0$ point matches the reference curve. Obviously, all these curves start off at a faster rate than the rate of the reference curve at the same HS fraction. The reason is that in all such cases where the decay starts at values of

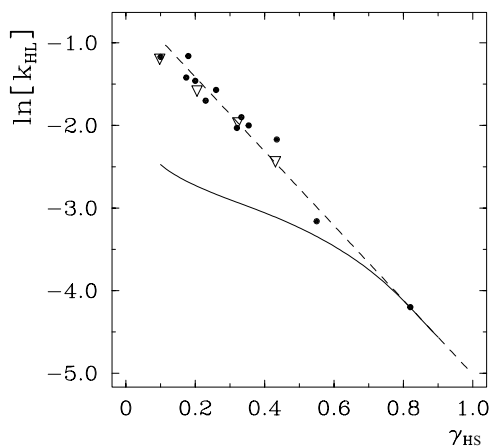


Fig. 19. Relaxation rate constants k_{HL} (at 23 K) plotted as $\ln(k_{HL})$ vs the HS fraction γ_{HS} for $[\text{Fe}(\text{2-pic})_3]\text{Cl}_2 \cdot \text{EtOH}$. The full circles are the rates at the starting values $\gamma_{HS}(t=0)$. The solid line is a spline function to the $\gamma_{HS}(t=0) = 1$ curve. The slope of the straight dashed line through the full circles is $\alpha = -4.5$. The open triangles are theoretical initial rates from Fig. 18d [189].

$\gamma_{HS}(t=0) < 1$, the crystal still contains the metastable HS molecules in random distribution, and the stabilizing correlations have not yet evolved. We consider this observation as a direct proof of correlations building up during the decay.

The findings are quantified in Fig. 19 using Eq. (33). The solid line is the spline through the logarithm of the rate constants of the reference curve. A straight line (dashed) fits to the initial rates with starting values $\gamma_{HS}(t=0) < 0.5$. These initial rates at different HS fractions are interpreted as rates belonging to a system with a random distribution of HS and LS molecules. Their dependence on the HS fraction is the same as was observed in the system $[\text{Fe}(\text{ptz})_6](\text{BF}_4)_2$ mentioned above which could be well explained within the frame of mean field theory. The open triangles in Fig. 19 are initial rates calculated with the Monte Carlo method starting from a random distribution of HS and LS molecules. The calculation of the dynamical process in the tunneling region requires a simplified Monte Carlo procedure as excitations from the LS to the HS state are negligible. The decay probability $W(\text{HS} \rightarrow \text{LS})$ depends on the energy separation ΔE_{HL} between the lowest vibronic HS state and the LS ground state of the molecule in the crystal:

$$W(\text{HS} \rightarrow \text{LS}) \propto \exp(\eta \Delta E_{HL}) \quad (34)$$

In the approximation of a non adiabatic multi-phonon process in the limit of strong vibronic coupling the parameter $\eta \approx \ln(S)/\hbar\omega$ depends on the Huang–Rhys parameter S , which is the reorganization energy in units of the quanta $\hbar\omega$ of the active vibrational mode [206]. Correlations as well as random distribution of molecules in the HS state cause a distribution of energy separations by the short range interaction term and in turn a distribution of decay times. So the initial k_{HL} value for random distribution of HS states is an average rate constant and principally different from its mean field value. But it turns out that these average values are very close to the mean field values.

With the slope $\alpha = -4.5$ of the dashed line (in Fig. 19) which was fitted to the initial decay rates, we can derive the parameter η from the expression $\alpha = -\eta 2\Gamma$ from

mean field theory. The resulting value of η comes out quite reasonable. Inserting $\Gamma = -175 \text{ cm}^{-1}$, the definition of the Huang–Rhys factor $S = 1/2f(\Delta Q_{\text{HL}})^2/\hbar\omega$ and values for Fe^{II} ($\Delta Q_{\text{HL}} = \sqrt{6} \times 0.18 \text{ \AA}$, $f = 2.0 \times 10^5 \text{ dyn cm}^{-1}$) [206] a frequency of $\hbar\omega = 290 \text{ cm}^{-1}$ for the active mode is derived, which is the value expected for the totally symmetric mode of the SC molecule.

Now we are in the position to simulate decay curves by the Monte Carlo method. The rate of HS \rightarrow LS transitions is defined by an adjustable scaling factor τ_{HL} :

$$k_{\text{HL}} = \frac{1}{\tau_{\text{HL}}} \exp(\eta\Delta E_{\text{HL}}) \quad (35)$$

The unknown time scaling factor was chosen large enough so that the result did not depend on a further increase of τ_{HL} . Then the simulation is parameter free, this means that the parameters used for the simulation of thermodynamic equilibrium transitions were also used here without any adjustments. The result is shown in Fig. 18. In Fig. 18c the simulation with and without (dashed line) short range interactions are plotted. The short range interactions stabilize the HS state for HS fractions below $\gamma_{\text{HS}} = 0.4$. The decay curves starting from random distribution at different HS fractions in Fig. 18d also show the characteristic features of the experimental one of Fig. 18b and the initial decay rates of these theoretical curves plotted as open triangles in Fig. 19 justify the whole procedure, because they are close to the mean field values we started out with. Correlation lengths have been estimated in [189] to be less than 2–3 neighboring spheres, which is of the same order as estimated in the step of the thermal transition.

It is clear that the rigorously simplified interaction scheme is far from reality. So the interaction will be different for neighbors with different relative orientation and to consider next and next nearest neighbors only is an arbitrary cut not justified in the present structure. Nevertheless, we learn that the model Hamiltonian catches the main features of the anomalous two-step transitions.

8.3.9 Nuclear Decay-induced Spin Crossover

Soon after the discovery of the Mössbauer effect more than forty years ago one learned that this technique can be used to study the physical and chemical after effects of the nuclear decay of ^{57}Co by electron capture into ^{57}Fe , $^{57}\text{Co}(\text{EC})^{57}\text{Fe}$, in solid coordination compounds. Conventional ^{57}Fe Mössbauer absorption spectroscopy uses radioactive ^{57}Co (half-life 270 days) fused into a noble metal (Pt, Rh) as the 14.4 keV γ -ray source; the emitted single line is swept over the hyperfine transition lines of the absorber material under study by normally moving the source relative to the absorber. The recorded **Mössbauer absorption spectrum** gives information on the electronic structure (valence and magnetic state) of the ^{57}Fe atoms in the absorber material [42c]. In so-called Mössbauer source experiments, one uses (in case of ^{57}Fe spectroscopy) the ^{57}Co labeled coordination compound of special interest as the Mössbauer source, normally fixed in a cryostat for variable temperature measurements, and a single-line absorber (e. g. $\text{K}_4[\text{Fe}(\text{CN})_6] \cdot 3\text{H}_2\text{O}$),

which is mounted on a transducer and moved relative to the source. In this case, one obtains a so-called **Mössbauer emission spectrum**, which bears information on the electronic structure of the nucleogenic ^{57}Fe atom during the lifetime of the 14.4 keV nuclear state.

Already some thirty years ago, we have observed anomalous resonance lines in the Mössbauer emission spectra of ^{57}Co labeled coordination compounds which could be assigned to metastable HS states of $^{57}\text{Fe}^{\text{II}}$ in the corresponding compounds, where Fe^{II} possesses a LS ground state at comparable temperatures [207–212]. Only with the discovery of the LIESST effect, we were able to understand the occurrence of such nuclear decay-induced metastable spin states. In analogy to the LIESST phenomenon, where spin state conversion and trapping is induced by an external light source, we speak here of “nuclear decay-induced excited spin state trapping” (NIESST), where the radioactive decay serves as the intrinsic molecular excitation source. A few examples will be recalled in the following.

The first observation of anomalous spin states arising from the $^{57}\text{Co}(\text{EC})^{57}\text{Fe}$ decay was made with phen complexes [208]. The system $[\text{M}(\text{phen})_3](\text{ClO}_4)_2$ with $\text{M} = ^{57}\text{Fe}_x/\text{Co}_{1-x}$, $x = 0.001$ was studied by temperature dependent Mössbauer absorption spectroscopy, and the one with $\text{M} = ^{57}\text{Co}_x/\text{Co}_{1-x}$, $x = 0.001$ by time-integral Mössbauer emission spectroscopy (TIMES). A selection of spectra for both series is shown in Fig. 20.

The neat iron complex ($\text{M} = \text{Fe}$) is a typical Fe^{II} LS compound with $^1\text{A}_1$ ground state, whereas the Co^{II} analog is HS with $^4\text{T}_1$ ground state. If Fe^{II} is doped into the host lattice of the Co^{II} compound to only 0.1% as in the present case, the tris-phen ligand field surrounding the Fe^{II} ions is still sufficiently strong such that the Fe^{II} exhibits LS behavior at all temperatures under study; Fig. 20a shows a typical Fe^{II} -LS quadrupole doublet between 300 K and 6 K. If, however, the Co^{II} compound is doped with radioactive $^{57}\text{Co}^{\text{II}}$ and used as a Mössbauer source against the single-line absorber $\text{K}_4[\text{Fe}(\text{CN})_6]$, emission spectra are obtained as shown in Fig. 20b. Down to ca. 250 K the emission spectra are much the same as the absorption spectra and show essentially only the typical Fe^{II} -LS doublet (A) and a small fraction of Fe^{III} -LS (B), arising from the loss of a valence electron after the nuclear decay. Toward lower temperatures two typical Fe^{II} -HS resonance doublets (C,D) appear with increasing intensities at the expense of the Fe^{II} -LS doublet; the Fe^{III} -LS doublet (B), however, remains practically unchanged in intensity. According to the area fractions about half of the nucleogenic ^{57}Fe ions are “trapped” in the metastable Fe^{II} -HS state in a strong field surroundings at ca. 10^{-7} s after the nuclear decay at 5 K.

If the ligand field strength is somewhat lowered such as in the ^{57}Co -labelled complex $[\text{Fe}(\text{phen})_2(\text{NCS})_2]$ as the Mössbauer source, in which thermal $\text{LS} \leftrightarrow \text{HS}$ transition occurs with $T_{1/2} \approx 175$ K [2], one obtains emission spectra as shown in Fig. 21 [207]. Clearly, the dominant or even only signal at all temperatures from 296 K down to 4.2 K is the Fe^{II} -HS quadrupole doublet, even at temperatures below 175 K, where ST occurs to the Fe^{II} -LS ground state in the iron(II) complex. A similar behavior was observed in the Mössbauer emission spectra of $[\text{Co}(\text{bipy})_2(\text{NCS})_2]$ [207, 208], $[\text{Co}(\text{Co}(2\text{-CH}_3\text{-phen})_3)(\text{ClO}_4)_2 \cdot 2\text{H}_2\text{O}]$ [209], $[\text{Co}(\text{Co}(2\text{-CH}_2\text{O-phen})_3)(\text{ClO}_4)_2 \cdot 2\text{H}_2\text{O}]$ [210], $[\text{Co}(\text{Co}(2\text{-pic})_3)\text{Cl}_2 \cdot \text{EtOH}]$ [211, 212] and $[\text{Co}(\text{Co}(\text{ptz})_6)(\text{BF}_4)_2]$ [213], whereas the corresponding iron(II) com-

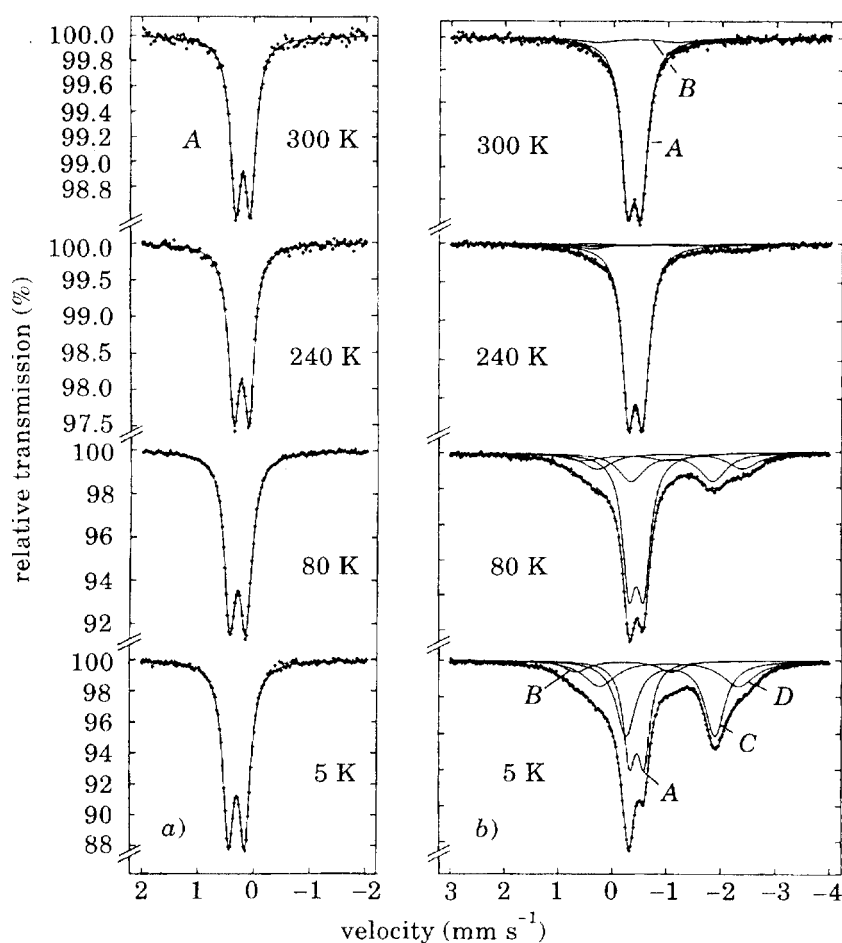


Fig. 20. (a) ^{57}Fe Mössbauer absorption spectra of $[\text{}^{57}\text{Fe}/\text{Co}(\text{phen})_3](\text{ClO}_4)_2$ as a function of temperature vs $^{57}\text{Co}/\text{Rh}$ (295 K) as source. (b) Time-integral ^{57}Fe Mössbauer emission spectra of a $[\text{}^{57}\text{Co}/\text{Co}(\text{phen})_3](\text{ClO}_4)_2$ source as a function of temperature vs $\text{K}_4[\text{Fe}(\text{CN})_6]$ (295 K) as absorber. Assignment: A $\text{Fe}^{\text{II}}\text{-LS}$, B $\text{Fe}^{\text{III}}\text{-LS}$, C $\text{Fe}^{\text{II}}\text{-HS1}$, D $\text{Fe}^{\text{II}}\text{-HS2}$. In (a) the source was moved relative to the absorber; in (b) the absorber was moved relative to the fixed source mounted in the crystal. For direct comparison, the sign of the velocities must be changed either in (a) or in (b) [214].

plexes exhibit thermal spin crossover. Obviously, in all these Fe^{II} SC systems metastable $\text{Fe}^{\text{II}}\text{-HS}$ states originating from the ^{57}Co nuclear decay are “trapped” and observed, to nearly 100% of all decay events, in the “Mössbauer window” of ca. 100 ns after nuclear decay, whereas the ground state of Fe^{II} in the same ligand surroundings at comparable temperatures is LS ($^1\text{A}_1$). Only with the discovery of the LIESST effect (see Section 8.3.7) we are close to understand these NIESST observations. The mechanism for both phenomena appears to be the same except

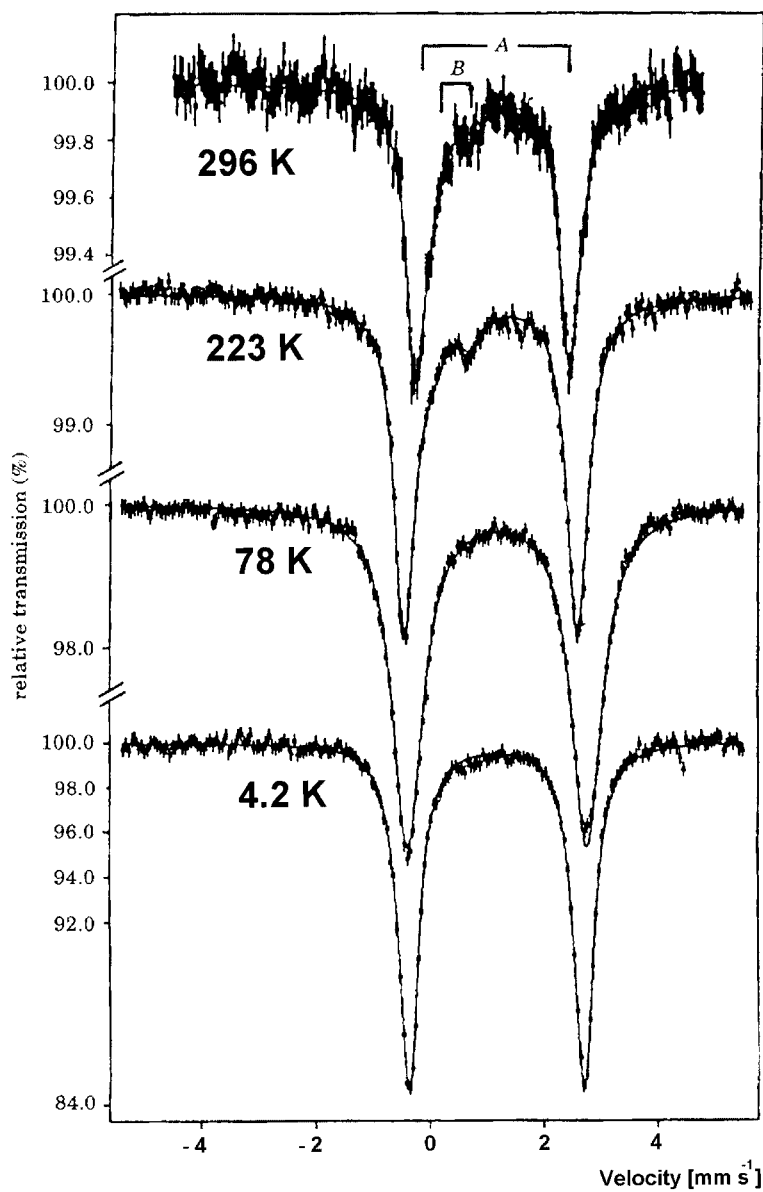


Fig. 21. ^{57}Fe Mössbauer emission spectra of a $[^{57}\text{Co}/\text{Co}(\text{phen})_2(\text{NCS})_2]$ source as a function of temperature vs $\text{K}_4[\text{Fe}(\text{CN})_6]$ (298 K) [207].

for the initial step, which is by external light irradiation in the case of LIESST, but $^{57}\text{Co}(\text{EC})^{57}\text{Fe}$ decay in the case of NIESST. The nuclear decay process is followed by a loss of electrons from outer shells leading to highly ionized species. There is very fast electron recombination ($\sim 10^{-15}$ s) in conducting materials. In insulating

materials, however, as in case of transition metal compounds of the present type electron recombination is much slower such that in the Mössbauer emission experiment with typical time window of ca. 10^{-7} s most of the nucleogenic iron species are observed in the +2 oxidation state [214]. From time-differential Mössbauer emission spectroscopy (TDMES) we know that metastable Fe^{II} -HS states exist already on the nanosecond time scale [215]. There are fast ($\ll 10^{-7}$ s) spin-allowed transitions to the $^1\text{A}_1$ ground state as well as fast ($\ll 10^{-7}$ s) ISC processes, which are favored by spin-orbit coupling as in the LIESST mechanism, populating the ^5E and then the metastable $^5\text{T}_2$ state (Fig. 14). The branching ratio for the two decay paths (prompt decay to $^1\text{A}_1$ and population of the $^5\text{T}_2$, respectively) depends on the ligand field strength and this in turn on ΔE_{HL}^0 (see Figs. 14 and 23). The weaker the ligand field strength and therefore the smaller ΔE_{HL}^0 , the higher the population of the $^5\text{T}_2$ state. This agrees with the experimental results, where the population of the $^5\text{T}_2$ state is found to be much more pronounced in the Mössbauer emission spectra of SC complexes than in a strong-field system like a $[\text{M}(\text{phen})_3]^{2+}$ complex. This “reduced energy gap law”, that is the smaller the energy difference ΔE_{HL}^0 between the lowest vibronic levels of the HS and LS states, the longer the lifetime of the trapped $^5\text{T}_2$ state, was demonstrated by Hauser [216] to hold for LIESST state relaxation in Fe^{II} SC complexes.

To prove that the LIESST mechanism also holds for the NIESST phenomenon, at least in its final step of ligand field state relaxations, we have constructed a coincidence spectrometer for TDMES experiments for lifetime measurements between ca. 5 ns and ca. 500 ns (resolution ≈ 3.5 ns) at variable temperatures down to 4 K [217]. The TDME spectra of ^{57}Co /tris-phen source prove that the intensity of the metastable Fe^{II} -HS state increases the lower the temperature and the shorter the time interval elapsed after nuclear decay. The lifetimes of one of the HS states derived from the TDME spectra were similar to that from time-resolved optical spectroscopy on $[\text{Fe}(\text{phen})_3]^{2+}$ embedded in a Nafion foil, for example 205 ns at 47 K for the HS state after NIESST [215], and 188 ns at 50 K after LIESST [218]. The agreement is very good and is strong evidence for the validity of the proposed mechanism. Further time-resolved studies of NIESST and LIESST on the very same system, viz. single crystal of $^{57}\text{Co}/\text{Mn}(\text{bpy})_3(\text{PF}_6)_2$ as Mössbauer source in TDMES and the corresponding single crystal iron complex for LIESST using optical spectroscopy yielded very similar results [219]. NIESST experiments have also been carried out with $^{57}\text{Co}/\text{M}(\text{phen})_3(\text{ClO}_4)_2$ ($\text{M} = \text{Fe}, \text{Ni}, \text{Co}, \text{Zn}$) as Mössbauer sources versus $\text{K}_4[\text{Fe}(\text{CN})_6]$ as absorber, in order to investigate the matrix influence, particularly the effect of different M^{2+} radii leading to different local pressure, on the relaxation rate of the metastable NIESST state ($^3\text{T}_2$). At a given temperature, the intensity of the nucleogenic ^{57}Fe -(HS) resonances was found to increase with increasing M^{2+} radius in the series $\text{M}^{2+} = \text{Fe}$ (61 pm in LS state) < Ni (70 pm) < Co (74 pm) < Zn (75 pm) [214]. A selection of relevant emission spectra recorded at 4.2 K are shown in Fig. 22.

In view of the fact that Fe^{II} -HS has the largest M^{2+} radius of 78 pm of all metal ions involved in this study, it is expected that the host with the smallest M^{2+} ion, which is the Fe^{II} -LS with 61 pm, should have the lowest formation probability of

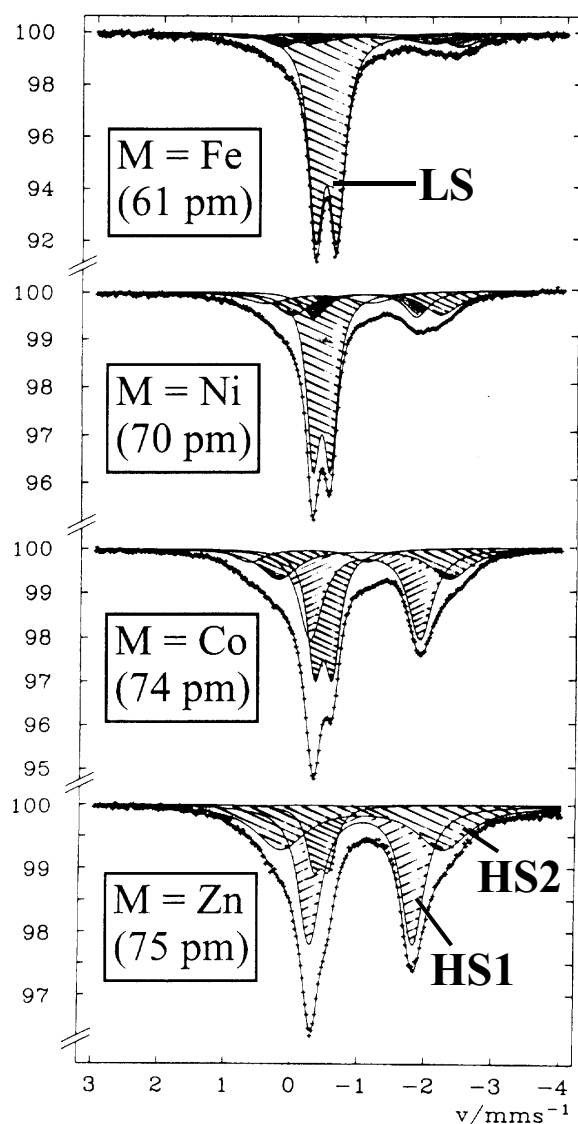


Fig. 22. ^{57}Fe Mössbauer emission spectra of $[\text{}^{57}\text{Co}/\text{M}(\text{phen})_3](\text{ClO}_4)_2$ vs $\text{K}_4[\text{Fe}(\text{CN})_6]\cdot 3\text{H}_2\text{O}$ recorded at 4.2 K. The spectra show increasing intensities of the nucleogenic $^{57}\text{Fe}(\text{II})$ -HS doublets with increasing M^{2+} radius due to decreasing local pressure [214].

$^{57}\text{Fe}(\text{II})$ -HS after NIESST. This is indeed the case (Fig. 22). The explanation can again be derived from Fig. 23: The smaller $r(\text{M}^{2+})$, the higher the local pressure, the larger ΔE_{HL}^0 , the shorter the lifetime (or faster the decay) of the $^{57}\text{Fe}(\text{HS})$ -HS state after NIESST.

Similar NIESST experiments have recently been performed with $[\text{}^{57}\text{Co}/$

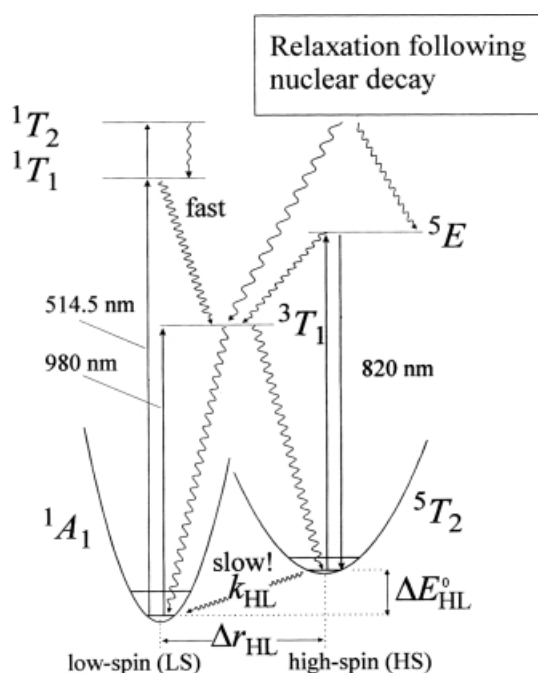


Fig. 23. Mechanism of nuclear-decay-induced excited spin state trapping (NIESST) [17].

$\text{Co}(\text{bpy})_3][\text{MCr}(\text{ox})_3]$ ($\text{M} = \text{Li}, \text{Na}$) and $[^{57}\text{Co}/\text{Co}(\text{bpy})_3][\text{Mn}_2(\text{ox})_3]$ as Mössbauer sources. These systems possess a cubic crystal structure, where the ^{57}Co -labelled cationic complex molecules sit in a cavity of slightly different dimension [220]. The a axis is smallest (15.387 Å) in the network with Li^+ and largest in that with Mn^{II} . Thus it is expected that in the former case the relaxation of the nucleogenic $^{57}\text{Fe}(\text{II})$ -HS state after NIESST is faster due to the somewhat higher local pressure in the former than in the latter case. This has indeed been observed: the intensity of the $^{57}\text{Fe}^{\text{II}}$ -HS resonances at a given temperature is larger in the system with $\text{Na}^+\text{Cr}^{3+}$ than in that with $\text{Li}^+\text{Cr}^{3+}$, but is largest in the host with $(\text{Mn}^{2+})_2$ [221]. These results are again well in accordance with the “reduced energy gap” law.

The NIESST effect was most recently studied for the first time in a Co^{II} SC compound, *viz.* $[^{57}\text{Co}/\text{Co}(\text{terpy})_2]\text{X}_2$ ($\text{X} = \text{ClO}_4^-, \text{Cl}^-$), where terpy is the tridentate ligand terpyridyl. The perchlorate derivative shows thermal spin transition, whereas the chloride derivative is still in the LS state at room temperature [222]. The former apparently possesses a weaker ligand field at the Co^{II} ion than the latter compound. In view of the “reduced energy gap law”, the perchlorate has a smaller ΔE_{HL}^0 value than the chloride and should therefore yield a higher population of the Fe^{II} -HS state after NIESST than the chloride. This has in fact been observed; the emission spectra in Fig. 24, which were recorded at 100 K, show a much larger fraction of the Fe^{II} -HS doublet for the perchlorate than for the chloride [223].

NIESST studies were also performed on $[^{57}\text{Co}/\text{Co}(\text{py})_2\text{Ni}(\text{CN})_4]$ ($\text{py} = \text{pyridine}$) [224]. The corresponding 2D cyano coordination $\text{Fe}^{\text{II}}\text{-Ni}^{\text{II}}$ polymer is known to

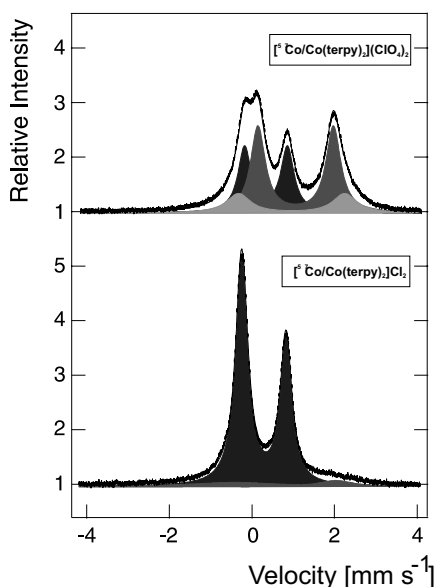


Fig. 24. Mössbauer emission spectra at 100 K for $[^{57}\text{Co}/\text{Co}(\text{terpy})_2]\text{A}_2$ ($\text{A} = \text{ClO}_4^-, \text{Cl}^-$) [223]. Black doublet: Fe(II)-LS. Dark grey, light grey doublets: Fe(II)-HS.

display an abrupt thermal ST $^1\text{A}_1 \leftrightarrow ^5\text{T}_2$ around 190 K with a hysteresis of 12 K [225]. The diamagnetic Ni^{II} ions are arranged in square planar configuration whereas Fe^{II} ions have octahedral surroundings. An interesting electron transfer from $\text{Fe}^{\text{II}}\text{-HS}$ to $\text{Fe}^{\text{III}}\text{-HS}$ above 210 K has been observed by Mössbauer spectroscopy [224].

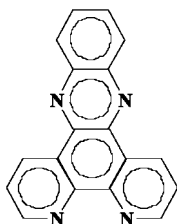
These examples convincingly demonstrate that the NIESST effect can be used to probe local ligand field or chemical pressure differences in a very sensitive manner.

8.4 New Trends in Spin Crossover Research

8.4.1 New Types of Spin Crossover Material

Most of the mononuclear SC systems exhibit weak cooperative behavior that is the spin state transitions are of a gradual type. If the transition is discontinuous, one usually observes a narrow hysteresis. The hysteresis becomes broader if the spin transition is accompanied by a crystallographic phase change like in $[\text{Fe}(\text{ptz})_6](\text{BF}_4)_2$ [153]. The crystal structure in this case is based on a molecular assembly of mononuclear entities mainly isolated from each other. A large number of ST materials of a new type have been discovered during the past ten years with the idea of increasing the cooperative interactions between the spin state changing molecules. The aim is to be able to propose materials exhibiting very abrupt ST along with strong thermal hysteresis effects around room temperature, these criteria being required for practical applications in displays and data processing [114]. Mainly two

strategies have been explored to enhance the electronic communication between the SC centers. The first one uses the tools of supramolecular chemistry and in the design of mononuclear compounds exhibiting strong intermolecular interactions such as hydrogen bonds or π - π interactions. $[\text{Fe}(\text{dpp})_2(\text{NCS})_2] \cdot \text{pyridine}$ with $\text{dpp} = \text{dipyrido}[3,2\text{-}a:2'3'\text{-}c]\text{phenazine}$ (Scheme 1) exhibits sharp ST with a hysteresis width of 40 K [226].



Scheme 1. Dipyrido[3,2-*a*:2'3'-*c*]phenazine (dpp).

Its room temperature crystal structure reveals strong π - π interactions as a consequence of the introduction of extended aromatic rings on the dpp ligand. In addition, van der Waals interactions were also found. Another example is given by $[\text{Fe}(\text{bpp})_2](\text{CF}_3\text{SO}_3)_2 \cdot \text{H}_2\text{O}$ which displays a ST with an unprecedented hysteresis loop of 138 K [144, 227]. This behavior is believed to be due to the presence of a strong hydrogen bonding network between the SC molecules, the anion and the lattice solvent molecules. However, this strategy can be considered as rather random as it is difficult to predict how the molecular contacts can be distributed in the crystal lattice. A more rational approach consists of directly linking the active SC centers by covalent bonds. For the resulting polynuclear compounds, it is believed that the molecular distortions accompanying the ST can be efficiently distributed throughout the whole crystal lattice by way of the ligands linking the SC sites. Several compounds of this kind have been reported; most of them incorporate 1,2,4-triazole derivatives as ligands [228]. Dinuclear, trinuclear, tetranuclear and pentanuclear SC compounds are now known [73, 187, 229–235]. An example is $[\text{Fe}_2(\text{totrz})_5(\text{NCS})_4]_2[\text{Fe}(\text{totrz})_2(\text{NCS})_2(\text{H}_2\text{O})_2] \cdot x\text{H}_2\text{O}$ with $\text{totrz} = 4\text{-}(p\text{-tolyl})\text{-}1,2,4\text{-triazole}$. The structure consists of two binuclear iron(II) entities linked to a non SC mononuclear unit via hydrogen bonding. This link allows an efficient communication between the active binuclear units leading to a very sharp spin transition. However, the cooperativity is not sufficient to induce hysteresis effect.

Iron(II) polymeric chain compounds of the following formula $[\text{Fe}(\text{Rtrz})_3](\text{anion})_2 \cdot \text{Sol}$ with $\text{Rtrz} = 4\text{-R-}1,2,4\text{-triazole}$ have also been prepared [49, 114, 147–152]. They generally exhibit sharp ST accompanied by wide thermal hysteresis around room temperature as well as an associated thermochromic effect between violet in the LS state and white in the HS state, making them potential candidates for practical application [114].

Their structure consists of iron(II) ions triply bridged by 1,2,4-triazole ligands through the nitrogen atoms occupying the 1 and 2 positions as shown in Fig. 25. The anions and the solvent molecules are located between the chains as it has been evidenced by X-ray diffraction for $[\text{Cu}(\text{hyetrz})_3](\text{ClO}_4)_2 \cdot 3\text{H}_2\text{O}$ [85].

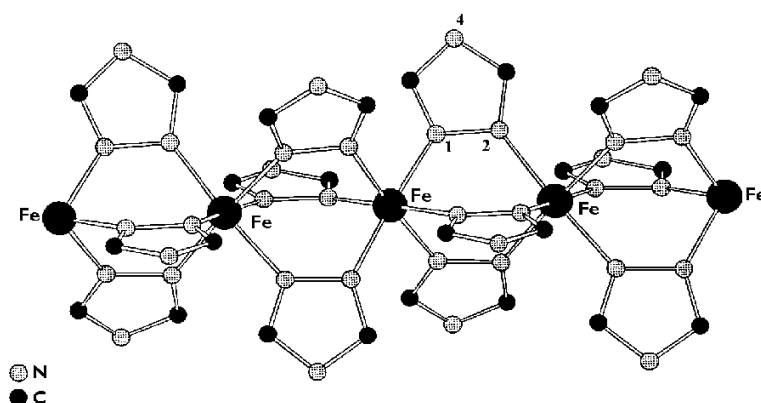


Fig. 25. Structure of the polymeric chain $[\text{Fe}(4\text{-R-1,2,4-triazole})_3]^{2+}$ as deduced by EXAFS spectroscopy [83].

$[\text{Fe}(1,2\text{-bis}(\text{tetrazole-1-yl})\text{propane})_3](\text{ClO}_4)_2$ is the first SC chain compound whose crystal structure has been determined by X-ray diffraction, both in the HS and LS state (Fig. 26). Despite its polymeric nature, the spin conversion is very gradual, with $T_{1/2} = 130$ K. The quasi absence of cooperativity has been attributed to the non-rigidity of the bridging network. This compound reveals in addition the LIESST effect, which is observed for an iron(II) linear chain compound for the first time [88].

A strategy towards obtaining polymeric systems of higher dimensionality makes use of ligands with several coordinating donor atoms. The use of multidentate ligands and/or spacers between the coordinating atoms increase the possibilities to raise up the dimensionality. The first ones can allow coordination to several metals whereas the second ones can increase the degrees of liberty of the coordinating groups in order to promote coordination in several directions. 2D and 3D SC networks have thus been obtained [228, 236–241].

$[\text{Fe}(\text{btr})_2(\text{NCS})_2] \cdot \text{H}_2\text{O}$ represents the first 2D ST compound [236]. Its crystal structure (Fig. 27) consists of iron(II) ions linked by btr ligands through the nitrogen

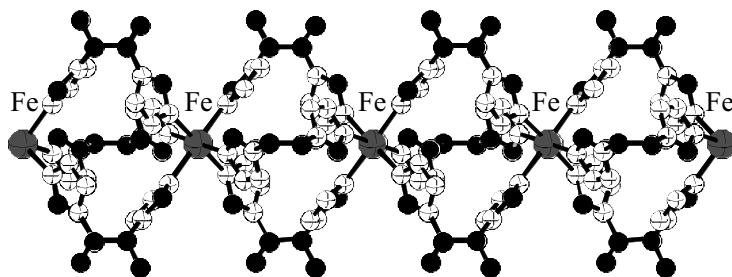


Fig. 26. View of the crystal structure of $[\text{Fe}(1,2\text{-bis}(\text{tetrazole-1-yl})\text{propane})_3](\text{ClO}_4)_2$ along the a axis [88]. C are shown in black and nitrogen in white.

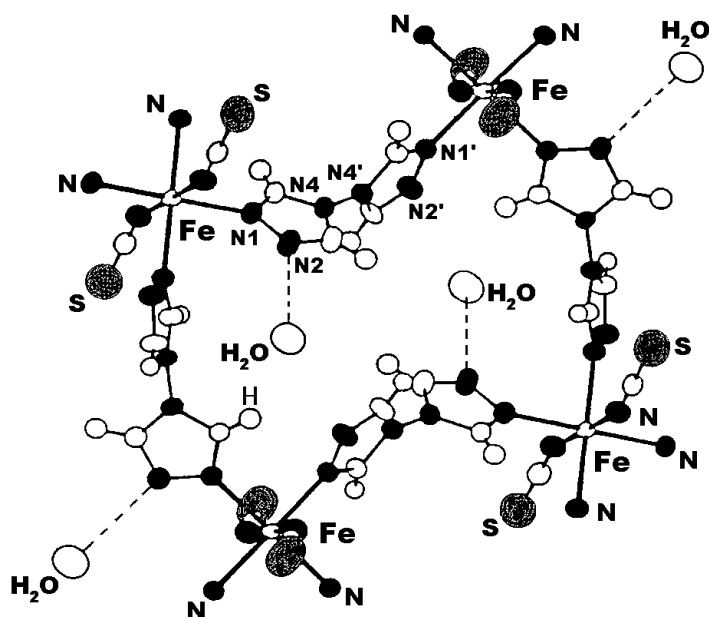


Fig. 27. Part of the crystal structure of $[\text{Fe}(\text{btr})_2(\text{NCS})_2] \cdot \text{H}_2\text{O}$ ($T = 293 \text{ K}$) [236].

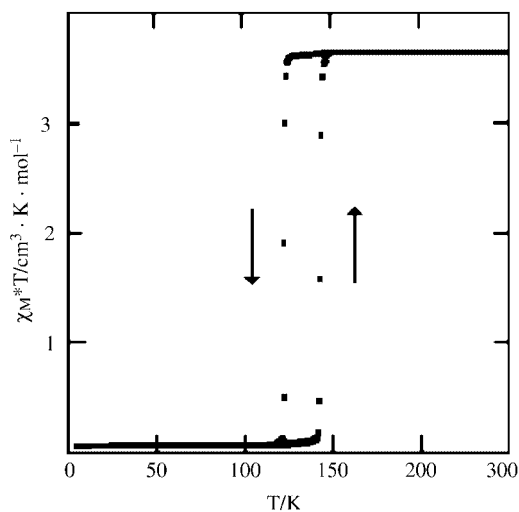


Fig. 28. $\chi_M T$ vs T plot of $[\text{Fe}(\text{btr})_2(\text{NCS})_2] \cdot \text{H}_2\text{O}$ [236].

atoms occupying the 1 and 1' positions. The thiocyanate anions are coordinated in *trans* position whereas the non-coordinated water molecules are linked by hydrogen bonding to the peripheral nitrogen atoms. The layers are connected by means of van der Waals forces and weak hydrogen bond bridges involving the water molecules. This compound reveals an extremely abrupt ST with a thermal hysteresis of 21 K as we can see in Fig. 28

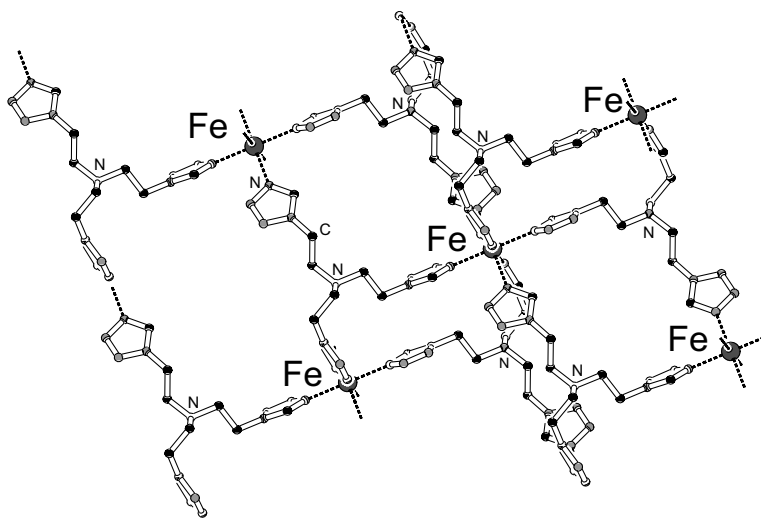


Fig. 29. Part of the crystal structure of $[\text{Fe}(\text{N}(\text{entz})_3)](\text{BF}_4)_2$ ($T = 293 \text{ K}$) [238].

$[\text{Fe}(\text{N}(\text{entz})_3)_2](\text{BF}_4)_2$ with $\text{N}(\text{entz})_3 = \text{tris}[(\text{tetrazole-1-yl})\text{ethane}]\text{amine}$, is the first example of a ST grid with 1-R-tetrazole as ligand [237].

The coordination occurs through the N4 nitrogen atoms of the tetrazole rings which are brought by the spider like ligand $\text{N}(\text{entz})$ (Fig. 29) [238]. Extremely abrupt ST with thermal hysteresis was observed ($T_{1/2 \uparrow} = 176 \text{ K}$ and $T_{1/2 \downarrow} = 167 \text{ K}$). Two other interesting 2D ST compounds were also recently reported. The structure of the catenane $[\text{Fe}(\text{tvp})_2(\text{NCS})_2] \cdot \text{CH}_3\text{OH}$ with $\text{tvp} = 1,2\text{-bis-(4-pyridyl)ethylene}$ consists of two interpenetrating orthogonal 2D networks [239]. It reveals quite an abrupt ST around 215 K. However, no hysteresis effect was observed. $[\text{Fe}(\text{py})_2\text{Ni}(\text{CN})_4]$ represents another example of a 2D compound revealing discontinuous ST [225]. Bridging cyano groups link the metal ions in this material.

$[\text{Fe}(\text{btr})_3](\text{ClO}_4)_2$ represents the first 3D ST compound [228]. Its structure (Fig. 30) consists of iron(II) ions connected in the three directions of space through the nitrogen atoms occupying the 1 and 1' positions of the btr ligand. The non-coordinated perchlorate anions are located in the voids of the 3D architecture. Upon cooling, an unusual spin conversion occurring in two steps is observed (Fig. 31).

A detailed single-crystal X-ray analysis together with temperature dependent ^{57}Fe Mössbauer spectroscopy have proved that this additional step was due to a consecutive spin conversion in two crystallographically inequivalent iron sites [228]. The narrow hysteresis observed in the lower branch of the curve can be attributed to cooperative interactions in the sense that no change of space group was observed.

2D and 3D SC catenanes were also recently obtained namely $[\text{Fe}(\text{bpb})_2(\text{NCS})_2] \cdot \text{MeOH}$ ($\text{bpb} = 1,4\text{-bis(4-pyridyl)butadiyne}$) [240] and $[\text{Fe}(\text{btzb})_3](\text{ClO}_4)_2$ ($\text{btzb} = 1,2\text{-bis(tetrazole-1-yl)butane}$) [241].

Research of SC compounds with multifunctional properties is currently carried out. The main goal is to obtain materials with original physical properties in ad-

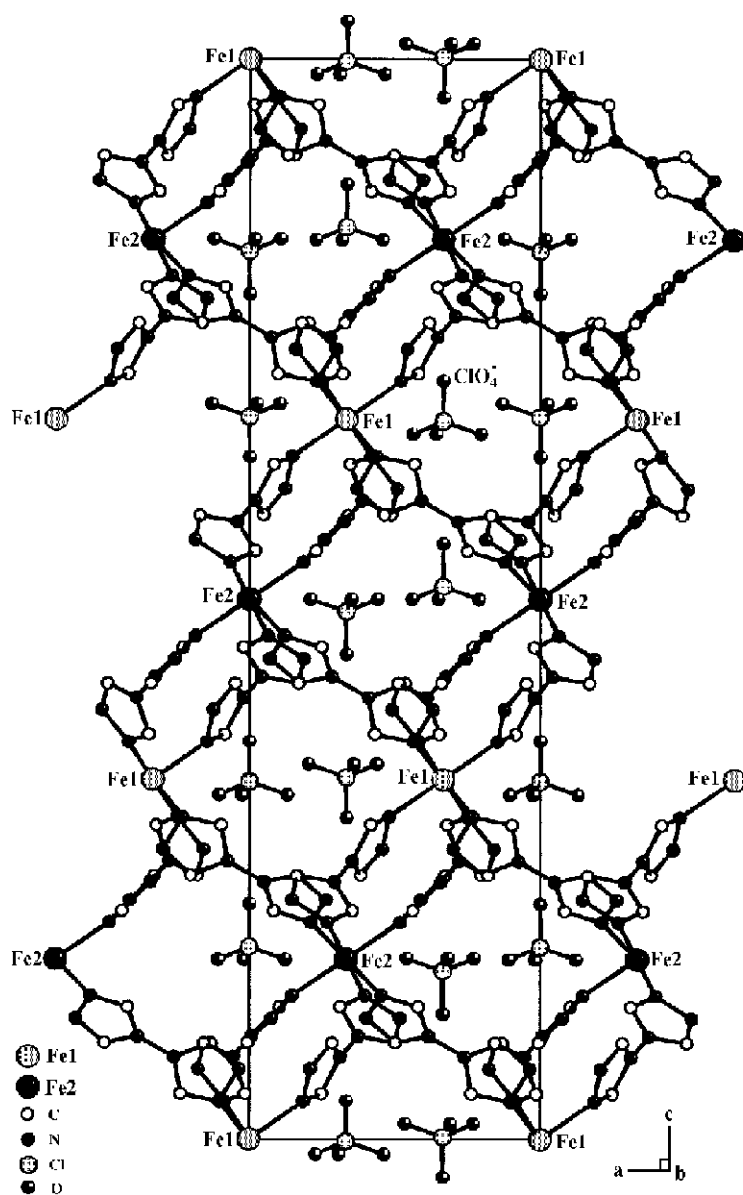


Fig. 30. Projection of the crystal structure of $[\text{Fe}(\text{btr})_3](\text{ClO}_4)_2$ along the c axis [228].

dition to spin crossover. For instance, $[\text{Co}_2\text{L}(\text{NCS})_2(\text{SCN})_2]$, L being a Schiff-base macrocyclic ligand obtained from the $[2 \times 2]$ condensation of 3,6-diformylpyridazine and 1,3-diaminopropane, represents the first compound exhibiting both antiferromagnetic coupling and spin crossover [242]. The crystal structure reveals a binuclear unit where Co^{II} ions are coordinated by two thiocyanate anions in *trans* position,

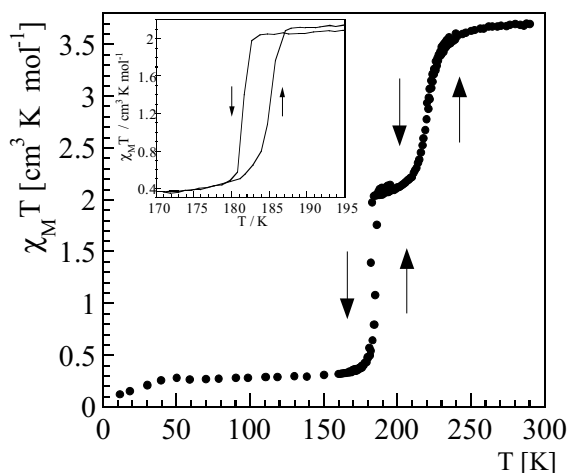


Fig. 31. $\chi_M T$ vs T plot of $[\text{Fe}(\text{btr})_3](\text{ClO}_4)_2$ [228].

one bound through the nitrogen atom and the other through the sulfur atom. SC materials exhibiting fluorescence [243] or non linear optics properties [244] were also recently reported, but the effect is observed only in solution.

8.4.2 New Effects and Phenomena

The past five years have seen an increasing number of reports dealing with new effects and phenomena, bringing a new breath to the rapidly expanding field of ST molecular materials.

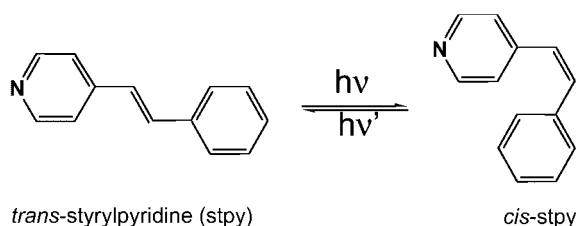
8.4.2.1 Soft X-ray Induced Excited Spin State Trapping

A new way to change spin states using soft X-ray irradiation at the iron $L_{2,3}$ edge has been discovered for $[\text{Fe}(\text{phen})_2(\text{NCX})_2]$ with $X = \text{S}, \text{Se}$ [245] which are known to undergo a ST around 200 K [53]. Irradiating a sample with a soft X-ray beam at ~ 45 K result in the population of a metastable HS state as a consequence of the $^1A_1 \rightarrow ^5T_2$ transition. Raising the temperature up to 80 K reveals thermal relaxation to the LS state as expected from LIESST experiments. This phenomenon called Soft X-ray Induced Excited Spin State Trapping (SOXIESST) is indeed analogous to the LIESST effect but occurs at much higher energy and is, in this regard, very comparable to the NIESST phenomenon. The energy involved is about 710 eV with soft X-ray in comparison with (2–3 eV for a standard UV–visible source [245].

8.4.2.2 Ligand Driven Light Induced Spin Change

Recently, a promising process towards the obtaining of photo-induced ST at room temperature was discovered [246–248]. The principle of the ligand-driven light-

induced spin change (LD-LISC) is based on ligands containing potentially photoisomerizable groups. However, this effect could in principle be extended to any other photochemical process like for instance bond forming/breaking rearrangements [249]. The first studies have taken advantage of the *cis*–*trans* photoisomerization of a C=C incorporated in a ligand coordinated to an iron(II) SC center like for instance with stpy = 4-styrylpyridine (see Scheme 2) [246–248].



Scheme 2. *cis*–*trans* Photoisomerization of 4-styrylpyridine.

This primary photoinduced isomerization in the ligand causes a change of the ligand field strength at the iron center as a secondary step. In the temperature region where the isomers are present in both spin states of the complex compound, the photoisomerization of the ligand directly results in SC behavior at the metal center. The LD-LISC phenomenon has, for the first time, been observed for $[\text{Fe}(\text{stpy})_4(\text{NCBPh}_3)_2]$, for which the compound containing the ligand in *trans* configuration exhibits quite an abrupt ST at 190 K, whereas the *cis* derivative remains in the HS state upon cooling (Fig. 32) [250].

Photoisomerization of the stpy ligand, at 140 K, in the complex embedded within a cellulose acetate matrix, was effectively shown, on the basis of UV–visible absorption measurements, to trigger the spin-state change of the iron(II) ions. Later, the phenomenon was also observed at room temperature for $[\text{Fe}(4\text{-methyl-4}'\text{-trans-styryl-2,2}'\text{-bipyridine})_2(\text{NCS})_2]$ [251] and for two several iron(III) SC compounds [252–254]. The limitation of the LD-LISC is that it has till now only been observed in diluted samples (in solution or in thin films), the reason being the enormous mechanical distortion of the molecules upon *cis*–*trans* isomerization. Therefore, the SC compounds under study do not show sharp thermal ST and the magnetic change regarding irradiation is not expected to be pronounced. This weak point regarding

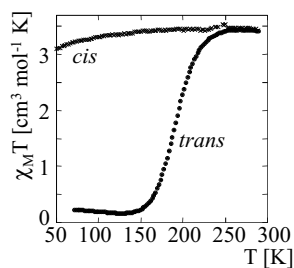


Fig. 32. Temperature dependence of $\chi_{\text{M}}T$ for the *trans* (C_t) and *cis* (C_c) forms of $[\text{Fe}(\text{stpy})_4(\text{NCBPh}_3)_2]$ [250].

practical applications could be overcome by embedding such materials in organized media on the mesoscopic scale, such as Langmuir–Blodgett films [255, 256].

8.4.2.3 New Photophysical Effects

Following the discovery of a light induced bistability on $[\text{Fe}(\text{etz})_6](\text{BF}_4)_2$ (see Section 8.3.7), several new photomagnetic phenomena have recently emerged. A light induced thermal hysteresis (LITH), which is another example of light induced bistability, has been discovered on the SC compound $[\text{Fe}(\text{pmbia})_2(\text{NCS})_2]$ (pmbia = *N*-(2-pyridylmethylene)aminobiphenyl) which undergoes a very abrupt thermal ST around 170 K with a hysteresis of 5 K [156]. Irradiating the sample at 10 K with green light resulted in the population of the LIESST state. The temperature was then raised up to 100 K and lowered to 10 K under continuous irradiation. A wide thermal hysteresis was observed (Fig. 33).

The same effect was also observed on the mixed crystal system $[\text{Fe}_{1-x}\text{Co}_x(\text{btr})_2(\text{NCS})_2] \cdot \text{H}_2\text{O}$ with $x = 0,3; 0,5; 0,85$ [257]. The explanation of this effect given by Varret et al. [257, 258] is based on the rate equation [206]:

$$k_{\text{HL}} = k_{\infty} \exp\left(-\frac{\Delta E_{\text{HL}}(\gamma_{\text{H}} = 0)}{k_{\text{B}}T}\right) \exp(-\alpha(T)\gamma_{\text{HS}}) \quad (36)$$

which at low temperatures is equal to the temperature independent tunneling limit of Eq. (34). The energy separation ΔE_{HL} at each site depends on the HS fraction of the crystal and the distribution of spin states in the neighborhood as described in the previous section. In mean field approximation only the dependence on the HS fraction is taken into account and the decay rate is the same for all molecules. The self-acceleration factor $\alpha(T) \approx 1/T$ was determined from experimental relaxation curves. The steady state condition is the equation of detailed balance $\Phi_{\text{up}} = \Phi_{\text{down}}$, where $\Phi_{\text{up}} = (1 - \gamma_{\text{HS}})k_{\text{LH}}$ is the number of LS \rightarrow HS excitations per second and $\Phi_{\text{down}} = \gamma_{\text{HS}}k_{\text{HL}}$ the number of molecules per second going from HS to LS state. In the temperature region, where all molecules are in the LS state in thermal equilibrium, thermal excitation can be neglected and k_{LH} is just proportional to the

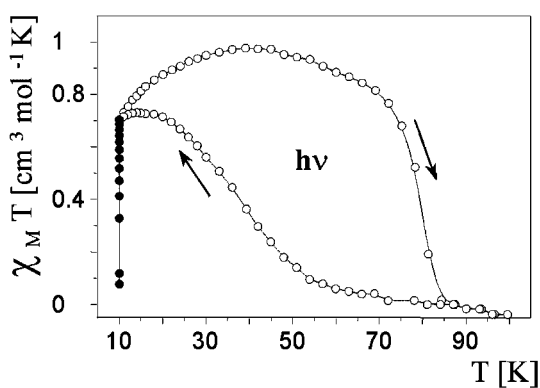


Fig. 33. $\chi_{\text{M}}T$ vs T plot of $[\text{Fe}(\text{pmbia})_2(\text{NCS})_2]$. The filled circles represent the data obtained at 10 K under irradiation. The open circles represent the data on heating and cooling modes under permanent irradiation [156].

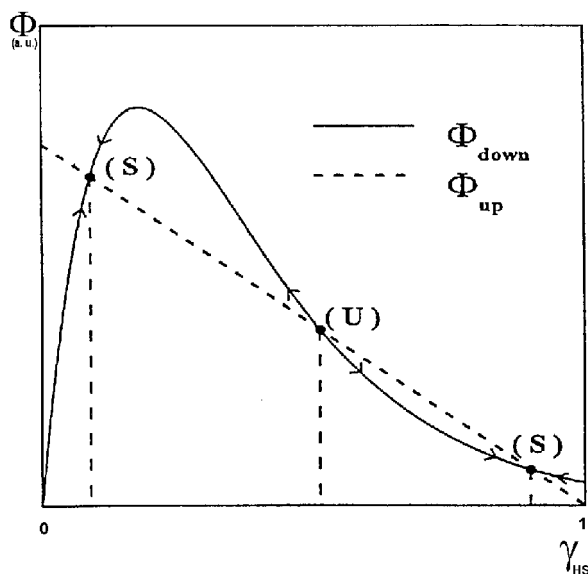


Fig. 34. Graphical resolution of Eq. (37) computed with $\alpha = 5.83$. The steady state values are given by the intersects of the curve and the straight line [257].

intensity of the laser light, the cross-section of the molecules times the probability to excite the metastable HS state by intersystem crossing. The implicit state equation for γ_{HS} at temperature T :

$$(1 - \gamma_{\text{HS}})k_{\text{LH}} = \gamma_{\text{HS}}k_{\infty} \exp\left(-\frac{\Delta E_{\text{HL}}(\gamma_{\text{H}} = 0)}{k_{\text{B}}T}\right) \exp(-\alpha(T)\gamma_{\text{HS}}) \quad (37)$$

depends on three terms k_{LH}/k_{∞} , $\Delta E_{\text{HL}}(\gamma_{\text{H}} = 0)$, and $\alpha(T)$, which can be determined independently from the decay curve at this temperature.

The functions Φ_{up} and Φ_{down} are plotted in Fig. 34 visualizing the bistability of the system. The steady state values are given by the intersects of the curve Φ_{down} and the straight line Φ_{up} . The two points (S) are both stable at that temperature and (U) is unstable with respect to small deviations of γ_{HS} . Starting from sufficiently low temperatures the maximum of the Φ_{down} curve is below the dashed line Φ_{up} and there is a single intersection at large HS fraction close to $\gamma_{\text{HS}} = 1$. With increasing temperature the Φ_{down} curve is shifting upwards. The bistability region begins as soon as the Φ_{down} curve intersects the Φ_{up} line in three positions (S, U, S). Upon further increasing the temperature, the Φ_{down} curve shifts up further and shows finally only one intersecting point with Φ_{up} close to $\gamma_{\text{HS}} = 0$. This determines the upper boundary of the bistability region. At a fixed temperature these different situations can also be reached by changing the slope of the Φ_{up} curve, which is proportional to the light intensity. The type of hysteresis measured this way has been called LIOH for light induced optical hysteresis.

Figure 35 shows the experimental γ_{HS} fraction of $[\text{Fe}_{0.5}\text{Co}_{0.5}(\text{btr})_2(\text{NCS})_2] \cdot \text{H}_2\text{O}$ versus temperature under continuous irradiation with light from a 100 W tungsten halogen lamp with an orange interferometric filter (100 nm wide, centered at

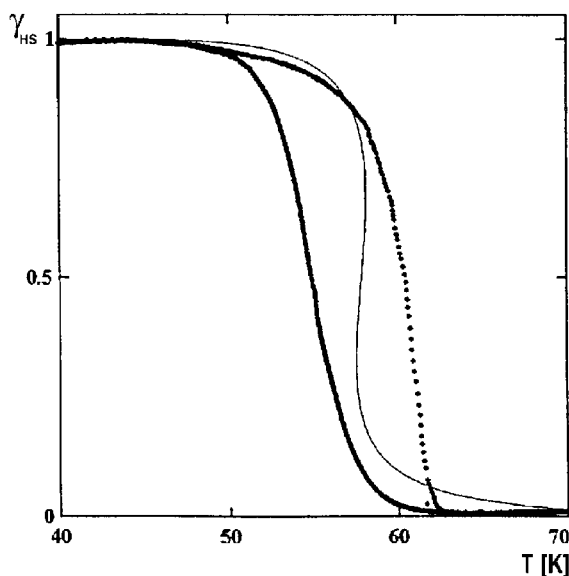


Fig. 35. Experimental γ_{HS} data for $[\text{Fe}_{0.5}\text{Co}_{0.5}(\text{btr})_2(\text{NCS})_2] \cdot x\text{H}_2\text{O}$ derived from optical reflectivity measurements. The solid line represents the steady state curve calculated with $\alpha T = 263 \text{ K}$ [257, 258].

600 nm). The γ_{HS} fraction was derived from optical reflectivity measurements. The solid line is the steady state curve calculated with $\alpha T = 263 \text{ K}$ as obtained from the decay curves in this temperature region. The experimental hysteresis width is much larger than the predicted one and the transitions are less steep as is usually found for classical thermal hysteresis curves. The poor prediction of the width of the hysteresis shows that mean field theory is not adequate to describe the interaction in this compound.

The prominent aspect of this theory is that it shows that the presence of a light induced hysteresis is the signature of cooperative effects among the SC centers. Thus, this method constitutes a simple and direct tool to probe qualitatively the presence of cooperativity for a given system provided the data are recorded in steady state conditions. This is particularly relevant in case strong cooperative effects are not directly observed, as indicated by a gradual thermal SC curve. This aspect has been convincingly illustrated on the first tetranuclear Fe_4^{II} $[2 \times 2]$ supramolecular SC grid [234]. This compound undergoes quite a gradual thermal SC behavior but nevertheless does show a light induced thermal hysteresis. This proves unambiguously the presence of cooperative effects within the tetranuclear unit unless the shape of the SC curve indicated apparently weak cooperative effects among the active centers [234].

A new photophysical effect called light perturbed thermal hysteresis (LiPTH) was recently found for $[\text{Fe}(\text{phy})_2](\text{BF}_4)_2$ with phy = 1,10-phenanthroline-2-carbaldehyde phenylhydrazone [259]. This compound shows a crystallographic phase transition [260] and undergoes a ST around room temperature with a hysteresis. Continuous irradiation during heating and cooling modes in the region of the thermal ST shifts the transition temperatures by ca. 10 K to the low temperature region using green light. Preliminary experiments indicate that a similar shift

of the hysteresis to higher temperatures ought to be observed using red light. This observation has been modeled in analogy to the theoretical description of the LITH effect. Since the relaxation rate above 250 K is too fast for the formation of a stable LIESST state, a light perturbed SC has been proposed.

Very surprising was the recent observation of the LIESST effect in the mixed crystal system $[\text{Fe}_{0.02}\text{Mn}_{0.98}(\text{terpy})_2](\text{ClO}_4)_2$ (terpy = 2,2':6',2'-terpyridine) [261] with ST temperature far above room temperature, contrary to what would be expected from the "inverse energy gap law", which predicts in this case a much shorter lifetime for the LIESST state by ca. 15 orders of magnitude [195]. Clearly, this unexpected observation escapes the normal LIESST mechanism (Section 8.3.7). Interestingly, no LIESST effect was observed for the pure Fe^{II} compound for which one can expect a similar ligand field strength. It might be possible that the crystal lattice plays an important role for this phenomenon as the host lattice $[\text{Mn}(\text{terpy})_2](\text{ClO}_4)_2$ is suitable to welcome HS Fe^{II} ions produced after photo-excitation, which would remain trapped and stabilized in it. Further investigations are necessary to clarify this behavior.

8.4.2.4 New Information from Pressure Experiments

Pressure represents a powerful tool in probing the cooperative interactions of SC materials by estimating its effect on the transition temperature and the hysteresis widths of first order SC phase transitions. Pressure work on such materials has started some thirty years ago but always at room temperature [262]. A new pressure cell was designed [47] allowing the application of hydrostatic pressure in a controlled manner. The first pressure experiments were carried out on $[\text{Fe}(\text{phy})_2](\text{BF}_4)_2$, a mononuclear SC compound that was reported to see its hysteresis width decreasing and increasing with pressure [263]. The increase of width with increasing pressure contradicts the expectation derived from mean field theory. Allowing for a pressure dependence of the elastic constants of the compound, the anomalous behavior of hysteresis width could be interpreted [264]. Another mononuclear compound, namely $[\text{Fe}(\text{pmaza})_2(\text{NCS})_2]$ with pmaza = *N*-(2-pyridylmethylene)4-azophenyl, was also pressurized. Its ST curve centered around 189 K flattened to a completely LS behavior at 10.8 kbar [265]. A calibration curve can be obtained when plotting the LS fraction versus pressure. In fact, this may be readily applied in a pressure sensor.

Polynuclear SC compounds were also the subject of extended pressure studies. Applying pressure on the chain compound $[\text{Fe}(\text{hyetrz})_3](3\text{-nitrophenylsulfonate})_2$ provokes a parallel shift upwards from 100 K to room temperature [149]. The steepness of the ST curves remains constant along with the hysteresis width. This lends support to the assertion that the cooperative interactions in this system are confined within the iron(II) triazole chain [149]. A similar pressure effect is observed on $[\text{Fe}(\text{hyptrz})_3](4\text{-chlorophenylsulfonate})_2 \cdot \text{H}_2\text{O}$ (hyptrz = hyptrz = 4-(3'-hydroxypropyl)1,2,4-triazole), but in this case above room temperature (Fig. 36) [266].

A peculiarity however is that the hysteresis width of this compound disappears and then reappears under pressure. Fig. 37 shows the pressure dependence of the

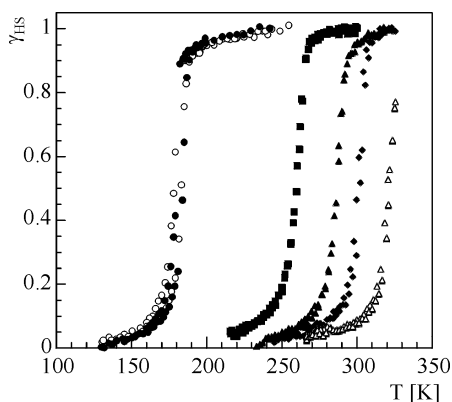


Fig. 36. γ_{HS} as a function of temperature for $[\text{Fe}(\text{hyprtz})_3](4\text{-chlorobenzenesulfonate})_2\cdot\text{H}_2\text{O}$ at different pressures. (\bullet , $P = 1$ bar; \blacksquare , $P = 4.1$ kbar; \blacktriangle , $P = 5$ kbar; \blacklozenge , $P = 5.3$ kbar; \triangle , $P = 5.9$ kbar; \circ , $P = 1$ bar after releasing the pressure) [266].

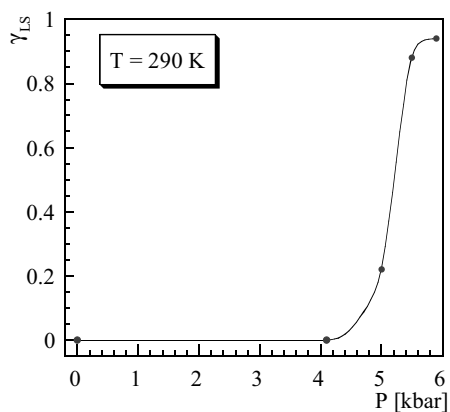


Fig. 37. Pressure dependence of the LS fraction for $[\text{Fe}(\text{hyprtz})_3](4\text{-chlorobenzenesulfonate})_2\cdot\text{H}_2\text{O}$ at room temperature [266].

LS fraction, γ_{LS} . A very steep $\text{HS} \rightarrow \text{LS}$ transition is observed at room temperature around ~ 6 kbar accompanied by a dramatic color change from white to deep purple. This particularity could be used for an application such as a pressure sensor or display [266]. Several theoretical models have been developed to rationalize such phenomena of linear SC chain compounds [267–269].

A layered SC compound has also recently been studied by pressure [270, 271]. Application of hydrostatic pressure (≤ 10.5 kbar) on $[\text{Fe}(\text{btr})_2(\text{NCS})_2]\cdot\text{H}_2\text{O}$, which is known to show a discontinuous ST around ≈ 132 K [236], results in an unexpected stabilization of the HS state. This result is surprising in the sense that pressure is known to stabilize the LS state as a consequence of the smaller volume for the LS iron(II) ion. On release of pressure, the HS state is found to be partially trapped. After thermal relaxation of the metastable HS state obtained by light switching (LIESST effect), which is obtained for this compound for the first time, a pure LS state is obtained in contrast to the pressure experiments. This different behavior supports the suggestion of a structural phase transition as the likely basis of the pressure-induced HS state [270].

New pressure effects were also recently observed on Fe^{II} compounds containing bpym ligands, revealing an intriguing interplay between antiferromagnetic coupling and SC behavior in the dinuclear compound [Fe(bpym)(NCS)₂]₂(bpym) [228] and in the chiral Fe^{II} chain, [Fe(bpym)(NCS)₂] [272]. A pressure induced SC was observed for these compounds exhibiting a global antiferromagnetic coupling in the HS state without pressure [273].

Structural insights can also be gained under perturbation conditions. This has been done for [Fe(phen)₂(NCS)₂] and [Fe(btz)₂(NCS)₂] with btz = 2,2'-bi-4,5-dihydrothiazine which were the first SC compounds to be structurally studied under pressure [274]. At room temperature, a HS to LS transition is observed under high pressure. The space group is retained and the overall molecular dimensions are very similar to those of the structure of the LS form obtained at ambient pressure after thermal SC. Structural aspects of the metastable HS state produced after light excitation were first examined some ten years ago [153] and are currently under investigations on the [Fe(Rtz)₆](anion)₂ family with the goal to gain greater understanding of light induced phenomena in general [275].

List of Abbreviations and Symbols

bpb	1,4-bis(4-pyridyl)butadiyne
bpp	2,6-bis(pyrazol-3-yl)pyridine
bpy	2,2'-bipyridine
bpym	2,2'-bipyrimidine
bt	2,2'-bithiazoline
btr	4,4'-bis-1,2,4-triazole
btz	2,2'-bis-4,5-dihydrothiazine
btzb	1,2-bis(tetrazole-1-yl)butane
btzp	1,2-bis(tetrazole-1-yl)propane
dpp	dipyrido[3,2- <i>a</i> :2'3'- <i>c</i>]phenazine
etz	1-ethyltetrazole
hyetrz	4-2'-hydroxyethyl-1,2,4-triazole
hyptrz	4-3'-hydroxypropyl-1,2,4-triazole
mtz	1-methyltetrazole
phen	1,10-phenanthroline
phy	1,10-phenanthroline-2-carbaldehyde phenylhydrazone
2-pic	2-picolyamine
pmaza	<i>N</i> -(2-pyridylmethylene)4-azophenyl
pmbia	<i>N</i> -(2-pyridylmethylene)aminobiphenyl
ptz	1-propyltetrazole
py	pyridine
stpy	4-styrylpyridine
terpy	2,2':6',2'-terpyridine
totrz	4-(<i>p</i> -tolyl)1,2,4-triazole
trz	1,2,4-triazolato
tvp	1,2-bis(4-pyridyl)ethylene

HB(trz) ₃	hydrotris(1,2,4-triazolyl)borate
Htrz	4- <i>H</i> -1,2,4-triazole
N(entz) ₃	tris[(tetrazole-1-yl)ethane]amine
NH ₂ trz	4-amino-1,2,4-triazole
5NO ₂ -sal-N(1,4,7,10)	2,2'-(2,5,8,11-tetraazadodeca-1,1,1-diene-1,12-diyl)4-nitrophenolato
<i>B</i>	Applied magnetic field
EFG	Electric field gradient
ISC	Intersystem crossing
LD-LISC	Ligand-driven light-induced spin change
LIESST	Light-induced excited spin state trapping
LIOH	Light-induced optical hysteresis
LITH	Light-induced thermal hysteresis
LIPTH	Light-perturbed thermal hysteresis
MAS	Mössbauer absorption spectroscopy
NIESST	Nuclear decay-induced excited spin state trapping
SC	Spin crossover
SOXIESST	Soft X-ray-induced excited spin state trapping
	Spin transition
TDMES	Time-differential Mössbauer emission spectroscopy
TIMES	Time-integral Mössbauer emission spectroscopy
ZFS	Zero-field splitting
<i>T</i> _{1/2}	Transition temperature
δ	Isomer shift
ΔE_Q	Quadrupole splitting
γ_{HS}	HS molar fraction

References

- [1] (a) L. Cambi, A. Cagnasso, *Atti Accad. Naz. Lincei* **1931**, *13*, 809. (b) L. Cambi, L. Szegö, *Ber. Dtsch. Chem. Ges.* **1931**, *64*, 259. (c) L. Cambi, L. Szegö, A. Cagnasso, *Atti. Accad. Naz. Lincei* **1932**, *15*, 266. (d) *ibid* **1932**, *15*, 329. (e) L. Cambi, L. Szegö, *Ber. Dtsch. Chem. Ges.* **1933**, *66*, 656. (f) L. Cambi, L. Malatesta, *Ber. Dtsch. Chem. Ges.* **1937**, *70*, 2067.
- [2] (a) K. Madeja, E. König, *J. Inorg. Nucl. Chem.* **1963**, *25*, 377. (b) W. A. Baker, H. M. Bobonich, *Inorg. Chem.* **1964**, *3*, 1184.
- [3] L. F. Lindoy, S. E. Livingstone, *Coord. Chem. Rev.* **1967**, *2*, 173.
- [4] R. L. Martin, A. H. White, *Transition Met. Chem.* **1968**, *4*, 113.
- [5] E. König, *Coord. Chem. Rev.* **1968**, *3*, 471.
- [6] H. A. Goodwin, *Coord. Chem. Rev.* **1976**, *18*, 293.
- [7] P. Gütllich, *Struct. Bonding (Berlin)* **1981**, *44*, 83.
- [8] P. Gütllich, *Ad. Chem. Ser.* **1981**, *194*, 405.

- [9] E. König, G. Ritter, S. K. Kulshreshtha, *Chem. Rev.* **1985**, 85, 219.
- [10] E. König, *Prog. Inorg. Chem.* **1987**, 35, 527.
- [11] J. K. Beattie, *Adv. Inorg. Chem.* **1988**, 32, 1.
- [12] H. Toftlund, *Coord. Chem. Rev.* **1989**, 94, 67.
- [13] P. Gütllich, A. Hauser, *Coord. Chem. Rev.* **1990**, 97, 1.
- [14] E. König, *Struct. Bonding (Berlin)* **1991**, 76, 51.
- [15] J. Zarembowitch, O. Kahn, *New. J. Chem.* **1991**, 15, 181.
- [16] O. Kahn, *Molecular Magnetism*, VCH, New York, **1993**, p. 53.
- [17] P. Gütllich, A. Hauser, H. Spiering, *Angew. Chem., Int. Ed.* **1994**, 33, 20.
- [18] (a) P. Gütllich, J. Jung, *J. Mol. Struct.* **1995**, 347, 21. (b) P. Gütllich, J. Jung, H. A. Goodwin, *NATO ASI Series E* **1996**, 321, 327. (c) P. Gütllich, J. Jung, *Il Nuovo Cimento* **1996**, 18D, 107.
- [19] O. Kahn, *Current Opinion Sol. State Mater. Sc.* **1996**, 1, 547.
- [20] P. Gütllich, *Mol. Cryst. Liq. Cryst.* **1997**, 305, 17.
- [21] P. Gütllich, H. Spiering, A. Hauser, in *Inorganic Electronic Structure and Spectroscopy*, (Eds. E. I. Solomon, A. B. P. Lever), vol II, Wiley, New York, **1999**, p. 575.
- [22] P. Gütllich, Y. Garcia, H. A. Goodwin, *Chem. Soc. Rev.* **2000**, 29, 419.
- [23] (a) R. C. Stouter, D. W. Smith, E. A. Cleavenger, T. E. Norris, *Inorg. Chem.* **1966**, 5, 1167. (b) J. G. Schmidt, W. S. Brey, R. C. Stouter, *Inorg. Chem.* **1967**, 6, 268.
- [24] R. Morassi, L. Sacconi, *J. Am. Chem. Soc.* **1970**, 92, 5241.
- [25] D. Gatteschi, C. A. Ghilardi, A. Orlandini, L. Sacconi, *Inorg. Chem.* **1978**, 17, 3023.
- [26] J. Zarembowitch, *New. J. Chem.* **1992**, 16, 255.
- [27] J. Faus, M. Julve, F. Loret, J. A. Real, J. Sletten, *Inorg. Chem.* **1994**, 33, 5535.
- [28] K. Heinze, G. Huttner, L. Zsolnai, P. Schober, *Inorg. Chem.* **1997**, 36, 5457.
- [29] (a) W. Kläui, *J. Chem. Soc., Chem. Comm.* **1979**, 700. (b) P. Gütllich, B. R. McGarvey, W. Kläui, *Inorg. Chem.* **1980**, 19, 3704. (c) W. Eberspach, N. El. Murr, W. Kläui, *Angew. Chem. Int. Ed. Engl.* **1982**, 21, 915. (d) G. Navon, W. Kläui, *Inorg. Chem.* **1984**, 23, 2722. (e) W. Kläui, W. Eberspach, P. Gütllich, *Inorg. Chem.* **1987**, 26, 3977.
- [30] (a) D. M. Halepoto, D. G. L. Holt, L. F. Larkworthy, G. J. Leigh, D. C. Povey, G. W. Smith, *J. Chem. Soc., Chem. Comm.* **1989**, 1322. (b) D. M. Halepoto, D. G. L. Holt, L. F. Larkworthy, D. C. Povey, G. W. Smith, G. J. Leigh, D. C. Povey, *Polyhedron* **1989**, 8, 1821. (c) M. Sorai, Y. Yumoto, D. M. Halepoto, L. F. Larkworthy, *J. Phys. Chem. Solids* **1993**, 54(4), 421.
- [31] A. K. Hughes, V. J. Murphy, D. Ohare, *J. Chem. Soc., Chem. Comm.* **1994**, 2, 163.
- [32] H. Sitzmann, M. Schär, E. Dormann, M. Kelemen, *Z. Anorg. Allg. Chem.* **1977**, 623, 1850.
- [33] (a) J. H. Ammeter, R. Bucher, N. Oswald, *J. Am. Chem. Soc.* **1974**, 96, 7833. (b) M. E. Switzer, R. Wang, M. F. Rettig, A. H. Maki, *J. Am. Chem. Soc.* **1974**, 96, 7669. (c) J. H. Ammeter, *J. Mag. Reson.* **1978**, 30, 299. (d) J. H. Ammeter, L. Zoller, J. Bachmann, E. Blatzer, E. Gamp, R. Bucher, E. Deiss, *Helv. Chim. Acta* **1981**, 64, 1063. (e) D. Cozak, F. Gauvin, *Organometallics* **1987**, 6, 1912.
- [34] N. Hebedanz, F. H. Köhler, G. Müller, J. Riede, *J. Am. Chem. Soc.* **1986**, 108, 3281.
- [35] (a) P. G. Sim, J. Sinn, *J. Am. Chem. Soc.* **1981**, 103, 241. (b) Y. Garcia, O. Kahn, J.-P. Ader, A. Buzdin, Y. Meurdesoif, M. Guillot, *Physics Letters A* **2000**, 271, 145.
- [36] H. J. Krokoszinski, C. Santandrea, E. Gmelin, K. Bärner, *Phys. Status Solidi B* **1982**, 113, 185.
- [37] L. Kaustov, M. E. Tal, A. I. Shames, Z. Gross, *Inorg. Chem.* **1997**, 36, 3503.
- [38] L. Sacconi, *Pure Appl. Chem.* **1971**, 27, 161.
- [39] R. H. Holm, M. J. O'Connor, *Prog. Inorg. Chem.* **1973**, 14, 241.
- [40] (a) W. Kläui, K. Schmidt, A. Bockmann, P. Hofmann, H. R. Schmidt, P. Staufert, *J.*

- Organomet. Chem.* **1985**, 286, 407. (b) H. Werner, B. Ulrich, U. Schubert, P. Hofmann, B. Zimmer-Gasser, *J. Organomet. Chem.* **1985**, 297, 27.
- [41] A. B. P. Lever, *Inorganic Electronic Spectroscopy*, vol. 33, Elsevier, Amsterdam, **1984**, p. 462.
- [42] (a) P. Gülich in *Chemical Mössbauer Spectroscopy* (Ed. R. H. Herber), Plenum, New York, **1984**, p. 27. (b) P. Gülich in *Mössbauer Spectroscopy Applied to Inorganic Chemistry*, (Ed. G. J. Long), vol 1., Plenum, New York, **1984**, p. 287. (c) P. Gülich, R. Link, A. X. Trautwein, *Mössbauer Spectroscopy and Transition Metal Chemistry*, Springer, Berlin, **1978**.
- [43] H. L. Schläfer, G. Gliemann, *Einführung in die Ligandenfeldtheorie*, (Akademische Verlagsgesellschaft, Wiesbaden) **1980**.
- [44] (a) M. Sorai, S. Seki, *J. Phys. Soc. Jap.* **1972**, 33, 575. (b) M. Sorai, S. Seki, *J. Phys. Chem. Solids* **1974**, 35, 555.
- [45] R. L. Carlin, A. J. van Duyneveldt, *Magnetic Properties of Transition Metal Compounds*, Springer, Berlin, **1977**.
- [46] (a) C. J. O'Connor, in *Molecule Based Magnetic Materials*, ACS Symp. Ser. **1996**, 644, 44. (b) F. Palacio, in *Localized and itinerant molecular magnetism. From molecular assemblies to the devices*, (Eds.: E. Coronado, P. Delhaes, D. Gatteschi, J. S. Müller), Kluwer Acad. Publ., NATO ASI Series C, Vol. 321, **1996**, p. 5.
- [47] M. Baran, G. Levchenko, V. P. Dyakonov, G. Shymchak, *Physica C* **1995**, 241, 383.
- [48] S. Sugano, Y. Tanabe, H. Kanimura, *Multiplets of Transition Metal Ions (Pure Appl. Phys.* **1970**, 33).
- [49] E. Codjovi, L. Sommier, O. Kahn, C. Jay, *New. J. Chem.* **1996**, 20, 503.
- [50] E. Codjovi, W. Morscheidt, J. Jeftic, J. Linares, M. Nogues, A. Goujon, O. Roubeau, H. Constant-Machado, A. Desaix, A. Bousseksou, M. Verdaguer, F. Varret, *Mol. Cryst. Liq. Cryst.* **1999**, 335, 583.
- [51] (a) J. H. Takemoto, B. Hutchinson, *Inorg. Nucl. Chem. Lett.* **1972**, 8, 769. (b) J. H. Takemoto, B. Hutchinson, *Inorg. Chem.* **1973**, 12, 705. (c) J. H. Takemoto, B. Streusand, B. Hutchinson, *Spectrochim. Acta Part A* **1974**, 30, 827.
- [52] A. Hofer, Dissertation Universität Mainz, **2000**.
- [53] (a) W. A. Baker Jr, G. J. Long, *J. Chem. Soc., Chem. Comm.* **1965**, 15, 368. (b) E. König, K. Madeja, *Inorg. Chem.* **1967**, 6, 48. (c) E. König, K. Madeja, *Spectrochim. Acta* **1967**, 23A, 45.
- [54] E. W. Müller, J. Ensling, H. Spiering, P. Gülich, *Inorg. Chem.* **1983**, 22, 2074.
- [55] (a) R. Herber, L. M. Casson, *Inorg. Chem.* **1986**, 25, 847. (b) R. H. Herber, *Inorg. Chem.* **1987**, 26, 173. (c) D. C. Figg, R. H. Herber, *Inorg. Chem.* **1990**, 29, 2170.
- [56] A. Bousseksou, J. J. McGarvey, F. Varret, J. A. Real, J.-P. Tuchagues, A. C. Dennis, M. L. Boillot, *Chem. Phys. Lett.* **2000**, 318, 409.
- [57] M. Konno, M. Mikami-Kido, *Bull. Chem. Soc. Jpn.* **1991**, 64, 339.
- [58] C. L. Zilverentant, G. A. van Albada, A. Bousseksou, J. G. Haasnoot, J. Reedijk, *Inorg. Chim. Acta* **2000**, 303, 287.
- [59] L. A. Sheludyakova, L. G. Lavrenova, *J. Struct. Chem.* **1997**, 38, 853.
- [60] P. J. van Koningsbruggen, J. S. Miller, unpublished results, **1998**.
- [61] (a) J. Jung, H. Spiering, Z. Yu, P. Gülich, *Hyperfine Inter.* **1995**, 95, 107. (b) J. Jung, H. Spiering, P. Gülich, *Conference Proceedings, ICAME* **1996**, 95, 879.
- [62] K. Kaji, M. Sorai, *Thermochim. Acta* **1985**, 88, 185.
- [63] R. Jakobi, H. Romstedt, H. Spiering, P. Gülich, *Angew. Chem. Int. Ed. Engl.* **1992**, 31, 178.
- [64] A. J. Conti, K. Kaji, Y. Nagano, K. M. Sena, Y. Yumoto, R. K. Chadha, A. L. Rheingold, M. Sorai, D. N. Hendrickson, *Inorg. Chem.* **1993**, 32, 2681.

- [65] (a) E. König, G. Ritter, S. K. Kulshreshta, J. Waigel, H. A. Goodwin, *Inorg. Chem.* **1984**, 23, 1896. (b) S. K. Kulshreshta, R. M. Iyer, E. König, G. Ritter, *Chem. Phys. Lett.* **1984**, 110, 201. (c) S. K. Kulshreshta, R. Sasikala, E. König, *Chem. Phys. Lett.* **1986**, 123, 215. (d) S. K. Kulshreshta, R. M. Iyer, *Chem. Phys. Lett.* **1987**, 134, 239.
- [66] K. D. M. Harris, M. Tremayne, *Chem. Mater.* **1998**, 8, 2554.
- [67] (a) C. Cartier, P. Thuéry, M. Verdagner, J. Zarembowitch, A. Michalowicz, *J. Phys.* **1986**, C8, 563. (b) P. Thuéry, J. Zarembowitch, A. Michalowicz, O. Kahn, *Inorg. Chem.* **1987**, 26, 851. (c) J. Zarembowitch, P. Thuéry, A. Dworkin, A. Michalowicz, *J. Chem. Research (S)* **1987**, 146. (d) C. Cartier, P. Rudolf, A.-M. Flank, C. T. Chen, *J. Phys. Chem.* **1992**, 96, 6196.
- [68] J. Etourneau, *Bull. Korean Chem. Soc.* **1998**, 19, 5.
- [69] J. E. Penner-Hahn, *Coord. Chem. Rev.* **1999**, 190, 1101.
- [70] G. Sankar, J. M. Thomas, V. Varma, G. U. Kulkarni, C. N. R. Rao, *Chem. Phys. Lett.* **1996**, 251, 79.
- [71] N. A. Young, *J. Chem. Soc., Dalton Trans.* **1996**, 1275.
- [72] (a) H. Welker, H. F. Grünsteudel, G. Ritter, R. Lübbbers, H. J. Hesse, G. Nowitzke, G. Wortmann, H. A. Goodwin, *Conference Proceedings, ICAME 95*, **1996**, 19. (b) R. Lübbbers, G. Nowitzke, H. A. Goodwin, G. Wortmann, *J. Phys. IV* **1997**, 7, 651.
- [73] J. A. Real, I. Castro, A. Bousseksou, M. Verdagner, R. Burriel, M. Castro, J. Linares, F. Varret, *Inorg. Chem.* **1997**, 36, 455.
- [74] C. Butzlaff, E. Bill, W. Meyer, H. Winkler, A. X. Trautwein, T. Beissel, K. Wieghardt, *Hyperfine Interact.* **1994**, 90, 453.
- [75] C. M. McGrath, C. J. O'Connor, C. Sangregorio, J. M. W. Seddon, E. Sinn, F. E. Sowrey, N. A. Young, *Inorg. Chem. Comm.* **1999**, 2, 536.
- [76] J. Zarembowitch, *New. J. Chem.* **1992**, 16, 255.
- [77] C. Hannay, M. J. Hubin-Franskin, F. Grandjean, V. Briois, J. P. Itié, A. Polian, S. Trofimenko, G. J. Long, *Inorg. Chem.* **1997**, 36, 5580.
- [78] H. Oyanagi, T. Iizuka, T. Matsushita, S. Saigo, R. Makino, Y. Ishimura, T. Ishiguro, *J. Phys. Soc. Jpn.* **1987**, 56, 3381.
- [79] (a) H. Winkler, A. Sawaryn, A. W. Trautwein, C. Hermes, H. Toftlund, *Recl. Trav. Chim. Pays. B.* **1987**, 106, 323. (b) H. Winkler, A. Sawaryn, A. X. Trautwein, A. S. Yousif, C. Hermes, H. Toftlund, R. Herber, *Hyperfine Interact.* **1988**, 42, 921.
- [80] V. Briois, C. Cartier, P. Saintavit, C. Brouder, A. M. Flank, *J. Am. Chem. Soc.* **1995**, 117, 1019.
- [81] M. Abbate, J. C. Fuggle, A. Fujimori, L. H. Tjeng, C. T. Chen, R. Potze, G. A. Sawatzky, H. Eisaki, S. Uchida, *Phys. Rev. B* **1993**, 47, 16124.
- [82] R. Boca, M. Vrbová, R. Werner, W. Haase, *Chem. Phys. Lett.* **2000**, 328, 188.
- [83] (a) A. Michalowicz, J. Moscovici, B. Ducourant, D. Cracco, O. Kahn, *Chem. Mater.* **1995**, 7, 1833. (b) A. Michalowicz, J. Moscovici, O. Kahn, *J. Phys. IV* **1997**, 7, 633.
- [84] (a) N. V. Bausk, S. B. Erenburg, L. G. Lavrenova, L. N. Mazalov, *J. Struct. Chem.* **1995**, 36, 925. (b) S. B. Erenburg, N. V. Bausk, V. A. Varnek, L. G. Lavrenova, *J. Mag. Mag. Mat.* **1996**, 157/158, 595. (c) S. B. Erenburg, N. V. Bausk, V. A. Varnek, L. N. Mazalov, *Sol. State Ionics* **1997**, 104-103, 571.
- [85] Y. Garcia, P. J. van Koningsbruggen, G. Bravic, P. Guionneau, D. Chasseau, G. L. Cascarano, J. Moscovici, K. Lambert, A. Michalowicz, O. Kahn, *Inorg. Chem.* **1997**, 36, 6357.
- [86] (a) T. Yokoyama, Y. Murakami, M. Kiguchi, T. Komatsu, N. Kojima, *Phys. Rev. B* **1998**, 58(21), 14238. (b) N. Kojima, Y. Murakami, T. Komatsu et al. *Synthetic Met.* **1999**, 103, 2154.
- [87] A. Michalowicz, J. Moscovici, Y. Garcia, O. Kahn, *J. Synchrotron Rad.* **1999**, 6, 231.

- [88] P. J. van Koningsbruggen, Y. Garcia, O. Kahn, H. Kooijman, A. L. Spek, J. G. Haasnoot, J. Moscovici, K. Provost, A. Michalowicz, L. Fournès, F. Renz, P. Gütllich, *Inorg. Chem.* **2000**, *39*, 1891.
- [89] M. Verelst, L. Sommier, P. Lecante, A. Mosset, O. Kahn, *Chem. Mater.* **1998**, *10*, 980.
- [90] (a) S. Erenburg, N. V. Bausk, L. G. Lavrenova, L. N. Mazalov, *J. Synchr. Rad.* **1999**, *6*, 576. (b) S. B. Erenburg, N. V. Bausk, L. G. Lavrenova, L. N. Mazalov, *Nucl. Inst. Meth. Phys. Res. A* **2000**, *448*, 351.
- [91] J.-J. Lee, H. Sheu, C.-R. Lee, J.-M. Chen, J.-F. Lee, C.-C. Wang, C.-H. Huang, Y. Wang, *J. Am. Chem. Soc.* **2000**, *122*, 5742.
- [92] Zs. Kajcsos, A. Vértes, Cs. Szeles, K. Burger, H. Spiering, P. Gütllich, J. Ch. Abbe, H. Haissler, C. P. Brauer, C. P. Köhler, in *Positron Annihilation* (Eds. P. C. Jain, R. M. Singru, K. P. Gopinathan), World Scientific, Singapore, **1985**, p. 195.
- [93] A. Vértes, Zs. Kajcsos, L. Marczis, E. Brauer, J. Hüller, I. Zay, K. Burger, *J. Phys. Chem.* **1984**, *88*, 3969.
- [94] A. Vértes, K. Süvegh, R. Hinek, P. Gütllich, *Hyperfine Interact.* **1994**, *84*, 483.
- [95] Y. Nagai, H. Saito, T. Hyodo, A. Vértes, K. Süvegh, *Phys. Rev. B* **1998**, *57*, 14119.
- [96] E. Gerdau, R. Ruffer, H. Winkler, W. Tolksdorf, C. P. Klages, J. P. Hannon, *Phys. Rev. Lett.* **1985**, *54*, 835.
- [97] U. van Bürck, G. V. Smirnov, *Hyperfine Interact.* **1994**, *90*, 313.
- [98] H. Grünsteudel, H. Paulsen, W. Meyer-Klaucke, H. Winkler, A. X. Trautwein, H. F. Grünsteudel, A. Q. R. Baron, A. I. Chumakov, R. Ruffer, H. Toftlund, *Hyperfine Interact.* **1998**, *113*, 311.
- [99] H. Grünsteudel, H. Paulsen, H. Winkler, A. X. Trautwein, H. Toftlund, *Hyperfine Interact.* **1999**, *123/124*, 841.
- [100] I. Dészi, B. Molnar, T. Tarnoczi, K. Tompa, *J. Inorg. Nucl. Chem.* **1967**, *29*, 2486.
- [101] H. L. Chum, J. A. Vanin, M. I. D. Holanda, *Inorg. Chem.* **1982**, *21*, 1146.
- [102] C. J. Janiak, T. G. Scharmann, T. Brauniger, J. Holubova, M. Nadvornik, *Z. Anorg. Allg. Chem.* **1998**, *624*, 769.
- [103] A. Ozarowski, Y. Shunzong, B. R. McGarvey, A. Mislankar, J. E. Drake, *Inorg. Chem.* **1991**, *30*, 3167.
- [104] (a) M. Bokor, T. Marek, K. Tompa, *J. Magn. Reson. Ser. A* **1996**, *122*, 157. (b) M. Bokor, T. Marek, K. Süvegh, K. Tompa, A. Vertes, Z. Nemes-Vetessy, K. Burger, *J. Radioan. Nucl. Ch.* **1996**, *211*, 247. (c) T. Marek, M. Bokor, G. Lansada, L. Parkanyi, J. Buschmann, *J. Phys. Chem. Solids* **2000**, *61*, 621.
- [105] M. Bokor, T. Marek, K. Tompa, P. Gütllich, A. Vertes, *Eur. Phys. J. D* **1999**, *7*, 567.
- [106] Y. Servant, C. Cantin, O. Kahn, J. Kliava, submitted.
- [107] P. S. Rao, A. Reuveni, B. R. McGarvey, P. Ganguli, P. Gütllich, *Inorg. Chem.* **1981**, *20*, 204.
- [108] W. Vreugdenhil, J. G. Haasnoot, O. Kahn, P. Thuéry, J. Reedijk, *J. Am. Chem. Soc.* **1987**, *109*, 5272.
- [109] A. Ozarowski, B. R. McGarvey, *Inorg. Chem.* **1989**, *28*, 2262.
- [110] (a) C. Cantin, J. Kliava, Y. Servant, L. Sommier, O. Kahn, *Appl. Magn. Res.* **1997**, *12*, 87 (b) C. Cantin, H. Daubric, J. Kliava, O. Kahn, *Solid State Comm.* **1998**, *108*, 17. (c) C. Cantin, H. Daubric, J. Kliava, Y. Servant, L. Sommier, O. Kahn, *J. Phys. Condens. Matt.* **2000**, *12*, 5484.
- [111] (a) H. Daubric, C. Cantin, C. Thomas, J. Kliava, J. F. Letard, O. Kahn, *Chem. Phys.* **1999**, *244*, 75. (b) H. Daubric, J. Kliava, P. Guionneau, D. Chasseau, J. F. Letard, O. Kahn, *J. Phys. Cond. Matter* **2000**, *12*, 5481.
- [112] C. Cantin, J. Kliava, Y. Servant, L. Sommier, O. Kahn, *Appl. Magn. Res.* **1997**, *12*, 81.

- [113] J. Fleisch, P. Gütlich, K. M. Hasselbach, *Inorg. Chem.* **1977**, *16*, 1979.
- [114] (a) O. Kahn, J. Kröber, C. Jay, *Adv. Mater* **1992**, *4*, 718. (b) O. Kahn, E. Codjovi, Y. Garcia, P. J. van Koningsbruggen, R. Lapouyade, L. Sommier, *ACS Symp. Ser.* **1996**, *644*, 298. (c) O. Kahn, C. Jay-Martinez, *Science* **1998**, *279*, 44.
- [115] G. A. Renovitch, W. A. Baker, Jr *J. Am. Chem. Soc.* **1967**, *89*, 6377.
- [116] M. Sorai, J. Ensling, P. Gütlich, *Chem. Phys.* **1976**, *18*, 199.
- [117] H. Köppen, E. W. Müller, C. P. Köhler, H. Spiering, E. Meissner, P. Gütlich, *Chem. Phys. Lett.* **1982**, *91*, 348.
- [118] H. Spiering, E. Meissner, H. Köppen, E. W. Müller, P. Gütlich, *Chem. Phys.* **1982**, *68*, 65.
- [119] P. Ganguli, P. Gütlich, E. W. Müller, *Inorg. Chem.* **1982**, *21*, 3429.
- [120] (a) J. P. Martin, J. Zarembowitch, A. Dworkin, J. G. Haasnoot, E. Codjovi, *Inorg. Chem.* **1994**, *33*, 2617. (b) J. P. Martin, J. Zarembowitch, A. Bousseksou, A. Dworkin, J. G. Haasnoot, F. Varret, *Inorg. Chem.* **1994**, *33*, 6325.
- [121] T. Buchen, P. Poganiuch, P. Gütlich, *J. Chem. Soc., Dalton Trans.* **1994**, *15*, 2285.
- [122] J. Jung, G. Schmitt, L. Wiehl, A. Hauser, K. Knorr, H. Spiering, P. Gütlich, *Z. Phys. B* **1996**, *100*, 523.
- [123] (a) L. G. Lavrenova, V. N. Ikorskii, V. A. Varnek, I. M. Oglezneva, S. V. Larionov, *J. Struct. Chem.* **1993**, *34*, 960. (b) Y. G. Shvedenkov, V. N. Ikorskii, L. G. Lavrenova, V. A. Drebuschak, N. G. Yudina, *J. Struct. Chem.* **1997**, *38*, 579. (c) Y. G. Shvedenkov, V. N. Ikorskii, L. G. Lavrenova, *Czech. J. Phys.* **1996**, *46*, 2147.
- [124] K. Drabent, R. Bronisz, M. F. Rudolf, *Conference Proceedings, ICAME 95*, **1996**, *50*, 7.
- [125] (a) I. Sanner, E. Meissner, H. Köppen, H. Spiering, P. Gütlich, *Chem. Phys.* **1984**, *86*, 227. (b) N. Willenbacher, H. Spiering, *J. Phys. C: Solid State Phys.* **1988**, *21*, 1423. (c) H. Spiering, N. Willenbacher, *J. Phys.: Condens. Matter* **1989**, *1*, 10089.
- [126] L. Wiehl, G. Kiel, C. P. Köhler, H. Spiering, P. Gütlich, *Inorg. Chem.* **1986**, *25*, 1565.
- [127] (a) M. Mikami, M. Konno, Y. Saito, *Chem. Phys. Lett.* **1979**, *63*, 566. (b) M. Mikamikido, Y. Saito, *Acta. Cryst. B.* **1982**, *38*, 452.
- [128] A. M. Greenaway, C. J. O'Connor, A. Schrock, E. Sinn, *Inorg. Chem.* **1979**, *18*, 2692.
- [129] A. M. Greenaway, E. Sinn, *J. Am. Chem. Soc.* **1978**, *100*, 8080.
- [130] B. A. Katz, C. E. Strouse, *J. Am. Chem. Soc.* **1979**, *101*, 6214.
- [131] B. A. Katz, C. E. Strouse, *Inorg. Chem.* **1980**, *19*, 658.
- [132] M. Sorai, J. Ensling, K. M. Hasselbach, P. Gütlich, *Chem. Phys.* **1977**, *20*, 197.
- [133] P. Gütlich, H. Köppen, H. G. Steinhäuser, *Chem. Phys. Lett.* **1980**, *74*, 3.
- [134] R. Claude, J. Zarembowitch, J. Philoche, M. Levisalles, F. D'Yvoire, *New. J. Chem.* **1991**, *15*, 635.
- [135] J. J. A. Kolnaar, M. I. de Heer, H. Kooijman, A. L. Spek, G. Schmitt, V. Ksenofontov, P. Gütlich, J. G. Haasnoot, J. Reedijk, *Eur. J. Inorg. Chem.* **1999**, 881.
- [136] L. Salmon, B. Donnadieu, A. Bousseksou, J.-P. Tuchagues, *C. R. Acad. Sci Paris* **1999**, *IIc*, 305.
- [137] B. R. Müller, G. Leibelng, E. G. Jäger, *Chem. Phys. Lett.* **2000**, *319*, 368.
- [138] Y. Garcia, P. Guionneau, G. Bravic, D. Chasseau, J. A. K. Howard, O. Kahn, V. Ksenofontov, S. Reiman, P. Gütlich, *Eur. J. Inorg. Chem.* **2000**, 1531.
- [139] H. Sugiyarto, H. A. Goodwin, *Aust. J. Chem.* **1988**, *41*, 1645.
- [140] H. Sugiyarto, D. C. Graig, A. D. Rae, H. A. Goodwin, *Aust. J. Chem.* **1993**, *46*, 1269
- [141] H. Sugiyarto, D. C. Graig, A. D. Rae, H. A. Goodwin, *Aust. J. Chem.* **1994**, *47*, 869.
- [142] B. J. Childs, D. C. Craig, A. D. Rae, H. A. Goodwin, *Aust. J. Chem.* **1994**, *47*, 891.
- [143] K. H. Sugiyarto, D. C. Craig, A. D. Rae, H. A. Goodwin, *Aust. J. Chem.* **1996**, *49*, 505.

- [144] K. H. Sugiyarto, K. Weitzner, D. C. Graig, H. A. Goodwin, *Aust. J. Chem.* **1997**, *50*, 869.
- [145] L. S. Harimanow, K. H. Sugiyarto, D. C. Craig, M. L. Scudder, H. A. Goodwin, *Aust. J. Chem.* **1999**, *52*, 109.
- [146] W. Vreugdenhil, J. H. van Diemen, R. A. G. de Graaff, J. G. Haasnoot, J. Reedijk, A. M. van der Kraan, O. Kahn, J. Zarembowitch, *Polyhedron* **1990**, *9*, 2971.
- [147] P. J. van Koningsbruggen, Y. Garcia, E. Codjovi, R. Lapouyade, O. Kahn, L. Fournès, L. Rabardel, *J. Mater. Chem.* **1997**, *7*, 2069.
- [148] Y. Garcia, P. J. van Koningsbruggen, E. Codjovi, R. Lapouyade, O. Kahn, L. Rabardel, *J. Mat. Chem.* **1997**, *7*, 857.
- [149] Y. Garcia, P. J. van Koningsbruggen, R. Lapouyade, L. Fournès, L. Rabardel, O. Kahn, V. Ksenofontov, G. Levchenko, P. Gütllich, *Chem. Mater.* **1998**, *10*, 2426.
- [150] Y. Garcia, P. J. van Koningsbruggen, R. Lapouyade, L. Rabardel, O. Kahn, M. Wierczorek, R. Bronisz, Z. Ciunik, M. F. Rudolf, *C. R. Acad. Sci. Paris IIC*, **1998**, 523.
- [151] S. Toyazaki, Y. Murakami, T. Komatsu, N. Kojima, T. Yokoyama, *Mol. Cryst. Liq. Cryst* **2000**, *343*, 493.
- [152] O. Kahn, C. Jay, Y. Garcia, E. Codjovi, Eur. Patent 842988- Philips Electronics NV, **1998**.
- [153] L. Wiehl, H. Spiering, P. Gütllich, K. Knorr, *J. Appl. Cryst.* **1990**, *23*, 151.
- [154] E. W. Müller, H. Spiering, P. Gütllich, *Chem. Phys. Lett.* **1982**, *93*, 567.
- [155] B. Gallois, J. A. Real, C. Hauw, J. Zarembowitch, *Inorg. Chem.* **1990**, *29*, 1152.
- [156] J.-F. Letard, P. Guionneau, L. Rabardel, J. A. K. Howard, A. E. Goeta, D. Chasseau, O. Kahn, *Inorg. Chem.* **1998**, *37*, 4432.
- [157] (a) M. S. Haddad, W. D. Federer, M. W. Lynch, D. N. Hendrickson, *J. Am. Chem. Soc.* **1980**, *102*, 1468. (b) M. S. Haddad, W. D. Federer, M. W. Lynch, D. N. Hendrickson, *Inorg. Chem.* **1981**, *20*, 131.
- [158] E. W. Müller, H. Spiering, P. Gütllich, *Inorg. Chem.* **1984**, *23*, 119.
- [159] P. Ganguli, P. Gütllich, E. W. Müller, W. Irlner, *J. Chem. Soc., Dalton Trans.* **1981**, 441.
- [160] J. Kröber, J. P. Audière, R. Claude, E. Codjovi, O. Kahn, J. G. Haasnoot, F. Grolière, C. Jay, A. Bousseksou, J. Linares, F. Varret, A. Gonthier-Vassal, *Chem. Mater.* **1994**, *6*, 1404.
- [161] E. König, K. Madeja, K. Watson, *J. Am. Chem. Soc.* **1968**, *90*, 1146.
- [162] G. S. Matouzenko, A. Bousseksou, S. Lecocq, P. J. van Koningsbruggen, M. Perrin, O. Kahn, A. Collet, *Inorg. Chem.* **1997**, *36*, 5869.
- [163] A. H. Ewald, R. L. Martin, G. I. Ross, A. H. White, *Proc. Roy. Soc. (London)* **1964**, *A 280*, 235.
- [164] E. König, K. Madeja, *Chem. Comm.* **1966**, *3*, 61.
- [165] D. B. Chesnut, *J. Chem. Phys.* **1964**, *40*, 405.
- [166] R. A. Bari, X. Sivardiè, *Phys. Rev. B* **1972**, *5*, 4466.
- [167] J. Wajnflasz, *Phys. Stat. Sol.* **1970**, *40*, 537.
- [168] J. P. Jesson, S. Trofimenko, D. R. Eaton, *J. Am. Chem. Soc.* **1967**, *89*, 3158.
- [169] C. P. Slichter, H. G. Drickamer, *J. Chem. Phys.* **1972**, *56*, 2142.
- [170] E. König, G. Ritter, *Solid State Comm.* **1976**, *18*, 279.
- [171] R. Zimmermann, E. König, *J. Phys. Chem. Solids* **1977**, *38*, 779.
- [172] E. König, G. Ritter, Mössbauer Effect Methodology, p. 1, 9. (Plenum Press, New York/London, **1974**).
- [173] P. Adler, L. Wiehl, E. Meissner, C. P. Köhler, H. Spiering, P. Gütllich, *J. Phys. Chem. Solids* **1987**, *48*, 517.
- [174] R. Jakobi, H. Spiering, P. Gütllich, *J. Phys. Chem. Solids* **1992**, *53*, 267.
- [175] J. D. Eshelby, *Sol. State. Phys.* **1956**, *3*, 79.

- [176] Y. Qi, E. W. Müller, H. Spiering, P. Gütllich, *Chem. Phys. Lett.* **1983**, *101*, 503.
- [177] A. Bousseksou, N. Negre, M. Goiran, L. Salmon, J.-P. Tuchagues, M.-L. Boillot, K. Boukheddaden, F. Varret, *Eur. Phys. J. B* **2000**, *13*, 451.
- [178] J. Lejay, A. G. M. Jansen, P. Wyder, W. Bronger, W. Kläui, *Phys. Rev. B* **1991**, *43*, 8196.
- [179] V. Petrouleas, J.-P. Tuchagues, *Chem. Phys. Lett.* **1987**, *137*, 21.
- [180] N. Sasaki, T. Kambara, *Phys. Rev. B* **1989**, *40*, 2442.
- [181] A. Bousseksou, J. Nasser, J. Linares, K. Boukheddaden, F. Varret, *J. Phys. I* **1992**, *2*, 1381.
- [182] B. G. Vekhter, *J. Appl. Physics* **1994**, *75*, 5863.
- [183] D. Boinard, A. Bousseksou, A. Dworkin, J. M. Savariault, F. Varret, J.-P. Tuchagues, *Inorg. Chem.* **1994**, *33*, 271.
- [184] H. Spiering, T. Kohlhaas, H. Romstedt, A. Hauser, C. Bruns-Yilmaz, J. Kusz, P. Gütllich, *Coord. Chem. Rev.* **1999**, *109-192*, 629.
- [185] R. Jakobi, H. Spiering, L. Wiehl, E. Gmelin, P. Gütllich, *Inorg. Chem.* **1988**, *27*, 1823.
- [186] H. Romstedt, H. Spiering, P. Gütllich, *J. Phys. Chem. Sol.* **1998**, *59*, 1353.
- [187] J. A. Real, H. Bolvin, A. Bousseksou, A. Dworkin, O. Kahn, F. Varret, J. Zarembowitch, *J. Am. Chem. Soc.* **1992**, *114*, 4650.
- [188] T. Kohlaas, H. Spiering, P. Gütllich, *Z. Physik B* **1997**, *102*, 455.
- [189] H. Romstedt, A. Hauser, H. Spiering, *J. Phys. Chem. Solids* **1998**, *59*, 265.
- [190] C. P. Köhler, R. Jakobi, E. Meissner, L. Wiehl, H. Spiering, P. Gütllich, *J. Phys. Chem. Solids* **1990**, *51*, 239.
- [191] E. Meissner, H. Köppen, H. Spiering, P. Gütllich, *Chem. Phys. Lett.* **1983**, *95*, 163.
- [192] T. Kohlhaas, Dissertation, Universität Mainz, **1995**.
- [193] S. Decurtins, P. Gütllich, C. P. Köhler, H. Spiering, A. Hauser, *Chem. Phys. Lett.* **1984**, *105*, 1.
- [194] S. Decurtins, P. Gütllich, K. M. Hasselbach, H. Spiering, A. Hauser, *Inorg. Chem.* **1985**, *24*, 2174.
- [195] A. Hauser, *Coord. Chem. Rev.* **1991**, *111*, 275 and references therein.
- [196] A. Hauser, *Chem. Phys. Lett.* **1986**, *124*, 543.
- [197] S. Decurtins, P. Gütllich, C. P. Köhler, H. Spiering, *Chem. Comm.* **1985**, 430.
- [198] A. Hauser, J. Adler, P. Gütllich, *Chem. Phys. Lett.* **1988**, *152*, 468.
- [199] A. Hauser, A. Vef, P. Adler, *J. Chem. Phys.* **1991**, *95*, 8710.
- [200] J.-F. Letard, O. Nguyen, H. Soyer, C. Mingotaud, P. Delhaès, O. Kahn, *Inorg. Chem.* **1999**, *38*, 3020.
- [201] K. U. Baldenius, A. K. Campen, H. D. Höhnk, A. J. Rest., *J. Mol. Struct.* **1987**, *157*, 295.
- [202] C.-C. Wu, J. Jung, P. K. Gantzel, P. Gütllich, D. N. Hendrickson, *Inorg. Chem.* **1997**, *36*, 5339.
- [203] S. Hayami, Z.-Z. Gu, M. Shiro, Y. Einaga, A. Fujishima, O. Sato, *J. Am. Chem. Soc.* **2000**, *122*, 7126.
- [204] A. Hauser, P. Gütllich, H. Spiering, *Inorg. Chem.* **1986**, *25*, 4245.
- [205] (a) R. Hinek, H. Spiering, D. Schollmeyer, P. Gütllich, A. Hauser, *Chem. Eur. J.* **1996**, *2*, 1427. (b) R. Hinek, H. Spiering, P. Gütllich, A. Hauser, *Chem. Eur. J.* **1996**, *2*, 1435.
- [206] A. Hauser, *Chem. Phys. Lett.* **1992**, *192*, 65.
- [207] J. Ensling, P. Gütllich, K. M. Hasselbach, B. W. Fitzsimmons, *Chem. Phys. Lett.* **1976**, *42*, 232.
- [208] J. Ensling, B. W. Fitzsimmons, P. Gütllich, *Angew. Chem.* **1970**, *9*, 637.
- [209] J. Fleisch, P. Gütllich, *Chem. Phys. Lett.* **1976**, *42*, 237.

- [210] J. Fleisch, P. Gütllich, *Chem. Phys. Lett.* **1977**, 45, 29.
- [211] J. Fleisch, P. Gütllich, H. Köppen, *Radiochem. Radioanalyt. Lett.* **1980**, 42, 279.
- [212] P. Gütllich, H. Köppen, *J. Phys. (Paris)* **1980**, 41-C1, 311.
- [213] C. Hennen, Master's thesis, University of Mainz, **1986**.
- [214] H. Sano, P. Gütllich, in *Hot Atom Chemistry*, edited by T. Matsuura (Kodanshi, Tokyo) **1984**, pp. 265-302.
- [215] R. Grimm, P. Gütllich, E. Kankeleit, R. Link, *J. Chem. Phys.* **1977**, 67, 5491.
- [216] A. Hauser, *Comments Inorg. Chem.* **1995**, 17, 17.
- [217] R. Albrecht, M. Alflen, P. Gütllich, Zs. Kajcsos, R. Schulze, H. Spiering, F. Tuczek, *Nucl. Instrum. Methods A* **1987**, 257, 209.
- [218] A. Hauser, *Chem. Phys. Lett.* **1990**, 173, 507.
- [219] S. Deisenroth, A. Hauser, H. Spiering, P. Gütllich, *Hyperf. Interact.* **1994**, 93, 1573.
- [220] R. Sieber, S. Decurtins, H. Stoeckli-Evans, C. Wilson, D. Yufit, J. A. K. Howard, S. C. Capelli, A. Hauser A., *Chem. Eur. J.* **2000**, 6, 361.
- [221] V. Chameko, M. Gross, P. Gütllich, S. Decurtins, unpublished results, **1999**.
- [222] S. Kremer, W. Henke, D. Reinen, *Inorg. Chem.* **1982**, 21, 3013.
- [223] H. Oshio, H. Spiering, V. Ksenofontov, F. Renz, P. Gütllich, *Inorg. Chem.*, **2001**, 40, 1143.
- [224] T. Sato, F. Ambe, T. Kitazawa, H. Sano, M. Takeda, *Chem. Lett.* **1997**, 12, 1287.
- [225] T. Kitazawa, Y. Gomi, M. Takahashi, M. Takeda, M. Enomoto, A. Miyazaki and T. Enoki, *J. Mater. Chem.* **1996**, 6, 119.
- [226] Z. J. Zhong, J-Q. Tao, Z. Yu, C-Y. Dun, Y-J. Liu, X-Z. You, *J. Chem. Soc., Dalton Trans.*, **1998**, 327.
- [227] T. Buchen, P. Gütllich, K. H. Sugiyarto, H. A. Goodwin, *Chem. Eur. J.* **1996**, 2, 1134.
- [228] Y. Garcia, O. Kahn, L. Rabardel, B. Chansou, L. Salmon, J-P. Tuchagues, *Inorg. Chem.* **1999**, 38, 4663.
- [229] J. A. Real, J. Zarembowitch, O. Kahn, X. Solans, *Inorg. Chem.* **1987**, 26, 2939.
- [230] (a) G. Vos, R. A. LeFèbre, R. A. G. de Graaf, J. G. Haasnoot, J. Reedijk, *J. Am. Chem. Soc.* **1983**, 105, 1682. (b) G. Vos, R. A. G. de Graaf, J. G. Haasnoot, A. M. van der Kraan, P. de Vaal, J. Reedijk, *Inorg. Chem.* **1984**, 23, 2905.
- [231] J. J. A. Kolnaar, G. van Dijk, H. Kooijman, A. L. Spek, V. G. Ksenofontov, P. Gütllich, J. G. Haasnoot, J. Reedijk, *Inorg. Chem.* **1997**, 36, 2433.
- [232] M. Thomann, O. Kahn, J. Guilhem, F. Varret, *Inorg. Chem.* **1994**, 33, 6029.
- [233] Y. Garcia, P. Guionneau, G. Bravic, D. Chasseau, J. A. K. Howard, O. Kahn, V. Ksenofontov, S. Reiman, P. Gütllich, *Eur. J. Inorg. Chem.* **2000**, 1531.
- [234] E. Breuning, M. Ruben, J. M. Lehn, F. Renz, Y. Garcia, V. Ksenofontov, P. Gütllich, E. Wegelius, K. Rissanen, *Angew. Chem. Int. Ed.* **2000**, 39, 2377.
- [235] J. J. A. Kolnaar, M. I. de Heer, H. Kooijman, A. L. Spek, G. Schmitt, V. Ksenofontov, P. Gütllich, J. G. Haasnoot, J. Reedijk, *Eur. J. Inorg. Chem.* **1999**, 881.
- [236] W. Vreugdenhil, J. H. van Diemen, R. A. G. de Graaff, J. G. Haasnoot, J. Reedijk, A. M. van der Kraan, O. Kahn, J. Zarembowitch, *Polyhedron* **1990**, 9, 2971.
- [237] R. Bronisz, Z. Ciunik, K. Drabent, M. F. Rudolf, Conf. Proc., ICAME-95, **1996**, 50, 15.
- [238] R. Bronisz, Ph D Thesis, University of Wroclaw, **1999**.
- [239] J. A. Real, E. Andrés, M. C. Muñoz, M. Julve, T. Granier, A. Bousseksou, F. Varret, *Science*, 1995, **268**, 265.
- [240] N. Moliner, C. Muñoz, S. Letard, X. Solans, N. Menendez, A. Goujon, F. Varret, J. A. Real, *Inorg. Chem.* **2000**, 39, 5390.
- [241] P. J. van Koningsbruggen, Y. Garcia, H. Koojmaan, A. L. Spek, J. G. Haasnoot, O. Kahn, J. Linares, E. Codjovi, F. Varret, *J. Chem. Soc., Dalton Trans.* **2001**, 4, 466.

- [242] S. Brooker, P. G. Plieger, B. Moubaraki, K. S. Murray, *Angew. Chem. Int. Ed.* **1999**, 38 (3), 408.
- [243] M. Engeser, L. Fabbrizzi, M. Licchelli, D. Sacchi, *Chem. Comm.* **1999**, 1191.
- [244] J.-F. Letard, S. Montant, P. Guionneau, P. Martin, A. Le Calvez, E. Freisz, D. Chasseau, R. Lapouyade, O. Kahn, *Chem. Comm.* **1997**, 745.
- [245] D. Collison, C. D. Garner, C. M. McGrath, J. F. W. Mosselmans, M. D. Roper, J. M. W. Seddon, E. Sinn, N. A. Young, *J. Chem. Soc., Dalton Trans.* **1997**, 22, 4371.
- [246] J. Zarembowitch, C. Roux, M. L. Boillot, R. Claude, J.-P. Itie, A. Polian, M. Bolte, *Mol. Cryst. Liq. Cryst.* **1993**, 34, 247.
- [247] C. Roux, J. Zarembowitch, B. Gallois, M. Bolte, *New J. Chem.* **1992**, 16, 671.
- [248] C. Roux, J. Zarembowitch, B. Gallois, T. Granier, R. Claude, *Inorg. Chem.* **1994**, 33, 2273.
- [249] L. B. Feringa, W. F. Jager, B. Delange, *Tetrahedron* **1993**, 49, 8267.
- [250] M. L. Boillot, C. Roux, J.-P. Audière, A. Dausse, J. Zarembowitch, *Inorg. Chem.* **1996**, 35, 3975.
- [251] M. L. Boillot, S. Chantraine, J. Zarembowitch, J. Y. Lallemand, J. Prunet, *New J. Chem.* **1999**, 179.
- [252] A. Sour, M. L. Boillot, E. Rivière, P. Lesot, *Eur. J. Inorg. Chem.* **1999**, 2117.
- [253] (a) S. Hayami, K. Inoue, Y. Maeda, *Chem. Phys. Lett.* **1998**, 10, 987. (b) S. Hayami, K. Inoue, Y. Maeda, *Mol. Cryst. Liq. Cryst.* **1999**, 334, 1285.
- [254] S. Hirose, S. Hayami, Y. Maeda, *Bull. Chem. Soc. Jpn* **2000**, 73, 2059.
- [255] (a) H. Soyer, C. Mingotaud, M. L. Boillot, P. Delhaès, *Thin Solid Films* **1998**, 435, 327. (b) *ibid., Langmuir* **1998**, 14, 5890.
- [256] M. L. Boillot, A. Sour, P. Delhaes, C. Mingotaud, H. Soyer, *Coord. Chem. Rev.* **1999**, 192, 47.
- [257] A. Desaix, O. Roubeau, J. Jeftic, J. G. Haasnoot, K. Boukheddaden, E. Codjovi, J. Linares, M. Nagues, F. Varret, *Eur. Phys. B.* **1998**, 6, 183.
- [258] F. Varret, K. Boukheddaden, J. Jeftic, O. Roubeau, *Mol. Cryst. Liq. Cryst.* **1999**, 335, 561.
- [259] F. Renz, H. Spiering, H. A. Goodwin, P. Gütllich, *Hyperfine Interact.* **2000**, 126, 155.
- [260] E. König, G. Ritter, S. K. Kulshreshtha, J. Waigel, H. A. Goodwin, *Inorg. Chem.* **1984**, 23, 1896.
- [261] F. Renz, H. Oshio, V. Ksenofontov, M. Waldeck, H. Spiering, P. Gütllich, *Angew. Chem. Int. Ed.* **2000**, 39, 3699.
- [262] H. G. Drickamer, C. W. Frank, *Electronic Transitions and the High Pressure Chemistry and Physics of Solids*, Chapman and Hall, London, **1973**.
- [263] E. König, G. Ritter, J. Waigel, H. A. Goodwin, *J. Chem. Phys.* **1985**, 83, 3055.
- [264] V. Ksenofontov, H. Spiering, A. Schreiner, G. Levchenko, H. A. Goodwin, P. Gütllich, *J. Phys. Chem. Solids* **1999**, 60, 393.
- [265] V. Ksenofontov, G. Levchenko, H. Spiering, P. Gütllich, J.-F. Letard, Y. Bouhedja, O. Kahn, *Chem. Phys. Lett.* **1998**, 294, 545.
- [266] Y. Garcia, V. Ksenofontov, G. Levchenko, P. Gütllich, *J. Mater. Chem.* **2000**, 10, 2274.
- [267] P. J. Camp, G. N. Patey, *J. Phys. Condens. Matter* **1998**, 10, 10909.
- [268] J. Linares, H. Spiering, F. Varret, *Eur. Phys. J. B* **1999**, 10, 271.
- [269] S. Klokishner, J. Linares, F. Varret, *Chem. Phys.* **2000**, 255, 317.
- [270] Y. Garcia, V. Ksenofontov, G. Levchenko, G. Schmidt, P. Gütllich, *J. Phys. Chem. B* **2000**, 104, 5045.
- [271] E. Codjovi, J. Jeftic, N. Menendez, F. Varret, *C. R. Acad. Sci. IIC* **2001**, 181.
- [272] G. De Munno, M. Julve, J. A. Real, F. Lloret, R. Scopelliti, *Inorg. Chim. Acta* **1996**, 250, 81.

- [273] V. Ksenofontov, A. B. Gaspar, J. A. Real, P. Gütlich, *J. Phys. Chem.* **2001**, *105*, 12266.
- [274] T. Granier, B. Gallois, J. Gaultier, J. A. Real, J. Zarembowitch, *Inorg. Chem.* **1993**, *32*, 5305.
- [275] J. Kusz, H. Spiering, P. Gütlich, *J. Appl. Cryst.* **2000**, *33*, 201.

9 Interpretation and Calculation of Spin-Hamiltonian Parameters in Transition Metal Complexes

Frank Neese and Edward I. Solomon

9.1 Introduction

Experimental techniques that employ external magnetic fields such as magnetic susceptibility, electron paramagnetic resonance (EPR), electron nuclear double resonance (ENDOR), magnetic circular dichroism (MCD) or Mössbauer spectroscopy (MB) have been found to be extremely useful in studying the geometric and electronic structures of open shell transition metal ions [1]. They yield key contributions to the understanding of the structures and reactivities of transition metal ions in many areas of research ranging from material science to biochemistry and pharmacology. The underlying physical phenomena are related to the magnetic moment of electrons that couple to the external magnetic fields and to the magnetic moments of nuclei with a nuclear spin I that is different from zero. It should be noted that electrons couple about 10^3 times stronger to an external magnetic field than nuclei. Therefore the techniques of EPR and nuclear magnetic resonance (NMR) are rather different in their experimental requirements. EPR techniques employ radiation in the microwave frequency region ($h\nu \approx 0.3 \text{ cm}^{-1}$) while NMR transitions are observed with radiofrequency radiation ($h\nu \approx 0.0004 \text{ cm}^{-1}$).

Part of the success of magnetic techniques is that they yield detailed information about the electronic ground state configuration of open shell molecules and this information can be related to the properties of the chemical bonds in these systems. Since the energy differences that are involved in the experiments are small relative to the strength of typical chemical bonds ($1\text{--}5 \text{ eV} \approx 8000\text{--}40\,000 \text{ cm}^{-1}$) the perturbation provided by the method of observation is rather small. Therefore the electronic structure of the ground state configuration is studied without complications due to the presence of electronic relaxation (the change of electronic structure between the two states connected by a spectroscopic transition). This is an important difference to the spectroscopies performed in the visible and X-ray regions that employ photon energies that are on the same order of magnitude or larger than the strengths of the chemical bonds being studied. Therefore significant changes in the electronic structure can take place upon excitation. Consequently, the information provided by magnetic and optical techniques is complementary and much insight can be obtained by simultaneously studying the optical and magnetic properties of transition metal complexes. An important technique that connects the two spectroscopic domains is MCD spectroscopy [2] that will not be developed in this review but will be used in Section 9.5.

An extremely important step in the development of magnetic spectroscopy was the invention of the spin-Hamiltonian (SH) concept [3–12]. As will be described below, the SH provides a means of parameterizing the experimental results in a simple, unified language that makes no explicit reference to the geometric and electronic structure of the compound under investigation. Instead, the SH contains only spin operators and operates on a manifold of states that span the electronic ground state configuration. This tremendous reduction in complexity compared to the problem of analyzing the electronic and geometric structure of a given compound in detail comes at the price of the introduction of free parameters. However, the number of parameters introduced is not very large. By this procedure the analysis proceeds in two steps. In the first step the SH parameters are extracted from experimental data by fitting procedures. In the second, more complicated, step the relationship between the SH parameters and the geometric and electronic structure of the compound is elucidated using theoretical techniques. In many investigations the second step is omitted and many empirical or semi-empirical relationships exist that explain trends in the measured SH parameters for classes of substances (for reviews see for example [13, 14]).

The focus of this review is the second step of the analysis. Namely, we will address the following questions:

- What is the relationship between the SH parameters and the electronic structure of a transition metal complex?
- How can experimental information be used to analyze the electronic structure contributions to SH parameters? And, finally, we will address the reverse question
- How can the SH be predicted from first principles given the geometric structure of a given complex and how accurate are the presently available procedures?

In this review we will limit ourselves to the most frequently encountered SH parameters, namely the g -values, zero-field splittings (ZFSs) and hyperfine couplings (HFCs). Excluded are properties such as quadrupole couplings or Mössbauer isomer shifts [15, 16]. Also excluded are the subtleties that arise from exchange and double exchange interactions in oligonuclear transition metal complexes [17].

The review is organized as follows. In Section 9.2 we will briefly introduce the SH, its matrix elements and its eigenstates. Section 9.3 is devoted to a fairly detailed derivation of general equations for the SH parameters of interest in terms of many electron wavefunctions. The results are presented in Section 9.3.4. Subsequently in Section 9.3.5 we will approximate the many electron wavefunctions by single determinants to obtain a formulation in terms of molecular orbitals (MOs). In the next step, presented in Section 9.4, the treatment will be further simplified to the special case of ligand field theory. We will provide the relevant equations that arise for SH parameters in d^N systems and discuss the influence of covalency on these parameters. Section 9.5 provides case studies of several prototypical transition metal complexes that have been studied in detail experimentally. The emphasis here is on the interplay between theory and experiment and the impact of excited state spectroscopies for a concise understanding of SH parameters. Finally, Section 9.6 deals with computational approaches to predict SH parameters. The emphasis here

is on computationally tractable algorithms that provide good numerical agreement with experimental data.

9.2 The Spin-Hamiltonian

9.2.1 The SH

The basis of the magnetic phenomena to be discussed in this review is that electrons as well as nuclei with a non-zero spin possess magnetic dipole moments that are directly related to the presence of a non-zero spin. For a free electron the magnetic dipole moment is [4, 18–20]:

$$\hat{\boldsymbol{\mu}}_e = -\beta g_e \hat{\mathbf{S}} \quad (1)$$

where β is the Bohr magneton ($1.3316 \times 10^{-4} \text{ MHz T}^{-1}$), g_e is the free-electron g-value ($g_e = 2.002319\dots$) and $\hat{\mathbf{S}}$ is the operator for the electron spin. Likewise a nucleus with spin \hat{I} has the magnetic moment:

$$\hat{\boldsymbol{\mu}}_N = \beta_N g_N \hat{\mathbf{I}} \quad (2)$$

where β_N is the nuclear magneton ($7.2521 \times 10^{-8} \text{ MHz T}^{-1}$), g_N the nuclear g-value and $\hat{\mathbf{I}}$ the operator for the nuclear spin. The classical interaction of a magnetic dipole moment with a magnetic field is given by $E = -\hat{\boldsymbol{\mu}}\mathbf{B}$ which can be straightforwardly translated into quantum mechanics.

In molecules that contain many electrons and nuclei with a spin different from zero many complications arise that will be dealt with at length in Section 9.3. At this point, it is sufficient to state the SH used in this review that effectively describes the interactions of the various magnetic dipole moments with the external magnetic field and among each other [4, 14, 18–20]:

$$\hat{H}_{\text{spin}} = \hat{\mathbf{S}}\mathbf{D}\hat{\mathbf{S}} + \beta\mathbf{B}g\hat{\mathbf{S}} + \sum_A \hat{\mathbf{S}}\mathbf{A}^{(A)}\hat{\mathbf{I}}^{(A)} - \beta_N g_N^{(A)}\hat{\mathbf{I}}^{(A)}\mathbf{B} \quad (3)$$

Here the first term describes the zero-field splitting (ZFS) and the second term represents the electronic Zeeman effect (the interaction of the net spin magnetic moment with the external magnetic field \mathbf{B}). The third term represents the magnetic interactions between the electrons magnetic moment and the nuclear spin magnetic moments and the last term is the interaction of the nuclear spin magnetic moments with the external magnetic field. The sum extends over all magnetic nuclei in the molecule. In the last term the nuclear g-factor, $g_N^{(A)}$, was taken to be a scalar with a value that corresponds to that of the free atom. In reality this is not accurate because, in molecules, deviations from this value occur and give rise to the phenomenon of “chemical shielding” that is of fundamental importance in NMR spectroscopy [19, 21]. However, the deviations are only of the order of parts per million (ppm)

and together with the low values of the nuclear magneton relative to the electron magneton the deviations of $g_N^{(A)}$ from their atomic values are unmeasurably small in EPR and related experiments that are dealt with in this review. We have also left out the NMR spin-spin coupling and the nuclear quadrupole interaction [22] that are both not being dealt with in this review. In summary, the SH parameters that we are concerned with are the elements of the 3×3 matrices \mathbf{D} , \mathbf{g} and $\mathbf{A}^{(A)}$. Note also that the operator \hat{S} represents the net spin of the electron ground state configuration (*vide infra*).

9.2.2 Eigenstates of the SH

The SH operates on a manifold of states $|SM, \mathbf{M}^{(I)}\rangle$, where:

$$|SM, \mathbf{M}^{(I)}\rangle = |SM\rangle \otimes \prod_{A=1}^{N_A} |I^{(A)} M^{(A)}\rangle \quad (4)$$

where N_A is the number of magnetic nuclei. $|SM\rangle$ is a function that exists in the space spanned by the spin variables of the electron spin and $|I^{(A)} M^{(A)}\rangle$ represents the nuclear spin degrees of freedom for nucleus A . Since for a spin S there are $2S+1$ values of M ($M = S, S-1, \dots, -S$) and for a spin $I^{(A)}$ there are $2I^{(A)}+1$ possible values of $M^{(A)}$, the total dimension of the set of basis states is:

$$\dim\left(\{|SM, \mathbf{M}^{(I)}\rangle\}\right) = (2S+1) \prod_{A=1}^{N_A} (2I^{(A)}+1) \quad (5)$$

A subtle point is that the value of S usually coincides with the true value of the total spin of the electronic ground state configuration denoted here as S_{GS} . However, this is not necessarily so and it is sometimes advantageous to choose a value $S \neq S_{GS}$ to set up an effective SH. S is therefore frequently called the ‘‘fictitious spin’’ [4]. Some of the complications that arise for $S \neq S_{GS}$ have been discussed by Harriman [8]. They are severe and often confusing; we prefer to only use a SH of the type Eq. (3) if the condition $S = S_{GS}$ is fulfilled and we shall assume this throughout this review.

The set of functions $\{|SM, \mathbf{M}^{(I)}\rangle\}$ provides a complete, orthonormal set of functions in which the eigenfunctions of the SH can be expanded. An exact solution to the Schrödinger equation with the model SH:

$$\hat{H}_{\text{spin}}\Theta = W\Theta \quad (6)$$

is obtained by diagonalizing the matrix representation of the SH in the basis of the states $\{|SM, \mathbf{M}^{(I)}\rangle\}$

$$(\mathbf{H}_{\text{spin}})_{K,L} = \left\langle SM_K, \mathbf{M}_K^{(I)} \mid \hat{H}_{\text{spin}} \mid SM_L, \mathbf{M}_L^{(I)} \right\rangle \quad (7)$$

where each label K or L selects one combination of M and $\mathbf{M}^{(I)}$ values. The eigenstates of the SH are written as:

$$\Theta_I = \sum_J p_{JJ} |SM_J, \mathbf{M}_J^{(I)}\rangle \quad (8)$$

The matrix \mathbf{p} collects the expansion coefficients that are the normalized eigenvectors of the matrix \mathbf{H}_{spin} .

9.2.3 Matrix Elements of the SH

The matrix elements of the SH are straightforward to calculate with the use of the standard quantum mechanical relations for angular momenta [23, 24]:

$$\hat{S}_z |SM\rangle = M |SM\rangle \quad (9)$$

$$\hat{S}_{\pm} |SM\rangle = (S_x \pm iS_y) |SM\rangle = \sqrt{(S \mp M)(S \pm M + 1)} |SM \pm 1\rangle \quad (10)$$

and corresponding relations for the nuclear spins. Instead of \hat{S}_z and \hat{S}_{\pm} we will frequently use the standard vector operator components \hat{S}_0 and $\hat{S}_{\pm 1}$ that are defined by:

$$\hat{S}_0 = \hat{S}_z \quad (11)$$

$$\hat{S}_{\pm 1} = \mp \frac{1}{\sqrt{2}} \hat{S}_{\pm} \quad (12)$$

This enables one to use the powerful apparatus of tensor operator theory in order to simplify the calculation of matrix elements [24]. In terms of the spherical components, a Cartesian second rank tensor \mathbf{T} becomes:

$$T_{00} = T_{zz} \quad (13a)$$

$$T_{01} = \frac{1}{\sqrt{2}} [T_{zx} - iT_{zy}] \quad (13b)$$

$$T_{10} = \frac{1}{\sqrt{2}} [T_{xz} - iT_{yz}] \quad (13c)$$

$$T_{0-1} = -\frac{1}{\sqrt{2}} [T_{zx} - iT_{zy}] \quad (13d)$$

$$T_{-10} = -\frac{1}{\sqrt{2}} [T_{xz} - iT_{yz}] \quad (13e)$$

$$T_{11} = \frac{1}{2} [T_{xx} - T_{yy} - iT_{xy} - iT_{yx}] \quad (13f)$$

$$T_{-1-1} = \frac{1}{2}[T_{xx} - T_{yy} + iT_{xy} + iT_{yx}] \quad (13g)$$

$$T_{1-1} = \frac{1}{2}[-T_{xx} - T_{yy} - iT_{xy} + iT_{yx}] \quad (13h)$$

$$T_{-11} = \frac{1}{2}[-T_{xx} - T_{yy} - iT_{xy} - iT_{yx}] \quad (13i)$$

9.2.3.1 Zero Field Splitting

The matrix elements of the ZFS in terms of the spherical vector operator components are:

$$\begin{aligned} \langle SM, \mathbf{M}^{(I)} | \hat{\mathbf{S}} \mathbf{D} \hat{\mathbf{S}} | SM', \mathbf{M}'^{(I)} \rangle &= \delta_{\mathbf{M}^{(I)}, \mathbf{M}'^{(I)}} \sum_{m, m'} (-1)^{m+m'} D_{mm'} \\ &\cdot \sum_{M''} \langle SM | \hat{S}_m | SM'' \rangle \langle SM'' | \hat{S}_{m'} | SM' \rangle \end{aligned} \quad (14)$$

with:

$$\delta_{\mathbf{M}^{(I)}, \mathbf{M}'^{(I)}} = \prod_{A=1}^{N_A} \delta_{M^{(A)}, M'^{(A)}} \quad (15)$$

and δ_{ij} is the Kronecker delta ($\delta_{ij} = 1$ for $i = j$ and $\delta_{ij} = 0$ otherwise). The multidimensional Kronecker symbol in Eq. (15) returns zero whenever the nuclear spin quantum numbers $M^{(A)}$ and $M'^{(A)}$ for any magnetic nucleus A are different.

If a coordinate system is chosen that diagonalizes \mathbf{D} , H_{ZFS} can be rewritten:

$$\hat{H}_{ZFS} = D \left[\hat{S}_z^2 - \frac{1}{3}S(S+1) \right] + E \left[\hat{S}_x^2 - \hat{S}_y^2 \right] \quad (16)$$

$$D = D_{zz} - \frac{1}{2}(D_{xx} + D_{yy}); \quad E = \frac{1}{2}(D_{xx} - D_{yy}) \quad (17)$$

A constant $\frac{1}{3}(D_{xx} + D_{yy} + D_{zz})S(S+1)$ is dropped because it shifts all levels equally and the factor $-\frac{1}{3}DS(S+1)$ is introduced for convenience. In a proper coordinate system x , y and z are chosen such that $0 \leq E/D \leq \frac{1}{3}$ [25]. Note that in general $D_{xx} + D_{yy} + D_{zz} \neq 0$; the \mathbf{D} tensor is not in general traceless as is sometimes stated (*vide infra*).

Alternatively, the matrix elements of the spin-operators are easily obtained from the spin-matrices for spin S . For zero-field splitting one has:

$$\begin{aligned} &\left\langle SM, \mathbf{M}^{(I)} \left| \sum_{p, q=x, y, z} \hat{S}_p D_{pq} \hat{S}_q \right| SM', \mathbf{M}'^{(I)} \right\rangle \\ &= \delta_{\mathbf{M}^{(I)}, \mathbf{M}'^{(I)}} \sum_{p, q=x, y, z} D_{pq} (\boldsymbol{\sigma}^{S; p} \boldsymbol{\sigma}^{S; q})_{MM'} \end{aligned} \quad (18)$$

the spin matrices $\sigma^{S;x}$, $\sigma^{S;y}$ and $\sigma^{S;z}$ with matrix elements $\sigma_{MM'}^{S;p} = \langle SM|\hat{S}_p|SM'\rangle$ are either tabulated [14] or can be obtained in an elementary way from Eqs. (9) and (10):

$$\sigma_{MM'}^{S;x} = \frac{1}{2}(\sqrt{(S-M')(S+M'+1)}\delta_{M-1,M'} + \sqrt{(S+M')(S-M'+1)}\delta_{M+1,M'}) \quad (19)$$

$$\sigma_{MM'}^{S;y} = \frac{i}{2}(\sqrt{(S-M')(S+M'+1)}\delta_{M-1,M'} + \sqrt{(S+M')(S-M'+1)}\delta_{M+1,M'}) \quad (20)$$

$$\sigma_{MM'}^{S;z} = \delta_{MM'}M \quad (21)$$

9.2.3.2 Electron Zeeman

The matrix elements of the electron Zeeman term are:

$$\begin{aligned} & \left\langle SM, \mathbf{M}^{(I)} \left| \beta \sum_{p,q=x,y,z} B_p g_{pq} \hat{S}_q \right| SM', \mathbf{M}'^{(I)} \right\rangle \\ & = \delta_{\mathbf{M}^{(I)}, \mathbf{M}'^{(I)}} \beta \sum_{p,q=x,y,z} B_p g_{pq} \sigma_{MM'}^{S;q} \end{aligned} \quad (22)$$

9.2.3.3 Nuclear Zeeman

Likewise, the matrix elements of the nuclear Zeeman term are given by:

$$\begin{aligned} & \left\langle SM, \mathbf{M}^{(I)} \left| -\beta_N g_N^{(A)} \sum_{p=x,y,z} B_p \hat{I}_p^{(A)} \right| SM', \mathbf{M}'^{(I)} \right\rangle \\ & = -\delta_{\mathbf{M}^{(I)}, \mathbf{M}'^{(I)}} \delta_{MM'} \beta_N g_N^{(A)} \sum_{p=x,y,z} B_p \sigma_{M^{(A)}M'^{(A)}}^{(A);p} \end{aligned} \quad (23)$$

where we have introduced a reduced Kronecker symbol:

$$\delta_{\mathbf{M}^{(I)}, \mathbf{M}'^{(I)}}^A = \prod_{B \neq A} \delta_{M^{(B)}, M'^{(B)}} \quad (24)$$

which returns zero if two nuclear spin quantum numbers $M^{(B)}$ and $M'^{(B)}$ for a nucleus differ except when the nucleus is nucleus A .

9.2.3.4 Hyperfine coupling

In analogy one finds for the matrix elements of the hyperfine interaction of the electron spin with nucleus A :

$$\begin{aligned} & \left\langle SM, \mathbf{M}^{(I)} \left| \sum_{p,q=x,y,z} \hat{S}_p A_{pq}^{(A)} \hat{I}_q^{(A)} \right| SM', \mathbf{M}'^{(I)} \right\rangle \\ & = \delta_{\mathbf{M}^{(I)}, \mathbf{M}'^{(I)}}^A \sum_{p,q=x,y,z} A_{pq}^{(A)} \sigma_{MM'}^{S;p} \sigma_{M^{(A)}M'^{(A)}}^{(A);q} \end{aligned} \quad (25)$$

9.2.4 Comments

The eigenstates of the SH depend explicitly on the strength of the external magnetic field and its orientation, the elements of the g -matrix as well as on the zero-field splitting and hyperfine parameters that are present to lift the degeneracy of the basis states even in zero field. Once the eigenstates, Θ_I , of the SH and the corresponding energies, W_I , are known all magnetic spectroscopic phenomena that occur within the space spanned by the SH eigenfunctions can be easily and exactly calculated. Thus, the problems associated with SHs are straightforward. They involve the calculation of the matrix elements of the SH in a basis that only contains spin variables and diagonalization of a complex valued matrix which is a standard problem of numerical mathematics [26]. As will be described below, the solution of this problem is much easier than the calculation of good approximations to the eigenstates of the complete molecular Hamiltonian that not only contains spin variables but also the space variables of the electrons and nuclei.

As the SH eigenstates and energies critically depend on the values of the SH parameters, the goal of the theoretical investigation is to interpret them in terms of the electronic and geometric structure of the compound under investigation. This requires a deeper look at the physical mechanisms that govern the values of the SH parameters as will be described in the next chapter.

9.3 The Physical Origin of Spin-Hamiltonian Parameters

9.3.1 Many-electron Wavefunctions and the Zeroth-order Hamiltonian

To set the stage for the developments to be presented below, we will first discuss the most commonly encountered “molecular Hamiltonian”, namely the Born–Oppenheimer (BO) Hamiltonian [27]. It is convenient to use atomic units throughout this review in which the elementary charge (e_0), the mass of the electron (m_e), Planck’s constant (\hbar) and the permittivity of free space ($4\pi\epsilon_0$) all assume unit values. The unit of length is the Bohr radius:

$$a_0 = \frac{4\pi\epsilon_0\hbar}{me_0^2} \quad (26)$$

and the unit of energy is the Hartree:

$$E_H = \frac{m_e e_0^4}{16\pi^2 \epsilon_0^2 \hbar^2} \quad (27)$$

In this units system the speed of light equals the inverse of the fine structure constant:

$$c = \alpha^{-1} = 137.03599\dots \quad (28)$$

and the Bohr magneton takes the value:

$$\beta = \frac{e_0\hbar}{2m_e c} = \frac{\alpha}{2} \approx 3.64868 \times 10^{-3} \quad (29)$$

Finally, the nuclear magneton takes on the value:

$$\beta_N = \beta \frac{m_e}{m_p} = \frac{\alpha}{2} \frac{m_e}{m_p} \approx 1.98713 \times 10^{-6} \quad (30)$$

where the ratio of proton and electron mass is $m_p/m_e \approx 1836.15274$. The BO Hamiltonian collects the terms that arise in the non-relativistic theory from the kinetic energies of the electrons as well as the electrostatic interactions of the particles (we consider a system of N_e electrons and N_A nuclei). The BO Hamiltonian does *not* contain terms for the kinetic energies of the nuclei as these are assumed to be “frozen”. The justification for this procedure comes from the much greater mass of nuclei compared to electrons that consequently move much slower and from the point of view of the electronic motion the nuclei are always static [27].

In atomic units the BO-Hamiltonian is:

$$\begin{aligned} \hat{H}_{BO} = & -\frac{1}{2} \sum_i \nabla_i^2 - \sum_i \sum_A \frac{Z_A}{|\mathbf{R}_A - \mathbf{r}_i|} + \frac{1}{2} \sum_i \sum_{j \neq i} \frac{1}{|\mathbf{r}_i - \mathbf{r}_j|} \\ & + \frac{1}{2} \sum_A \sum_B \frac{Z_A Z_B}{|\mathbf{R}_A - \mathbf{R}_B|} \end{aligned} \quad (31)$$

Here i sums over electrons and A over nuclei. Z_A is the nuclear charge of the A th nucleus at position \mathbf{R}_A and \mathbf{r}_i is the position of the i th electron. The first term represents the kinetic energy of the electrons, the second term is the nucleus–electron attraction and the third term is the interelectronic electrostatic repulsion. The final term is the internuclear repulsion and is a constant at any given nuclear configuration.

The Schrödinger equation to be solved in the BO picture is:

$$\hat{H}_{BO} \Psi(\mathbf{x}_1, \dots, \mathbf{x}_N) = E \Psi(\mathbf{x}_1, \dots, \mathbf{x}_N) \quad (32)$$

where $\mathbf{x}_i = (\mathbf{r}_i, \sigma_i)$ represents the spatial and spin degrees of freedom for the i th electron.

Obviously, the BO Hamiltonian is a linear operator. The BO eigenfunctions depend on the coordinates of N_e -electrons and parametrically on the positions of the N_A -nuclei. Such N_e -electron wavefunctions are tremendously complicated objects that cannot be exactly obtained for any but the smallest systems. However, efficient methods of approximation exist as will be briefly described in Sections 9.6.1–9.6.3. The many electron wavefunction Ψ should obey the fundamental symmetries of the BO Hamiltonian. First, it must be antisymmetric in the coordinates of the electrons (Pauli principle).

$$\Psi(\mathbf{x}_1, \dots, \mathbf{x}_i, \dots, \mathbf{x}_j, \dots, \mathbf{x}_N) = -\Psi(\mathbf{x}_1, \dots, \mathbf{x}_j, \dots, \mathbf{x}_i, \dots, \mathbf{x}_N) \quad (33)$$

Second it should be an eigenfunction to the total spin squared and the \hat{S}_z component of the total spin. Since the BO Hamiltonian does not explicitly contain spin variables both \hat{S}^2 and \hat{S}_z commute with \hat{H}_{BO} and consequently the eigenfunctions of \hat{H}_{BO} are also eigenfunctions of \hat{S}^2 and \hat{S}_z . Thirdly, Ψ should transform under one of the irreducible representations of the molecular symmetry group spanned by the (fixed) nuclei. Again, the symmetry operations commute with H_{BO} which means that the eigenfunctions of \hat{H}_{BO} must also be eigenfunctions of the symmetry operators [28].

For the purposes of this chapter we assume that a set of eigenfunctions of \hat{H}_{BO} has been calculated either approximately or exactly. This set of functions can be denoted as: $\{|a\Gamma M_\Gamma SM\rangle\}$. Here Γ is the spatial irreducible representation under which the state transforms and M_Γ is used to distinguish different components of Γ should it be more than one-dimensional. S is the total spin quantum number and M the projection onto the z -axis. The remaining label “ a ” is used to distinguish between different functions with identical Γ , M_Γ , S and M . The energy of such a state is E_a and all $\dim(\Gamma)(2S+1)$ components of a state $|a\Gamma M_\Gamma SM\rangle$ are energetically degenerate.

However, in the present review we will not make use of the spatial symmetry and therefore use a simpler notation in which the spatial symmetry labels Γ and M_Γ are absorbed in the compound label $\alpha \equiv a\Gamma M_\Gamma$. Good use of spatial symmetry can be made by using the powerful irreducible tensor operator method pioneered for point groups by Griffith [29] and elaborated by others [2, 24, 30]. It is, however, our desire to keep the notation as simple as possible and we will therefore only make use of spatial symmetry where appropriate. Consequently, the set of functions is written $\{|\alpha SM\rangle\}$. We will refer to the $2S+1$ components ($M = -S, \dots, S$) of such a state with total S as the “magnetic sublevels”.

To summarize this section, a set of many-electron wavefunctions, $\{|\alpha SM\rangle\}$, is introduced that either exactly or approximately diagonalizes the BO Hamiltonian, \hat{H}_{BO} . At this point, each of the functions $|\alpha SM\rangle$ is $2S+1$ fold degenerate with the energy of state $|\alpha SM\rangle$ being E_α . Typically, the energy differences between the ground state configuration, $|0SM\rangle$, and excited configurations $|\alpha SM\rangle$ ($\alpha = 1, 2, \dots$), is on the order of a few electron volts unless the ground state is orbitally degenerate or almost degenerate in which case there are several configurations $|\alpha SM\rangle$ which

are close in energy and the theoretical description of the magnetic experiments becomes much more involved. However, typically the energetic separation between the ground state configuration $|0SM\rangle$ and the excited configurations, $|\alpha SM\rangle$, is much larger than the energies employed in the experimental magnetic techniques and we will assume henceforth that this is the case.

As has been pointed out above, the BO Hamiltonian is not able to describe the lifting of the degeneracy of the magnetic sublevels and is therefore not complete enough to describe magnetic experiments. Thus, the next step is to include the small interactions either between the particles or between the particles and the external fields that lifts the degeneracy of the magnetic sublevels and enables magnetic spectroscopists to observe transitions among them. We will first introduce the necessary operators in the next section (Section 9.3.2) and then describe a convenient technique that allows us to include these operators in the electronic structure treatment (Section 9.3.3) to arrive at a theory that has the same mathematical structure as the SH of Section 9.2.

9.3.2 Perturbing Operators for Magnetic Interactions

The BO-Hamiltonian discussed in the previous section is sufficient to discuss the major effects of structure and bonding of molecules except for those that contain very heavy elements beyond the second transition row. However, as it does not contain electric or magnetic fields or the spins of electrons and nuclei it is not appropriate to discuss magnetic resonance experiments.

9.3.2.1 Zeeman Interaction

To introduce the external fields we make use of the so-called “minimal coupling” [31–33] procedure. We will focus on the effect of an external magnetic field. The introduction of external electric fields is of no interest in the present context and, in addition, is straightforward. (Note however the interesting possibility of modifying spin-Hamiltonian parameters experimentally through external electric fields. A detailed discussion is available elsewhere [34].) In the case of a magnetic field, the particle momenta are simply replaced by:

$$\mathbf{p}_i \xrightarrow{\text{substitute}} \boldsymbol{\pi}_i = \mathbf{p}_i + \alpha \mathbf{A}_i \quad (34)$$

where the momentum of the i th electron is $\mathbf{p}_i = -\nabla$ and \mathbf{A}_i is the vector potential defined in the Coulomb gauge ($\text{div } \mathbf{A}_i = 0$). Note that α denotes the fine structure constant here. For a uniform magnetic field it takes the form:

$$\mathbf{A}_i = \frac{1}{2} \mathbf{B} \times \mathbf{r}_i \quad (35)$$

If one replaces \mathbf{p}_i by $\boldsymbol{\pi}_i$ in the BO Hamiltonian the only change that is required is in the electronic kinetic energy of the i th electron that is given by $\frac{1}{2}\boldsymbol{\pi}_i^2$. Insertion

of this Ansatz results in two additional one-electron terms in the Hamiltonian that are:

$$\begin{aligned}\hat{H}_{LB} &= \frac{\alpha}{2} \sum_i \mathbf{B} \mathbf{l}_i \\ &= \frac{\alpha}{2} \mathbf{B} \mathbf{L}\end{aligned}\quad (36)$$

which simply is the orbital Zeeman term that describes the interaction between the external magnetic field and the magnetic moment caused by the orbital motion of the electrons. The second term is:

$$\hat{H}_{BB} = \frac{\alpha^2}{8} \sum_i (\mathbf{B} \times \mathbf{r}_i)^2 \quad (37)$$

This familiar diamagnetic term is quadratic in the external magnetic field. It is important for the calculation of magnetizabilities but is of no further consequence in the present context.

Thus, even in this non-relativistic approximation there arises a coupling between the orbital angular momentum of the electrons and the magnetic field. However, molecules in non-degenerate electronic states have “quenched” angular momentum. Mathematically this means that the expectation value of the orbital Zeeman operator over the ground state wavefunction is zero. This arises because the orbital Zeeman operator is purely imaginary while the BO wavefunction for an orbitally non-degenerate state can always be chosen to be real.

Therefore there are a number of terms missing in the Hamiltonian that can be systematically derived from the Dirac equation and its generalizations to more than one particle [8]. Since the theoretical apparatus to systematically introduce the necessary terms is beyond the scope of this review [8] the necessary operators will be introduced in an *ad hoc* fashion. The necessary terms are given in the so-called Breit–Pauli approximation and are correct to α^2 with $\alpha = c^{-1}$ in atomic units.

The first term is the coupling of the spin-magnetic moment to the external magnetic field. The spin-Zeeman operator is:

$$\begin{aligned}\hat{H}_{SB} &= \frac{\alpha g_e}{2} \sum_i \mathbf{B} \mathbf{s}_i \\ &= \frac{\alpha g_e}{2} \mathbf{B} \hat{\mathbf{S}}\end{aligned}\quad (38)$$

(We will not make any difference between the various g -values such as g_e and g' . Their difference is much smaller than the presently obtainable experimental or theoretical accuracy. A full discussion is given in the monograph by Harriman [8].)

In contrast to the orbital Zeeman term it contains the additional “anomalous” factor g_e . From the fully relativistic treatment there arises a “kinetic energy correction” (relativistic mass correction) to the spin-Zeeman energy that is given by:

$$\hat{H}_{SB}^{RMC} = \frac{\alpha^3 g_e}{2} \sum_i \nabla_i^2 \mathbf{B} \mathbf{s}_i \quad (39)$$

As this term is of order α^3 it will give a correction of order α^2 to the g -tensor (Section 9.3.4.2).

9.3.2.2 Spin–Orbit Coupling

The largest, and most important additional term in the Hamiltonian is the spin–orbit coupling (SOC) (a recent review is available [35]). The SOC describes a coupling of the electronic spin-magnetic moment to the orbital magnetic moment of the same electron as well as of the other electrons. In the Breit–Pauli approximation the SOC operator is:

$$\hat{H}_{SO} = \hat{H}_{SO}^{(1)} + H_{SO}^{(2)} \quad (40)$$

The one electron part, $\hat{H}_{SO}^{(1)}$, is given by:

$$\hat{H}_{SO}^{(1)} = \frac{\alpha^2}{2} \sum_A \sum_i \frac{Z_A}{|\mathbf{R}_A - \mathbf{r}_i|^3} \mathbf{I}_i^A \mathbf{s}_i \quad (41)$$

where \mathbf{I}_i^A is the angular momentum of the i th electron relative to nucleus A .

$$\mathbf{I}_i^A = (\mathbf{r}_i - \mathbf{R}_A) \times \mathbf{p}_i \quad (42)$$

The two electron part consists of two terms and is given by:

$$\hat{H}_{SO}^{(2)} = -\frac{\alpha^2}{2} \sum_i \mathbf{s}_i \sum_{j \neq i} \frac{1}{|\vec{r}_i - \vec{r}_j|^3} (\mathbf{I}_i^j + 2\mathbf{I}_j^i) \quad (43)$$

where \mathbf{I}_i^j is the angular momentum of electron i relative to electron j .

$$\mathbf{I}_i^j = (\mathbf{r}_i - \mathbf{r}_j) \times \mathbf{p}_i \quad (44)$$

This form of the spin–orbit coupling was derived by Bethe and Salpeter [36] from the Breit equation [37–39] and with classical arguments by Slater [40]. The first term in $\hat{H}_{SO}^{(2)}$ arises from the movement of electron i in the Coulomb field of electron j and the second term describes the coupling of the spin magnetic moment of electron i with the orbital current of electron j (the spin-other orbit, SOO, contribution). The one-electron term $\hat{H}_{SO}^{(1)}$ has the familiar interpretation as described in popular textbooks (e. g. Ref [41], page 1215).

This operator is evidently a complicated two-electron operator that is quite difficult to handle computationally. For this reason approximations to it are frequently used. Historically the studies of Blume, Watson and Freeman [42–44], Horie [45] and Elliot [46] suggest that, for atoms, it is a reasonable approximation to substitute the full SOC operator by an effective one-particle operator. The main effects of the two-electron part can thus be absorbed in the effective SOC coupling constant ζ' .

The detailed expressions are given by Blume and Watson and application to atoms lead to good agreement with experiment for 2p and 3d elements [42–44].

A widely used approximation for molecules is to assume that the two electron term basically provides a “screening” of the nuclear charge and that the overall behavior of the SOC term is reasonably approximated by the one-electron term. Furthermore, owing to the r^{-3} dependence, the one-electron SOC is rather local in nature and it is a good approximation to only consider one-center matrix elements of this operator. The effective SOC operator can thus be written:

$$\hat{H}_{SO} = \sum_A \sum_i \xi(r_{iA}) \mathbf{l}_i^A \mathbf{s}_i \quad (45)$$

where the function $\xi(r_{iA})$ is usually taken to be:

$$\xi(r_{iA}) = \frac{\alpha^2}{2} \frac{Z_{\text{eff}}^A}{r_{iA}^3} \quad (46)$$

where $\mathbf{r}_{iA} = \mathbf{r}_i - \mathbf{R}_A$ and $r_{iA} = |\mathbf{r}_{iA}|$. The effective nuclear charges, Z_{eff}^A , entering this SOC Hamiltonian are semi-empirical parameters that need to be determined either with reference to experimental results or to more accurate calculations. For *ab initio* calculations a reasonable set of effective nuclear charges has been obtained by Koseki et al. [47–49] for most of the periodic table and has been shown to give good results for the SOC in a variety of molecules.

An alternative to the effective nuclear charge method is to define the SOC via the “molecular potential”, V , as:

$$\hat{H}_{SO} = \frac{\alpha^2}{2} \left\langle \frac{1}{r} \frac{\partial V}{\partial r} \right\rangle \sum_i \mathbf{l}_i \mathbf{s}_i \quad (47)$$

This treatment leads to a SOC of the form:

$$\hat{H}_{SO} = \zeta \sum_i \mathbf{l}_i \mathbf{s}_i \quad (48)$$

a one-electron SOC “constant” ζ which is most commonly determined from fitting atomic spectra. In this way empirical values for the SOC constants of many elements in varying configurations and oxidation states have been determined (Section 9.4.1.3).

For the potential one has to introduce either the Hartree–Fock or the density functional theory potential which leads to one- and two-electron terms. However, at least for the Hartree–Fock case, it has been shown that the results with the effective potential method will tend to be 20–25% too large [42–44]. This is because the important spin-other orbit contributions are missing from the two-electron part and therefore the one-electron terms are insufficiently cancelled and the calculated SOC will be too large.

The apparently simplest method to accurately approximate the full Breit–Pauli treatment of SOC is the atomic-mean field method of Hess and co-workers [50].

Their treatment is inspired by the Hartree–Fock method in which a two body interaction (the electron–electron repulsion) is approximated by a much simpler pseudo-single particle operator (see Section 9.6.1). Finally, it is of course also possible to introduce SOC via effective core potentials [51–58] but a detailed description is not appropriate here.

Before leaving this section two further aspects of SOC should be mentioned. First, we have used throughout the momentum \mathbf{p}_i rather than the gauge invariant momentum $\boldsymbol{\pi}_i$. Use of $\boldsymbol{\pi}_i$ will give rise to one- and two-electron gauge correction terms to the SOC that lead to observable effects on g-values. We will derive the correction to the effective one-electron operator in Eq. (45). Remembering the definition of the angular momentum operator and inserting Eqs. (34) and (35) into Eq. (45) we obtain:

$$\begin{aligned}\hat{H}_{SOC} &= \sum_{i,A} \xi(r_{iA}) \mathbf{l}_i^A \mathbf{s}_i \\ &= \sum_{i,A} \xi(r_{iA}) (\mathbf{r}_{iA} \times \mathbf{p}_i) \mathbf{s}_i \\ &= \sum_{i,A} \xi(r_{iA}) (\mathbf{r}_{iA} \times (\mathbf{p}_i + \frac{1}{2} \alpha \mathbf{B} \times \mathbf{r}_i)) \mathbf{s}_i\end{aligned}\quad (49)$$

We are interested in the *correction* to the SOC and therefore drop the terms involving \mathbf{p}_i . We obtain the gauge-correction for the effective SOC operator as:

$$\hat{H}_{SOC}^{GC} = \frac{\alpha}{2} \sum_{i,A} \xi(r_{iA}) \{(\mathbf{s}_i \mathbf{B})(\mathbf{r}_{iA} \mathbf{r}) - (\mathbf{s}_i \mathbf{r}_i)(\mathbf{B} \mathbf{r}_{iA})\} \quad (50)$$

where we have used the vector identity $\mathbf{a} \times (\mathbf{b} \times \mathbf{c}) = (\mathbf{a}\mathbf{b})\mathbf{c} - (\mathbf{a}\mathbf{c})\mathbf{b}$.

The second aspect of SOC concerns the use of the “atom-like” SOC operator:

$$\hat{H}_{SL} = \lambda \mathbf{L} \mathbf{S} \quad (51)$$

where $\mathbf{L} = \sum_i \mathbf{l}_i$ is the total angular momentum and $\mathbf{S} = \sum_i \mathbf{s}_i$ is the total spin. This operator can be derived in the context of Russell–Saunders coupling for atoms [59]. It is only valid *within a single atomic term*. For example, since it is proportional to the total spin rather than incorporating the individual electron spins it will not have matrix elements between states of different total spin, in contrast to the more complete SOC operator. In addition, in molecules the total angular momentum \mathbf{L} is not a good quantum number and the advantage of using \hat{H}_{SL} instead of \hat{H}_{SO} is less apparent. Moreover, the “many-electron SOC constant” λ that proves to be so eminently useful in atomic spectroscopy [59] is rather poorly defined in a molecular context where SOC of all atoms in the molecule should be considered. In contrast to the atomic SOC constants ζ , λ is a signed quantity and related to ζ by:

$$\lambda = \pm \frac{\zeta}{2S} \quad (52)$$

where S is the total spin of the term of interest, the positive sign holds for a more than half-filled shell and the negative sign otherwise.

9.3.2.3 Operators for Coupling of Electron Spins

The direct magnetic dipole–dipole interaction leads to a familiar term in the Hamiltonian that reads:

$$\hat{H}_{SS} = \frac{\alpha^2}{2} \sum_i \sum_{j \neq i} \frac{\mathbf{s}_i \mathbf{s}_j}{r_{ij}^3} - 3 \frac{(\mathbf{s}_i \mathbf{r}_{ij})(\mathbf{s}_j \mathbf{r}_{ij})}{r_{ij}^5} \quad (53)$$

where $\mathbf{r}_{ij} = \mathbf{r}_i - \mathbf{r}_j$ and $r_{ij} = |\mathbf{r}_i - \mathbf{r}_j|$. The contribution \hat{H}_{SS} therefore is a genuine two-electron effect and its accurate calculation is anything but straightforward. It is less well known that there also exists an electron–electron contact interaction that is described by the operator:

$$\hat{H}_{SS}^{(c)} = -\frac{8\pi}{3} \frac{\alpha^2}{2} \sum_i \sum_{j \neq i} \mathbf{s}_i \mathbf{s}_j \delta(r_{ij}) \quad (54)$$

It is, however, possible to show [8] that this operator leads to no observable consequences and can usually be omitted from the discussion.

9.3.2.4 Operators for Coupling of Electron and Nuclear Magnetic Moments

For the coupling of the nuclear magnetic moments with the electronic magnetic and orbital moment we will consider three terms. The first term arises from the classical magnetic dipole–dipole interaction of the electron spin magnetic moment with the nuclear magnetic moments and is given by:

$$\hat{H}_{SI}^{(d)} = \frac{\alpha}{2} g_e \beta_N \sum_A g_N^{(A)} \sum_i \frac{\mathbf{s}_i \hat{\mathbf{I}}^{(A)}}{r_{iA}^3} - 3 \frac{(\mathbf{s}_i \mathbf{r}_{iA})(\hat{\mathbf{I}}^{(A)} \mathbf{r}_{iA})}{r_{iA}^5} \quad (55)$$

The second term has no classical analogue and is given by the famous Fermi-contact interaction (for a detailed discussion see Kutzelnigg [60]) term that reads:

$$\hat{H}_{SI}^{(c)} = \frac{\alpha}{2} \frac{8\pi}{3} g_e \beta_N \sum_A g_N^{(A)} \sum_i \mathbf{s}_i \hat{\mathbf{I}}^{(A)} \delta(r_{iA}) \quad (56)$$

Finally, the third term that we will consider is the coupling of the nuclear magnetic moment with the orbital moment of the electrons. The relevant operator can be derived from the magnetic dipole–dipole interaction equation with the result:

$$\hat{H}_{LI} = \frac{\alpha}{2} \beta_N \sum_A g_N^{(A)} \sum_i \frac{\mathbf{l}_i^A \hat{\mathbf{I}}^{(A)}}{r_{iA}^3} \quad (57)$$

9.3.2.5 Scalar Relativistic Operators

In addition to the magnetic terms described in the preceding paragraphs there are two relativistic operators (the so called “scalar” relativistic effects) that may be considered [61]. These operators do not have a direct influence of the SH parameters. However, their action leads to significant modification of the electron density and the electronic wavefunctions close to the nuclei. Since several of the magnetic operators have a dependence on r^{-3} and $\delta(r)$ this is an important region and therefore the scalar relativistic operators indirectly affect SH parameters.

The first term arises from the variation of the electron mass with velocity for electrons that move close to the speed of light such as is the case for core electrons in heavy elements. The mass-velocity term reads:

$$\hat{H}_{MV} = -\frac{\alpha^2}{8} \sum_i \nabla^4 \quad (58)$$

The second scalar relativistic term is the so-called “Darwin” term has the form:

$$\hat{H}_{\text{Darwin}} = \alpha^2 \frac{\pi}{2} \sum_A \sum_i Z_A \delta(r_{iA}) \quad (59)$$

It is thought to describe a “Zitterbewegung” (“trembling motion”) of the electron.

9.3.2.6 Summary of Terms

In the preceding paragraphs the different terms have been described that need to be added to the BO Hamiltonian in order to describe the leading terms in the SH, namely, the zero-field splitting, the g-tensor and the hyperfine couplings. The additional terms cover the interaction of the spin- and orbital magnetic moments with the external magnetic field (\hat{H}_{LB} , \hat{H}_{SB} and \hat{H}_{SB}^{RMC} , Eqs. 36, 38 and 39), the spin-orbit coupling ($\hat{H}_{SO}^{(1)}$ and $\hat{H}_{SO}^{(2)}$ or the effective one-electron form, \hat{H}_{SO} , Eq. (45) together with its gauge correction \hat{H}_{SOC}^{GC} , Eq. (50)), the spin-spin interaction ($\hat{H}_{SS}^{(d)}$ and $\hat{H}_{SS}^{(c)}$, Eqs. 53 and 54), and the coupling of electron and nuclear magnetic moments ($\hat{H}_{SI}^{(d)}$, $\hat{H}_{SI}^{(c)}$ and \hat{H}_{LI} , Eqs. 55, 56 and 57). In addition there are scalar relativistic operators (\hat{H}_{MV} and \hat{H}_{Darwin} , Eqs. 58 and 59) that will influence the SH parameters indirectly. In the approximations that we use here all of these operators with the exception of $\hat{H}_{SS}^{(d,c)}$ appear in the form of one-electron operators and this will lead to essential simplifications in the derivation of explicit expressions for the SH parameters.

9.3.3 Theory of Effective Hamiltonians

Having defined the zero-order states and the necessary perturbing operators the question arises how to incorporate these terms in the electronic structure treatment

in a form that is compatible with the SH formalism. There are a variety of ways to achieve this goal. In this section we will follow an elegant treatment that has been advocated by McWeeny [9, 11, 12] and which is based on the partitioning treatment of Löwdin [62, 63]. In this “effective-Hamiltonian” [62–65] treatment one defines a zeroth order model space that already contains the main physics of the problem. Then an effective Hamiltonian is set up in this basis that approximately incorporates the effects of the additional terms in the Hamiltonian. This effective Hamiltonian is then compared term by term to the matrix of the Spin-Hamiltonian and in this way the SH parameters are defined in terms of matrix elements of the perturbing operators over zeroth order (non-relativistic) wavefunctions.

The treatment starts by assuming that the Hamiltonian can be divided into a major part and a perturbation:

$$\hat{H} = \hat{H}_0 + \hat{H}_1 \quad (60)$$

where in the present case $\hat{H}_0 = \hat{H}_{BO}$ and \hat{H}_1 represents the sum of the various magnetic operators described in Section 9.3.2. The full set of states $\{|\alpha SM\rangle\}$ is divided into two sets: (i) the “a” set $\{|0SM\rangle\}$ of the $2S + 1$ function which make up the orbitally non-degenerate electronic ground state and (ii) the “b” set $\{|\alpha SM\rangle, \alpha = 1, 2 \dots\}$ of excited state wavefunctions. Any wavefunction can then be represented as a superposition of the form:

$$\Psi = \sum_M c_M^a |0S_0M\rangle + \sum_{\alpha SM} c_{\alpha SM}^b |\alpha S_\alpha M_\alpha\rangle \quad (61)$$

The secular equations arising from the variation principle can be set up in matrix form like:

$$\mathbf{H}\mathbf{c} = E\mathbf{c} \quad (62)$$

where \mathbf{c} is the vector that collects the expansion coefficients and \mathbf{H} is the matrix of the complete Hamiltonian with elements:

$$H_{\alpha SM, \alpha' S' M'} = \langle \alpha SM | \hat{H} | \alpha' S' M' \rangle \quad (63)$$

Applying the partitioning into “a” and “b” sets Eq. (62) can be written in the partitioned form:

$$\begin{pmatrix} \mathbf{H}_{aa} & \mathbf{H}_{ab} \\ \mathbf{H}_{ba} & \mathbf{H}_{bb} \end{pmatrix} \begin{pmatrix} \mathbf{c}^a \\ \mathbf{c}^b \end{pmatrix} = E \begin{pmatrix} \mathbf{c}^a \\ \mathbf{c}^b \end{pmatrix} \quad (64)$$

The second equation can formally be solved for \mathbf{c}^b to give:

$$\mathbf{c}^b = -(\mathbf{H}_{bb} - \mathbf{I}E)^{-1} \mathbf{H}_{ba} \mathbf{c}^a \quad (65)$$

If this is inserted into the first set of equations one obtains:

$$\mathbf{H}_{aa} \mathbf{c}^a - \mathbf{H}_{ab} (\mathbf{H}_{bb} - \mathbf{I}E)^{-1} \mathbf{H}_{ba} \mathbf{c}^a = E \mathbf{c}^a \quad (66)$$

which is equivalent to the matrix eigenvalue equation of an effective Hamiltonian:

$$\mathbf{H}_{\text{eff}}\mathbf{c}^a = E\mathbf{c}^a \quad (67)$$

with

$$\mathbf{H}_{\text{eff}} = \mathbf{H}_{aa} - \mathbf{H}_{ab}(\mathbf{H}_{bb} - \mathbf{I}E)^{-1}\mathbf{H}_{ba} \quad (68)$$

According to McWeeny [12] the value of E in Eq. (68) can to a first approximation be set equal to the unperturbed energy of the ground state E_0 . If it is assumed that the basic set of states, $\{|\alpha SM\rangle\}$, diagonalizes \hat{H}_0 we have for the inverse term in Eq. (68) the equation $(\mathbf{H}_{bb} - \mathbf{I}E_0)^{-1} = (E_\alpha - E_0)^{-1} \equiv \Delta_\alpha^{-1}$ which means that the effective Hamiltonian assumes the form:

$$\begin{aligned} & \langle 0SM | \hat{H}_{\text{eff}} | 0SM' \rangle \\ &= E_0 \delta_{MM'} + \langle 0SM | \hat{H}_1 | 0SM' \rangle \\ & \quad - \sum_{\alpha S' M''} \Delta_\alpha^{-1} \langle 0SM | \hat{H}_1 | \alpha S' M'' \rangle \langle \alpha S' M'' | \hat{H}_1 | 0SM' \rangle \end{aligned} \quad (69)$$

where $\Delta_\alpha = E_\alpha - E_0$, is a positive quantity. The matrix of the effective Hamiltonian is of the same dimension as the matrix of the SH. Yet it contains the effect of the magnetic perturbations and the interaction of the ground state magnetic sublevels with the excited states up to second order. In order to make the connection to the SH formalism the parameters that occur in the SH must be chosen such that they match one by one the matrix elements of the effective Hamiltonian in Eq. (69).

9.3.4 Equations for Spin-Hamiltonian Parameters

Having derived the necessary zeroth-order wavefunctions, the perturbing operators and the method of effective Hamiltonians we are now in a position to derive explicit expressions for the SH parameters. A technically more advanced subject is the calculation of the SOC matrix elements. This subject is developed in the appendix (Section 9.8) and here we proceed with the derivation of the SH parameters.

9.3.4.1 Zero-Field Splittings

The ZFS appears in the SH as a term that is quadratic in the electron spin operators. The terms that are candidates for contributing to the ZFS are therefore the first order terms that contain products of electron spin operators ($\hat{H}_{SS}^{(d)}$, Eq. (53)) and the second order terms that contain the spin operators but not the external magnetic field or the nuclear spin which leaves \hat{H}_{SOC} (Eq. (45)).

The first order contribution to the D-tensor follows from the manipulations described by Harriman and reads:

$$D_{\mu\nu}^{(SS)} = \frac{1}{2} \frac{\alpha^2}{2(2S-1)} \cdot \left\langle 0SS \left| \sum_i \sum_{j \neq i} \frac{r_{ij}^2 \delta_{\mu\nu} - 3(\mathbf{r}_{ij})_\mu (\mathbf{r}_{ij})_\nu}{r_{ij}^5} \{2s_{zi}s_{zj} - s_{xi}s_{xj} - s_{yi}s_{yj}\} \right| 0SS \right\rangle \quad (70)$$

This contribution is symmetric and traceless as expected for a dipolar interaction. It does, however, involve fairly complicated two electron matrix elements.

The second order contribution to the D-tensor is relatively difficult to derive and we shall not repeat all details of the original derivation that has been described in detail elsewhere [66]. The derivation shows that to second order the D-tensor has three contributions that come from excited states with either the same spin as the ground state and excited states with the total spin-quantum number increased or decreased by one relative to the ground state. In order to see what is involved, the contributions of excited states with the same spin as the ground state are derived here. Let us initially focus on a single element of the D-tensor, namely D_{zz} . The relevant SH matrix element is:

$$\langle SS | \hat{S}_z^2 D_{zz} | SS \rangle = S^2 D_{zz} \quad (71)$$

This expression is to be compared with the second order part of Eq. (69) with \hat{H}_{SOC} substituted for \hat{H}_1 . We can focus on the case that $M = S$ since we want to derive an expression for D_{zz} . The second order equation is:

$$\langle 0SS | \hat{H}_{\text{eff}} | 0SS \rangle^{(2)} = - \sum_{b(S_b=S)} \Delta_b^{-1} \langle 0SS | \hat{H}_{SOC} | bSS \rangle \langle bSS | \hat{H}_{SOC} | 0SS \rangle \quad (72)$$

To calculate the SOC matrix elements we make use of Eqs. (348) and (351) in the appendix (Section 9.8) and get:

$$\langle 0SS | \hat{H}_{SOC} | bSS \rangle = \left\langle 0SS \left| \sum_{i,A} \xi(r_{iA}) l_{i,z}^A s_{i,z} \right| bSS \right\rangle \quad (73)$$

which leads to:

$$\begin{aligned} \langle 0SS | \hat{H}_{\text{eff}} | 0SS \rangle^{(2)} = & - \sum_{b(S_b=S)} \Delta_b^{-1} \left\langle 0SS \left| \sum_{i,A} \xi(r_{iA}) l_{i,z}^A s_{i,z} \right| bSS \right\rangle \\ & \cdot \left\langle bSS \left| \sum_{i,A} \xi(r_{iA}) l_{i,z}^A s_{i,z} \right| 0SS \right\rangle \end{aligned} \quad (74)$$

If this expression is compared with Eq. (71) it is found that:

$$\begin{aligned} D_{zz}^{SOC-(0)} = & - \frac{1}{S^2} \sum_{b(S_b=S)} \Delta_b^{-1} \left\langle 0SS \left| \sum_{i,A} \xi(r_{iA}) l_{i,z}^A s_{i,z} \right| bSS \right\rangle \\ & \cdot \left\langle bSS \left| \sum_{i,A} \xi(r_{iA}) l_{i,z}^A s_{i,z} \right| 0SS \right\rangle \end{aligned} \quad (75)$$

where the superscript “SOC-(0)” has been added to indicate that this contribution to the D-tensor derives from the SOC and excited states with $S_b - S = 0$ where S is the total spin of the ground state and S_b is the total spin of excited state b . The derivation is same for all other components of the D-tensor from this mechanism. One finds [12, 66]:

$$D_{\mu\nu}^{SOC-(0)} = -\frac{1}{S^2} \sum_{b(S_b=S)} \Delta_b^{-1} \left\langle 0SS \left| \sum_{i,A} \xi(r_{iA}) l_{i,\mu}^A s_{i,z} \right| bSS \right\rangle \cdot \left\langle bSS \left| \sum_{i,A} \xi(r_{iA}) l_{i,\nu}^A s_{i,z} \right| 0SS \right\rangle \quad (76)$$

where $(\mu, \nu = x, y, z)$ It is much more involved to derive expressions for the contributions of excited states of different spin than the ground state. We merely quote the result of the derivation [66] which gives for excited states of lower multiplicity than the ground state:

$$D_{\mu\nu}^{SOC-(-1)} = -\frac{1}{S(2S-1)} \sum_{b(S_b=S-1)} \Delta_b^{-1} \cdot \left\langle 0SS \left| \sum_{i,A} \xi(r_{iA}) l_{i,\mu}^A s_{i,+1} \right| bS-1S-1 \right\rangle \cdot \left\langle bS-1S-1 \left| \sum_{i,A} \xi(r_{iA}) l_{i,\nu}^A s_{i,-1} \right| 0SS \right\rangle \quad (77)$$

and for excited states with a multiplicity that is higher than that of the ground state:

$$D_{\mu\nu}^{SOC-(+1)} = -\frac{1}{(S+1)(2S+1)} \sum_{b(S_b=S+1)} \cdot \left\langle 0SS \left| \sum_{i,A} \xi(r_{iA}) l_{i,\mu}^A s_{i,-1} \right| bS+1S+1 \right\rangle \cdot \left\langle bS+1S+1 \left| \sum_{i,A} \xi(r_{iA}) l_{i,\nu}^A s_{i,+1} \right| 0SS \right\rangle \quad (78)$$

All three second-order contributions have a very similar appearance. First they involve a constant factor that is universal and only depends the multiplicity of the contributing excited state. These factors take into account that the matrix elements of the SH are calculated with the fictitious “pure” spin S whereas the perturbed wavefunction contains contributions from states with differing S because the SOC mixes different multiplicities. Since the matrix elements of the spin operators between the components of two multiplets with different total spin are different from those of two multiplets with the same spin one has to correct for the inherent assumption of the SH formalism that “everything” can be effectively described within a *single* multiplicity. It is interesting to note that this can be so easily achieved with

the prefactors of Eqs. (77) and (78). Furthermore, all three second order contributions involve matrix elements of the reduced SOC operator $\sum_{i,A} \xi(r_{iA})l_{i,\mu}^A$ which, is, however, multiplied by different spin operators. For states of the same spin, the operator $s_{i,0} = s_{i,z}$ is involved which does not lead to spin-flips. For excited states with a lower multiplicity the operator $s_{i,+1}$ is involved which does lead to spin flips of spin-down electrons to become spin-up. This is what is needed to make the matrix element of the SOC non-zero because the excited states of lower multiplicity will have a smaller number of spin-up and a larger number of spin-down electrons compared to the ground state. Similarly, the operator $s_{i,-1}$ takes care of excited states with higher multiplicity than the ground state. It should also be noticed that in Eqs. (76)–(78) only the standard components of the ground state and the excited states with $S = M$ occur. Thus instead of having to calculate $(2S + 1)(2S_b + 1)$ matrix elements only *one* matrix element is needed. This is a consequence of applying the Wigner–Eckhard theorem in the form described in the appendix (Section 9.8). In conclusion, the derivation has taken into account all of the complications that arise from the spin parts of the wavefunctions. What remains is to specify the space parts of the many electron wavefunctions and to evaluate the matrix elements of the reduced spin–orbit operator $\sum_{i,A} \xi(r_{iA})l_{i,\mu}^A$ that will govern the actual values of the ZFS tensor elements. Note however, that the *observable* part of the ZFS arises from a *difference* of ZFS-tensor elements (see Eq. (17)) and therefore it is more important to correctly predict the *relative* values of the elements $D_{\mu\nu}$ rather than their absolute values.

In summary, the ZFS tensor has one first order and three second-order contributions and the complete ZFS is given by:

$$D_{\mu\nu} = D_{\mu\nu}^{(SS)} + D_{\mu\nu}^{SOC-(0)} + D_{\mu\nu}^{SOC-(-1)} + D_{\mu\nu}^{SOC-(+1)} \quad (79)$$

In general, in organic molecules made of light atoms with small SOC constants the first term is thought to often dominate [67–72] and ZFSs of a fraction of a wavenumber are common. The opposite situation is thought to be the case in transition metal complexes where the ZFS can easily reach magnitudes of several wavenumbers. Here the ZFS is thought to be dominated by the SOC term. Very little experience exists in the calculation of the first order term $D_{\mu\nu}^{(SS)}$. It is however recognized as a genuine two-electron property that involves the average of the inverse third power of the interelectronic distance which consequently needs to be accurately predicted (especially for short interelectronic distances) in order to give good predictions for the ZFS. Unfortunately even the best available wavefunctions do not appear to give good values for the average interelectronic distance in the short range which lead Kutzelnigg to describe the prediction of such two-electron observables as “almost hopeless” with the presently available theoretical methodology [73].

9.3.4.2 g-Tensors

To derive expressions for the g-tensor we study the terms that involve the electron spin and the magnetic field. Two terms already considered involve the product of the spin magnetic moment and the magnetic field and will give rise to first order

contributions in the sense of Eq. (69). The first term is the spin-Zeeman term \hat{h}_{SB} (Eq. (38)). Comparing a typical element of the SH:

$$\frac{\alpha}{2} \langle SS | g_{zz} B_z \hat{S}_z | SS \rangle = \frac{\alpha}{2} B_z S g_{zz} \quad (80)$$

with the matrix element of \hat{H}_{SB} :

$$\begin{aligned} \langle 0SS | \hat{H}_{SB}(z - \text{component}) | 0SS \rangle &= \frac{\alpha g_e}{2} \langle 0SS | B_z \hat{S}_z | 0SS \rangle \\ &= \frac{\alpha g_e}{2} B_z S \end{aligned} \quad (81)$$

it is evident that:

$$g_{zz}^{(SB)} = g_e \quad (82)$$

and more generally one obtains from this mechanism:

$$g_{\mu\nu}^{(SB)} = \delta_{\mu\nu} g_e \quad (83)$$

which is the familiar isotropic contribution to the g-tensor that equals the free-electron g-value.

The second term of first order is the relativistic mass correction \hat{H}_{SB}^{RMC} . According to the results of the appendix (Section 9.8) and using the key Eq. (348) one obtains for the contribution to the g-tensor:

$$g_{zz}^{(RMC)} = \frac{\alpha^2}{2} \frac{g_e}{S} \left\langle 0SS \left| \sum_i \nabla_i^2 s_{zi} \right| 0SS \right\rangle \quad (84)$$

and more generally:

$$g_{\mu\nu}^{(RMC)} = \delta_{\mu\nu} \frac{\alpha^2}{2} \frac{1}{S} \frac{g_e}{2} \left\langle 0SS \left| \sum_i \nabla_i^2 s_{zi} \right| 0SS \right\rangle \quad (85)$$

This contribution is evidently also isotropic and gives a diagonal correction to the g-tensor of order α^2 . Due to the ∇_i^2 term that is proportional to the kinetic energy $\hat{T}_i = -\frac{1}{2}\nabla_i^2$ this is also sometimes called a kinetic energy correction. It will later become evident that this correction is fairly small, on the order of a few hundred ppm.

The third first order term arises from the gauge correction to the SOC (\hat{H}_{SOC}^{GC} , Eq. (50)). It is of a similar nature as the \hat{H}_{SB}^{RMC} term. For example, consider the terms that are proportional to $s_{iz} B_z$:

$$\hat{H}_{SOC}^{GC}(zz) = \frac{\alpha}{2} \sum_{i,A} \xi(r_{iA}) s_{iz} B_z \{x_{iA} x_i + y_{iA} y_i\} \quad (86)$$

which gives for the g_{zz} element:

$$g_{zz}^{(GC)} = \frac{1}{S} \left\langle 0SS \left| \sum_{i,A} \xi(r_{iA}) s_{iz} \{x_{iA} x_i + y_{iA} y_i\} \right| 0SS \right\rangle \quad (87)$$

and more generally:

$$g_{\mu\nu}^{(GC)} = \frac{1}{S} \left\langle 0SS \left| \sum_{i,A} \xi(r_{iA}) \{r_{iA} r_i - r_{iA,\mu} r_{i,\nu}\} s_{iz} \right| 0SS \right\rangle \quad (88)$$

This term, which was derived for the first time by Stone [74], is of the same order of magnitude as the kinetic energy correction ($\xi(r_{iA})$ is of order α^2 , Eq. (46)) and frequently of different sign. Thus, as will be elaborated in Section 9.6.7 there is some cancellation between the two small first order terms.

The most important term that is of second order is the cross term that arises in Eq. (69) from the orbital Zeeman and the SOC terms (\hat{H}_{LB} , Eq. (36) and \hat{H}_{SOC} , Eq. (45)). In deriving this term it is important to note that the orbital angular momentum operator is diagonal in the total spin. Thus the sum over excited states in Eq. (69) will *only* involve those states that have the same spin as the ground state. This is an important and not widely acknowledged difference to the ZFS tensor that incorporates excited states of the same spin as the ground state *as well as* spin states of higher and lower multiplicity because the SOC operator is *not* diagonal in the total spin. To derive the explicit form of the g-tensor $\hat{H}_{LB} + \hat{H}_{SOC}$ is inserted for \hat{H}_1 in Eq. (69). The matrix elements of \hat{H}_{LB} pose no difficulties while those of \hat{H}_{SOC} *between functions of the same total spin* are given by Eqs. (348) and (351) of the appendix. Finally, the g-tensor from this mechanism becomes:

$$g_{\mu\nu}^{(OZ/SOC)} = -\frac{1}{S} \sum_{b(S_b=S)} \Delta_b^{-1} \left\{ \left\langle 0SS \left| \sum_i l_{i\mu} \right| bSS \right\rangle \left\langle bSS \left| \sum_{i,A} \xi(r_{iA}) l_{i\nu}^A s_{iz} \right| 0SS \right\rangle \right. \\ \left. + \left\langle 0SS \left| \sum_{i,A} \xi(r_{iA}) l_{i\mu}^A s_{iz} \right| bSS \right\rangle \left\langle bSS \left| \sum_i l_{i\nu} \right| 0SS \right\rangle \right\} \quad (89)$$

where S is the total spin of the ground state and the summation has been explicitly restricted to excited states of the same spin. This term is a genuine second order term. In order to evaluate it one has to have knowledge of the “standard components” of the excited state multiplets (i. e. the states $|bSM\rangle$ with $M = S$) and has to evaluate the matrix elements of the angular momentum and the reduced SOC operator between these excited states and the standard components of the ground state multiplet. In addition the transition energy from the ground state multiplet to the excited state multiplet, Δ_b^{-1} , enters in the denominator and it is important to know good values for it in order for the second order sum to give accurate predictions. While the sum over excited states is, in principal, infinite, it is fortunately usually the case that only a few excited states make dominant contributions to the g-tensor.

In summary, the g -tensor contains four main contributions and is written:

$$g_{\mu\nu} = g_{\mu\nu}^{(SB)} + g_{\mu\nu}^{(RMC)} + g_{\mu\nu}^{(GC)} + g_{\mu\nu}^{(OZ/SOC)} \quad (90)$$

The first term equal the free g -value. The first three terms are of first order and the last term is of second order and usually dominates over the second and third terms. Note that frequently rather than \mathbf{g} itself the difference to the g -tensor of a free electron $\Delta\mathbf{g} = \mathbf{g} - g_e\mathbf{1}$ is discussed. There is one further complication in the prediction of g -tensors (the gauge problem) that will be discussed in Section 9.6.7.1.

9.3.4.3 Hyperfine Couplings

For prediction of hyperfine coupling terms proportional to the product of the electron spin with the nuclear spin must be found. Two of these terms are immediately evident from the list of perturbing operators and will contribute in first order to the SH parameters.

The first term that will contribute to the HFC is the Fermi contact term $\hat{H}_{SI}^{(c)}$, Eq. (56). For illustrative purposes we make the comparison to the SH matrix elements of the z -component of the HFC for a given nucleus A with nuclear spin $I^{(A)}$:

$$\langle SS, I^{(A)} I | A_{zz}^{(A)} \hat{S}_z \hat{I}_z^{(A)} | SS, I^{(A)} I \rangle = A_{zz}^{(A)} S I^{(A)} \quad (91)$$

Once more using Eqs. (348) and (351) of the appendix (Section 9.8) we obtain for the matrix elements of the $\hat{H}_{SI}^{(c)}$ at nucleus A :

$$\begin{aligned} & \langle 0SS \otimes I^{(A)} I^{(A)} | \hat{H}_{SI}^{(c)} | 0SS \otimes I^{(A)} I^{(A)} \rangle \\ &= \frac{\alpha}{2} \frac{8\pi}{3} g_e \beta_N g_N^{(A)} I^{(A)} \left\langle 0SS \left| \sum_i s_{zi} \delta(r_{iA}) \right| 0SS \right\rangle \end{aligned} \quad (92)$$

and consequently we find for the HFC:

$$A_{zz}^{(A;c)} = \frac{8\pi}{3} \frac{\alpha}{2} \frac{1}{S} g_e \beta_N g_N^{(A)} \left\langle 0SS \left| \sum_i s_{zi} \delta(r_{iA}) \right| 0SS \right\rangle \quad (93)$$

where the superscript (A, c) indicates the contact contribution to the HFC of nucleus A . Again, this is a more general result. For the complete Fermi-contact terms one finds:

$$A_{\mu\nu}^{(A;c)} = \delta_{\mu\nu} \frac{8\pi}{3} \frac{\alpha}{2} \frac{1}{S} g_e \beta_N g_N^{(A)} \left\langle 0SS \left| \sum_i s_{zi} \delta(r_{iA}) \right| 0SS \right\rangle \quad (94)$$

This is the well-known isotropic contribution to the HFC of nucleus A and is abbreviated $A_{iso}^{(A)}$.

The derivation of the second contribution proceeds along the exactly same lines. It involves the dipolar hyperfine operator $\hat{H}_{SI}^{(d)}$. The result is an anisotropic contribution of the form:

$$A_{\mu\nu}^{(A;d)} = \frac{\alpha}{2} \frac{1}{S} g_e \beta_N g_N^{(A)} \left\langle 0SS \left| \sum_i s_{zi} r_{iA}^{-5} \{ \delta_{\mu\nu} r_{iA}^2 - 3r_{iA,\mu} r_{iA,\nu} \} \right| 0SS \right\rangle \quad (95)$$

Note that this contribution is symmetric in the indices μ, ν and has a vanishing trace as is characteristic for dipolar interactions.

The remaining contributions to the HFC are of second order. If we look for terms that are either proportional to the electron spin or the nuclear spin but not both and not on the magnetic field, one is left with the operators \hat{H}_{SOC} and \hat{H}_{LI} . The derivation proceeds in the same way as shown for the second order contribution to the g-tensor in Section 9.3.4.2 and will not be repeated here. The result is a contribution of the form:

$$\begin{aligned} A_{\mu}^{(A;SO)} = & -\frac{\alpha}{2S} g_e \beta_N g_N^{(A)} \\ & \cdot \sum_{b(S_b=S)} \Delta_b^{-1} \left\{ \left\langle 0SS \left| \sum_i l_{i\mu}^A r_{iA}^{-3} \right| bSS \right\rangle \left\langle bSS \left| \sum_{B,i} \xi(r_{iB}) l_{i\nu}^B s_{zi} \right| 0SS \right\rangle \right. \\ & \left. + \left\langle 0SS \left| \sum_{B,i} \xi(r_{iB}) l_{i\mu}^B s_{zi} \right| bSS \right\rangle \left\langle bSS \left| \sum_i l_{i\nu}^A r_{iA}^{-3} \right| 0SS \right\rangle \right\} \quad (96) \end{aligned}$$

where the superscript (A, SO) indicates the SOC contribution to the HFC of nucleus A . Note, that – as for the g-tensor – only excited states of the same spin multiplicity as the ground state contribute because the operator \hat{H}_{LI} is diagonal in the total spin. In addition $A_{\mu\nu}^{(A;SO)}$ is *not* traceless. This is the reason why the trace of the total HFC does *not* simply reduce to the isotropic Fermi contact term. For organic molecules or the HFCs of light nuclei it may be a reasonable approximation to neglect $A_{\mu\nu}^{(A;SO)}$ but for metal nuclei this contribution is fairly large and can reach a few hundred MHz as will become evident in Section 9.4.

In summary, there are three contributions to the HFC of nucleus A which are given by:

$$A_{\mu\nu}^{(A)} = \delta_{\mu\nu} A_{iso}^{(A)} + A_{\mu\nu}^{(A;d)} + A_{\mu\nu}^{(A,SO)} \quad (97)$$

The first two terms are of first order while the second term is of second order and will only be significant for heavier elements with large SOC constants.

There is one further subtlety in the prediction of HFCs that arises from a special term that has frequently been added to the $\hat{\mathbf{S}}\mathbf{A}\hat{\mathbf{I}}$ term of the SH. This term arises in second order as a cross term between \hat{H}_{SOC} and $\hat{H}_{SI}^{(d)}$. It is immediately evident that this term does not reduce naturally to the form $\hat{\mathbf{S}}\mathbf{A}\hat{\mathbf{I}}$ as it contains the electron spin *twice* and is therefore proportional to $\hat{\mathbf{S}}^2$ rather than to $\hat{\mathbf{S}}$ itself. The question arises in which sense this term can still be incorporated into the $\hat{\mathbf{S}}\mathbf{A}\hat{\mathbf{I}}$ term of the SH. We will not pursue the general case [75] but rather state the result of Keijzers and DeBoer [76] in Section 9.3.5.4.

9.3.5 Formulation in Terms of Molecular Orbitals

Up to this point we have presented a fairly rigorous derivation of a many electron theory of SH parameters. This section and the entire Section 9.4 will be devoted to approximations that simplify these equations up to the point where they are useful for “back of the envelope” calculations which are important for gaining insight into the main factors that influence SH parameters in transition metal complexes.

9.3.5.1 Many-electron Wavefunctions in Terms of Molecular Orbitals

We start by introducing a suitable set of molecular orbitals that are denoted by $\{\psi\}$. The many electron wavefunctions are then constructed by distributing the N_e electrons among these orbitals and taking linear combinations of Slater determinants in order to make these configuration state functions eigenfunctions of the \hat{S}^2 operator. A Slater determinant is given by [77]:

$$\Psi(\mathbf{x}_1, \dots, \mathbf{x}_{N_e}) = \frac{1}{\sqrt{N_e!}} \begin{vmatrix} \psi_1(\mathbf{x}_1) & \psi_1(\mathbf{x}_2) & \dots & \psi_1(\mathbf{x}_{N_e}) \\ \psi_2(\mathbf{x}_1) & \psi_2(\mathbf{x}_2) & \dots & \psi_2(\mathbf{x}_{N_e}) \\ \vdots & \vdots & \ddots & \vdots \\ \psi_{N_e}(\mathbf{x}_1) & \psi_{N_e}(\mathbf{x}_2) & \dots & \psi_{N_e}(\mathbf{x}_{N_e}) \end{vmatrix} \quad (98)$$

It will be abbreviated as:

$$\Psi(\mathbf{x}_1, \dots, \mathbf{x}_{N_e}) = |\psi_1 \psi_2 \dots \psi_{N_e}| \quad (99)$$

A bar over a orbital indicates it is occupied by a spin-down electron while unbarred orbitals are occupied by a spin-up electron. The Slater determinants are the simplest form of many electron wavefunctions of the single configuration type that take into account the Pauli principle because it changes sign whenever the coordinates of a pair of electrons are interchanged.

Ultimately we will expand the space parts of the MOs in terms of a basic set of auxiliary functions $\{\varphi\}$ (“atomic” orbitals; “linear combination of atomic orbitals”, LCAO expansion). The expansion is:

$$\psi_i(\mathbf{r}) = \sum_p c_{pi} \varphi_p(\mathbf{r}) \quad (100)$$

The expansion coefficients are collected in a matrix \mathbf{c} that has to be determined by some kind of energy minimization process as will be described in detail in the subsequent section.

9.3.5.1.1 Configuration State Functions (CSF)

We will assume that the ground state of the system with total spin S can be represented by a single normalized Slater determinant with n doubly and m singly occupied MOs. It is then said to be of the “high-spin type” and reads:

$$|0SS\rangle = |\psi_1 \bar{\psi}_1 \psi_2 \bar{\psi}_2 \dots \psi_n \bar{\psi}_n \psi_{o1} \dots \psi_{om}| \quad (101)$$

It will prove convenient to define the charge and spin densities of the ground state wavefunction. The charge density of spin-up and spin down electrons is respectively:

$$\rho^\alpha(\mathbf{r}) = \sum_{i=1}^{n+m} |\psi_i(\mathbf{r})|^2 \quad (102)$$

$$\rho^\beta(\mathbf{r}) = \sum_{i=1}^n |\psi_i(\mathbf{r})|^2 \quad (103)$$

and therefore the spin density is:

$$\rho^{\alpha-\beta}(\mathbf{r}) = \rho^\alpha(\mathbf{r}) - \rho^\beta(\mathbf{r}) = \sum_{i=1}^m |\psi_{o_i}(\mathbf{r})|^2 \quad (104)$$

and only involves the singly occupied MOs (SOMOs). In terms of the auxiliary set $\{\varphi\}$ the spin-density is:

$$\rho^{\alpha-\beta}(\mathbf{r}) = \sum_{p,q} P_{pq}^{\alpha-\beta} \varphi_p(\mathbf{r}) \varphi_q(\mathbf{r}) \quad (105)$$

where the spin density matrix $\mathbf{P}^{\alpha-\beta}$ is:

$$P_{pq}^{\alpha-\beta} = \sum_{i=1}^m c_{po_i} c_{qo_i} \quad (106)$$

Likewise the excited states will be represented by many electron wavefunctions of the single configuration type. An excited state in which an electron is promoted from a doubly occupied into one of the singly occupied MOs is also an eigenfunction of S^2 and S_z with the same eigenvalues:

$$|I_i^{o_j} SS\rangle = |\psi_1 \bar{\psi}_1 \dots \psi_i \bar{\psi}_{o_j} \dots \psi_n \bar{\psi}_n \psi_{o_1} \dots \psi_{o_m}| \quad (107)$$

Likewise, if an electron is promoted from one of the singly occupied MOs into an empty orbital, a single determinant spin eigenfunction is obtained:

$$|II_{o_i}^a SS\rangle = |\psi_1 \bar{\psi}_1 \dots \psi_n \bar{\psi}_n \psi_{o_1} \dots \psi_a \dots \psi_{o_m}| \quad (108)$$

The case where an electron is promoted from one of the doubly occupied MOs into an empty MO is more complicated because it increases the number of unpaired electrons by two. This means that the highest spin state that can be reached in this configuration $S+1$. This state is unique and is also represented by a single Slater determinant.

$$|Q_i^a S+1S+1\rangle = |\psi_1 \bar{\psi}_1 \dots \psi_i \psi_a \dots \psi_n \bar{\psi}_n \psi_{o_1} \dots \psi_{o_m}| \quad (109)$$

By contrast, there are *several* CSFs with spin S . In general for u unpaired electrons the number of CSFs with spin S is:

$$f_u^S = \binom{u}{\frac{1}{2}u - S} - \binom{u}{\frac{1}{2}u - S - 1} \quad (110)$$

Thus for $u = 2S + 2$ we have $f_u^S = 2S + 1$. One of these excitations can be chosen to be the spin singlet-coupling of the excited electron with the electron “left behind” and reads:

$$\begin{aligned} |III_i^a SS\rangle = \frac{1}{\sqrt{2}} \{ & |\psi_1 \bar{\psi}_1 \dots \psi_i \bar{\psi}_a \dots \psi_n \bar{\psi}_n \psi_{o_1} \dots \psi_{o_m} | \\ & + |\psi_1 \bar{\psi}_1 \dots \psi_a \bar{\psi}_i \dots \psi_n \bar{\psi}_n \psi_{o_1} \dots \psi_{o_m} | \} \end{aligned} \quad (111)$$

For a ground state spin of $S = \frac{1}{2}$ there is one additional singly excited spin-doublet CSF that is given by:

$$\begin{aligned} |IV_i^a \frac{1}{2} \frac{1}{2}\rangle = \frac{1}{\sqrt{6}} \{ & 2|\psi_1 \bar{\psi}_1 \dots \psi_i \psi_a \dots \psi_n \bar{\psi}_n \bar{\psi}_{o_1} | \\ & - |\psi_1 \bar{\psi}_1 \dots \psi_i \bar{\psi}_a \dots \psi_n \bar{\psi}_n \psi_{o_1} | \\ & + |\psi_1 \bar{\psi}_1 \dots \psi_a \bar{\psi}_i \dots \psi_n \bar{\psi}_n \psi_{o_1} | \} \end{aligned} \quad (112)$$

This state corresponds to a triplet excitation from the doubly occupied MOs coupled to a spin flip in the singly occupied MO.

For general ground state spin S the construction of the $2S + 1$ singly excited CSFs of spin $S - 1$ is more involved but efficient and general methods exist and are described in the books by Pauncz [78, 79].

These single configuration wavefunctions described above are not in general accurate descriptions of the actual molecular states as they neglect excited state electronic relaxation. In addition they do not satisfy our assumption of Sections 9.3.3 and 9.3.4 and do not diagonalize the BO Hamiltonian, that is, we do neglect configuration interaction (CI) in this section. The single CSF representation of the many electron wavefunctions is nevertheless extremely useful from a conceptual point of view as it links physical observables to individual MOs.

9.3.5.1.2 Energies of CSFs

The energies of the CSFs can be chosen as the expectation value of the BO operator and, in addition, can be measured relative to the ground state energy. Thus, the energy denominators that are needed in order to evaluate the expressions set up in Sections 9.3.5.2–9.3.5.4 are:

$$\Delta_b = \langle bSS | \hat{H}_{BO} | bSS \rangle - \langle OSS | \hat{H}_{BO} | OSS \rangle \quad (113)$$

For example, for a system with a single unpaired electron (CSFs 107, 108, 111, and 112), the energy denominators are given by:

$$\begin{aligned} \Delta_{I_i^o} = \varepsilon_o - \varepsilon_i - & \langle \psi_i \psi_i | r_{12}^{-1} | \psi_o \psi_o \rangle + \langle \psi_o \psi_o | r_{12}^{-1} | \psi_o \psi_o \rangle \\ & + \frac{1}{2} \langle \psi_i \psi_o | r_{12}^{-1} | \psi_i \psi_o \rangle \end{aligned} \quad (114)$$

$$\Delta_{II_o^a} = \varepsilon_a - \varepsilon_o - \langle \psi_o \psi_i | r_{12}^{-1} | \psi_a \psi_a \rangle + \langle \psi_o \psi_a | r_{12}^{-1} | \psi_o \psi_a \rangle \quad (115)$$

$$\begin{aligned} \Delta_{III_i^a} = \varepsilon_a - \varepsilon_i - \langle \psi_i \psi_i | r_{12}^{-1} | \psi_a \psi_a \rangle + 2 \langle \psi_i \psi_a | r_{12}^{-1} | \psi_i \psi_a \rangle \\ + \frac{1}{2} \langle \psi_o \psi_a | r_{12}^{-1} | \psi_i \psi_a \rangle \end{aligned} \quad (116)$$

$$\begin{aligned} \Delta_{IV_i^a} = \varepsilon_a - \varepsilon_i - \langle \psi_i \psi_i | r_{12}^{-1} | \psi_a \psi_a \rangle - \frac{1}{2} \langle \psi_i \psi_a | r_{12}^{-1} | \psi_i \psi_a \rangle \\ + \frac{3}{2} \langle \psi_o \psi_a | r_{12}^{-1} | \psi_o \psi_a \rangle \end{aligned} \quad (117)$$

Here and everywhere else the Mulliken notation for the two electron integrals is used:

$$\langle \psi_i \psi_j | r_{12}^{-1} | \psi_k \psi_l \rangle = \int \int \frac{\psi_i(\mathbf{r}_1) \psi_j^*(\mathbf{r}_1) \psi_k(\mathbf{r}_2) \psi_l^*(\mathbf{r}_2)}{|\mathbf{r}_1 - \mathbf{r}_2|} d\mathbf{r}_1 d\mathbf{r}_2 \quad (118)$$

The important point in Eqs. (114)–(117) is that the energy denominators that enter the perturbation calculation are *not* simply given by orbital energy differences but contain corrections with certain two electron integrals that are potentially large. For example, the largest integrals are those of the “Coulomb type” for which $i = j$ and $k = l$ in Eq. (118). These integrals can amount to ≈ 20 eV. The “exchange type” integrals over MOs ($i = k$ and $j = l$ in Eq. (118)) are much smaller and may range from ≈ 0 –3 eV. They are therefore also not negligible. The correction terms arise naturally from the changes in electron repulsion in the excited state. As a consequence the states of type “III” and type “IV” are *not* degenerate in zeroth order. This assumption is sometimes made in the literature in order to identify canceling contributions. In fact, the splittings between states of these type play an important role in spectroscopy [80]. Specifically, states of type “IV” are called “trip-doublets” because they formally correspond to a triplet excitation from MO ψ_i to MO ψ_a coupled antiparallel to a spin flip in the singly occupied MO ψ_o . A detailed discussion of the subject has been given by Cory and Zerner [80]. (As a slight caveat we note that the construction of type III and type IV states is not unique and a linear combination of the two types could also be used as a many electron basis. This would make a difference because the states interact through the Born–Oppenheimer Hamiltonian. However, the canonical form used here has a particularly transparent physical interpretation. Note also, that the energy denominators depend on how exactly the MOs have been obtained. For these equations it was assumed that the MOs have been determined by the ROHF procedure of Edwards and Zerner [81], or an equivalent method.)

9.3.5.1.3 Spin–Orbit Coupling Matrix Elements

Using Slater’s rules [77] gives for the SOC matrix elements:

$$\left\langle 0SS \left| \sum_{A,i} \xi(r_A) l_{i,\mu}^A s_{0,i} \right| I_i^{o_j} SS \right\rangle = -\frac{1}{2} \left\langle \psi_i \left| \sum_A \xi(r_A) l_{\mu}^A \right| \psi_{o_j} \right\rangle \quad (119)$$

$$\left\langle 0SS \left| \sum_{A,i} \xi(r_{iA}) l_{i,\mu}^A s_{0,\mu} \right| II_{o_i}^a SS \right\rangle = +\frac{1}{2} \left\langle \psi_{o_i} \left| \sum_A \xi(r_A) l_{\mu}^A \right| \psi_a \right\rangle \quad (120)$$

$$\left\langle 0SS \left| \sum_{A,i} \xi(r_{iA}) l_{i,\mu}^A s_{i,0} \right| III_i^a SS \right\rangle = 0 \quad (121)$$

$$\left\langle 0SS \left| \sum_{A,i} \xi(r_{iA}) l_{i,\mu}^A s_{-1,i} \right| Q_i^a S + 1S + 1 \right\rangle = \frac{1}{\sqrt{2}} \left\langle \psi_i \left| \sum_A \xi(r_A) l_{\mu}^A \right| \psi_a \right\rangle \quad (122)$$

and in the particular case of $S = \frac{1}{2}$:

$$\left\langle 0 \frac{1}{2} \frac{1}{2} \left| \sum_{A,i} \xi(r_{iA}) l_{i,\mu}^A (i) s_{0,i} \right| IV_i^a \frac{1}{2} \frac{1}{2} \right\rangle = \frac{1}{\sqrt{6}} \left\langle \psi_i \left| \sum_A \xi(r_A) l_{\mu}^A \right| \psi_a \right\rangle \quad (123)$$

For real MOs these two matrix elements are purely imaginary and Hermitian.

9.3.5.1.4 Other One-electron Matrix Elements

For a general spin-independent one-electron operator of the form $\hat{O} = \sum_i \hat{o}(i)$ one obtains:

$$\langle 0SS | \hat{O} | I_i^{o_j} SS \rangle = \langle \psi_i | \hat{o} | \psi_{o_j} \rangle \quad (124)$$

$$\langle 0SS | \hat{O} | II_{o_i}^a SS \rangle = \langle \psi_{o_i} | \hat{o} | \psi_a \rangle \quad (125)$$

$$\langle 0SS | \hat{O} | III_i^a SS \rangle = \sqrt{2} \langle \psi_i | \hat{o} | \psi_a \rangle \quad (126)$$

and in the particular case of $S = \frac{1}{2}$:

$$\left\langle 0 \frac{1}{2} \frac{1}{2} \left| \hat{O} \right| IV_i^a \frac{1}{2} \frac{1}{2} \right\rangle = 0 \quad (127)$$

9.3.5.1.5 Symmetry-adapted Single Excitations

In higher than Abelian point groups it may sometimes be necessary to use linear combination of single excitations rather than the single excitations themselves in order to make the CSFs transform properly under one of the irreps of the group. In any configuration interaction treatment one would automatically obtain properly symmetry adapted states. However, since we work with single CSFs here it is necessary to take the appropriate precaution before entering the perturbation calculation with the singly excited CSFs as a basis. The modifications that are needed to adapt

the treatment to linear combinations of singly excited CSFs are rather minimal. Consider for example the situation that:

$$|CSF\rangle = \cos \eta |I_i^{ok} SS\rangle + \sin \eta |I_j^{ok} SS\rangle \quad (128)$$

where $i \neq j$. Then the SOC matrix element with the ground state becomes (compare Eq. (119)):

$$\begin{aligned} \left\langle 0SS \left| \sum_{A,i} \xi(r_{iA}) I_{i,\mu}^A s_{0,i} \right| CSF \right\rangle &= -\frac{\cos \eta}{2} \left\langle \psi_i \left| \sum_A \xi(r_A) I_\mu^A \right| \psi_{ok} \right\rangle \\ &\quad - \frac{\sin \eta}{2} \left\langle \psi_j \left| \sum_A \xi(r_A) I_\mu^A \right| \psi_{ok} \right\rangle \end{aligned} \quad (129)$$

Closely analogous equations result for the other single excitations. We will use equations of this form several times in Section 9.4.1.9 where we deal with highly symmetric transition metal complexes. In the following derivations the possibility of having linear combinations of CSFs as basis will, for simplicity, be suppressed but it should be kept in mind that straightforward modifications of the resulting equations are necessary if linear combinations of CSFs are taken as many electron basis functions due to symmetry constraints. The general case of CI wavefunctions where potentially every state contains contributions from all possible CSFs will be dealt with in Section 9.6.2.

9.3.5.2 Zero-field Splittings

Consider first the contributions of the excited states of “type I” and “type II” to the contribution $\mathbf{D}^{SOC-(0)}$. Using the matrix elements Eqs. (119) and (120) they are given by:

$$\begin{aligned} D_{\mu\nu}^{SOC-(0)} &= -\frac{1}{4S^2} \left\{ \sum_{i(\text{doubly})o_j} \sum_{(\text{singly})} \Delta_{I_i}^{-1} \bar{L}_{1\mu}^{io_j} \bar{L}_{1\nu}^{io_j} \right. \\ &\quad \left. + \sum_{a(\text{empty})o_j} \sum_{(\text{singly})} \Delta_{I_{\sigma_j}^a}^{-1} \bar{L}_{1\mu}^{o_j a} \bar{L}_{1\nu}^{o_j a} \right\} \end{aligned} \quad (130)$$

where $\bar{L}_{1\mu}^{ij} = \text{Im} \left(\left\langle \psi_i \left| \sum_A \xi(r_A) I_\mu^A \right| \psi_j \right\rangle \right)$. Note that $\bar{L}_{1\mu}^{ij} = -\bar{L}_{1\mu}^{ji}$. The states of

“type III” do not contribute to $\mathbf{D}^{SOC-(0)}$ because they have zero SOC matrix elements with the ground state (Eq. (121)). The contributions to the D-tensor of type $\mathbf{D}^{SOC-(1)}$ are also straightforward to evaluate because of the simple form of Eq. (122). Thus, Eq. (78) becomes:

$$D_{\mu\nu}^{SOC-(1)} = \frac{1}{2(S+1)(2S+1)} \sum_{i(\text{doubly})} \sum_{a(\text{empty})} \Delta_{Q_i^a}^{-1} L_{1\mu}^{ia} L_{1\nu}^{ia} \quad (131)$$

which is a slight extension of our earlier treatment [66] that only listed the contribution $\mathbf{D}^{SOC-(0)}$. The contributions of states of lower spin multiplicity are more difficult to treat in the general case due to the necessity of choosing a spin coupling among the open shell orbitals. First of all note that the “spin flips” where simply one electron changes its spin in one of the open shell orbitals $\psi_{o_i} \rightarrow \overline{\psi}_{o_i}$ do not contribute to the D-tensor because $L_{1\mu}^{o_i o_i} = 0$ for real orbitals $\{\psi\}$.

9.3.5.3 g-Tensors

For the g-tensor the derivation of the relevant contributions in terms of MOs is straightforward. We will first look at the first order terms. The RMC contribution (Eq. (85)) becomes:

$$\left\langle 0SS \left| \frac{\alpha^2}{4} \frac{g_e}{S} \sum_i \nabla_i^2 s_{zi} \right| 0SS \right\rangle = \frac{\alpha^2}{4} \frac{g_e}{S} \sum_{i=1}^m \langle \psi_{o_i} | \nabla^2 | \psi_{o_i} \rangle \quad (132)$$

and therefore:

$$g_{\mu\nu}^{(RMC)} = -\delta_{\mu\nu} \frac{\alpha^2}{2} \frac{g_e}{S} \sum_{i=1}^m \langle \psi_{o_i} | \hat{T} | \psi_{o_i} \rangle \quad (133)$$

This can be more conveniently and more generally expressed in terms of the spin-density matrix (Eq. 106):

$$g_{\mu\nu}^{(RMC)} = -\delta_{\mu\nu} \frac{\alpha^2}{2} \frac{g_e}{S} \sum_{p,q} P_{pq}^{\alpha-\beta} \langle \varphi_p | \hat{T} | \varphi_q \rangle \quad (134)$$

Similarly, for the gauge correction (Eq. (88)) one finds:

$$\begin{aligned} & \left\langle 0SS \left| \sum_{i,A} \xi(r_{iA}) \{ \mathbf{r}_{iA} \mathbf{r}_i - r_{iA,\mu} r_{i,\nu} \} s_{zi} \right| 0SS \right\rangle \\ &= \frac{1}{2} \sum_{i=1}^m \left\langle \psi_{o_i} \left| \sum_A \xi(r_A) \{ \mathbf{r}_A \mathbf{r} - r_{A,\mu} r_\nu \} \right| \psi_{o_i} \right\rangle \end{aligned} \quad (135)$$

and therefore:

$$g_{\mu\nu}^{(GC)} = \frac{1}{2S} \sum_{i=1}^m \left\langle \psi_{o_i} \left| \sum_A \xi(r_A) \{ \mathbf{r}_A \mathbf{r} - r_{A,\mu} r_\nu \} \right| \psi_{o_i} \right\rangle \quad (136)$$

Again, it is more convenient to define this in terms of the ground state spin density:

$$g_{\mu\nu}^{(GC)} = \frac{1}{2S} \sum_{pq} P_{pq}^{\alpha-\beta} \left\langle \varphi_p \left| \sum_A \xi(r_A) \{ \mathbf{r}_A \mathbf{r} - r_{A,\mu} r_\nu \} \right| \varphi_q \right\rangle \quad (137)$$

For the dominant contribution $\mathbf{g}^{(OZ/SOC)}$ it can readily be shown that only excited states of “type I” and “type II” contribute. This arises because for excited states of “type III” the SOC matrix element with the ground state vanishes while for “type IV” excited states it is readily shown that the orbital Zeeman matrix element vanishes (Eq. (127)). Thus, using the matrix elements Eq. (119) and (120), the $\mathbf{g}^{(OZ/SOC)}$ (Eq. (89)) becomes:

$$g_{\mu\nu}^{(OZ/SOC)} = +\frac{1}{2S} \sum_{i(\text{doubly})} \sum_{o_j(\text{singly})} \Delta_{I_i^{o_j}}^{-1} \{ \bar{L}_{2\mu}^{i o_j} \bar{L}_{1\nu}^{i o_j} + \bar{L}_{1\mu}^{i o_j} \bar{L}_{2\nu}^{i o_j} \} \\ - \frac{1}{2S} \sum_{a(\text{empty})} \sum_{o_j(\text{singly})} \Delta_{I_{o_j^a}^{-1}} \{ \bar{L}_{2\mu}^{o_j^a} \bar{L}_{1\nu}^{o_j^a} + \bar{L}_{1\mu}^{o_j^a} \bar{L}_{2\nu}^{o_j^a} \} \quad (138)$$

where:

$$\bar{L}_{2p}^{ij} \equiv \text{Im} (\langle \psi_i | l_p | \psi_j \rangle) \quad (139)$$

The positive sign for the first contribution arises from the s_0 term in the SOC operator. This is related to the fact that in order to create an excited state $|I_i^{o_j} SS\rangle$ a spin down electron must be excited while in order to create an excited state $|II_{o_j^a} SS\rangle$ a spin up electron is excited. This accounts for the fact that d^1 systems have negative g-shifts while d^9 systems have positive g-shifts (*vide infra*) as long as only d-d transitions contribute to the g-shift (no low lying charge transfer states). The same sign change does not occur for the \mathbf{D} -tensor because each term in Eq. (76) contains s_0 twice. The present treatment is valid for orbitally non-degenerate ground states. In orbitally degenerate states other techniques have been found convenient [82, 83]. Also, the treatment has been extended to third order by Atkins and Jamieson [84].

9.3.5.4 Hyperfine Couplings

The derivation of the relevant expressions for the HFC is also straightforward using the results of Sections 9.3.4.3 and 9.3.5.1. We will write for the field gradient integral over MOs:

$$F_{\mu\nu;A}^{ij} = \langle \psi_i | r_A^{-5} \{ \delta_{\mu\nu} r_A^2 - 3r_{A,\mu} r_{A,\nu} \} | \psi_j \rangle \quad (140)$$

and for the proportionality constant:

$$P^A = \frac{\alpha}{2} g_e \beta_N g_N^{(A)} \quad (141)$$

For the Fermi contact term Eq. (94) becomes:

$$A_{iso}^{(A)} = \frac{8\pi}{3} \frac{1}{2S} \frac{\alpha}{2} g_e \beta_N g_N^{(A)} \sum_{pq} P_{pq}^{\alpha-\beta} \langle \varphi_p | \delta(\mathbf{r} - \mathbf{R}_A) | \varphi_q \rangle \\ = \frac{4\pi}{3S} P^A \rho^{\alpha-\beta}(\mathbf{R}_A) \quad (142)$$

which is the familiar result, that the Fermi term is directly proportional to the spin density at the nucleus in question. In the same way one finds for the dipolar HFC from Eq. (95) the expression:

$$A_{\mu\nu}^{(A;d)} = \frac{1}{2S} P^A \sum_{pq} P_{pq}^{\alpha-\beta} \langle \varphi_p | r_A^{-5} \{ \delta_{\mu\nu} r_A^2 - 3r_{A,\mu} r_{A,\nu} \} | \varphi_q \rangle \quad (143)$$

Thus, from the knowledge of the spin density matrix and the field gradient integrals the dipolar HFC tensor can be readily calculated.

The most difficult term is the SO contribution to the HFC, Eq. (96). Using the matrix elements in Eqs. (119) and (120) one gets:

$$A_{\mu\nu}^{(A;SO1)} = \frac{1}{2S} P^A \left\{ \sum_{i(\text{doubly})} \sum_{o_j(\text{singly})} \Delta_{I_i^{o_j}}^{-1} \{ L_{3\mu}^{io_j} L_{1\nu}^{io_j} + L_{1\mu}^{io_j} L_{3\nu}^{io_j} \} \right. \\ \left. - \sum_{o_i(\text{singly})} \sum_{a(\text{empty})} \Delta_{II_o_i^a}^{-1} \{ L_{3\mu}^{ao_i} L_{1\nu}^{ao_i} + L_{1\mu}^{ao_i} L_{3\nu}^{ao_i} \} \right\} \quad (144)$$

where:

$$L_{3\mu}^{ij} = \text{Im} \langle \psi_i | l_{\mu}^A r_A^{-3} | \psi_j \rangle \quad (145)$$

Note that, again, states of higher or lower spin multiplicity do not contribute to the second order HFC because operator \hat{H}_{LI} is diagonal in the total spin. This equation has obvious similarities with the second order g-tensor expression, Eq. (138), at the same level of approximation. The main difference is that instead of the orbital Zeeman operator which gives rise to the L_2 integrals the nuclear-spin/electron orbit operator contributes and gives rise to the L_3 integrals. These also feature an angular momentum operator but with two important differences to the L_2 terms: (a) the angular momentum is measured relative to nucleus A for which the HFC is calculated and (b) there also is a factor r_A^{-3} present which makes these integrals much shorter in range than the corresponding L_2 integrals, i. e. only the parts of the MOs that are centered close to nucleus A will contribute to the L_3 integrals while pretty much all parts of a given MO pair will contribute to the L_2 integrals. This subject will be further discussed in Section 9.4 in connection with ligand field theory.

The second SOC contribution to the HFC arises from a cross term between the electron–nuclear dipole–dipole Hamiltonian and the SOC. Below we have adapted the equation obtained by Keijzers and DeBoer for a single unpaired electron ($S = \frac{1}{2}$) to the present treatment (“ o ” is the index of the singly occupied MO). The result is:

$$A_{\mu\nu}^{(A;SO2)} = -P^A \left\{ \sum_{i(\text{doubly})} \Delta_{I_i^o}^{-1} \sum_{\kappa, \tau=x,y,z} \varepsilon_{\kappa\tau\mu} F_{\kappa\nu}^{io} L_{1\tau}^{io} \right. \\ \left. - \sum_{a(\text{empty})} \Delta_{II_o^a} \sum_{\kappa, \tau=x,y,z} \varepsilon_{\kappa\tau\mu} F_{\kappa\nu}^{ao} L_{1\tau}^{ao} \right\} \quad (146)$$

where ε_{ijk} is the Levi–Civita symbol that is +1 for an even permutation of i, j, k , -1 for an odd permutation and zero otherwise. One approximation that has been made is that only excited states of the same spin as the ground state contribute to $A_{\mu\nu}^{(A;SO2)}$. This will, in general, not be true, as both the HFC operator and the SOC operator depend on the electron spin and will mix a state of spin S with states of spin $S' - S = 0, \pm 1$.

9.4 Ligand Field and Covalency Effects on SH Parameters

In this section we will apply the molecular orbital expression derived in Sections 9.3.5.2–9.3.5.4 to the specific case of transition metal ions in d^N electron configurations. Some further approximations will be introduced and the relation between MO theory, ligand field theory (LFT) and crystal field theory (CFT) should become apparent. Given the large number of possible geometric and electronic structures we restrict the treatment to a few typical electronic structures met in inorganic complexes. Extensive collections of experimental data can be found elsewhere [85–87].

9.4.1 Molecular Orbitals for Inorganic Complexes

We consider a typical mononuclear transition metal complex and focus our attention on the five MOs that derive mainly from the metal d-orbitals. To lower energy there will be doubly occupied mainly ligand based orbitals that need to be taken into account in more refined treatments and to higher energies there will be the metal (n+1)s and (n+1)p orbitals as well as unoccupied orbitals of the ligands. The focus on the five metal-derived MOs is referred to as the “ligand field limit” and is distinguished from the MO description which includes at least the valence orbitals of all atoms in the complex.

The metal d-derived MOs are written:

$$\psi_i = N_i \{ \varphi_{d_i} + \kappa_i \varphi_{L_i} \} \quad (147)$$

where for simplicity it is assumed that each MO ψ_i contains contributions from only one (normalized) metal derived d-orbital φ_{d_i} . φ_{L_i} is a suitably constructed, normalized ligand group orbital (LGO). Specific forms for a variety of complex geometries have for example been given by Ballhausen and Gray [88]. The factor N_i is the normalization constant and is given by:

$$N_i = \frac{1}{\sqrt{1 + \kappa_{L_i}^2 + 2\kappa_i S_{M_i, L_i}}} \quad (148)$$

where S_{M_i, L_i} is the overlap integral between φ_{d_i} and φ_{L_i} and κ_i is a factor that determines the amount of ligand character that is mixed into the mainly metal-d

derived MOs, i. e. it relates to the covalency of the metal–ligand bond. This factor can be substantially different for different MOs in which case the bonding is said to show an “*anisotropic covalency*”. It is more convenient to absorb the normalization factor into the expansion coefficients and write:

$$\psi_i = c_{Mi}\phi_{d_i} + c_{Li}\phi_{L_i} \quad (149)$$

where $c_{Mi} = N_i^{-1}$ and $c_{Li} = \kappa_i N_i^{-1}$. Note that $c_{Mi}^2 + c_{Li}^2 = 1$ only for $S_{Mi,Li} = 0$. In general the metal–ligand overlap will not be negligible and the normalization condition is $c_{Mi}^2 + c_{Li}^2 + 2c_{Mi}c_{Li}S_{Mi,Li} = 1$. Note also that the metal d-derived MOs are usually antibonding. This means that the metal–ligand overlap integral is negative (destructive interference). An exception is the presence of metal–ligand backbonding where the overlap will be constructive.

The “crystal field limit” of the ligand field is obtained by letting the metal-derived orbitals be of pure metal character, i. e. $\kappa_i \rightarrow 0$ for all i .

9.4.2 Ligand Field Energies

Ligand field theory has two important limits which are called the strong-field limit and the weak field limit respectively. The strong field coupling scheme treats the effects of the crystal field first and then takes into account SOC and configuration interaction while in the weak field case the opposite route is taken and the atomic states of the ion are modified by SOC and crystal field effects in this order. It is the strong field case that directly maps onto the MO theory described so far. I.e. each electronic state of the complex is described by a single configuration wavefunction that is constructed from the five metal based MOs described in the previous section. Configuration interaction between these strong field configurations can be admitted at a later stage but for the present purposes it is sufficient to consider these “pure” strong field configurations as a basis of our treatment. Furthermore we will take the crystal field limit ($\kappa_i \rightarrow 0$) in order to derive the energies of these strong field configurations.

The energy of a single Slater determinant composed of the crystal field orbitals is given by:

$$E = \sum_{i=1}^5 n_i \langle \psi_i | \hat{h} | \psi_i \rangle + \frac{1}{2} \sum_{i=1}^5 \sum_{j=1}^5 n_i n_j \langle \psi_i \psi_i | r_{12}^{-1} | \psi_j \psi_j \rangle - (n_i^\alpha n_j^\alpha + n_i^\beta n_j^\beta) \langle \psi_i \psi_j | r_{12}^{-1} | \psi_i \psi_j \rangle \quad (150)$$

where n_i is the occupation number of the i th MO ($n_i = 0, 1, 2$) and $n_i^\alpha = 0, 1$ indicates whether the i th MO is occupied by a spin-up electron or not. It is observed that the diagonal terms with $i = j$ vanish in order to cancel contributions to the energy that would describe the interaction of an electron with itself.

The one-electron operator in the Hamiltonian is taken in the crystal field approximation to arise from the electrostatic interaction of the ligand with the metal d-electrons. The ligands are approximated as point charges with negative charge q_i at positions \mathbf{R}_{L_i} and the metal is placed at the origin. This arrangement of ligands leads to a charge distribution:

$$\rho(\mathbf{R}) = \sum_{i=1}^{N_L} q_i \delta(\mathbf{R} - \mathbf{R}_{L_i}) \quad (151)$$

where N_L is the number of ligands and \mathbf{R} is measured relative to the metal nucleus. The potential from this charge distribution of the ligands at point \mathbf{r} becomes:

$$V_{LF}(\mathbf{r}) = \int \frac{\rho(\mathbf{R})}{|\mathbf{R} - \mathbf{r}|} d\mathbf{R} \quad (152)$$

The inverse distance can be expanded as:

$$\frac{1}{|\mathbf{R} - \mathbf{r}|} = \sum_{l=0}^{\infty} \frac{4\pi}{2l+1} \frac{r_{<}^l}{r_{>}^{l+1}} \sum_{m=-l}^l S_{lm}(\mathbf{R}) S_{lm}(\mathbf{r}) \quad (153)$$

where $r_{<}$ is the smaller of R ($\equiv |\mathbf{R}|$) and r ($\equiv |\mathbf{r}|$) and $r_{>}$ the larger of the two quantities. S_{lm} is a real spherical harmonic. The expansion in complex spherical harmonics is more common but since we work with real orbitals throughout, the expansion in real spherical harmonics is more convenient. Since one can assume in ligand field theory $r_{<} = r$ and $r_{>} = R$ one obtains the potential:

$$V_{LF}(\mathbf{r}) = \sum_{l=0}^{\infty} r^l \sum_{m=-l}^l S_{lm}(\mathbf{r}) A_{lm} \quad (154)$$

where:

$$A_{lm} = \sum_{i=1}^{N_L} \frac{4\pi}{2l+1} \frac{1}{R_{L_i}^{l+1}} S_{lm}(\mathbf{R}_{L_i}) \quad (155)$$

Thus, A_{lm} can be immediately calculated once the charges and positions of the ligands are known. The one-electron operator then becomes:

$$\hat{h} = -\frac{1}{2}\nabla^2 + V_{LF}(\mathbf{r}) \quad (156)$$

The matrix elements of the ligand field potential are also easily evaluated over atomic d-orbitals as:

$$\langle d_i | V_{LF} | d_j \rangle = \sum_{l=0}^{\infty} \langle r^l \rangle \sum_{m=-l}^l A_{lm} G_{l_i l_j l}^{m_i m_j m} \quad (157)$$

where $G_{l_i l_j l}^{m_i m_j m}$ is a Gaunt coefficient that arises from the integral of three spherical harmonics over the angular coordinates ($l_i = l_j = 2$ for d-orbitals and m_i and m_j are

the quantum numbers that distinguish the five real d-orbitals). It is readily evaluated or can be looked up in tables. It is zero unless $m_i + m_j = m$ and $|l_i - l_j| \leq l \leq l_i + l_j$. Thus, the highest possible l in the case of d-orbitals is 4.

In the familiar case of an octahedral ligand field with six equivalent ligands around the metal (O_h point group) the ligand field leads to a splitting of the five d-orbital into a triply degenerate t_{2g} and a doubly degenerate e_g set. The energy difference is defined as $10Dq$ which therefore parameterizes the ligand field seen by the central metal ion. In ligand fields of lower symmetry further splittings arise as is clearly explained in the standard works on ligand field theory [89, 90]. The central theme, however, is that the ligand field potential leads to a splitting of the degeneracy of the d-orbitals with the orbitals that have their lobes closer to the ligands being higher in energy and those further away being lower in energy. The splittings are parameterized by a small number of ligand field parameters such as $10D$ that are fitted to spectral data.

The electron–electron repulsion is also easily treated in the strong crystal field limit. All of the integrals are “pure” electron–electron repulsion integrals over metal d-orbitals. These integrals are well known from atomic spectroscopy [59] and can be expressed in terms of either Slater–Condon or Racah parameters. In terms of Slater Condon parameters the relevant expressions for the Coulomb and Exchange integrals are:

$$\langle d_i d_i | r_{12}^{-1} | d_i d_i \rangle = F_{dd}^0 + \frac{4}{49} F_{dd}^2 + \frac{36}{441} F_{dd}^4 \quad (158)$$

$$\langle d_\sigma d_\sigma | r_{12}^{-1} | d_\pi d_\pi \rangle = \langle d_\sigma d_\sigma | r_{12}^{-1} | d_{\pi'} d_{\pi'} \rangle = F_{dd}^0 + \frac{2}{49} F_{dd}^2 - \frac{24}{441} F_{dd}^4 \quad (159)$$

$$\langle d_\sigma d_\sigma | r_{12}^{-1} | d_\delta d_\delta \rangle = \langle d_\sigma d_\sigma | r_{12}^{-1} | d_{\delta'} d_{\delta'} \rangle = F_{dd}^0 - \frac{4}{49} F_{dd}^2 + \frac{6}{441} F_{dd}^4 \quad (160)$$

$$\langle d_\pi d_\pi | r_{12}^{-1} | d_{\pi'} d_{\pi'} \rangle = \langle d_\pi d_\pi | r_{12}^{-1} | d_\delta d_\delta \rangle = F_{dd}^0 - \frac{2}{49} F_{dd}^2 - \frac{4}{441} F_{dd}^4 \quad (161)$$

$$\langle d_\delta d_\delta | r_{12}^{-1} | d_{\delta'} d_{\delta'} \rangle = F_{dd}^0 + \frac{4}{49} F_{dd}^2 - \frac{34}{441} F_{dd}^4 \quad (162)$$

$$\langle d_\sigma d_\pi | r_{12}^{-1} | d_\sigma d_\pi \rangle = \langle d_\sigma d_{\pi'} | r_{12}^{-1} | d_\sigma d_{\pi'} \rangle = \frac{1}{49} F_{dd}^2 + \frac{30}{441} F_{dd}^4 \quad (163)$$

$$\langle d_\sigma d_\delta | r_{12}^{-1} | d_\sigma d_\delta \rangle = \langle d_\sigma d_{\delta'} | r_{12}^{-1} | d_\sigma d_{\delta'} \rangle = \frac{4}{49} F_{dd}^2 + \frac{15}{441} F_{dd}^4 \quad (164)$$

$$\begin{aligned} \langle d_\pi d_{\pi'} | r_{12}^{-1} | d_\pi d_{\pi'} \rangle &= \langle d_\pi d_\delta | r_{12}^{-1} | d_\pi d_\delta \rangle = \langle d_\pi d_{\delta'} | r_{12}^{-1} | d_\pi d_{\delta'} \rangle \\ &= \langle d_{\pi'} d_\delta | r_{12}^{-1} | d_{\pi'} d_\delta \rangle = \langle d_{\pi'} d_{\delta'} | r_{12}^{-1} | d_{\pi'} d_{\delta'} \rangle \\ &= \frac{3}{49} F_{dd}^2 + \frac{20}{441} F_{dd}^4 \end{aligned} \quad (165)$$

$$\langle d_\delta d_{\delta'} | r_{12}^{-1} | d_\delta d_{\delta'} \rangle = \frac{35}{441} F_{dd}^4 \quad (166)$$

where the abbreviations $d_\sigma = d_{z^2}$, $d_{\pi,\pi'} = d_{xz,yz}$ and $d_{\delta,\delta'} = d_{x^2-y^2,xy}$ were used. Note that the exchange integrals $\langle d_i d_j | r_{12}^{-1} | d_i d_j \rangle$ ($i \neq j$) do not carry the factor F_{dd}^0 which is otherwise the largest term. It can be estimated from atomic spectroscopy as $I - A$ where I is the ionization energy and A the electron affinity of the atom or ion. However, F_{dd}^0 enters in the same way into all Coulomb integrals. It will therefore not appear in equations for *energy differences* and is therefore usually dropped.

The relation between the Slater–Condon and the more familiar Racah parameters is:

$$A = F_{dd}^0 - \frac{49}{441} F_{dd}^0 \quad (167)$$

$$B = \frac{1}{49} F_{dd}^2 - \frac{5}{441} F_{dd}^4 \quad (168)$$

$$C = \frac{35}{441} F_{dd}^4 \quad (169)$$

where A , B and C are the Racah parameters (A is not to be confused with the electron affinity mentioned above). In terms of Racah parameters the term energies usually take a simpler form compared to Slater–Condon parameters. In practical calculations A is again dropped and $C \simeq 4B$ is commonly assumed. Therefore the electron–electron repulsion in ligand field theory is approximated by a *single* parameter B which is very convenient for the analysis of experimental data. The free ion Racah parameters for the first transition series are collected in Table 1.

As expected for interelectronic repulsion, the Racah B parameter increases with increasing effective nuclear charge, i. e. down the series and with the oxidation state of the metal. In general, the effect of covalent bonding will be to reduce electron–electron repulsion parameters from their atomic values. In practice this is usually done by simply fitting the parameters to experimental observations. In the general case, where there is orbital degeneracy, more complicated expressions result for the ligand field energies. The details of the necessary procedures are well covered for example in the classic texts by Griffith [90], Ballhausen [89] and more recently also in a review article [91]. The simple relations derived here, however, serve to illustrate the general principles.

Table 1. Racah parameters B for the atoms and ions of the first transition series in cm^{-1} .

	0	1+	2+	3+	4+
Ti	560	680	720		
V	580	660	765	860	
Cr	790	710	830	1030	1040
Mn	720	870	960	1140	
Fe	805	870	1060		
Co	780	880	1120		
Ni	1025	1040	1080		
Cu		1220	1240		

In summary, the effects of the crystal field and the interelectronic repulsion are incorporated in a small set of numerical parameters that can be fitted to experimental transition energies. This procedure is remarkably successful. On the other hand, if the symmetry becomes low, the number of necessary parameters is increasing and the fits tend to become overdetermined.

9.4.3 Matrix Elements over Molecular Orbitals

To derive expressions for the SH parameters it is necessary to evaluate matrix elements of fairly complicated one-electron operators between MOs. In this section we will introduce an approximate evaluation of these integrals in the framework of ligand field theory. The first operator to be treated is the reduced SOC operator with the matrix elements:

$$L_{1\mu}^{ij} = \text{Im} \left(\left\langle \psi_i \left| \sum_A \xi(r_A) l_{\mu}^A \right| \psi_j \right\rangle \right) \quad (170)$$

In a normal complex the ligands are made of light atoms with small SOC constants. It is therefore a good approximation to restrict the sum over atoms to the metal only which gives:

$$\begin{aligned} L_{1\mu}^{ij} &\approx \text{Im} \left(\langle \psi_i | \xi(r_M) l_{\mu}^M | \psi_j \rangle \right) \\ &= \text{Im} (c_{M_i} c_{M_j} \langle d_i | \xi(r_M) l_{\mu}^M | d_j \rangle + c_{M_i} c_{L_j} \langle d_i | \xi(r_M) l_{\mu}^M | L_j \rangle \\ &\quad + c_{M_j} c_{L_i} \langle L_i | \xi(r_M) l_{\mu}^M | d_j \rangle + c_{L_i} c_{L_j} \langle L_i | \xi(r_M) l_{\mu}^M | L_j \rangle) \end{aligned} \quad (171)$$

The first term is a one-center integral and the last three are at least two center integrals. Since the operator $\xi(r_M)$ has a r_M^{-3} dependence it will be a good approximation to neglect these multicenter integrals and end up with:

$$\begin{aligned} L_{1\mu}^{ij} &\approx c_{M_i} c_{M_j} \text{Im} (\langle d_i | \xi(r_M) l_{\mu}^M | d_j \rangle) \\ &= c_{M_i} c_{M_j} \zeta_{ij} \text{Im} (\langle d_i | l_{\mu}^M | d_j \rangle) \end{aligned} \quad (172)$$

where:

$$\zeta_{ij} = \langle d_i | \xi(r_M) | d_j \rangle \quad (173)$$

is the radial integral over the operator $\xi(r_M)$. (There are, of course, also situations where ligands like sulfur, chlorine or even heavier atoms can make significant contributions to the SOC integrals. It should be kept in mind, however, that the ligands contribute only s- and p-orbitals which have one unit lower angular momentum than d-orbitals which in addition to the smaller intrinsic SOC constants compared to the metal leads to smaller SOC integrals.) The next approximation is to assume that all metal d-orbitals have the same radial function. In this case the radial integration becomes independent of i and j and one gets $\zeta_{ij} = \bar{\zeta}$. $\bar{\zeta}$ may be identified as the

Table 2. Empirically determined SOC constants for first row transition metal ions in d^N electron configurations (in cm^{-1}) (from Bendix et al. [92]).

	2+	3+	4+	5+	6+
Sc	79				
Ti	118	153			
V	169	206	250		
Cr	229	274	319	376	
Mn	315	351	408	466	540
Fe	427	464	505	578	649
Co	533	619	656	700	
Ni	668	749	858	888	863
Cu	829	911	1009	1139	

one-electron SOC constant of the free atom or ion (ζ). However, one has to account the possibility that the metal radial function changes upon complex formation which leads to a differences between $\bar{\zeta}$ and ζ (Section 9.4.1.4).

A comprehensive collection of ζ values for ions in d^N configurations taken from the paper by Bendix et al. [92] is given in Table 2. As expected, the SOC constants increase with increasing effective nuclear charge and oxidation state of the metal ion.

The one-center integrals of the angular momentum operator are easy to evaluate. Their values are given in Table 3.

The factor $c_{M_i}c_{M_j}$ is very important as it determines the effect of metal–ligand covalent bonding on the SOC constants. It could be absorbed into the radial integral, i. e. $\zeta_{\text{eff}} = \zeta c_{M_i}c_{M_j}$ which defines a covalently *reduced* SOC “constant” ($c_{M_i}c_{M_j} \leq 1$) which shows up as a result of the “dilution” of the metal orbitals with ligand orbitals. However, this “dilution” will in general be *anisotropic* ($c_{M_i} \neq c_{M_j}$) which would seem to preclude the use of a single SOC constant for the treatment of SOC in inorganic complexes. However, in a number cases it will be an acceptable approximation to take an average (\bar{c}_M) of the c_{M_i} over all metal d-derived MOs to define an average covalently reduced SOC constant as $\bar{\zeta}_{\text{eff}} = \bar{c}_M^2 \zeta$ and to use this value in all SOC matrix elements. It should however be noticed that the anisotropy in the covalency is an important effect that is sensitively connected to the bonding in the complex. In general the more strongly antibonding MOs at higher energy will have larger covalencies (smaller c_{M_i}) than the less antibonding or non-bonding orbitals and this can have important effects on some properties such as zero-field splittings (Sections 9.4.1.9.6, 9.5.2, and 9.6.5).

From Eq. (46) an appropriate form of the operator $\xi(r_M)$ is:

$$\xi(r_M) = \frac{\alpha^2 Z_{\text{eff}}^M}{2 r_M^3} \quad (174)$$

This equation predicts that the one-electron SOC constant should be directly proportional to the expectation value of r_M^{-3} taken over the metal d-orbital radial function. The proportionality constant should be proportional to the effective nu-

Table 3. Values of the one center integrals $\langle i|l_\mu|j\rangle$ for real s-, p- and d-orbitals. Only non-zero values are given.

$l_{A,x}$	s	p_z	p_x	p_y	d_{z^2}	d_{xz}	d_{yz}	$d_{x^2-y^2}$	d_{xy}
s									
p_z				i					
p_x									
p_y		$-i$							
d_{z^2}							$i\sqrt{3}$		
d_{xz}									i
d_{yz}					$-i\sqrt{3}$			$-i$	
$d_{x^2-y^2}$							i		
d_{xy}						$-i$			
$l_{A,y}$	s	p_z	p_x	p_y	d_{z^2}	d_{xz}	d_{yz}	$d_{x^2-y^2}$	d_{xy}
s									
p_z			$-i$						
p_x		i							
p_y									
d_{z^2}						$-i\sqrt{3}$			
d_{xz}					$i\sqrt{3}$			$-i$	
d_{yz}									$-i$
$d_{x^2-y^2}$						i			
d_{xy}							i		
$l_{A,z}$	s	p_z	p_x	p_y	d_{z^2}	d_{xz}	d_{yz}	$d_{x^2-y^2}$	d_{xy}
s									
p_z									
p_x				$-i$					
p_y			i						
d_{z^2}									
d_{xz}							$-i$		
d_{yz}						i			
$d_{x^2-y^2}$									$-2i$
d_{xy}								$2i$	

clear charge felt by the d-electrons. Figure 1 shows the correlation between empirically determined SOC constants for a series of Fe ions in d^N configurations [92] with $\langle r^{-3} \rangle_d$ values from accurate Hartree–Fock calculations [66]. From the slope of the regression line one finds $Z_{\text{eff}}^{Fe} = 14.0$ in reasonable agreement with Slater’s rules [27, 77] that predict $Z_{\text{eff}}^{Fe} = 13.2$. While the agreement is rather satisfactory at this point one has to be careful because in inorganic complexes the metal radial functions can be distorted from the situation found in the free d^N -ion and this will give additional “central field” covalency effects on the SOC “constants”. This subject will be further discussed in Section 9.6.5.

For some heavier ligands like sulfur, chlorine or bromine it will prove necessary to include the ligand SOC in the treatment as it can become appreciable. In this case

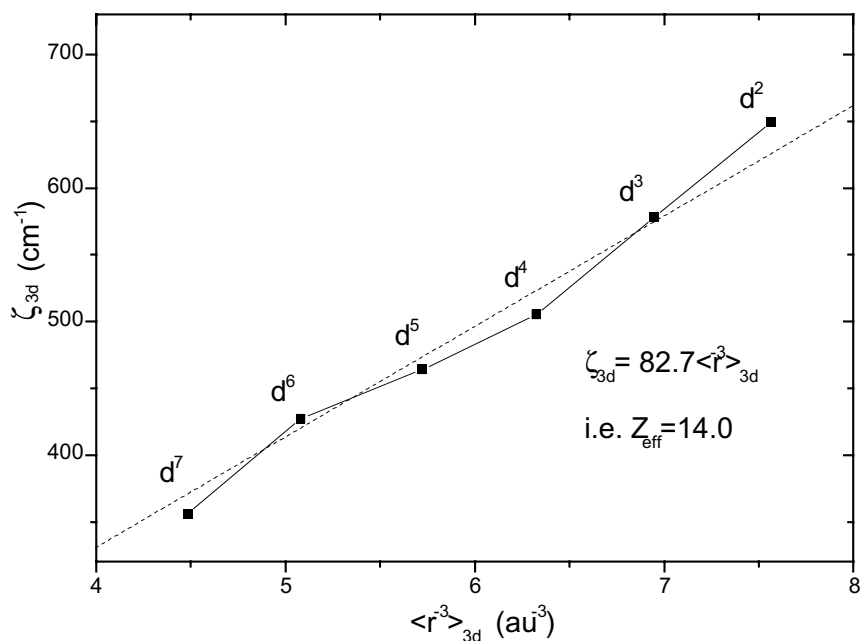


Fig. 1. Correlation between the empirically determined values of SOC constants ζ_{3d} [92] and $\langle r_{Fe}^{-3} \rangle_{3d}$ calculated from accurate Hartree-Fock wavefunctions [66].

one should include the ligand nuclei in the sum over nuclei. However, a one-center approximation will still be appropriate. In place of Eq. (171) one finds:

$$\begin{aligned} L_{1\mu}^{ij} &\approx \text{Im}(\langle \psi_i | \xi(r_M) l_\mu^M + \xi(r_L) l_\mu^L | \psi_j \rangle) \\ &\approx \text{Im}(c_{Mi} c_{Mj} \langle d_i | \xi(r_M) l_\mu^M | d_j \rangle + c_{Li} c_{Lj} \langle L_i | \xi(r_L) l_\mu^L | L_j \rangle) \end{aligned} \quad (175)$$

This equation can be expressed in terms of the metal SOC constant alone by keeping Eq. (172) but redefining the effective SOC constant in Eq. (173) as:

$$\zeta_{ij} \rightarrow \langle d_i | \xi(r_M) | d_j \rangle + \nu_L \frac{c_{Li} c_{Lj} \langle L_i | l_\mu^L | L_j \rangle}{c_{Mi} c_{Mj} \langle d_i | l_\mu^M | d_j \rangle} \quad (176)$$

where ν_L can to a good approximation be taken to be the ratio of the atomic SOC constants of the ligand and the metal [85].

Finally note the symmetry requirements for non-zero integrals. Although we have chosen not to introduce spatial symmetry at the many electron level it can be easily incorporated at the one electron level. The angular momentum operators transform under the same irreducible representations as the molecular rotations. Thus it can be readily decided whether $\Gamma(\psi_i) \otimes \Gamma(R_\mu) \otimes \Gamma(\psi_j)$ contains the totally symmetric representation in which case $L_{1\mu}^{ij}$ is non-zero (as is $L_{2\mu}^{ij}$ and $L_{3\mu}^{ij}$).

Closely related to the matrix elements of the SOC are the matrix elements of the nucleus-orbit coupling, Eq. (145). Using the same approximation as for the SOC one finds:

$$L_{3\mu}^{ij} \approx c_{Mi}c_{Mj}\langle r^{-3} \rangle_d \text{Im}(\langle d_i | l_{\mu}^M | d_j \rangle) \quad (177)$$

that is, these integrals differ only by the constant factor $\frac{1}{2}\alpha^2 Z_{\text{eff}}^M$ from the SOC integrals. They can therefore be either related to empirically determined SOC constants or can be estimated by using free atom or ion values for $\langle r^{-3} \rangle_d$ (*vide infra*; Table 6). Of course, the same covalency effects as for the SOC “constants” arise.

The next operator to be discussed is the nucleus-electron spin dipolar coupling that arise in Eq. (143). For the prediction of metal hyperfine coupling the operator once more has a dependence r_M^{-3} and therefore it will be sufficient to only keep the one-center parts of the integrals to get:

$$\begin{aligned} & \langle \psi_i | r_M^{-5} \{ \delta_{\mu\nu} r_M^2 - 3r_{M,\mu} r_{M,\nu} \} | \psi_j \rangle \\ & \approx c_{Mi}c_{Mj}\langle r^{-3} \rangle_d \langle d_i | \delta_{\mu\nu} - 3r_{M,\mu}^{-2} r_{M,\nu} | d_j \rangle \end{aligned} \quad (178)$$

The one-center reduced field gradient integrals are easy to evaluate. The operator for the reduced field gradient integrals is denoted $f_{\mu\nu}$ and its matrix elements over real s-, p- and d-orbitals are given in Table 4. For the ligand HFC likewise:

$$\begin{aligned} & \langle \psi_i | r_L^{-5} \{ \delta_{\mu\nu} r_L^2 - 3r_{L,\mu} r_{L,\nu} \} | \psi_j \rangle \\ & \approx c_{Li}c_{Lj}\langle r^{-3} \rangle_L \langle L_i | \delta_{\mu\nu} - 3r_{L,\mu}^{-2} r_{L,\nu} | L_j \rangle \end{aligned} \quad (179)$$

The most critical integrals are the orbital Zeeman integrals (the L_2 integrals, Eq. (139)). Making the natural choice that the metal ion is placed at the origin the integrals become:

$$\begin{aligned} L_{2p}^{ij} = & \text{Im}(c_{Mi}c_{Mj}\langle d_i | l_p^M | d_j \rangle + c_{Mi}c_{Lj}\langle d_i | l_p^M | L_j \rangle \\ & + c_{Li}c_{Mj}\langle L_i | l_p^M | d_j \rangle + c_{Li}c_{Lj}\langle L_i | l_p^L - i(\mathbf{R}_{LM} \times \nabla)_p | L_j \rangle) \end{aligned} \quad (180)$$

Where in the last term the general equation to shift an angular momentum operator from one center to the other has been used:

$$\mathbf{l}^M = \mathbf{l}^L - i\mathbf{R}_{LM} \times \nabla \quad (181)$$

where $\mathbf{R}_{LM} = \mathbf{R}_L - \mathbf{R}_M$. Thus, a two center integral has been transformed to a one-center integral at the expense of introducing an extra term that depends on the gradient of the orbital in the ket with respect to the electronic coordinates. The important point nevertheless is that the operator contains no factors of r^{-3} that would justify a one-center approximation. The order of magnitude of the terms can be most easily estimated by considering the third term in Eq. (180). The effect of operating with the angular momentum operator on an d-orbital is another d-orbital multiplied by a complex valued factor (Table 3). If this d-orbital overlaps with the ligand orbital in the bra a contribution proportional to the metal-ligand overlap

Table 4. The values of the one-center reduced field gradient integrals. In order to get the field gradient themselves multiply with the matrix element of r^{-3} evaluated over the radial parts of the orbitals involved.

f_{xx}	s	p_z	p_x	p_y	d_{z^2}	d_{xz}	d_{yz}	$d_{x^2-y^2}$	d_{xy}
s					$-\frac{1}{5}\sqrt{5}$			$\frac{1}{5}\sqrt{15}$	
p_z		$-\frac{2}{5}$							
p_x			$\frac{4}{5}$						
p_y				$-\frac{2}{5}$					
d_{z^2}	$-\frac{1}{5}\sqrt{5}$				$-\frac{2}{7}$			$-\frac{2}{7}\sqrt{3}$	
d_{xz}						$\frac{2}{7}$			
d_{yz}							$-\frac{4}{7}$		
$d_{x^2-y^2}$	$\frac{1}{5}\sqrt{15}$				$-\frac{2}{7}\sqrt{3}$			$\frac{2}{7}$	
d_{xy}									$\frac{2}{7}$
f_{yy}	s	p_z	p_x	p_y	d_{z^2}	d_{xz}	d_{yz}	$d_{x^2-y^2}$	d_{xy}
s					$-\frac{1}{5}\sqrt{5}$			$-\frac{1}{5}\sqrt{15}$	
p_z		$-\frac{2}{5}$							
p_x			$-\frac{2}{5}$						
p_y				$\frac{4}{5}$					
d_{z^2}	$-\frac{1}{5}\sqrt{5}$				$-\frac{2}{7}$			$\frac{2}{7}\sqrt{3}$	
d_{xz}						$-\frac{4}{7}$			
d_{yz}							$\frac{2}{7}$		
$d_{x^2-y^2}$	$-\frac{1}{5}\sqrt{15}$				$\frac{2}{7}\sqrt{3}$			$\frac{2}{7}$	
d_{xy}									$\frac{2}{7}$
f_{zz}	s	p_z	p_x	p_y	d_{z^2}	d_{xz}	d_{yz}	$d_{x^2-y^2}$	d_{xy}
s					$\frac{2}{5}\sqrt{5}$				
p_z		$\frac{4}{5}$							
p_x			$-\frac{2}{5}$						
p_y				$-\frac{2}{5}$					
d_{z^2}	$\frac{2}{5}\sqrt{5}$				$\frac{4}{7}$				
d_{xz}						$\frac{2}{7}$			
d_{yz}							$\frac{2}{7}$		
$d_{x^2-y^2}$								$-\frac{4}{7}$	
d_{xy}									$-\frac{4}{7}$
f_{xy}	s	p_z	p_x	p_y	d_{z^2}	d_{xz}	d_{yz}	$d_{x^2-y^2}$	d_{xy}
s									$\frac{1}{5}\sqrt{15}$
p_z									
p_x				$\frac{3}{5}$					
p_y			$\frac{3}{5}$						
d_{z^2}									$-\frac{2}{7}\sqrt{3}$
d_{xz}							$\frac{3}{7}$		
d_{yz}						$\frac{3}{7}$			
$d_{x^2-y^2}$									
d_{xy}	$\frac{1}{5}\sqrt{15}$				$-\frac{2}{7}\sqrt{3}$				

Table 4. (continued.)

f_{xz}	s	p_z	p_x	p_y	d_{z^2}	d_{xz}	d_{yz}	$d_{x^2-y^2}$	d_{xy}
s						$\frac{1}{5}\sqrt{15}$			
p_z			$\frac{3}{5}$						
p_x		$\frac{3}{5}$							
p_y									
d_{z^2}						$\frac{1}{7}\sqrt{3}$			
d_{xz}	$\frac{1}{5}\sqrt{15}$				$\frac{1}{7}\sqrt{3}$			$\frac{3}{7}$	
d_{yz}									$\frac{3}{7}$
$d_{x^2-y^2}$						$\frac{3}{7}$			
d_{xy}							$\frac{3}{7}$		
f_{yz}	s	p_z	p_x	p_y	d_{z^2}	d_{xz}	d_{yz}	$d_{x^2-y^2}$	d_{xy}
s							$\frac{1}{5}\sqrt{15}$		
p_z				$\frac{3}{5}$					
p_x									
p_y		$\frac{3}{5}$							
d_{z^2}							$\frac{1}{7}\sqrt{3}$		
d_{xz}									$\frac{3}{7}$
d_{yz}	$\frac{1}{5}\sqrt{15}$				$\frac{1}{7}\sqrt{3}$			$-\frac{3}{7}$	
$d_{x^2-y^2}$							$-\frac{3}{7}$		
d_{xy}						$\frac{3}{7}$			

will arise. Even if all overlap integrals are neglected the fourth term will survive and make a non-negligible contribution. We do not enter into a detailed calculation of the various contributions [85, 93–97]. The terms are fairly easily evaluated numerically (*vide infra*). In anticipating a result from Section 9.6.7 it is noted that the ligand contributions account for a *reduction* of the orbital Zeeman matrix elements by up to ≈ 20 – 25% . The reduction always arises for antibonding molecular orbitals. Physically, this means that the ligand angular momentum in antibonding MOs opposes the metal-angular momentum and thereby leads to a reduction of the orbital Zeeman matrix elements. For the purposes of this section it is sufficient to model the reduction in a rather global way by writing:

$$L_{2p}^{ij} \approx \text{Im}(c_{Mi}c_{Mj}\langle d_i || l_p^M || d_j \rangle \varepsilon_{ij}^p) \quad (182)$$

where ε_{ij}^p maybe as low as 0.75–0.80. It should be noted, however, that in the crystal field limit ($c_{Mi} \rightarrow 1$ and $c_{Li} \rightarrow 0$) the ligand angular momentum corrections to the orbital Zeeman vanishes exactly ($\varepsilon_{ij}^p \rightarrow 1$).

To further illustrate this important point, consider the data collected in Table 5 where the differences in the SOC and Zeeman matrix elements were derived from a density functional calculation [98]. In ligand field theory the reduced SOC and Zeeman matrix elements would be equal. However, it is seen from the table that the SOC matrix element is much larger than the Zeeman matrix element. Thus, the

Table 5. SOC versus Zeeman matrix elements for $[\text{Cu}(\text{NH}_3)_4]^{2+}$ from Ref. [98]. The matrix elements are the SOC and Zeeman matrix elements between the metal $d_{x^2-y^2}$ and d_{xy} based MOs. The angular momentum matrix element between the pure $d_{x^2-y^2}$ and d_{xy} metal orbitals is 2i. The SOC constant of Cu(II) from atomic spectroscopy is 829 cm^{-1} . The calculations were done with the B3LYP density functional method.

	Calc.
ζ_{Cu} (free Cu(II) ion)	821 cm^{-1}
$\left \left\langle \psi_{x^2-y^2} \left \sum_A \zeta(r_A) \vec{L}_{A,Z} \right \psi_{xy} \right\rangle \right / \zeta_{Cu}$	1.619
Reduction from crystal field	19%
$\left \left\langle \psi_{x^2-y^2} \left \vec{L}_z \right \psi_{xy} \right\rangle \right $	1.295
Reduction from crystal field	34%
$\varepsilon_{x^2-y^2,xy}^z$	0.799

SOC “constant” is reduced by 19% from its crystal field limit while the Zeeman matrix element is reduced by as much as 34% because of the aforementioned effects (i. e. $\varepsilon_{x^2-y^2,xy}^z \approx 0.80$). Complete neglect of the ligand contributions to the Zeeman matrix elements therefore leads to sizeable errors and consequently the results are necessarily at most qualitatively correct.

9.4.4 “Central Field” versus “Symmetry Restricted” Covalency

In the preceding section we have discussed the main factors that need to be taken into account in evaluating the relevant matrix elements of the various magnetic operators in a ligand field framework. Most of the integrals can be satisfactorily approximated as of the one-center type. By this procedure one can clearly observe one consequence of covalent bonding – the dilution of metal d-orbitals with ligand orbitals reduces all of the matrix elements from their atomic values. The crystal field limit is obtained by letting $c_{Mi} \rightarrow 1$ and $c_{Li} \rightarrow 0$ wherever they occur. This type of covalency has been termed the “symmetry restricted covalency” because the symmetry of the complex determines which metal orbitals can interact with ligand orbitals in order to form covalent bonds. This covalency is manifestly *anisotropic*, i. e. different metal d-orbitals can have grossly different admixtures of ligand orbitals and, as will be elaborated below, this has interesting consequences on the spectroscopic properties of the complexes. The ligand admixtures will be the largest for the orbitals that interact most strongly with the ligand and these are the most antibonding orbitals that are highest in energy. Exceptions from this rule only occur for exceptionally strong π -bonding effects.

There is, however, a second kind of covalency that is more subtle than the symmetry restricted covalency that already shows up in the most primitive molecular orbital

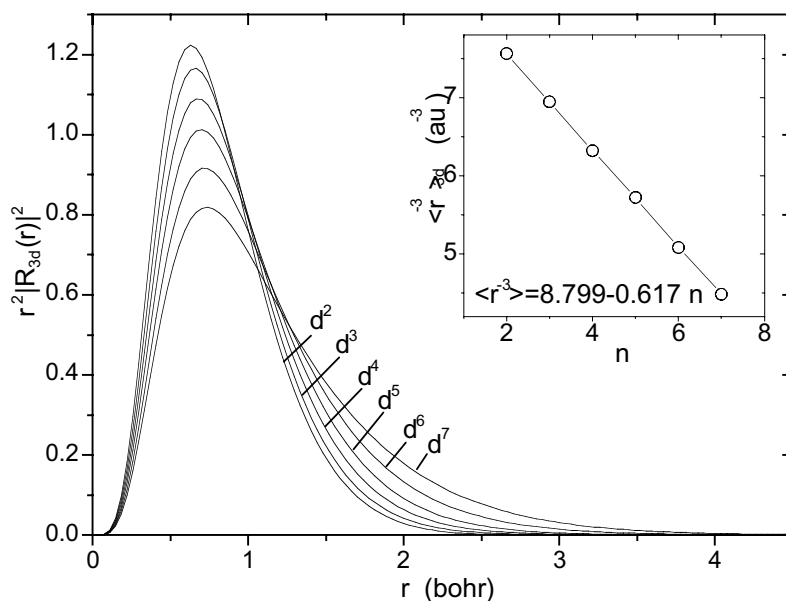


Fig. 2. Radial distribution functions of iron ions in d^N configurations from accurate Hartree–Fock calculations (reproduced with permission from Ref. [66]). The inset shows the variation of the variation of the $\langle r^{-3} \rangle_{3d}$ expectation value with the d^N configuration.

calculations. This second kind of covalency is termed “central field covalency” and shows up as a change of the radial expectation values from their atomic values. The origin of this effect – which is to be separated from the simple dilution effect – is a change of the radial distribution function of the metal ion upon being placed in the ligand field. To illustrate the effect, Fig. 2 shows the radial distribution functions of different iron ions in d^N configurations as found from accurate Hartree–Fock calculations. Evidently, the functions become more diffuse (i. e. extend to larger distances from the nucleus) as the number of d-electrons is increased. This is due to a decreased effective nuclear charge seen by the 3d electrons as more other 3d-electrons tend to shield the nuclear charge. This change in metal-radial functions of course also leads to a modification of the radial expectation values that are sensitive to the shape of these functions. The inset in Fig. 2 shows that variation of the most important $\langle r^{-3} \rangle_{3d}$ value that decreases with increasing d-electron count because the peak of the radial distribution function moves to larger distances with increasing d^N electron count. Since the HFC and the SOC are both directly proportional to this value a $\approx 8\text{--}10\%$ decrease of these values per one-electron increase is predicted by this plot.

However, as we have discussed recently [66] following classic work of Ammeter [97, 99], the pure nuclear shielding effect, that was anticipated early on [100–104] is not the only effect that contributes to the central field covalency. Especially, the formation of covalent bonds (i. e. bonding and antibonding molecular orbitals) leads to

rather pronounced effects on the radial distribution function of the metal. In general, the radial distribution function of the metal will become *more diffuse* in *antibonding* orbitals which is a consequence of the virial theorem. Since the bonding and antibonding character of the metal d-orbitals in a complex is evidently not isotropic, this expansion of the radial function is also anisotropic. Thus, there not only is an *anisotropic* “symmetry restricted covalency” but there also is an anisotropic “central field covalency”. The anisotropic central field covalency is a significant effect that account for up to $\approx 20\%$ reduction of the $\langle r^{-3} \rangle_{3d}$ value from its atomic value and is therefore of the same order of magnitude as the symmetry restricted covalency. If the “central field covalency” is not taken into account a significant overestimate of the “symmetry restricted covalency” may be the consequence. The effect is illustrated in Fig. 3 for the case of FeCl_4^- where we have plotted the molecular radial distribution functions of the central iron in comparison to atomic radial distribution functions [66]. It is observed that the molecular radial functions do not reflect the atomic radial functions of the ${}^6\text{S Fe}^{3+}$ ion but are rather intermediate between Fe(I) and Fe(II). Thus, the molecular radial distribution function is significantly more diffuse than the expected atomic one. Moreover, the expansion of the molecular radial function is *anisotropic* because the bonding characteristics of the t_2 and e orbitals are different. This has important consequences for the $\langle r^{-3} \rangle_{3d}$ expectation value that also becomes anisotropic and up to 20% smaller than the one for the parent ion. Consequently, the same reduction is to be expected for the

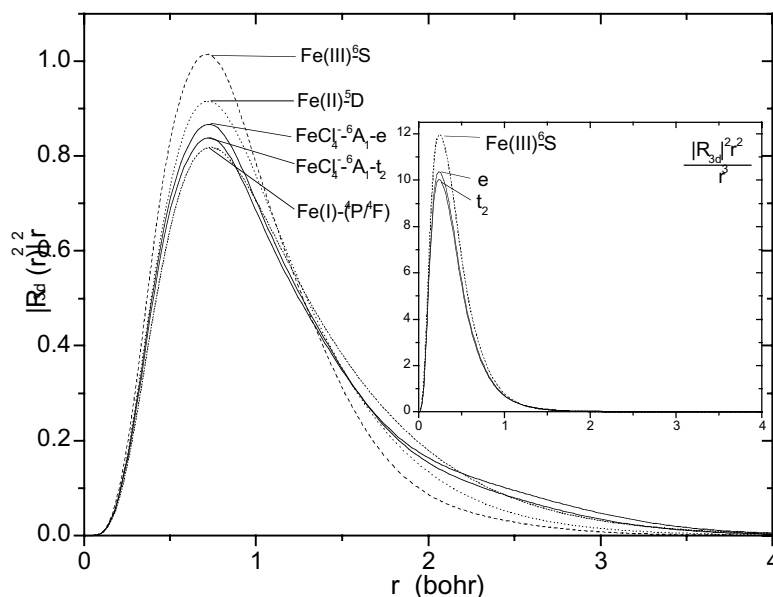


Fig. 3. Molecular radial functions of the central iron in FeCl_4^- in comparison with atomic radial functions for several Fe ions of different d^N configuration (reproduced with permission from Ref. [66]).

SOC constant which underlines the importance of taking these effects into account in a quantitative analysis of the magnetic resonance parameters in transition metal complexes.

Having discussed the relevant matrix elements and the effects of covalency in a general sense, we are now in a position to discuss the SH parameters of transition metal complexes in a ligand field framework.

9.4.5 Ligand-field Theory of Zero-field Splittings

The ZFS contribution $\mathbf{D}^{SOC-(0)}$ to the D-tensor follows from Eq. (130) using the matrix elements Eq. (173) and (172) and neglecting the ligand contribution to the SOC matrix elements (Eq. (176)):

$$D_{\mu\nu}^{SOC-(0)} = -\frac{1}{4S^2} \sum_i \sum_j \Delta_{ij}^{-1} \zeta_{ij}^2 c_{Mi}^2 c_{Mj}^2 \langle d_i | l_\mu^M | d_j \rangle \langle d_j | l_\nu^M | d_i \rangle \quad (183)$$

where i is either a doubly occupied orbital or an empty orbital and j is a singly occupied orbital in the ground state. Δ_{ij} is the transition energy for the promotion of an electron from orbital i to j if i is double occupied and the transition energy from j to i if i is empty in the ground state. In the approximation where the covalency is averaged one finds:

$$D_{\mu\nu}^{SOC-(0)} = -\frac{\bar{\zeta}_{\text{eff}}^2}{4S^2} \sum_i \sum_j \Delta_{ij}^{-1} \langle d_i | l_\mu^M | d_j \rangle \langle d_j | l_\nu^M | d_i \rangle \quad (184)$$

According to Eq. (52) prefactor of Eq. (184) equals λ^2 , the square of the many SOC constant. In this approximation the D-tensor becomes equivalent to the standard ligand field expression:

$$D_{\mu\nu}^{LFT} = -\lambda^2 \sum_n \frac{\langle 0 | L_\mu | n \rangle \langle n | L_\nu | 0 \rangle}{E_n - E_0} \quad (185)$$

where $|0\rangle$ is the ground state and $|n\rangle$ is an excited state that arises from the same term as the ground state [3]. If $|0\rangle$ and $|n\rangle$ are approximated by single Slater determinants built from pure metal d-orbitals Eq. (184) is recovered. Since a one-electron approximation to the SOC is used it is clear that $|n\rangle$ must be singly excited relative to $|0\rangle$ in order to make a non-zero contribution.

It is evident from this discussion that the ligand field treatment of ZFSs makes two severe assumptions: (a) The covalency effects can be absorbed into a single, unique, covalently reduced many electron SOC constant and (b) The contributions of excited states of the same spin dominate the D-tensor. As will be explained in detail below and illustrated with experimental data in Section 9.5, both assumptions are critical and will only provide reasonable approximations under certain circumstances.

9.4.6 Ligand-field Theory of the g-Tensor

The g-tensor in the ligand field approximation is derived exactly along the same lines as the D-tensor. First of all the two small terms (Eqs. 134 and 137) can be safely neglected for the g-tensors of transition metal complexes which generally show rather large g-shifts on the order of 0.1 and more. Making use of Eqs. (172) (or 176) and (182) in Eq. (138) one finds:

$$g_{\mu\nu} = \delta_{\mu\nu}g_e + \frac{1}{2S} \sum_i \sum_j \Delta_{ij}^{-1} c_{Mi}^2 c_{Mj}^2 \zeta_{ij} \{ \langle d_i | l_\mu^M | d_j \rangle \varepsilon_{ij}^\mu \langle d_j | l_\nu^M | d_i \rangle + \langle d_i | l_\mu^M | d_j \rangle \varepsilon_{ji}^\nu \langle d_j | l_\nu^M | d_i \rangle \} \quad (186)$$

The phase factor p_{ij} is zero if i is doubly occupied and unity if i is empty. If the ligand terms are neglected and the covalency is averaged over the various molecular orbitals this becomes:

$$g_{\mu\nu} = \delta_{\mu\nu}g_e + \frac{\bar{\zeta}^{\text{eff}}}{S} \sum_i \sum_j \Delta_{ij}^{-1} (-1)^{p_{ij}} \langle d_i | l_\mu^M | d_j \rangle \langle d_j | l_\nu^M | d_i \rangle \quad (187)$$

which is equivalent to the standard ligand field expression [3, 4]:

$$g_{\mu\nu}^{LFT} = \delta_{\mu\nu}g_e - 2\lambda \sum_n \frac{\langle 0 | L_\mu | n \rangle \langle n | L_\nu | 0 \rangle}{E_n - E_0} \quad (188)$$

where again, the summation n is over singly excited states that arise from the same term as the ground state. If it is furthermore assumed that the index i sums only over occupied or only over empty orbitals there is a close connection between the D- and g-tensor which is:

$$D_{\mu\nu} = \pm \frac{\bar{\zeta}^{\text{eff}}}{4S} \Delta g_{\mu\nu} \quad (189)$$

where the upper sign holds for summations over doubly occupied orbitals and the lower one for empty orbitals i . It should however be reiterated that several rather severe assumptions, in addition to the simplification to a MO type picture, have been made to arrive at this familiar result: (a) contributions to the D-tensor from states of different spin than the ground state have been neglected, (b) the covalency was averaged over all orbitals, (c) the ligand contribution to the SOC and much more severely to the orbital Zeeman matrix elements has been neglected and (d) the relevant excited states were restricted to either promotion from a doubly occupied into a singly occupied MO or from a singly occupied MO into an empty MO but *not* both types. The two different types of excited states enter with the same sign into the D-tensor expression but with *opposite* signs into the g-tensor. These four assumptions are so severe that quantitative accuracy at any level cannot be expected. The relation between the D- and the g-tensor has, however, still been found to be useful in certain circumstances.

9.4.7 Ligand-field Theory of Hyperfine Couplings

9.4.7.1 Metal HFCs

The dipole contribution to the metal HFC is usually large being proportional to the expectation value of r_M^{-3} over the rather compact d-orbitals and the value P that can be substantial for some metal nuclei (Table 6).

Inserting Eq. (178) into Eq. (143) one finds (remembering that in atomic units $\beta_e = \frac{1}{2}\alpha$):

$$A_{\mu\nu}^{(A;d)} = \frac{1}{2S} P_d \sum_i c_{Mi}^2 \langle d_i | f_{\mu\nu} | d_i \rangle \quad (190)$$

with

$$P_d = \frac{\alpha}{2} g_e \beta_N g_N^{(A)} \langle r_M^{-3} \rangle_d \quad (191)$$

where the sum over i includes the singly occupied MOs and the expectation value $\langle r_M^{-3} \rangle_d$ is to be understood as an appropriate average over the singly occupied MOs. The second order contribution to the metal HFC is also usually large. Since in the ligand field approximation the L_1 and L_3 integrals are proportional, an approximate relation between the second order HFC and the g-tensor can be established. Inserting Eqs. (172) and (177) into Eq. (144) one obtains:

$$A_{\mu\nu}^{(M;SO)} = \frac{1}{S} P_d \sum_i \sum_j \Delta_{ij}^{-1} (-1)^{p_{ij}} c_{Mi}^2 c_{Mj}^2 \zeta_{ij} \langle d_i | l_\mu^M | d_j \rangle \langle d_j | l_\nu^M | d_i \rangle \quad (192)$$

where all symbols have the same meaning as in Eq. (186). In fact comparing the two equations and once more neglecting the ligand terms in the g-tensor one deduces that:

$$A_{\mu\nu}^{(M;SO1)} = P_d \Delta g_{\mu\nu} \quad (193)$$

It should, however, be realized that the approximations for the second order part of the HFC and the g-tensor are quite different – the neglect of ligand terms is a good approximation in the case of the HFC but is a less accurate approximation for the g-tensor (see also Section 9.3.5.4). Nevertheless, the relation between the g-tensor and the second order metal HFC is a highly useful one.

For the second SOC contribution to the HFC one has ($S = \frac{1}{2}$ case):

$$A_{\mu\nu}^{(M;SO2)} = -P_d \sum_i \sum_j \Delta_{ij}^{-1} (-1)^{p_{ij}} \zeta_{ij} c_{Mi}^2 c_{Mj}^2 \cdot \sum_{\kappa, \tau=x,y,z} i \varepsilon_{\kappa\tau\mu} \langle d_j | f_{\kappa\nu} | d_i \rangle \langle d_i | l_\tau^M | d_j \rangle \quad (194)$$

This term will also give contributions that are related to g-tensor elements although the proportionality is not as direct as for $A_{\mu\nu}^{(M;SO1)}$.

The Fermi contact contribution to the metal nucleus HFC Eq. (142) is zero in the ligand field approximation because d-orbitals have zero amplitude at the nucleus. In reality, however, the Fermi contact interaction in inorganic complexes is non-zero due to the presence of core-polarization (*vide infra*). The Fermi term is therefore introduced as an empirical parameter into LFT and treated together with the dipole term. Since the core polarization is usually negative the Fermi term is written:

$$A_{iso}^{(M)} = -\frac{P_d}{2S}\kappa \quad (195)$$

where κ is an empirical parameter.

9.4.7.2 Ligand HFCs

Ligand HFCs do not arise in the crystal field approximation because the singly occupied orbitals are all of purely metal character in this approximation. In fact, observation of ligand HFCs were instrumental in proving experimentally that the crystal field picture is incomplete [105]. In a ligand field framework, the ligand HFC arises from the ligand character in the predominantly metal-based singly occupied orbitals.

To be more specific consider the case where the ligand orbital is an sp hybrid of the form:

$$|L\rangle = n|p\rangle + \sqrt{1-n^2}|s\rangle \quad (196)$$

where $|p\rangle$ is the valence shell p-orbital and $|s\rangle$ is the valence shell s-orbital of the ligand. Let us also assume that the hybrid orbital is oriented along the metal–ligand axis and that the coefficient multiplying $|L\rangle$ in the singly occupied MO is c_L . Then from Eq. (142) one estimates for the isotropic part of the ligand HFC:

$$A_{iso}^{(L)} \approx \frac{4\pi}{3S} P^L c_L^2 (1-n^2) |\psi_s(0)|^2 \quad (197)$$

This equation has frequently been used to estimate c_L^2 from an assumed value of n and an atomic value of $|\psi_s(0)|^2$ which is identified with the value of the amplitude of the atomic valence s-orbital at the nucleus. The validity of this approach will be discussed in Section 9.6.8.

For the dipolar part of the ligand HFC one finds from Eqs. (143) and (179) and the values in Table 4:

$$A_{\sigma}^{(L;d)} \approx \frac{4}{5} \frac{1}{2S} P^L \langle r_L^{-3} \rangle_p c_L^2 n^2 \quad (198)$$

$$A_{\pi}^{(L;d)} \approx -\frac{2}{5} \frac{1}{2S} P^L \langle r_L^{-3} \rangle_p c_L^2 n^2 \quad (199)$$

where $A_{\sigma}^{(L;d)}$ and $A_{\pi}^{(L;d)}$ are the values of the ligand HFC along and perpendicular to the metal–ligand bond respectively.

The SOC contribution to the ligand HFC can be estimated from Eqs. (144) and (146). From the form of the ligand contribution, Eq. (196), and the fact that for the ligand HFC the L_3 and F integrals are measured relative to the ligand nucleus it is clear that the contributions are on the order of $n^2 c_L^2 P_L \langle r_L^{-3} \rangle_P \bar{\zeta}_M / \Delta$ where Δ is some average excitation energy. In most cases $\bar{\zeta}_M / \Delta$ is on the order of 0.1 or smaller and this means that the second order contribution to the ligand HFC are at least an order of magnitude smaller than the first order contributions and it is customary to neglect them. Additional evidence for the validity this approximation will be discussed in Section 9.6.8.

Thus, in most cases the ligand HFC will be dominated by the Fermi and dipolar contributions and the ligand HFC tensor will consequently be traceless. This means that the Fermi term can, for example, be measured from fluid solution spectra where the dipolar term averages out, while measurement of the anisotropy requires high-resolution data of frozen solutions or single crystals in order to obtain the desired information.

Finally it is noted that ligands that are not directly coordinated to the metal ion and do not carry significant spin density by themselves will also show small HFCs. These are due to through space dipolar interactions and small residual Fermi contact contributions. These contributions will be briefly discussed in Section 9.6.8 as they form the basis of obtaining geometric information from techniques like ENDOR, ESEEM or NMR.

9.4.8 Table of Hyperfine Parameters

For convenience, we have tabulated the g_N , P , $\langle r^{-3} \rangle$, $P \langle r^{-3} \rangle$ and $|\psi(0)|^2$ values that enter the estimation of HFCs in Table 6. (The calculations were performed with the Hartree–Fock method for the average of the spatial multiplets that have the same spin multiplicity as the ground state multiplet (SAHF method [106]. The Ahlrichs triple-zeta basis set [107] was used for the calculations and is supposed to give results that are reasonably close to the basis set limit (FN, unpublished results).) As a convenient unit to quote the values of HFCs MHz ($= 10^6 \text{ s}^{-1}$) has been chosen. The conversion to cm^{-1} is $1 \text{ cm}^{-1} = 29\,979.24 \text{ MHz}$ and the conversion to eV is $1 \text{ eV} = 2.418\,044\,6 \times 10^8 \text{ MHz}$. Finally, $1 \text{ au} = 6.579\,668\,50 \times 10^9 \text{ MHz}$. It is evident from the table that some of the metal nuclei have sizeable magnetic moments leading to large HFCs on the order of more than 1000 MHz. However, variations of more than two order of magnitudes are observed over the first transition series. This is also partially due to a pronounced increase of the $\langle r^{-3} \rangle$ values over the series which indicates relatively poor shielding of the nuclear charge by the 3d-electrons. For several nuclei more than one isotope is available that differ in their nuclear magnetic moments. This feature can be profitably used to prove the origin of a given set of resonance lines if samples are enriched with only one of the isotopes. As discussed at length in Sections 4.1.3 and 4.1.4, the $\langle r^{-3} \rangle$ values quoted in the table were derived from atomic Hartree–Fock calculations and should be viewed as order of magnitude estimates for several reasons: (a) they have been computed with an approximate physical model, (b) they will vary with the effective nuclear charge (i. e. oxidation

Table 6. Hyperfine parameters for a number of neutral main group atoms (in the ns^2np^x configuration) and the metal atoms of the first transition series (in the $3d^{x-2}4s^2$ configuration). For the ligand atoms the $\langle r^{-3} \rangle$ expectation value over the outermost p-shell is given while for the metals the values refers to the 3d shell.

Isotope	I	NA (%) ^a	g_N	$P \equiv g_e g_N \beta \beta_N$ (MHz au ³) ^b	$\langle r^{-3} \rangle$ (au ⁻³)	$P \langle r^{-3} \rangle$ (MHz)	$\rho^{\alpha-\beta}(0)$ (au ⁻³) ^c	$\frac{4\pi}{3} P \rho^{\alpha-\beta}(0)$ (MHz)
¹ H	$\frac{1}{2}$	99.98	5.5857	533.552	–	–	0.318	711.40
² H	1		0.8574	81.900	–	–	0.318	109.09
⁶ Li	1		0.8221	78.528	–	–	0.170	55.92
⁷ Li	$\frac{3}{3}$		2.1710	207.376	–	–	0.170	147.67
⁹ Be	$\frac{3}{3}$		–0.7850	–74.984	–	–	0.570	–179.03
¹⁰ B	$\frac{3}{3}$	19.8	0.6002	57.332	0.769	44.09	1.410	338.61
¹¹ B	$\frac{3}{3}$	80.2	1.7924	171.212	0.769	131.66	1.410	1011.21
¹³ C	$\frac{1}{2}$	1.11	1.4048	134.188	1.678	225.17	2.770	1556.98
¹⁴ N	1	99.63	0.4038	38.571	3.074	118.57	4.770	770.67
¹⁵ N	$\frac{1}{2}$	0.37	–0.5664	–54.103	3.074	–166.31	4.770	–1081.01
¹⁷ O	$\frac{3}{2}$	0.04	–0.7575	–72.357	4.737	–342.76	7.640	–2315.59
¹⁹ F	$\frac{3}{2}$	100	5.2577	502.22	7.172	3601.93	11.410	24 003.15
²² Na	3	<0.1	0.5820	55.933	–	–	0.530	124.17
²³ Na	$\frac{3}{3}$	100	1.4784	141.218	–	–	0.530	313.51
²⁵ Mg	$\frac{3}{3}$	10.0	–0.3422	–32.687	–	–	1.210	–165.67
²⁷ Al	$\frac{3}{3}$	100	1.4566	139.136	1.092	151.94	2.360	1375.44
²⁹ Si	$\frac{3}{3}$	4.67	–1.1106	–106.086	2.074	220.02	3.810	–1693.06
³¹ P	$\frac{3}{3}$	100.0	2.2632	216.183	3.638	786.48	5.630	5098.22
³³ S	$\frac{3}{3}$	0.75	0.4291	40.988	4.964	203.465	7.950	1364.94
³⁵ Cl	$\frac{3}{3}$	75.77	0.5479	52.336	6.792	355.47	10.640	2332.55
³⁷ Cl	$\frac{3}{3}$	24.23	0.4561	43.567	6.792	295.91	10.640	1941.73
³⁹ K	$\frac{3}{2}$	93.26	0.2610	24.931	–	–	0.740	77.279
⁴¹ K	$\frac{3}{2}$	6.73	0.1433	13.688	–	–	0.740	42.43
⁴³ Ca	$\frac{3}{2}$	0.135	–0.3764	–35.954	–	–	1.380	207.83
⁴⁵ Sc	$\frac{7}{2}$	100.0	1.3591	129.823	1.405	182.40		
⁴⁷ Ti	$\frac{7}{2}$	7.4	–0.3154	–30.127	1.967	–59.26		
⁴⁹ Ti	$\frac{7}{2}$	5.4	–0.3155	–30.137	1.967	–59.28		
⁵⁰ V	6	0.25	0.5566	53.167	2.595	137.97		
⁵¹ V	$\frac{7}{2}$	99.75	1.4684	140.263	2.595	363.98		
⁵³ Cr	$\frac{7}{2}$	9.50	–0.3147	–30.060	3.274	–98.418		
⁵⁵ Mn	$\frac{7}{2}$	100	1.3819	132.001	4.097	540.81		
⁵⁷ Fe	$\frac{7}{2}$	2.15	0.1806	17.251	5.522	95.26		
⁵⁹ Co	$\frac{7}{2}$	100	1.218	116.344	5.841	679.57		
⁶¹ Ni	$\frac{7}{2}$	1.13	–0.5000	–47.760	6.884	328.78		
⁶³ Cu	$\frac{7}{2}$	69.2	1.484	141.753	8.006	1134.88		
⁶⁵ Cu	$\frac{7}{2}$	30.8	1.588	151.688	8.006	1214.41		
⁶⁷ Zn	$\frac{7}{2}$	4.10	0.3503	33.461	9.323	311.96		

Table 6. (continued.)

Isotope	I	NA (%) ^a	g_N	$P \equiv g_e g_N \beta \beta_N$ (MHz au ³) ^b	$\langle r^{-3} \rangle$ (au ⁻³)	$P \langle r^{-3} \rangle$ (MHz)	$\rho^{\alpha-\beta}(0)$ (au ⁻³) ^c	$\frac{4\pi}{3} P \rho^{\alpha-\beta}(0)$ (MHz)
⁶⁹ Ga	3	60.1	1.3444	128.418	2.807	360.47	6.920	3722.38
⁷¹ Ga	3	39.9	1.7082	163.169	2.807	458.02	6.920	4729.69
⁷³ Ge	1	7.8	-0.1954	-18.665	4.692	-87.58	9.540	-745.87
⁷⁵ As	1	100	0.9596	91.662	7.238	633.45	12.430	4772.53
⁷⁷ Se	1	7.6	1.0693	102.141	9.629	983.51	15.720	6725.69
⁷⁹ Br	3	50.69	1.4043	134.140	12.407	1664.28	19.400	10900.56
⁸¹ Br	3	49.31	1.5137	144.590	12.407	1793.93	19.400	11749.75

^a NA = natural abundance

^b $g_e \beta \beta_N$ has been taken as 95.521 MHz au³.

^c From the Hartree–Fock limit functions of Clementi and Rötti [302] as evaluated by Koh and Miller [303].

state) of the atoms and (c) they are influenced by changes in the radial functions of the orbitals that are involved in the bonding. Nevertheless, the parameters listed in Table 6 are useful in order to estimate metal–ligand covalencies from magnetic resonance parameters or to obtain insight into the bonding trends in a series of related compounds.

For the transition metals no value of $\rho^{\alpha-\beta}$ is provided. The partially filled 3d-orbitals have no spin density on their own at the nucleus. The observed HFC arises from a combination of core-polarization and direct 4s-contributions and thus, the tabulated values would be of little use.

9.4.9 Examples of Ligand-field Expressions for Spin Hamiltonian Parameters

In this section we will apply the equations derived above to some standard cases. The goal is not to derive the most general equations possible but instead to develop the information content of the SH parameters of transition metal complexes. We will use α_1 , β_1 , γ_1 , γ_2 and δ_1 for the MO coefficients of the $d_{x^2-y^2}$, d_{xy} , d_{yz} , d_{xz} and d_{z^2} orbitals in the corresponding MOs respectively. The averaged metal SOC constant is denoted as $\bar{\zeta}_M$. According to our discussion of the central field covalency in Section 9.4.1.4 it may be reduced by up to 10–20% from their atomic values (Table 2).

9.4.9.1 d¹ and d⁹ Configurations (S = 1/2)

The d⁹ configuration in a square planar ligand field belongs to the best studied examples of SH parameters. The most common cases are Cu(II) and Ni(I) complexes.

In a square planar ligand field where the ligands are placed along the x - and y -axes respectively, the highest MO among the metal-d-derived orbitals is $d_{x^2-y^2}$. From group theory it is clear that the only contribution to the element g_{zz} arises from the transition $d_{xy} \rightarrow d_{x^2-y^2}$.

9.4.9.1.1 g-Values

Neglecting all ligand terms Eq. (186) becomes:

$$\begin{aligned} g_{zz} &\approx g_e + 2\Delta_{xy \rightarrow x^2-y^2}^{-1} \bar{\zeta}_M \alpha_1^2 \beta_1^2 \langle d_{xy} | l_z^M | d_{x^2-y^2} \rangle \langle d_{x^2-y^2} | l_z^M | d_{xy} \rangle \\ &= g_e + 8\Delta_{xy \rightarrow x^2-y^2}^{-1} \bar{\zeta}_M \alpha_1^2 \beta_1^2 \end{aligned} \quad (200)$$

where use has been made of Table 3 and the positive sign arises because the d_{xy} based MO is doubly occupied in the ground state. $\Delta_{xy \rightarrow x^2-y^2}^{-1}$ is the transition energy for the promotion of an electron from the d_{xy} based MO to the $d_{x^2-y^2}$ based MO. In the same way the contributions to the other diagonal elements of the g-tensor are found to be:

$$g_{xx} \approx g_e + 2\Delta_{yz \rightarrow x^2-y^2}^{-1} \bar{\zeta}_M \alpha_1^2 \gamma_1^2 \quad (201)$$

$$g_{yy} \approx g_e + 2\Delta_{xz \rightarrow x^2-y^2}^{-1} \bar{\zeta}_M \alpha_1^2 \gamma_1^2 \quad (202)$$

9.4.9.1.2 Metal Hyperfine Couplings

The isotropic contribution is by definition (Eq. (195)):

$$A_{iso}^{(M)} = -P_d \kappa \quad (203)$$

For the dipolar contribution to the metal HFC one finds from Table 4 and Eq. (191)

$$A_{zz}^{(M;d)} = -\frac{4}{7} P_d \alpha_1^2 \quad (204)$$

$$A_{xx}^{(M;d)} = A_{yy}^{(M;d)} = \frac{2}{7} P_d \alpha_1^2 \quad (205)$$

For the first part of the second order contribution one has from Eq. (193):

$$A_{zz}^{(M;SO1)} = P_d \Delta g_{zz} \quad (206)$$

$$A_{xx}^{(M;SO1)} = P_d \Delta g_{xx} \quad (207)$$

$$A_{yy}^{(M;SO1)} = P_d \Delta g_{yy} \quad (208)$$

The second part of the second order contribution requires a little more work. Take the $A_{xx}^{(M;SO2)}$ component and consider Eq. (194). The only cases for which the Levi-Civita symbol can be non-zero are $\kappa, \tau = z, y$ for which $\varepsilon_{zyx} = -1$ and $\kappa, \tau = y, z$ for which $\varepsilon_{yzx} = 1$. Since the only singly occupied MO is $\psi_{x^2-y^2}$ we have to find the functions in Table 4 that give a non-zero contribution with $d_{x^2-y^2}$ for f_{xy} or for f_{zx} . For f_{xy} no contribution is found, but for f_{zx} we have $\langle d_{x^2-y^2} | f_{xz} | d_{xz} \rangle = \frac{3}{7}$. In addition

we have from Table 3, $\langle d_{x^2-y^2} | l_y^M | d_{xz} \rangle = +i$. Thus we obtain the contribution:

$$\begin{aligned}
 A_{xx}^{(M-SO_2)} &= -P_d \frac{\bar{\zeta}_M}{\Delta_{xz \rightarrow x^2-y^2}} \underbrace{\alpha_1^2 \gamma_2^2}_{c_{Mi}^2 c_{Mj}^2} \underbrace{(-i)}_{i \varepsilon_{zyx}} \underbrace{\frac{3}{7}}_{\langle d_{xz} | f_{xz} | d_{x^2-y^2} \rangle} \underbrace{+i}_{\langle d_{x^2-y^2} | l_y^M | d_{xz} \rangle} \\
 &= -P_d \frac{3}{7} \frac{\alpha_1^2 \gamma_2^2 \bar{\zeta}_M}{\Delta_{xz \rightarrow x^2-y^2}} \\
 &= -P_d \frac{3}{14} \Delta g_{yy}
 \end{aligned} \tag{209}$$

In the same way the other contributions are obtained. Putting the four contributions to the metal HFC together, we have obtained the well known equations:

$$A_{zz}^{(M)} \approx P_d \left[-\kappa - \frac{4}{7} \alpha_1^2 + \Delta g_{zz} + \frac{3}{14} \Delta g_{xx} + \frac{3}{14} \Delta g_{yy} \right] \tag{210}$$

$$A_{xx}^{(M)} \approx P_d \left[-\kappa + \frac{2}{7} \alpha_1^2 + \Delta g_{xx} - \frac{3}{14} \Delta g_{yy} \right] \tag{211}$$

$$A_{yy}^{(M)} \approx P_d \left[-\kappa + \frac{2}{7} \alpha_1^2 + \Delta g_{yy} - \frac{3}{14} \Delta g_{xx} \right] \tag{212}$$

Together with the corresponding equations for the g-tensor and an educated guess for the “quasi-atomic” values $\bar{\zeta}_M$ and P_d , they can be used to get rough estimates of κ , α_1^2 , β_1^2 , γ_1^2 and γ_2^2 . It is, however, necessary to have accurate optical data available in order to estimate $\Delta_{xy \rightarrow x^2-y^2}$, $\Delta_{xz \rightarrow x^2-y^2}$ and $\Delta_{yz \rightarrow x^2-y^2}$; otherwise the number of unknowns is larger than the number of known quantities (see Section 9.5.1). In this form, these equations have found extremely widespread application. However, they have also been criticized for being too simplistic [96, 97, 99, 108].

A mechanism for the reduction of the HFC in d^9 complexes is the mixing of $4p_z$ character into the $d_{x^2-y^2}$ based SOMO [109]. However, this mechanism has certainly been overused [110] and in many cases the covalency contribution is more important as in the case of blue copper centers in proteins (Section 9.5.1).

9.4.9.1.3 Ligand Hyperfine Couplings

The ligand HFC is approximated by the equations given in Section 9.4.1.7.2. A further discussion is provided in Section 9.6.8.

9.4.9.1.4 Trigonal-bipyramidal Complexes

In this ligand field geometry the d_{z^2} based orbital is highest in energy and singly occupied. The following expressions are found for the g-values and metal HFCs.

$$g_{zz} \approx g_e \tag{213}$$

$$g_{xx} \approx g_e + \frac{6\delta_1^2 \gamma_1^2 \bar{\zeta}_M}{\Delta_{yz \rightarrow z^2}} \tag{214}$$

$$g_{yy} \approx g_e + \frac{6\delta_1^2 \gamma_2^2 \bar{\zeta}_M}{\Delta_{xz \rightarrow z^2}} \tag{215}$$

and:

$$A_{zz}^{(M)} \approx P_d \left[-\kappa + \frac{4}{7}\delta_1^2 - \frac{1}{14}\Delta g_{xx} - \frac{1}{14}\Delta g_{yy} \right] \quad (216)$$

$$A_{xx}^{(M)} \approx P_d \left[-\kappa - \frac{2}{7}\delta_1^2 + \Delta g_{xx} + \frac{1}{14}\Delta g_{yy} \right] \quad (217)$$

$$A_{yy}^{(M)} \approx P_d \left[-\kappa - \frac{2}{7}\delta_1^2 + \Delta g_{yy} + \frac{1}{14}\Delta g_{xx} \right] \quad (218)$$

9.4.9.1.5 d¹ Complexes

The d¹ case is very similar to the d⁹ case with VO²⁺ square pyramidal complexes being typical members of this class. In this case, the d_{xy} based MO is commonly lowest in energy. The expressions found for the g-tensor are formally the same as for the d⁹ configuration with the $d_{x^2-y^2}$ based MO being singly occupied. However, the signs of the g-shifts are reversed because now all relevant ligand field excitations are from the singly occupied MO into empty MOs. Specifically, at the same level of approximation as before:

$$g_{zz} \approx g_e - 8\Delta_{xy \rightarrow x^2-y^2}^{-1} \bar{\zeta}_M \beta_1^2 \alpha_1^2 \quad (219)$$

$$g_{xx} \approx g_e - 2\Delta_{xy \rightarrow yz}^{-1} \bar{\zeta}_M \beta_1^2 \gamma_1^2 \quad (220)$$

$$g_{yy} \approx g_e - 2\Delta_{xy \rightarrow xz}^{-1} \bar{\zeta}_M \beta_1^2 \gamma_2^2 \quad (221)$$

For the metal HFC one finds:

$$A_{zz}^{(M)} \approx P_d \left[-\kappa - \frac{4}{7}\beta_1^2 + \Delta g_{zz} + \frac{3}{14}\Delta g_{xx} + \frac{3}{14}\Delta g_{yy} \right] \quad (222)$$

$$A_{xx}^{(M)} \approx P_d \left[-\kappa + \frac{2}{7}\beta_1^2 + \Delta g_{xx} - \frac{3}{14}\Delta g_{yy} \right] \quad (223)$$

$$A_{yy}^{(M)} \approx P_d \left[-\kappa + \frac{2}{7}\beta_1^2 + \Delta g_{yy} - \frac{3}{14}\Delta g_{xx} \right] \quad (224)$$

Note that despite the formal similarities, there are several differences compared to the d⁹ case – (a) in the d⁹ case the most antibonding MO in the metal d-set is singly occupied and the covalent reduction of the metal HFC is therefore quite pronounced. In the case of the d¹ system it is the least antibonding (i. e. non-bonding) MO in the metal d-set that is singly occupied. Therefore the covalency effects are much smaller here ($\beta_1^2 > \alpha_1^2$), (b) the second order effects on $A_{zz}^{(M)}$ have the same sign as the orbital dipolar contribution because the signs of the g-shifts are negative and (c) as a consequence of the mainly non-bonding nature of the singly occupied MO in the d¹ systems the ligand HFCs will be very small.

9.4.9.1.6 Concluding Remarks

A number of refinements can be made to the ligand field treatment of the SH parameters for d⁹ systems. Perhaps the most important one is to include the ligand terms for the orbital Zeeman term and, for complexes with coordinating sulfur or chlorine ligands, to include the ligand SOC into the equations. These enhancements have been thoroughly discussed in the literature [85, 96, 97, 99, 108] and we will not repeat them here. Furthermore from Eq. (138) it is clear that the doubly occupied ligand based orbitals will also make some contribution. These relevant excited states are to be classified as ligand-to-metal charge (LMCT) transfer states. As will

be further discussed in Section 9.5.1 they may make small but noticeable contributions especially for ligands like thiolates, that form highly covalent bonds and lead to low lying LMCT transitions.

9.4.9.2 High-spin d^8 ($S = 1$)

The most commonly met case is Ni(II) in an distorted octahedral field. In this case the $d_{x^2-y^2}$ and d_{z^2} based MOs are singly occupied and highest in energy while d_{xy} , d_{xz} and d_{yz} are lower in energy and doubly occupied. There are six one-electron promotions from the three doubly filled t_{2g} derived orbitals into the two half-filled e_g derived orbitals. From group theory in octahedral symmetry these give rise to a ${}^3T_{1g}$ and a ${}^3T_{2g}$ state of which only the ${}^3T_{2g}$ contributes to the g-shift as it is the only state that spin-orbit couples with the ${}^3A_{2g}$ ground state. Rather than directly using Eq. (186) we should take the correct linear combinations of the single excitations (compare the discussion in Section 9.3.5.1) to produce the three components of the ${}^3T_{1g}$ state which are:

$$|{}^3T_{2g}^x\rangle = \cos \eta |\psi_{yz} \rightarrow \psi_{x^2-y^2}\rangle + \sin \eta |\psi_{yz} \rightarrow \psi_{z^2}\rangle \quad (225)$$

$$|{}^3T_{2g}^y\rangle = \cos \eta |\psi_{xz} \rightarrow \psi_{x^2-y^2}\rangle - \sin \eta |\psi_{xz} \rightarrow \psi_{z^2}\rangle \quad (226)$$

$$|{}^3T_{2g}^z\rangle = |\psi_{xy} \rightarrow \psi_{x^2-y^2}\rangle \quad (227)$$

where $\eta = \pi/3$. $|\psi_{yz} \rightarrow \psi_{x^2-y^2}\rangle$ is a Slater determinant where a spin-up electron in ψ_{yz} has been replaced by a spin-up electron in $\psi_{x^2-y^2}$. As discussed in Section 9.3.5.1 these linear combination of single excitations should be inserted into Eq. (89) to get an equation closely resembling Eq. (138) except for the presence of the terms that contain η . These equations are then simplified making the usual ligand field approximations, using Table 3 and taking $S = 1$ to get (ligand terms neglected):

$$g_{zz} \approx g_e + \frac{4\alpha_1^2\beta_1^2\bar{\zeta}_M}{\Delta({}^3T_{2g}^z)} \quad (228)$$

$$g_{xx} \approx g_e + \frac{1}{4} \frac{\gamma_1^2\bar{\zeta}_M(\alpha_1 + 3\delta_1)^2}{\Delta({}^3T_{2g}^x)} \quad (229)$$

$$g_{yy} \approx g_e + \frac{1}{4} \frac{\gamma_2^2\bar{\zeta}_M(\alpha_1 + 3\delta_1)^2}{\Delta({}^3T_{2g}^y)} \quad (230)$$

where $\Delta({}^3T_{2g}^{x,y,z})$ are the transition energies to the three components of the possibly low-symmetry split ${}^3T_{2g}$ state. In the case that the covalency is isotropic all energy denominators are equal and $\alpha_1 = \delta_1$ as well as $\beta_1 = \gamma_1 = \gamma_2$. In this case the g-tensor becomes isotropic with a g-value greater than g_e . This is what is usually observed in close to octahedral Ni(II) compounds. For a tetragonal distortion that lowers $d_{xz,yz}$ in energy one would predict $g_{xx,yy} > g_{zz}$ and vice versa for a tetragonal distortion that increases $d_{xz,yz}$ in energy.

At the same level of approximation one finds for the D and E values from the excited states of the same spin:

$$D(^3T_{2g}) = \frac{\bar{\zeta}_M}{4} [g_{zz} - \frac{1}{2}(g_{xx} + g_{yy})] \quad (231)$$

$$E(^3T_{2g}) = \frac{\bar{\zeta}_M}{8} [g_{xx} - g_{yy}] \quad (232)$$

McGarvey reports reasonable agreement between theory and experiment with this approximation [85].

9.4.9.3 d^3 Configuration (High-spin; $S = 3/2$)

The most commonly met cases are Cr(III) and V(II) in distorted octahedral fields. The calculation proceeds in a way that is quite similar to the case of high-spin d^8 in the previous section. In the distorted octahedral case the ground state has the d_{xy} , d_{xz} and d_{yz} orbitals singly occupied which gives rise to a $^4A_{2g}$ ground state. There are again six one-electron promotions that give rise to a $^4T_{1g}$ and a $^4T_{2g}$ state that are different in energy but only the $^4T_{2g}$ state spin-orbit couples with the ground state. The three components of the $^4T_{2g}$ state may be taken as:

$$|^4T_{2g}^x\rangle = \cos \eta |\psi_{yz} \rightarrow \psi_{x^2-y^2}\rangle + \sin \eta |\psi_{yz} \rightarrow \psi_{z^2}\rangle \quad (233)$$

$$|^4T_{2g}^y\rangle = \cos \eta |\psi_{xz} \rightarrow \psi_{x^2-y^2}\rangle - \sin \eta |\psi_{xz} \rightarrow \psi_{z^2}\rangle \quad (234)$$

$$|^4T_{2g}^z\rangle = |\psi_{xy} \rightarrow \psi_{x^2-y^2}\rangle \quad (235)$$

and $\eta = \pi/3$. The g -tensor is found in the same way as in the d^8 case. Here one has to take into account that $S = \frac{3}{2}$ and that all transitions are from half-filled into empty orbitals. The result is:

$$g_{zz} = g_e - \frac{8 \alpha_1^2 \beta_1^2 \bar{\zeta}_M}{3 \Delta(^4T_{2g}^z)} \quad (236)$$

$$g_{xx} = g_e - \frac{1 \gamma_1^2 \bar{\zeta}_M (\alpha_1 + 3\delta_1)^2}{6 \Delta(^4T_{2g}^x)} \quad (237)$$

$$g_{yy} = g_e - \frac{1 \gamma_2^2 \bar{\zeta}_M (\alpha_1 + 3\delta_1)^2}{6 \Delta(^4T_{2g}^y)} \quad (238)$$

Again, for pure octahedral symmetry it is expected to find an isotropic g -tensor but this time with a g -values that is smaller than g_e . These expectations are in agreement with experimental observations.

At the same level of approximation as for the d^8 case the ZFS that results from the $^4T_{2g}$ derived states is:

$$D(^4T_{2g}) = -\frac{\bar{\zeta}_M}{6}[g_{zz} - \frac{1}{2}(g_{xx} + g_{yy})] \quad (239)$$

$$E(^4T_{2g}) = -\frac{\bar{\zeta}_M}{12}[g_{xx} - g_{yy}] \quad (240)$$

For d^3 ions, however, there is an important contribution of spin doublet states to the ZFS. From group theory the only states that can spin-orbit couple with the ground state are states of ${}^2T_{2g}$ symmetry. The lowest ${}^2T_{2g}$ state arises from the t_{2g}^3 configuration and its energy is thus largely independent of the ligand field strength. To estimate the contribution from this term the ${}^2T_{2g}$ components are constructed as:

$$|^2T_{2g}^z(t_{2g}^3)\rangle = \cos \eta |\psi_{xz}\rangle \rightarrow \bar{\psi}_{yz}\rangle + \sin \eta |\psi_{yz}\rangle \rightarrow \bar{\psi}_{xz}\rangle \quad (241)$$

$$|^2T_{2g}^x(t_{2g}^3)\rangle = \cos \eta |\psi_{xy}\rangle \rightarrow \bar{\psi}_{xz}\rangle + \sin \eta |\psi_{xz}\rangle \rightarrow \bar{\psi}_{xy}\rangle \quad (242)$$

$$|^2T_{2g}^y(t_{2g}^3)\rangle = \cos \eta |\psi_{yz}\rangle \rightarrow \bar{\psi}_{xy}\rangle + \sin \eta |\psi_{yz}\rangle \rightarrow \bar{\psi}_{xy}\rangle \quad (243)$$

($\eta = \pi/2$). Insertion of these states into Eq. (77) and making the usual approximation that ligand contributions are negligible one obtains:

$$D(^2T_{2g}(t_{2g}^3)) = -\frac{\bar{\zeta}_M^2}{3} \left[\frac{\gamma_1^2 \gamma_2^2}{\Delta(^2T_{2g}^z)} - \frac{1}{2} \left(\frac{\beta_1^2 \gamma_2^2}{\Delta(^2T_{2g}^x)} + \frac{\gamma_1^2 \beta_1^2}{\Delta(^2T_{2g}^y)} \right) \right] \quad (244)$$

$$E(^2T_{2g}(t_{2g}^3)) = -\frac{\bar{\zeta}_M^2}{6} \left[\frac{\beta_1^2 \gamma_2^2}{\Delta(^2T_{2g}^x)} - \frac{\gamma_1^2 \beta_1^2}{\Delta(^2T_{2g}^y)} \right] \quad (245)$$

The second ${}^2T_{2g}(t_{2g}^2 e_g^1)$ will, of course, also contribute to the ZFS but we will not enter a detailed calculation of this contribution here [111–113].

It is evident that for perfect octahedral symmetry the ZFS vanishes and it is a combination of anisotropic covalency and low-symmetry distortions that make the ZFS non-zero. Consequently, depending on the interplay between these two effects the ZFS can be either positive or negative.

9.4.9.3.1 Hyperfine Couplings

For the t_{2g}^3 configuration the anisotropic HFC vanishes if the covalency is isotropic. Thus the isotropic contribution $A_{iso}^{(M)} = -\frac{1}{3}P_d\kappa$ should be dominant and this is what is commonly observed. In the case of anisotropic covalency one obtains from Eq. (191) for the dipolar part:

$$A_{zz}^{(M;d)} = \frac{1}{3}P_d \left[\frac{2}{7}\gamma_1^2 + \frac{2}{7}\gamma_2^2 - \frac{4}{7}\beta_1^2 \right] \quad (246)$$

$$A_{xx}^{(M;d)} = \frac{1}{3}P_d \left[\frac{2}{7}\gamma_2^2 - \frac{4}{7}\gamma_1^2 + \frac{2}{7}\beta_1^2 \right] \quad (247)$$

$$A_{yy}^{(M;d)} = \frac{1}{3}P_d \left[\frac{2}{7}\gamma_1^2 - \frac{4}{7}\gamma_2^2 + \frac{2}{7}\beta_1^2 \right] \quad (248)$$

9.4.9.4 d⁷ Configuration (Low-spin; S = 1/2)

This case is realized for some complexes of Ni(III). We will consider a tetragonally distorted complex with a weak ligand field along the z -axis. This leaves the $d_{x^2-y^2}$ based MO empty and the d_{z^2} based MO half-filled. The resulting expressions for the magnetic parameters are given by Eqs. (213)–(218) because the $d_{z^2} \rightarrow d_{x^2-y^2}$ transition does not contribute to the g - or A -values in this approximation.

9.4.9.5 d⁴ Configuration (High-spin; S = 2)

High-spin d^4 is often encountered in compounds of Mn(III). We first consider a distorted octahedral complex with a strong ligand field along the z -axis, which will leave a hole in the d_{z^2} orbital. From Eq. (186), taking $S = 2$ and using Table 3 one gets for the three diagonal elements of the g -tensor (ligand terms neglected):

$$g_{zz} = g_e \quad (249)$$

$$g_{xx} \approx g_e - \frac{3\delta_1^2 \gamma_1^2 \bar{\zeta}_M}{\Delta_{yz \rightarrow z^2}} \quad (250)$$

$$g_{yy} \approx g_e - \frac{3\delta_1^2 \gamma_2^2 \bar{\zeta}_M}{\Delta_{xz \rightarrow z^2}} \quad (251)$$

For the alternative case with a strong equatorial ligand field and a hole in the $d_{x^2-y^2}$ orbital, one obtains the analogous equations:

$$g_{zz} \approx g_e - \frac{2\alpha_1^2 \beta_1^2 \bar{\zeta}_M}{\Delta_{xy \rightarrow x^2-y^2}} \quad (252)$$

$$g_{xx} \approx g_e - \frac{1}{2} \frac{\alpha_1^2 \gamma_1^2 \bar{\zeta}_M}{\Delta_{yz \rightarrow x^2-y^2}} \quad (253)$$

$$g_{yy} \approx g_e - \frac{1}{2} \frac{\alpha_1^2 \gamma_2^2 \bar{\zeta}_M}{\Delta_{xz \rightarrow x^2-y^2}} \quad (254)$$

Thus, in both cases g -values smaller than or equal to the free electron g -value are expected which in agreement with observations for Mn(III) and Cr(II) complexes. These complexes have ${}^5T_{2g}$ ground states in the octahedral limit and thus undergo large Jahn–Teller distortions which will frequently leave a hole in the $d_{x^2-y^2}$ based MO.

At the same level of approximation, the contributions of d–d excited states with $S = 2$ to the ZFS follows again from Eq. (189):

$$D \approx -\frac{\bar{\zeta}_M}{8} [g_{zz} - \frac{1}{2}(g_{xx} + g_{yy})] \quad (255)$$

$$E \approx -\frac{\bar{\zeta}_M}{16} [g_{xx} - g_{yy}] \quad (256)$$

It is however, readily appreciated that triplet terms that arise from the octahedral ${}^3T_{1g}$ and ${}^3T_{2g}$ states are likely to make a significant contribution to the ZFS.

9.4.9.6 d⁵ Configuration (High-spin; S = 5/2)

This is the important case which is met for example in Fe(III) and Mn(II). In the case of high-spin d⁵ the metal d-based MOs are all half filled to produce the spin state of $S = \frac{5}{2}$. There can be no ligand field excited state of the same multiplicity. Consequently one expects no deviations of the g-values from the free electron value and this is what is commonly observed. However, although one does also not expect ligand field contributions from excited states of the same spin to the D-tensor, the observed zero-field splittings are often on the order of a few wavenumbers. This indicates that it is important to include the low-lying quartet states in the prediction of ZFSs. We will pursue an approximate calculation described in Ref. [66] (see also Section 9.5.2).

9.4.9.6.1 Zero-field Splittings

Consider first a high spin d⁵ ion in a distorted tetrahedral ligand field. In such a ligand field the orbitals are split into a lower energy e-set ($d_{z^2}, d_{x^2-y^2}$) and a higher-energy t₂ set (d_{xz}, d_{yz}, d_{xy}). In this symmetry (T_d point group) the ground state 6A_1 state can only spin-orbit couple to states of T_1 symmetry. In a distorted tetrahedral molecule the lowest 4T_1 is dominated by the $t \rightarrow e$ excitations that are represented by:

$$|{}^4T_{1z}^a\rangle = |\psi_{xy} \rightarrow \bar{\psi}_{x^2-y^2}\rangle \quad (257a)$$

$$|{}^4T_{1x}^a\rangle = \cos \eta |\psi_{yz} \rightarrow \bar{\psi}_{x^2-y^2}\rangle + \sin \eta |\psi_{yz} \rightarrow \bar{\psi}_{z^2}\rangle \quad (257b)$$

$$|{}^4T_{1y}^a\rangle = \cos \eta |\psi_{xz} \rightarrow \bar{\psi}_{x^2-y^2}\rangle - \sin \eta |\psi_{xz} \rightarrow \bar{\psi}_{z^2}\rangle \quad (257c)$$

once more with $\eta = \pi/3$. Using these states in Eq. (77) together one finds for the ZFS parameter D :

$$D({}^4T_1^a) = \frac{\bar{\zeta}_M^2}{20} \left[\frac{4\alpha_1^2\beta_1^2}{\Delta({}^4T_{1z}^a)} - \frac{1}{8} \left(\frac{\gamma_1^2(\alpha_1\gamma_1 + 3\delta_1)^2}{\Delta({}^4T_{1x}^a)} + \frac{\gamma_2^2(\alpha_1 + 3\delta_1)^2}{\Delta({}^4T_{1y}^a)} \right) \right] \quad (258)$$

where the Δ s in the denominator are the relevant transition energies. In perfectly cubic environments symmetry demands that the energy denominators are equal and also $\gamma_1 = \gamma_2 = \beta_1$ and $\alpha_1 = \delta_1$, i. e. $D({}^4T_1^a) = 0$. Non-zero contributions in lower symmetries can be mainly traced back to two sources, namely distortions that lift the degeneracy of the three quartet states and changes in covalencies of individual MOs that reflect differences in bonding interactions.

Let us initially assume that all MO coefficients are equal to 1 and that the distortion splits the quartet states in a manner consistent with ligand field theory:

$$E({}^4T_{1z}^a) = E_0^{(a)} + \frac{1}{2}\Delta_e + \frac{1}{2}\Delta_{t_2} \quad (259a)$$

$$E({}^4T_{1x,y}^a) = E_0^{(a)} - \frac{1}{4}\Delta_e - \frac{1}{2}\Delta_{t_2} \quad (259b)$$

Here Δ_e is positive if $\psi_{x^2-y^2}$ is above ψ_{z^2} , Δ_{t_2} is positive if $\psi_{xz,yz}$ are above ψ_{xy} and $E_0^{(a)} = E({}^4T_1^a)_{T_d}$. Using the series $(a+b)^{-1} = \sum_i (-1)^i b^i a^{-i-1}$ which converges rapidly for $b \ll a$ one arrives at a contribution to D from this mechanism that is

given by:

$$D(^4T_1^a)_{\text{dist}} \simeq -\frac{1}{5} \left(\frac{\bar{\zeta}_M}{E_0^{(a)}} \right)^2 \left[\Delta_e + \frac{3}{4} \Delta_{t_2} - \frac{1}{4} \Delta_e \Delta_{t_2} / E_0^{(a)} \right] \quad (260)$$

Thus, if Δ_e is small this approximation, which is essentially the same as Griffith's [114], suggests that D should be positive if $\psi_{xz,yz}$ is below ψ_{xy} (flattened tetrahedron) and negative if $\psi_{xz,yz}$ is above ψ_{xy} (compressed tetrahedron).

To see the effect of covalency one might assume $\delta_1 = \alpha_1$ and $\gamma_1 = \gamma_2 = \gamma$. Equation (260) is then modified to:

$$D(^4T_1^a)_{\text{cov}} \simeq \frac{1}{5} \frac{\bar{\zeta}_M^2}{E_0^{(a)}} \alpha_1^2 \left[\beta_1^2 \left(1 - \frac{1}{2} x_e - \frac{1}{2} x_{t_2} + \frac{1}{2} x_e x_{t_2} \right) - \gamma^2 \left(1 + \frac{1}{2} x_e + \frac{1}{4} x_{t_2} + \frac{1}{4} x_e x_{t_2} \right) \right] \quad (261)$$

where $x_e = \Delta_e / E_0^{(a)}$ and $x_{t_2} = \Delta_{t_2} / E_0^{(a)}$. For the typical case of negative x_{t_2} and small x_e one can also expect $\beta_1^2 < \gamma^2$ and therefore in this case the effect of covalency on the ZFS is negative while the distortion gives a positive contribution.

This situation changes for the higher lying 4T_1 states. $^4T_1^c$ is mainly composed of the $e \rightarrow t$ excitations that give rise to states with analogous determinantal descriptions. The only difference is that now Δ_e and Δ_{t_2} change sign because the one electron energy is increased in the excited state. Therefore the contribution from $^4T_1^c$ is:

$$D(^4T_1^c)_{\text{cov}} \simeq \frac{1}{5} \frac{\bar{\zeta}_M^2}{E_0^{(b)}} \alpha_1^2 \left[\beta_1^2 \left(1 + \frac{1}{2} x'_e + \frac{1}{2} x'_{t_2} + \frac{1}{2} x'_e x'_{t_2} \right) - \gamma^2 \left(1 - \frac{1}{2} x'_e - \frac{1}{4} x'_{t_2} + \frac{1}{4} x'_e x'_{t_2} \right) \right] \quad (262)$$

where $x'_e = \Delta_e / E_0^{(a)}$ and $x'_{t_2} = \Delta_{t_2} / E_0^{(c)}$. It is important to note that for $^4T_1^c$ the covalency and distortion contributions work in the *same* direction, i. e. for negative x'_{t_2} , small x'_e and $\beta_1^2 < \gamma^2$ the effects of both covalency and distortion are negative. Thus, although $^4T_1^c$ is typically $> 10\,000 \text{ cm}^{-1}$ higher in energy than $^4T_1^a$, it is likely to make a significant contribution to the ZFS.

The third 4T_1 state, $^4T_1^b$, is dominated by the spin flip transitions within the t_2 -set. It does not split to first order with a geometric distortion but has a small contribution to the ZFS arising from anisotropic covalency:

$$D(^4T_1^b) = \frac{1}{10} \bar{\zeta}_M^2 \gamma^2 \left[\frac{\gamma^2}{E(^4T_{1z}^b)} - \frac{\beta_1^2}{E(^4T_{1x,y}^b)} \right] \quad (263)$$

The case of octahedral sites is slightly more complicated because the anisotropic covalency pattern will differ from the tetrahedral case. Here it may be assumed that

$\gamma_1 = \gamma_2 = \beta_1 = \gamma$. Instead of Eq. (261) the contribution from ${}^4T_1^a$ is now given by:

$$D({}^4T_1^a) = \frac{3}{80} \frac{\zeta_M^2}{E_0} \gamma^2 [(\alpha_1 - \delta_1)(5\alpha_1 + 3\delta_1) + \alpha_1^2 (\frac{17}{6}x_{t_{2g}} + \frac{11}{4}x_{e_g} + \frac{31}{12}x_{t_{2g}}x_{e_g}) + \delta_1^2 (\frac{3}{2}x_{t_{2g}} + \frac{3}{4}x_{e_g} - \frac{3}{4}x_{t_{2g}}x_{e_g}) + \alpha_1\delta_1(x_{t_{2g}} + \frac{1}{2}x_{e_g} - \frac{1}{2}x_{t_{2g}}x_{e_g})] \quad (264)$$

Again, for the typical case of small $x_{t_{2g}}$, positive x_{e_g} and $\alpha_1^2 < \delta_1^2$ one has a negative contribution to the D-value from anisotropic covalency and a positive from the low symmetry distortion. The contribution from ${}^4T_1^c$ is given by the same equation with the signs of $x_{t_{2g}}$ and x_{e_g} reversed.

In addition to the contributions described here there will be additional contributions that arise from the ${}^6\Gamma$ charge-transfer excited state that are not present in a ligand field treatment but that nevertheless give important contributions that will be described in Section 9.5.2.

9.4.9.6.2 g-Values

For the high-spin d^5 configuration there are no ligand field excited states of the same total spin as the ground state. Consequently in this approximation the deviations of the g-values from the value of the free-electron are negligible. If there are ligands present that give rise to low lying charge transfer state small deviations from the free-electron g-value may arise.

9.4.9.6.3 Hyperfine Couplings

For the metal HFC are rather similar situation exists. If the covalency is isotropic it is readily appreciated from Table 4 and Eq. (191) that the dipolar part of the metal HFC equals zero. Likewise the SOC contribution to the metal HFC is zero because the deviations of the g-values from the free-electron g-value are zero. Therefore one is left with the isotropic part that is given $A_{iso}^{(M)} = -\frac{1}{5}P_d\kappa$. If the covalency is not isotropic one will have small dipolar contributions to the metal HFC that are given by:

$$A_{zz}^{(M;d)} = \frac{1}{35}P_d \sum_i 4\delta_1^2 + 2\gamma_1^2 + 2\gamma_2^2 - 4\alpha_1^2 - 4\beta_1^2 \quad (265)$$

$$A_{xx}^{(M;d)} = \frac{1}{35}P_d \sum_i -2\delta_1^2 + 2\gamma_2^2 - 4\gamma_1^2 + 2\alpha_1^2 + 2\beta_1^2 \quad (266)$$

$$A_{yy}^{(M;d)} = \frac{1}{35}P_d \sum_i -2\delta_1^2 - 4\gamma_2^2 + 2\gamma_1^2 + 2\alpha_1^2 + 2\beta_1^2 \quad (267)$$

9.4.9.7 d^5 Configuration (Low-spin; $S = 1/2$)

The low-spin d^5 configuration with $S = \frac{1}{2}$ has received much attention because it occurs very frequently in Fe(III) porphyrins and many other complexes of Fe(III) or Ru(III). The theory is not quite standard because in an octahedral ligand field the

ground term is ${}^2T_{2g}$ which is orbitally triply degenerate. The corresponding electronic configuration is t_{2g}^5 which has altogether five electrons in the d_{xy} , d_{xz} and d_{yz} based MOs. In the case of (near) orbital degeneracy the standard perturbation theory is not valid and special techniques have to be used.

We will first look at the situation of a significantly distorted octahedron, where the low-symmetry splittings are so large that they become significantly larger than the one-electron SOC constant of the metal which is $\approx 400 \text{ cm}^{-1}$ in the case of Fe(III) after making a reasonable covalent reduction. This situation is met in a number of low symmetry environments such as present in heme or certain non-heme enzyme active sites [115]. The general features of the g-tensor of such sites can, in fact, be understood from perturbation theory. Initially only the three components of the ${}^2T_{2g}$ ground state are taken into account. If the situation is such that the distortion leaves the d_{yz} orbital singly occupied the expressions for the g-tensor from Eq. (186) become:

$$\Delta g_{zz}({}^2T_{2g}) \approx \frac{2\bar{\zeta}_M \gamma_1^2 \gamma_2^2}{\Delta_{xz \rightarrow yz}} \quad (268)$$

$$\Delta g_{xx}({}^2T_{2g}) \approx \frac{2\bar{\zeta}_M \gamma_1^2 \beta_1^2}{\Delta_{xy \rightarrow yz}} \quad (269)$$

$$\Delta g_{yy}({}^2T_{2g}) \approx 0 \quad (270)$$

In the alternative case of the d_{xy} -based MO being singly occupied in the ground state one finds:

$$\Delta g_{zz}({}^2T_{2g}) \approx 0 \quad (271)$$

$$\Delta g_{xx}({}^2T_{2g}) \approx \frac{2\bar{\zeta}_M \beta_1^2 \gamma_2^2}{\Delta_{xz \rightarrow xy}} \quad (272)$$

$$\Delta g_{yy}({}^2T_{2g}) \approx \frac{2\bar{\zeta}_M \beta_1^2 \gamma_1^2}{\Delta_{yz \rightarrow xy}} \quad (273)$$

and thus, it differs mainly by the orientation of the g-tensor in the molecular frame. In this approximation there are two g-values larger than the free electron g-value and one g-value equal to it. This is not what is actually observed because there will usually be one g-value that is significantly smaller than the free electron g-value. This is, in part, due to higher order terms that become important when the energy denominators become small [84, 116]. However, the second reason for g_{\min} values smaller than g_e are the $t_{2g} \rightarrow e_g$ excitations. These excitations may occur at energies between 15000 and 30000 cm^{-1} and are thus low enough in energy to make significant contributions to the g-shift. As explained in detail elsewhere, there is a rather large number of many electron states that arise from the $t_{2g} \rightarrow e_g$ excitations [116]. In an order-of-magnitude treatment one may, however, look at the one-electron excitations only. Since the excitations are from the singly occupied MO into an empty MO, the contributions to the g-shift are negative and are given by:

$$\Delta g_{xx}(^2E_g) \approx -\frac{2\bar{\zeta}_M \gamma_1^2 \alpha_1^2}{\Delta_{yz \rightarrow xy}} - \frac{6\bar{\zeta}_M \gamma_1^2 \delta_1^2}{\Delta_{yz \rightarrow z^2}} \quad (274)$$

when the d_{yz} based MO is singly occupied in the ground state and:

$$\Delta g_{zz}(^2E_g) \approx -\frac{8\bar{\zeta}_M \beta_1^2 \alpha_1^2}{\Delta_{xy \rightarrow x^2-y^2}} \quad (275)$$

when the d_{xy} based MO is singly occupied in the ground state.

In the case that the perturbation expressions diverge or are too inaccurate, one has to first remove the degeneracies by diagonalizing the matrix of the SOC operator in the basis of the low-symmetry $^2T_{2g}$ components. In a second step the resulting states may be perturbed to second order by the higher d-d excitations and finally, in a third step the g-tensor is obtained by using the Zeeman operator in the basis of the lowest Kramers doublet found from the diagonalization. The procedure is rather straightforward although the second step is omitted in almost all treatments. The crystal field equations have first been worked out by Griffith [90, 117]. His model has then undergone some minor modifications [118–122] with the most commonly used one being due to Taylor [121]. We will briefly describe the Griffith–Taylor model.

Consider a situation where the one-electron SOC constant is averaged for the three t_{2g} derived MOs. The main effects of SOC are obtained by diagonalizing the BO plus SOC Hamiltonian in the basis of the six components of the low symmetry split $^2T_{2g}$ term. The component where the d_{xy} derived MO is singly occupied with a spin-up electron is written:

$$|^2T_{2g}; xy\rangle = |\psi_{xz}\bar{\psi}_{xz}\psi_{yz}\bar{\psi}_{yz}\psi_{xy}| \quad (276)$$

and corresponding notations for the other five states. The matrix of the BO plus SOC Hamiltonian is then found to be factored into two identical 3×3 submatrices (as required from time reversal symmetry) which read:

$$\begin{array}{ccc} & |^2T_{2g}; yz\rangle & |^2T_{2g}; xz\rangle & |^2T_{2g}; \bar{xy}\rangle \\ \begin{array}{l} \langle ^2T_{2g}; yz| \\ \langle ^2T_{2g}; xz| \\ \langle ^2T_{2g}; \bar{xy}| \end{array} & \left(\begin{array}{ccc} 0 & -\frac{i}{2}\bar{\zeta}_{\text{eff}} & \frac{1}{2}\bar{\zeta}_{\text{eff}} \\ \frac{i}{2}\bar{\zeta}_{\text{eff}} & -A & -\frac{i}{2}\bar{\zeta}_{\text{eff}} \\ \frac{1}{2}\bar{\zeta}_{\text{eff}} & \frac{i}{2}\bar{\zeta}_{\text{eff}} & -B \end{array} \right) & \end{array} \quad (277)$$

Where the diagonal elements contain ligand field parameters that describe the low-symmetry splitting of the three spatial components.

$$A = V \quad (278)$$

$$B = \Delta + \frac{1}{2}V \quad (279)$$

where Δ describes a tetragonal splitting and V a rhombic ligand field splitting. Diagonalization of the Hamiltonian matrix yields three pairs of degenerate states (Kramers doublets). The lowest Kramers doublet in Taylors notation is written

as:

$$|+\rangle = a|^2T_{2g}; yz\rangle - ib|^2T_{2g}; xz\rangle - c|^2T_{2g}; \overline{xy}\rangle \quad (280)$$

$$|-\rangle = -a|^2T_{2g}; \overline{yz}\rangle - ib|^2T_{2g}; \overline{xz}\rangle - c|^2T_{2g}; xy\rangle \quad (281)$$

where a , b and c are the components of the lowest eigenvector and the signs and phases have been chosen by Taylor for convenience. Application of the Zeeman operator within this Kramers doublet, which amounts to first order perturbation theory, and comparison to the matrix of the SH then yields the g -values as [121]:

$$g_{zz} = 2[(a + b)^2 - c^2] \quad (282)$$

$$g_{xx} = 2[a^2 - (b + c)^2] \quad (283)$$

$$g_{yy} = 2[(a + c)^2 - b^2] \quad (284)$$

A useful feature of the model is that the ligand field parameters can be extracted from the measured g -values in units of the SOC constant as [121]:

$$\frac{A}{\zeta_{\text{eff}}} = \frac{g_{xx}}{g_{yy} + g_{zz}} + \frac{g_{yy}}{g_{zz} - g_{xx}} \quad (285)$$

$$\frac{B}{\zeta_{\text{eff}}} = \frac{g_{xx}}{g_{zz} + g_{yy}} + \frac{g_{zz}}{g_{yy} - g_{xx}} \quad (286)$$

In this form the model has been found extremely widespread application and many empirical relationships are known [122, 123] that relate the ligand field parameters to specific ligation patterns. A useful prediction of the model is that $g_{xx}^2 + g_{yy}^2 + g_{zz}^2 \leq 16$ [90] and this has sometimes been used to estimate a lower limit for the g_{min} value which is helpful for quantification purposes [124]. A drawback of the model is that it leaves the signs of the g -values in doubt and this has led to much discussion in the literature about the correct assignment of magnetic axes for low-spin d^5 systems (a discussion is available elsewhere [125]).

9.5 Case Studies of SH Parameters

From the ligand field expressions given in Section 9.4.1.8, the spin Hamiltonian parameters are underdetermined depending on both the energies of excited states and on the covalencies of the different d orbitals. Electronic spectroscopy (polarized single crystal absorption, magnetic circular dichroism (MCD), and X-ray absorption (XAS) combined with their selection rules) allows the relevant excited states to be assigned and their energies determined from experiment. Thus a combination of ground and excited state data gives a direct probe of the covalency of the valence orbitals allowing experimental evaluations of electronic structure calculations and insight into physical properties and reactivity. $S = 1/2$ (g and A values) and $S = 5/2$ (zero field splitting) examples are developed below.

9.5.1 CuCl_4^{2-} and the Blue Active Site: g and A^M Values

9.5.1.1 g Values

Square planar cupric chloride is one of the most well studied molecules in physical-inorganic chemistry [126]. It has been spectroscopically studied over ten orders of magnitude in photon energy and treated by the complete range of electronic structure methods. Its g values are $g_{\parallel} = 2.220$, $g_{\perp} = 2.041$. From the ligand field expressions (Eqs. 200–202) these are dependent on the energies of the ligand field transitions to the $d_{xy} \rightarrow d_{x^2-y^2}$ and $d_{xz}, d_{yz} \rightarrow d_{x^2-y^2}$ excited states, respectively, and the covalencies of the different d orbitals in the CuCl_4^{2-} environment (α_1^2 for $d_{x^2-y^2}$, β_1^2 for γ_1^2, γ_2^2 for d_{xz}, d_{yz}). The relevant ligand field excited state energies can be obtained from polarized single crystal electronic absorption spectroscopy. From Fig. 4, the band at $12\,500\text{ cm}^{-1}$ is forbidden in z polarization. Vibronic selection rules for a square planar system show that this must be the $d_{xy} \rightarrow d_{x^2-y^2}$ transition [126–128] which gives the energy denominator in Eq. (200). The transition centered at $\sim 14\,200\text{ cm}^{-1}$ is split in x and y polarizations. This must be a transition to the doubly degenerate excited state, $d_{xz}, d_{yz} \rightarrow d_{x^2-y^2}$, that splits in energy due to the low site symmetry of the cupric chloride complex in the crystal lattice. These transitions give the energy denominators in Eqs. (201) and (202).

Using these experimental energy denominators and assuming pure d orbitals, the ligand field expressions give the calculated g values in the second column of Table 7.

These deviate too much from the spin angular momentum value of 2.0023 relative to experiment indicating that there is too much orbital angular momentum in the ground state. Covalency decreases this by delocalizing the metal d electron density onto p hybrid orbitals of the ligands. This corresponds to $\alpha_1^2, \beta_1^2, \gamma_1^2, \gamma_2^2 < 1$ in Eqs. (200)–(202). Since there are still four unknowns required for three experimental g values, these are best estimated from molecular orbital theory and used to evaluate the calculations. This was addressed in the mid eighties using the simplest density functional method, $X\alpha$ -scattered wave developed by Slater and Johnson

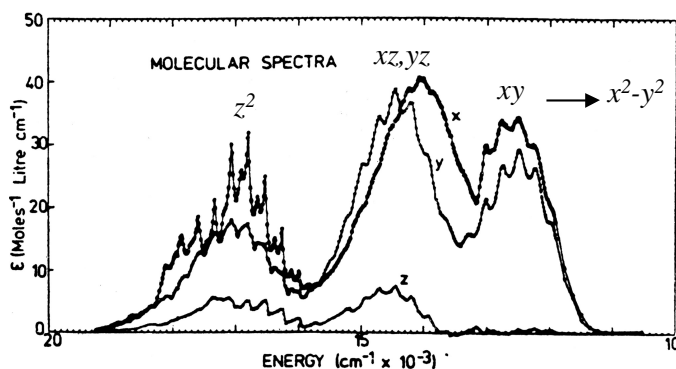


Fig. 4. Polarized absorption spectra of the ligand field region for a single crystal of D_{4h} - CuCl_4^{2-} at 10 K.

Table 7. Experimental and calculated g-values of $D_{4h}^- \text{CuCl}_4^{2-}$.

	Exp	LFT	X α -SW	X α Adjusted
g_{\parallel}	2.220	2.531	2.144	2.220
g_{\perp}	2.041	2.117	2.034	2.041

[129, 130]. From the third column in Table 7, the g values calculated (using more complete expressions than Eqs. (200)–(202) which include ligand orbital angular momentum, ligand centered spin–orbit coupling, and charge transfer contributions to the g values) were reduced relative to the ligand field calculated values due to covalency. However, they are closer to 2.0023 than the experimental values indicating that these calculations give too covalent a description of the ground state. There is a set of parameters in these calculations, the sphere sizes used in the scattered wave solutions, which could then be adjusted until there was agreement between the calculated and experimental g values. This then gives an experimentally calibrated description of the ground state of D_{4h} - CuCl_4^{2-} , Fig. 5A, which has 61% copper $d_{x^2-y^2}$ character in the SOMO with the rest of the wave function equivalently distributed over the 3p orbitals of the four chloride ligands that are involved in σ -antibonding interactions with the metal [131]. This description is supported by a wide range of experiments and has been recently used to evaluate and improve modern DFT methods [132].

The blue copper active site, which has a Cu(II) in a distorted tetrahedral geometry with a short thiolate ligand, has played a central role in bioinorganic chemistry due to its unique spectroscopic features (*vide infra*). It is involved in long-range electron transfer (ET) and its unique spectroscopic features reflect a novel electronic structure that activates the ground state for rapid directional ET [133–138]. The experimental g values of the blue copper site in plastocyanin are given in Table 8 [139,140].

The unique absorption features of the blue copper site (intense absorption band at ~ 600 nm in Fig. 6A) make assignment of the ligand field transitions inaccessible

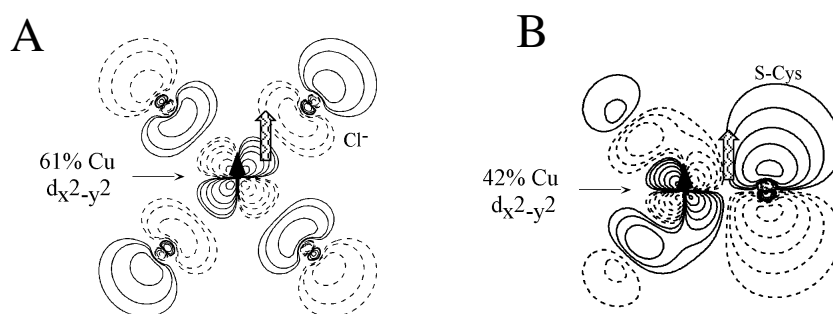


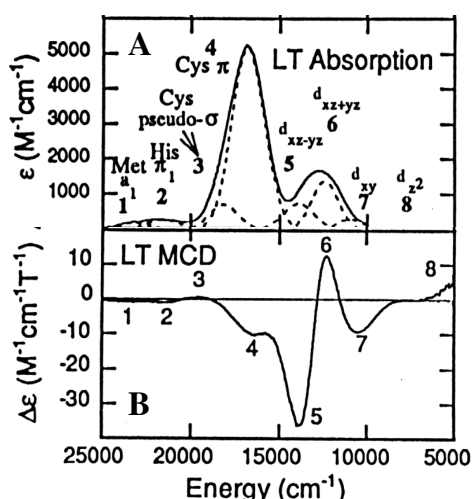
Fig. 5. Contour plots of ground state wavefunctions generated from SCF-X α -SW calculations of A) CuCl_4^{2-} and B) plastocyanin, the latter showing significantly more covalency involving the Cys-thiolate sulfur.

Table 8. g-Value analysis for the blue copper active site.

	Exp	LFT	X α -SW	X α Adjusted
g_{\parallel}	2.226	2.615	2.159	2.226
g_{\perp}	2.053	2.124	2.056	2.067

using only polarized crystal absorption methods. However, low temperature MCD spectroscopy allowed assignment of the ligand field excited states [141].

From Fig. 6B, bands 5–8 in the low temperature MCD spectrum are intense, while they are weak in absorption. Low temperature MCD intensity involves a C-term mechanism requiring two perpendicular transition moments [142, 143]. Since in a low symmetry protein active site environment all states are non-degenerate, all transitions to excited states must be unidirectional. Thus C-term MCD intensity requires SOC between these excited states which have different polarization directions. Since the SOC constant for Cu(II) ($\zeta \sim 830 \text{ cm}^{-1}$) is much larger than for the ligands (ζ (O, N) $\sim 70 \text{ cm}^{-1}$, ζ (S) $\sim 325 \text{ cm}^{-1}$) the C-term intensity is dominated by d character in the excited states. Therefore d \rightarrow d transitions are intense in the low temperature MCD relative to absorption spectrum (i. e. high C/D ratios). From the signs and magnitudes of the C/D ratios, the excited states can be assigned as indicated in Fig. 6. This gives the $d_{xy} \rightarrow d_{x^2-y^2}$ excited state at 10800 cm^{-1} and the average energy of the $d_{xz,yz} \rightarrow d_{x^2-y^2}$ transitions at 13375 cm^{-1} . Using these in Eqs. (200)–(202) gives the non-covalent ligand field calculated g values in the second column of Table 8 which again are too large relative to experiment. Allowing for covalency using X α -scattered wave DFT and adjusting the calculations to fit the experimental g values as described above, gives the ground state description of the blue copper site in Fig. 5B. This is very covalent with only 42% Cu $d_{x^2-y^2}$ character in the SOMO and the covalency is highly anisotropic with 36% delocalization

**Fig. 6.** Low temperature absorption (upper) and low temperature MCD (lower) spectra of plastocyanin with transition assignments.

into the sulfur 3p π orbital of the thiolate ligand. This activates protein pathways involving this ligand for rapid directional long-range electron transfer.

9.5.1.2 A^M Values

The A^M values of square planar CuCl_4^{2-} are $A_{\parallel} = -164 \times 10^{-4} \text{ cm}^{-1}$ and $A_{\perp} = -35 \times 10^{-4} \text{ cm}^{-1}$. Note that while only their magnitude is obtained from a standard powder pattern EPR spectrum, their sign can be determined from off-axis single crystal and circularly polarized EPR data [144]. The ligand field expressions for these A^M values are given by Eqs. (210)–(212). Inserting the experimental g values (*vide supra*), κ (Cu(II)) = 0.43, $\text{Pd}(\text{Cu(II)}) = 400 \times 10^{-4} \text{ cm}^{-1}$ and initially assuming the ionic limit ($\alpha_1^2 = 1$) gives individual ligand field contributions to the A^M values listed in the top two rows of Table 9.

These sum to give too large a magnitude for the hyperfine coupling of the electron spin to the nuclear spin of the copper. Covalency reduces this coupling by delocalizing the electron spin onto the four chloride ligands. Using the ground state wave function from the $X\alpha$ -scattered wave calculations adjusted to the g values to describe this covalency, Fig. 5A, gives the individual contributions to the A^M values listed in the bottom two rows of Table 9. Covalency reduces the spin dipolar term since α_1^2 in Eqs. (210)–(212) is 0.61. While the experimental g values have covalency effects included, they must be modified as the ligand orbital angular momentum contributes to these g values but not the A values since the latter are more localized on the copper (Section 9.4). κ is also reduced by covalency; while in some treatments this term is included as $\kappa\alpha_1$ [2], the dependence on covalency is more complex, not easily calculated by DFT and best obtained from a fit to experimental EPR data [145]. Table 9 bottom gives the best available estimates for the individual contributions to A^M ; all are of similar magnitude, Fermi contact and spin dipolar both have negative contributions to A_{\parallel} , and the orbital dipolar term is of opposite sign.

As shown in Fig. 7, upon going from D_{4h} - CuCl_4^{2-} to the blue copper active site the A_{\parallel} value greatly decreases.

This was originally attributed to Cu $4p_z$ mixing into the $d_{x^2-y^2}$ orbital due to the distorted tetrahedral site symmetry [110]. The idea as sketched in Fig. 8 is that the spin dipolar interaction of the electron with the nuclear spin on the copper averaged over the Cu p_z orbital is of opposite sign and would reduce the spin dipolar interaction of the electron averaged over the $d_{x^2-y^2}$ orbital with the copper nucleus [109].

Table 9. A^M Values of $D_{4h}^- \text{CuCl}_4^{2-}$ ($\times 10^{-4} \text{ cm}^{-1}$).

		A^{iso}	A^{dip}	A^{SO}	Total	Exp
LFT	A_{\parallel}	-172	-229	+95	-306	-164
	A_{\perp}	-172	+114	+13	-4	-35
$X\alpha$	A_{\parallel}	-123	-155	+114	-164	-164
Adjusted	A_{\perp}	-123	+78	+17	-28	-35

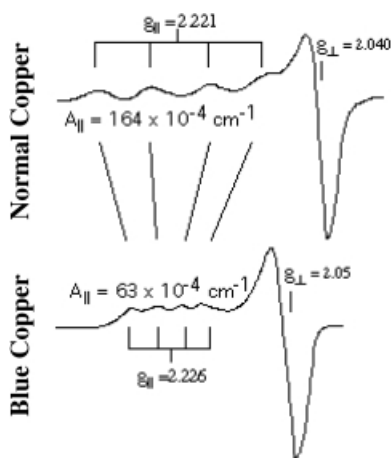


Fig. 7. EPR spectra of normal copper, CuCl_4^{2-} (upper) and the blue (Type I) copper center in plastocyanin (lower) which shows the characteristic extremely small parallel hyperfine splitting.

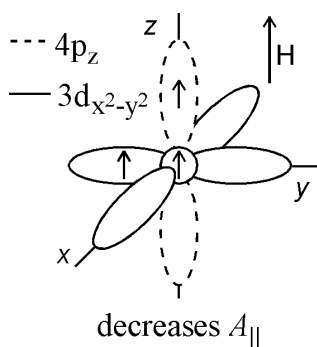


Fig. 8. Spin dipolar contribution to the parallel hyperfine coupling of the nuclear spin on the copper to an electron in a $4p_z$ relative to one in a $3d_{x^2-y^2}$ orbital.

This could be evaluated by polarized single crystal X-ray absorption spectroscopy at the Cu K-edge [146]. This involves the $1s \rightarrow 3d$ transition at 8979 eV which is only quadrupole allowed but gains electric dipole absorption intensity through Cu 4p mixing into the $d_{x^2-y^2}$ orbital due to the distorted tetrahedral site symmetry. From Fig. 9 this behavior clearly is observed in the orientation averaged edges, as the intensity at 8979 eV is much larger for blue copper relative to square planar CuCl_4^{2-} which has a center of inversion and thus no Cu 4p mixing. The nature of the 4p mixing could be determined from single crystal XAS. Polarized absorption data taken along the molecular z axis (determined by single crystal EPR) shows no 8979 eV intensity indicating no $4p_z$ mixing, while all the 8979 eV intensity is observed when the crystal is oriented such that the E vector of light is in the x,y plane. Thus Cu $4p_{x,y}$ mixes with the $d_{x^2-y^2}$ orbital and this would increase not decrease A_{\parallel} [146].

Thus polarized single crystal XAS data experimentally evaluated this generally accepted model for small parallel hyperfine in distorted copper complexes [146]. Elimination of this model allowed us to focus on the alternative explanation of the highly covalent site reducing the electron spin coupling to the Cu nuclear spin by delocalization onto the ligands. Using the ground state wave function from $X\alpha$ -

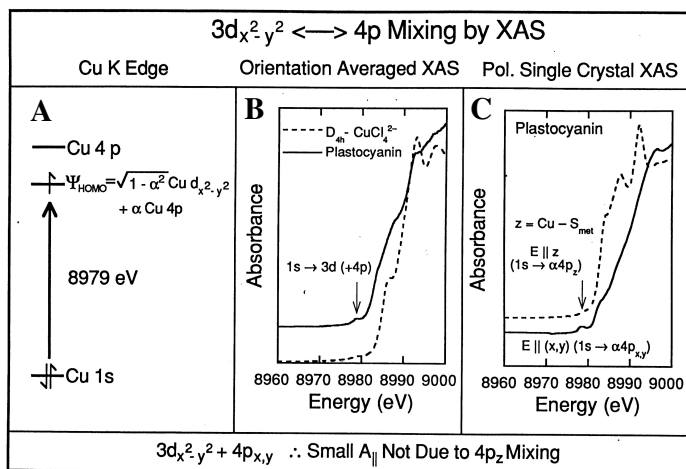


Fig. 9. XAS determination of 4p mixing into 3d orbital with Cu pre-K edge at 8979 eV. A) Energy level diagram for the Cu pre-edge. B) Orientation averaged XAS spectra of D_{4h} - CuCl_4^{2-} and the blue copper site in plastocyanin. C) Polarized single crystal XAS edge spectra of the blue copper site in plastocyanin.

scattered wave calculations adjusted to the g values in Fig. 5B gives the individual contributions to the hyperfine coupling of the blue copper site listed in Table 10. Both the Fermi contact and spin dipolar terms are greatly reduced relative to square planar CuCl_4^{2-} in Table 9 by the highly covalent nature of the blue copper active site ground state wavefunction. The functional significance of this covalency is described above.

Table 10. A^M Values of the blue copper active ($\times 10^{-4} \text{ cm}^{-1}$).

	A^{iso}	A^{dip}	A^{SO}	Total	Exp
A_{\parallel}	-79	-90	+106	-65	[63]
A_{\perp}	-79	+45	+18	-15	< [17]

9.5.2 FeCl_4^- and the $\text{Fe}(\text{SR})_4^-$ Active Site: Zero-field Splitting (ZFS)

From ligand field theory, to a first approximation the ZFS of the 6A_1 ground state of high spin d^5 complexes derives from second order spin-orbit coupling with a low lying ${}^4T_1^a$ state which is split in energy due to the axial distortion of the ligand environment around the iron (Section 9.4.1.9.6). This is often referred to as the Griffith model and is described by Eq. (287) which derives from Eq. (258) setting the coefficients of the orbitals to 1.0 for the ionic limit.

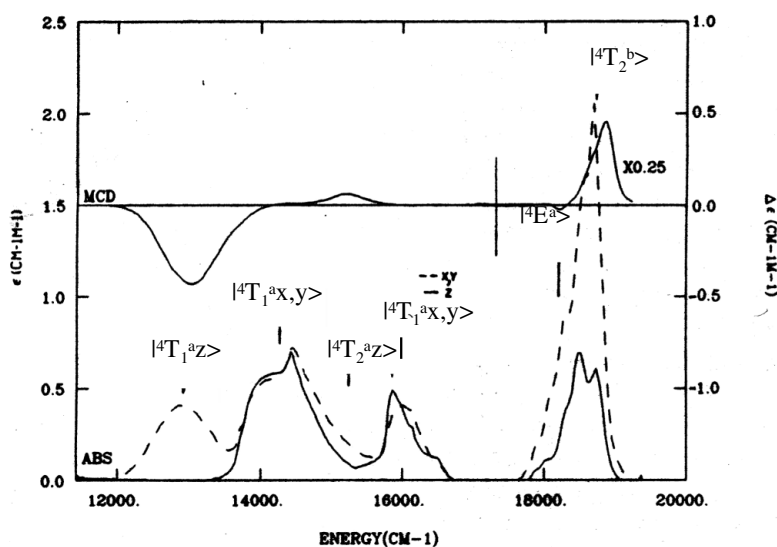


Fig. 10. Polarized single crystal absorption and MCD spectra of $[\text{FeCl}_4][\text{PPh}_4]$.

$$D = \frac{\zeta^2}{5} \left[\frac{1}{\Delta(^4T_{1z}^a)} - \frac{1}{\Delta(^4T_{1x,y}^a)} \right] \quad (287)$$

To test this model experimentally, the energies of the ${}^4T_1^a$ axial components are needed. This has been accomplished for the $D_{2d}\text{-FeCl}_4^-$ and $S_4\text{-Fe}(\text{SR})_4^-$ complexes using polarized single crystal electronic absorption and magnetic circular dichroism spectroscopies [147, 148]. For $D_{2d}\text{-FeCl}_4^-$ in Fig. 10, the energies of ${}^4T_{1z}^a$ and ${}^4T_{1x,y}^a$ are 12890 and 14240 cm^{-1} respectively.

The energy order is as predicted by Eq. (258) with the d_{xy} above the d_{xz}, d_{yz} which is appropriate for a flattened tetrahedral structure with the chlorides moved into the xy plane by 5.1° . Using these energies in Eq. (287) with $\zeta_{\text{Fe(III)}} = 430\text{ cm}^{-1}$, gives $D(\text{calc}) = +0.27\text{ cm}^{-1}$. The experimentally observed value for the ground state zero field splitting is $D(\text{exp}) = -0.04\text{ cm}^{-1}$ [147, 148]. Thus even the sign is wrong, demonstrating that differential orbital covalency, that is $\beta_1^2 \neq \gamma_1^2$, etc. in Eq. (258), plays a key role in determining the ZFS. This is again under-determined as one parameter, D , depends on a number of orbital coefficients in addition to the energies of the axial split excited state and is best obtained from molecular orbital calculations. On a qualitative level when the d_{xy} orbital energy is increased due to the flattened D_{2d} axial distortion splitting the ${}^4T_1^a$ state, its covalency also increases due to the increased antibonding interactions with the ligands. Thus $\beta_1^2 < \gamma_1^2, \gamma_2^2$ and from Eq. (258) this will have the opposite effect on D relative to the energy splitting of the ${}^4T_1^a$ state. Quantitatively, these opposing effects reduce the impact of the lowest energy ${}^4T_1^a$ state on the ZFS and higher energy quartet ligand field excited states become more important. Also covalency leads to additional contribu-

Table 11. Contributions of excited states to the ZFS in FeCl_4^- at an distortion angle of 2.7° as calculated by the ROHF-INDO/S-CI method (reproduced from Ref. [66]).

State	E_{calc}^a	D_{total} (cm^{-1})	D_{Griffith} (cm^{-1})	D_{metal} (cm^{-1})	D_{lig} (cm^{-1})	D_{mixed} (cm^{-1})
${}^4T_1^a$	15 100 (4A_2) 15 773 (4E)	+0.070	+0.089	+0.086	+0.001	-0.017
${}^4T_1^{b,b}$	24 582 (4E) 24 990 (4A_2)	-0.077 ^c	-0.021	-0.078	0.000	+0.001
${}^4T_1^{c,b}$	30 666 (4E) 31 027 (4A_2)	-0.009	-0.006	-0.002	-0.001	-0.006
${}^4\Gamma$ total		-0.016	+0.055	+0.005	0.000	-0.022
${}^6\Gamma$ total		-0.031 ^d	-	-0.016	-0.002	-0.013
total		-0.047	+0.062	-0.011	-0.002	-0.035
exp.		-0.042				

D_{Griffith} = considering the low symmetry distortions only; D_{metal} = contributions of metal-SOC alone; D_{lig} = contributions of ligand-SOC alone; $D_{\text{mixed}} = D_{\text{total}} - D_{\text{metal}} - D_{\text{lig}}$

^a Note that these number can not be directly compared to the experimental transition energies since the experimental numbers in contrast to the theoretical ones contain spin-orbit coupling.

^b There is considerable configurational mixing among the ${}^4T_1^b$ (e^2t^3) and ${}^4T_1^c$ (e^1t^4) states.

^c This number contains a -0.012 cm^{-1} contribution from the 4E state following from ${}^4T_2^b$.

^d This number contains contributions from many states. There is a significant amount of electronic relaxation in the CT excited states of FeCl_4^- that will be analyzed elsewhere.

tions from sextet charge transfer excited states and from ligand spin-orbit coupling ($\zeta(\text{Cl}^-) = 550 \text{ cm}^{-1}$). These contributions are summarized in Table 11 [66] leading to a reasonable estimate of the different contributions to the experimental value of D .

The polarized single crystal absorption and MCD data for $\text{Fe}(\text{SR})_4^-$ given in Fig. 11 show that the ${}^4T_1^a$ S_4 -axial splitting is reversed from that of D_{2d} - FeCl_4^- with the ${}^4T_{1x,y}^a$ lower in energy than ${}^4T_{1z}^a$ (7975 and $10\,525 \text{ cm}^{-1}$, respectively).

Using Eq. (287) these give a $D(\text{calc})$ of -0.7 cm^{-1} . From EPR, $D(\text{exp}) = +2.4 \text{ cm}^{-1}$. Again the calculated sign is opposite experiment demonstrating the dominant role of differential orbital covalency in determining the sign and magnitude of D . The positive sign of $D(\text{exp})$ requires that $\beta_1^2 > \gamma_1^2, \gamma_2^2$. This combined with the experimental energy order of the axial splitting of the ${}^4T_1^a$ indicate that the d_{xz}, d_{yz} set is at higher energy than d_{xy} and more antibonding with the ligands.

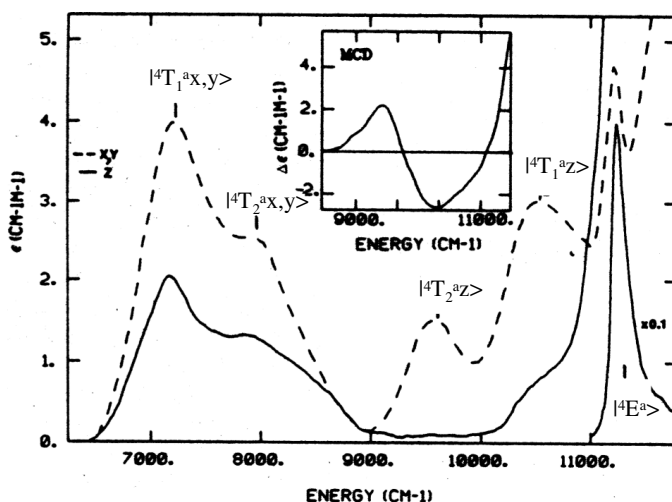


Fig. 11. Polarized single crystal absorption and MCD spectra of $[\text{Fe}(\text{SR})_4][\text{NEt}_4]$ ($\text{R} = 2,3,5,6\text{-Me}_4\text{C}_6\text{H}$).

This is important since the $\text{Fe}(\text{SR})_4^-$ complex has a flattened sulfur core congruent with that of FeCl_4^- . However, the bonding of the sulfur to the R group with a R–S–Fe angle of 102.4° tilts the p orbital of the sulfur involved in σ -bonding to the iron off the S–Fe axis (i.e. a pseudo- σ interaction) and into the xz, yz plane. This demonstrates that the orientation of the thiolate–metal bond in the protein can play a major role in determining the electronic structure of iron sulfur active sites and its contribution to reactivity in electron transfer.

9.6 Computational Approaches to SH Parameters

This chapter is devoted to an overview of computational approaches to SH parameters. This requires an, at least, superficial understanding of the types of electronic structure theories that can presently be applied to molecules the size of some tens of atoms. These theories are either based on the Hartree–Fock (HF) method or density functional theory (DFT) both of which will be briefly described. It will then be shown how these theories can be used to predict SH parameters and it will be found that in practice algorithms have to be used that are significantly different from the general theory developed in the previous chapters. This is because in practice it turns out to be exceedingly difficult to accurately calculate wavefunctions of sufficient accuracy for a large number of states (HF based theories) or to the fact that many electron wavefunctions are not available (DFT).

9.6.1 Hartree–Fock Theory

In Hartree–Fock theory [77] the many electron wavefunction of the ground state is approximated by a single Slater determinant of the form of Eq. (98). According to the variational principle the energetically best possible solution within this approximation is obtained by varying the MOs $\{\psi\}$ to make the energy expectation value $\langle \Psi | \hat{H}_{BO} | \Psi \rangle$ stationary. For practical reasons the MOs are always expanded in a linear combination of basis functions according to Eq. (100) using a one-electron basis $\{\varphi\}$ that in most cases consists of Gaussian or Slater functions. This procedure is the well-known Hartree–Fock–Roothaan (HF) approximation. When applied to open-shell systems at least two variants of the HF procedure are known. In the spin-unrestricted (UHF) formalism, the orbitals for spin-up and spin-down electrons are allowed to have different spatial parts, leading to a Slater determinant of the form:

$$\Psi = |\psi_1^\alpha \dots \psi_{n_\alpha}^\alpha \bar{\psi}_1^\beta \dots \bar{\psi}_{n_\beta}^\beta| \quad (288)$$

where n_α is the number of spin-up electrons and n_β is the number of spin-down electrons. A state with total spin S is approximated by a UHF determinant with $n_\alpha - n_\beta = 2S$. The MOs $\{\psi^\alpha, \psi^\beta\}$ satisfy the canonical UHF equations:

$$\hat{F}^\alpha \psi_i^\alpha = \varepsilon_i^\alpha \psi_i^\alpha \quad (289)$$

$$\hat{F}^\beta \psi_i^\beta = \varepsilon_i^\beta \psi_i^\beta \quad (290)$$

where \hat{F}^σ ($\sigma = \alpha, \beta$) is the Fock operator for spin- σ :

$$\hat{F}^\sigma = \hat{h} + \sum_{j \in \alpha} \hat{J}_j^\alpha - \hat{K}_j^\alpha + \sum_{j \in \beta} \hat{J}_j^\beta \quad (291)$$

where \hat{h} is the one-electron operator:

$$\hat{h} = -\frac{1}{2}\nabla^2 - \sum_A \frac{Z_A}{|\mathbf{R}_A - \mathbf{r}|} \quad (292)$$

J_j^σ is the Coulomb-operator:

$$\hat{J}_j^\sigma = \int \frac{|\psi_j^\sigma(\mathbf{r}')|^2}{|\mathbf{r} - \mathbf{r}'|} d\mathbf{r}' \quad (293)$$

and K_j^σ is the non-local exchange operator that is defined by its action on any orbital ψ :

$$\hat{K}_j^\sigma \psi(\mathbf{r}) = \int \frac{\psi_j^\sigma(\mathbf{r}')\psi(\mathbf{r}')}{|\mathbf{r} - \mathbf{r}'|} d\mathbf{r}' \psi_j^\sigma(\mathbf{r}) \quad (294)$$

Solution of the UHF equations yields the two sets of MO coefficients $\{\mathbf{c}^\alpha, \mathbf{c}^\beta\}$ and orbital-energies $\{\varepsilon^\alpha, \varepsilon^\beta\}$ as well as the total energy E_{UHF} :

$$\begin{aligned}
 E_{UHF} = & \sum_{i,\sigma} n_i^\sigma \langle \psi_i^\sigma | \hat{h} | \psi_i^\sigma \rangle \\
 & + \frac{1}{2} \sum_{\sigma,i} \sum_{\sigma',j} n_i^\sigma n_j^{\sigma'} (\langle \psi_i^\sigma \psi_i^\sigma | r_{12}^{-1} | \psi_j^{\sigma'} \psi_j^{\sigma'} \rangle - \delta_{\sigma\sigma'} \langle \psi_i^\sigma \psi_j^{\sigma'} | r_{12}^{-1} | \psi_i^{\sigma'} \psi_j^\sigma \rangle) \\
 & + E_{NN}
 \end{aligned} \tag{295}$$

The HF method delivers the best possible energy within the restriction that the wavefunction has the form of a single Slater determinant. It treats the electron–electron repulsion in an average way in the sense that each electron moves in the potential created by the nuclei and the average potential created by the other electrons. Thus, still lacking from the HF approximation is the instantaneous electron–electron interaction (the so-called “dynamical correlation”). Also lacking from the HF approximation is the flexibility to describe situations (like bond breaking) where a single Slater determinant does not constitute a reasonable approximation (this is the so-called “static correlation”). The correlation energy is not very large in relation to the total energy. However, it is chemically significant. While the HF approximation gives $\approx 99\%$ of the correct non-relativistic energy, the remaining percent corresponds to hundreds or thousands of kcal mol⁻¹ and therefore the errors of the HF approximation are large on a chemical scale and methods to treat the interelectronic correlation are required. For an introduction see Szabo and Ostlund [77] or Jensen [149].

The strong point of the spin-unrestricted method is that it allows for a polarization of the electron cloud and is therefore able to describe negative spin-densities and phenomena such as core-polarization that are indispensable for the accurate calculation of HFCs. The polarization arises from the exchange terms that only exist for electrons of like spin. Since there are more spin-up than spin-down electrons, the spin-up electrons move in a more attractive potential. Consequently, the distribution of spin-up and spin-down electrons in formally doubly occupied MOs will be slightly different. The spin-density from the UHF wavefunction is:

$$\begin{aligned}
 \rho_{UHF}^{\alpha-\beta}(\mathbf{r}) &= \sum_i n_i^\alpha |\psi_i^\alpha(\mathbf{r})|^2 - n_i^\beta |\psi_i^\beta(\mathbf{r})|^2 \\
 &= \sum_{pq} P_{pq}^{\alpha-\beta} \varphi_\mu(\mathbf{r}) \varphi_\nu(\mathbf{r})
 \end{aligned} \tag{296}$$

where n_i^α and n_i^β are the occupation numbers of the relevant MOs. with the spin-density matrix:

$$P_{pq}^{\alpha-\beta} = \sum_i n_i^\alpha c_{pi}^\alpha c_{qi}^\alpha - n_i^\beta c_{pi}^\beta c_{qi}^\beta \tag{297}$$

Using this spin-density, all first order properties considered above can be calculated. These are the relativistic mass correction to the g-tensor ($g_{\mu\nu}^{(RMC)}$, Eq. 134),

the gauge correction ($g_{\mu\nu}^{(GC)}$, Eq. 137), the spin dipolar HFC ($A_{\mu\nu}^{(A;d)}$, Eq. 143) and the Fermi-contact term ($A_{iso}^{(A)}$, Eq. 142). The remaining second order terms (the ZFS and the second order spin-orbit coupling contributions to the g-tensors and the HFC) cannot be dealt with in this way. Techniques to treat these terms are described below.

However, the UHF method has the well-known defect that it is not an eigenfunction of the total spin squared, i. e. $\langle \hat{S}^2 \rangle_{UHF} \neq S(S+1)$ and this can have undesirable consequences. In many cases, however, $\langle \hat{S}^2 \rangle_{UHF} \approx S(S+1)$ and the UHF wavefunction is a reasonable approximation to a state of spin S .

The alternative to the UHF method is the restricted open-shell HF (ROHF) method. In this case the trial wavefunction Ψ is of the form of Eq. (101) and thus has a set of doubly occupied and a set of singly occupied MOs. The ROHF equations are somewhat different from the UHF equations. Their solution yields a set of orbitals and orbital energies and the complete formalism of Section 9.3.5 is directly applicable. The ROHF wavefunction has less variational degrees of freedom than the UHF wavefunction and therefore gives a slightly higher energy. In addition, at the ROHF level one cannot describe core-polarization because the spin density (Eq. 104) is positive everywhere. However, the ROHF determinant is a spin-eigenfunction.

Thus, both the UHF and the ROHF have certain advantages and will be used in different contexts. The UHF procedure is usually preferable for the calculation of HFCs while the ROHF wavefunction is a suitable starting point for more accurate treatments.

9.6.2 Configuration Interaction

The theory of SH parameters in Section 9.3 was formulated in a set of many electron wavefunctions for the ground- as well as excited states. Computationally, a set of many electron wavefunctions may be obtained from the procedure of configuration interaction (CI). In this method the many electron wavefunctions are expanded in terms of CSFs as:

$$\Psi_I = \sum_J C_{JI} \Phi_j \quad (298)$$

where the $\{\Phi\}$ are CSFs as described in Section 9.3.5.1. In Section 9.3.5.1 the treatment was focused on CSFs that are singly excited relative to the ground state. However, in the general case the set $\{\Phi\}$ may also contain doubly, triply, etc. excited CSFs. The CI coefficients \mathbf{C} are obtained from solving the secular equations:

$$\mathbf{HC} = E\mathbf{C} \quad (299)$$

where \mathbf{H} is the matrix of the BO Hamiltonian in the $\{\Phi\}$ basis:

$$H_{IJ} = \langle \Phi_I | \hat{H}_{BO} | \Phi_j \rangle \quad (300)$$

The matrix elements (300) are fairly difficult to calculate and contain the one-electron integrals $\langle \psi_i | \hat{h} | \psi_j \rangle$ and the two electron integrals $\langle \psi_i \psi_j | r_{12}^{-1} | \psi_k \psi_l \rangle$. It is clear, that the number of two-electron integrals as well as the number of possible CSFs $\{\Phi\}$ is enormous. Accurate CI calculations may involve as many as 10^6 – 10^{10} CSFs and are computationally extremely demanding. However, efficient algorithms to calculate the ground and a number of excited states by this procedure exist [150–152].

Given a set of many electron CI wavefunctions $\{\Psi\}$ and their energies $\{E\}$, the general equations derived in Sections 9.3.4.1–9.3.4.3 may be directly evaluated without any further approximation. The matrix elements that occur in these equations present considerable technical challenges (for details see [153–155]). Furthermore, it is clear that the infinite summations that occur in Sections 9.3.4.1–9.3.4.3 must be truncated since only a limited number of excited states can be calculated with a reasonable effort. However, in many cases the SH parameters are dominated by only a few excited states and some of the most accurate calculations of SH parameters have been done with the CI formalism (*vide infra*). In general, however, the method is computationally too demanding to be applied to large molecules and alternative procedures are needed and will be described below.

9.6.3 Density Functional Theory

DFT is a fundamentally different approach to electronic structure theory that has become extremely popular in recent years because it gives results that are significantly better than those delivered by the HF method with about the same computational effort. The theory is fairly involved [156] and only a cursory introduction can be presented here. DFT is based on the Hohenberg–Kohn theorems [157] the first of which states that the exact ground state energy of a non-degenerate ground state is a unique functional of the electron density only. The exact non-relativistic total energy can thus be written:

$$E_0[\rho_\alpha, \rho_\beta] = T[\rho_\alpha, \rho_\beta] + V_{en}[\rho_\alpha, \rho_\beta] + J[\rho_\alpha, \rho_\beta] + E_{XC}[\rho_\alpha, \rho_\beta] + V_{NN} \quad (301)$$

where ρ_α and ρ_β are the densities of spin-up and spin-down electrons, T is the electronic kinetic energy, V_{en} the electron–nuclear attraction, J the Coulomb energy and E_{XC} is the exchange correlation functional that describes all contributions to the energy in terms of only the spin-up and spin-down densities.

In practice the so-called Kohn–Sham (KS) method [158] is used in order to calculate the electron density. The KS construction features a fictitious system of non-interacting electrons that share the same electron density with the real interacting system. The wavefunction of the non-interacting reference system can be taken as a single determinant of the UHF type. Application of the variational principle (which is valid due to the second Hohenberg–Kohn theorem) then leads to the KS equations in their spin-polarized form:

$$\left\{ -\frac{1}{2}\nabla^2 + \hat{V}_{en} + \hat{V}_C + \hat{V}_{XC}^\sigma \right\} \psi_i^\sigma(\mathbf{r}) = \varepsilon_i^\sigma \psi_i^\sigma(\mathbf{r}) \quad (302)$$

where the KS molecular orbitals $\{\psi\}$ and their energies $\{\varepsilon\}$ were introduced and the Coulomb operator, \hat{V}_C , is:

$$\hat{V}_C = \sum_{j\sigma} \hat{j}_j^\sigma \quad (303)$$

The exchange-correlation potential V_{XC}^σ is given by the functional derivative of $\tilde{E}_{XC}[\rho_\alpha, \rho_\beta]$ with respect to ρ_σ :

$$V_{XC}^\sigma = \frac{\delta \tilde{E}_{XC}[\rho_\alpha, \rho_\beta]}{\delta \rho_\sigma(\mathbf{r})} \quad (304)$$

Here, \tilde{E}_{XC} is essentially E_{XC} but also contains a small contribution to the kinetic energy that is not covered directly in the KS method [156]. Thus, if the exchange-correlation functional were known, DFT in the KS formalism would give the exact energy and electron density of the ground state. However, the exact many electron wavefunction that leads to the exact energy remains unknown as is the exact exchange-correlation functional. However, successful approximate forms for \tilde{E}_{XC} have been under intense development in the past three decades and have led to computationally tractable expressions that are widely used (reviews are available elsewhere [159–168]). Essentially three variants are presently in common use (a) the local density approximation (LDA) in which only the densities ρ_α and ρ_β enter V_{XC}^σ , (b) the generalized gradient approximation (GGA) where the densities as well as their gradients $\nabla\rho_\alpha$ and $\nabla\rho_\beta$ contribute and (c) the hybrid functionals where in addition to the densities and their gradients a part of the HF exchange term is mixed into the density functional. In many applications it is found that the accuracy of the functions increases in order (a) < (b) < (c) with the hybrid B3LYP functional [169–172] being the most popular member of class (c) and the Becke–Perdew (BP) functional [169, 173] the most popular member of class (b) [174].

From a computational perspective, the KS equations look quite similar to the HF equations of Section 9.6.1 although they have been derived from a completely different perspective. The main difference is the replacement of the HF exchange term by the local exchange-correlation potential V_{XC}^σ . For a full discussion of the many subtleties and problems associated with DFT, the excellent monographs of Parr and Yang [156] and Koch and Holthausen [174] should be consulted. The exchange-correlation potential is, in general, fairly complicated and its matrix elements are usually calculated by efficient three dimensional numerical integration techniques [175, 176].

9.6.4 Coupled-perturbed SCF Theory

The coupled perturbed SCF (CP-SCF) theory [177–183] is an attractive alternative to the use of computationally demanding CI type procedure for the calculation of

second order properties such as the spin-orbit coupling contributions to the g-tensor and the HFC. It is the basis of all modern approaches to second order properties that are tractable for large molecules. The main idea is to express the second order property as a mixed second derivative of the total energy with respect to two perturbations λ and μ .

$$T_{\lambda\mu} = \frac{\partial^2 E(\lambda, \mu)}{\partial\lambda\partial\mu} \quad (305)$$

where “ T ” represents a second order property and λ and μ symbolize two perturbations that are associated with the perturbing one-electron operators $\lambda\hat{h}_\lambda$ and $\mu\hat{h}_\mu$. In this form infinite summations over excited states are avoided. If the zero-order wavefunction is variational (as is the case for the HF and KS methods), it can be shown that it is sufficient to calculate the response of the wavefunction with respect to one perturbation in order to evaluate the mixed second derivative. Also, it is immaterial in which order the two perturbations are treated [183]. This is known as the interchange theorem of double-perturbation theory [12, 183].

For convenience, the self-consistent field (SCF) operator, \hat{F}^σ , is written in a form that is valid for either HF, pure DFT or hybrid DFT:

$$\hat{F}^\sigma = \hat{h}(\vec{r}) + \hat{V}_C(\vec{r}) + c_{HF}\hat{K}^\sigma + c_{DF}\hat{V}_{XC}^\sigma[\rho_\alpha, \rho_\beta](\vec{r}) \quad (306)$$

The parameter c_{HF} equals one in HF theory, zero in “pure” DFT and assumes values in the range between 0.05 and 0.5 in hybrid DFT. The parameter c_{DF} equals zero in HF theory and one in form of DFT.

The perturbation treatment consists of supplementing the SCF operator by the perturbing operator $\lambda\hat{h}_\lambda$ (i. e. $\hat{F}^\sigma \rightarrow \hat{F}^\sigma + \lambda\hat{h}_\lambda$) and expanding the SCF-operator, the spin-orbitals and the orbital energies as Taylor series in the perturbation parameter λ :

$$\varepsilon_i^\sigma(\lambda) = \varepsilon_i^{\sigma(0)} + \lambda\varepsilon_i^{\sigma(1)} + O(\lambda^2) \quad (307)$$

$$\psi_i^\sigma(\lambda) = \psi_i^{\sigma(0)} + \lambda\psi_i^{\sigma(1)} + O(\lambda^2) \quad (308)$$

$$\hat{F}^\sigma(\lambda) = \hat{F}^{\sigma(0)} + \lambda\hat{F}^{\sigma(1)} + O(\lambda^2) \quad (309)$$

Collecting terms of the same order in the perturbation gives:

$$(\hat{F}^{\sigma(0)} - \varepsilon_i^{\sigma(0)})\psi_i^{\sigma(1)} + (\hat{F}^{\sigma(1)} - \varepsilon_i^{\sigma(1)})\psi_i^{\sigma(0)} = 0 \quad (310)$$

The most difficult part is the calculation of the first order perturbed SCF operator $\hat{f}^{\sigma(1)}$ that is defined by:

$$\hat{f}^{\sigma(1)} = \left. \frac{\partial\hat{F}^\sigma(\lambda)}{\partial\lambda} \right|_{\lambda=0} \quad (311)$$

The derivative is complicated in so far as the operator $\hat{F}^\sigma(\lambda)$ involves the λ -dependent term $\lambda\hat{h}_\lambda$ and also the perturbed orbitals $\psi_i^{\sigma(1)}$. Without compromising

the generality of the treatment, the first order orbitals can be written as a sum over the zeroth order virtual orbitals of the same spin:

$$\psi_i^{\sigma(1)}(\mathbf{r}) = \sum_{a \in \sigma} U_{ia}^{\sigma} \psi_a^{\sigma(0)}(\mathbf{r}) \quad (312)$$

where the U 's are the first order wavefunction coefficients (throughout indices i, j, k refer to occupied orbitals, a, b to empty orbitals and the zero order orbitals are assumed real). This gives for the derivative of the density with respect to the perturbation parameter:

$$\frac{\partial \rho_{\sigma}(\mathbf{r})}{\partial \lambda} = 2 \sum_{i, a \in \sigma} n_i^{\sigma} \operatorname{Re}(U_{ia}^{\sigma}) \psi_i^{\sigma(0)}(\mathbf{r}) \psi_a^{\sigma(0)}(\mathbf{r}) \quad (313)$$

Proceeding term by term, the one-electron operator, \hat{h} , does not contribute, while the Coulomb operator gives the term:

$$\frac{\partial \hat{V}_C}{\partial \lambda} = 2 \sum_{\sigma=\alpha, \beta} \sum_{i, a \in \sigma} n_i^{\sigma} \operatorname{Re}(U_{ia}^{\sigma}) \int \frac{\psi_i^{\sigma(0)}(\mathbf{r}') \psi_a^{\sigma(0)}(\mathbf{r}')}{|\mathbf{r} - \mathbf{r}'|} d\mathbf{r}' \quad (314)$$

The exchange operator contributes the following term to the derivative:

$$\begin{aligned} \left\langle \psi_a^{\sigma'} \left| \frac{\partial \hat{K}^{\sigma}}{\partial \lambda} \right| \psi_i^{\sigma'} \right\rangle &= - \sum_{j, b \in \sigma} n_j^{\sigma} \left((U_{jb}^{\sigma})^* \langle \psi_a^{\sigma'(0)} \psi_j^{\sigma(0)} | r_{12}^{-1} | \psi_b^{\sigma(0)} \psi_i^{\sigma'(0)} \rangle \right. \\ &\quad \left. + U_{jb}^{\sigma} \langle \psi_a^{\sigma'(0)} \psi_b^{\sigma(0)} | r_{12}^{-1} | \psi_j^{\sigma(0)} \psi_i^{\sigma'(0)} \rangle \right) \end{aligned} \quad (315)$$

Finally, the exchange correlation potential contributes the following term (Parr and Yang [156], appendix A):

$$\begin{aligned} \frac{\partial \hat{V}_{XC}[\rho_{\alpha}, \rho_{\beta}](\mathbf{r})}{\partial \lambda} &= \sum_{\sigma'=\alpha, \beta} \int \frac{\partial \hat{V}_{XC}[\rho_{\alpha}, \rho_{\beta}]}{\partial \rho_{\sigma'}(\mathbf{r}')} \Big|_{\rho_{\sigma'}=\rho_{\sigma'}(\lambda=0)} \frac{\partial \rho_{\sigma'}(\mathbf{r}')}{\partial \lambda} \Big|_{\lambda=0} d\mathbf{r}' \\ &= \sum_{\sigma'=\alpha, \beta} \int f_{xc}^{\sigma\sigma'}[\rho_{\alpha}, \rho_{\beta}](\mathbf{r}, \mathbf{r}') \frac{\partial \rho_{\sigma'}(\mathbf{r}')}{\partial \lambda} \Big|_{\lambda=0} d\mathbf{r}' \\ &= 2 \sum_{\sigma'=\alpha, \beta} \sum_{j, b \in \sigma'} n_j^{\sigma'} \operatorname{Re}(U_{jb}^{\sigma'}) \\ &\quad \cdot \int f_{xc}^{\sigma\sigma'}[\rho_{\alpha}, \rho_{\beta}](\mathbf{r}, \mathbf{r}') \psi_j^{\sigma'(0)}(\mathbf{r}') \psi_b^{\sigma'(0)}(\mathbf{r}') d\mathbf{r}' \end{aligned} \quad (316)$$

The exchange-correlation kernel $f_{xc}^{\sigma\sigma'}[\rho_{\alpha}, \rho_{\beta}](\mathbf{r}, \mathbf{r}')$ is familiar from time dependent DFT in the adiabatic approximation [184–186]. In the commonly encountered case where the exchange-correlation potential is a simply function of the density and its gradients, a delta-function $\delta(\mathbf{r} - \mathbf{r}')$ arises in the integral (see Parr and Yang [156], appendix A).

Separating the real and imaginary parts gives the following coupled-perturbed SCF equations:

$$\begin{aligned} \operatorname{Re}(V_{ai}^\sigma) + \sum_{\sigma'=\alpha,\beta} \sum_{j,b} E_{ia,jb}^{\sigma\sigma'} \operatorname{Re}(U_{jb})^{\sigma'} + \operatorname{Im}(V_{ai}^\sigma) \\ + \sum_{\sigma'=\alpha,\beta} \sum_{j,b} M_{ia,jb}^{\sigma\sigma'} \operatorname{Im}(U_{jb})^{\sigma'} = 0 \end{aligned} \quad (317)$$

where the vector \mathbf{V}^σ has the elements:

$$V_{ai}^\sigma = \langle \psi_a^{\sigma(0)} | \hat{h}_\lambda | \psi_i^{\sigma(0)} \rangle \quad (318)$$

As first discussed in the framework of the closed shell HF method by Stevens, Pitzer and Lipscomb [177], the matrices $E_{ia,jb}^{\sigma\sigma'}$ and $M_{ia,jb}^{\sigma\sigma'}$ are the “electric” and “magnetic” Hessians respectively. For the spin-polarized hybrid DFT case one obtains:

$$\begin{aligned} E_{ia,jb}^{\sigma\sigma'} = & (\varepsilon_a^{\sigma(0)} - \varepsilon_i^{\sigma(0)}) \delta_{ia,jb} \delta_{\sigma\sigma'} + 2 \langle \psi_a^{\sigma(0)} \psi_i^{\sigma(0)} | r_{12}^{-1} | \psi_j^{\sigma'(0)} \psi_b^{\sigma'(0)} \rangle \\ & - c_{HF} \delta_{\sigma\sigma'} \langle \psi_a^{\sigma(0)} \psi_j^{\sigma'(0)} | r_{12}^{-1} | \psi_b^{\sigma'(0)} \psi_i^{\sigma(0)} \rangle \\ & - c_{HF} \delta_{\sigma\sigma'} \langle \psi_a^{\sigma(0)} \psi_b^{\sigma'(0)} | r_{12}^{-1} | \psi_j^{\sigma'(0)} \psi_i^{\sigma(0)} \rangle \\ & + 2c_{DF} \langle \psi_a^{\sigma(0)} \psi_i^{\sigma(0)} | f_{XC}^{\sigma\sigma'} | \psi_b^{\sigma'(0)} \psi_j^{\sigma'(0)} \rangle \end{aligned} \quad (319)$$

$$\begin{aligned} M_{ia,jb}^{\sigma\sigma'} = & (\varepsilon_a^{\sigma(0)} - \varepsilon_i^{\sigma(0)}) \delta_{ia,jb} \delta_{\sigma\sigma'} + c_{HF} \delta_{\sigma\sigma'} \langle \psi_a^{\sigma(0)} \psi_j^{\sigma'(0)} | r_{12}^{-1} | \psi_i^{\sigma(0)} \psi_b^{\sigma'(0)} \rangle \\ & - c_{HF} \delta_{\sigma\sigma'} \langle \psi_a^{\sigma(0)} \psi_b^{\sigma'(0)} | \psi_i^{\sigma(0)} \psi_j^{\sigma'(0)} | \rangle \end{aligned} \quad (320)$$

Note that neither the Coulomb nor the DFT exchange-correlation terms contribute to the magnetic Hessian due to their simple multiplicative nature. The corresponding equations for the closed shell case and in the presence of current dependent terms in the exchange correlation potential have been discussed [187, 188]. Thus, the main quantities that enter the CP-SCF equations are the orbital energies, the matrix elements of the perturbing operator and two electron integrals over occupied and virtual molecular orbitals.

In the case that the matrix element of the perturbation are purely imaginary the coefficients U_{ia}^σ are also purely imaginary. Furthermore, in this particular case the magnetic Hessian is diagonal (as long as $c_{HF} = 0$) and one obtains [187, 188]:

$$U_{ia}^\sigma = \frac{i \operatorname{Im} \langle \psi_a^\sigma | h_\lambda | \psi_i^\sigma \rangle}{\varepsilon_a^{\sigma(0)} - \varepsilon_i^{\sigma(0)}} \quad (321)$$

which is just the result one would obtain from standard Rayleigh–Schrödinger perturbation theory, where the fact that the SCF operator \hat{F}^σ depends on the perturbed molecular orbitals is neglected. This is known as the uncoupled approximation which only becomes exact for pure density functionals and in the case where the matrix

elements of the perturbation are purely imaginary. However, for the HF method and hybrid density functionals the following linear equation system must be solved:

$$\begin{pmatrix} \mathbf{M}^{\alpha\alpha} & \mathbf{0} \\ \mathbf{0} & \mathbf{M}^{\beta\beta} \end{pmatrix} \begin{pmatrix} \text{Im}(\mathbf{U}^\alpha) \\ \text{Im}(\mathbf{U}^\beta) \end{pmatrix} = - \begin{pmatrix} \text{Im}(\mathbf{V}^\alpha) \\ \text{Im}(\mathbf{V}^\beta) \end{pmatrix} \quad (322)$$

The linear equation system is of large dimension and can, in general, only be solved iteratively. For details we refer to the literature [180, 189, 190].

Having obtained the coefficients of the first order perturbed wavefunction the second-order property is calculated as:

$$T_{\mu\lambda} = \sum_{\sigma} \sum_{i,a \in \sigma} U_{ai}^{\lambda\sigma} \langle \psi_i^\sigma | h_\mu | \psi_a^\sigma \rangle + U_{ia}^{\lambda\sigma*} \langle \psi_a^\sigma | h_\mu | \psi_i^\sigma \rangle \quad (323)$$

where the sum is over the occupied orbitals i and empty orbitals a of spin σ .

9.6.5 Relativistic Methods

As an alternative to the use of perturbation theory, the relativistic effects (i. e. the scalar relativistic effects, Section 9.3.2.5 and the spin-orbit coupling, Section 9.3.2.2) can be directly incorporated into the HF or DFT electronic structure calculation. In this case, first order perturbation theory is sufficient to calculate all magnetic parameters. The resulting methods do not suffer from divergence problems that are occasionally a problem for perturbation treatments.

However, the direct inclusion of relativistic effects presents a challenging problem for electronic structure calculations. This arises because the relativistic operator in the Breit-Pauli form discussed in this review are not bounded from below and when applied in a variational procedure leads to variational collapse. Thus, these operators should only be used in perturbation calculations and operators with regular behavior must be derived in a different form from the Dirac equation.

One of the most popular relativistic method at present is the ZORA (zero order regular approximation) method that can be traced back to the work of Chang, Pelissier and Durand [191] and that has been extensively developed by the Amsterdam group in the context of DFT [192-195]. In this method one starts from the split form of the Dirac equation for the so-called large component ψ (electron like states):

$$(V - E)\psi + \frac{\alpha^2}{2} [\boldsymbol{\sigma} \mathbf{p} \omega(\mathbf{r}) \boldsymbol{\sigma} \mathbf{p}] \psi = 0 \quad (324)$$

where V is the effective molecular potential (i. e. the DFT potential $\hat{V} = \hat{V}_{eN} + \hat{V}_C + \hat{V}_{XC}$, Section 9.6.3), \mathbf{p} is the momentum operator and $\boldsymbol{\sigma}$ is the vector with Pauli spin matrices. The function $\omega(r)$ is given by:

$$\omega(\mathbf{r}) = \left(1 - \frac{V - E}{2\alpha^{-2}} \right)^{-1} \quad (325)$$

Expansion of this equation in powers of α^2 and elimination of the energy dependence gives to first order the familiar terms described above (Sections 3.2.2 and 3.2.5). An alternative family of relativistic methods is obtained by partitioning the function $\omega(\mathbf{r})$ as follows:

$$\omega(\mathbf{r}) = \frac{2\alpha^{-2}}{2\alpha^{-2} - V} \left(1 + \frac{E}{2\alpha^{-2} - V} \right)^{-1} \quad (326)$$

and expansion of the term in parenthesis. To zeroth order in this expansion the ZORA method is obtained and the molecular ZORA equations therefore take the form:

$$\{\hat{T}_{ZORA} + \hat{V}\}\psi_i = \varepsilon_i \psi_i \quad (327)$$

where:

$$\hat{T}_{ZORA} = \boldsymbol{\sigma} \mathbf{p} \frac{\alpha^{-2}}{2\alpha^{-2} - V} \boldsymbol{\sigma} \mathbf{p} \quad (328)$$

Solution of these equations in a molecular context with either inclusion of only scalar relativistic effects and/or SOC has been extensively discussed in the literature by van Lenthe et al. [192–195] and by Van Wüllen [196]. A HF version has also been reported [197]. Furthermore, van Lenthe and coworkers have discussed the calculation of g-values [198], HFCs [199] and quadrupole couplings [200] on the basis of the ZORA method. The results are discussed below.

Other relativistic methods are possible and in particular we note those based on the application of the Douglas–Kroll–Hess transformation [201–206]. However, for details we refer to the specialist literature, in particular to an excellent recent review by Hess and Marian [61].

9.6.6 Calculation of Zero-field Splittings

Very few general methods for the calculation of ZFSs of transition metal complexes outside the domain of ligand field theory [207] exist. However, as has been argued in Sections 4.1.5 and 5.2, ligand field theory is not entirely reliable for the prediction of ZFSs due to the important contributions of anisotropic covalency that often tend to counteract the contributions from the low-symmetry ligand field splittings. The fundamental complication in the first principle prediction of ZFSs is, that excited states of different spin than the ground state contribute to the ZFS (Sections 9.3.4.2, 9.3.5.2, and 9.4.1.5). In such a situation it is not clear how to formulate a proper CP-SCF theory. This appears to have precluded so far a proper calculation of ZFSs by DFT.

In the *ab initio* HF field some large scale CI calculations were reported that obtain the ZFSs from a CI that includes the SOC. This procedure yields only the eigenvalues of the ZFS tensor but not its orientation. However, the calculations were

done for a fairly large molecule and have lead to good agreement with experiment [113].

We have developed a general method for the calculation of ZFSs from general multireference CI (MR-CI) wavefunctions [66]. The method includes all SOC contributions to the ZFS including excited states with a total spin different from that of the ground state but neglects the direct spin–spin coupling. It is also formulated for any ground state spin S . However, in order to be able to apply it to large molecules a semi-empirical Hamiltonian was chosen. This Hamiltonian is the INDO/S Hamiltonian of Zerner and coworkers [208–210] that has proven its ability to predict spectroscopic properties of transition metal complexes in many applications (reviews are available elsewhere [211–213]).

As an example of this general methodology consider the case of FeCl_4^- that has been treated in some detail [66, 147, 148] (Section 9.5.2). Here the calculations give insight into the interplay between low-symmetry distortions, covalency effects and charge-transfer contributions to the observed ZFS. FeCl_4^- exists as an almost regular tetrahedron in a $S = \frac{5}{2}$ ground state that closely corresponds to the ligand field picture. In Fig. 12 the contribution from $S = \frac{3}{2}$ spin-forbidden, ligand field excited states and $S = \frac{5}{2}$ metal-to-ligand charge transfer excited states to the ZFS are shown as a function of molecular geometry. The coordinate describes a distortion from a elongated tetrahedron to a flattened tetrahedron, the latter is observed experimentally [147, 148]. It is observed that the sign of the ZFS changes as the system goes from a elongated to a flattened tetrahedron and that the contributions of d–d and MLCT excited states have the same sign, with the d–d states being more important. However, the sign of the ZFS is opposite of the predictions from ligand field theory that only consider the low-symmetry distortion but not the differential

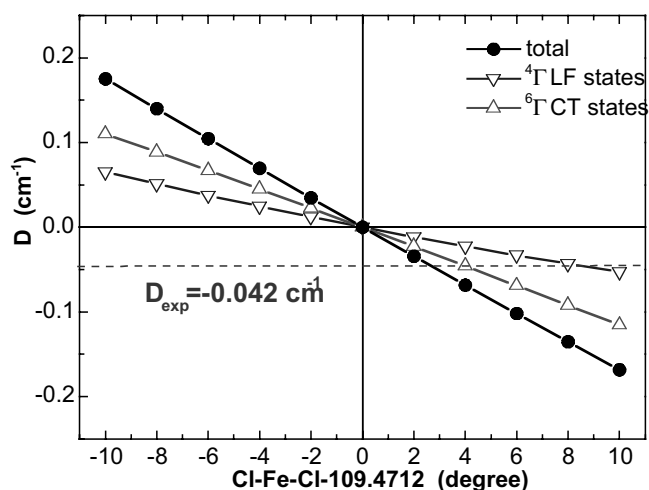


Fig. 12. Contributions of quartet (d–d excited states) and sextet (MLCT excited states) to the observed ZFS in FeCl_4^- as a function of low-symmetry distortion. The experimental D -value is indicated by a dashed horizontal line (reproduced from Ref. [66]).

covalencies (Ref. [114], see Section 9.5.2). However, the calculations are in agreement with experiment while ligand field theory is not. The ZFS of FeCl_4^- can be further analyzed in terms of metal- and ligand SOC contributions and for details we refer to the literature [66, 147, 148] and Sections 5.2 and 4.1.4.

While the semi-empirical procedure used is open to critique, the emerging applications [214, 215] to low symmetry high-spin Fe(III) and Mn(III) [216] protein active sites demonstrate that the method is capable of predicting the correct sign of the ZFSs and their magnitudes to within a factor of two. In addition, it appears that the orientation of the ZFS tensors is predicted with reasonable accuracy which is particularly useful in combination with MCD spectroscopy [143, 214]. While these initial results appear to be promising it is clear that further developments are needed. Especially a DFT method for ZFSs is needed in order to provide increasingly reliable prediction of this important magnetic property (a review is available elsewhere [217]).

9.6.7 Calculation of g-Values

Compared to ZFSs a variety of general methods are available for the prediction of g-tensors. These have partly been inspired by the close analogy of g-tensors to NMR chemical shifts [218–223], and closely analogous computational procedures have been used to predict the two quantities.

9.6.7.1 The Gauge Problem

There is one further complication that must be considered in the context of g-tensor calculations. In the equations of Sections 3.4.2, 3.5.3, and 4.1.6 for the g-tensor the orbital-Zeeman operator appears which includes the angular momentum operator. However, the angular momentum is measured *relative to the chosen origin of the coordinate system*. This means that if a different choice for the origin of the overall coordinate system is made, the predictions for the g-tensor will change. This obviously is an undesirable feature of the theory as the g-tensor is of course independent of the origin. As explained in detail by Harriman [8] and McWeeny [12] a change of gauge is offset by a phase change in the wavefunction in the exact treatment. (In a more general context the gauge dependence arises from the arbitrariness of the vector potential. Addition of the gradient of an arbitrary gauge potential to the vector potential does not change the electric and magnetic fields and therefore not the basic physics. Such a change of gauge can consequently not change the values of observables. The origin dependence discussed here is only one particular aspect of the more general gauge problem.) However, in the present context we are involved in a perturbation calculation with fixed zero order functions and the flexibility for the phase change is not built in into the basic set of states. This problem is widely acknowledged in the prediction of magnetic properties such as NMR chemical shifts, magnetizabilities and g-tensors. It appears that the g-tensor is the least sensitive of the three properties with respect to the choice of origin. Thus, if

a “reasonable” origin is chosen, the gauge dependence of the results is fairly small and may be ignored. This is referred to as the “common gauge” (CG) approach to the problem. The origin may be chosen to be coincident with the center of mass or the center of nuclear charge. However, there is one choice that is superior from a theoretical point of view. Luzanov et al. [224] have argued that if one chooses the center of electronic charge as the origin it is to be expected that the results most closely resemble the fully gauge invariant results. The electronic charge centroid is computed from:

$$\mathbf{R}_G = \frac{1}{N_e} \left\langle 0SS \left| \sum_i \mathbf{r}_i \right| 0SS \right\rangle \quad (329)$$

Thus, the computation of \mathbf{R}_G only involves the evaluation of electric dipole integrals which are easy to calculate. There are at least two more rigorous approaches to the gauge problem. The more involved solution is the use of one electron orbitals that are dependent on the magnetic field [225, 226]. These orbitals are known as “London orbitals” [225] and the method is identified by the acronym GIAO (Gauge Including Atomic Orbital). The GIAOs are given by:

$$\varphi_i^{GIAO}(\mathbf{r}, \mathbf{B}) = \varphi_i(\mathbf{r}) \exp\left(-\frac{i\alpha}{2}(\mathbf{B} \times \mathbf{R}_A)\mathbf{r}\right) \quad (330)$$

where $\varphi_i(\mathbf{r})$ is a member of the “normal” atomic orbital basis set which is centered at position \mathbf{R}_A . The use of GIAOs in place of normal orbitals leads to technical complications in the calculation of magnetic properties but is known to converge fast with basis set size and give good results [227–230]. The second popular approach to the treatment of the gauge dependence of magnetic properties is known by the acronym IGLO (Individual Gauge for Localized Orbitals) and has been developed by Kutzelnigg and coworkers [218, 219]. In this case the magnetic field dependent phase factors are not attached to the basis functions but to the MOs themselves that, however, have been localized according to one of the popular criteria [231–233]. The IGLO equations are somewhat easier to evaluate than the GIAO equations and the convergence of the IGLO and GIAO procedure appears to be similar with, perhaps, a slight advantage for the GIAO method [227, 230]. A related method that has found application in the field of NMR chemical shifts is the LORG (Localized orbital local origin) due to Hansen and Bouman [234].

9.6.7.2 Methods for g-Tensor Calculations

There have been some early *ab initio* attempts to calculate g-values that are, however, not particularly conclusive because rather small basis sets had to be used at the time. The field was revived by Lushington and Grein [235, 236] who made important contributions to the *ab initio* prediction of g-values at the Hartree–Fock (HF) and more recently, the MR-CI level [235–240]. While the HF level methods can also be applied to larger molecules, the much more demanding MR-CI methodology is restricted to small molecules where, however, it gives accurate results. Since all of

these *ab initio* approaches are formulated as sum-over-states (SOS) theories it is necessary to explicitly generate a “sufficient number” of excited state wavefunctions which is a laborious and time consuming task. These explicit constructions can be avoided by the elegant response theory treatment developed by Engström et al. [241–245] that has already proved useful for the calculation of g-values of biologically relevant phenoxyl radicals [244] and nitroxide spin labels [245]. However, this methodology has not yet been applied to transition metal complexes. An alternative to perturbation theory is to include the relevant operators in the SCF treatment. This route has been followed by Jayatilaka who has obtained promising results with a generalized two component HF methodology [246]. However, in cases where electron correlation is important the method is expected to break down. The only reported transition metal application has been CoCl_4^- and in this case the method gives reasonable agreement with experiment [246]. (Note that CoCl_4^- is an $S = 3/2$ system and that the calculated g-values were effective g-values of the lowest Kramers doublet rather than real ones.) A systematic study for transition metal complexes is lacking.

As for the ZFSs we have previously developed a MR-CI approach to g-values [66, 155] but have chosen to implement it in connection with semi-empirical quantum chemical methods which allowed application to transition metal complexes of Cu(II) [155] and Mo(V) [247]. It appears from these studies that the approach is capable of giving semi-quantitative agreement with experimental values. In the study of 18 Cu(II) complexes the g-values were predicted with a standard deviation of 21 ppt, a slope of the correlation line of unity and an R-factor of 0.97 [155]. The results were taken as an indication that the INDO/S semi-empirical methods give a reasonable description of Cu(II) complexes. However, the remaining errors due to the crude approximations made in the semi-empirical treatment can not be remedied.

Other semi-empirical approaches for g-values have been described in the literature [83, 108, 248–258] but none has been systematically evaluated for transition metal complexes. The shortcoming of the semi-empirical approach is the limited reliability due to the crude approximations made and the parameterization that may only be valid for certain classes of compounds.

There have been a number of significant contributions to the field of g-value calculations with density functional theory. The earliest attempts to use DFT to calculate magnetic resonance parameters appear to be due to Geurts et al. [259] using uncoupled perturbation theory and the Hartree–Fock–Slater (HFS) variant of DFT. This perturbation method (but in conjunction with more modern functionals based on the generalized gradient approximation (GGA)) has more recently been applied by Belanzoni et al. to TiF_3 [260, 261]. Early work with the $X\alpha$ -scattered wave method should also be mentioned [140, 141] (*vide supra*).

More recently, Schreckenbach and Ziegler [221, 262] reported the development of a gauge including atomic orbital (GIAO) method for LSD and GGA functionals and provided a valuable collection of test results. They demonstrated that their method is more accurate than the older HF based treatments. However, some failures were also noted [221, 262]. Patchkovskii and Ziegler reported several applications to large transition metal complexes with this methodology and demonstrated its usefulness for the interpretation of experimental data [263–266]. In particular

the methods has been applied to d^1 porphyrins [265], nitrosoporphyrins [264] and also to small anionic transition metal complexes [263]. A generalization of their method to calculate g -values to high-spin radicals with mostly encouraging results has recently been published [266].

Van Lenthe et al. made significant contributions to relativistic DFT within the ZORA approach and applied it to the prediction of g -values in small molecules [198] and iron-porphyrins [267]. The latter study [267] demonstrates the potential of the ZORA method for orbitally nearly degenerate molecules where traditional perturbation theory is difficult to apply. Recently, g -value and HFC calculations for two Ni complexes were reported with this method by Stein et al. [268] and most recently by the same authors for the active site of Hydrogenase [269]. These studies and those of Patchkovskii and Ziegler [263–266] demonstrate the potential of DFT for the elucidation of the structures of biologically relevant intermediates that may not be crystallographically characterized but are amenable to spectroscopic analysis. Belanzoni et al. reported a detailed evaluation of the ZORA approach for two and three atomic linear molecules in $^2\Sigma$ states that contain heavy atoms [270]. Reasonable agreement with experimental g -values was observed with no systematic error in the g_{\parallel} -component and an overestimation of the g -shift in the g_{\perp} -component. Limitations of the presently available ZORA method are that it is valid only for a single unpaired electron and can only be used in spin-restricted formalisms.

An important contribution to the DFT prediction of g -values and its extensive numerical evaluation was presented by Malkina et al. [271]. The latter authors also used uncoupled SCF perturbation theory in the spin unrestricted formalism. In particular Malkina et al. used accurate mean field spin-orbit operators [50, 61] and evaluated the potential of relativistic effective core potentials for g -value calculations. It was demonstrated that the method in combination with the popular BP functional [169, 173] gives accurate predictions for radicals made of light atoms. When applied to transition metal complexes, Malkina et al. found that the slope of the regression line was ≈ 0.6 which indicates a systematic underestimation of the g -shifts by this approach [271].

Most recently the DFT approach to g -values was extended to also include hybrid functionals [98]. In this work, the coupled-perturbed KS theory had to be used because the magnetic hessian (Section 9.6.4) is not diagonal for hybrid functionals.

The most important results gathered from all of the DFT studies that have been reported so far may be summarized as follows: (1) g -tensor calculations are only moderately sensitive to the basis sets used. Standard valence-double zeta basis sets with a single set of polarization functions yield reasonable results; (2) The effects of the gauge dependence of the g -tensor are not very large as long as the basis sets used are of reasonable quality (see (1)) and the origin is reasonably chosen; (3) The performance of different density functionals is rather similar (GGA functionals offer at best minor improvements over LDA functionals and hybrid functionals are not grossly superior to either GGA or LDA functionals); (4) The DFT methods are capable of giving reasonable to good agreement with experiment for main group radicals but none of them has been found to be capable of providing uniformly quantitative agreement with experiment for transition metal complexes.

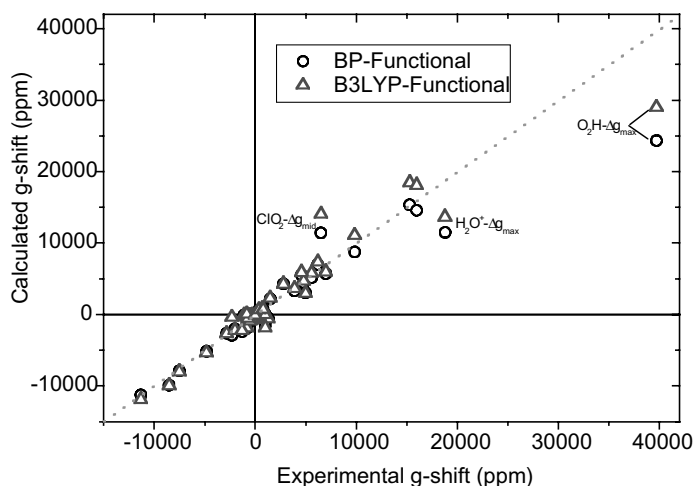


Fig. 13. Correlation between theoretical and experimental g-shifts for small radicals as predicted from two different popular density functionals. Triangles – hybrid B3LYP functional. Circles – GGA BP functional. The dotted line is a correlation line with unit slope. For individual results see Table 12.

In order to make these statements more quantitative we have compiled the results of different DFT and *ab initio* approaches for a series of small radicals in Table 12. From the table it is evident that all DFT method provide rather good agreement with the experimental values (Fig. 13). The typical error is ± 500 – 1000 ppm for most of the methods. Given that g-values are difficult to measure to an accuracy better than ≈ 100 ppm this agreement should be regarded as satisfactory, especially since none of the calculations took effects of the environment (mostly inert gas matrices) into account. From the comparison it also appears that the performance of the LDA, GGA and hybrid density functional methods is roughly comparable and that all methods perform better than the HF method. The most accurate values are delivered by the *ab initio* MR-CI method but, as discussed above, this method is not applicable to large molecules, at least not in the near future.

The application to a number of transition metal complexes is made in Table 13 and Fig. 14. Here, it is seen that the prediction of g-values is far more difficult and disagreement with the experimentally measured g-shifts by a factor of two is not uncommon. It appears that the hybrid density functionals such as B3LYP and PBE0 have a slight advantage over GGA and LSD functionals. One of the underlying reasons is that hybrid DFTs predict the covalencies of the chemical bonds in transition metal complexes somewhat better than the LSD and GGA functionals. However, even the hybrid functionals, that predict HFCs in transition metal complexes well, lead to sometimes seriously underestimated g-shifts. This has been attributed, at least in part, to too large energy denominators that make the systems too “stiff” with respect to the external perturbation provided by the magnetic field [98].

Table 12. Comparison of different ab initio and density functional methods for the prediction of the g-shifts of small radicals in doublet states (adapted from ref98).

Molecule	g-value	Exp	HF	LSD	BP	PBE	B3LYP	PBE0	GHF	MR-CI	ZORA	SZ	UDFT
CO ⁺	-2600,-3200	-3271	-2715	-2622	-2613	-2690	-2687	-2798	-2674	-2674	-3464	-3129	-2458
	0,-1400	-103	-166	-165	-163	-167	-158	-42	-178	-178	-157	-138	-93
CN	-2000	-2264	-2119	-2033	-2019	-2206	-2166	-1983			-2701	-2514	
	-800	-105	-147	-145	-143	-145	-138	-63			-186	-137	
BO	-800	-2148	-1972	-1924	-1919	-1883	-1923		-1899	-1899	-2455	-2298	
	-1100	-58	-92	-92	-92	-94	-83		-99	-99	-117	-72	
BS	-8100,-8900	-10502	-10759	-9928	-9926	-9955	-9914				-11743	-9974	
	-700,-800	-109	-127	-128	-132	-130	-127				-476	-83	
MgF	-1300	-1935	-2533	-2433	-2401	-2258	-2226	-1314	-1092	-1092	-1967	-2178	-1869
	-300	-75	-90	-88	-87	-94	-85	+20	-59	-59	-81	-60	+14
AlO	-1900,-2600		-3050	-2920	-2974	-389	-962			-2506	+855	-1222	
	-200,-900		-154	-153	-151	-170	-161			-114	-338	-142	
H ₂ O ⁺	200	-150	-183	-185	-185	-186	-182	-229	-292	-292	-780	103	-142
	18800	13124	17683	11475	11870	13624	12638	12704	16019	16019	46527	13824	10205
HCO	4800	4056	5440	4412	4491	4693	4482	3306	4217	4217	7765	5126	3702
	1500	2104	2328	2183	2184	2281	2232				3095	2749	2275
NF ₂	0	-516	-302	-307	-295	-280	-308				-175	-270	-224
	-7500	-7680	-9528	-7891	-8045	-8001	-8068				-12196	-9468	-7476
NO ₂	-100	-1062	-627	-636	-617	-680	-700	-447			-318	-738	-617
	6200	5968	7789	6970	7074	7318	7033	5649			10576	7619	6288
O ₂ H	2800	2916	4608	4264	4318	4261	4100	2892			6254	4678	3928
	3900	4265	3350	3281	3261	3606	3604	3368	3806	3806	5000	4158	3400
CO ₂ ⁻	-11300	-12590	-12283	-11270	-11288	-11871	-11839	-11008	-10322	-10322	-16000	-13717	-11229
	-300	-1212	-695	-706	-692	-724	-735	-623	-235	-235	-600	-760	-688
O ₂ H	-800	-283	-284	-305	-299	-312	-314	-690			-2150	-	-
	39720	39590	36206	24300	25124	28969	28353	37321			85158	-	-
CO ₂ ⁻	5580	5964	5445	5120	5126	5796	5748	5140			5127	-	-
	700	1007	519	490	415	750	767	805			2236	1522	-
CO ₂ ⁻	-4800	-5765	-5380	-5151	-5149	-5361	-5430	-4767			-8056	-7210	-
	-500	-966	-977	-969	-1000	-900	-901	-571			-624	-803	-

Table 12. (continued.)

Molecule	g-value	Exp	HF	LSD	BP	PBE	B3LYP	PBE0	GHF	MR-CI	ZORA	SZ	UDFT
O3-	200,1300	-1522	-457	-476	-463	-556	-576	-597	-	-	-439	-554	-
	16400,14700	23754	16590	15323	15380	18465	18565	17933	-	-	25475	19380	-
	10000,9700	16083	9170	8736	8728	11045	11260	10954	-	-	12710	10542	-
ClO2	1300	-1063	-471	-512	-504	-587	-612	-	-	-	-659	-455	-
	16000	34292	15284	14569	14634	18092	19330	-	-	-	17120	12292	-
H2CO+	6500	28225	11663	11416	11380	14051	14314	-	-	-	13428	10606	-
	200	3085	7	18	10	240	265	2976	1296	-	-286	76	-
	-800	654	-1277	-678	-750	79	122	927	-30	-	-1131	-1220	-
NF3+	4600	5794	6007	5507	5543	5905	5812	5427	5510	-	8046	6231	-
	1000	-3802	-1351	-1561	-1524	-1826	-1946	-	-	-	-373	-511	-
	7000	3984	6071	5683	5720	5964	5770	-	-	-	8241	8046	-
SiH3	1000	11	-7	1	11	-23	15	-	-	-	-147	-105	-
	5000	2155	3722	3025	3083	2952	2894	-	-	-	3679	2402	-
C3H5	0	-64	-90	-79	-79	-88	-78	-	-	-	-152	-115	-65
	400	576	701	634	639	641	633	-	-	-	854	769	497
	800	589	839	731	743	726	712	-	-	-	1023	660	603

For references to the original works see Refs. [98, 262, 271] and [246]

HF = Hartree-Fock; LSD = local spin density approximation; BP = Becke-Perdew density functional; PBE = Perdew, Burke, Ernzerhoff density functional; B3LYP = Becke-3 parameter density functional with Lee-Yang-Parr correlation part; PBE0 = PBE functional with 25% HF exchange mixed in; GF = generalized two-component Hartree-Fock; MR-CI = multireference CI; ZORA = zero order regular approximation; SZ = Gauge including atomic orbital DFT method of Schreckenback and Ziegler [262]; UDFT = spin unrestricted DFT results from Malkina et al. [271].

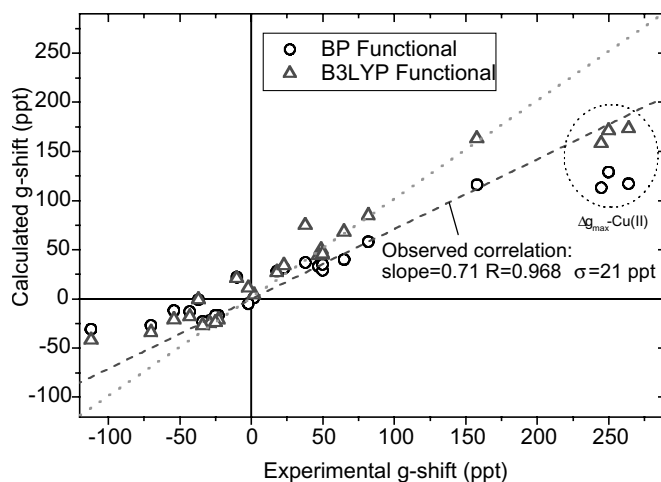


Fig. 14. Correlation between theoretical and experimental g-shifts for transition metal complexes as predicted from two different popular density functionals. Triangles – hybrid B3LYP functional. Circles – GGA BP functional. The dotted line is a correlation line with unit slope. The dashed line is the observed correlation for the B3LYP functional. For individual results see Table 13.

9.6.7.3 Some Challenges for DFT Treatments

It is presently not clear which factors are responsible for the errors in the density functionals. It appears that the excessive covalency found in the LSD and GGA functionals is a consequence of the self-interaction error in DFT as has been early on discussed by Perdew and Zunger [272]. Presently methods are being developed that correct these deficiencies [273–276] but much remains to be done before they enter the standard arsenal of mainstream computational methods. As an alternative it appears to be promising to develop density functionals that, by construction, have no self-interaction and Görling has recently developed methods that feature an exact (i. e. self-interaction free) local exchange part [277, 278]. Again, more work is needed before these methods become commonplace. Both, self-interaction corrections and exact exchange methods also solve the problem that the presently used density functionals show an erroneously fast decay of the exchange-correlation potential in the long distance limit which is responsible for the fact that orbital energies of the occupied MOs in DFT methods are several eV higher than minus the lowest ionization energy of the system [165]. A shortcoming of all presently existing DFT methods is that they do not have a dependence of the current density,

$$\mathbf{j} = -\alpha \mathbf{A} \sum_i \psi_i^* \psi_i + i \frac{\alpha}{2} \sum_i \psi_i^* \nabla \psi_i - \psi_i \nabla \psi_i^* \quad (331)$$

as they should for systems placed in magnetic fields [185, 187, 188]. Methods which do include current terms have been developed [185, 187, 188] but these are not available in standard computational packages and do not lead to the improved pre-

Table 13. Comparison of different density functional methods for the prediction of the *g*-shifts of transition metal complexes in doublet states (adapted from [98]).

Exp.	Neese [98]		Malkina et al. [271]		PZ/SZ [262]		ZORA [268, 198, 98]	
	BP	B3LYP	PBE0	BP	BP	BP	BP	
TiF ₃	-0.9	-1.1	-1.2	-1.1	-1.7	-0.7*	-0.7*	
	-111.1, -3.7	-41.8	-46.1	-26.6	-42.8	-64.7*	-64.7*	
VOF ₄ ²⁻	-30.7	-34.1	-36.1	-	-36.0	-58.8	-58.8	
	-111.9, -123.7	-25.0	-26.4	-	-28.0	-51.1	-51.1	
VOCl ₄ ²⁻	-21.9	-20.5	-23.7	-	-18.0	-32.2	-32.2	
	-54	-20.6	-22.1	-	-20.0	-27.3	-27.3	
CrOF ₄ ⁻	-17.2	-18.1	-19.6	-13.6	-19.0	-33.5	-33.5	
	-43	-27.0	-29.2	-21.8	-29.0	-50.7	-50.7	
CrOCl ₄ ⁻	-22.6	+20.6	+16.9	+20.3	+18.0	+22.7	+22.7	
	-10	-23.7	-26.8	-18.1	-21.0	-26.7	-26.7	
Ni(CO) ₃ H	-16.9	4.3	5.4	1.3	-	-2	-2	
	2	67.7	77.8	39.8	-	46	46	
Ni(mnt) ₂ ⁻	65	11.3	26.0	-	-	-28	-28	
	-2, -12	75.2	95.1	-	-	31	31	
Cu(acac) ₂	38	163.2	211.8	-	-	99	99	
	158, 138	46.2	51.9	30.6	-	26.4	26.4	
[Cu(NH ₃) ₄] ²⁺	48.7, 49.6	50.3	55.8	34.7	-	33.0	33.0	
	48.7	173.0	193.3	115.5	-	126.9	126.9	
Cu(dtc) ₂	285.2, 263.8	158.4	175.8	-	-	119.8	119.8	
	245	44.2	49.3	-	-	31.1	31.1	
Cu(NO ₃) ₂	47	27.0	31.1	-	-	11.3	11.3	
	18.0	33.9	36.7	-	-	22.1	22.1	
Cu(NO ₃) ₂	23.0	85.0	100.4	-	-	44.2	44.2	
	82.0	44.6	50.3	28.2	-	27.0	27.0	
Cu(NO ₃) ₂	49.9	46.0	51.5	31.0	-	29.2	29.2	
	49.9	171.2	191.3	116.3	-	126.9	126.9	
246.6	128.9	191.3	116.3	-	126.9	126.9		

For original references see [98, 262] and [271]. For other abbreviations see caption to Table 12.

diction of magnetic properties [187, 188]. A subtle problem is that the SOC is a two electron operator but only the one-electron electron and spin densities are known in DFT. It is not clear how to calculate two electron properties in this approach. While the use of the non-interacting reference wavefunction in place of the real many electron wavefunction appears to give reasonable results in many cases, it is clear that it does not have a Coulomb hole and therefore may give erroneous results for operators that are strongly dependent on the interelectronic distance (as is the case for the two electron part of the SOC).

From these considerations and the results presented in the previous section, the prediction of g -values by DFT methods is presently under development and already provides a powerful complement to experimental studies. However, a number of problems need to be solved before DFT has the same accuracy for the prediction of g -values that has been obtained for the prediction of energetic quantities like reaction or atomization energies [174].

9.6.8 Calculation of Hyperfine Couplings

According to the discussion in Sections 3.4.3, 3.5.4, and 4.1.7 there are three distinct contributions to the HFCs which are: (a) the Fermi-contact term, (b) the spin-dipolar contribution and (c) the spin-orbit coupling contribution. The first two terms are of first order and the third term is of second order. The three terms behave differently for the metal and ligand nuclei and are also associated with different technical challenges. We therefore first review the concept of spin-polarization in the case of transition metal complexes, then turn to the technical aspects of performing calculations for HFCs and finally separately discuss the metal- and ligand HFCs.

9.6.8.1 Spin Polarization in Transition Metal Complexes

The concept of spin-polarization has been found to be extremely useful for understanding the HFCs of organic radicals which are dominated by the Fermi contact contribution [279, 280]. The situation for transition metal complexes is rather different in several respects. The present discussion is based on a study by Munzarova, Kubacek and Kaupp [281] which follows the classic work by Watson and Freeman [282].

The idea of spin polarization is relatively simple and is best understood from the UHF energy expression (Eq. 295). According to this expression the electron repulsion that a given electron feels is obtained by summing up the interactions with all other electrons. Electrons of like spin contribute a positive Coulomb integral and a *positive* exchange integral but with a *negative* sign to the repulsion, while electrons of opposite spin only contribute positive Coulomb integrals. Consequently, the interelectronic repulsion is minimized within the set of spin-up electrons if the exchange interaction with the singly occupied MOs is maximized. This means that the optimum situation for spin-up electrons is different than for spin-down electrons because there is a larger number of spin-up than spin-down electrons in open shell

molecules. Consequently the shape of the spin-up orbitals will be slightly different than for the spin-down electrons and upon taking the difference of the squares of the orbitals a net spin density arises even from the formally doubly occupied MOs. However, the spin-up orbitals must stay mutually orthogonal and overall the virial theorem (potential energy/kinetic energy equals two) must be obeyed. In general, orbitals that have little spatial overlap with the singly occupied orbitals are distorted towards the singly occupied orbitals and orbitals that occupy the same region in space are “repelled”. Thus, in organic radicals where the singly occupied orbitals are of the 2p type the spin-up 2s orbitals are repelled from the singly occupied MOs leaving a net *positive* contribution to the spin density at the nucleus while the spin-up 1s orbitals are attracted towards the 2p shell which leaves a *negative* spin-polarization at the nucleus [281]. Prototypical examples are the proton HFCs in the methyl radical or the benzene anion radical.

A similar, but more complicated situation exists in first row transition metal complexes. Here the singly occupied MOs are derived from the metal 3d-orbitals. Thus, the 3s shell is polarized to leave *positive* spin density at the nucleus because the 3s and 3d shells occupy a similar region in space. By contrast, the 2s shell is polarized in the opposite direction and leaves a *negative* spin density at the nucleus. The 1s shell is also polarized to give negative spin density but here the spin-polarization is found to be very small.

Again, we follow Munzarova et al. [281] and illustrate the points by plotting the radial distribution functions for the neutral Mn atom (Fig. 15). It is evident from the figure that the orbitals with the same main quantum number occupy similar regions in space and are relatively well separated in space from the next higher and next lower shell. In particular, the 4s orbital is rather diffuse and shows its maximum close to typical bonding distances while the 3d orbitals are much more compact.

At the resolution of the plot in Fig. 15, the spin-polarization of the spin-up and spin-down components is barely visible. Therefore the difference of the densities of each orbital is plotted in the inner atomic region in Fig. 16. It is clearly observed in this plot how the 3s shell is polarized to give a positive spin-density at the nucleus while the 2s shell is negatively polarized. The spin-polarization of the 1s shell is very small and contributes very little spin density at the nucleus. The contribution of the 4s subshell is also large and parallels that of the 3s subshell. As long as the 4s subshell is not occupied as is the case with most di- and trivalent ions of the first transition row the negative contribution of the 2s subshell is larger than the contribution from the 3s subshell and the net spin density at the nucleus is negative which results in a large negative contribution to the metal HFC.

The analysis by Munzarova et al. [281] suggests the following interpretation of these findings: the polarization of the metal 2s shell is due to the enhanced exchange interaction with the singly occupied metal 3d orbitals and causes the spin-up 2s orbital to move closer to the metal 3d subshell which leaves a net negative spin density at the nucleus. The behavior of the 3s subshell is strictly opposite to that of the 2s subshell (Fig. 16). The reason for this is the orthogonality requirement between the 2s and the 3s orbital. Thus, the exchange interaction between the 3d and 3s shells is *not* optimized by the spin-polarization. On the contrary, this exchange interaction is increased. The reason for the 2s subshell spin-polarization dominating

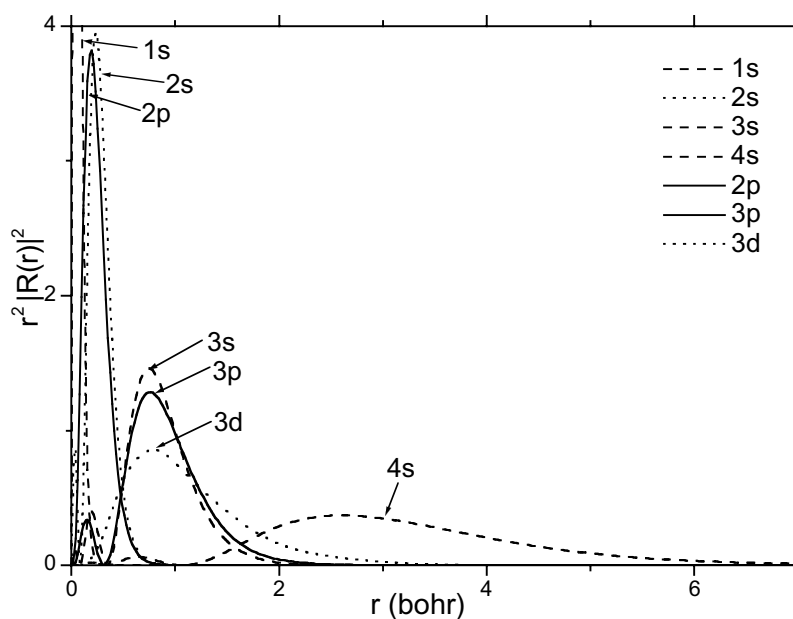


Fig. 15. Normalized radial distribution function for the neutral Mn atom ($3d^5 4s^2; {}^6S$) as calculated by the UHF method.

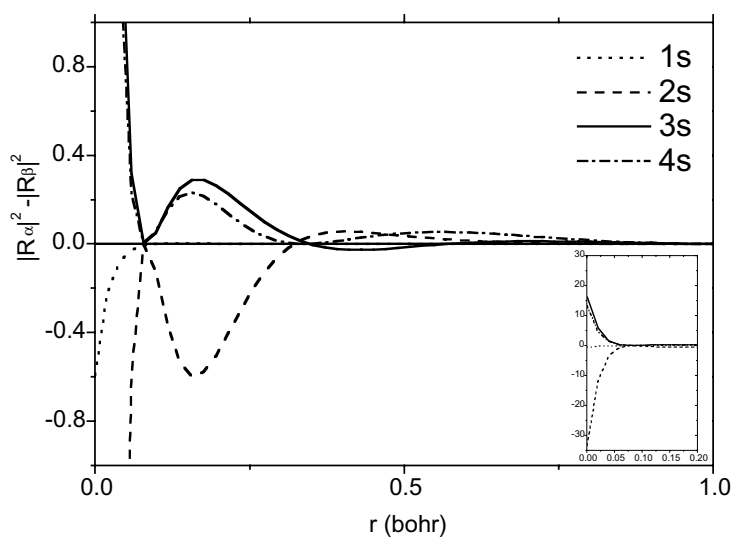


Fig. 16. Spin-polarization of the s-orbitals in the neutral Mn atom ($3d^5 4s^2; {}^6S$) as calculated by the UHF method. The inset shows the region at the nucleus in more detail.

over the 3s one is that the *gain* in 2s/3d exchange energy is larger than the possible 3s/3d exchange gain. In other words, there is little to gain by distorting the 3s shell but much to gain by distorting the 2s subshell. Therefore, the 3s subshell merely reacts to the distortion of the 2s subshell rather than taking an “active” role in the spin polarization and these changes are necessary in order to “re-equilibrate” the total energy and wavefunction according to the virial theorem and the orthogonality requirements. Similar considerations apply to the very small spin-polarization of the 1s shell. (It should be noted, however, that the percentage spin-polarization of the 3s shell is larger than that of the 2s shell. Because of the much larger value of the 2s orbital at the nucleus, however, the negative contribution to the spin density must dominate.)

9.6.8.2 Metal Hyperfine Couplings

For the calculation of metal HFCs three contributions must be taken into account: (1) the isotropic HFCs which is directly proportional to the spin density at the nucleus, (2) the metal dipolar coupling which is proportional to the spin density in the metal p- and d-orbitals and (3) the SOC corrections to the HFC (Sections 9.3.4.3, 9.3.5.4, and 9.4.1.7). The three contributions have rather different demands in computational complexity and will be discussed in turn.

9.6.8.2.1 Isotropic HFCs

If the formally singly occupied orbitals do not carry significant 4s character, the isotropic metal HFCs arise from the subtle spin-polarization mechanisms described above. In order to describe this spin-polarization accurately (i. e. close to the basis set limit), it is necessary to use basis sets that are flexible in the core region. Unfortunately Gaussian functions that are commonly used in electronic structure calculations have a poor behavior close to the nucleus where they lack the characteristic “cusp” (for a review see [149, 283]). It is then necessary to include primitive Gaussian orbitals in the basis that have very large exponents in order to mimic the cusp behavior. Given this, it appears that isotropic HFCs can be well predicted with Gaussian basis sets. Slater orbitals are better in that the 1s orbitals have the correct cusp behavior and a finite amplitude at the nucleus and therefore convergence to the basis set limit should be faster with these basis functions. However, for high-quality basis sets the difference between the two approaches will vanish. It is important to point out that the standard basis sets used for quantum chemical calculations and that are widely available in the commercial packages are *not* suitable for HFC predictions because they lack the essential flexibility in the core region. Barone has standardized basis sets for HFC calculations and these are available for first row atoms [284]. No basis sets appear to have been standardized for transition metals.

Since the spin-polarization of the core is so important for the accurate predictions of metal HFCs, spin-restricted wavefunctions can not be used for the prediction of this property. Unfortunately, the UHF method is known to overestimate the spin-polarization and therefore to give HFCs that are too negative. Munzarova and Kaupp have performed a comparison between high-level correlated *ab initio*

and DFT methods and have found that DFT in the LDA and GGA variants *underestimates* the core polarization and therefore tends to give isotropic HFCs that are too small in magnitude [131, 285]. Thus, once again, the hybrid density functionals that mix in part of the HF exchange into the DFT formalism appear to give an error compensation that adjusts the isotropic HFCs in the right direction. However, according to Munzarova and Kaupp, there is caveat here that is caused by the spin contamination [285]. If the spin-polarization is caused by significant spin contamination ($\langle S^2 \rangle$ significantly different from $S(S+1)$), the results of the hybrid DFTs tend to get unreliable. In conclusion, Munzarova and Kaupp in their study of 21 representative transition metal complexes have not found a density functional that performs satisfactory for all types of bonding situations. DFT is nevertheless the method of choice for the prediction of isotropic HFCs due to the lack of computationally attractive alternatives and its much better performance compared to HF methods [285]. Indeed, a number of workers have found DFT to be a useful tool in the calculation of transition metal HFCs [199, 259–261, 268–270, 285–290]. If the 4s contribution to the formally singly occupied MOs is significant more or less all of the presently used functionals give good predictions of isotropic metal HFCs [285].

9.6.8.2.2 Dipolar HFCs

The anisotropic HFCs depend on the expectation value of the r^{-3} operator which becomes large for tight orbitals. Thus, it is also advisable to have flexible basis sets that describe the tight p- and d-functions. For first row atoms, the 2p orbitals are valence orbitals and standard basis sets are suitable for dipolar HFC predictions. For first row transition metal complexes the most important orbitals are the 3d ones and these have to be described accurately anyway, probably at least with triple-zeta quality basis sets [291].

It has been widely assumed in the analysis of transition metal HFCs that spin-polarization is unimportant for the anisotropic HFCs and thus, the anisotropic couplings can be used to estimate the metal contribution to the singly occupied MOs. However, Belanzoni et al. [260] found a significant effect of spin-polarization to the dipolar HFCs of TiF_3 . The same conclusion was reached and analyzed in depth by Munzarova et al. [285] who point out that the same mechanisms that lead to the spin-polarization of their 2s and 3s shells will also polarize the 2p and 3p shells. Since the expectation values over the r^{-3} operator are one to two orders of magnitude larger for the 2p and 3p orbitals than for the 3d orbitals (for example, for the neutral Mn atom the HF values for 2p, 3p and 3d are 403.03 au^{-3} , 46.58 au^{-3} and 4.10 au^{-3} respectively) relatively small spin-polarization contributions from the 2p and 3p shells can significantly influence the dipolar metal HFCs. The contribution from the 2p subshell has been estimated to be 5–10% of the total A_{dip} for some complexes containing Mn [285]. However, the contribution of 3p tends to cancel the 2p polarization and the net effect is a limited contribution from core polarization. The valence shell polarization may also influence the dipolar HFCs and will vary greatly between different systems. So far only limited computational experience with these effects is available [260, 285]. It appears that they are present and

should be included in the analysis. While it is unlikely that they will obscure the ligand field description, they add another complication in the analysis.

9.6.8.2.3 SOC Contributions

Limited experience is available for the SOC contributions to the metal HFCs. The early work of Geurts et al. [259] used the equations derived by Keijzers and De-Boer to successfully estimate the effects for $[\text{Cu}(\text{dte})_2]$ and the same methodology was used by Belanzoni et al. to discuss the HFCs in TiF_3 [260, 261] as well as by Noodleman to discuss the properties of 2Fe/2S Ferredoxins [292]. The only generally available, modern method is the ZORA method of van Lenthe and co-workers [199]. It has been used in a number of studies and has demonstrated its ability for the prediction of SOC contributions in a similar way to the g-tensor. Belanzoni et al. [270] have used this method to obtain insight into the metal HFCs of a series of 22 small, linear molecules that contain transition metals. The results are in good agreement with experiment. The calculations highlight the importance of both, spin-polarization and SOC on the metal HFCs. In addition it is pointed out that in highly accurate models finite sized nuclei should be employed, at least for the heavy elements like mercury or gold [270]. Recently, Stein et al. [268, 269] have used the ZORA method to calculate the SOC contributions to the metal HFCs for a series of Ni complexes that are designed to mimic the active site of hydrogenases with mostly encouraging results. The importance of SOC contributions to the metal HFCs has been stressed in this study. The limitations of the ZORA approach are the same as for g-tensor calculations – presently it is only available in spin-restricted form and for a single unpaired electron. However, the necessary generalizations are said to be under development [199, 268–270]. From the discussion in Section 9.6.4 it is clear that CP-SCF theory is an attractive alternative to the ZORA method, at least throughout the first transition series where perturbation theory appears to be satisfactory for the inclusion of SOC. In this case spin-polarization and extension to all ground state spins S is straightforward [75].

9.6.8.3 Ligand Hyperfine Couplings

Compared to metal HFCs ligand HFCs are somewhat easier to calculate because the SOC contributions are much smaller. Therefore somewhat more experience is available for these terms.

The early study of Geurts et al. showed that good agreement with experiment could be obtained for $[\text{Cu}(\text{dte})_2]$ using the Hartree–Fock–Slater (HFS) variant of DFT [259]. Belanzoni et al. discussed the fluorine HFCs in TiF_3 [260, 261] and more recently reported a study of a series of small transition metal containing molecules [270]. The ZORA method has been developed and tested by van Lenthe et al. for HFC calculations [199]. Stein et al. applied this method to predict the HFCs of several intermediates in the reaction cycle of Hydrogenases [269] and also reported a detailed evaluation study on the two Ni complexes $[\text{Ni}(\text{mnt})_2]^-$ and $[\text{Ni}(\text{H})(\text{CO})_3]$ [268]. Rather satisfactory agreement with experiment was obtained for HFCs to ^1H , ^{13}C , ^{14}N and ^{33}S by using standard GGA functionals and spin polarized, scalar

relativistic ZORA calculations. More traditional DFT calculations in $[\text{Ni}(\text{mnt})_2]^-$ were also reported but the basis sets used were not flexible in the core region and SOC was not considered [289]. It appears that the performance of GGA and hybrid density is rather similar in these systems. Knight et al. have reported a rather detailed experimental as well as HF and DFT study the ^{17}O HFCs in ScO, YO and LaO [288]. The result given by the B3LYP method compared favorably with the experimental values while the HF calculations were not successful. In another recent study Jaszewski and Jezerska have computed HFCs for the blue copper protein Azurin and its M121Q mutant with the B1LYP hybrid functional [293]. The agreement for the copper HFC was unsatisfactory because SOC effects have not been taken into account. The ligand HFCs for the directly coordinating nitrogens compared favorably with the experimental values with the isotropic values being slightly underestimated and the dipolar contributions slightly overestimated by the calculations. The large proton HFCs arising from one of the cysteine C_β -protons was predicted too large by a factor of almost two. Smaller nitrogen and proton HFCs were predicted in qualitative agreement with experiment. These studies consistent with the well-understood electronic structure of blue copper centers [133, 136–141, 294] and show that quantum chemical calculations can help to understand high resolution magnetic resonance experiments [295–299].

9.6.8.3.1 Ligand HFCs in Cu(II) Complexes

A DFT study of ^{14}N HFCs in Cu(II) complexes was recently been reported [290]. Complexes of Cu(II) were chosen because the singly occupied MO is the one that is most involved in the bonding to the ligand and therefore will most clearly show the shortcomings of DFT in describing these bonds.

9.6.8.3.2 Breakdown of Ligand HFC Contributions

In the interest of interpreting the calculated HFCs it is instructive to decompose Eqs. (142) and (143) into several parts:

$$A_{iso}^A = A_{iso;loc}^A + A_{iso;nonloc}^A \quad (332)$$

$$\mathbf{A}^{(A;d)} = \mathbf{A}_{1-center}^{(A;d)} + \mathbf{A}_{2-center}^{(A;d)} + \mathbf{A}_{3-center}^{(A;d)} \quad (333)$$

The local contribution to the isotropic HFC arises from the spin density in the s-orbitals on atom A and the one-center contribution to the dipolar HFC is due to the spin-density in the ligand p-orbitals as outlined in Section 9.4.1.7.2. The non-local correction to the isotropic HFC divides into two parts:

$$A_{nonloc}^A = A_{nonloc-cf}^A + A_{nonloc-bond}^A \quad (334)$$

$$A_{nonloc-cf}^A = \frac{4\pi}{3S} P^A \sum_{B \neq A} \sum_{C \neq A} \sum_{\mu}^B \sum_{\nu}^C P_{\mu\nu}^{\alpha-\beta} \varphi_{\mu}^B(\vec{R}_A) \varphi_{\nu}^C(\vec{R}_A) \quad (335)$$

$$A_{nonloc-bond}^A = \frac{8\pi}{3S} P^A \sum_{B \neq A} \sum_{\mu}^B \sum_{\nu}^A P_{\mu\nu}^{\alpha-\beta} \varphi_{\mu}^B(\vec{R}_A) \varphi_{\nu}^A(\vec{R}_A) \quad (336)$$

The superscript on the summation indicates that the sum includes only the basis functions that belong to the indicated atom. The non-local part is divided into a “crystal-field” contribution involving basis functions are on neighboring atoms and a “bond” contribution, where only one function is located on another center. The two-center corrections to the first-order anisotropic part of the nitrogen HFC also divide into “crystal-field” and “bond” contributions:

$$\mathbf{A}_{2\text{-center}}^{(A;d)} = \mathbf{A}_{2\text{-center};cf}^{(A;d)} + \mathbf{A}_{2\text{-center};bond}^{(A;d)} \quad (337)$$

where:

$$\mathbf{A}_{2\text{-center};cf}^{(A;d)} = P^A \sum_{B \neq A} \sum_{\mu}^B \sum_{\nu}^B P_{\mu\nu}^{\alpha-\beta} \langle \varphi_{\mu}^B | \hat{\mathbf{F}}(\mathbf{R}_A) | \varphi_{\nu}^B \rangle \quad (338)$$

$$\mathbf{A}_{2\text{-center};bond}^{(A;d)} = 2P^A \sum_{B \neq A} \sum_{\mu}^B \sum_{\nu}^A P_{\mu\nu}^{\alpha-\beta} \langle \varphi_{\mu}^B | \hat{\mathbf{F}}(\mathbf{R}_A) | \varphi_{\nu}^A \rangle \quad (339)$$

The “crystal-field” contribution arises from the spin density located at remote atoms. At large distances this term can be presented by a point-dipole approximation (*vide infra*). The “bond” contribution arises from the unpaired spin density in the bonds surrounding atom *A*. Finally, the three-center terms arise from the spin density in remote bonds and are given by:

$$\mathbf{A}_{3\text{-center}}^{(A;d)} = P^A \sum_{B \neq A} \sum_{C \neq A, B} \sum_{\mu}^B \sum_{\nu}^C P_{\mu\nu}^{\alpha-\beta} \langle \varphi_{\mu}^B | \hat{\mathbf{F}}(\mathbf{R}_A) | \varphi_{\nu}^C \rangle \quad (340)$$

This partitioning has been applied in Ref. [290]. A similar partitioning has been carried out before by Keijzers and Snaathorst and the individual terms were evaluated with STO-6G fits to extended Hückel orbitals for [Cu(dtc)₂] [300].

9.6.8.3.3 Directly Coordinating Ligands

For directly coordinating ligands one expects the one-center contributions to dominate the ligand HFCs as was assumed in Section 9.4.1.7.2. The example of [Cu(NH₃)₄]²⁺ is shown in Table 14 [290]. It is observed, that the values are dominated by the one-center parts. However, this result is due to a near cancellation of

Table 14. One, two and three center contributions to the calculated HFCs in [Cu(NH₃)₄]²⁺ using the B3LYP functional. (reproduced from Ref. [290]).

	A_{iso}^N (MHz)	$A_{dip-max}^N$ (MHz)	$A_{dip-mid}^N$ (MHz)	$A_{dip-min}^N$ (MHz)
1-Center	34.96	-4.93	-4.95	9.87
2-Center crystal field	-0.02	-0.68	-0.53	1.21
2-Center bond	2.76	+0.47	+0.45	-0.91
3-Center	0.06	<0.01	<0.01	<0.01
Total	37.76	-5.09	-5.03	10.12

the two-center bond and point-charge terms that are of similar magnitude but opposite sign. Since the two contributions have a different distance dependence (*vide infra*), the cancellation is expected to be system dependent and a 10–20% contribution from two-center terms to the ligand HFC is not unreasonable. Three center terms are apparently negligible.

9.6.8.3.4 Remote Ligands

It is often found in ENDOR and ESEEM experiments that remote nuclei (in particular protons) show HFCs even if these nuclei carry no or very little spin density on their own. In addition, these HFCs are anisotropic even though protons do not have p-orbitals available that would give dipolar HFCs. The origin of these HFCs are twofold: (a) very small residual spin densities that give rise to isotropic HFCs and (b) through space dipolar couplings. The through space dipolar couplings are the more interesting because they carry geometric information that is the basis of extracting structural information from ENDOR and ESEEM data. The relation to the more rigorous theory is made with reference to the partitioning described above. For protons, both the one-center and the three center contributions to the dipolar HFCs are negligible. However, the two two-center terms have a rather different distance dependence. The two-center bond contributions have the two basis functions located on different centers and therefore these contributions mainly reflect orbital overlap that decays exponentially with distance. For ligands in the second coordination sphere or even further these contributions become small. The “crystal-field” contribution to the dipolar HFCs is, in more detail:

$$\mathbf{A}_{dip-2-centre;cf}^A = P^A \sum_{B \neq A} \sum_{\mu}^B \sum_{\nu}^B P_{\mu\nu}^{\alpha-\beta} \cdot \int \varphi_{\mu}^B(\mathbf{r} - \mathbf{R}_B) \varphi_{\nu}^B(\mathbf{r} - \mathbf{R}_B) \hat{\mathbf{F}}(\mathbf{R}_A) d\mathbf{r} \quad (341)$$

at large distances $|\mathbf{R}_A - \mathbf{R}_B|$ it is reasonable to “collapse” the product of the two orbitals under the integral to a delta-function $\varphi_{\mu}^B(\mathbf{r} - \mathbf{R}_B) \varphi_{\nu}^B(\mathbf{r} - \mathbf{R}_B) \rightarrow \delta_{\mu\nu} \delta(\mathbf{r} - \mathbf{R}_B)$ (point charge approximation). Thereby one gets:

$$\mathbf{A}_{\mu\nu}^{(A;d)} \approx P^A \sum_{B \neq A} \rho_B R_{AB}^{-5} \{ R_{AB}^2 \delta_{\mu\nu} - 3 R_{\mu}^{BA} R_{\nu}^{BA} \} \quad (342)$$

where R_{AB} is the distance between centers A and B and $\mathbf{R}^{BA} = \mathbf{R}_B - \mathbf{R}_A$. The quantity ρ_B is the brut spin population on center ρ_B given by $\rho_B = \sum_{\mu}^B P_{\mu\mu}^{\alpha-\beta}$. It is *not* the Mulliken spin population since these would contain overlap terms. Consequently $\sum_B \rho_B \neq 1$. In addition, one frequently finds expressions for the point dipole approximation that incorporate the molecular g-values. However, these expressions do not follow easily from the general theory of HFCs. The numerical performance of the point dipole approximation is shown in Fig. 17, where the “crystal-field” contribution to the zz-component of the HFC of a proton located along the positive z-axis of a unit spin density spin-carrying center. It is observed that the point dipole approximation fails badly for small distances where it diverges whereas it gives a fairly good approximation to the exactly evaluated HFC at distances larger than

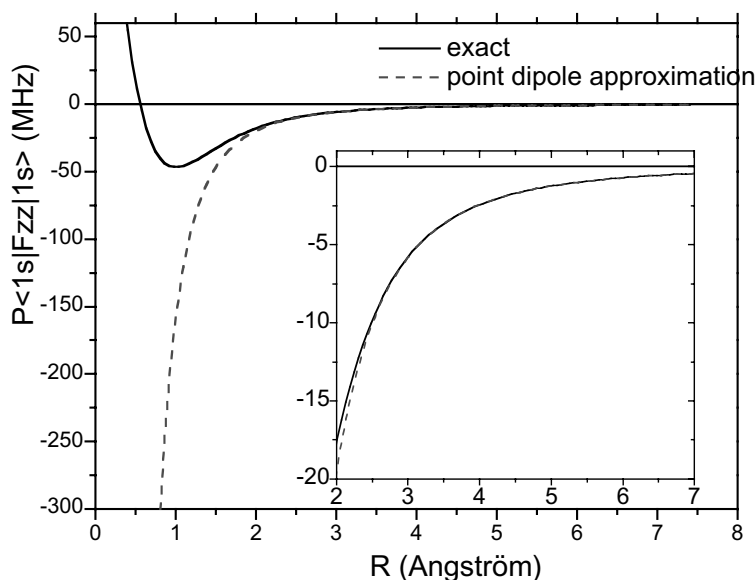


Fig. 17. Comparison of the point dipole approximation to exactly evaluated “crystal-field” contributions to the HFC of a proton located along the positive z -axis of a center that carries a unit spin density. The $1s$ orbital of the hydrogen was approximated by a single Slater orbital with exponent 1.2.

2 Angström. Thus, the point dipole approximation will be unreliable for protons directly bound to spin carrying centers but allows reliable estimates of distances of more distant protons.

9.6.8.3.5 Covalency

The results of the study show that the HF method largely underestimates the ligand HFCs which can be traced back to a bonding description which is far too ionic. For example, for $[\text{Cu}(\text{NH}_3)_4]^{2+}$, the HF method predicts a spin density on the copper of $\approx 90\%$ which is far too high based on the combined analysis of optical spectra, g -values, metal HFCs and ligand HFCs. The GGA functionals were found to overestimate the ligand HFCs and this has been taken as further evidence for the commonly held belief that the GGA functionals tend to overestimate the covalency of metal–ligand bonds. The best results were found for hybrid density functionals that appear to lead to error compensation. While either the hybrid or GGA functionals predict reasonably accurate values for the isotropic HFCs, all density functionals overestimated the dipolar ligand HFCs by about a factor of two. This result can be clearly seen in Fig. 18. Either hybrid or GGA functionals predict the isotropic HFCs in a series of Cu(II) complexes with nitrogen donors within a few MHz of the experimental values. Both types of density functionals significantly overestimate the dipolar couplings ($A_{\text{max}}^{(N;d)} - A_{\text{min}}^{(N;d)}$) with the GGA functionals being worse than the hybrid functionals.

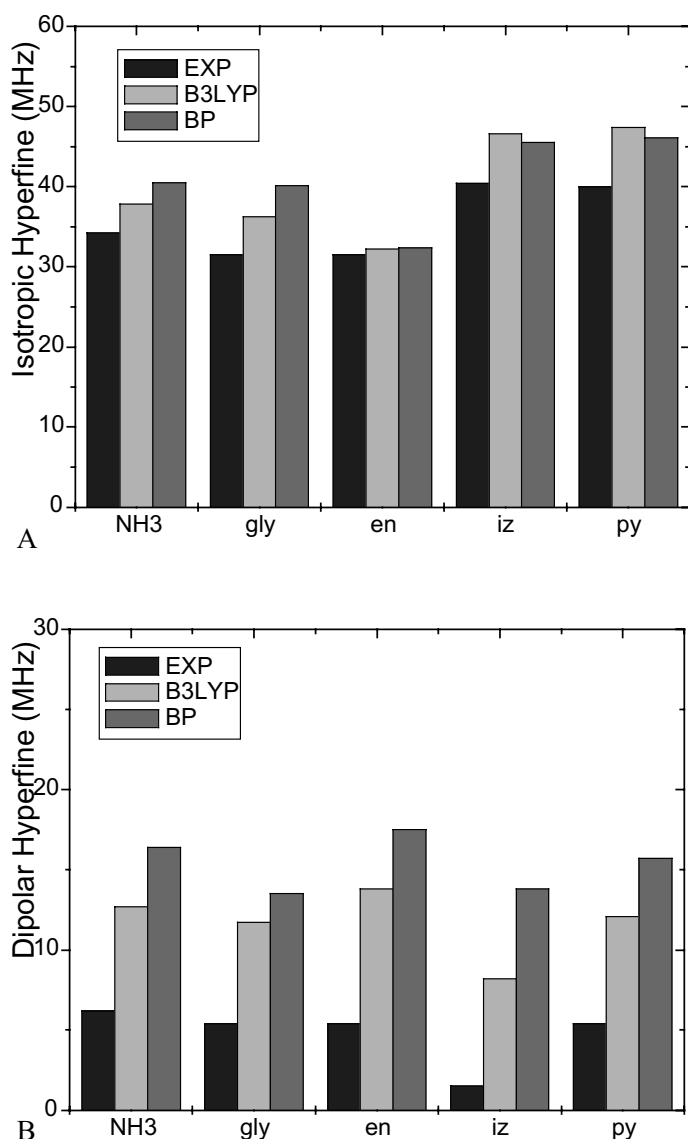


Fig. 18. Comparison of theoretically calculated and experimental ligand HFCs in a series of Cu(II) complexes. A gradient corrected (BP86) and a hybrid (B3LYP) density functional were used. (A) isotropic HFCs, (B) dipolar HFCs. Abbreviations used for ligands – NH3 = ammonia, gly = glycine, en = ethylenediamine, iz = imidazole, py = pyridine.

This result has been attributed to a spin-polarization of the valence shell that is too low and a spin density on the ligands that is too high [290]. Spin density in the out-of-plane ligand orbitals will tend to cancel the direct sigma contribution to

the HFCs and will thereby reduce the observed anisotropy of the HFCs. This is, however, precisely what is observed experimentally, where for example Scholl and Hüttermann in their ENDOR study of $[\text{Cu}(\text{imidazole})_4]^{2+}$ did not find significant anisotropy in the ^{14}N -HFC tensor [301].

9.6.8.3.6 SOC Contributions

Scalar relativistic and SOC contributions to the ligand HFCs have also been evaluated and were both found to be negligible (<1 MHz) [290]. This is in qualitative agreement with the results of Stein et al. who found limited contributions from SOC to the HFCs of light ligand nuclei while they may become discernible for second- and third-row atoms [268, 269] that form highly covalent bonds to the metal, such as is the case for sulfur.

9.7 Concluding Remarks

In this review we have tried to provide a rather detailed and self-contained overview of the origin of spin Hamiltonian parameters in transition metal complexes. The treatment started from a fairly general point of view with many electrons wavefunctions and was simplified up to the point where the ligand field expressions were obtained. We hope that in this process it became evident which approximations have to be introduced in order to arrive at these expressions and in which way they have to be generalized in more detailed treatments. It is also evident that ligand field theory forms a firm basis for understanding most of the general features of SH parameters in transition metal complexes. However, the numerical predictions of ligand field theory may not be highly accurate due to the crudeness of some of the approximations made, especially in the treatment of anisotropic covalency.

We have then proceeded to several case studies for which detailed experimental results are available and have stressed the impact of excited state data for getting insight into the observed ground state magnetic properties. In particular, excited state methods offer the information necessary to invert the underdetermined ligand field equations for covalency parameters. In addition excited state methods feature independent selection rules that are also related to metal–ligand covalent bonding and thereby complement the ground state magnetic resonance methods.

Finally we have outlined the present state of the art of first principle computational methods for predicting SH parameters in transition metal complexes. While it appears that the general theory of SH parameters is fairly well understood, the goal of predicting these parameters with high accuracy (i. e. comparable to experiment) has only partially been met. However, the existing methods do provide a highly useful complement to experiment, in particular for hyperfine couplings. In addition, new methods are rapidly emerging and there are good reasons to be optimistic about the future of SH calculations.

The development of these methods is important to critically evaluate the validity of the bonding descriptions provided by the calculations. If the agreement between

calculation and experiment is good, one can have confidence that the calculated bonding scheme is also reasonable and can then be used to obtain insight into the electronic structure and reactivity of short lived intermediates along a given reaction coordinate.

9.8 Appendix: Calculation of Spin-Orbit Coupling Matrix Elements

According to the discussion in Section 9.3.2.2 it is customary to write the spin-orbit coupling operator in molecules as an effective one electron operator:

$$\begin{aligned}\hat{H}_{SO} &= \sum_{A,i} \xi(r_{Ai}) \vec{l}_A(i) \vec{s}(i) \\ &= \sum_{p=x,y,z} \sum_{A,i} \xi(r_{Ai}) l_{A,p}(i) s_p(i) \\ &= \sum_{m=0,\pm 1} (-1)^m \sum_{A,i} \xi(r_{Ai}) l_{A,-m}(i) s_m(i)\end{aligned}\quad (343)$$

where $r_{iA} = |\vec{r}_i - \vec{R}_A|$, the distance of the i th electron to nucleus A . As the total spin is given by the sum over the individual spins of all electrons ($\vec{S} = \sum_i \vec{s}(i)$) and spin operators for different electrons commute ($[\vec{s}(i), \vec{s}(j)] = 0$, for $i \neq j$) it follows that each $\vec{s}(i)$ is of "type T" [90] with respect to the total spin \vec{S} .

$$\begin{aligned}[S_x, s_x(j)] &= 0 & [S_x, s_y(j)] &= +i\hbar s_z(j) & [S_x, s_z(j)] &= -i\hbar s_y(j) \\ [S_y, s_x(j)] &= -i\hbar s_z(j) & [S_y, s_y(j)] &= 0 & [S_y, s_z(j)] &= -i\hbar s_x(j) \\ [S_z, s_x(j)] &= +i\hbar s_y(j) & [S_z, s_y(j)] &= -i\hbar s_x(j) & [S_z, s_z(j)] &= 0\end{aligned}\quad (344)$$

This leads to a replacement theorem:

$$\langle \alpha S M | S_m | \alpha' S' M' \rangle = \begin{pmatrix} S' & 1 & S \\ M' & m & M \end{pmatrix} \langle \alpha S || S || \alpha' S' \rangle \quad (345)$$

$$\langle \alpha S M | s_m(i) | \alpha' S' M' \rangle = \begin{pmatrix} S' & 1 & S \\ M' & m & M \end{pmatrix} \langle \alpha S || s || \alpha' S' \rangle \quad (346)$$

If both matrix elements are non-zero the ratio of the two equations can be taken and rearrangement leads to:

$$\begin{aligned}\langle \alpha S M | s_m(i) | \alpha' S' M' \rangle &= \langle \alpha S M | S_m | \alpha' S' M' \rangle \frac{\langle \alpha S || s || \alpha' S' \rangle}{\langle \alpha S || S || \alpha' S' \rangle} \\ &= \langle \alpha S M | S_m | \alpha' S' M' \rangle \gamma\end{aligned}\quad (347)$$

where γ is a constant. For the present purpose a slightly more powerful form is required. the Wigner-Eckhardt theorem [23, 24] for vector operators can be applied

to an operator of the form $\sum_i f(i)s_m(i)$ to yield:

$$\left\langle \alpha SM \left| \sum_i f(i)s_m(i) \right| \alpha' S' M' \right\rangle = \begin{pmatrix} S' & 1 & S \\ M' & m & M \end{pmatrix} \left\langle \alpha S \left| \sum_i f(i) \right| \alpha' S' \right\rangle \quad (348)$$

This equation is valid because every $s_m(i)$ is proportional to S_m and this in turn is proportional to the Clebsch–Gordon coefficient. The reduced matrix element can be calculated for any convenient choice of m .

Equation (348) finally allows the matrix elements for the spin–orbit coupling operator (343) to be written as:

$$\begin{aligned} & \left\langle \alpha SM \left| \sum_m (-1)^m \sum_{A,i} \xi(r_{Ai}) l_{A,-m} s_m \right| \alpha' S' M' \right\rangle \\ &= \sum_m (-1)^m \begin{pmatrix} S' & 1 & S \\ M' & m & M \end{pmatrix} \left\langle \alpha S \left| \sum_{A,i} \xi(r_{Ai}) l_{A,-m} \right| \alpha' S' \right\rangle \\ &\equiv \sum_m (-1)^m \begin{pmatrix} S' & 1 & S \\ M' & m & M \end{pmatrix} Y_{SS'}^{\alpha\alpha'}(-m) \end{aligned} \quad (349)$$

The remaining task is now to calculate the reduced matrix elements $Y_{SS'}^{\alpha\alpha'}(-m)$. The selection rules contained in the Clebsch–Gordon coefficients requires that three different types of matrix elements are to be calculated for $S' = S, S + 1$ and $S - 1$. In theory we can chose any convenient combination of M, M' and m . However, the practical setup of the calculations put some constraints on the choices.

For $S' = S$ we will always have the function for $M = M' = S$ and choose $m = 0$. Hence:

$$\begin{aligned} \left\langle \alpha SS \left| \sum_{A,i} \xi(r_{Ai}) l_{A,-m}(i) s_0(i) \right| \alpha' SS \right\rangle &= \begin{pmatrix} S & 1 & S \\ S & 0 & S \end{pmatrix} Y_S^{\alpha\alpha'}(-m) \\ &= \frac{S}{\sqrt{S(S+1)}} Y_S^{\alpha\alpha'}(-m) \end{aligned} \quad (350)$$

and inversion yields:

$$Y_S^{\alpha\alpha'}(m) = \frac{\sqrt{S(S+1)}}{S} \left\langle \alpha SS \left| \sum_{A,i} \xi(r_{Ai}) l_{A,m}(i) s_0(i) \right| \alpha' SS \right\rangle \quad (351)$$

For the matrix elements with $S' = S + 1$ we will have the states $|\alpha' S + 1 S + 1\rangle$ available, a natural choice is $M = S, M' = S + 1$ and $m = -1$. This gives:

$$\begin{aligned} \left\langle \alpha SS \left| \sum_{A,i} \xi(r_{Ai}) l_{A,-m}(i) s_{-1}(i) \right| \alpha' S + 1 S + 1 \right\rangle &= \begin{pmatrix} S+1 & 1 & S \\ S+1 & -1 & S \end{pmatrix} Y_{SS+1}^{\alpha\alpha'}(-m) \\ &= \sqrt{\frac{(2S+1)}{(2S+3)}} Y_{SS+1}^{\alpha\alpha'}(-m) \end{aligned} \quad (352)$$

Inversion results in:

$$Y_{SS+1}^{\alpha\alpha'}(m) = \sqrt{\frac{2S+3}{2S+1}} \left\langle \alpha S S \left| \sum_{A,i} \xi(r_{Ai}) l_{A,m}(i) s_{-1}(i) \right| \alpha' S + 1 S + 1 \right\rangle \quad (353)$$

Likewise one obtains the matrix elements:

$$Y_{SS-1}^{\alpha\alpha'}(m) = \left\langle \alpha S S \left| \sum_{A,i} \xi(r_{Ai}) l_{A,m}(i) s_{+1}(i) \right| \alpha' S - 1 S - 1 \right\rangle \quad (354)$$

References

- [1] EI Solomon, MA Hanson (1999) In: EI Solomon and ABP Lever (Eds.): *Inorganic Electronic Structure and Spectroscopy*. Wiley, New York, pp 1ff.
- [2] SB Piepho, PN Schatz (1983) *Group Theory in Spectroscopy with Applications to Magnetic Circular Dichroism*, Wiley, New York.
- [3] A Abragam, MHL Pryce (1951) *Proc. Roy. Soc. London (A)*, **205**, 131.
- [4] A Abragam, B Bleaney (1970) *Electron Paramagnetic Resonance of Transition Ions*, Clarendon Press, Oxford.
- [5] JHE Griffith, J Owen (1954) *Proc. Roy. Soc. (London)*, **A 226**, 96.
- [6] JS Griffith (1959) *Molec. Phys.*, **3**, 79.
- [7] KHW Stevens (1963) In: GT Rado and H Suhl (Eds.): *Magnetism*. Academic Press, New York, pp 1ff.
- [8] JE Harriman (1978) *Theoretical foundations of electron spin resonance*, Academic Press, New York.
- [9] R McWeeny (1965) *J. Chem. Phys.*, **42**, 1717.
- [10] R McWeeny, GHF Dierksen (1968) *J. Chem. Phys.*, **49**.
- [11] R McWeeny (1970) *Spins in Chemistry*, Academic Press, New York.
- [12] R McWeeny (1992) *Methods of Molecular Quantum Mechanics*, Academic Press, London.
- [13] FE Mabbs, D Collison (1992) *Electron Paramagnetic Resonance of d-Transition Metal Compounds*, Elsevier, Amsterdam.
- [14] JR Pilbrow (1990) *Transition Ion Electron Paramagnetic Resonance*, Clarendon Press, Oxford.
- [15] P Gütlich, R Link, A Trautwein (1978) *Mössbauer Spectroscopy and Transition Metal Chemistry*, Springer, Heidelberg, New York.
- [16] P Gütlich, J Ensling (1999) In: EI Solomon and ABP Lever (Eds.): *Inorganic Electronic Structure and Spectroscopy*. Wiley, New York, pp 161.
- [17] A Bencini, D Gatteschi (1990) *EPR of Exchange Coupled Systems*, Springer, Heidelberg.
- [18] NM Atherton (1993) *Principles of Electron Spin Resonance, 2nd ed.*, Ellis Horwood, Prentice-Hall, New York.
- [19] A Carrington, M A.D. (1967) *Introduction to Magnetic Resonance*, Wiley, New York
- [20] GE Pake, TL Estle (1973) *The Physical Principles of Electron Paramagnetic Resonance*, W.A. Benjamin Inc., London.
- [21] CP Slichter (1990) *Principles of magnetic resonance*, Springer, Heidelberg.

- [22] EAC Luken (1969) *Nuclear Quadrupole Coupling Constants*, Academic Press, London.
- [23] ME Rose (1957) *Elementary Theory of Angular Momentum*, Wiley, New York.
- [24] BL Silver (1976) *Irreducible Tensor Methods. An Introduction of Chemists*, Academic Press, New York.
- [25] WE Blumberg (1967) In: A Ehrenberg and B Malmström (Eds.): *Magnetic Resonance in Biological Systems*. Pergamon Press. Oxford., pp. 110ff.
- [26] WH Press, SA Teukolsky, WT Vetterling, BP Flannery (1988) *Numerical Recipes in C. 2nd Edition.*, Cambridge University Press, Cambridge.
- [27] PW Atkins (1983) *Molecular Quantum Mechanics. Second Edition*, Oxford University Press, Oxford.
- [28] V Heine (1960) *Group Theory in Quantum Mechanics*, Pergamon Press, London.
- [29] JS Griffith (1962) *The Irreducible Tensor Method for Molecular Symmetry Groups*, Prentice-Hall Inc., Englewood Cliffs.
- [30] PH Butler (1981) *Point Group Symmetry Applications*, Plenum Press, New York.
- [31] DP Craig, T Thirunamachandran (1984) *Molecular Quantum Electrodynamics*, Academic Press, London.
- [32] DW Davies (1966) *The Theory of the Electric and Magnetic Properties of Molecules*, Wiley, Chichester.
- [33] P Swannstrom, F Hegelund (1975) In: GHF Diercksen (Eds.): *Computational Techniques in Quantum Chemistry and Molecular Physics*. D. Reidel, Dordrecht, pp. 299ff.
- [34] WB Mims (1976) *The linear electric field effect in paramagnetic resonance*, Clarendon Press, Oxford.
- [35] BA Hess, CM Marian, SD Peyerimhoff (1995) In: D Yarkony (Eds.): *Modern Electronic Structure Theory*. World Scientific Publishing Company, Singapore.
- [36] H Bethe, E Salpeter (1957) *Quantum Mechanics of One- and Two-Electron Atoms*, Springer, Berlin.
- [37] G Breit (1929) *Phys. Rev.*, **34**, 553.
- [38] G Breit (1930) *Phys. Rev.*, **36**, 363.
- [39] G Breit (1932) *Phys. Rev.*, **39**, 616.
- [40] JC Slater (1960) *The Quantum Theory of Atomic Structure. Vol II*, McGraw-Hill, New York.
- [41] C Cohen Tanudji, B Diu, F Laloe (1977) *Quantum Mechanics. Vol. 2*, Wiley, Paris.
- [42] M Blume, RE Watson (1962) *Proc. Roy. Soc. A*, **270**, 127.
- [43] M Blume, RE Watson (1963) *Proc. Roy. Soc. A*, **271**, 565.
- [44] M Blume, AJ Freeman, RE Watson (1964) *Phys. Rev. A*, **134**, 320.
- [45] H Horie (1953) *Prog. Theor. Phys.*, **10**, 296.
- [46] JP Elliot (1953) *Proc. Roy. Soc. (London)*, **218**, 345.
- [47] S Koseki, MW Schmidt, MS Gordon (1992) *J. Chem. Phys.*, **96**, 10768.
- [48] S Koseki, MS Gordon, MW Schmidt, N Matsunaga (1995) *J. Phys. Chem.*, **99**, 12764.
- [49] S Koseki, MW Schmidt, MS Gordon (1998) *J. Phys. Chem. A.*, **102**, 10430.
- [50] BA Hess, CM Marian, U Wahlgren, O Gropen (1996) *Chem. Phys. Lett.*, **251**, 365.
- [51] D Andrae, Häussermann U, M Dolg, H Stoll, H Preuss (1990) *Theor. Chim. Acta*, **77**, 123.
- [52] M Dolg, H Stoll, H Preuss (1989) *J. Chem. Phys.*, **90**, 1730.
- [53] M Dolg, H Preuss (1995) In: KA Gschneider and L Eyring (Eds.): *Handbook of Physics and Chemistry of Rare Earths. Vol 22*. Elsevier, Amsterdam, chapter 12.
- [54] M Dolg (1996) *Theor. Chim. Acta*, **93**, 141.
- [55] W Küchle, M Dolg, H Stoll (1991) (74,
- [56] T Leininger, A Berning, A Nicklass, H Stoll, HJ Werner, HJ Flad (1997) *Chem. Phys.*, **217**, 19.

- [57] RM Pitzer, NW Winter (1988) *J. Chem. Phys.*, **92**, 3061.
- [58] L Seijo (1995) *J. Chem. Phys.*, **102**, 8078.
- [59] EU Condon, GH Shortly (1959) *The Theory of Atomic Spectra*, Cambridge University Press, Cambridge.
- [60] W Kutzelnigg (1988) *Theoret. Chim. Acta*, **73**, 173.
- [61] BA Hess, CM Marian (2000) In: P Jensen and PR Bunker (Eds.): *Computational Molecular Spectroscopy*. John Wiley & sons, New York, pp. 169ff.
- [62] PO Löwdin (1962) *J. Math. Phys.*, **3**, 969
- [63] PO Löwdin (1966) In: CH Wilcox (Eds.): *Perturbation Theory and its Applications in Quantum Mechanics*. Wiley, New York.
- [64] BG Wyborne (1968) *J. Chem. Phys.*, **48**, 2596
- [65] JC Barthelat, P Durand (1992) In: S Fraga (Eds.): *Computational Chemistry: Structure, Interactions and Reactivity. Studies in physical and Theoretical Chemistry, Vol 77*. Elsevier, Amsterdam.
- [66] F Neese, EI Solomon (1998) *Inorg. Chem.*, **37**, 6568.
- [67] E Wassermann, LC Snyder, WA Yager (1964) *J. Chem. Phys.*, **41**, 1763.
- [68] SR Langhoff, ER Davidson (1973) *Int. J. Quant. Chem.*, **7**, 759.
- [69] ER Davidson, JC Ellenbogen, SR Langhoff (1980) *J. Chem. Phys.*, **73**, 865.
- [70] D Feller, WT Borden, ER Davidson (1981) *J. Chem. Phys.*, **74**, 2256.
- [71] PR Surjan, K Nemeth, M Bennati, A Grupp, M Mering (1996) *Chem. Phys. Lett.*, **251**, 115.
- [72] B Bomfleur, M Sironi, M Raimondi, J Voigtländer (2000) *J. Chem. Phys.*, **112**, 1066.
- [73] W Kutzelnigg (1994) *Einführung in die Theoretische Chemie. Band 2*, VCH, Weinheim.
- [74] AJ Stone (1963) *Proc. Roy. Soc. London (A)*, **271**, 424.
- [75] F Neese (2002) (manuscript in preparation).
- [76] CP Keijzers, E DeBoer (1972) *J. Chem. Phys.*, **57**, 1277.
- [77] A Szabo, NS Ostlund (1998) *Modern Quantum Chemistry. Introduction to Advanced Electronic Structure Theory*, McGraw-Hill, New York.
- [78] R Pauncz (1979) *Spin Eigenfunctions. Construction and use*, Plenum Press, New York.
- [79] R Pauncz (1995) *The Symmetric Group in Quantum Chemistry*, CRC Press, Boca Raton.
- [80] MG Cory, MC Zerner (1991) *Chem. Rev.*, **91**, 813.
- [81] WD Edwards, MC Zerner (1987) *Theor. Chem. Acta*, **72**, 347.
- [82] M Gerloch, RF McMeeking (1975) *J. Chem. Soc. Dalton*, 2443.
- [83] RE Moss, AJ Perry (1971) *Molec. Phys.*, **22**, 789.
- [84] PW Atkins, AM Jamieson (1967) *Molec. Phys.*, **14**, 425.
- [85] BR McGarvey (1966) *Transition Metal Chemistry*, **3**, 89.
- [86] BA Goodman, JB Raynor (1970) In: HJ Emeleus and AG Sharpe (Eds.): *Adv. Inorg. Radiochem.* Academic Press, New York, pp 135.
- [87] A Benchini, D Gatteschi (1979) *Transition Metal Chemistry*, **8**, 1.
- [88] CJ Ballhausen, HB Gray (1964) *Molecular Orbital Theory*, Benjamin, New York.
- [89] CJ Ballhausen (1962) *Introduction to Ligand Field Theory*, McGraw-Hill, New York.
- [90] JS Griffith (1964) *The Theory of Transition Metal Ions*, Cambridge University Press, Cambridge.
- [91] EI Solomon, ABP Lever (1999) In: EI Solomon and ABP Lever (Eds.): *Inorganic Electronic Structure and Spectroscopy. Vol 1*. Wiley, New York, p. 1.
- [92] J Bendix, M Brorson, CE Schäffer (1993) *Inorg. Chem.*, **32**, 2838.
- [93] A Lupei, JA McMillan (1972) *J. Chem. Phys.*, **57**, 827.
- [94] NM Atherton, AJ Horsewill (1980) *J. Chem. Soc., Faraday Tans.*, **76**, 660.

- [95] R Sheahan, B Hathaway (1979) *J. Chem. Soc., Dalton Trans.*, 17.
- [96] DW Smith (1970) *J. Chem. Soc. A*, 3108.
- [97] J Ammeter (1968) *Chimia*, **22**, 469.
- [98] F Neese (2001) *J. Chem. Phys.*, **115**, 11080.
- [99] J Ammeter, G Rist, HH Günthard (1972) *J. Chem. Phys.*, **57**, 3852
- [100] CK Jørgensen (1962) *Orbitals in Atoms and Molecules*, Academic Press, London, New York.
- [101] CK Jørgensen (1963) *Adv. Chem. Phys.*, 33.
- [102] CK Jørgensen (1966) *Struc. Bond*, **1**, 3.
- [103] CK Jørgensen (1969) *Struc. Bond*, **6**, 94.
- [104] RL Belford, M Karplus (1959) *J. Chem. Phys.*, **31**, 394.
- [105] JHE Griffith, J Owen (1954) *Proc. Roy. Soc. (London)*, **A 205**, 96.
- [106] KK Stavrev, MC Zerner. (1997) *Int. J. Quant. Chem.*, **65**, 877.
- [107] A Schäfer, C Huber, R Ahlrichs (1994) *J. Chem. Phys.*, **100**, 5829.
- [108] HA Kuska, MT Rogers (1971) In: CNR Rao and JR Ferraro (Eds.): *Spectroscopy in Inorganic Chemistry. Vol 2*. Academic Press, New York, pp. 175.
- [109] M Sharnoff (1965) *J. Chem. Phys.*, **42**, 3383.
- [110] AS Brill, GF Bryce (1968) *J. Chem. Phys.*, **48**, 4398.
- [111] LL Lohr, WN Lipscomb (1963) *J. Chem. Phys.*, **38**, 1607.
- [112] BR McGarvey (1964) *J. Chem. Phys.*, **41**, 3743.
- [113] C Ribbing, K Pierloot, A Ceulemans (1998) *Inorg. Chem.*, **37**, 5227.
- [114] JS Griffith (1964) *Mol. Phys.*, **8**, 213.
- [115] EI Solomon, TC Brunold, MI Davis, JN Kemsley, SK Lee, N Lehnert, F Neese, AJ Skulan, YS Yang, J Zhou (2000) *Chem. Rev.*, **100**, 235.
- [116] F Neese, JM Zaleski, KE Loeb, EI Solomon (2000) *J. Am. Chem. Soc.*, **122**, 11703.
- [117] JS Griffith (1957) *Nature*, **180**, 30.
- [118] M Kotani (1961) *Prog. Theoret. Phys. Suppl.*, 4.
- [119] M Weissbluth *Hemoglobin: Cooperativity and Electronic Processes*, Springer, Berlin, **1973**
- [120] SM Soltis, CE Strouse (1988) *J. Am. Chem. Soc.*, **110**, 2824.
- [121] CPS Taylor (1977) *Biochim. Biophys. Acta*, **491**, 137.
- [122] G Palmer (1983) In: ABP Lever and HB Gray (Eds.): *The Porphyrins. Vol. 2*. Addison-Wesley, London, pp. 43.
- [123] WE Blumberg, J Peisach (1971) In: B Chance, T Yonetani and AS Mildvan (Eds.): *Probes of structure and function of macromolecules and membranes*. Academic Press, New York.
- [124] S DeVries, PJ Albracht (1979) *Biochim. Biophys. Acta*, **546**, 334.
- [125] NV Shokirev, FA Walker (1998) *J. Am. Chem. Soc.*, **120**, 981.
- [126] EI Solomon (1984) *Comments Inorg. Chem.*, **3**, 227.
- [127] J Ferguson (1964) *J. Chem. Phys.*, **40**, 3406.
- [128] SR Desjardins, KW Penfield, SL Cohen, RL Musselman, EI Solomon (1983) *J. Am. Chem. Soc.*, **105**, 4590.
- [129] JC Slater (1951) *Phys. Rev.*, **81**, 385.
- [130] KH Johnson (1966) *J. Chem. Phys.*, **45**, 3085.
- [131] AA Gewirth, SL Cohen, HJ Schugar, EI Solomon (1987) *Inorg. Chem.*, **26**, 1133.
- [132] R Szilagyi, EI Solomon (2001) *J. Phys. Chem. A*, **106**, 2994.
- [133] EI Solomon, AA Gewirth, TD Westmoreland (1989) In: AJ Hoff (Eds.): *Advanced EPR. Applications in Biology and Biochemistry*. Elsevier, Amsterdam, pp. 865.
- [134] EI Solomon, MJ Baldwin, MD Lowery (1992) *Chem. Rev.*, **92**, 521.
- [135] EI Solomon, MD Lowery (1993) *Science*, **259**, 1575.

- [136] EI Solomon, MD Lowery (1993) In: AJ Welch and SK Chapman (Eds.): *The Chemistry of Copper and Zinc Triads*. Royal Society of Chemistry, Cambridge, pp. 12.
- [137] EI Solomon, MD Lowery, LB LaCroix, DE Root (1993) *Meth. Enzymol.*, **226**, 1.
- [138] EI Solomon, MD Lowery, DE Root, BL Hemming (1995) In: HH Thorp and VL Pecoraro (Eds.): *Mechanistic Inorganic Biochemistry*. American Chemical Society, Washington DC, pp. 121.
- [139] KW Penfield, RR Gay, RS Himmelwright, NC Eickman, VA Norris, HC Freeman, EI Solomon (1981) *J. Am. Chem. Soc.*, **103**, 4382.
- [140] KW Penfield, AA Gewirth, EI Solomon (1985) *J. Am. Chem. Soc.*, **107**, 4519.
- [141] AA Gewirth, EI Solomon (1988) *J. Am. Chem. Soc.*, **110**, 3811.
- [142] BS Gerstman, AS Brill (1985) *J. Chem. Phys.*, **82**, 1212.
- [143] F Neese, EI Solomon (1999) *Inorg. Chem.*, **38**, 1847.
- [144] RL Belford (1982) *Inorg. Chem.*, **22**, 577.
- [145] BR McGarvey (1967) *J. Phys. Chem.*, **71**, 51.
- [146] SE Shadle, JE Penner-Hahn, HJ Schugar, B Hedman, KO Hodgson, EI Solomon (1993) *J. Am. Chem. Soc.*, **115**, 767.
- [147] JC Deaton, MS Gebhard, EI Solomon (1989) *Inorg. Chem.*, **28**, 877.
- [148] MS Gebhard, JC Deaton, SA Koch, M Millar, EI Solomon (1990) *J. Am. Chem. Soc.*, **112**, 2217.
- [149] F Jensen (1999) *Introduction to computational chemistry*, Wiley, New York.
- [150] I Shavitt (1977) In: HF Schaefer III (Eds.): *Methods of Electronic Structure Theory*. Plenum Press, New York, pp. 189ff.
- [151] PEM Siegbahn (1992) In: BO Roos (Eds.): *Lecture Notes in Quantum Chemistry*. Springer, Berlin, pp. 255 ff.
- [152] CD Sherill, HF Schaefer III (1999) *Adv. Quant. Chem.*, **34**, 143.
- [153] R Manne, MC Zerner (1986) *Int. J. Quant. Chem. Symp.*, **19**, 165.
- [154] M Kotzian, N Rösch, MC Zerner (1991) *Int. J. Quant. Chem. Symp.*, **25**, 545.
- [155] F Neese (2001) *Int. J. Quant. Chem.*, **83**, 104.
- [156] RG Parr, W Yang (1989) *Density Functional Theory of Atoms and Molecules*, Oxford University Press, Oxford.
- [157] P Hohenberg, W Kohn (1964) *Phys. Rev. B*, **136**, 864.
- [158] W Kohn, LJ Sham (1965) *Phys. Rev.*, **A140**, 1133.
- [159] T Ziegler (1991) *Chem. Rev.*, **91**, 651.
- [160] RG Parr, W Yang (1995) *Annu. Rev. Phys. Chem.*, **46**, 701.
- [161] AD Becke (1995) In: DR Yarkony (Eds.): *Modern Electronic Structure Theory. Part II*. World Scientific, Singapore, pp. 1022.
- [162] NC Handy (1995) In: D Bicout and M Field (Eds.): *Quantum Mechanical Simulation Methods For Studying Biological Systems*. Springer, Berlin, pp. 1.
- [163] JC Slater (1972) *Adv. Quant. Chem.*, **6**, 1.
- [164] BB Laird, RB Ross, T Ziegler (1996) In: BB Laird, RB Ross and T Ziegler (Eds.): *Chemical Applications of Density Functional Theory*. American Chemical Society, Washington D.C., pp. 1.
- [165] EJ Baerends, OV Gritsenko, R van Leeuwen (1996) In: BB Laird, RB Ross and T Ziegler (Eds.): *Chemical Applications of Density-Functional Theory*. American Chemical Society, Washington DC.
- [166] JP Perdew, K Burke, M Ernzerhof (1996) In: BB Laird, RB Ross and T Ziegler (Eds.): *Chemical Applications of Density Functional Theory*. American Chemical Society, Washington D.C., pp. 453.
- [167] FM Bickelhaupt, EJ Baerends (2000) In: KB Lipkowitz and DB Boyd (Eds.): *Reviews in Computational Chemistry. Vol. 15*. Wiley-VCH, New York, pp 1.

- [168] C Adamo, A di Matteo, V Barone (2000) *Adv. Quant. Chem.*, **36**, 45.
- [169] AD Becke (1988) *Phys. Rev. A.*, **38**, 3098.
- [170] AD Becke (1993) *J. Chem. Phys.*, **98**, 1372.
- [171] AD Becke (1993) *J. Chem. Phys.*, **98**, 5648.
- [172] C Lee, W Yang, RG Parr (1988) *Phys. Rev. B.*, **37**, 785.
- [173] JP Perdew (1986) *Phys. Rev. B.*, **33**, 8822.
- [174] W Koch, MC Holthausen (2000) *A Chemist's guide to Density Functional Theory*, Wiley-VCH, Weinheim.
- [175] AD Becke (1988) *J. Chem. Phys.*, **88**, 2547.
- [176] O Treutler, R Ahlrichs (1994) *J. Chem. Phys.*, **102**, 346.
- [177] RM Stevens, RM Pitzer, WN Lipscomb (1963) *J. Chem. Phys.*, **38**, 550.
- [178] R Moccia (1970) *Chem. Phys. Lett.*, **5**, 260.
- [179] R Moccia (1970) *Chem. Phys. Lett.*, **5**, 265.
- [180] M Häser, R Ahlrichs, HP Baron, P Weis, H Horn (1992) *Theor. Chim. Acta*, **83**, 455.
- [181] JL Dodds, R McWeeny, AJ Sadlej (1977) *Molec. Phys.*, **34**, 1779.
- [182] GHF Diercksen, R McWeeny (1966) *J. Chem. Phys.*, **44**, 3554.
- [183] ST Epstein (1974) *The Variation Method in Quantum Chemistry*, Academic Press, New York.
- [184] R Bauernschmitt, R Ahlrichs (1996) *Chem. Phys. Lett.*, **256**, 454.
- [185] G Vignale, M Rasolt, DJW Geldart (1990) *Advan. Quant. Chem.*, **21**, 235.
- [186] EKV Gross, JF Dobson, M Petersilka (1996) *Density functional theory*, Springer, Berlin.
- [187] SM Colwell, NC Handy (1994) *Chem. Phys. Lett.*, **217**, 271.
- [188] SM Colwell, CW Murray, NC Handy, RD Amos (1993) *Chem. Phys. Lett.*, **210**, 261.
- [189] JA Pople, R Krishnan, HB Schlegel, JS Binkley (1979) *Int. J. Quant. Chem.: Quant. Chem. Symp.*, **13**, 225.
- [190] Y Osamura, Y Yamaguchi, P Saxe, DJ Fox, MA Vincent, HF Schaefer III (1983) *J. Mol. Struct. (Theochem)*, **103**, 183.
- [191] C Chang, M Pelissier, P Durand (1986) *Physica Scripta*, **34**, 394.
- [192] E van Lenthe, JG Snijders, EJ Baerends (1993) *J. Chem. Phys.*, **99**, 4597.
- [193] E van Lenthe, EJ Baerends, JG Snijders (1994) *J. Chem. Phys.*, **101**, 4783.
- [194] E van Lenthe, JG Snijders, EJ Baerends (1996) *J. Chem. Phys.*, **105**, 6505.
- [195] PHT Phillipsen, E van Lenthe, JG Snijders, EJ Baerends (1996) *Phys. Rev. B*, **56**, 13556.
- [196] C van Wüllen (1998) *J. Chem. Phys.*, **109**, 392.
- [197] S Faas, JH van Lenthe, AC Hennum (2000) *J. Chem. Phys.*, **113**, 4052.
- [198] E van Lenthe, PES Wormer, A van der Avoird (1997) *J. Chem. Phys.*, **107**, 2488.
- [199] E van Lenthe, A van der Avoird, ES Wormer (1998) *J. Chem. Phys.*, **108**, 4783.
- [200] E van Lenthe, EJ Baerends (2000) *J. Chem. Phys.*, **112**, 8279.
- [201] M Douglas, NM Kroll (1974) *Annals Phys.*, **82**, 89.
- [202] BA Hess (1985) *Phys. Rev. A*, **32**, 756.
- [203] BA Hess (1986) *Phys. Rev. A*, **33**, 3742.
- [204] M Mayer, S Krüger, N Rösch (2001) *J. Chem. Phys.*, **115**, 4411.
- [205] L Gagliardi, NC Handy, AG Ioannou, CK Skylaris, S Spencer, A Willets, AM Simper (1998) *Chem. Phys. Lett.*, **283**, 187.
- [206] L Gagliardi, B Schimmelpfennig, L Maron, U Wahlgren, A Willets (2001) *Chem. Phys. Lett.*, **344**, 207.
- [207] A Bencini, C Benelli, D Gateschi (1984) *Coord. Chem. Rev.*, **60**, 131.
- [208] J Ridley, MC Zerner (1973) *Theor. Chim. Acta*, **32**, 111.

- [209] MC Zerner, GH Loew, RF Kirchner, UT Mueller-Westerhoff (1980) *J. Am. Chem. Soc.*, **102**, 589.
- [210] WP Anderson, WD Edwards, MC Zerner (1986) *Inorg. Chem.*, **25**, 272.
- [211] MC Zerner (1990) In: KB Lipkowitz and DB Boyd (Eds.): *Reviews in Computational Chemistry. Vol. 2*. VCH, Heidelberg, pp. 315.
- [212] MC Zerner (1992) In: DR Salahub and N Russo (Eds.): *Metal-Ligand Interactions: from Atoms, to Clusters, to Surfaces*. Kluwer Academic publishers, Amsterdam, pp. 101.
- [213] MC Zerner (1996) In: N Russo and DR Salahub (Eds.): *Metal Ligand Interactions*. Kluwer Academic, Amsterdam, pp. 493.
- [214] F Neese, EI Solomon (1998) *J. Am. Chem. Soc.*, **120**, 12829.
- [215] MI Davis, AM Orville, F Neese, JM Zaleski, JD Lipscomb, EI Solomon (2001) *J. Am. Chem. Soc.* (in press).
- [216] TC Brunold (2001) personal communication.
- [217] O Kahn (1993) *Molecular Magnetism*, VCH Publishers, New York.
- [218] W Kutzelnigg (1980) *Isr. J. Chem.*, **19**, 193.
- [219] W Kutzelnigg, U Fleischer, M Schindler (1990) In: P Diehl, E Fluck, H Günther, R Kosfield and J Seeling (Eds.): *NMR basic principles and progress*. Springer, Heidelberg.
- [220] VG Malkin, OL Malkina, LA Eriksson, DR Salahub (1994) In: JM Seminario and P Politzer (Eds.): *Modern density functional theory: a tool for chemistry*. Elsevier, Amsterdam.
- [221] G Schreckenbach, T Ziegler (1998) *Theor. Chem. Acc.*, **99**, 71.
- [222] T Helgaker, M Jaszunski, K Ruud (1999) *Chem. Rev.*, **99**, 293.
- [223] M Kaupp, VG Malkin, OL Malkina (1998) In: PvR Schleyer (Eds.): *Encyclopedia of Computational Chemistry*. Wiley, Chichester.
- [224] AV Luzanov, EN Babich, VV Ivanov (1994) *J. Mol. Struct. (Theochem)*, **311**, 211.
- [225] F London (1937) *J. Phys. Radium*, **8**, 397.
- [226] R Ditchfield (1974) *Molec. Phys.*, **27**, 789.
- [227] K Wolinski, JF Hinton, P Pulay (1990) *J. Am. Chem. Soc.*, **112**, 8251.
- [228] K Ruud, T Helgaker, R Kobayashi, P Jorgensen, HJA Jensen (1993) *J. Chem. Phys.*, **99**, 3847.
- [229] K Ruud, T Helgaker, KL Bak, HJA Jensen (1994) *J. Chem. Phys.*, **100**, 8178.
- [230] JCC Chan, SCF Au-Yeung (1997) *J. Mol. Struct. (Theochem)*, **393**, 93.
- [231] JM Foster, SF Boys (1963) *Rev. Mod. Phys.*, **32**, 296.
- [232] C Edminton, K Rüdénberg (1963) *Rev. Mod. Phys.*, **35**, 457.
- [233] J Pipek, PG Mezey (1989) *J. Chem. Phys.*, **90**, 4916.
- [234] AE Hansen, TD Bouman (1985) *J. Chem. Phys.*, **82**, 5035.
- [235] GH Lushington, P Bündgen, F Grein (1995) *Int. J. Quant. Chem.*, **55**, 377.
- [236] GH Lushington, F Grein (1996) *Theor. Chim. Acta*, **93**, 259.
- [237] GH Lushington, F Grein (1996) *Int. J. Quant. Chem.: Quant. Chem. Symp.*, **30**, 467.
- [238] GH Lushington, F Grein (1997) *J. Chem. Phys.*, **106**, 3292.
- [239] GH Lushington (2000) *J. Phys. Chem. A.*, **104**, 2969.
- [240] PJ Bruna, F Grein (2000) *Int. J. Quant. Chem.*, **77**, 324.
- [241] O Vahtras, B Minaev, H Agren (1997) *Chem. Phys. Lett.*, **281**, 186.
- [242] M Engström, B Minaev, O Vahtras, H Agren (1998) *Chem. Phys. Lett.*, **237**, 149.
- [243] M Engström, O Vahtras, H Agren (1999) *Chem. Phys. Lett.*, **243**, 263.
- [244] M Engström, F Himo, H Agren (2000) *Chem. Phys. Lett.*, **319**, 191.
- [245] M Engström, R Owenius, O Vahtras (2001) *Chem. Phys. Lett.*, **338**, 407.
- [246] D Jayatilaka (1998) *J. Chem. Phys.*, **108**, 7587.

- [247] ML Mader, F Neese, MD Carducci, AM Raitsimring, AV Astashkin, JH Enemark (2000) *ABS. PAP. AM. CHEM. SOC.*, **219**, 79.
- [248] R Angstl (1989) *Chem. Phys.*, **132**, 435.
- [249] E Dalgaard (1978) *Proc. Roy. Soc. London (A)*, **361**, 487.
- [250] YH Hsiao, MC Zerner (1999) *Int. J. Quant. Chem.*, **75**, 577.
- [251] CP Keijzers, HJM De Vries, A van der Avoird (1971) *Inorg. Chem.*, **11**, 1338.
- [252] CP Keijzers, E De Boer (1974) *Molec. Phys.*, **29**, 1007.
- [253] GH Loew, DA Chadwick (1974) *Theor. Chim. Acta*, **33**, 125.
- [254] T Morikawa, O Kikuchi (1971) *Theor. Chim. Acta*, **22**, 224.
- [255] G Peng, J Nichols, EA McCullough, JT Spence (1994) *Inorg. Chem.*, **33**, 2857.
- [256] M Rudin, A Schweiger, HH Günthard (1982) *Molec. Phys.*, **47**, 171.
- [257] J Stach, R Kirmse (1979) *Z. Chem.*, **19**, 205.
- [258] JT Törring, S Un, M Knüpfling, M Plato, K Möbius (1997) *J. Chem. Phys.*, **107**, 3905.
- [259] PJM Geurts, PCP Bouten, A van der Avoird (1980) *J. Chem. Phys.*, **73**, 1306.
- [260] P Belanzoni, EJ Baerends, S van Asselt, PB Langewen (1995) *J. Phys. Chem.*, **99**, 13094.
- [261] P Belanzoni, EJ Baerends, M Gribneau (1999) *J. Phys. Chem. A.*, **103**, 3732.
- [262] G Schreckenbach, T Ziegler (1997) *J. Phys. Chem. A.*, **101**, 3388.
- [263] S Patchkovskii, T Ziegler (1999) *J. Chem. Phys.*, **111**, 5730.
- [264] S Patchkovskii, T Ziegler (2000) *Inorg. Chem.*, **39**, 5354.
- [265] S Patchkovskii, T Ziegler (2000) *J. Am. Chem. Soc.*, **122**, 3506.
- [266] S Patchkovskii, T Ziegler (2001) *J. Phys. Chem. A.*, **105**, 5490.
- [267] E van Lenthe, A van der Avoird, WR Hagen, EJ Reijerse (2000) *J. Phys. Chem. A.*, **104**.
- [268] M Stein, E van Lenthe, EJ Baerends, W Lubitz (2001) *J. Phys. Chem. A.*, **105**, 416.
- [269] M Stein, E Van Lenthe, EJ Baerends, W Lubitz (2001) *J. Am. Chem. Soc.*, **123**, 5839.
- [270] P Belanzoni, E Van Lenthe, EJ Baerends (2001) *J. Chem. Phys.*, **114**, 4421.
- [271] OL Malkina, J Vaara, B Schimmelpfenning, M Munzarova, V Malkin, M Kaupp (2000) *J. Am. Chem. Soc.*, **122**, 9206.
- [272] JP Perdew, A Zunger (1981) *Phys. Rev. B*, **23**, 5048.
- [273] J Garza, JA Nichols, DA Dixon (2000) *J. Chem. Phys.*, **112**, 7880.
- [274] J Garza, R Varga, JA Nichols, DA Dixon (2001) *J. Chem. Phys.*, **114**, 639.
- [275] S Patchkovskii, J Autschbach, T Ziegler (2001) *J. Chem. Phys.*, **115**, 26.
- [276] U Ludin, O Eriksson (2001) *Int. J. Quant. Chem.*, **81**, 247.
- [277] A Görling (1999) *Phys. Rev. Lett.*, **83**, 5459.
- [278] F Della Sala, A Görling (2001) *J. Chem. Phys.*, **115**, 5718.
- [279] LA Eriksson (1998) In: PvR Schleyer (Eds.): *Encyclopedia Computational Chemistry*. John Wiley and Sons, Chichester, pp. 952.
- [280] B Engels, LA Eriksson, S Lunell (1996) *Adv. Quant. Chem.*, **27**, 297.
- [281] ML Munzarova, P Kubacek, M Kaupp (2000) *J. Am. Chem. Soc.*, **122**, 11900.
- [282] RE Watson, A Freeman (1961) *Phys. Rev.*, **123**, 2027.
- [283] T Helgaker, PR Taylor (1995) In: D Yarkony (Eds.): *Modern Electronic Structure Theory*, World Scientific, Singapore, pp. 725.
- [284] V Barone (1996) In: DP Chong (Eds.): *Recent Advances in Density Functional Methods*, World Scientific, Singapore.
- [285] ML Munzarova, M Kaupp (1999) *J. Phys. Chem. A.*, **103**, 9966.
- [286] C Balagopalakrishna, JT Kimbrough, TD Westmoreland (1996) *Inorg. Chem.*, **35**, 7758.
- [287] JE Huyett, SB Choudhury, DM Eichorn, PA Bryngelson, MJ Maroney, BM Hoffman (1998) *Inorg. Chem.*, **37**, 1361.

- [288] LB Knight, JG Kaup, B Petzold, R Ayyad, TK Ghanty, ER Davidson (1999) *J. Chem. Phys.*, **110**, 5658.
- [289] RG Hayes (2000) *Inorg. Chem.*, **39**, 156.
- [290] F Neese (2001) *J. Phys. Chem. A.*, **105**, 4290.
- [291] PJ Hay (1978) *J Am Chem Soc.*, **100**, 2411.
- [292] L Noodelman, EJ Baerends (1984) *J. Am. Chem. Soc.*, **106**, 2316.
- [293] AR Jaszewski, J Jezierska (2001) *Chem. Phys. Lett.*, **343**, 571.
- [294] EI Solomon, MJ Baldwin, MD Lowery (1992) *Chem. Rev.*, **92**, 521.
- [295] MM Werst, CE Davoust, BM Hoffman (1991) *J. Am. Chem. Soc.*, **113**, 1533.
- [296] M van Gastel, JWA Coremans, LJC Jeuken, GW Canters, EJJ Groenen (1997) *J. Am. Chem. Soc.*, **119**, 4726.
- [297] JWA Coremans, M van Gastel, OG Poluektov, T Groenen, T den Blaauwen, G van Pouderoyen, GW Canters, H Nar, C Hammann, A Messerschmidt (1995) *Chem. Phys. Lett.*, **235**, 202.
- [298] JWA Coremans, OG Poluektov, EJJ Groenen, GW Canters, H Nar, A Messerschmidt (1996) *J. Am. Chem. Soc.*, **118**, 12141.
- [299] JE Roberts, JF Cline, V Lum, H Freeman, HB Gray, J Peisach, B Reinhammar, BM Hoffman (1984) *J. Am. Chem. Soc.*, **106**, 5324.
- [300] CP Keijzers, D Snaathorst (1980) *Chem. Phys. Lett.*, **69**, 348.
- [301] HJ Scholl, J Hüttermann (1992) *J. Phys. Chem.*, **96**, 9684.
- [302] E Clementi, DL Raimondi (1963) *J. Chem. Phys.*, **38**, 2686.
- [303] AK Koh, DJ Miller (1985) *At. Nucl. Data Tables*, **33**, 235.

10 Chemical Reactions in Applied Magnetic Fields

Quentin A. Pankhurst and Ivan P. Parkin

10.1 Introduction

Research in the last ten years has highlighted the dramatic influence that magnetic fields can have on chemical reactions in gases, liquids and solids. In the gaseous state, magnetic fields improve the combustion process in various engines, probably by influencing the behavior of dioxygen. An external field can also affect the shape and distribution of fullerenes and carbon nanotubes synthesized by arc-discharge. In the liquid state a magnetic field can influence the population balance of opposing-chirality organic molecules. It can also affect the phase and morphology of electrodeposited phases, such as the handedness of spirals of copper crystals. In the solid state, and in particular in solid flame combustion reactions, applied fields can modify both reaction pathways and product compositions, as well as a host of structural and magnetic properties ranging from lattice parameters to saturation magnetizations.

It is a remarkable fact that despite the ubiquity and profundity of these observations of definite, measurable effects, there remains in many cases little in the way of understanding their origins – even to the extent of uncertainty about whether the field influences the reactions directly or indirectly. In this review we present an overview of current research in this fascinating and challenging area.

10.2 Gas-phase Reactions

10.2.1 Gaseous Combustion

Combustion reactions are well known to be influenced by electric fields [1]. Less work has been published on the effect of magnetic field on gaseous combustion reactions. Michael Faraday was the first to report the effect of an external magnetic field gradient on a candle flame [2]. He found that the fuel gas flowed towards a stronger magnetic field and the candle flame was deflected towards a weaker field. Furthermore, he found that the diamagnetic gases hydrogen and nitrogen make a detour around magnetic poles in air while paramagnetic gases such as oxygen are attracted toward the stronger fields. More recently, magnetic field gradients have also been found to have a considerable effect on advancing gas streams in air, and

it has been shown that the magnetic force per unit volume is:

$$F = \frac{1}{2} P_{O_2} \chi_{O_2} \nabla H^2 \quad (1)$$

where χ_{O_2} is the magnetic susceptibility of oxygen gas, P_{O_2} is the oxygen partial pressure, and H is the magnetic field strength [3].

Flames can be categorized as ‘diffusion’, ‘partially mixed’ or ‘premixed’ flames, depending on the origin of the oxygen source. In diffusion flames the oxygen supplied to the flame is provided by diffusion from the surrounding air. The combustion in such flames is greatly altered in the presence of an external magnetic field. Wakayama [4] has studied this effect, and shown that for methane/oxygen flames application of an external field immediately made the flame shorter in length, sharper and more brilliant (Fig. 1). The flame temperature increased while the magnetic field was in place but decreased once the magnetic field was removed, returning to its original burning pattern. The flame temperature was found to vary almost linearly with magnetic field gradient changing from 790°C at zero field to 900°C in a gradient of 40 T² m⁻¹. The magnetic field promoted combustion when the fuel gas flowed in the direction of decreasing field strength. Magnetic acceleration of combustion was found only in diffusion or partially mixed flames and not premixed flames (air/methane). This indicates that magnetically induced air-flows promote combustion in diffusion flames.

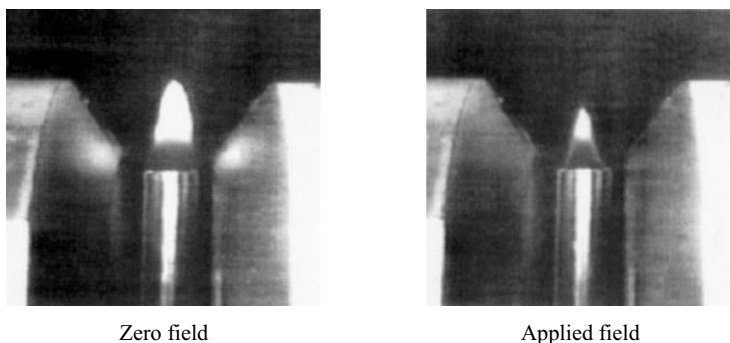


Fig. 1. Comparison of diffusion flames in zero field and in an homogeneous magnetic field with a gradient of 35 T² m⁻¹.

10.2.2 Carbon Nanotube and Fullerene Synthesis

Carbon nanotubes are long microtubules of carbon atoms [5]. They comprise nested cylinders of carbon sheets, of typical dimension 200 nm long by 5–50 nm wide. The nanotubes have an inter-wall separation of 0.34 nm that is comparable to that found in graphite. The cylindrical carbon sheets form a series of concentric cylinders and have been described as a series of ‘Russian dolls’. Carbon nanotubes are synthesized

by dc-arc discharge using carbon rods in a partial vacuum containing helium [6]. The carbon nanotubes are found in the soot-like material that forms at the cathode. In the same process a series of fullerene molecules such as C_{60} and C_{70} are also isolated. Yokomichi has studied the formation of nanotubes and fullerenes in magnetic fields up to 10 T [7]. The magnetic field was found to greatly change the yield and morphology of the nanotubes and also to affect the abundance of the fullerene molecules.

The principal finding of Yokomichi's work was that the carbon nanotubes formed at 10 T had greater curvature than those synthesized in zero field (Fig. 2). The nanotubes were also found to have a collapsed core, and the nanotube yields decreased with field strength. The nanotubes that did form at high fields tended to have thinner walls than those synthesized in zero fields (less nested carbon sheets). Another important result was that the ratio of C_{60} to C_{70} isolated in the experiment was found to vary with magnetic field. The fullerene yield decreased by an order of magnitude on the application of an external magnetic field. Interestingly, under conventional zero field synthesis, C_{60} makes up the dominant fullerene synthesized by arc discharge, ca. 90%. The ratio of C_{70} fraction increases steadily with external field strength such that at 5 T the proportion of C_{70} isolated is greater than that of C_{60} . These effects have been tentatively explained on the basis of broadening and deformation in the discharge column due to gradients in ion density. The effect has thus been ascribed to plasma confinement in the magnetic field and the subsequent alteration of the arc-current density rather than spin polarization or Zeeman effects. The authors believe that a high magnetic field may enable control of the curvature of nanotubes and selective synthesis of fullerenes [7].

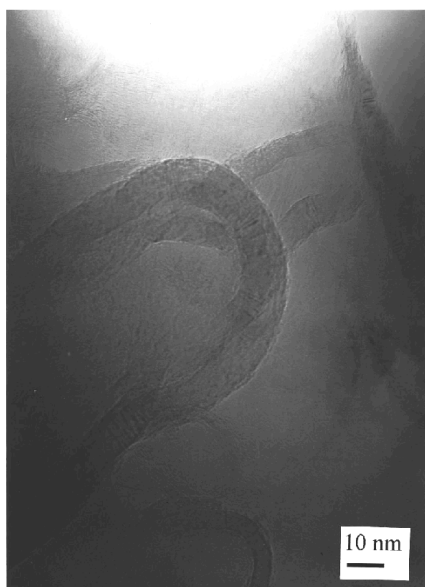


Fig. 2. Transmission electron micrograph of carbon nanotubes made in a magnetic field of 10 T, showing that nanotubes with a large amount of curvature can be obtained when synthesis is performed in an applied field.

10.2.3 Liquid-phase Reactions

10.2.4 Asymmetric Synthesis

It has been widely reported that magnetic fields can affect the mechanisms and rates of reactions, and the subject has been reviewed for both biological and chemical processes [8, 9]. One aspect of this question that has been plagued by controversy, fraud and frequent misunderstanding is whether an external magnetic field can induce chirality (or, more precisely, 'enantiomeric excess') in a reaction.

Much of the natural world is chiral [10]. Chirality is a phenomenon arising from the handedness of molecules at an atomic center. It is most commonly found in organic chemistry in cases where a carbon atom has four different groups attached. The carbon atom is defined as chiral and can exist in one of two forms which have been classified variously as *R* or *S*, *D* or *L*, + or −, or *d* or *l* (exact definitions of these forms are given elsewhere [11]). These chiral centers have two possible configurations, either right or left handed, with the two different forms of the same molecule being known as 'enantiomers'. Enantiomers have exactly the same chemical activity except when they react with other chiral molecules. In that case significant increases in rates of reaction are often observed between different enantiomers, leading to enhancement in the products with one particular handedness – the so-called enantiomeric excess or e. e. of the reaction [12]. Enantiomers also show a further difference in that they rotate the plane of polarized light in different directions, a phenomenon that has been used in the study of reactions via techniques such as polarimetry, circular dichroism and optical rotatory dispersion [13]. The key point to note is that enantiomeric excess in chemical reactions can only be induced by the presence of other chiral molecules [13].

Field-induced enantiomeric excess was first investigated over 100 years ago by Pasteur [14]. Pasteur reasoned that as a magnetic field can cause optical rotation through the Faraday effect [15], the asymmetric influence of the field, he reasoned, was similar to that induced by chiral molecules. Hence the two phenomena were probably interrelated and an external magnetic field should be able to influence the enantiomeric excess in a reaction. However, despite intensive effort no proven link could be established. Indeed this link has caused some confusion even to today. The Faraday effect and optical rotation observed from a collection of chiral molecules are in fact different phenomena [16]. The quantum states for chiral rotation and the Faraday effect are fundamentally different. Chiral induction requires quantum states of mixed parity but definite reversibility, whereas the Faraday effect has states of definite parity but mixed reversibility [17].

In 1994 Eisenbraun et al. claimed that an external magnetic field of 1.2 T was sufficient to induce enantiomeric excesses of 98% and 67% in certain chemical reactions [18]. This remarkable result generated intense interest in the chemical community, as the control of enantiomeric excess in chemical reactions up to that time could only be invoked by the use of expensive chiral reagents. The result promised to revolutionize the synthesis of natural products in chemistry and lead to much faster production of important drugs. However, the enantiomeric excesses found in Eisenbraun's experiments could not be duplicated by other research groups [19, 20].

After careful detective work it was found that G. Zadel, one of the workers in the original experiment, was guilty of manipulating the results by adding chiral product to the reactions. Despite this case of scientific fraud, combined external electric and magnetic fields have been theoretically shown to produce a minimal chiral induction effect of the order of 10^{-5} [21]. Other reports, as yet unsubstantiated, have shown that chiral induction of the order of 1% can be obtained [22].

10.2.5 Electrodeposition

Far more obvious and measurable field effects have been reported in electrodeposited films. Coey has studied the effects of an external magnetic field on electrochemical metal deposition [23]. He found that a uniform magnetic field unexpectedly alters the form of copper deposits grown in a flat electrochemical cell (Fig. 3). The patterns of the electrodeposit change substantially in nature depending on the orientation of the cell and the external field. The electrodeposits can be categorized by their fractal dimension and apparent chirality. Coey's work builds on earlier reports that state that fields in the range of 1 T could influence the rate of deposition of a metal in simple redox reactions, although it should be noted that no mechanism had then (or since) been established [24, 25]. Speculation had focused on the hypothesis that the field alters ion concentration near an electrode surface or that convection currents were enhanced by the Lorentz force acting on charged species in solution.

Coey's work showed that the morphology of copper electrodeposits formed from CuSO_4 solution was critically dependent of field orientation (Fig. 3). In a flat cell radial growth of copper in zero field showed a dense growth pattern. When an applied magnetic field was applied perpendicular to the plain of the cell a branching spiraling pattern was observed. If the field direction was inverted the chirality of the electrodeposit was in exactly the reverse sense. If the magnetic field was applied parallel to the plane of the cell string-like deposits were noted. The experiments were repeated on a number of occasions and in every experiment the form of the electrodeposit was a function of the applied magnetic field.

The origin of this effect is thought to derive primarily from a field-dependence of the rate of transport of ions to the surface of the working electrode [25]. In the vicinity of the electrode the net current density associated with ion transport through the solution can be large enough so that the Lorentz force acting on it becomes comparable to the gravitational force, thereby providing a mechanism by which to influence convection.

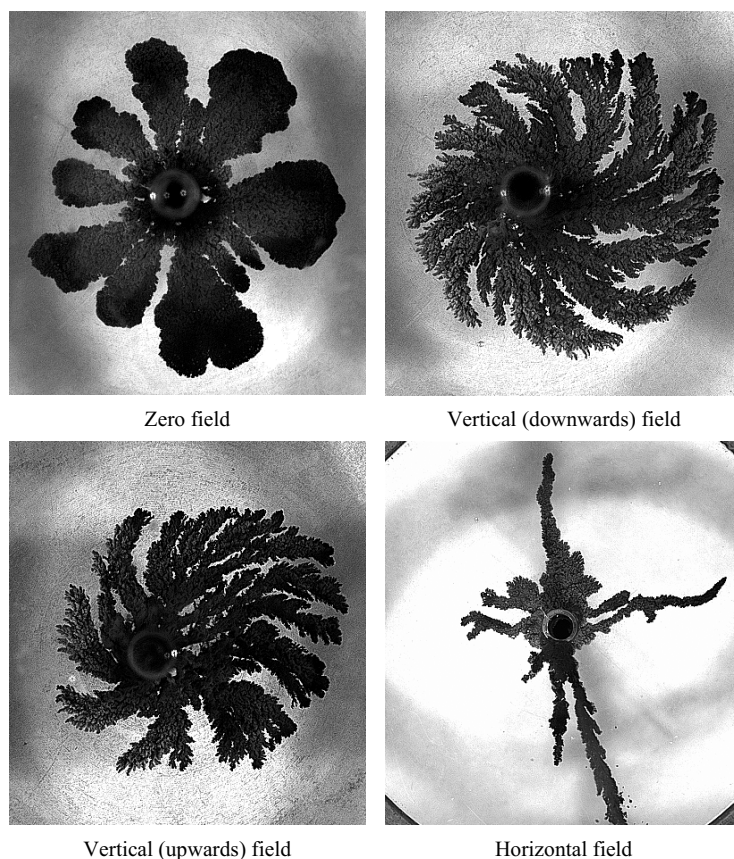


Fig. 3. Electrodeposited copper particles obtained in a horizontal cell, in zero field and in horizontal or vertical fields of 1 T.

10.3 Solid-phase Reactions

10.3.1 Self-propagating High-temperature Synthesis (SHS)

In the last few years there has been a major upsurge in research activity into the effect of magnetic fields on solid phase chemical reactions. This work has focused on a particular family of reactions – the ‘self-propagating high-temperature synthesis’ (SHS) reactions – all of which involve highly exothermic solid state combustion processes [26]. The best known examples are the thermite reaction that is used to weld railway tracks:



and the Goldsmidt reaction:

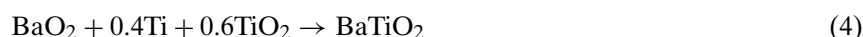


that is used commercially to produce chromium metal.

Commonly, SHS reactions use the elements or element oxides as the starting materials, with $M + E$ transforming to ME , where M is a metal or metal oxide and E is a non-metal. The reactions can be started by point source initiation, where a hot wire or filament is brought into contact with the green mixture, igniting the powder. A synthesis wave or thermal flash moves through the solid, promoting the reaction of successive layers of powder – as illustrated in Fig. 4. The synthesis wave is extremely hot (often more than 1200°C), is highly directional (away from the source of ignition), and has a uniform velocity.

Although the prototypical SHS reactions – the thermite and Goldsmidt reactions – have been known for over a hundred years, it was only in 1986 that the first report appeared of an SHS reaction performed in an applied magnetic field [27]. This study dealt with the SHS of titanium carbide, and reported an increased reaction rate and reaction temperature in the applied field. In 1994 a second paper was published, reporting similar enhanced reaction rates and temperatures in the synthesis of strontium hexaferrite $\text{SrFe}_{12}\text{O}_{19}$ [28]. Since then many reports have been published on SHS reactions in applied fields, especially with regard to the formation of ferrites [29–38], and a variety of different effects have been identified. These include observations of increased reaction temperature and propagation velocity; differences in phase compositions and microstructures in post-SHS products; and differences in structural and magnetic properties in post-annealing products, such as changes in coercivity, magnetization, Curie temperature, atomic site occupancy and site inversion, and cationic homogeneity.

An important feature of these reactions that has only recently come to light is that the passage of the wave induces an electrical pulse [39] and/or a small magnetic field [40], both of which are thought to be caused by the movement of ions and electrons at the molten reactant front. The latter ‘chemomagnetic fields’ have been observed in reactions involving both non-magnetic reactants and products, for example:



with a maximum field of 6.5 nT (at a point 10 mm from the reaction front) measured by SQUID magnetometry [40]. They have also been observed for reactions involving magnetic products, including the thermite reaction (Fig. 5), which gave a maximum field of 4.6 nT [40].

The fact that such electrical and magnetic phenomena can be attributed to the combustion wavefront itself is significant in that it gives a possible clue to the origins of the observed field effects. In this context we now review the published data that has been accumulated on applied field SHS reactions in the ferrite family of hard and soft magnets. In particular we focus on macroscopic effects evidenced by experiments conducted in large magnetic fields (of up to 20 T) and on short-lived structural effects evidenced by time-resolved X-ray diffraction experiments.

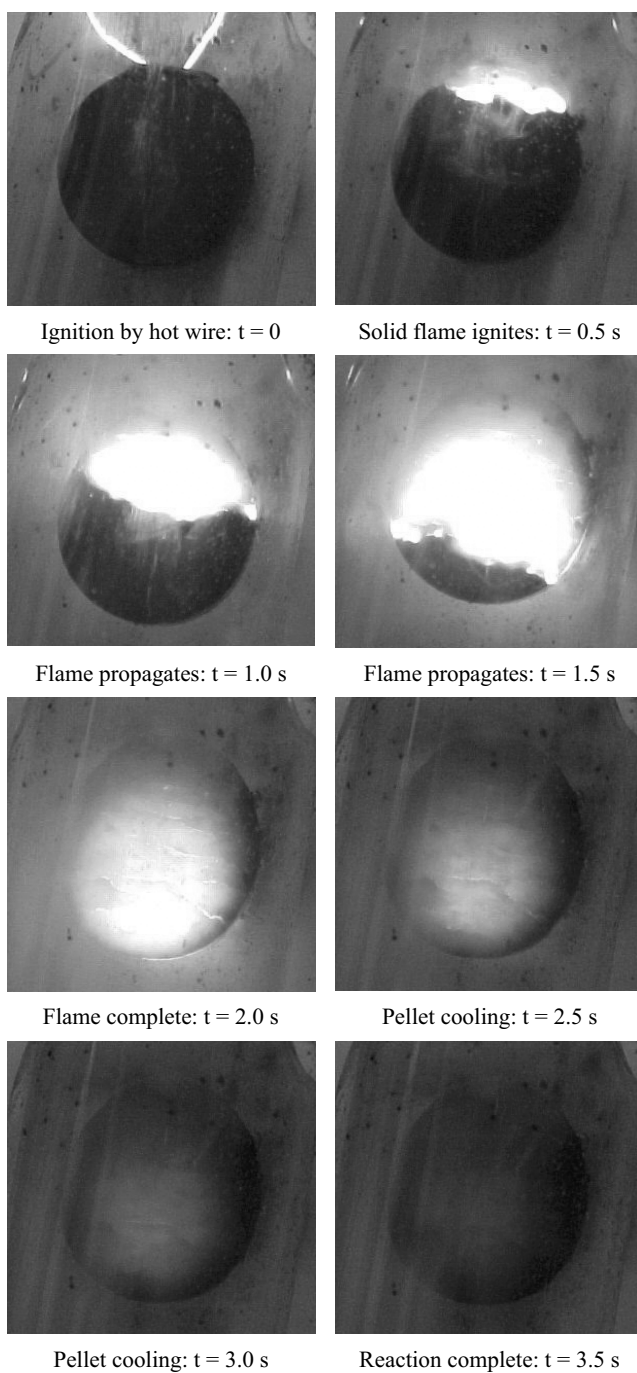


Fig. 4. Self-propagating synthesis wave moving through a 13-mm diameter pellet of MgO, ZnO, Fe, Fe₂O₃, and NaClO₄ under a flow of oxygen gas.

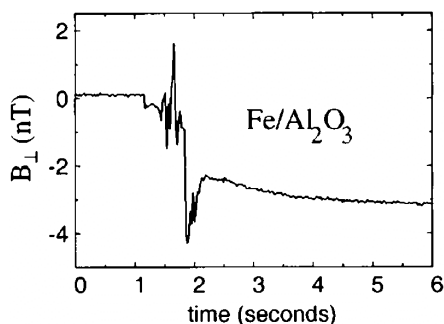
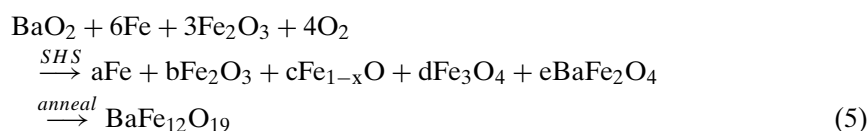


Fig. 5. Magnetic signal measured by means of a SQUID magnetometer placed 10 mm from the reaction wavefront of the SHS thermite reaction, $\text{Fe}_2\text{O}_3 + 2\text{Al} \rightarrow 2\text{Fe} + \text{Al}_2\text{O}_3$.

10.3.2 SHS Reactions in High Fields (1 to 20 T)

The effect of magnetic fields on the preparation via SHS of both hard and soft ferrite magnets was first explored in University College London in 1997. Ferrite production by SHS is a two-step process, illustrated below for the M-type ferrite $\text{BaFe}_{12}\text{O}_{19}$:



The first step is the SHS reaction step, which results in an intimately mixed product comprising a number of phases, sometimes including a small proportion of unreacted reagents. The second step is a grind-and-anneal step carried out at a relatively low temperature, typically ca. 1200°C, for a relatively short time, typically ca. 2 h, after which a single-phase product is obtained.

Comprehensive studies of the hard ferrites $\text{BaFe}_{12-x}\text{Cr}_x\text{O}_{19}$ [33, 34, 41] and the soft ferrites $\text{Li}_{0.5}\text{Fe}_{2.5-x}\text{Cr}_x\text{Fe}_2\text{O}_4$ [29, 34] and $\text{Mg}_{0.5}\text{Zn}_{0.5}\text{Fe}_{2-x}\text{Cr}_x\text{O}_4$ [30, 41] revealed that in a field of 1.1 T the SHS reactions proceeded faster and had higher combustion temperatures than the corresponding zero field reactions. The applied field also resulted in changes to the bulk magnetic properties of the ground and sintered end-products, compared to those made either by zero field SHS or ceramic methods. These changes included a 20% decrease in coercivity in $\text{BaFe}_{12}\text{O}_{19}$, and a magnetization increase of 15% in MgFe_2O_4 and 35% in $\text{Mg}_{0.5}\text{Zn}_{0.5}\text{Fe}_2\text{O}_4$ [30, 34]. Incorporating chromium into the samples modified these results, with the coercivity change in $\text{BaFe}_{12}\text{O}_{19}$ rising to almost 100% for $\text{BaFe}_{10}\text{Cr}_2\text{O}_{19}$ [34]. The unit cell volumes of the sintered end-products were also modified, with a 0.14% reduction in MgFe_2O_4 , a 0.75% reduction in LiFe_5O_8 , and a 0.22% expansion in $\text{BaFe}_{12}\text{O}_{19}$ [30, 34].

Subsequent experiments on SHS reactions of BaO_2 , Fe and Fe_2O_3 (Eq. 5) in fields of up to 20 T yielded further new results [37], including the observation of two macroscopically distinct parts in the post-SHS product, one having a shiny appearance, the other a matt appearance (Fig. 6). The amount of shiny phase formed

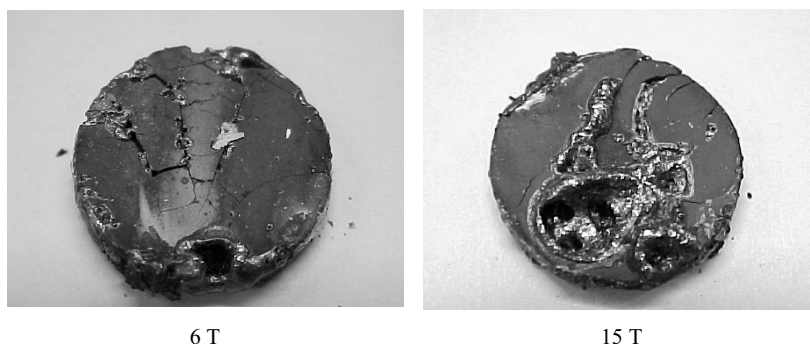


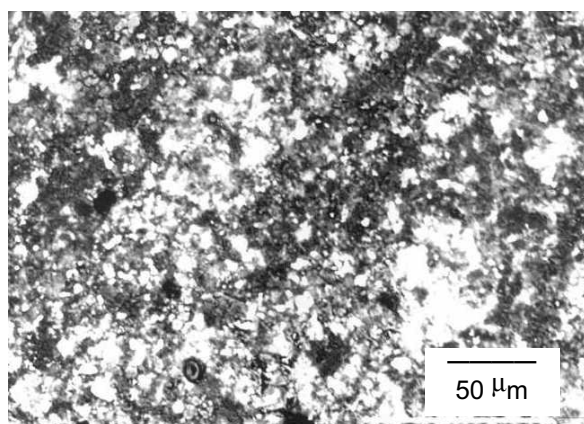
Fig. 6. The as-made products (17-mm diameter pellets) of SHS reaction of SrO_2 , Fe, and Fe_2O_3 in large, steady-state applied fields.

increased as the applied field strength increased. The shiny and matt parts had different phase compositions, microstructures and magnetic properties. The shiny parts were more fully combusted than the matt parts, with the latter having a greater proportion of unreacted starting mixture. This result shows that the applied field has a direct influence on the combustion process itself, and that higher fields promote more complete combustion – an observation that correlates with the observed hotter and faster nature of the SHS wave propagation. The microstructures of the shiny and matt parts were found to be significantly different, with the latter closely resembling that found in zero field reaction products (Fig. 7). Acicular grains of order $100\text{--}300\ \mu\text{m}$ long and $10\text{--}20\ \mu\text{m}$ wide appeared in the shiny parts only, while the matt parts had a random distribution of components. The acicular grains were deduced via electron probe analysis and X-ray diffraction to comprise fine scale mixtures of BaFe_2O_4 and Fe_3O_4 [35–37].

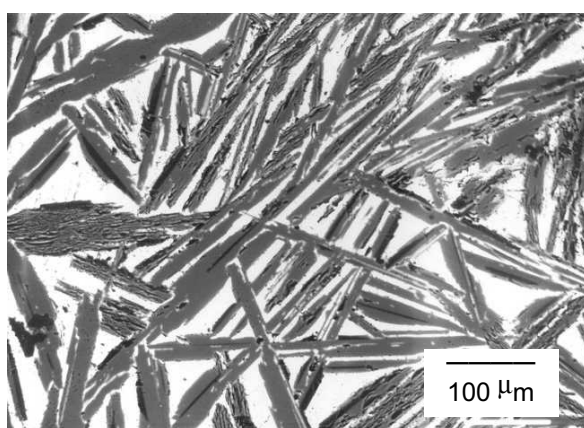
The structural properties of the monophasic $\text{BaFe}_{12}\text{O}_{19}$ samples obtained after annealing also showed a memory of the field applied during SHS. Differences were seen in lattice parameters, up to a maximum of an 0.5% reduction in cell volume $\text{BaFe}_{12}\text{O}_{19}$ annealed from the shiny part of the 15 T reaction [37].

10.3.3 Time-resolved X-ray Diffraction Studies

To better understand the effect of an applied field on the very rapid SHS reactions, it is desirable to obtain high quality, relevant data that can be obtained on the time-scale of a second or less. Research in the last five years in France and the US has shown that an excellent method for such a purpose is time-resolved X-ray diffraction (TRXRD) using synchrotron radiation. Experiments at LURE in Orsay on the formation of Al–Ni–Ti intermetallic compounds [42], and at Brookhaven on the reaction $\text{Ta} + \text{C} \rightarrow \text{TaC}$ [43], have shown kinetic features and intermediate phases that are only revealed given the 50–100 ms timing resolution possible with a synchrotron source.



Zero field



Applied field 1.1 T

Fig. 7. Electron microprobe compositional maps of the product of the SHS reaction of BaO_2 , Fe, and Fe_2O_3 under oxygen, in zero field and in a magnetic field of 1 T. Gray-scale mapping shows regions of higher iron content as darker features.

However, these experiments were performed in zero field. The first TRXRD experiments on applied field SHS reactions were performed by the UCL group in 1999 [35, 44]. TRXRD scans were recorded on both hard and soft ferrites, in zero field and in an applied field of 1.1 T, on time-scales down to 0.1 s measurement time, interspersed with data readout times of ca. 1.0 s. Very rapid structure and phase changes were observed (Fig. 8). In a series of experiments on $\text{BaFe}_{12}\text{O}_{19}$, LiFe_5O_8 and $\text{Mg}_{0.5}\text{Zn}_{0.5}\text{Fe}_2\text{O}_4$ first-step SHS reactions, intermediate phases were observed only in applied field reactions, and not in the corresponding zero field reactions. Attention was focused on the $\text{BaFe}_{12}\text{O}_{19}$ reaction, where Fe_3O_4 was seen in four of five cases to be a dominant transient intermediary (see Figure 8), while no intermediate phase at all was observed in any of eight different scans of the zero field

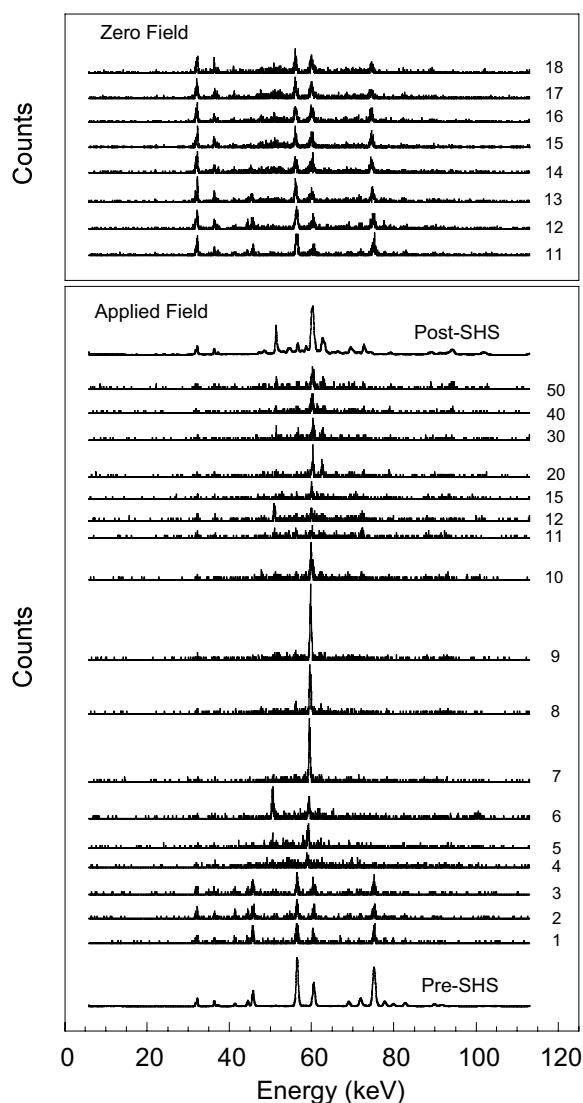


Fig. 8. Time-resolved X-ray powder diffraction patterns of the SHS reaction of BaO_2 , Fe, and Fe_2O_3 under an oxygen atmosphere and in a magnetic field of 1 T. Scans were each recorded for 0.25 s, with a read-out time of 1.25 s. Scan numbers are as noted on the figure.

reaction. The scans in Figure 8 show that at the onset of the SHS wave the diffraction pattern becomes diffuse (scan 4). A strong peak due to the (111) reflection for Fe_3O_4 dominates scans 7–10. After the passage of the combustion wavefront, the product cools and the X-ray patterns tend towards those of the post-SHS product (scan 20 and beyond).

These results show that the applied field is directly influencing the combustion reaction pathways themselves, and is not simply speeding up or enlarging the reaction wavefront.

10.3.4 Possible Field-dependent Reaction Mechanisms

There is as yet no consensus in the literature regarding the mechanism by which an applied magnetic field can influence the SHS combustion wave. There has been some speculation that there would be a field-induced rearrangement (alignment or texturing) of the powder reactants that could allow a more efficient surface-to-surface reaction pathway through the reactant mixture. However, this hypothesis fails to account for the high field experiments on pressed pellets, in which it would have been impossible for the reagents to move, and where field-dependent effects were still observed [37].

Another possibility is that the availability of oxygen is the determining aspect of the reaction, and that more oxygen brings hotter reaction temperatures. This view is supported by recent work on the $\text{BaFe}_{12}\text{O}_{19}$ reaction in air and in various oxygen-flow atmospheres (as well as in the presence of an internal oxidizing agent), where the more oxygen-rich reactions burned hotter and faster, went further to completion, and in some cases gave rise to the acicular microstructure previously seen only in applied field reactions [45]. However, this raises again the question of how the applied field can affect the flow of oxygen, or its availability, at the reaction wavefront – an aspect which intriguingly has echoes of the effect of fields on gaseous combustion discussed in Section 10.2.1.

A third possibility arises from the evidence [39, 40] that the SHS wavefront constitutes a moving electrical and magnetic pulse generated by the motion of charged and mobile ions at the high-temperature heart of the SHS wave. Given this, it may be reasonable to suppose that the applied field could directly influence the ions and their motion and/or energetics at the wavefront, thereby enhancing the combustion process. This, however, is a highly speculative suggestion, and one that requires further theoretical exploration. Nevertheless, it serves to illustrate that the mechanisms by which these applied field effects arise are still far from being well understood.

10.4 Conclusions

Recent progress in studies of the effect of applied magnetic fields on chemical reactions have uncovered a wealth of intriguing phenomena in three states of matter – gases, liquids and solids. In each case it is clear that our current understanding of the mechanisms and physical processes at work is still limited. Nevertheless it is equally clear that our ability to probe and measure these effects is improving and yielding increasingly valuable and relevant data. The prospects for future work in this area are positive, especially given that in many cases there are strong technological potentials waiting to be exploited in the use of applied magnetic fields to not just influence but also to control a wide range of chemical reactions.

References

- [1] Lawton, J.; Weinberg, F.J. *Electrical Aspects of Combustion*, Clarendon Press, Oxford, **1969**.
- [2] Faraday, M. *Phil. Mag.* **1847**, S3 210, 401.
- [3] Wakayama, N.I. *Combust. Flame* **1993**, 93, 207.
- [4] Wakayama, N.I.; Sugie, M. *Physica B* **1996**, 216, 403.
- [5] Iijima, S. *Nature* **1991**, 354, 56.
- [6] Hamada, N.; Sawanda, S.; Oshiyama, A. *Phys. Rev. Lett.* **1992**, 68, 1579.
- [7] Yokomichi, H.; Sakima, H.; Ichihara, M.; Sakai, F.; Itoh, K.; Kishimoto, N. *Appl. Phys. Lett.* **1999**, 74, 1827.
- [8] Steiner, V.E.; Ulrich, T. *Chem. Rev.* **1989**, 89, 51.
- [9] Grissom, C.B. *Chem. Rev.* **1995**, 95, 3.
- [10] Mason, S.F. *Chem. Soc. Rev.* **1988**, 17, 347.
- [11] Streitweiser, A.; Heathcock, C.H. *Introduction to Organic Chemistry*, 2nd edn, Macmillan, New York, **1981**.
- [12] Morrison, J.D.; Moshar, H.S. *Asymmetric Organic Reactions*, Prentice Hall, Englewood Cliffs, NJ, **1971**.
- [13] Jonas, J. *Chem. Pap.* **1997**, 51, 161.
- [14] Pasteur, L. *Rev. Sci.* **1884**, 7, 2.
- [15] Lord Kelvin *Baltimore Lectures*, C.J. Clay and Sons, London, **1904**.
- [16] Barron, L.D. *Molecular Light Scattering and Optical Activity*, Cambridge University Press, Cambridge, **1982**.
- [17] Avalos, M.; Babino, R.; Contas, P.; Jimenez, J.L.; Palacios, J.C.; Barron, L.D. *Chem. Rev.* **1998**, 98, 2391.
- [18] Zadel, G.; Eisenbraun, C.; Wolff, J.; Brietmaier, E. *Angew. Chem.* **1994**, 106, 460.
- [19] Feringa, B.L.; Kellogg, R.M.; Hulst, R.; Zondervan, C.; Kruizinger, W.H. *Angew. Chem. Int. Ed. Engl.* **1994**, 33 1458.
- [20] Kaupp, G.; Marquardt, T. *Angew. Chem. Int. Ed. Engl.* **1994**, 33, 1460.
- [21] Rhodes, W.; Dougherty, R.C. *J. Am. Chem. Soc.* **1978**, 100, 6247.
- [22] Gerike, P. *Naturwissenschaften* **1975**, 62, 38.
- [23] Coey, J.M.D.; Hinds, G.; Lyons, M.E.G. *Europhys. Lett.* **1999**, 47, 267.
- [24] Kelly, E. *J. Electrochem. Soc.* **1977**, 124, 987.
- [25] Hinds, G.; Coey, J.M.D.; Lyons, M.E.G. *J. Appl. Phys.* **1998**, 83, 6447.
- [26] Yi, H.C.; Moore, J.J. *J. Mater. Sci.* **1990**, 25, 1159.
- [27] Kiriyashkin, A.I.; Maksimov, Y.M.; Merzhanov, A.G. *Combust. Explos. Shock Waves* **1986**, 22, 700.
- [28] Komarov, A.V.; Morozov, Y.G.; Avakyan, P.B.; Nersesyan, M.D. *Int. J. SHS* **1994**, 3, 207.
- [29] Kuznetsov, M.V.; Pankhurst, Q.A.; Parkin, I.P. *J. Phys. D* **1998**, 31, 2886.
- [30] Kuznetsov, M.V.; Pankhurst, Q.A.; Parkin, I.P. *J. Mater. Chem.* **1998**, 8, 2701.
- [31] Cross, W.B.; Affleck, L.; Kuznetsov, M.V.; Parkin, I.P.; Pankhurst, Q.A. *J. Mater. Chem.* **1999**, 9, 2545.
- [32] Fernández Barquín, L.; Kuznetsov, M.V.; Morozov, Y.G.; Pankhurst, Q.A.; Parkin, I.P. *Int. J. Inorg. Mater.* **1999**, 1, 311.
- [33] Kuznetsov, M.V.; Fernández Barquín, L.; Pankhurst, Q.A.; Parkin, I.P. *J. Phys. D* **1999**, 32, 2590.
- [34] Parkin, I.P.; Kuznetsov, M.V.; Pankhurst, Q.A. *J. Mater. Chem.* **1999**, 9, 273.
- [35] Affleck, L.; Aguas, M.D.; Pankhurst, Q.A.; Parkin, I.P.; Steer, W.A. *Adv. Mater.* **2000**, 12, 1359.

- [36] Affleck, L.; Aguas, M.D.; Parkin, I.P.; Pankhurst, Q.A.; Kuznetsov, M.V. *J. Mater. Chem.* **2000**, *10*, 1925.
- [37] Aguas, M.D.; Affleck, L.; Parkin, I.P.; Kuznetsov, M.V.; Steer, W.A.; Pankhurst, Q.A.; Fernández Barquín, L.; Roberts, M.A.; Boamfa, M.I.; Perenbloom, J.A.A.J. *J. Mat. Chem. Commun.* **2000**, *10*, 235.
- [38] Kuznetsov, M.V.; Pankhurst, Q.A.; Parkin, I.P.; Affleck, L.; Morozov, Y.G. *J. Mater. Chem.* **2000**, *10*, 755.
- [39] Morozov, Y.G.; Kuznetsov, M.V.; Nersesyan, M.D.; Merzhanov, A.G. *Doklady Akademii Nauk SSSR* **1997**, *351*, 780.
- [40] Nersesyan, M.D.; Claycomb, J.R.; Ming, Q.; Miller, J.H.; Richardson, J.T.; Luss, D. *Appl. Phys. Lett.* **1999**, *75*, 1170.
- [41] Pankhurst, Q.A.; Parkin, I.P. *Mater. World* **1998**, *6*, 743.
- [42] Javel, J.F.; Dirand, M.; Nassik, F.Z.; Gachon, J.C. *J. de Physique IV* **1996**, *6*, C2 229.
- [43] Larson, E.M.; Wong, J.; Holt, J.B.; Waide, P.A.; Nutt, G.; Rupp, B.; Terminello, L.J. *J. Mater. Res.* **1993**, *8*, 1533.
- [44] Parkin, I.P.; Pankhurst, Q.A.; Affleck, L.; Aguas, M.D.; Kuznetsov, M.V. *J. Mater. Chem.* **2000**, *10*, 235.
- [45] Affleck, L.; Parkin, I.P.; Pankhurst, Q.A.; Aguas, M.D. *J. Mater. Chem.* **2000**, *10*, 1925.

Subject Index

- 1-D, *see* one-dimensional
2-D, *see* two-dimensional
- Anisotropy, 32, 34, 215–217
Antiferromagnetic coupling, 54, 60, 61, 88–89
Asymmetric synthesis, 470–471
- Bacterial magnetotaxis mechanism, 223–227
Bimetallic magnets, 1–37, 148–159
Biogenic magnets, 205–227
Blocking temperature, 243
- Calorimetry, 279–280, 300–302
Canted antiferromagnet, 258
Chemical reactions in applied magnetic fields, 467–479
Chirality, 10, 11
Co/Pt interfaces, 253
Coercivity, 13–14, 17, 18, 20, 21, 26, 30, 34
Compensation temperature, 18–20
Configuration interaction, 426–427
Copper nitroxide complexes, 41–62
 $\text{CuCl}_4(\text{C}_m\text{H}_{2m+1}\text{NH}_3)_2$, 260
- Density functional theory, 427–428, 442–444
Density matrix renormalization, 137–144
DFT, *see* Density functional theory
Diffraction, 280–281
Dimerized spin chains, 144–148
Dipolar hyperfine coupling, 448–449
Dipolar interaction, 89, 233–266
- Electrodeposition, 471–472
EPR, 284–285
 EuSO_4 , 238
EXAFS, 281–282
- Faraday effect, 470
[$\text{Fe}(\text{C}_5\text{Me}_5)_2$][TCNE], 89
[$\text{Fe}(\text{etz})_6$](BF_4)₂, 307, 309
 Fe_3O_4 , *see* Magnetite, 205
 Fe_3S_4 , *see* Greigite, 205
[$\text{Fe}(\text{2-pic})_3$] Cl_2 , 286, 287, 289, 296, 299, 305, 310–312
[$\text{Fe}(\text{Htrz})_2\text{trz}$](BF_4), 282
Fe Mössbauer spectroscopy, 195, 277, 279, 283, 313–330
[$\text{Fe}(\text{phen})_2(\text{NCS})_2$], 271, 277, 280, 282, 285, 286, 291, 294–295, 299, 314–316, 333
[$\text{Fe}(\text{ptz})_6$](BF_4)₂, 277–279, 284, 289, 308, 312, 320
Ferrimagnetic spin chains, 148–159
Ferromagnetic coupling, 45–46, 54, 59, 61, 88–89, 234
Ferromagnetic films, 247
- Greigite, 205, 208–210, 218, 219
Grids, structures, 174–188
g-Tensors, 366, 369–370, 377–378, 396, 402, 405, 406, 408, 411–414, 415–417, 435–422
- Haldane chains, 129
Hamiltonian spin, 345–456
Hamiltonian, 188–191, 193, 195, 196, 199
Hamiltonian, spin, 119–168, 345–456
Hamiltonians, effective, 361–363
Hartee-Fock theory, 424–426
Heisenberg chains, 129
Heptacyanomolybdenum-based magnets, 31–37
HFC, *see* Hyperfine coupling
High-temperature synthesis, 472–476
Hyperfine coupling, 346, 352, 369, 378–380, 397–399, 400–403, 407–411, 418–420, 444–447, 449–451

- Hysteresis, 20, 49, 56
- Interlocked two-dimensional lattice, 17
- Interpenetrated two-dimensional nitronyl nitroxide, 12–14, 17–20
- Ising model, 120
- Jahn-Teller effect, 44–45, 61
- Ladder and honeycomb lattices, 14–17
- Layered magnet, *see* Two-dimensional magnet,
- LISSST, 306–310
- Ligand field theory, 380–414
- Light-induced magnetism, 36, 37
- Light-induced spin change, 326–331
- $M_2(OH)_3A$ ($M = Co, Cu$), 259–261
- Magnetic dots, 252–255
- Magnetic grids, 173, 188–200
- Magnetic ordering, dipolar, 234–243
- Magnetic quantum tunneling, 242
- Magnetic susceptibility measurements, 274–275
- Magnetic wires, 250–252
- Magnetite, 205–227
- Magneto-crystalline anisotropy, 234
- Magneto-structural correlations, 102–112
- Magnetotactic bacteria, 205–227
- Magnets, low dimensional, 255–261
- McConnell-I mechanism, 89–94
- McConnell-II mechanism, 89
- Mean field theory, 18, 235–238
- Mean-field model, *see* Mean field theory
- Mechanisms of exchange coupling, 3, 4
- Metal hexafluoroacetylacetonates, 46–62
- Metal nitroxide complexes, 43–62
- Micromagnetism, 220
- Mn_{12} cluster, *see*
 $Mn_{12}O_{12}(OAc)_{16}(H_2O)_4$
 $[Mn(CN)_7]^{4-}$, *see*
 heptacyanomolybdenum-based
 magnets
- $Mn_{12}O_{12}(OAc)_{16}(H_2O)_4$, 125–127, 242
- $[MnTPP][TCNE]$, 286–289
- $MnCu(pba)(H_2O)_3 \cdot 2H_2O$, 8
- $Mn(hfac)_2NITR$, 256
- Molecular field theory, *see* mean field theory
- Mössbauer spectroscopy,
see Fe Mössbauer spectroscopy
- $[NMe_4][MnCl_3]$, 256
- Nanotube and fullerene synthesis, 468–469
- Negative magnetization, 20
- Nitronyl nitroxide, 65–112
 – electronic structure, 68–89
 – spin distribution, 78–87
- Nitrophenyl nitronyl nitroxide, 66
- Nitroxides, 42–43
- NMR, 284–295
- NPNN, *see* Nitrophenyl nitronyl nitroxide
- Nuclear resonant scattering, 283–284
- One-dimensional magnets, 7–9, 20–26
- Optical spectroscopy, 275–276, 306–310
- Orthogonal orbitals, 45
- Oxalate based magnetic materials, 28–31
- Oxamato-based magnetic materials, 2–31
- Peierls distortion, 144
- Photo-induced magnets, 36, 37
- Photo-induced spin change, 326–331
- Photo-induced magnets, *see*
 Light-induced magnets
- Photo-induced spin change, *see*
 Light-induced spin change
- Positron-annihilation spectroscopy, 282–283
- Rare earth ions, 14–17
- Relativistic methods, 432–433
- Rhombic lattice, 244–246, 249–250
- $Ru(acac)_2(CN)_2$, 31
- Second-row metal based magnets, 28–35
- Single molecule magnet, 125–129, 242
- Single-domain, 211–212
- Spin chains, 129–137
- Spin clusters, 125–129
- Spin crossover, *see* spin transition, 271
- Spin density, *see* spin distribution
- Spin distribution, 8, 26–28, 31, 33, 78–87
- Spin Hamiltonian, *see* Hamiltonian, spin
- Spin polarization, 444–447
- Spin rotator state, 245
- Spin rotators, 244

- Spin transition, 46–62, 271–333
– theory, 292–298, 303–306
Spin-ladder, 160–167
Spin-orbit coupling, 357–359, 374–375,
456–458
Square and honeycomb lattice, 243–244
Superexchange, 88–89
Superparamagnetic, 211–212, 241
Synchrotron radiation, 283–284
- Thermochromism, 275–276
Third-row metal based magnets, 31, 35,
37
Through-space coupling, 89, 94–102
- Two-dimensional layered magnets, 9–17
Two-dimensional magnet, 24
- Vibrational spectroscopy, 271, 276–277
- X-Ray absorption spectroscopy, 228–282
XY chain, 144
XY model, 120
- Zeeman, 351, 355–256
Zero field splitting, 194, 195, 276–277,
295, 346, 350–351, 363–366, 406–409,
420–423, 433–434
ZFS, *see* Zero-field splitting